Research Topics

Optimal design and efficiency improvement of fluid machinery and systems

Edited by
Leilei Ji, Ramesh K. Agarwal, Kan Kan, Yongfei Yang,
Ran Tao, Yang Yang and Alexandre Presas

Published in
Frontiers in Energy Research

ISSN 1664-8714
ISBN 978-2-8325-3001-6
DOI 10.3389/978-2-8325-3001-6

About Frontiers

Frontiers is more than just an open access publisher of scholarly articles: it is a pioneering approach to the world of academia, radically improving the way scholarly research is managed. The grand vision of Frontiers is a world where all people have an equal opportunity to seek, share and generate knowledge. Frontiers provides immediate and permanent online open access to all its publications, but this alone is not enough to realize our grand goals.

Frontiers journal series

The Frontiers journal series is a multi-tier and interdisciplinary set of open-access, online journals, promising a paradigm shift from the current review, selection and dissemination processes in academic publishing. All Frontiers journals are driven by researchers for researchers; therefore, they constitute a service to the scholarly community. At the same time, the *Frontiers journal series* operates on a revolutionary invention, the tiered publishing system, initially addressing specific communities of scholars, and gradually climbing up to broader public understanding, thus serving the interests of the lay society, too.

Dedication to quality

Each Frontiers article is a landmark of the highest quality, thanks to genuinely collaborative interactions between authors and review editors, who include some of the world's best academicians. Research must be certified by peers before entering a stream of knowledge that may eventually reach the public - and shape society; therefore, Frontiers only applies the most rigorous and unbiased reviews. Frontiers revolutionizes research publishing by freely delivering the most outstanding research, evaluated with no bias from both the academic and social point of view. By applying the most advanced information technologies, Frontiers is catapulting scholarly publishing into a new generation.

What are Frontiers Research Topics?

Frontiers Research Topics are very popular trademarks of the *Frontiers journals series*: they are collections of at least ten articles, all centered on a particular subject. With their unique mix of varied contributions from Original Research to Review Articles, Frontiers Research Topics unify the most influential researchers, the latest key findings and historical advances in a hot research area.

Find out more on how to host your own Frontiers Research Topic or contribute to one as an author by contacting the Frontiers editorial office: frontiersin.org/about/contact

Optimal design and efficiency improvement of fluid machinery and systems

Topic editors
Leilei Ji — Jiangsu University, China
Ramesh K. Agarwal — Washington University in St. Louis, United States
Kan Kan — College of Energy and Electrical Engineering, China
Yongfei Yang — Nantong University, China
Ran Tao — China Agricultural University, China
Yang Yang — Yangzhou University, China
Alexandre Presas — Universitat Politecnica de Catalunya, Spain

Citation
Ji, L., Agarwal, R. K., Kan, K., Yang, Y., Tao, R., Yang, Y., Presas, A., eds. (2023).
Optimal design and efficiency improvement of fluid machinery and systems.
Lausanne: Frontiers Media SA. doi: 10.3389/978-2-8325-3001-6

Table of contents

Frontiers in Energy Research

TYPE Editorial
PUBLISHED 30 June 2023
DOI 10.3389/fenrg.2023.1238721

Editorial: Optimal design and efficiency improvement of fluid machinery and systems

Leilei Ji[1], Ramesh K. Agarwal[2], Kan Kan[3], Ran Tao[4], Yang Yang[5]* and Alexandre Presas[6]

[1]National Research Center of Pumps, Jiangsu University, Zhenjiang, China, [2]Department of Mechanical Engineering and Materials Science, Washington University in St. Louis, St. Louis, United States, [3]College of Energy and Electrical Engineering, Hohai University, Nanjing, China, [4]College of Water Resources and Civil Engineering, China Agricultural University, Beijing, China, [5]College of Hydraulic Science and Engineering, Yangzhou University, Yangzhou, China, [6]Centre of Industrial Diagnostics and Fluid Dynamics (CDIF), Universitat Politècnica Catalunya (UPC), Barcelona, Spain

OPEN ACCESS

EDITED AND REVIEWED BY
Ellen B. Stechel,
Arizona State University, United States

*CORRESPONDENCE
Yang Yang,
✉ yang_yang@yzu.edu.cn

RECEIVED 12 June 2023
ACCEPTED 23 June 2023
PUBLISHED 30 June 2023

CITATION
Ji L, Agarwal RK, Kan K, Tao R, Yang Y and Presas A (2023), Editorial: Optimal design and efficiency improvement of fluid machinery and systems.
Front. Energy Res. 11:1238721.
doi: 10.3389/fenrg.2023.1238721

KEYWORDS

fluid machinery and system, design and optimization, efficiency improvement, unsteady flow, computational fluid dynamics

Editorial on the Research Topic
Optimal design and efficiency improvement of fluid machinery and systems

Introduction

Fluid machinery plays a pivotal role in facilitating human development by encompassing vital equipment such as water turbines, wind turbines, pumps, torque converters, and low-pressure fans. However, despite its extensive applications, practical engineering encounters several challenges, including suboptimal equipment efficiency, unstable operation, and system discrepancies. The introduction of concepts such as "carbon peak" and "carbon neutrality" has further underscored the significance of high-efficiency fluid machinery in energy conservation and carbon reduction efforts. As a result, the advancement of fluid machinery technology has garnered substantial global attention and emerged as a crucial research area in the realm of energy-saving and carbon reduction. This Research Topic specifically focuses on the design and optimization of fluid machinery and its associated systems, employing experimental and numerical calculation methods to enhance operational efficiency, safety, and economic benefits. Notably, following a rigorous peer-to-peer review process, 17 articles have been accepted for inclusion in this Research Topic, which encompass the following categories.

Optimization of geometric structure or system of fluid machinery

Qi et al. conducted an optimization study on centrifugal pumps to enhance theirperformance. They combined entropy generation theory with particle swarm optimization to compare and analyze the energy losses between the original and optimized models. As a result, the pump efficiency increased by 3.89%. The optimization method employed in this research offers valuable support to the theory of centrifugal pump optimization. In order to improve the operational optimization of water pump production models, Xu et al. compared various indicators, including inventory, productivity, and delivery rate of water pumps, among traditional make-to-order (MTO) model, make-to-stock (MTS) model, and MTO and MTS model. Following a comprehensive evaluation, the MTO and MTS production model was determined as the most favorable choice for pumps. Sun et al. acknowledged the significant changes in the geometric characteristics of leading edge erosion on wind airfoils. They explored the impact of different blade shapes on the aerodynamic performance of NACA series airfoils under various working conditions. The results indicated that an optimal blade thickness range exists when considering leading edge erosion. Tian et al. conducted a study on the optimal design of submersible mixers using the coupled CFD-DEM method within the Euler-Lagrange framework. They examined the solid-liquid two-phase flow field of submersible mixers installed at different heights and analyzed the motion characteristics of particles, the extent of mixing, and the reasons for aggregation. The article demonstrated that adjusting the installation position of submersible mixers can enhance their energy utilization efficiency. Furthermore, Tian et al. utilized installation position parameters as design variables and performed a multi-objective optimized design using the Non-dominated Sorting Genetic Algorithm (NSGA-II). The results revealed an improvement of approximately 0.47% in mixing efficiency compared to pre-optimization values. To address the limitation of using a single type of parameter as the design parameter, Chen et al. selected a typical mixed-flow pump as the research subject and improved its efficiency using the Taguchi method. Their aim was to overcome the decrease in the optimization upper limit. Cheng et al. investigated the internal flow and rotor force characteristics of Canned Motor Pumps (CMP) under different radial clearances of front or back wear-rings and varying volute partitions. They discovered that adding a clapboard to the volute can enhance the balance of the radial force, providing a theoretical basis and reference for the hydraulic optimization of CMP.

Internal flow mechanism and energy loss analysis of fluid machinery

Lv et al. conducted a numerical analysis of the internal flow and pressure pulsation characteristics of a submersible tubular electric pump device. The validity of the numerical simulation was confirmed through physical model testing. Their findings indicate that the impeller of the submersible tubular electric pump is primarily responsible for the inlet pressure pulsation of the impeller. Guo et al. investigated the fluid movement law, energy transfer, and loss mechanism in the impeller of an axial flow pump. They successfully identified the main cause of hydraulic losses in the impeller flow passage. This research provides valuable insights into understanding the flow field structure within the impeller of the axial flow pump. Liu et al. (Liu et al., 2023) studied the flow characteristics and evolution of vorticity force in liquid nitrogen cavitation flow using a two-phase flow model and an improved thermal cavitation model. Their research reveals the internal flow mechanism of fluid machinery and offers theoretical guidance for the design of such machinery. Tian et al. examined the internal flow characteristics of low-head bulb perfusion pumps and analyzed the entropy production of essential components. They discovered that the water entropy production head decreases gradually and then increases, with the ratio of entropy production at the impeller to total entropy production being the largest. Xu et al. presented an adaptive mesh refinement technique for simulating compressible flows. This technique effectively refines the mesh in regions containing shock waves and vortices. Numerical results demonstrate that the proposed technique successfully captures shock waves and vortices, leading to improved solution accuracy.

Flow control technology and other techniques of fluid machinery

Hong et al. introduced a two-dimensional vortex model to gain insights into the characteristics of shedding vortices in a blade-divergent passage. They proposed a negative circulation unsteady flow control technique as a means to compensate for the viscous effect. The study revealed that this technique is more efficient than conventional flow control methods in mitigating shedding vortex strength. Xu et al. developed an electro-hydraulic composite drive winch and energy recovery system for mobile cranes. Based on electric construction machinery equipped with high-pressure energy-density electric energy storage units, this system incorporates a control strategy to ensure high torque output even at near-zero speeds. Li et al. presented a flywheel-based boom energy regeneration system for hydraulic excavators (HEs) utilizing load sensing systems. In a typical digging and dumping cycle, the energy-saving rate achieved with this system is approximately 32.7% higher compared to conventional load-sensing systems. This method holds promise for the development of energy-efficient HEs. To enhance the uniformity of water distribution under low pressure conditions, Qureshi et al. introduced the aeration jet method for the design of an aeration impact sprinkler. They also presented the structural details of the aeration impact sprinkler. The study demonstrated the feasibility of this method in reducing the operational pressure of sprinklers and improving water uniformity coefficient. Considering the insufficient accuracy of existing cavitation fault feature identification, (Chen et al., 2023) constructed a cavitation state recognition model. By combining current and vibration signals and leveraging information fusion theory, this model aims to improve the recognition rate of cavitation states and enhance anti-interference performance.

In summary, this Research Topic encompasses a wide range of research articles focused on the optimal design and efficiency improvement of fluid machinery and systems. The published articles delve into various aspects of this field, exploring innovative approaches and methodologies. Notably, there is a growing trend towards integrating advanced technologies such as the Internet of Things (IoT) and next-generation communication technologies to enhance the performance and intelligence of fluid machinery. By highlighting these advancements, this Research Topic aims to enrich people's understanding of fluid machinery and elevate its application level across diverse fields. The knowledge shared through this Research Topic of articles will contribute to the continuous improvement and evolution of fluid machinery, driving innovation and progress in various industries. Ultimately, the goal is to optimize the performance, efficiency, and intelligence of fluid machinery, enabling its widespread application and benefiting society as a whole.

Author contributions

All authors listed have made a substantial, direct, and intellectual contribution to the work and approved it for publication.

Funding

LJ was supported by the China Postdoctoral Science Foundation (No.2022TQ0127). YY was supported by the Natural Science Foundation of Jiangsu Province (No. BK20220587).

Conflict of interest

The authors declare that the research was conducted in the absence of any commercial or financial relationships that could be construed as a potential conflict of interest.

Publisher's note

References

Chen, L., Yan, H., Xie, T., Li, Z., Zhou, C., and Zhang, D. (2023b). Geostatistical analysis of the spatial variation of *Chrysolina aeruginosa* larvae at different stages in desert ecosystems. *Front. Energy Res.* 11, 379. doi:10.3390/insects14040379

Frontiers in Energy Research

TYPE Original Research
PUBLISHED 04 January 2023
DOI 10.3389/fenrg.2022.1107524

EDITED BY
Yang Yang,
Yangzhou University, China

REVIEWED BY
Daoxing Ye,
Xihua University, China
Yibin Li,
Lanzhou University of Technology,
China
Fei Tian,
Jiangsu University, China

*CORRESPONDENCE
Jinjing Sun,
✉ sunjinjing0916@163.com

SPECIALTY SECTION
This article was submitted to Process and Energy Systems Engineering, a section of the journal Frontiers in Energy Research

RECEIVED 25 November 2022
ACCEPTED 13 December 2022
PUBLISHED 04 January 2023

CITATION
Sun J, Zhang S, Cao P and Qi L (2023), Influence of blade maximum thickness on airfoil performance with varied leading edge erosion rate.
Front. Energy Res. 10:1107524.
doi: 10.3389/fenrg.2022.1107524

Influence of blade maximum thickness on airfoil performance with varied leading edge erosion rate

Jinjing Sun*, Shuhan Zhang, Peiyu Cao and Linze Qi

University of Shanghai for Science and Technology, Shanghai, China

In this study, the effect of different blade shapes on the aerodynamic performance of NACA series airfoils under a wide variety of working conditions at Reynolds number Re = 700,000 was explored. The SST k-ω turbulence model was used for the CFD method to investigate the effect of leading edge erosion on the aerodynamic performance of NACA series airfoils. The results indicated that an optimal thickness range of the blade exists considering the leading edge erosion. If the airfoil was too thin or too thick, the leading edge erosion increased, and the aerodynamic performance was significantly reduced. However, the aerodynamic performance will not decrease greatly when the thickness was moderate, even if the leading edge erosion increased. For the same airfoil, the less the leading edge erosion, the better its aerodynamic performance will be. When the erosion degree (depth) of the leading edge airfoil was small, the variation of the erosion size would significantly affect the aerodynamic performance of the airfoil. When the erosion size of the leading edge increases to a certain extent, the performance of the blade decreases greatly compared with the original cases, but the sensitivity of the erosion blade performance to the change of the leading edge erosion size decreases.

KEYWORDS

leading edge erosion, wind turbine, airfoil, thickness, aerodynamic performance

1 Introduction

The burning of fossil fuels has caused considerable greenhouse gas (GHGs) emissions. In 2016, the greenhouse gas emissions attributed to fossil fuels accounted for 73.2% of the 49.4 billion tons of CO_2 equivalent greenhouse gas emissions worldwide (Ritchie and Roser, 2017). Greenhouse gas emissions will further increase the greenhouse effect, thus causing climate change disasters [e.g., global warming and extreme weather (Hussain et al., 2020)]. From the global perspective, people are shifting their focus from fossil fuel-based energy sources to cleaner sources [e.g., solar, wind, geothermal and biomass (Eshiemogie et al., 2022)]. Compared with other energy sources (Chien et al., 2021), wind energy is one of the most promising clean energy sources since it is sustainable and cost-effective.

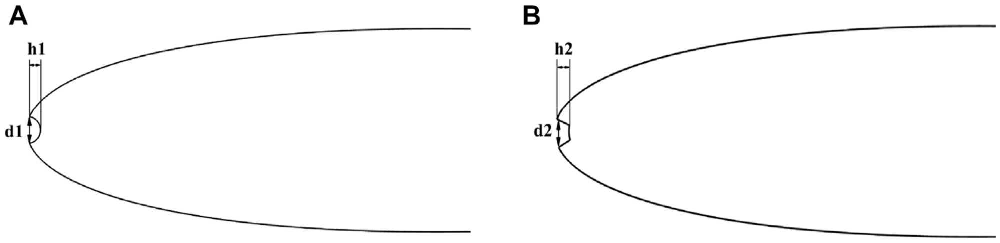

FIGURE 1
Two erosion shape applied on airfoil leading edge. (**(A)**: Semi-circleerosion; **(B)**: Square erosion).

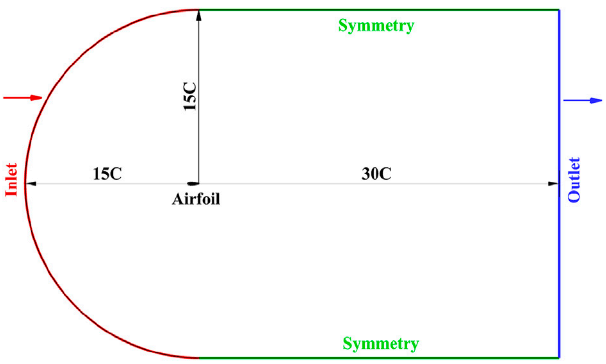

FIGURE 2
Fluid domain of the airfoil.

In the actual installation environment, the working position of wind turbines is often arranged in northwest wind resources (e.g., sandstorm and coastal typhoon frequency areas). The above areas are characterized by dust caused by drought (Dong et al., 2019; Wang et al., 2021), hailstones washed away by extreme weather (Mishnaevsky et al., 2021), rain generated by Pacific current on the sea surface, wave corrosion caused by lunar attraction (Elhadi Ibrahim and Medraj, 2019; Doagou-Rad et al., 2020). All these factors will cause irreversible erosion on the leading edge of the wind turbine blade, thus seriously affecting the aerodynamic performance of the blade and resulting in the increase of wind turbine power loss (Wang et al., 2017; Cappugi et al., 2021; Manatbayev et al., 2021).

At present, many scholars worldwide have studied the effect of the generation, development and erosion of the leading edge on the aerodynamic performance of the wind turbine (Khalfallah and Koliub, 2007). investigated the mechanism of dust and accumulation of the wind turbine blades, and examined the effect of the operation cycle of the wind turbine on the surface roughness of the blades. By examining the power performance of the leading edge of a 1.5 MW wind turbine blade to varying degrees of pollution or erosion Vestas (Spruce, 2006) has suggested that high levels of pollution and erosion are capable of reducing annual electricity generation (AEP) by 10%–13% (Keegan et al., 2012; Keegan et al., 2013). established the dynamic model of rain and hail using the display dynamics module in ANSYS and then simulated the hail on the airfoil leading impact process using SPH method. The result has suggested that hailstones and impacts on wind turbine blades are continuous and will cause erosion and deformation on wind turbine blades during long-term operation in rainy conditions (Han et al., 2018). has suggested that the leaf lift and resistance coefficients decrease and increase by 53% and 314%, depending on the severity of the contamination and leading edge erosion conditions, respectively.

There are three major changes in the geometric characteristics of the leading edge erosion of wind airfoil (Sareen et al., 2014). The surface of the wind airfoil is erosion, and when the erosion depth reaches 0.51 mm, a sand hole is generated. The sand hole continues to expand into smaller pits of higher size. When the depth is 2.54 mm, it can be considered as a small pit. The small pit develops into local peeling and becomes delamination, which can be considered as delamination when the depth is 3.81 mm (Li et al., 2017). modified the leading edge of DU 96-W-180 wind airfoil. The leading edge of the erosion airfoil primarily comprises sand holes, small pits, and grooves. When the angle of attack is 10.3°, the lift-drag ratio of erosion airfoil of sand holes and small pits is reduced by nearly 10% compared with the value of smooth airfoil, and the lift-drag ratio of trench erosion airfoil decreases by nearly 60% compared with the value of smooth airfoil (Papi et al., 2020). built a 2-dimensional FFAW3-241 airfoil erosion model to investigate different modeling stratification methods (stratification depth and leaf head cover area), reducing the lift-drag ratio by 57.74% at Re = $1.85*10^6$ with a stratification depth of 5 (Wang et al., 2016). mainly studied the rectangular erosion at the leading edge of S809 airfoil. The erosion depths of the airfoil with erosion thickness of 12%*t*, 18%*t* and 25%*t* reached 1.0%*c*, 2.0%*c*, and 3.0%*c*, respectively, and the corresponding relative reduction values of lift-drag ratio were obtained as 48.08%, 64.56%, and 77.53%, respectively. In this study, the effect of different leading edge erosion degree on the maximum thickness of different blade airfoil performance was investigated based on two leading edge erosion forms using the CFD method, which can guide wind turbine airfoil design and erosion blade performance evaluation.

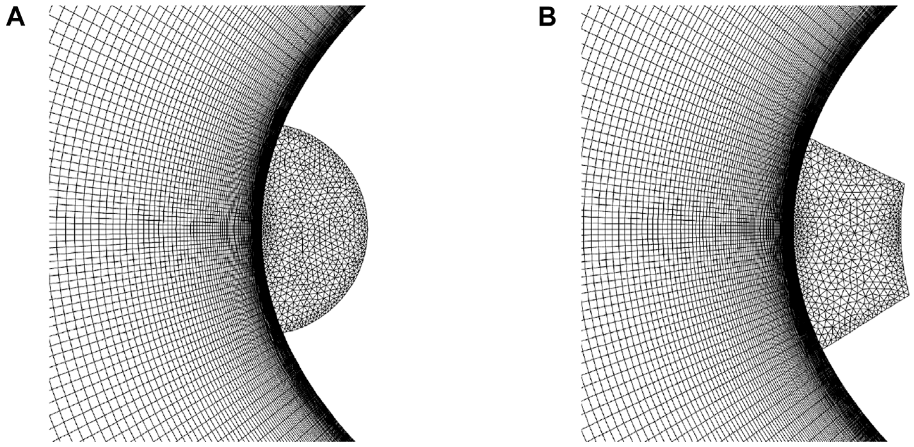

FIGURE 3
Local mesh amplification of the leading edge of the airfoil. (**(A)**: Semi-circle erosion; **(B)**: Square erosion).

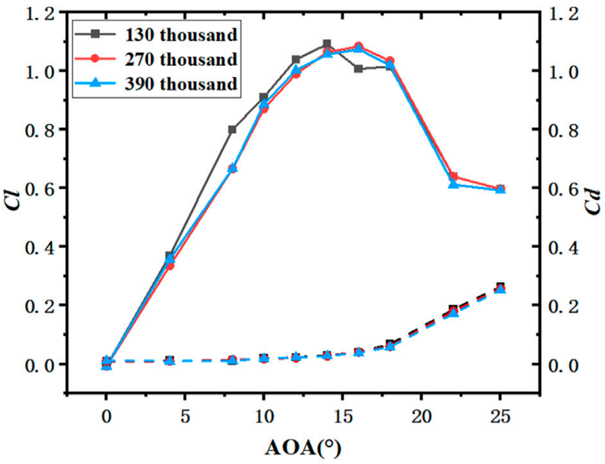

FIGURE 4
Lift-drag coefficient for different mesh quantities of the NACA0021 airfoil.

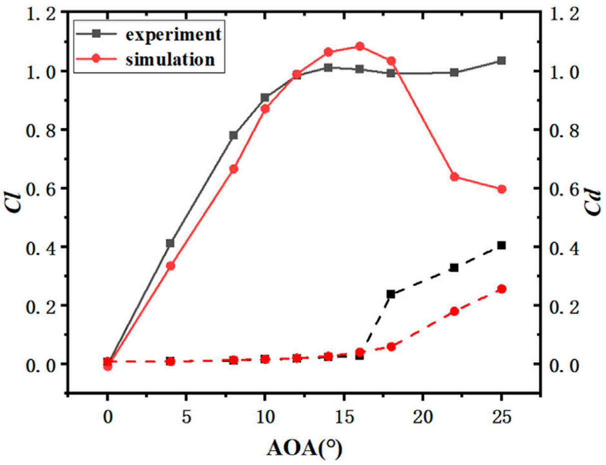

FIGURE 5
Comparing NACA0021 simulation data and experimental data.

2 Numerical method

2.1 Erosion model

In this study, the aerodynamic performance of NACA airfoil was primarily explored at different erosion depths (Sapre, 2012). highlighted that the chord depth of erosion is up to 13% of the chord length. For the airfoil, three degree of erosion depth were studied, with h_1 of 0.3%c, 0.5%c, and 1%c, and erosion thickness $d_1 = 2h_1$ (Gharali and Johnson, 2012). examined the amount of wind turbine blade wear after years of operation and have suggested that the maximum erosion thickness can account for 23% of the maximum airfoil thickness when the entire leading edge of the blade is largely eroded by erosion. In the study by Sareen et al. (2014), as derived from the blade erosion provided by 3 M, the deformation ratio of airfoil suction surface and pressure surface is nearly 1:1.3. Accordingly, for the square erosion setting on the leading edge of airfoil presented in Figure 1B, the erosion depth h_2 was 0.3%c, 0.5%c, 1%c, and the erosion thickness $d_2 = 13\%t$ (t is the maximum thickness of airfoil, the erosion thickness on the suction and pressure surfaces of the airfoil is 1: 1.3).

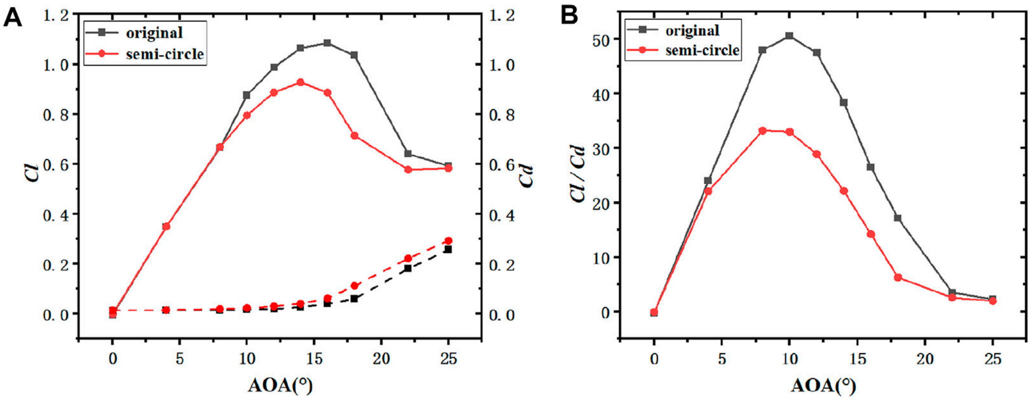

FIGURE 6
NACA0021 aerodynamic characteristic curve comparison diagram of the original airfoil with the leading edge semi-circular erosion airfoil (h_1 = 0.5%c). ((**A**): Lift and drag coefficient; (**B**): Lift-drag ratio coefficient).

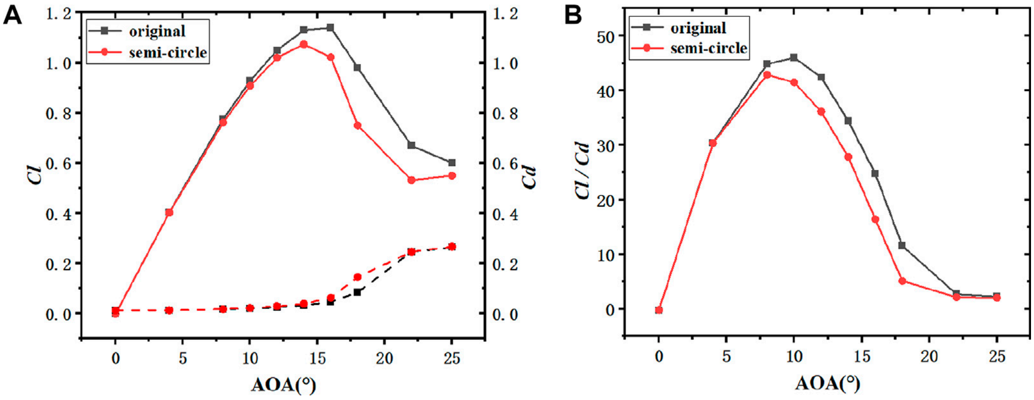

FIGURE 7
NACA0018 aerodynamic characteristic comparison curve of the original airfoil and the leading edge semi-circular erosion airfoil (h_1 = 0.5%c). ((**A**): Lift and drag coefficient; (**B**): Lift-drag ratio coefficient).

2.2 Computing domain and grid division

The airfoil calculation domain is presented in Figure 3 as an overall C shape, with a semi-circular inlet 15 times the chord length from the leading edge as well as an exit 30 times the chord length from the caudal edge of the blade. The vertical distance of the upper and lower boundaries from the blade was 15 times the chord length. The inlet was set as velocity inlet, and the outlet was set as pressure outlet. As depicted in Figures 2, 3, the calculation domain was filled with structural grid and with the unstructured grid filled in the erosion part. The grid near the airfoil surface was encrypted to conform to the $y^{+} < 1$ requirements in the turbulence model. Furthermore, the Reynolds number was taken as Re = 700,000.

2.3 Turbulence model

The selection of turbulence model significantly affects the calculation, verification and evaluation of airfoil performance. For the region close to the wall, the k-ε model with low Reynolds numbers cannot be taken. Thus, the k-ω model was built by combining considerable

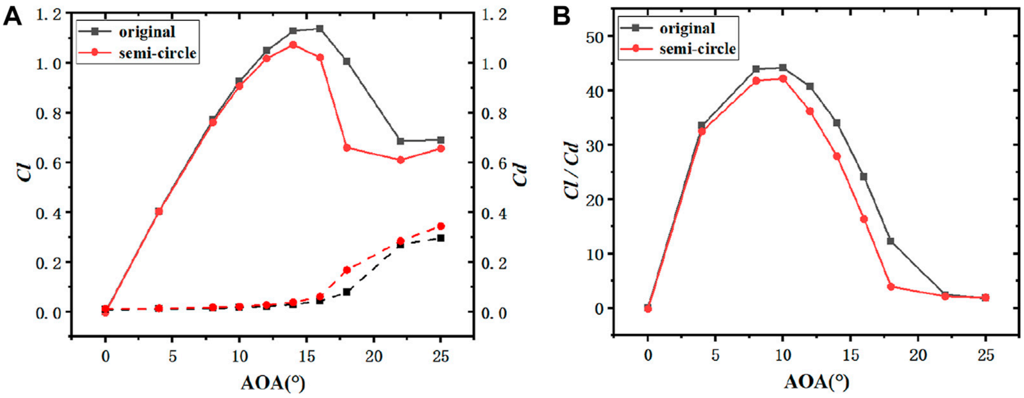

FIGURE 8
NACA0015 aerodynamic characteristic comparison curve of the original airfoil and the leading edge semi-circular erosion airfoil (h_1 = 0.5%c). (**(A)**: Lift and drag coefficient; **(B)**: Lift-drag ratio coefficient).

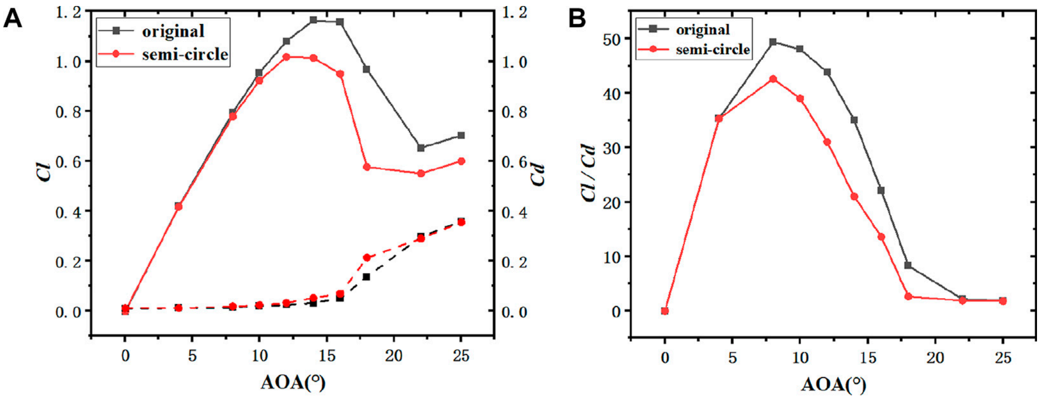

FIGURE 9
NACA0012 aerodynamic characteristic comparison curve of the original airfoil with the leading edge semi-circular erosion airfoil (h_1 = 0.5%c). (**(A)**: Lift and drag coefficient; **(B)**: Lift-drag ratio coefficient).

experimental data and the calculation method of the turbulence model. Moreover, based on Wilcox k-ω, the standard k-ω model was built through optimization calculation. To obtain a result with less error for the calculation near the wall (Menter, 1994), revised the model again after obtaining a large number of experimental data, and also took the transport of turbulent shear stress in the flow field into account. Finally, the SST k-ω model was obtained. With high calculation accuracy, this model has been used in the CFD software frequently. Accordingly, the SST k-ω model was used to simulate the airfoil aerodynamic performance in this study.

2.4 Grid-independent validation and model validation

To ensure the independence of the calculation grid, the number of nodes on the airfoil surface was 201,238 and 286, respectively. Three sets of grids with different number of grids were drawn, and the calculation results are presented in Figure 4. When the number of grids exceeded 270 thousand, the simulation results varied slightly, while 130 thousand and 270 thousand grid amount showed a significant gap in the rising resistance coefficient. Thus, the following conclusion was drawn: 130 thousand mesh was too large for the overall calculation error, so it cannot be used. However, there was little difference in accuracy between

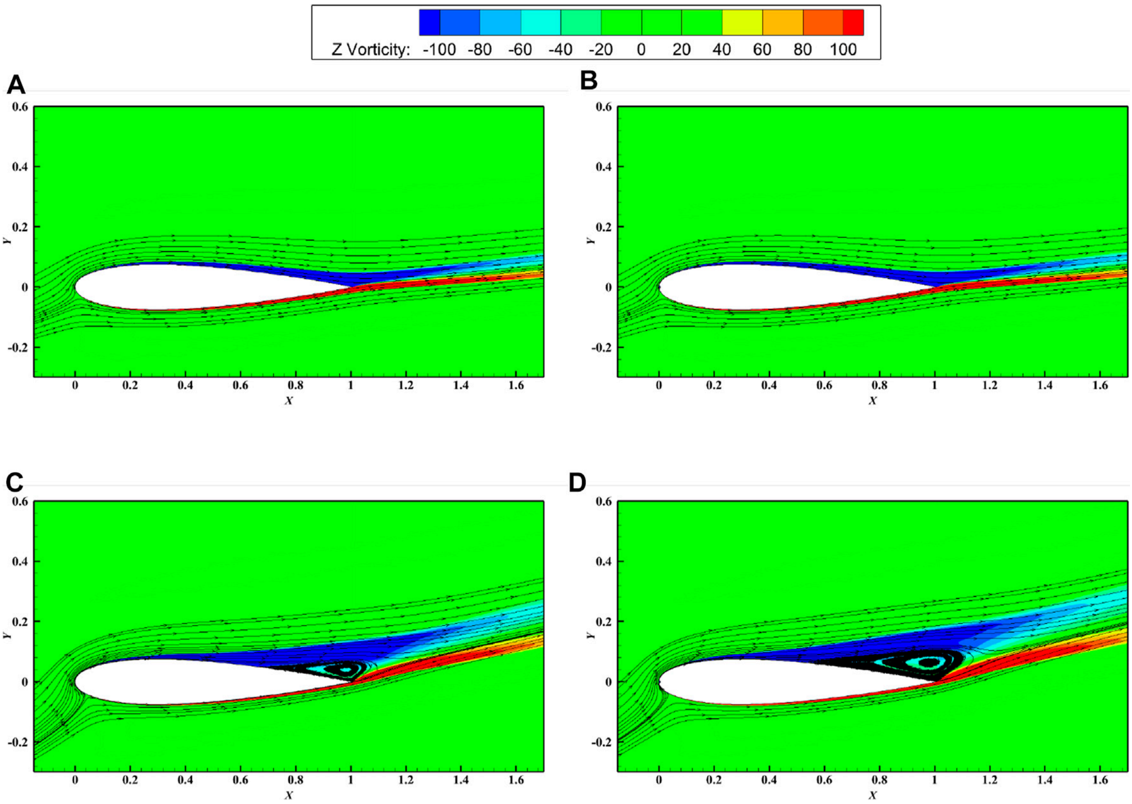

FIGURE 10
Schematic diagram of the surface streamline and vorticity of the NACA0015 original and semi-circular leading edge erosion airfoil (h_1 = 0.5%c). ((**A**): Original airfoil (*i* = 8°); (**B**): Semi-circular erosion airfoil (*i* = 8°); (**C**): Original airfoil (*i* = 16°); (**D**): Semicircular erosion airfoil (*i* = 16°).

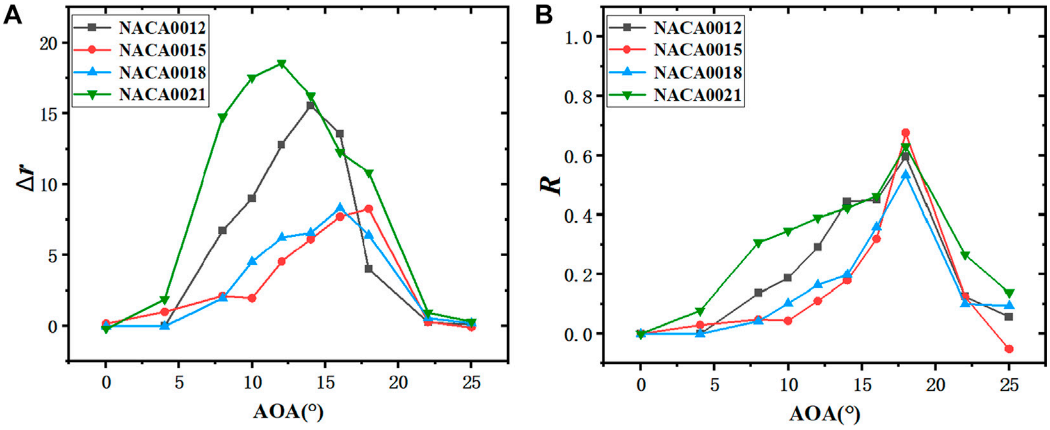

FIGURE 11
Difference of lift-drag ratio between original airfoil with different thickness and semi-circular leading edge erosion airfoil (h_1 = 0.5%c). ((**A**): Absolute difference in the lift-drag ratio; (**B**): Relative difference in the lift-drag ratio).

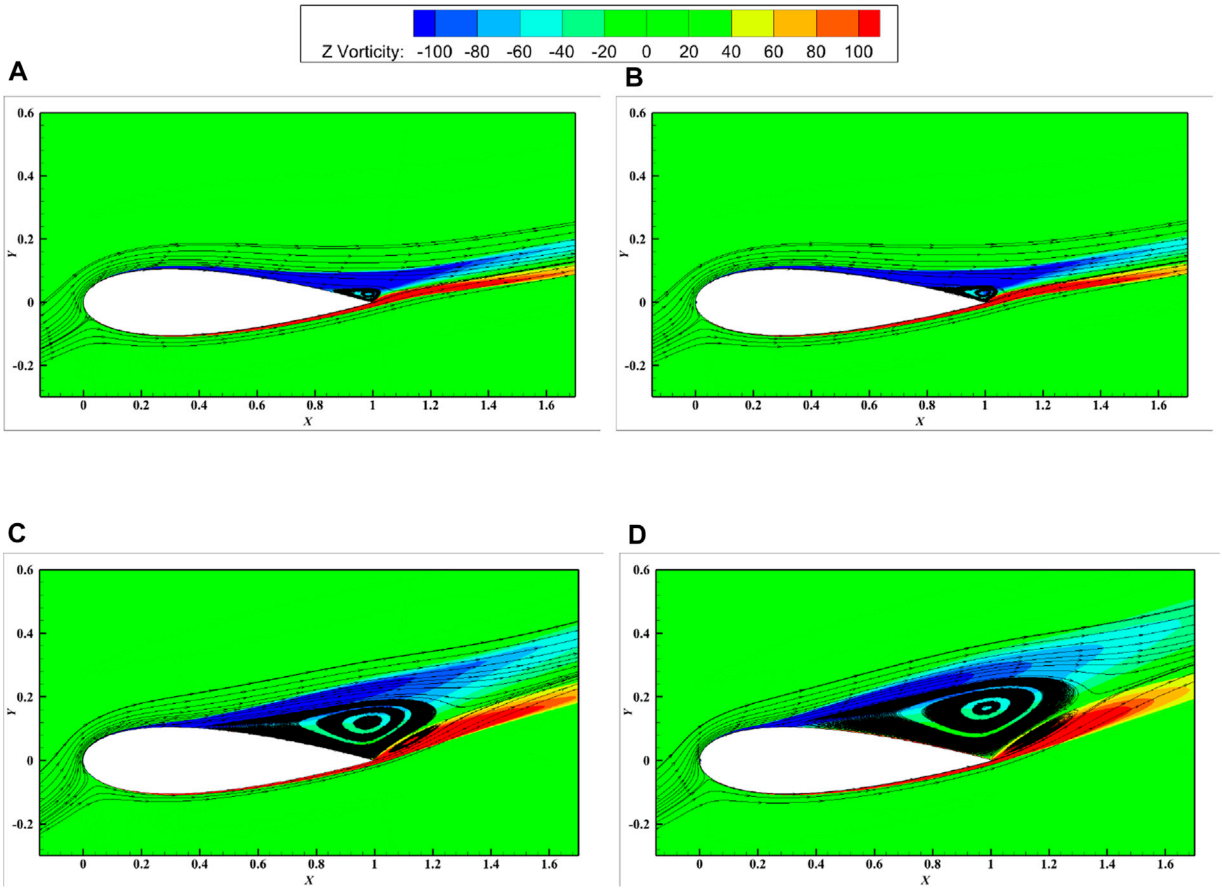

FIGURE 12
Schematic diagram of the surface streamline and vorticity of the NACA0021 primitive and semi-circular leading edge erosion airfoil (h_1 = 0.5%*c*). (**(A)**: Original airfoil (*i* = 12°); **(B)**: Semi-circular erosion airfoil (*i* = 12°); **(C)**: Original airfoil (*i* = 18°); **(D)**: Semi-circular erosion airfoil (*i* = 18°)).

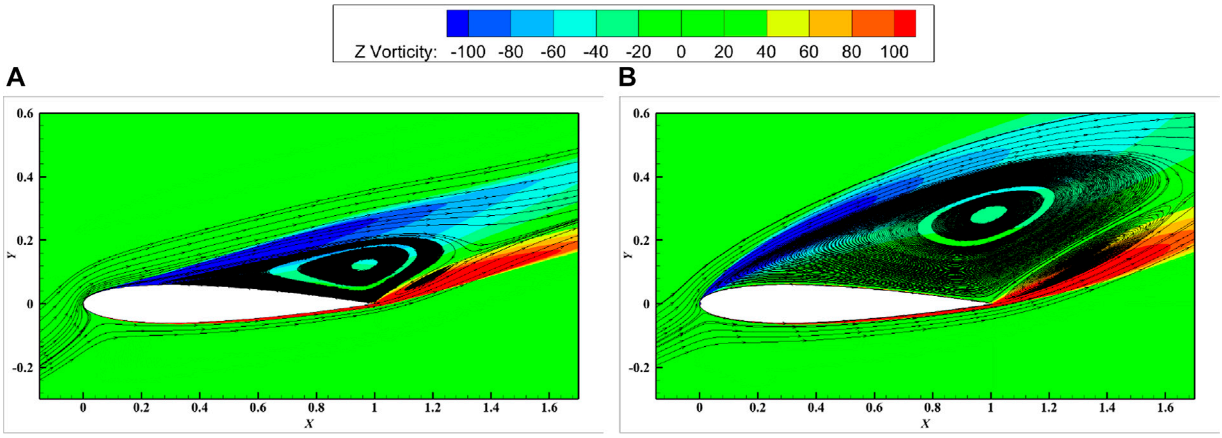

FIGURE 13
Schematic diagram of the surface streamline and vorticity of the NACA0012 original and semi-circular leading edge erosion airfoil (h_1 = 0.5%*c*). (**(A)**: Original airfoil (*i* = 18°); **(B)**: Semi-circular erosion airfoil (*i* = 18°)).

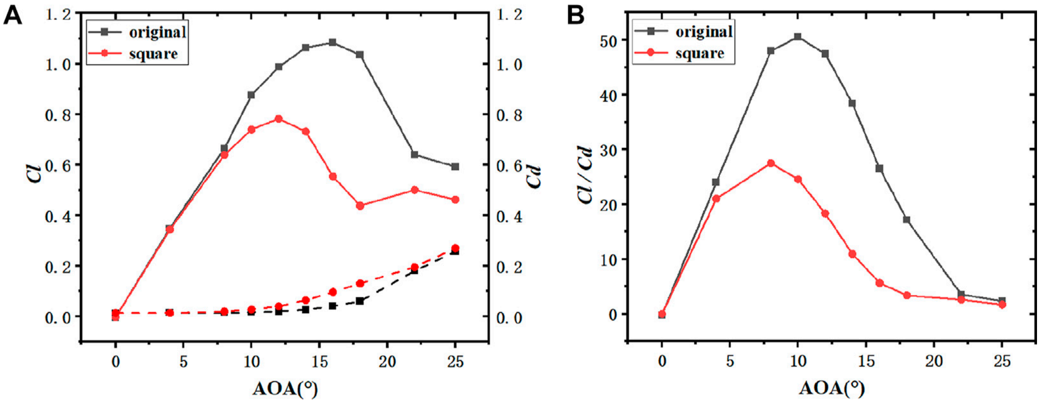

FIGURE 14
Comparison of aerodynamic characteristic curves between the original airfoil of NACA0021 and the square erosion airfoil with leading edge (h_2 = 0.5%c). (**(A)**: Lift and drag coefficient; **(B)**: Lift-drag ratio coefficient).

270 thousand and 390 thousand grids. For the consideration of the accuracy of the calculation results and the rationality of the overall computing resource allocation, 270 thousand grids were selected as the grid for simulation calculation in this study.

When the 270 thousand grid amount was used, the maximum lift coefficient was 1.08534, not significantly different from the experimental data (Figure 5), but only 6%. Moreover, close to the maximum lift coefficient and the corresponding angle in existing research (Sun et al., 2020), the data trend of the simulation was smooth without mutation, and it was also close to the current simulation data. In conclusion, the grid setting and numerical calculation method applied to the simulation of low-speed airfoil NACA in wind turbines are reliable, as verified by the data simulation calculation of NACA0021 on the suitable SST k-ω turbulence model, thus laying a good numerical calculation basis for the subsequent simulation experiments to increase the airfoil leading edge erosion and change the maximum thickness of the airfoil.

3 Results and analysis

3.1 Effect of airfoil thickness on aerodynamic performance of erosion airfoil

In this study, NACA0012, NACA0015, NACA0018 and NACA0021 were selected as the research objects and modified into two erosion forms (semi-circular/square) to explore the effect of airfoil thickness on the aerodynamic performance of

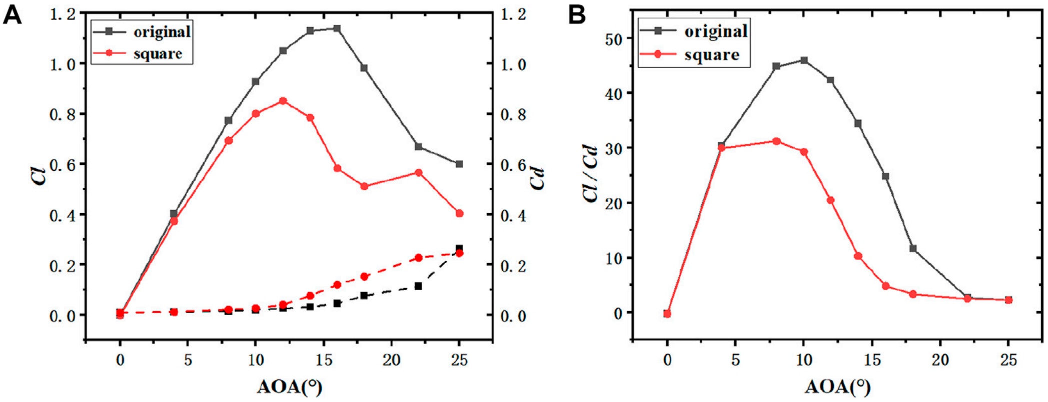

FIGURE 15
Comparison of aerodynamic characteristics between NACA0018 original airfoil and square erosion leading edge airfoil (h_2 = 0.5%c). (**(A)**: Lift and drag coefficient; **(B)**: Lift-drag ratio coefficient).

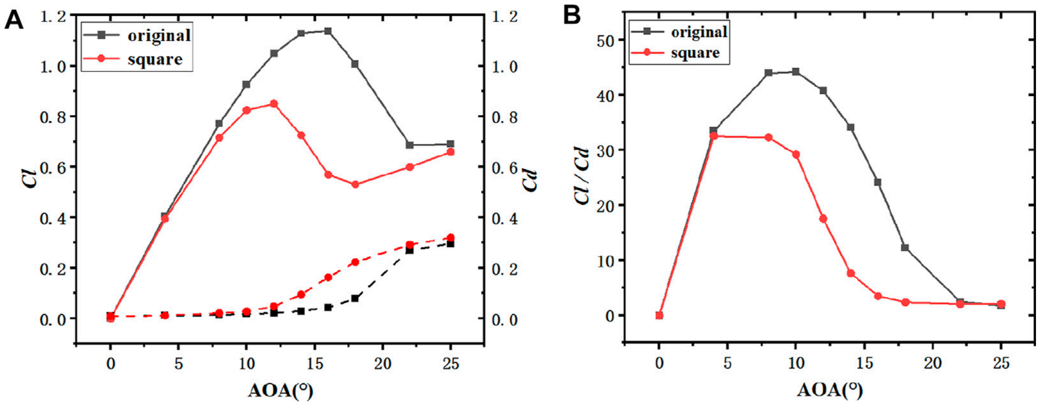

FIGURE 16
Comparison of aerodynamic characteristics between NACA0015 original airfoil and square-erosion leading edge airfoil (h_2 = 0.5%c). ((**A**): Lift and drag coefficient; (**B**): Lift-drag ratio coefficient).

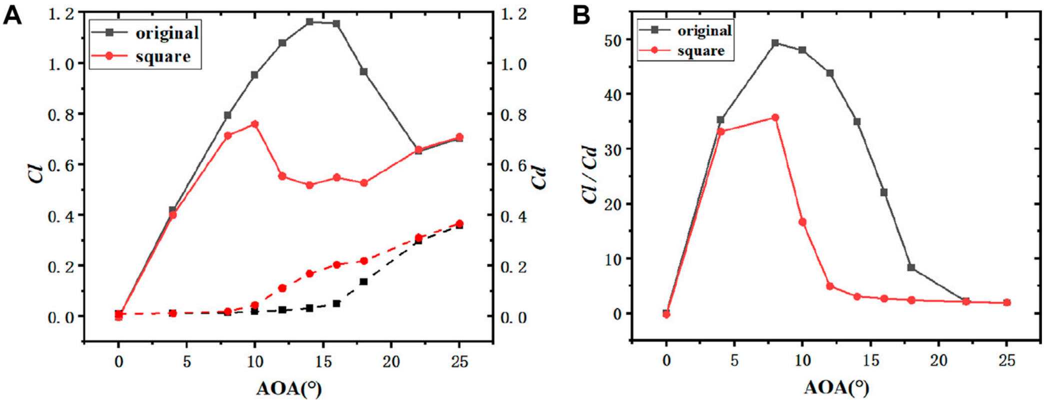

FIGURE 17
Comparison of aerodynamic characteristics between NACA0012 original airfoil and square-erosion leading edge airfoil (h_2 = 0.5%c). ((**A**): Lift and drag coefficient; (**B**): Lift-drag ratio coefficient).

erosion airfoil. Two sets of simulations were performed on the respective airfoil, i.e., airfoil with semi-circular erosion (erosion depth ratio of 0.5%c), airfoil with square erosion (erosion depth ratio of 0.5%c) and the original airfoil. The calculation results are presented as follows:

According to the lift-drag coefficients of airfoils with different thickness presented in Figure 6A, Figure 7A, Figure 8A and Figure 9A, the lift coefficient increased first and then decreased after reaching a maximum peak value. Moreover, from 0° to 8° (Figures 10A, B), the lift coefficient of the semicircle erosion airfoil was basically the same as that of the original airfoil. On that basis, the vorticity remained nearly unchanged, and the fitting degree of streamline was basically the same. When it was higher than 8° (Figures 10C, D), the lift coefficient of the original airfoil was significantly higher than that of the erosion airfoil, and the vorticide of the erosion airfoil was significantly higher than that of the original airfoil. However, there was no detachment, the fluid velocity in the upper part of the erosion airfoil was significantly smaller, and the lift coefficient decreased. With the increase of the angle of attack, the lift difference between the erosion airfoil and the original airfoil tended to decrease. The analysis reason is that with the increase of the angle of attack, the flow field environment deteriorated significantly, and the effect of the erosion part of the leading edge on the overall airfoil decreased, such that the difference was

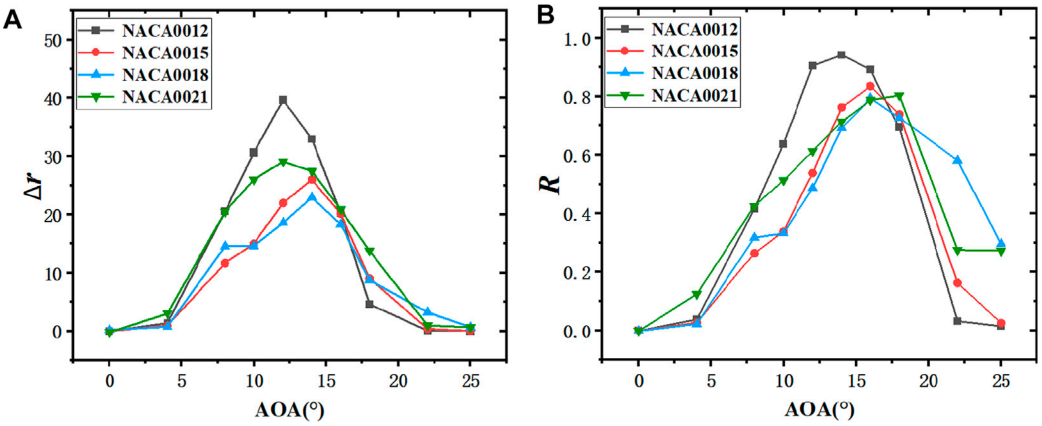

FIGURE 18
Difference of lift-drag ratio between the original airfoil with different thickness and the square leading edge erosion airfoil (h_2 = 0.5%*c*). (**(A)**: Absolute difference in the lift-drag ratio; **(B)**: Relative difference in the lift-drag ratio).

reduced. However, the drag coefficient of the erosion airfoil was higher than that of the prototype from 0° to 25°. As depicted in Figure 6B, Figure 7B, Figure 8B and Figure 9B, variation trend of lift-drag ratios of airfoils with different thickness remained nearly unchanged, whereas the maximum lift-drag ratios of the original airfoils of NACA0012 and the erosion airfoils were 8°. The maximum lift-drag ratios of the original airfoil of the remaining three airfoils were 10°, and the maximum lift-drag ratios of the erosion airfoils reached 8°.

As depicted in Figure 11A, the difference of lift-drag ratio between the original airfoil and the erosion airfoil of NACA0021 was the most significant among the four thicknesses, and the absolute difference of lift-drag ratio reached 18.6 at 12° angle of attack. However, as depicted in Figure 11B, the relative difference of lift-drag ratio of NACA0021 at 12° angle of attack was only 0.39, whereas the maximum decrease was 63.1% at 18° angle of attack. Moreover, as depicted in Figure 12, at 12°angle of attack, the size of vortex for the original airfoil near blade trailing edge did not change significantly compared to the erosion airfoil. However, at 18° angle of attack, the size of vortex for the semi-circular erosion airfoil is significantly increased compared to the original airfoil. ($R = \frac{r}{\Delta r}$; *R*: Relative difference in the lift-drag ratio; *r*: Lift-drag ratio of original airfoil; Δr: Absolute difference in the lift-drag ratio).

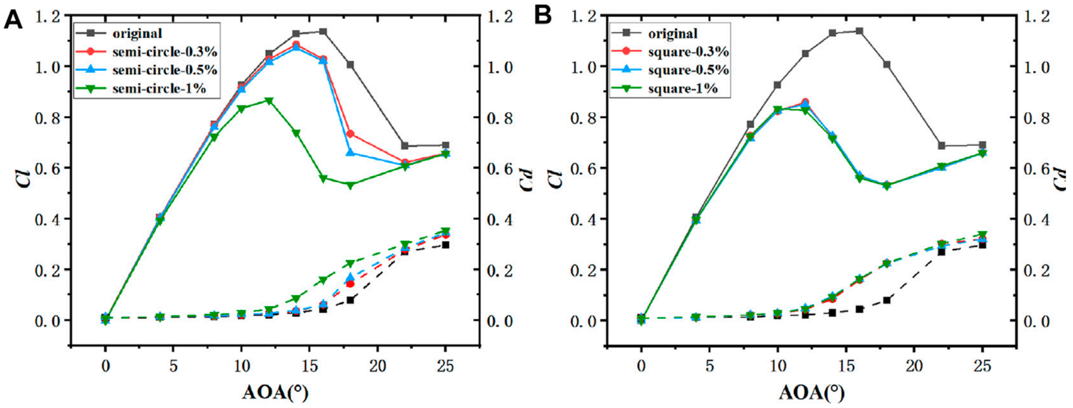

FIGURE 19
Comparison of the Lift and drag coefficient between the original airfoil and the semi-circular/square leading edge erosion airfoil for NACA0015. (**(A)**: Semi-circular erosion airfoil; **(B)**: Square erosion airfoil).

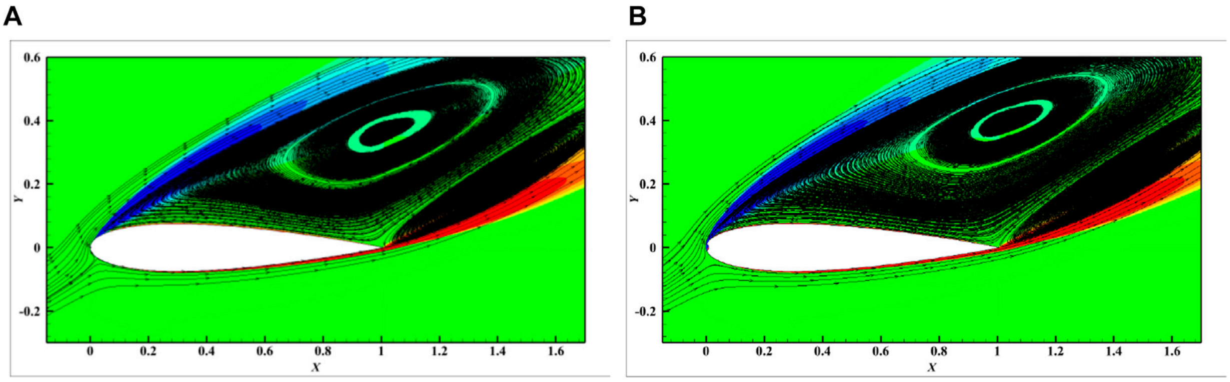

FIGURE 20
Surface streamline and vorticity of the Semi-circular erosion on the leading edge of the NACA0015 airfoil at 22° angle of attack. (**(A)**: $h_1 = 0.3\%c$; **(B)**: $h_1 = 1\%c$).

The second was the NACA0012 airfoil. At 18° angle of attack, as presented in Figure 11, compared with the other three airfoils, it showed the smallest reduction in the lift-drag ratio, whereas the relative reduction in the lift-drag ratio accounted for 59.7%. The vorticity diagram in Figure 13 indicates that the vorticity increased significantly at 18° compared with The original. The overall trend of the whole lift-drag ratio difference curve of NACA0015 and NACA0018 was smaller than that of NACA0012 and NACA0021 airfoils.

In addition, as depicted in Figure 11, the difference of lift-drag ratio of the four blade thicknesses was relatively small at 0° and 25° angles of attack, and the leading edge erosion slightly affected the aerodynamic performance of airfoils with 0° angles of attack and angles of attack greater than 25° (including 25°). At the 0° angle of attack, the flow was not separated, there was basically no lift, and the leading edge erosion geometry was also symmetric on the suction and pressure surfaces, such that the effect was small. However, at 25° angle of attack, the flow separation developed from the trailing edge to the leading edge of the airfoil, and the lift to drag ratio of the original airfoil was relatively small at this time. Besides, the effect of the deterioration of aerodynamic performance caused by the erosion of the leading edge was small.

For the leading edge erosion airfoil with square erosion pattern, as depicted in Figure 14A, Figure 15A and Figure 16A, at the angle of attack from 0° to 8°, the lift coefficient values of the original airfoil and the leading edge square erosion airfoil remained nearly unchanged, thus indicating that there was little difference between the flow on the suction surface and pressure surface of the leading edge square erosion airfoil and the original airfoil at this time. At the lift coefficient higher than 8°, the lift coefficient of the original airfoil was significantly higher than that of the leading edge square airfoil. Moreover, the angle of attack when the maximum lift coefficient of the square erosion airfoil moved forward from the original 16°–12° of the square erosion airfoil of the leading edge.

The resistance curves of the original and square erosion airfoil with different thickness remained nearly unchanged with the exponential curve growth. The drag coefficient curve of the leading edge square airfoil rose slowly before the angle of attack from 0° to 12° and then increased after the angle of attack from 12°. Notably, the drag coefficient value of the leading edge square airfoil was always higher than that of the original airfoil (0°–25° angle of attack).

As depicted in Figure 14B, Figure 15B and Figure 16B, the maximum lift-to-drag ratio of the square erosion airfoil was at 8° angle

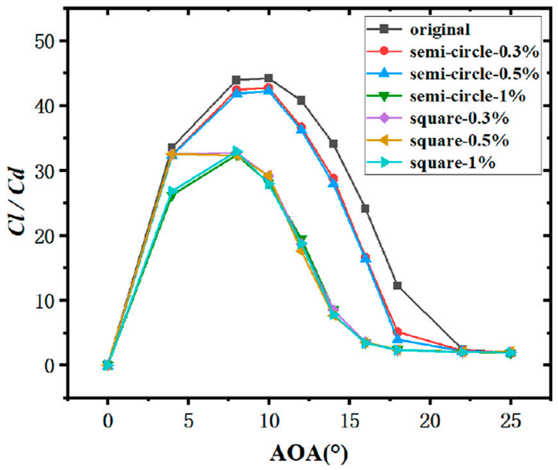

FIGURE 21
Comparison of the lift-drag ratio coefficient between the original airfoil and the semi-circular/square leading edge erosion airfoil for NACA0015.

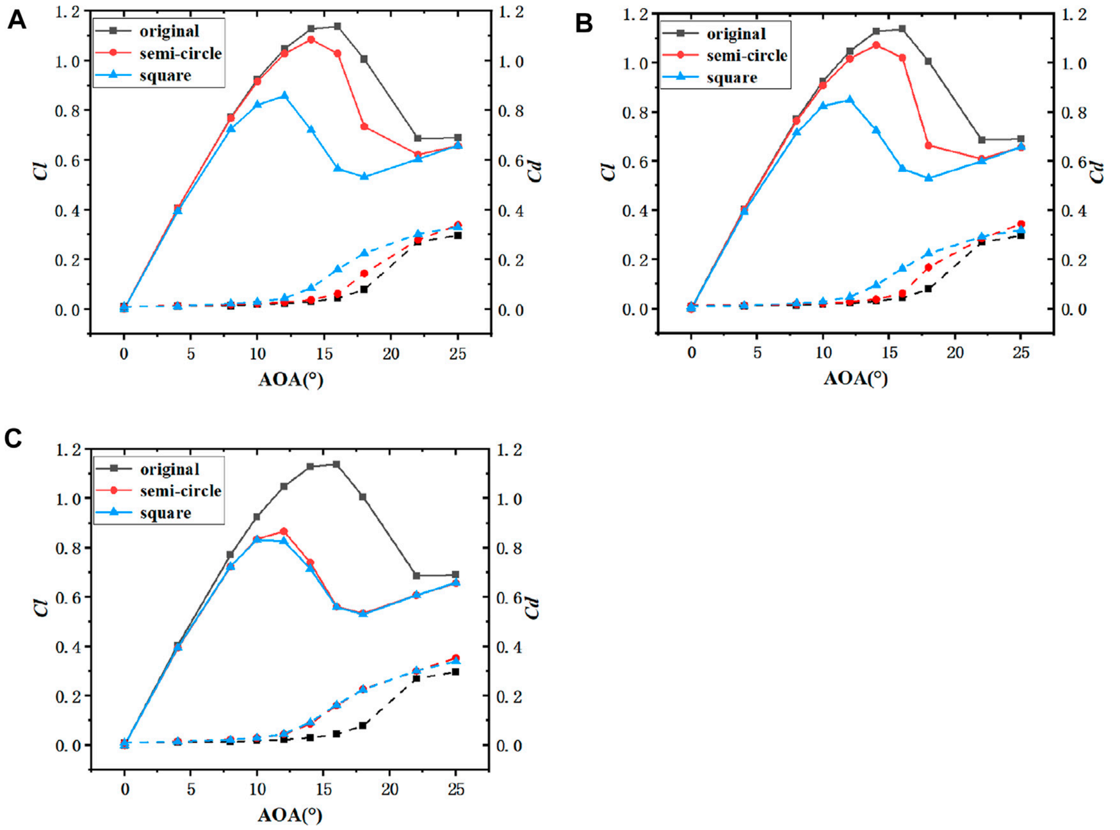

FIGURE 22
Comparison of Lift and drag coefficients of NACA0015 original airfoil with semi-circle and square leading edge erosion airfoil. (**(A)**: $h_1 = h_2 = 0.3\%c$; **(B)**: $h_1 = h_2 = 0.5\%c$; **(C)**: $h_1 = h_2 = 1\%c$).

of attack, nearly 2° forward compared with the 10° angle of attack when the lift-to-drag ratio of the original airfoil reached its maximum. The higher the lift-drag ratio, the better the aerodynamic performance of the airfoil will be. As depicted in the figure, the maximum lift-drag ratio of the original airfoil of NACA0021 was obtained as 50.6, whereas the maximum lift-drag ratio of the square erosion airfoil was 27.6, and the reduction range was the largest among the four thickness blades, up to 45.5%. The maximum difference of lift-drag ratio between the original airfoil and leading edge deformation of NACA0015 and NACA0018 airfoils was smaller than that of NACA0021 airfoils, with a decrease of 33.9% and 33.1%, respectively.

As depicted in Figure 17, the maximum lift-drag ratio curve of NACA0012 square erosion airfoil was obtained at 4° angle of attack, nearly 4° ahead of the 8° angle of attack when the lift-drag ratio of the original airfoil was at its maximum value. In addition, there was a significant difference between the maximum lift-drag ratio of the original airfoil and the square-erosion airfoil. The maximum lift-drag ratio of the original airfoil was 46.7, and the maximum lift-drag ratio of the square-erosion airfoil was obtained as 29.2, marking a decrease of 37.5%.

Figure 18 presents the difference in the lift-drag ratio between the square erosion airfoil with four thicknesses and the original airfoil. The difference in the lift-drag ratio between the original and erosion airfoil of NACA0012 was the largest among the four thicknesses, followed by the NACA0021 airfoil. The absolute difference of lift-drag ratio between NACA0012 airfoil and erosion airfoil was obtained as 39.7, and the relative difference in the lift-drag ratio was 90.5% at 12° angle of attack, and the maximum decrease was 94.2% at 14° angle of attack. The difference of lift-drag ratio between NACA0015 airfoil and NACA0018 airfoil and their erosion airfoils is significantly smaller than that of NACA0012 and NACA0021 airfoils between 0° and 16° angles of attack, and slightly higher than that of NACA0012 and NACA0021 airfoils between 16° and 25° angles of attack.

In brief, NACA0012 and NACA0021 were the two airfoils with the largest thickness and the smallest thickness among the four airfoils studied in this study. One of them was thinner, resulting in less differential pressure and less lift; the other was thicker, causing easy separation of the flow, interfering with the flow field, thus resulting in a reduction in the lift coefficient and a rise in the drag coefficient. As a

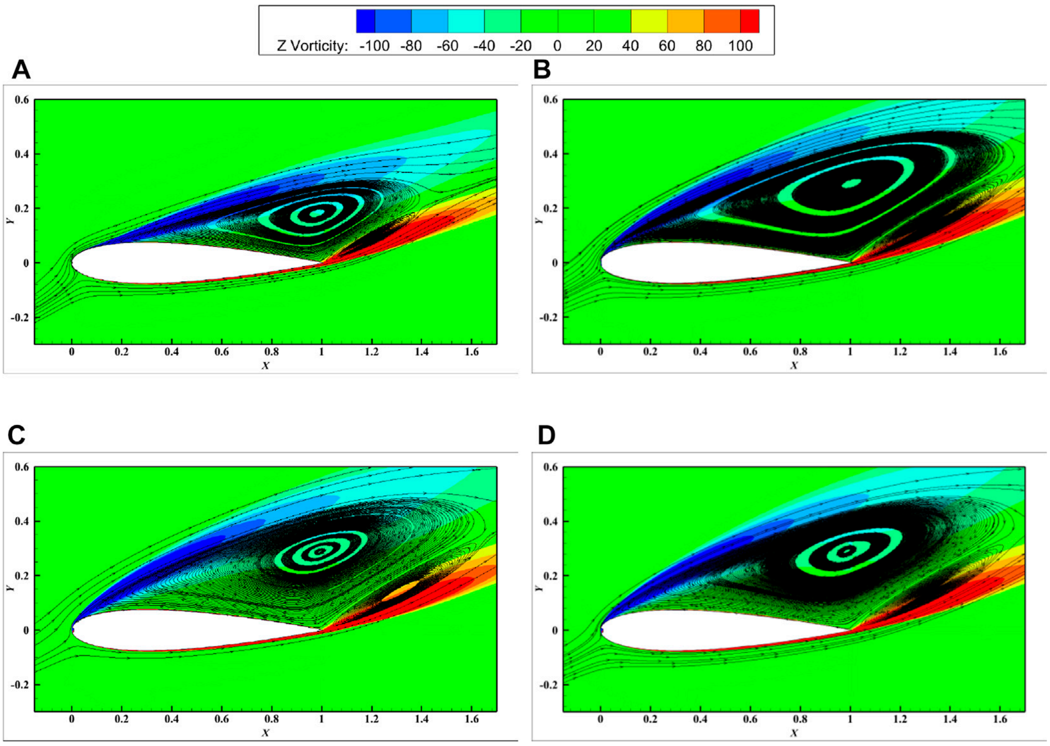

FIGURE 23
Surface streamlines and vorticity of NACA0015 airfoil with different erosion patterns at 18° angle of attack. **(A)**: Semicircular erosion (h_1 = 0.3% *c*); **(B)**: Square erosion (h_2 = 0.3%*c*); **(C)**: Semi-circular erosion (h_1 = 1%*c*); **(D)**: Square erosion (h_2 = 1%*c*)).

result, the aerodynamic performance will be reduced. NACA0015 and NACA0018 were the two airfoil types with medium thickness among the four blade types.

3.2 Effect of leading erosion on aerodynamic performance of airfoil

In this study, airfoil NACA0015 was selected as the research object to explore the effect of leading edge erosion degree on aerodynamic performance of airfoil. Three groups of simulations were performed to compare the two erosion (semi-circular and square) airfoils, respectively, with the leading edge erosion depth ratios of 0.3%*c*, 0.5%*c*, and 1%*c*.

As depicted in Figure 19A, the overall trend of lift-drag of airfoils with three erosion degrees was to increase at small angles of attack. At the angle of attack close to 12°, the lift-drag was peaked. At the angle of attack close to the large angle of attack, the lift coefficient decreased, whereas the drag coefficient continued to increase. The higher the angle of attack, the more significant the change of Lift-drag coefficient will be. The difference between lift coefficient and drag coefficient of airfoil with three erosion degrees tended to decrease to the same value after 20° angle of attack. As depicted in Figure 20, this is because at high angle of attack, the drag increment caused by the erosion part of the leading edge accounted for a too small proportion for the overall airfoil after large flow separation and slightly affected it when the flow field environment was harsh, such that the coefficients tended to be the same. As depicted in Figure 21, the lift-drag ratio of the erosion airfoil with the leading edge erosion degree of 1% decreased the most in the range of 0°–25° angle of attack, and the lift-drag ratio of the erosion airfoil with the leading edge erosion degree of 0.5% decreased by 26.3% at 8° angle of attack (at the maximum lift-drag ratio of the airfoil). The lift-drag ratio of an airfoil with 0.3% leading edge erosion decreased by only 3.5%. The above results suggest that for the same airfoil, the smaller the leading edge erosion, the better its aerodynamic performance will be.

As depicted in Figure 19B, the aerodynamic performance of the airfoil was reduced significantly when the square erosion of the airfoil leading edge increased. Even if the square erosion of the airfoil leading edge was only 0.3% of the chord length of the airfoil, the lift of the erosion airfoil decreased to 50.3% of the original airfoil, and the drag increased by 263.6% at 16° angle of attack. However, the increase of square erosion degree slightly affected the aerodynamic changes of the airfoil. As depicted in Figure 21, the lift-drag ratio of the square erosion airfoil with leading edge erosion depth of 0.3%*c* and 0.5%*c* was slightly higher than that of 1%*c* when the erosion depth of the square erosion airfoil ranged from 0° to 8°, and the lift-drag ratio of the three erosion degrees of the square airfoil at other attack angles remained nearly unchanged.

3.3 Effect of different leading edge erosion on the aerodynamic performance of the airfoil

To explore the morphology of different leading edge erosion (different depth and thickness), two groups of simulation were performed on the airfoil NACA0015 under the same leading edge erosion depth ($h_1 = h_2$) for comparison. The two sets of simulations included the leading edge Semi-circular erosion airfoil $d_1 = 2h_1$ ($h_1 = 0.3\%c$, $0.5\%c$, $1\%c$) and the leading edge square erosion airfoil $d_2 = 13\%t$.

As depicted in Figure 21 and Figure 22, when the leading edge erosion shape is semi-circle, the change of airfoil erosion thickness significantly affected the aerodynamic performance of airfoil from 0.3%c to 1%c. For the square leading edge erosion shape, the aerodynamic performance for the eroded airfoil little varied by the erosion depth, but the lift coefficient can be much lower than the semi-circle erosion airfoil at 0.3%c an 0.5%c erosion depth. As depicted in Figures 23A, B, at the erosion depth of 0.3%, the vorticity of the two erosion patterns was significantly different. However, with the increase of the leading edge erosion degree, the difference between the lift drag coefficient of the Semi-circular erosion airfoil and the square erosion airfoil decreased. When the leading edge erosion reached to 1%, the lift drag coefficient curves of the Semi-circular erosion airfoil and the square erosion airfoil were basically the same. Figures 23C,D shows that the vorticity generated by the two erosion airfoil is the same. At this time, the aerodynamic performance of the original NACA0015 airfoil changed to a similar extent by both. The results indicated that the effect of the change of airfoil erosion thickness on airfoil aerodynamic performance decreases, when the leading edge erosion depth reached a certain level.

4 Conclusion

In this study, four NACA series airfoils were investigated and the influence of blade maximum thickness on airfoil performance under different leading edge erosion rates were studied by two erosion forms through the CFD method. The main conclusions are drawn as follows:

1) The result indicated that due to the thin or thick airfoil of NACA0012 and NACA0021, the increase of leading edge erosion resulted in a significantly reduced aerodynamic performance compared with the medium thickness airfoil. However, due to the moderate thickness of NACA0015 and NACA0018, the variation range of aerodynamic performance was small even with the increase of the leading edge erosion. Among the four different thickness airfoils, the aerodynamic performance of the NACA0015 and NACA0018 airfoils with increased leading edge erosion was proved to be higher than that of thicker or thinner airfoils.
2) For NACA0015, semi-circular erosion airfoil, at 8° angle of attack (when the lift-drag ratio of airfoil was peaked), the lift-drag ratio of airfoil with the leading edge erosion degree of 1% decreased by 26.3%, followed by the airfoil with 0.5%leading edge erosion, and the lift-drag ratio of airfoil with the leading edge erosion degree of 0.3% decreased by only 3.5%. For square erosion airfoil, the drop of lift-drag ratio of the erosion airfoil with 1% leading edge erosion was also the largest. The above results suggest that for the same airfoil, the smaller the leading edge erosion, the better the aerodynamic performance will be.
3) When the erosion degree (depth) of the leading edge airfoil was small, the varation of the erosion size would significantly affect the aerodynamic performance of the airfoil. When the erosion size of the leading edge increases to a certain extent, the performance of the blade decreases greatly compared with the original cases, but the sensitivity of the erosion blade performance to the change of the leading edge erosion size decreases.

Data availability statement

The original contributions presented in the study are included in the article/supplementary material, further inquiries can be directed to the corresponding author.

Author contributions

JS: Conceptualization, Funding acquisition, Resources Writing—review and editing, Funding acquisition. SZ: Writing—original draft, Visualization. PC: Investigation, Data curation. LQ: Validation, Formal analysis.

Funding

This work was funded by National Natural Science Foundation of China (Grant Nos. 51906156) and Natural Science Foundation of Shanghai (Grant Nos. 22ZR1443500).

Conflict of interest

The authors declare that the research was conducted in the absence of any commercial or financial relationships that could be construed as a potential conflict of interest.

Publisher's note

References

Cappugi, L., Castorrini, A., Bonfiglioli, A., Minisci, E., and Campobasso, M. S. (2021). Machine learning-enabled prediction of wind turbine energy yield losses due to general blade leading edge erosion. *Energy Convers. Manag.* 245, 114567. doi:10.1016/j.enconman.2021.114567

Chien, F. S., Kamran, H. W., Albashar, G., and Iqbal, W. (2021). Dynamic planning, conversion, and management strategy of different renewable energy sources: A sustainable solution for severe energy crises in emerging economies. *Int. J. Hydrogen Energy* 46 (11), 7745–7758. doi:10.1016/j.ijhydene.2020.12.004

Doagou-Rad, S., Mishnaevsky, L., Jr, and Bech, J. I. (2020). Leading edge erosion of wind turbine blades: Multiaxial critical plane fatigue model of coating degradation under random liquid impacts. *Wind Energy* 23 (8), 1752–1766. doi:10.1002/we.2515

Dong, M., Wang, C., Liu, H., Shen, C., and Zhang, J. (2019). Enhanced solid particle erosion properties of thermoplastic polyurethane-carbon nanotube nanocomposites. *Macromol. Mater. Eng.* 304 (5), 1900010. doi:10.1002/mame.201900010

Elhadi Ibrahim, M., and Medraj, M. (2019). Water droplet erosion of wind turbine blades: Mechanics, testing, modeling and future perspectives. *Materials* 13 (1), 157. doi:10.3390/ma13010157

Eshiemogie, S. O., Ighalo, J. O., and Banji, T. I. (2022). Knowledge, perception and awareness of renewable energy by engineering students in Nigeria: A need for the undergraduate engineering program adjustment. *Clean. Eng. Technol.* 6, 100388. doi:10.1016/j.clet.2021.100388

Gharali, K., and Johnson, D. A. (2012). Numerical modeling of an S809 airfoil under dynamic stall, erosion and high reduced frequencies. *Appl. Energy* 93, 45–52. doi:10.1016/j.apenergy.2011.04.037

Han, W., Kim, J., and Kim, B. (2018). Effects of contamination and erosion at the leading edge of blade tip airfoils on the annual energy production of wind turbines. *Renew. energy* 115, 817–823. doi:10.1016/j.renene.2017.09.002

Hussain, M., Butt, A. R., and Uzma, F. (2020). A comprehensive review of climate change impacts, adaptation, and mitigation on environmental and natural calamities in Pakistan[J]. *Environ. Monit. Assess.* 192 (1), 1–20. doi:10.1007/s10661-019-7956-4

Keegan, M. H., Nash, D., and Stack, M. (2012). Modelling rain drop impact on offshore wind turbine blades[J]. *ASME Turbo Expo.* 2012, 8–10. doi:10.1115/GT2012-69175

Keegan, M. H., Nash, D., and Stack, M. (2013). Numerical modelling of hailstone impact on the leading edge of a wind turbine blade[J]. *EWEA Annu. Wind Energy Event* 2013, 5–10.

Khalfallah, M. G., and Koliub, A. M. (2007). Effect of dust on the performance of wind turbines. *Desalination* 209 (1-3), 209–220. doi:10.1016/j.desal.2007.04.030

Li, D., Wang, C., and Li, Y. (2017). Influence of blade leading edge erosion features on aerodynamic characteristics of wind turbine airfoil[J]. *Trans. Chin. Soc. Agric. Eng.* 33 (22), 269–275. doi:10.11975/j.issn.1002-6819.2017.22.035

Manatbayev, R., Baizhuma, Z., Bolegenova, S., and Georgiev, A. (2021). Numerical simulations on static Vertical Axis Wind Turbine blade icing. *Renew. Energy* 170, 997–1007. doi:10.1016/j.renene.2021.02.023

Menter, F. R. (1994). Two-equation eddy-viscosity turbulence models for engineering applications. *AIAA J.* 32 (8), 1598–1605. doi:10.2514/3.12149

Mishnaevsky, L., Jr, Hasager, C. B., Bak, C., Tilg, A. M., Bech, J. I., Doagou Rad, S., et al. (2021). Leading edge erosion of wind turbine blades: Understanding, prevention and protection. *Renew. Energy* 169, 953–969. doi:10.1016/j.renene.2021.01.044

Papi, F., Ferrara, G., and Bianchini, A. (2020). Practical considerations on wind turbine blade leading edge erosion modelling and its impact on performance and loads[C]//Journal of physics: Conference series. *IOP Publ.* 1618 (5), 052005. doi:10.1088/1742-6596/1618/5/052005

Ritchie, H., and Roser, M. (2017). *CO_2 and greenhouse gas emissions*. UK: Our World in Data. [J]. Cited on, 3.

Sapre, C. (2012). "Turbine blade erosion and the use of wind protection tape,". M S Thesis.

Sareen, A., Sapre, C. A., and Selig, M. S. (2014). Effects of leading edge erosion on wind turbine blade performance. *Wind Energy* 17 (10), 1531–1542. doi:10.1002/we.1649

Spruce, C. J. (2006). "Power performance of active stall wind turbines with blade contamination," in Proceedings of the European Wind Energy Conference, Greece, 27 Feb-2 Mar.

Sun, J., Sun, X., and Huang, D. (2020). Aerodynamics of vertical-axis wind turbine with boundary layer suction – effects of suction momentum. *Energy* 209, 118446. doi:10.1016/j.energy.2020.118446

Wang, Y., Zheng, X., Hu, R., and Wang, P. (2016). Effects of leading edge defect on the aerodynamic and flow characteristics of an S809 airfoil. *PloS one* 11 (9), e0163443. doi:10.1371/journal.pone.0163443

Wang, Y., Hu, R., and Zheng, X. (2017). Aerodynamic analysis of an airfoil with leading edge pitting erosion. *J. Sol. Energy Eng.* 139 (6). doi:10.1115/1.4037380

Wang, Y., Wang, L., Duan, C., Zheng, J., Liu, Z., and Ma, G. (2021). CFD simulation on wind turbine blades with leading edge erosion. *J. Theor. Appl. Mech.*, 579–593. doi:10.15632/jtam-pl/141546

frontiers | Frontiers in Energy Research

TYPE Original Research
PUBLISHED 04 January 2023
DOI 10.3389/fenrg.2022.1094717

Performance optimization of centrifugal pump based on particle swarm optimization and entropy generation theory

Handong Qi[1], Wei Li[1,2]*, Leilei Ji[1,3,4]*, Mingjiang Liu[1], Rui Song[1], Yunxin Pan[1] and Yi Yang[1]

[1]National Research Center of Pumps, Jiangsu University, Zhenjiang, China, [2]Institute of Fluid Engineering Equipment Technology, Jiangsu University, Zhenjiang, China, [3]Key Laboratory of Fluid and Power Machinery, Xihua University, Chengdu, China, [4]Wenling Fluid Machinery Technology Institute of Jiangsu University, Wenling, China

EDITED BY
Muhammad Wakil Shahzad,
Northumbria University,
United Kingdom

REVIEWED BY
Aqiang Lin,
Northwestern Polytechnical University,
China
Muhammad Ahmad Jamil,
Northumbria University,
United Kingdom

*CORRESPONDENCE
Wei Li,
✉ lwjiangda@ujs.edu.cn
Leilei Ji,
✉ leileiji@ujs.edu.cn

SPECIALTY SECTION
This article was submitted to Process and Energy Systems Engineering, a section of the journal Frontiers in Energy Research

RECEIVED 10 November 2022
ACCEPTED 05 December 2022
PUBLISHED 04 January 2023

CITATION
Qi H, Li W, Ji L, Liu M, Song R, Pan Y and Yang Y (2023), Performance optimization of centrifugal pump based on particle swarm optimization and entropy generation theory.
Front. Energy Res. 10:1094717.
doi: 10.3389/fenrg.2022.1094717

Centrifugal pumps are frequently utilized in general machinery, but they have issues with low efficiency, unstable operation, and high-power consumption in actual engineering, making performance improvements necessary. In this paper, the particle swarm algorithm is utilized to find the optimal solution among the Pareto front solutions and obtain the most suitable impeller for the centrifugal pump with the lowest entropy generation and highest efficiency as the optimization objectives. Based on the entropy generation theory, the energy losses of the original model and the optimized model are compared and analyzed. The results show that the centrifugal pump impeller and volute are the two areas with the largest entropy generation ratio, the optimized centrifugal pump entropy generation decreases by 5.41%, and the efficiency increases by 3.89%. Turbulent entropy generation and wall entropy generation are the important causes of hydraulic losses. Most of the losses within the impeller occur mainly at leading edge and trailing edge of blade. As the flow rate increases, the closer the distribution of the high entropy generation rate at the front cover of the impeller, the more serious the flow losses. This paper can provide a theoretical reference for the performance optimization of centrifugal pumps.

KEYWORDS

centrifugal pump, particle swarm algorithm, entropy generation analysis, numerical calculation, optimization

1 Introduction

As a general fluid machinery and equipment, centrifugal pumps are widely utilized in petrochemical, nuclear power, irrigation, urban water supply, heating systems, and other fields. With the deepening research in the field of blade pumps, the optimization and numerical calculation of blade pumps such as mixed-flow pumps and centrifugal pumps have become a key direction of current research (Li et al., 2016a; Li et al., 2021; Li et al., 2020; Ji et al., 2021; Jaluria, 2009). At present, centrifugal pumps generally have low efficiency, unsafe operation, high power consumption, and other problems. Therefore, improving centrifugal pumps' operational stability, efficiency, and service life is of great importance to energy efficiency and response to global carbon neutrality targets (Cong et al., 2015; Pei, Yi, Yuan, Wang, Wang, 2017).

In recent years, many researchers have devoted themselves to studying the relationship between energy loss and entropy generation in the internal flow of fluid machinery and have obtained specific research results (Jiang et al., 2011; Fan et al., 2022; Lai et al., 2022; Zhang and Tang, 2022). Entropy generation theory is a method of calculating energy loss in a practical process based on the second law of thermodynamics, which is combined with heat transfer theory and fluid mechanics (Saha and Mahanta, 2001; Chen, 2012). Gong et al. (2013) analyzed the energy loss in hydraulic turbines and found that the entropy generation analysis method has the advantage of determining the amount of energy dissipation and the location of dissipation. Li et al. (2016b) combined the velocity distribution and entropy generation theory to study the hydraulic loss distribution in centrifugal pumps and found that the entropy generation rate changed with the decrease in flow rate. Ahmed et al. (2016) conducted a numerical study of incompressible viscous flow around the blades to investigate the entropy generation characteristics of turbine blades under oscillatory flow conditions. Hou et al. (2016) investigated the magnitude and location of irreversible energy losses in a two-stage LNG cryogenic submersible pump based on the entropy generation theory to find that the entropy generation theory is advantageous for evaluating the energy characteristics of LNG pumps. Li et al. (2017) utilized the entropy generation theory to obtain the variation law of hydraulic loss distribution and entropy generation of hydraulic turbines in pump mode. Li et al. (2018) utilized the local flow analysis method to study the relationship between the vacuole distribution and entropy generation. Ji et al. (Ji et al., 2020a; Ji et al., 2020b) utilized the entropy generation theory to study the relationship between internal energy loss and the size of the impeller clearance in mixed-flow pumps. The results show that the increase in the impeller tip clearance may cause an increase in the energy loss within the impeller. Zhang et al. (2018) found that the losses by direct dissipation were much smaller than by turbulent dissipation within a single-stage side-runner pump based on the entropy generation theory. Yang et al. (2019) utilized entropy generation theory to correct for wall effects in turbine pumps and to evaluate energy losses in pumps as well as entropy generation analysis of components to point out the effect of timing effects on pump performance. Majeed et al. (2019) utilized entropy generation theory to study turbulent dissipation in centrifugal pumps to select the location of optimized losses. Hou et al. (2019) optimize the design of an ultra-low specific speed centrifugal pump based on entropy generation theory and orthogonal design, in which the efficiency is improved and the entropy generation value is reduced. Chang et al. (2019) use entropy generation theory to investigate the type, size, and location of hydraulic losses in centrifugal pumps at different blade thicknesses. Qian et al. (2019) studied the internal flow of centrifugal pumps from energy distribution and entropy generation to find that entropy generation analysis could provide a basis for improving pump efficiency from another perspective. Lu et al. (2019) analyzed the internal flow state by the distribution of entropy generation in the pump-turbine and obtained the vortex generation mechanism. Mohammad et al. (2020) pointed out the advantages of entropy generation theory in determining the exact location and quantity of energy dissipation in PAT. Ren et al. (2021) and Guan et al. (2020) utilized entropy generation theory and the Q-criterion to investigate and analyze the hydraulic losses of over-flow components within centrifugal pumps. The entropy production theory can describe the system work loss, the optimization goal that reduces entropy production is to minimize the system work loss, while the whole system has a maximum working ability. Therefore, it can be used as an indicator and method to evaluate pump performance improvement.

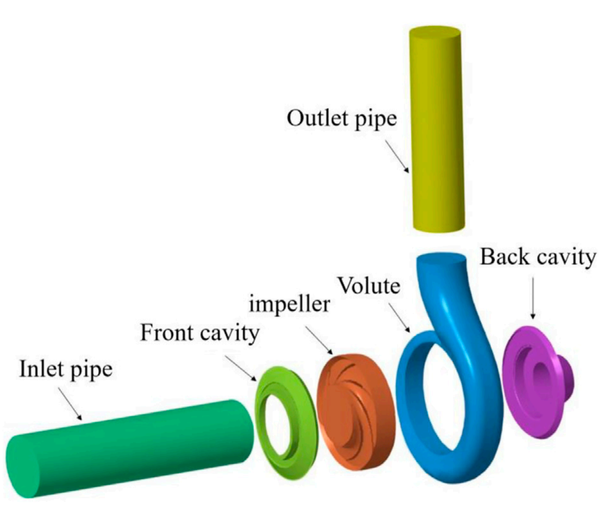

FIGURE 1
Centrifugal pump 3D model.

Undeniably, numerous scholars have extensively and deeply investigated pump optimization. However, centrifugal optimization based on entropy generation theory and particle swarm optimization (PSO) still needs further study. Therefore, based on previous research, this paper carried out research on the above-mentioned, and the results can provide a theoretical reference for improving the centrifugal pump stability. The remainder of this paper is organized as follows: in Section 2, numerical models are described. In Section 3, the centrifugal Pump Impeller has been optimized based on entropy

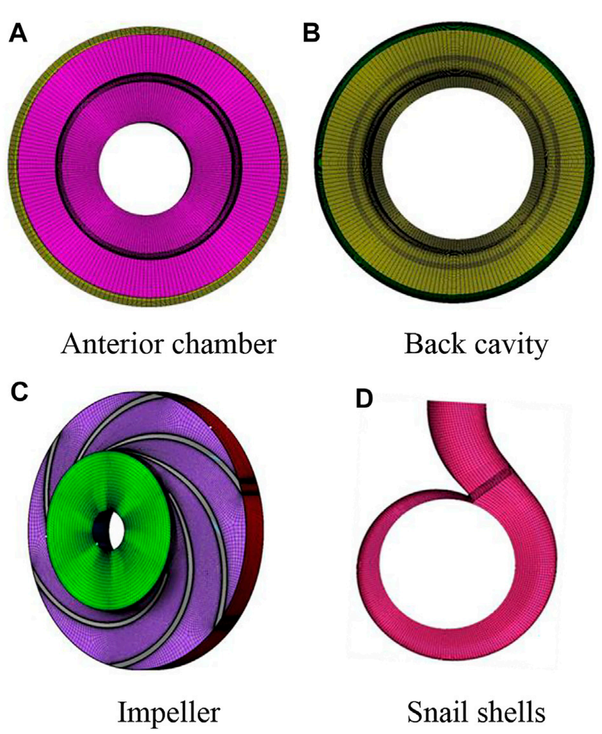

FIGURE 2
Centrifugal pump meshing.**(A)** Anterior chamber, **(B)** Back cavity, **(C)** Impeller, **(D)** Snail shells

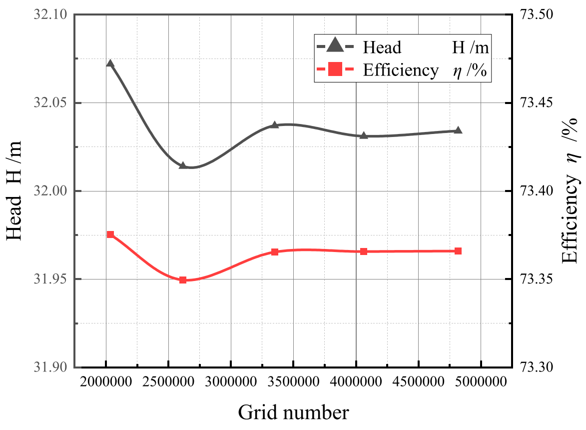

FIGURE 3
Grid independence verification.

TABLE 1 Essential parameters of the Centrifugal pump

Parameter	Symbol	Value
Flow rate	Q	100m3/h
Head	H	32m
Rotational speed	n	2950r/min
Efficiency	η	73%
Number of blades	Z	6

generation theory and particle swarm optimization. In Section 4, the energy losses of the original and optimized models are compared and analyzed based on the entropy generation theory.

2 Numerical method

2.1 Configuration of the calculation domain

The research object is the centrifugal pump developed by Jiangsu University. It uses Creo software for 3D modeling and adds inlet extensions and outlet extensions respectively to better match the actual flow conditions. Its components include an inlet pipe, front cavity, impeller, volute, back cavity, and outlet pipe, as shown in Figure 1. The main performance parameters of the model pump are shown in Table 1.

2.2 Meshing

The accuracy of the numerical results and the rate of convergence directly depend on the quality of the mesh, the quantity of meshes, and the division of the mesh. Turbogrid is used for the unstructured hexahedral meshing of the impeller, and ICEM is used for the structured hexahedral meshing of the volute, front and rear chambers, and inlet and outlet pipes respectively. In addition, to ensure that the turbulence model has y + requirements for the near-wall surface, the mesh at the near-wall surface of the overflow components is locally encrypted. Finally, each overflow component has then assembled. The components are then assembled. Figure 2 shows the meshing of the centrifugal pump.

2.3 Turbulence model

SST *k-ω* model combines the advantages of standard *k-ε* model and *k-ω* model to simulate the flow well. The application of *k-ω* model in the near wall region can well predict the adverse pressure gradient in the boundary layer, and the use of *k-ε* model in the far field region. SST k-ω model makes the main shortcomings of Wilcox turbulence model to be greatly

FIGURE 4
Real scenery of the performance test.

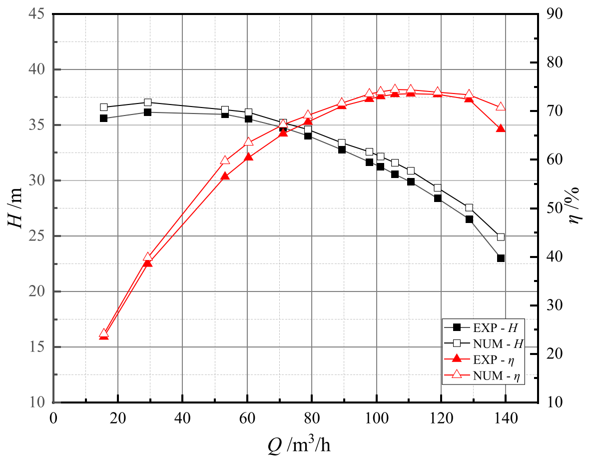

FIGURE 5
Comparison between numerical calculation value and test value.

resolved. It is also recognized as a more accurate model for turbulence simulation in the field of rotating machinery. Its relevant equations are as follows:

$$\frac{\partial(\rho k)}{\partial t} + \frac{\partial(\rho \bar{u}_i k)}{\partial x_i} = \tilde{P}_k - \beta^* \rho k \omega + \frac{\partial}{\partial x_i}\left[(\mu + \sigma_k \mu_t)\frac{\partial k}{\partial x_j}\right] \tag{1}$$

$$\begin{aligned}\frac{\partial(\rho\omega)}{\partial t} + \frac{\partial(\rho \bar{u}_l \omega)}{\partial x_i} &= \left[\frac{5}{9}F_1 + 0.44(1 - F_1)\right]\frac{1}{\nu_t}\tilde{P}_k - \beta\rho\omega^2 \\ &\quad + \frac{\partial}{\partial x_i}\left[(\mu + \sigma_\omega \mu_t)\frac{\partial \omega}{\partial x_i}\right] \\ &\quad + 2(1 - F_1)\frac{\rho\sigma_{\omega 2}}{\omega}\frac{\partial k}{\partial x_i}\frac{\partial \omega}{\partial x_i}\end{aligned} \tag{2}$$

The calculation of Reynolds stresses in the model is based on the Bossiness assumptions:

$$\overline{u_i' u_j'} = -\nu_t\left(\frac{\partial \overline{u_i}}{\partial x_j} + \frac{\partial \overline{u_j}}{\partial x_i}\right) + \frac{2}{3}k\delta_{ij} \tag{3}$$

where the turbulent kinetic energy viscosity ν_t is defined as

$$\nu_t = \frac{a_1 k}{\max\left(a_1\omega, \sqrt{2S_{ij}S_{ij}}\,F_2\right)} \tag{4}$$

where F_1 and F_2 are mixing functions; k is the turbulent kinetic energy, m^2/s^2; $\tilde{P}_k$ is the turbulence productivity, W/kg; ω is the turbulence frequency, 1/s.

2.4 Boundary condition

The calculation area in the numerical calculation is divided into two settings: stationary area and rotating domain, the rotating domain is set for the impeller domain of the centrifugal pump, the other over-flow components are stationary domain, the interface of the volute and the inlet and outlet sections connected to the impeller is set for the dynamic static interface, the rest interface is static-static interface. The boundary conditions of the wall are an adiabatic and non-slip wall. The calculation domain reference pressure is set to 1 atm, the inlet boundary condition is the mass flow inlet with a value of 27.7278 kg/s and the outlet boundary condition is the pressure outlet. Considering the accuracy of the results, the convergence accuracy is set to 10^{-5} and the number of iteration steps is 1000.

2.5 Grid independence verification

In addition to the grid quality, the overall grid amount also significantly affects the calculation's speed and accuracy. The right grid amount must be chosen for numerical calculations since a bigger grid quantity would lengthen

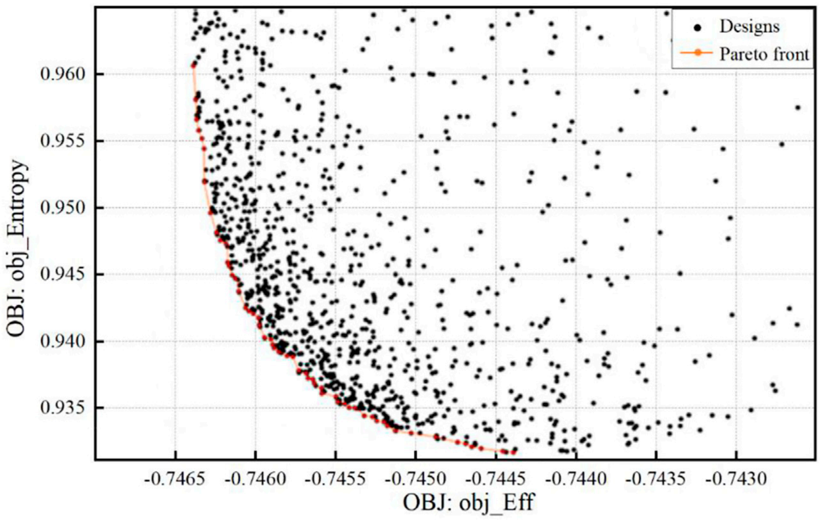

FIGURE 6
Pareto solution set.

calculation times and cost more in calculation resources while increasing calculation accuracy. Under the condition that the quality of the grid remains unchanged, five structural grid calculation schemes with different grid quantities are obtained by adjusting the number of grid nodes of the same topology. The same calculation conditions are set for the five different numbers of calculated model meshes and the pump head and efficiency are used as reference standards for comparison, and the results are shown in Figure 3. When the overall grid number of the model is greater than 3.35 million, the calculated head and efficiency do not vary much and tend to be stable, and the calculation error is less than 1%, which meets the requirements of the grid irrelevance test. Therefore, considering the calculation accuracy and the limitation of calculation resources, the overall grid number of 3.35 million is chosen for the subsequent numerical calculation.

2.6 Validation

To verify the accuracy of the numerical results, the prototype centrifugal pump is tested under the same flow conditions, and the test diagram is shown in Figure 4. The parameters of the measuring instrument are: power less than or equal to 400kW, pressure range from −0.1 MPa to 6.8 MPa, flow rate range from 0 m^3/h to 10000 m^3/h and total uncertainty of the measured value is 0.68%.

Figure 5 shows the comparison of the results obtained by the simulation and the experiment. As can be seen from the figure, the numerically calculated head and efficiency are slightly lower than the experimental values, with a maximum error of 3.89% and a minimum error of 1.65% for the head and a maximum error of 3.46% and a minimum error of 0.63% for the efficiency, both of which are within 5% of the error range, and the numerical simulation results are in high agreement with the experimental results.

3 Entropy generation theory and particle swarm arithmetic

3.1 Mathematical model of entropy generation theory

The entropy generation theory based on the second law of thermodynamics can be used to evaluate the energy loss in centrifugal pumps, including the direct dissipation entropy generation $\dot{S}'''_{\mathrm{D}}$ W/(m3·K) caused by the average velocity, the turbulent dissipation entropy generation $\dot{S}'''_{\mathrm{D}'}$W/(m3·K) caused by the fluctuating velocity and the wall entropy generation $\dot{S}''_{\mathrm{w}}$ W/(m2·K) caused by the wall shear stress. The expression is as follows.

Direct dissipation entropy generation:

$$\dot{S}'''_{\bar{\mathrm{D}}} = \frac{\mu}{T}\left[\left(\frac{\partial \bar{u}}{\partial y}+\frac{\partial \bar{v}}{\partial x}\right)^2+\left(\frac{\partial \bar{u}}{\partial z}+\frac{\partial \bar{w}}{\partial x}\right)^2+\left(\frac{\partial \bar{v}}{\partial z}+\frac{\partial \bar{w}}{\partial y}\right)^2\right] + 2\frac{\mu}{T}\left[\left(\frac{\partial \bar{u}}{\partial x}\right)^2+\left(\frac{\partial \bar{v}}{\partial y}\right)^2+\left(\frac{\partial \bar{w}}{\partial z}\right)^2\right] \tag{5}$$

Turbulent dissipative entropy generation:

TABLE 2 Comparison of parameters before and after optimization.

Parameters	θ1/°	θ2/°	θ3/°	θ4/°	Wrap/°	Entropy generation/W/K	Efficiency/%
Original	40	19.632	16.3	19.632	130	1.145	0.734
Optimization	39.63	21.85	40.42	16.02	127	1.074	0.755
Effects	-	-	-	-	-	↓5.41%	↑3.89%

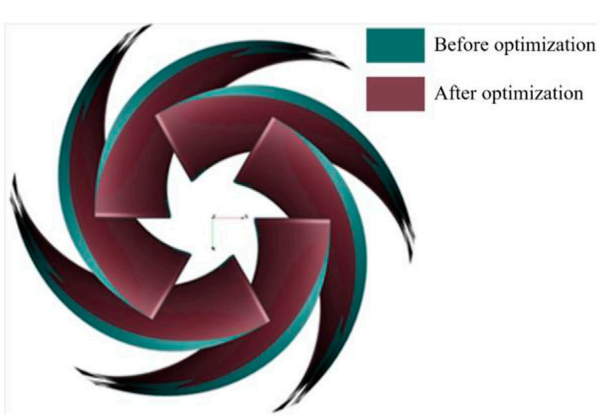

FIGURE 7
3D drawing of impeller before and after optimization.

$$\dot{S}'''_{D'} = \beta_{*}\frac{\rho\omega k}{T} \tag{6}$$

Wall entropy generation:

$$\dot{S}''_{\mathrm{w}} = \frac{\boldsymbol{\tau}_{\mathrm{w}} \cdot \boldsymbol{u}_{\mathrm{p}}}{T} \tag{7}$$

Where ū' v̄' w̄ are the mean velocity components in the *x*, *y*, and *z* directions, m/s; μ is the dynamic viscosity, Pa·s; the empirical coefficient $\beta = 0.09$, ω is the turbulent vortex frequency; k is the turbulent kinetic energy, m^2/s^2; τ_{w} is the wall shear stress, Pa; $\boldsymbol{u}_{\mathrm{p}}$ is the mean velocity vector at the center of the first grid layer near the wall, m/s.

Therefore, the entropy generation in the mainstream zone is:

$$\dot{S}'''_{D} = \dot{S}'''_{\bar{D}} + \dot{S}''_{D''} \tag{8}$$

Integral of each entropy generation in the corresponding region:

$$S_{\bar{\mathrm{D}}} = \int_{\mathrm{v}} \dot{S}'''_{\bar{\mathrm{D}}} \mathrm{d}V, S_{\mathrm{D}'} = \int_{\mathrm{v}} \dot{S}'''_{\mathrm{D}'} \mathrm{d}V, S_{\mathrm{w}} = \int_{\mathrm{s}} \dot{S}''_{\mathrm{w}} \mathrm{d}S \tag{9}$$

As a result, the total entropy generation in the computational domain is:

$$S_{\mathrm{D}} = S_{\bar{\mathrm{D}}} + S_{\mathrm{D}'} + S_{\mathrm{w}} \tag{10}$$

3.2 Particle swarm algorithms

Researchers solve multi-objective optimization problems mainly by transforming multi-objective optimization problems into single-objective optimization problems. However, when setting the weight of a single objective, it is often the weight set by the researchers themselves, which cannot accurately describe the optimization objectives. Therefore, many intelligent optimization algorithms have emerged for multi-objective optimization problems. At present, PSO (Bashiri et al., 2019) and genetic algorithm (GA) (Şahin et al., 2011; Zhou et al., 2012) are widely used. Because the search of each bird in PSO is directional, and the mutation in GA is random. To some extent, PSO is more efficient than GA. Therefore, this paper selects the PSO algorithm as the research.

Eberhart and Kennedy et al. (1995) proposed the PSO algorithm based on the evolutionary algorithm, and it is a simplified model inspired by the predatory behavior of bird flocks. The basic idea of PSO is that individuals in a swarm pass information to each other, collaborate, and then find the optimal solution through iteration. Each individual in the

TABLE 3 Comparison of entropy generation value before and after optimization under rated working conditions.

	Before optimization			After optimization			Total rate of cnage
	Impeller	Other components	Total value	Impeller	Other components	Total value	
S1/W/K	0.2453	0.0035	0.2488	0.2592	0.0034	0.2626	5.5%
S2/W/K	0.8999	0.8080	1.7079	0.8151	0.7088	1.5239	−6.3%
S3/W/K	0.1201	0.7185	0.8386	0.1246	0.6689	0.7935	−6.4%
S/W/K	1.2653	1.5300	2.7953	1.1989	1.3811	2.5800	−2.8%

Before optimization After optimization

Direct entropy generation S1

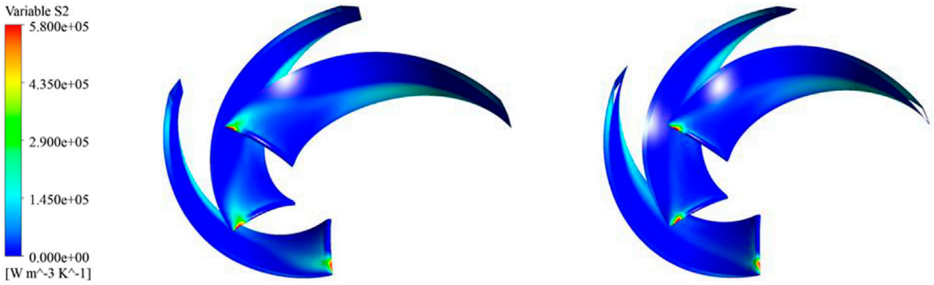

Before optimization After optimization

Turbulent entropy generation S2

Before optimization After optimization

Wall entropy generation S3

FIGURE 8
Different types of entropy generation cloud map.

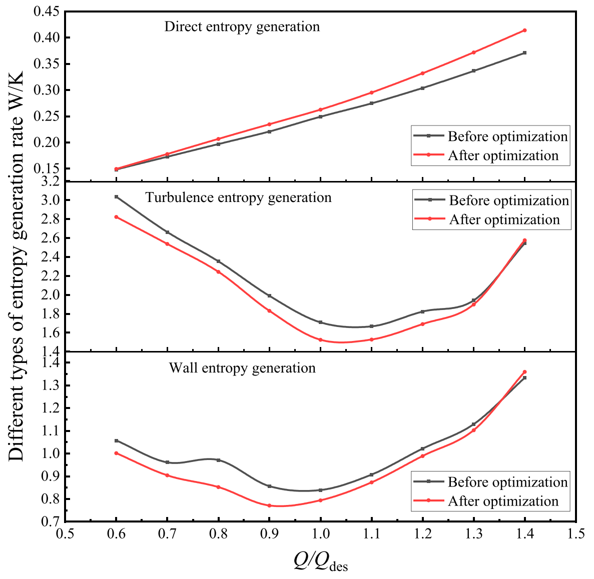

FIGURE 9
Comparison of different types of entropy generation in centrifugal pump before and after optimization.

solution space is referred to as a particle, and the individual is the solution in each optimization problem (Jordehi, 2015; Tang et al., 2021; Jain et al., 2022). The particle is given two properties: position and velocity. Moreover, the velocity and position of the particle are updated in the solution space according to the following equations.

$$v_i = \omega \times v_i + c_1 \times rand\,() \times (pbest_i - x_i) + c_2 \times rand\,() \times (gbest_i - x_i) \tag{11}$$

$$x_i = x_i + v_i \tag{12}$$

where $i = 1, 2, \ldots,$ N, N is the total number of particles; ω is the inertia factor, taking the value of 0.9; v_i is the particle velocity; *rand* () is a random number between 0 and 1; x_i is the current particle position; c_1, c_2 are the learning factors, taking the value of 2.

3.3 Definition of objective functions

In engineering application problems, there are often two or more objectives to be optimized, and in most cases, it is difficult to optimize all sub-objectives. Due to the contradictory relationship between each objective, when dealing with multi-objective optimization problems, it is necessary to make appropriate ' concessions ' for each sub-objective, to achieve overall consideration. A multi-objective optimization problem can be defined as:

$$\begin{aligned} &\min{}_x F(x) = [f_1(x), f_2(x), \ldots, f_K(x)] \\ &g_i(x) \geq 0, \quad i \in [1, M] \\ &h_j(x) = 0, \quad j \in [1, L] \end{aligned} \tag{13}$$

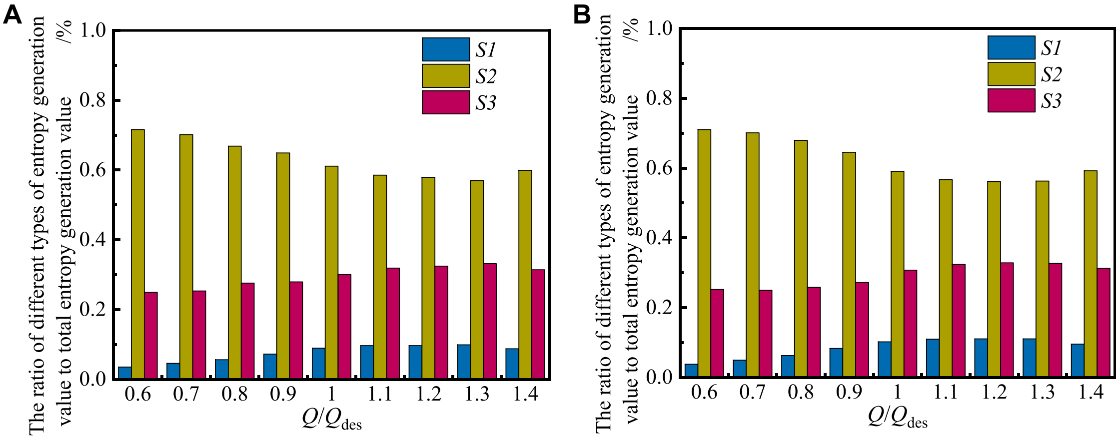

before optimization

after optimization

FIGURE 10
Ratio of different types of entropy generation to total entropy generation before and after optimization.**(A)** before optimization **(B)** after optimization.

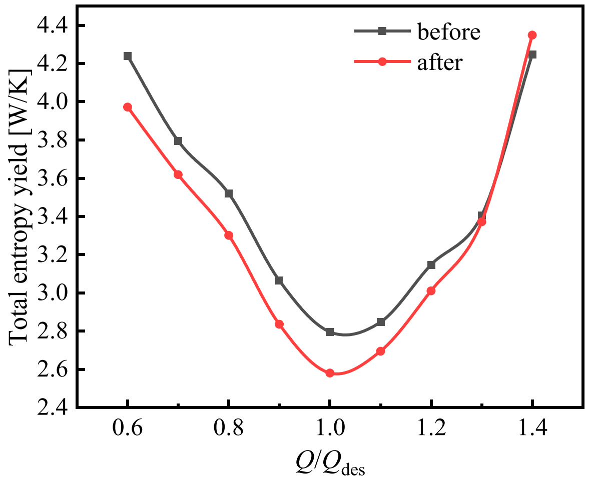

FIGURE 11
Total entropy generation value under different flows before and after optimization.**(A)** before optimization **(B)** after optimization.

Let D be the feasible region of the above multi-objective optimization problem:

$$D = \left\{x \middle| g_i(x) \geq 0, i \in [1, M], h_j(x) = 0, j \in [1, L]\right\} \quad (14)$$

In this paper, the first optimization objective of multi-objective optimization is to reduce the entropy production rate, and the second objective is to improve the efficiency of the centrifugal pump and meet the head as a constraint condition.

3.4 Optimization results

The multi-objective optimization of the approximate model is carried out by the particle swarm algorithm. The final Pareto solution set is obtained as shown in Figure 6. The figure depicts the efficiency as the horizontal coordinate and the entropy generation value as the vertical coordinate, corresponding to the maximum efficiency and the minimum entropy generation value of the optimization target. Respectively, and the points in the figure represent each optimization sample, and the points on the red line are the Pareto front distribution. The minimum entropy generation value. From this line, an optimization sample is selected as the final optimization solution, and the optimization model is determined.

After optimization by the particle swarm algorithm, a solution is found in the Pareto front solution that satisfied the head constraint, had a reduced entropy generation value, and had an increased efficiency value. The comparison of the parameters before and after optimization is shown in Table 2. As shown in the table, the optimized blades have no significant change in the blade inlet angle at the back cover (θ_1), the blade outlet angle at the back cover (θ_2) is increasing, the blade inlet angle at the back cover (θ_3) has increased the most, the blade outlet angle at the front cover (θ_4) has decreased and the wrap angle value (wrap) has decreased. Overall, the entropy value of the optimized centrifugal pump has decreased by 5.41% and the efficiency value has increased by 3.89%. The blade model of the centrifugal pump before and after optimization is shown in Figure 7.

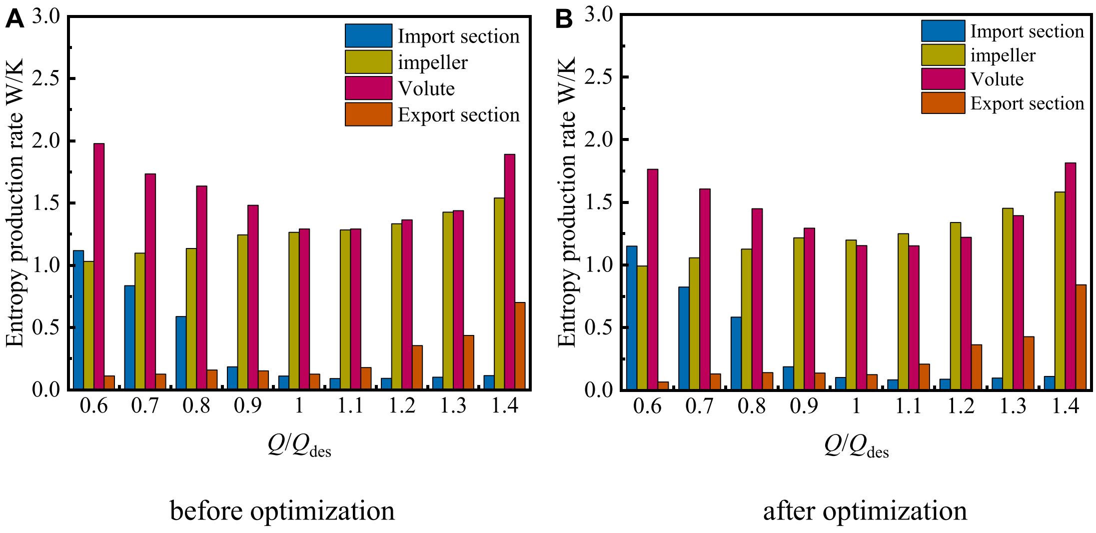

FIGURE 12
Entropy generation distribution of components under different working conditions.**(A)** before optimization **(B)** after optimization.

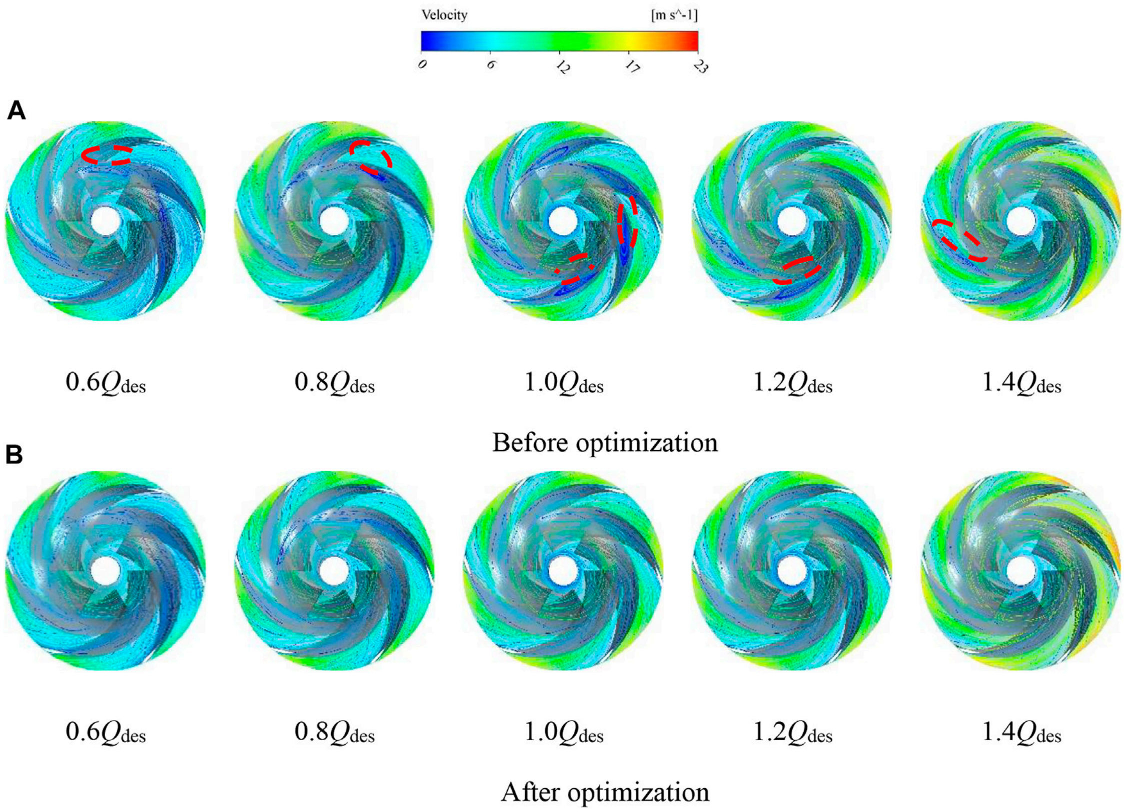

FIGURE 13
Velocity streamline diagram in impeller under different working conditions before and after optimization.**(A)** before optimization **(B)** after optimization.

4 Results and analysis

4.1 Distribution of the entropy generation

Table 3 shows the comparison of the entropy generation values of the different types of entropy within the centrifugal pump before and after optimization at rated operating conditions. As can be seen from the table, the total entropy generation value is reduced after optimization by 0.2153 W/K, and the losses are reduced by 2.8%, indicating that the flow performance of the optimized centrifugal pump has been improved. The value of the different types of entropy generation changed before and after the optimization, except for the direct entropy generation utilized by the time-averaged pulsation, which increases after the optimization, the turbulent entropy generation and the wall entropy generation decrease by 0.184 W/K and 0.0451 W/K respectively, and the losses decrease by 6.3% and 6.4% respectively. It can be seen that entropy generation due to turbulent dissipation and entropy generation to wall dissipation are optimized best, with both entropy generation values reduced by more than 6%.

Figure 8 shows the contour of the distribution of the different types of entropy generation on the blade at rated operating conditions. From the figure, it can be seen that the entropy generation values of each type are not in the same order of magnitude, the wall entropy generation level is much smaller than the direct entropy generation and turbulent entropy generation. While the direct entropy generation value is smaller than the turbulent entropy generation, the entropy generation is mainly distributed at the blade’s leading edge and trailing edge, which may be due to impact loss at the inlet and the existence of a jet wake at the outlet. The direct entropy generation is mainly distributed at the blade’s leading edge, and the turbulent entropy generation is mainly distributed at the leading edge against the tip of the blade. Then the wall entropy generation is mainly distributed at the leading and trailing edges of the blade.

To further analyze the trend of irreversible losses in the centrifugal pump before and after optimization, Figure 9 shows the variation of different types of entropy generation values with flow rate. It can be seen from the figure that the direct entropy generation value of the optimized model is larger than before, indicating that parameter optimization is not effective in

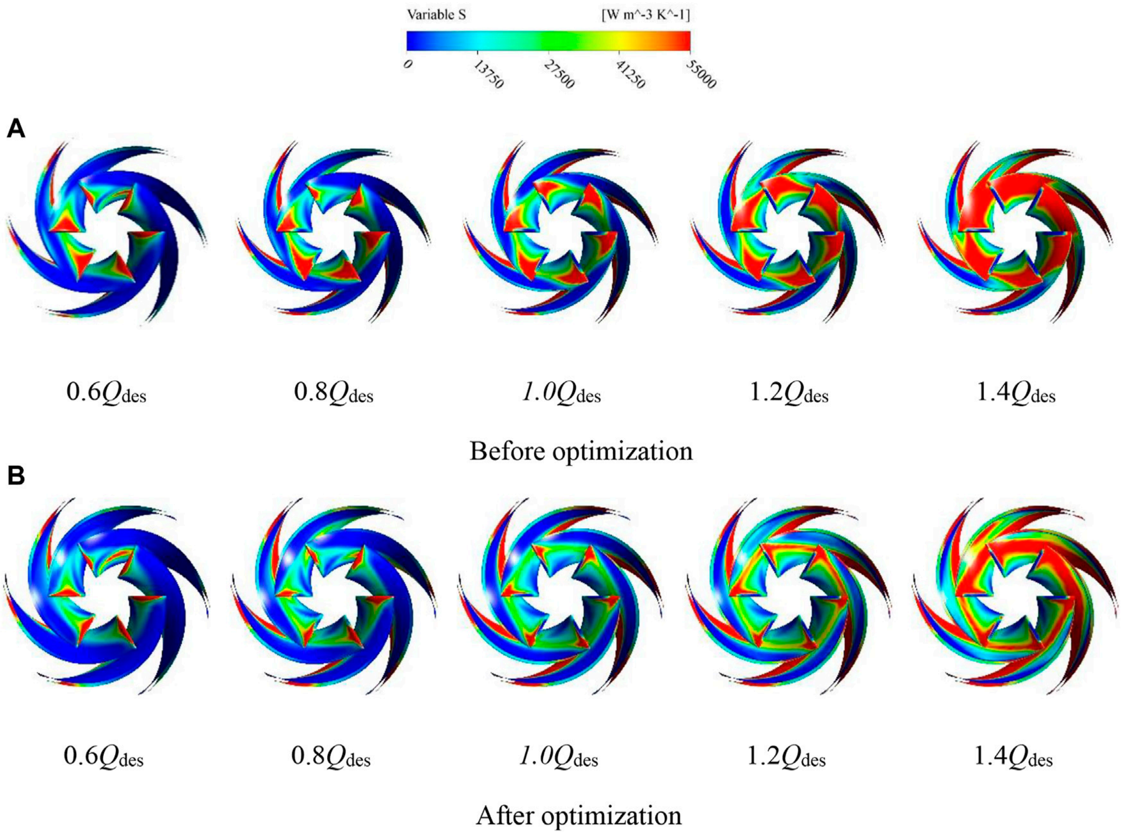

FIGURE 14
Distribution of blade entropy generation under different working conditions before and after optimization.**(A)** before optimization **(B)** after optimization.

optimizing the entropy generation of this category, while on the contrary, turbulent entropy generation and wall entropy generation both decrease; Both before and after optimization, the direct entropy generation value is positively proportional to the flow rate, and the entropy generation value increases as the flow rate increases. At low flow rates, the entropy generation due to turbulent dissipation decreases more rapidly and then increases slowly after rated operating conditions; the entropy generation to wall friction decreases slowly and then starts to increase rapidly after rated operating conditions.

Figure 10 shows the ratio of the different types of entropy generation to the total entropy generation before and after optimization. The histogram shows more clearly that turbulent losses due to turbulent dissipation in the impeller account for the largest proportion, followed by wall losses due to wall friction. Finally, direct dissipation is due to time averaging. Comparing Figure 10A and Figure 10B, the trend of the different types of entropy generation to total entropy generation ratio before and after optimization is the same. In summary, the turbulent entropy generation and wall entropy generation of the impeller of the centrifugal pump are optimized to a certain extent after the optimization, and the overall pump performance is improved.

4.2 Distribution of entropy generation in the overflow components

To investigate the relationship between the irreversible losses utilized by entropy generation and the flow rate in the centrifugal pump, CFX simulation software is utilized to numerically simulate the flow conditions from $0.6Q_{des}$ to $1.4Q_{des}$, and the total entropy generation value with a flow rate in the centrifugal pump is obtained as shown in Figure 11. As can be seen from the graph, the changing pattern of the relationship graph before and after the optimization is the same, the total entropy output is first falling and then rises when the flow rate from $0.6Q_{des}$ to the rated condition $1.0Q_{des}$, the total entropy output value in the pump is rapidly decreasing, when the flow rate from $1.0Q_{des}$ to $1.4Q_{des}$, the total entropy output value is increasing. The total entropy output decreases after optimization, especially from the small flow rate to the design condition. Then the total entropy generation value before and after optimization is the

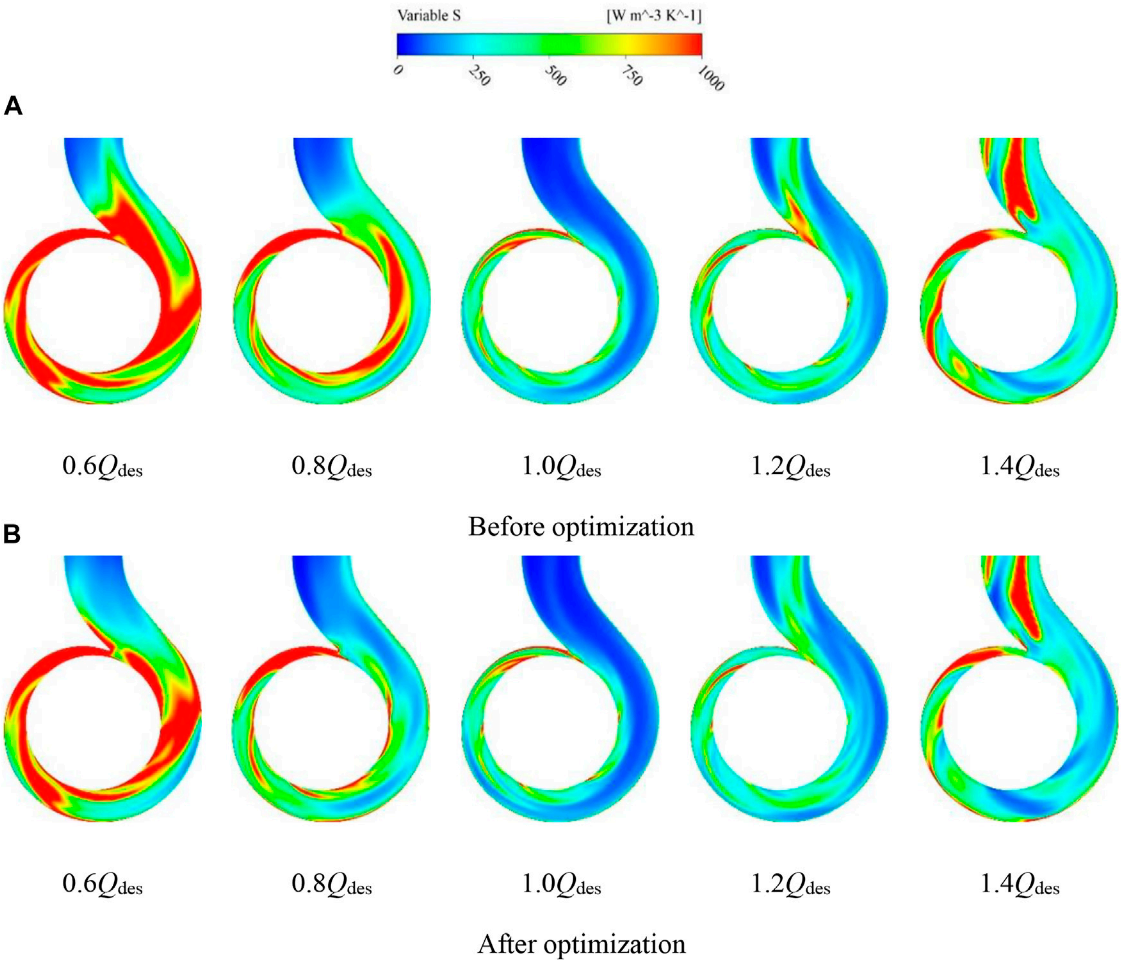

FIGURE 15
Entropy generation of volute cross-section at different working conditions before and after optimization.**(A)** before optimization **(B)** after optimization.

FIGURE 16
Different section display.

smallest at 1.0Q_{des}, which is consistent with the internal flow field flow of the centrifugal pump and further illustrates that the hydraulic performance of the centrifugal pump is related to the stability of the internal flow field flow.

Figure 12 shows the entropy generation values of each overflow component in the centrifugal pump under different operating conditions before and after optimization. It is seen from the figure that the entropy generation in the inlet section, impeller, and volute are relatively large at a low flow rate. In contrast, the entropy generation value for the outlet section is smaller. The value of the inlet section decreases under rated conditions, while the value of the outlet section increases. However, the impeller and volute are always the larger sections, with the entropy generation value of the impeller increasing slowly and the volute entropy generation value decreasing and then increasing. Figure 12B shows the entropy generation generated in each overflow component within the optimized centrifugal pump. Comparing Figure 12A; Figure 12B, the development of entropy generation in each overflow component with operating conditions after optimization is similar to that before optimization. At the rated condition, the

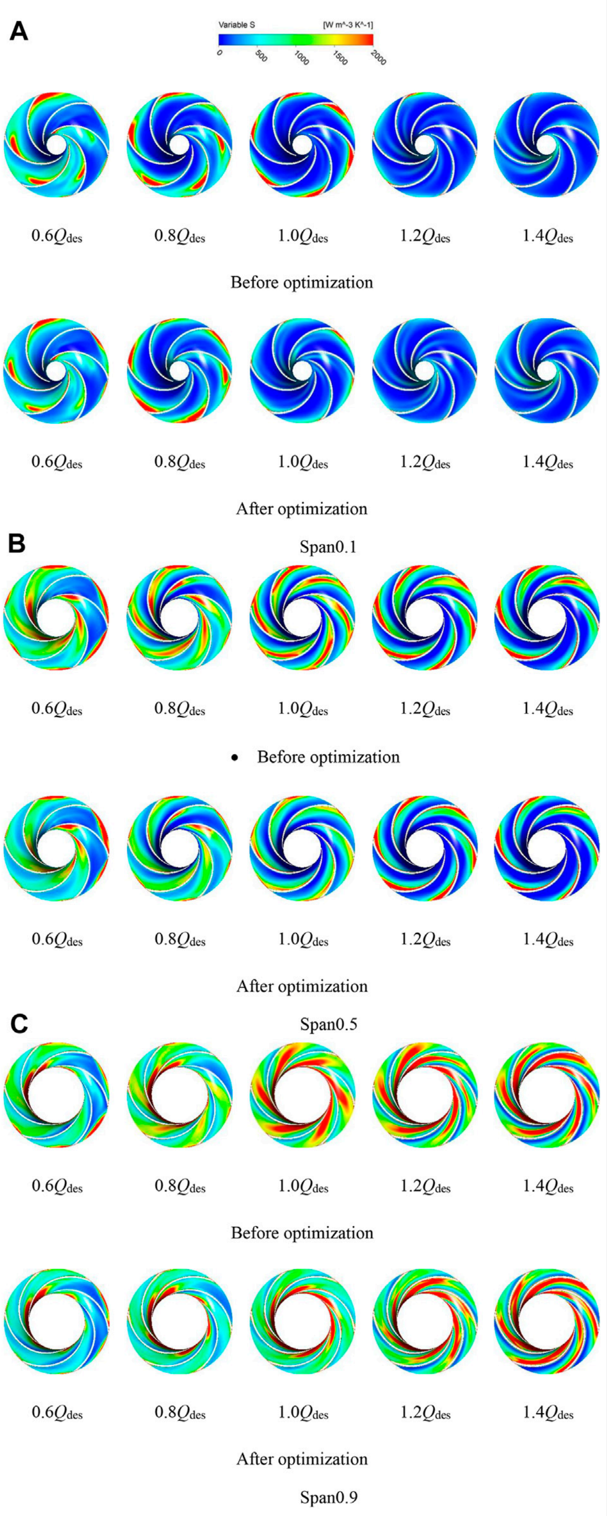

FIGURE 17
Entropy generation clouds of different sections before and after optimization.**(A)** Span0.1, **(B)** Span0.5, **(C)** Span0.9.

optimized impeller entropy generation is smaller, indicating a significant improvement in the optimization effect because of the reduction in turbulence entropy generation and wall entropy generation. The optimized impeller design significantly reduces the entropy generation value within the entire centrifugal pump, thereby reducing the hydraulic losses.

Figure 13 shows the velocity streamwise in the impeller runners before and after optimization. From the figure, it can be seen that the velocity streamlines in the different runners of the impeller are distributed differently, and the swirls occurring mainly in the middle of the runner before optimization. Under the same conditions, there are fewer swirls in the impeller runners after optimization, which means that the flow losses are smaller. According to existing research (Zhu, 2019), it is known that the vortex has a large turbulent kinetic energy, which leads to an increase in the entropy value utilized by turbulent dissipation in the passage. It can be deduced that where vortices occur, hydraulic losses are generated and that the hydraulic losses in the passage are mainly due to turbulent dissipation.

Figure 14 shows the contour of the distribution of entropy generation value on the blades of the centrifugal pump before and after optimization under different operating conditions. As seen above, the entropy generation value produced by the impeller and the entropy generation value produced by the volute are similar; both account for a larger proportion of centrifugal pumps. As shown in the figure, the blade on the entropy generation value increases with the flow rate increase. Moreover, the occupied area in the spread, especially the blade suction surface high entropy generation area from the initial blade leading edge to the blade trailing edge development. In the leading edge, there is a high entropy generation area, which may be due to the inlet's easy to produce a large number of vortex and backflow phenomena, resulting in energy loss, appear a high entropy generation area. As the flow rate increases, the impact loss of the fluid at the leading edge of the blade intensifies, resulting in a further deterioration of the energy loss from the leading edge of the blade to the middle of the blade. Under high flow conditions, the entropy generation loss in the impeller passage is higher under the dual action of high velocity and gravity. A high entropy generation region is formed at the edge of the blade suction surface. Comparing the entropy generation distribution before and after optimization, the high entropy generation region is significantly reduced, indicating that the flow conditions at the impeller inlet and in the runner are effectively improved and the losses are reduced.

To further analyze the distribution of entropy generation values in the volute, Figure 15 shows the distribution of entropy generation in the middle section of the volute of the centrifugal pump before and after optimization under different operating conditions. It can be seen from the graph that the entropy generation in the volute is mainly distributed at the volute inlet, the volute outlet, and the volute wall surface. As the flow rate increases from 0.6Q_{des} to 1.0 Q_{des}, the entropy generation distribution in the volute gradually decreases. As the flow rate increases from 1.0 Q_{des} to 1.4 Q_{des}, the entropy generation distribution in the volute gradually increases. The entropy generation in the volute section is minimized at the design flow rate. It is found that at 1.0 Q_{des}, the change in entropy generation in the volute is not significant before and after the optimization, because there are no obvious changes at the blade trailing edge. While the distribution of entropy generation of turbulent flow in the volute is reduced at the rest of the flow rate.

4.3 Entropy generation of impellers with different blade heights

As can be seen from the previous section, the over-flow component with the high entropy generation within the centrifugal pump is the impeller and the main over-flow component to be optimized is also the impeller, so an in-depth analysis of this component is necessary to determine the main cause of irreversible losses within the pump passage. Figure 16 shows the display of different cross-sections of the impeller. Three different cross-sections within the impeller runner are defined in the post-processing step, span 0.1 near the back cover plate, span 0.5 in the middle runner section of the impeller, and span 0.9 near the front cover plate.

Figure 17 shows the contour of total entropy yield distribution for each section of the impeller before and after optimization. Figure 17A shows the cross-section near the rear cover plate, where the high entropy generation is distributed in the middle and rear part of the blade suction surface at low flow rate conditions and moves towards the trailing edge of the blade as the flow rate increases until it disappears. At a flow rate of 1.0Q_{des}, comparing the entropy generation distribution on the span0.1 cross-section before and after optimization, the entropy generation after optimization is significantly lower than that before optimization, indicating that the flow condition in the impeller runner after optimization has improved and the hydraulic loss has been reduced. As seen from the contour of the entropy generation distribution in the middle section of the impeller in Figure 17B, the high entropy generation is mainly distributed at the impeller inlet, blade suction surface, and impeller outlet, and the loss in the impeller runner decreases as the flow rate increases. The optimized total entropy generation is the smallest at the nominal operating condition of 1.0 Q_{des}. Figure 17C shows the cross-section near the front cover of the impeller where the entropy generation increases with increasing flow rate. At low flow rates, the high entropy generations are mainly at the impeller inlet and the impeller outlet, and as the flow rate increases, the entropy generations spread from the blade pressure into the impeller outlet. In general, the closer to the front cover the higher the distribution of high entropy generation, and the more serious the flow losses.

5 Conclusion

In the present paper, the centrifugal pump impeller carries out optimization by combining entropy generation theory and particle swarm optimization. The energy losses of the original and optimized models are compared and analyzed. The following major conclusions have been drawn from the present study.

1) The result of optimization indicates that the entropy generation of the centrifugal pump is reduced by 5.41%, and the efficiency is increased by 3.89%. The numerical calculation value and experimental value of centrifugal pump performance are within the error range, indicating that the numerical simulation can well reflect the real flow of the internal flow field of the centrifugal pump.
2) Comparing the different types of entropy generation before and after optimization, it is found that the entropy generation utilized by turbulent dissipation and the entropy generation utilized by wall dissipation are optimized to be the most effective, with both entropy generation values reduced by more than 6%. Turbulent entropy generation and wall entropy generation are the important causes of hydraulic losses. Most of the losses within the impeller occur mainly at the blade's leading edge and the blade's trailing edge.
3) The total entropy generation value at the rated operating condition is the smallest, which further illustrates that the centrifugal pump operating away from the design conditions will lead to increased fluid instability in the pump, resulting in a decline in hydraulic performance. Optimizing the impeller of the centrifugal pump significantly reduces the internal flow loss and improves its efficiency of the centrifugal pump.
4) At low flow rates, the high entropy generations are mainly at the impeller inlet and the impeller outlet. The closer to the front cover the higher the distribution of high entropy generation, and the more serious the flow losses. The optimization content studied in this article can provide support for the optimization theory of centrifugal pump. At the same time, it provides a new idea for the

optimization of rotating machinery such as the mixed-flow pump.

Data availability statement

The raw data supporting the conclusions of this article will be made available by the authors, without undue reservation.

Author contributions

Conceptualization: HQ; Methodology: HQ, WL; Formal analysis: HQ, LJ; Investigation: HQ, RS, and ML; Writing–original draft preparation: HQ, WL; Writing–review and editing: HQ, WL, and LJ; Supervision: HQ, YY, and YP.

Funding

The work was sponsored by the Key International Cooperative research of National Natural Science Foundation of China (No.52120105010), National Natural Science Foundation of China (No.52179085), the National Key R&D Program Project (No.2020YFC1512405), China Postdoctoral Science Foundation (No.2022TQ0127), the Fifth "333 High Level Talented Person Cultivating Project" of Jiangsu Province, Funded projects of "Blue Project" in Jiangsu Colleges and Universities, "Belt and Road" Innovation Cooperation Project of iangsu Province (No.BZ2020068), Independent Innovation Fund Project of Agricultural Science and Technology in Jiangsu Province (No.CX(20)2037), Open Research Subject of Key Laboratory of Fluid and Power Machinery (Xihua University), Ministry of Education (LTDL-2022010).

Conflict of interest

The authors declare that the research was conducted in the absence of any commercial or financial relationships that could be construed as a potential conflict of interest.

Publisher's note

References

Ahmed, S., Khalid, M., Qing, X., Shehadeh, M. F., and Day, A. (2016). Performance analysis of wells turbine blades using the entropy generation minimization method. *Renew. Energy* 86, 1123–1133. doi:10.1016/j.renene.2015.09.045

Bashiri, M., Derakhshan, S., and Shahrabi, J. (2019). Design optimization of a centrifugal pump using particle swarm optimization algorithm. *Int. J. Fluid Mach. Syst.* 12 (4), 322–331. doi:10.5293/ijfms.2019.12.4.322

Chang, H., Shi, W., Li, W., and Liu, J. (2019). Energy loss analysis of novel self-priming pump based on the entropy production theory. *J. Therm. Sci.* 28 (2), 306–318. doi:10.1007/s11630-018-1057-5

Chen, L. G. (2012). Progress in entransy theory and its applications. *Chin. Sci. Bull.* 57 (34), 4404–4426. doi:10.1007/s11434-012-5477-4

Cong, X., Zhou, R., Han, Y., Zhang, F., and Chen, L. (2015). Optimization design of deep-well centrifugal pump based on CFX orthogonal test [J]. *Fluid Mach.* 43 (9), 22–25.

Eberhart, R., and Kennedy, J. (1995). IEEE, 39–43.A new optimizer using particle swarm theory MHS'95, Proceedings of the sixth international symposium on micro machine and human science, Beijing China, June 1995

Fan, B., Liang, Z., Fan, R., and Chen, S. (2022). Numerical study on entropy generation of the multi-stage centrifugal pump. *Entropy* 24 (7), 923. doi:10.3390/e24070923

Gong, R., Wang, H., Chen, L., Li, D., Zhang, H., and Wei, X. (2013). Application of entropy production theory to hydro-turbine hydraulic analysis. *Sci. China Technol. Sci.* 56 (7), 1636–1643. doi:10.1007/s11431-013-5229-y

Guan, H., Jiang, W., Yang, J., Wang, Y., Zhao, X., and Wang, J. (2020). Energy loss analysis of the double-suction centrifugal pump under different flow rates based on entropy production theory. *Proc. Institution Mech. Eng. Part C J. Mech. Eng. Sci.* 234 (20), 4009–4023. doi:10.1177/0954406220919795

Hou, H., Zhang, Y., Li, Z., Jiang, T., Zhang, J., and Xu, C. (2016). Numerical analysis of entropy production on a LNG cryogenic submerged pump. *J. Nat. Gas Sci. Eng.* 36, 87–96. doi:10.1016/j.jngse.2016.10.017

Hou, H., Zhang, Y., Zhou, X., Zuo, Z., and Chen, H. (2019). Optimal hydraulic design of an ultra-low specific speed centrifugal pump based on the local entropy production theory. *Proc. Institution Mech. Eng. Part A J. Power Energy* 233 (6), 715–726. doi:10.1177/0957650918825408

Jain, M., Saihjpal, V., Singh, N., and Singh, S. B. (2022). An overview of variants and advancements of PSO algorithm. *Appl. Sci.* 12 (17), 8392. doi:10.3390/app12178392

Jaluria, Y. (2009). Simulation-based optimization of thermal systems. *Appl. Therm. Eng.* 29 (7), 1346–1355. doi:10.1016/j.applthermaleng.2008.01.008

Ji, L., Li, W., Shi, W., Chang, H., and Yang, Z. (2020). Energy characteristics of mixed-flow pump under different tip clearances based on entropy production analysis. *Energy* 199–117447. doi:10.1016/j.energy.2020.117447

Ji, L., Li, W., Shi, W., Tian, F., and Agarwal, R. (2020). Diagnosis of internal energy characteristics of mixed-flow pump within stall region based on entropy production analysis model. *Int. Commun. Heat Mass Transf.* 117–104784. doi:10.1016/j.icheatmasstransfer.2020.104784

Ji, L., Li, W., Shi, W., Tian, F., and Agarwal, R. (2021). Effect of blade thickness on rotating stall of mixed-flow pump using entropy generation analysis. *Energy* 236–121381. doi:10.1016/j.energy.2021.121381

Jiang, J., Wang, R., Pezeril, M., and Wang, Q. A. (2011). Application of varentropy as a measure of probabilistic uncertainty for complex networks. *Chin. Sci. Bull.* 56 (34), 3677–3682. doi:10.1007/s11434-011-4697-3

Jordehi, A. R. (2015). A review on constraint handling strategies in particle swarm optimisation. *Neural Comput. Applic.* 26 (6), 1265–1275. doi:10.1007/s00521-014-1808-5

Lai, F., Huang, M., Wu, X., Nie, C., and Li, G. (2022). Local entropy generation analysis for cavitation flow within a centrifugal pump. *J. Fluids Eng.* 144 (10)–101206. doi:10.1115/1.4054467

Li, D., Wang, H., Qin, Y., Han, L., Wei, X., and Qin, D. (2017). Entropy production analysis of hysteresis characteristic of a pump-turbine model. *Energy Convers. Manag.* 149, 175–191. doi:10.1016/j.enconman.2017.07.024

Li, W., Ji, L., Li, E., Shi, W., Agarwal, R., and Zhou, L. (2021). Numerical investigation of energy loss mechanism of mixed-flow pump under stall condition. *Renew. Energy* 167, 740–760. doi:10.1016/j.renene.2020.11.146

Li, W., Ji, L., Shi, W., Hui, C., and Jin, M. (2016). Starting characteristic of mixed-flow pump based on quasi-steady state assumption[J]. *Trans. Chin. Soc. Agric. Eng.* 32 (7), 86–92.

Li, W., Li, E., Ji, L., Zhou, L., Shi, W., and Zhu, Y. (2020). Mechanism and propagation characteristics of rotating stall in a mixed-flow pump. *Renew. Energy* 153, 74–92. doi:10.1016/j.renene.2020.02.003

Li, X., Jiang, Z., Zhu, Z., Si, Q., and Li, Y. (2018). Entropy generation analysis for the cavitating head-drop characteristic of a centrifugal pump. *Proc. Institution Mech. Eng. Part C J. Mech. Eng. Sci.* 232 (24), 4637–4646. doi:10.1177/0954406217753458

Li, X., Zhu, Z., Li, Y., and Chen, X. (2016). Experimental and numerical investigations of head-flow curve instability of a single-stage centrifugal pump with volute casing. *Proc. Institution Mech. Eng. Part A J. Power Energy* 230 (A7), 633–647. doi:10.1177/0957650916663326

Lu, J., Wang, L., Liao, W., Wan, N., and Zin, A. (2019). Entropy generation analysis for vortex rope of a turbine model [J]. *J. Hydraulic Eng.* 50 (2), 233–241.

Majeed, K., Wang, W., Yuan, J., Zhao, J., Wang, Y., and Liu, J. (2019). Flow loss analysis of a two-stage axially split centrifugal pump with double inlet under different channel designs. *Proc. Institution Mech. Eng. Part C J. Mech. Eng. Sci.* 233 (15), 5316–5328. doi:10.1177/0954406219843573

Mohammad, M., Mohammad, H., Ali, M., and Riasi, A. (2020). A numerical study on mechanisms of energy dissipation in a pump as turbine (PAT) using entropy generation theory. *Renew. Energy* 162, 1036–1053. doi:10.1016/j.renene.2020.08.102

Pei, J., Yi, T., Yuan, S., Wang, W., and Wang, J. (2017). Cavitation optimization for a centrifugal pump impeller by using orthogonal design of experiment. *Chin. J. Mech. Eng.* 30 (1), 103–109. doi:10.3901/cjme.2016.1024.125

Qian, B., Chen, J., Wu, P., Wu, D. z., Yan, P., and Li, S. y. (2019). Investigation on inner flow quality assessment of centrifugal pump based on Euler head and entropy production analysis. *IOP Conf. Ser. Earth Environ. Sci.* 240 (9)–092001. doi:10.1088/1755-1315/240/9/092001

Ren, Y., Zhu, Z., Wu, D., Chen, A., and Wing, L. (2021). Flow loss characteristics of a centrifugal pump based on entropy generation [J]. *J. Harbin Eng. Univ.* 42 (2), 266–272.

Saha, S. K., and Mahanta, D. K. (2001). Thermodynamic optimization of solar flat-plate collector. *Renew. energy* 23 (2), 181–193. doi:10.1016/s0960-1481(00)00171-3

Şahin, A. Ş., Kılıç, B., and Kılıç, U. (2011). Optimization of heat pump using fuzzy logic and genetic algorithm. *Heat. Mass Transf.* 47 (12), 1553–1560. doi:10.1007/s00231-011-0818-4

Tang, J., Liu, G., and Pan, Q. (2021). A review on representative swarm intelligence algorithms for solving optimization problems: Applications and trends. *IEEE/CAA J. Autom. Sin.* 8 (10), 1627–1643. doi:10.1109/jas.2021.1004129

Yang, B., Li, B., Chen, H., and Liu, Z. (2019). Entropy production analysis for the clocking effect between inducer and impeller in a high-speed centrifugal pump. *Proc. Institution Mech. Eng. Part C J. Mech. Eng. Sci.* 233 (15), 5302–5315. doi:10.1177/0954406219843946

Zhang, F., Yuan, S., Wei, X., and Zhan, B. (2018). Study on flow loss characteristics of side channel pump based on entropy production. *J. Mech. Eng.* 54 (22), 137–144. doi:10.3901/jme.2018.22.137

Zhang, X., and Tang, F. (2022). Energy loss evaluation of axial flow pump systems in reverse power generation operations based on entropy production theory[J]. *Sci. Rep.* 12 (1), 1–19.

Zhou, J. S., Zhang, S. J., and Mao, P. Z. (2012). Performance optimization based on genetic algorithm of double suction centrifugal pump. *Adv. Mat. Res.* 468, 2565–2568. doi:10.4028/www.scientific.net/amr.468-471.2565

Zhu, K. (2019). *Study on internal flow and cavitation characteristics of centrifugal pump with jetting device [D]*. China: Zhejiang Sci-tech University.

frontiers | Frontiers in Energy Research

TYPE Original Research
PUBLISHED 05 January 2023
DOI 10.3389/fenrg.2022.1104248

Numerical analysis of the internal flow and pressure pulsation characteristics of a submersible tubular electric pump device

Yuting Lv[1], Ping Ding[1,2], Jinsheng Liu[2], Hengjun Ge[3], Fan Yang[1]* and Fangping Tang[1,4]

[1]College of Hydraulic Science and Engineering, Yangzhou University, Yangzhou, China, [2]Water Conservancy Project Construction Center of Yangzhou City, Yangzhou, China, [3]Yangzhou Surveying and Design Institute Co.,Ltd, Yangzhou, China, [4]Hydrodynamic Engineering Laboratory of Jiangsu Province, Yangzhou University, Yangzhou, China

OPEN ACCESS

EDITED BY
Leilei Ji,
Jiangsu University, China

REVIEWED BY
Kan Kan,
College of Energy and Electrical Engineering, China
Shibiao Fang,
Shenzhen University, China

*CORRESPONDENCE
Fan Yang,
fanyang@yzu.edu.cn

SPECIALTY SECTION
This article was submitted to Process and Energy Systems Engineering, a section of the journal Frontiers in Energy Research

RECEIVED 21 November 2022
ACCEPTED 01 December 2022
PUBLISHED 05 January 2023

CITATION
Lv Y, Ding P, Liu J, Ge H, Yang F and Tang F (2023), Numerical analysis of the internal flow and pressure pulsation characteristics of a submersible tubular electric pump device.
Front. Energy Res. 10:1104248.
doi: 10.3389/fenrg.2022.1104248

In order to clarify the non-constant flow characteristics of the impeller and bulb body of the submersible tubular electric pump device, the entire flow rate conduit of the pump device is numerically calculated using the numerical simulation method, focusing on the analysis of the non-constant flow field characteristics of the guide vane body and bulb body and the time−frequency variation law of the pressure pulsation, and the results of the physical model testing confirm the validity of the numerical simulation. The findings demonstrate that the impeller of a submersible tubular electric pump is mostly responsible for the impeller's inlet pressure pulsation, and the number of impeller blades to the number of peaks and valleys is consistent. Under the high flow rate condition of 1.2 Q_d, the pressure fluctuation in the impeller inlet, between the impeller and the guide vane is small, and the main frequency is located at three times the rotational frequency, and the pressure pulsation at the outlet of the guide vane body has no obvious pattern and small amplitude. As the flow rate increases, the peak value of pressure pulsation at each monitoring point in the characteristic section of the pump device gradually decreases. The pressure pulsation peak value varies widely, ranging from 0.058 to 0.15, at each monitoring location of the impeller inlet. The peak value of pressure pulsation at each monitoring point of the impeller outlet fluctuates less due to the change of flow rate. The size and scale of the omega vortex structure in the guide vane body at different moments of the same cycle is small, and the number of vortex structures from the guide vane body inlet to the outlet direction shows a gradual increase in the trend; with a rise in flow rate, there is a tendency for the velocity and deflection angle of the guide vane body outlet and bulb body outlet surface to decrease.

Abbreviations: δ, relative error; ε, absolute error; H, head; η, efficiency; n, rotational velocity; Q_d, design flow rate; D, nominal impeller diameter; T, rotational period; C_p, pressure coefficient; P, instantaneous pressure; $\bar{P}$, average pressure; ρ, water density; N, number of grid nodes on the coupling surface; Q, flow rate; f_n, impeller rotational frequency; γ, deflected flow angle; V_t, lateral velocity; V_z, axial velocity; u_2, circumferential velocity of the impeller outlet; V_i, instantaneous velocity; V_a, average velocity; CFD, computational fluid dynamics; TKE, turbulent kinetic energy; SST, shear stress transport; FFT, fast Fourier transform.

KEYWORDS

submersible tubular electric pump, pump device, flow field, pressure pulsation, numerical simulation

1 Introduction

The installation method of submersible tubular electric pump device is horizontal or tilting type, which is mostly applied to river water lifting and urban drainage projects, which mainly has the following characteristics: 1) the inlet and outlet water conduit is straight, the water flow is stable, and the total hydraulic loss of the flow rate conduit is small; 2) compared to the conventional bulb tubular pump, the bulb body volume is smaller, and the device has a high hydraulic efficiency; and 3) the motor of the submersible tubular electric pump device can run in water, which is simple to operate, generates low noise, does not produce high temperature, and has good cavitation performance. In the 1970s, Japan used submersible tubular electric pump devices in the agricultural government Sijue Lujin pumping station and other large pumping station projects. Early 21st century, China began to develop large submersible tubular electric pumping devices and promote the application of large submersible tubular electric pumping devices in 2008 for the first time in China's Jiangsu Province, Tongyu River North Extension Water Supply Project irrigation River North, Shan Hou Henan pumping station. In good operating condition, the device has an efficiency of up to 79%, changing the *status quo* of the traditional tubular pumping device's low efficiency (Xie et al., 2010). Optimizing the relevant parameters of the impeller and guide vane is of great significance to improve the hydraulic performance of the submersible tubular electric pump.

So far, many scholars at home and abroad have carried out some research on the submersible tubular electric pump device. The research methods mainly use CFD technology and model tests (Wang et al., 2019a; Munih et al., 2020; Yang et al., 2022a) to study the internal and external characteristics and pressure pulsation of the pump device. The three-dimensional steady numerical analysis and structural optimization of the flow field in each flow structure (Lu et al., 2018; Arocena et al., 2021; Sun et al., 2021) have achieved fruitful research results. Zhang et al. (2014) investigated the three-dimensional turbulent flow and the pressure fluctuation in a submersible axial-flow pump by adopting the RNG k-ε turbulence model and the SIMPLEC algorithm, with which the pressure pulsation distribution of the impeller inlet and outlet was obtained (Ji et al., 2021). The influence of shaft position on the performance of tubular pump devices was studied by three-dimensional steady and unsteady numerical simulation combined with a model test. The results showed that the hydraulic performance of the two inlet conduits was excellent, and the hydraulic loss was close. In the study by Xiao et al. (2019), two-dimensional (2D) particle image velocimetry (PIV) was applied to test the blood pump under three different conditions, and the results show that under the medium rotation velocity condition, the flow field is stable and the velocity distribution is even (Choi et al., 2008). The variation of turbine performance with blade angle is analyzed by CFD. The results show that the inlet and outlet angles of the runner blade have great influence on turbine performance. In the study by Miyabe et al. (2006), dynamic particle image velocimetry and pressure fluctuation measurement were used to investigate the unstable flow of a mixed-flow pump with a vane diffuser. It is concluded that the key to improving the positive slope of the flow-head curve is to suppress the growth of the vortex at the diffuser inlet.

Due to the pump's actual operation's high-velocity rotation, it is very easy for the water flow to produce flow separation, vortex, secondary flow, and other complex flow phenomena (Khalifa et al., 2011). The flow characteristics of the pump device and the flow state of the fluid in the pump have a great influence on its operational reliability and performance stability. Pressure pulsation is one of the main causes of vibration and noise in pump devices, and some scholars have carried out studies on the internal pressure pulsation characteristics of pump devices of different structural forms (Chu et al., 1995; Li et al., 2018; Ji et al., 2020; Yang et al., 2021a). Li et al. (2021) examine the cavitation performance of an LNG submerged pump and the pressure pulsation characteristics during cavitation excitation using CFD analytical technologies. Jin et al. (2019) present an investigation of external flow characteristics and pressure fluctuation of a submersible tubular pumping system by using a combination of numerical simulation and experimental methods. In the work by Shi et al. (2021), CFD is used to compare the difference in pressure pulsation characteristics between a full tubular pump and an axial flow pump. The results show that the pressure pulsation at the inlet of the impeller of the full tubular pump is larger than that of the axial flow pump, while the pressure pulsation of the full tubular pump is smaller than that of the axial flow pump. In the study by Zhang et al. (2015), in order to find a practical way to lower high pressure pulsation levels, a slope volute is explored. The results demonstrate that unique pressure pulsation peaks at fBPF, together with non-linear components, are captured. Results demonstrate that distinct pressure pulsation peaks at fBPF are caught, together with non-linear components. In the study by Al-Obaidi (2020), the influence of different blade numbers on the flow and pressure pulsation in the pump is studied by computational fluid dynamics technology. The impeller blade has a great influence on the pressure, shear stress, magnitude velocity, and axial velocity.

The internal flow of a submersible tubular electric pump device is a complex three-dimensional non-constant turbulent flow, and the water flows through the impeller to obtain energy, so the numerical simulation of the internal flow characteristics of the pump device can help to optimize the pump device structure. This study focuses on the numerical simulation of the internal non-constant flow of the submersible tubular electric pump device at different flow rate conditions by CFD technology, focusing on the time–frequency characteristics of the pressure pulsation in the impeller and guide vane domain to study the internal flow characteristics of the submersible tubular electric pump device, and it elaborates the development law of the pump device's internal flow characteristics and vortex structure at various points in order to optimize the pump device's structure and assure the safety of the pumping station.

2 Calculation object and numerical method

2.1 Three-dimensional model establishment of the pump device

The submersible tubular electric pump device consists of five parts: straight inlet conduit, impeller, guide vane body, bulb body, and straight outlet conduit. In order to ensure the full development of the water flow into the inlet conduit during the numerical simulation and to be closer to the actual inlet flow field, an inlet extension section was set in front of the straight pipe inlet conduit with a length of 1.0 times the length of the inlet conduit and a height of 1.2 times the height of the inlet conduit; the outlet conduit extension section was set at the outlet of the straight outlet conduit, and its dimensions were set the same as the inlet extension section. Unigraphics NX modeling software was used to model the straight inlet conduit, bulb body, and straight outlet conduit in three dimensions. The complex shape of the blade in the meshing of the rotating equipment may be produced by ANSYS TurboGrid software, so ANSYS TurboGrid was used to provide structured mesh for the impeller domain and guide vane domain. The impeller model is ZM25N, the nominal diameter of the impeller is 300 mm, the rotational velocity is 1,352 r/min, and the impeller nD value is according to the hydraulic performance of the selected ZM25N impeller of the submersible tubular electric pump device and the operating parameters such as the design head and design flow rate of the pump device. The number of impeller blades is 3, the top clearance is 0.20 mm, the number of guide vanes is 5, and the axial distance between the impeller and the guide vanes is $0.25D$. The length of the straight inlet conduit is $6.01D$, the height of the inlet conduit is $1.72D$, and the width of the inlet conduit is $2.21D$. The length of the straight outlet conduit is $5.42D$, the height of the outlet conduit is $1.72D$, and the width of the outlet conduit is $2.21D$; the length of the bulb body is $1.67D$, the bulb body is supported on the support segment, and the cross-sectional shape of the support is stream-lined; the number of support strucutre is five evenly spaced in the flow conduit, with a length of $0.58D$, a width of $0.025D$, and an average height of $0.26D$. Figure 1 depicts the submersible tubular electric pump device's primary geometric measurements, and Table 1 presents the pump device's primary calculation parameters.

2.2 Calculation method and boundary conditions

The SST-CC turbulence model can better handle the transport of turbulent shear stress in the inverse pressure gradient and separation boundary layer (Chalghoum et al., 2018; Smirnov and Menter, 2009) and predict the flow separation in the inverse pressure gradient region by using ANSYS CFX to perform three-dimensional non-constant numerical values of the internal flow field of a submersible tubular electric pump device at different flow rate conditions. Also, the turbulence model has been well applied in rotating mechanical energy performance and three-dimensional flow field prediction (Tao et al., 2014; Yang et al., 2022b), so this study uses the SST-CC turbulence model with rotation and curvature-adjusted vortex viscosity model. Pressure is the inlet boundary condition, the reference total pressure size is set to 1 atm, and the inlet surface of the inlet extension is designed to have the entire pressure. The outlet condition is mass flow rate, which is set on the outlet surface of the outlet extension. The impeller, guide vane body, bulb body, and the solid wall surface of the flow rate conduit are set as no-slip boundary conditions, and the intersection surface between the impeller and the inlet water conduit and guide vane body is set as the dynamic–static intersection interface, as shown in Table 2, and the transient frozen rotor intersection interface is used for non-stationary flow field calculation. Referring to the time step setting of the non-constant numerical calculation in the literature (Wang, 2020; Yang et al., 2022c), the time step for the non-constant calculation of the submersible tubular electric pump device is set to 3.6988×10^{-4} (1/120 of the impeller rotational period), and one time step is set for every 3° of impeller rotation, 8 calculation periods are selected for a total of 960 steps, and the total time is set to 0.35552 s. The range of flow rate conditions is calculated by changing the inlet flow rate and monitoring the inlet and outlet pressure, the efficiency and head under different flow rate conditions are calculated, and 1.0×10^{-5} is the convergence accuracy setting.

3 Comparison of mesh dissection and model test validation

3.1 Mesh dissection and irrelevance analysis

There are two main types of mesh segmentation methods: structured and unstructured. The structure of the pump device is

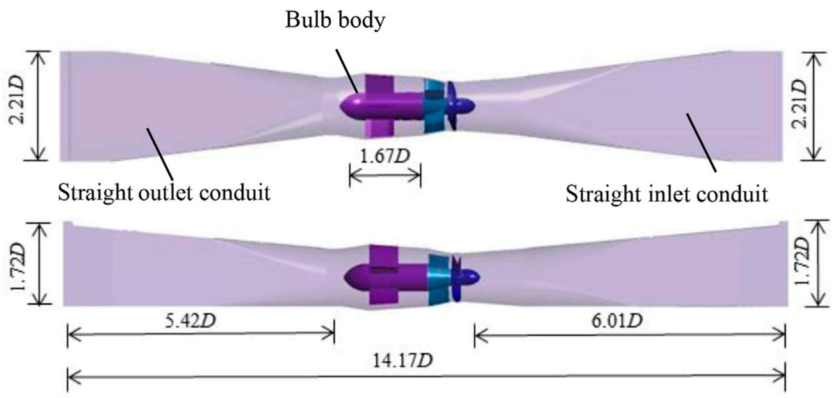

FIGURE 1
Dimensional drawing of the whole submersible tubular electric pump device.

TABLE 1 Main parameters of the submersible tubular electric pump device.

Parameter	Value
Design flow	300 L/s
Design head	2.84 m
Rotational velocity	1,352 r/min
Nominal diameter of impeller	300 mm
Number of impeller blades	3
Number of guide vane blades	5
Blade angle	0°

TABLE 2 Setting of boundary conditions.

Position	Boundary condition
Pump device boundary conditions	——
Pump device inlet extension section	Pressure
Pump device outlet extension section	Mass flow
Solid wall	Non-slip wall
Interface on both sides of impeller domain	——
Steady state	Stage
Transient state	Transient rotor–stator
Transient solution settings	——
Time step	3.6988×10^{-4} s
Total time	0.35552 s

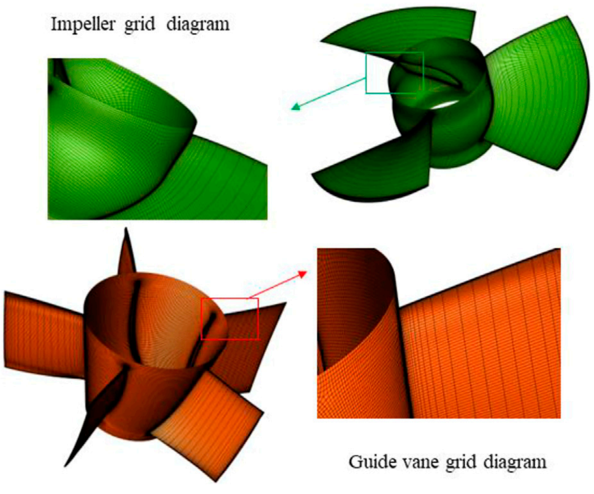

FIGURE 2
Grid of impeller and guide vane.

complex, and the block mesh separation strategy is used. The complicated shape of the blades in the mesh section of rotating machinery can be generated by ANSYS TurboGrid software as a high-quality structured mesh, the fluid domain of the impeller and guide vane body is separated by structured mesh through TurboGrid, the inlet and outlet water conduits are generated in ICEM CFD software to generate structured mesh, and the bulb body's fluid domain is dissected by ICEM CFD software with an unstructured grid, the accuracy of the internal flow of the pump device's, and the Jacobi determinant value is used to judge the grid quality, and the grid quality of each overflow structure is greater than 0.6. The impeller and impeller grid y^+ are within 20. This satisfies the near-wall grid quality requirements of the SST-CC turbulence model (Yang et al., 2021b). The impeller and guide vane body meshes of the submersible tubular electric pump device are shown in Figure 2.

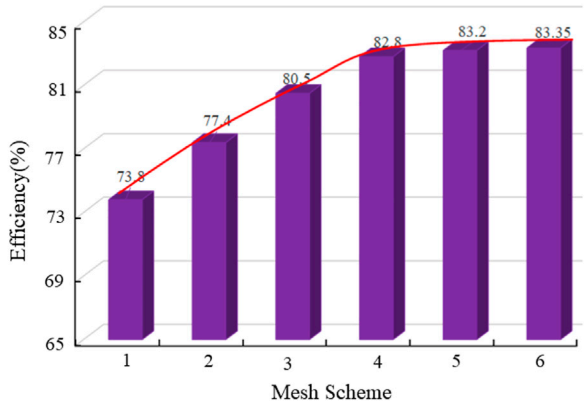

FIGURE 3
Grid number irrelevance.

In the numerical simulation calculation of the internal flow of the pump device, the grid dissection nodes contain physical quantities. Thus, while in theory, a larger number of grid nodes would result in more precise calculations, in fact, the accuracy of the calculations is not in a linear relationship with the number of grids. When the number of grids reaches a certain value, the increase in calculation accuracy tends to be stable. In order to select a suitable number of grids for the pump device, the predicted values of the pump device efficiency at seven grid quantities were selected as the basis for the evaluation of the grid quantities, and the grid quantities of schemes 1 to 6 were 2514527, 3345478, 4224561, 5143695, 5854427, and 7185921, respectively. The results of the calculation of the efficiency of the device are shown in Figure 3. When there are 5.85 million grids, the efficiency of the pump device changes noticeably more slowly. The absolute error of the device efficiency of scheme 4 and scheme 5 is 0.4%, the absolute error of the device efficiency of scheme 5 and scheme 6 is 0.15%, and the absolute difference of the pump device efficiency of scheme 4, scheme 5, and scheme 6 is less than 0.5% to meet the accuracy requirements; this study adopts 5.85 million grids. The submersible tubular electric pump device is numerically simulated using the grid number of scheme 5.

3.2 Test bench and pump device predicted performance verification

3.2.1 Test bench and test contents

To verify the validity of the numerical calculations, the energy performance of the submersible tubular electric pump device was tested on a high-precision hydro-mechanical test bench at the Key Laboratory of Hydraulic Power Engineering in Jiangsu Province, China, as shown in Figure 4. The pump device's physical model test used an impeller and guide vane with the same geometry as the numerically calculated model, and the head, flow rate, and torque of the pump device were measured under different flow rate conditions at a blade placement angle of 0° and a rated rotational speed of 1,352 r/min. A reputable metrology calibration department in China confirmed the system uncertainties of the test equipment, and Table 3 lists the system uncertainties of each piece of test equipment. The system uncertainty of the test bench and pump device energy performance efficiency is 0.274%, the random uncertainty of the pump device efficiency test is 0.11%, and then the comprehensive uncertainty of the test bench is 0.296%. The comprehensive uncertainty of the efficiency test is in line with the requirements of the water industry standard of the People's Republic of China "Code of practice for model pump and its installation acceptance tests (SL140-2006)."

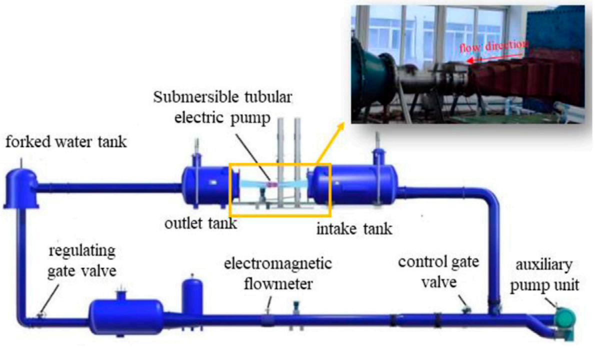

FIGURE 4
High-precision hydro-mechanical test bench.

3.2.2 Numerical calculation of energy characteristic results

The head ~ flow rate and efficiency ~ flow rate curves of the submersible tubular electric pump device at different flow rate conditions are shown in Figure 5. The trends of flow rate ~ efficiency curve and flow rate ~ head curve of numerical simulation and model test are consistent, and the test results of head and efficiency in the high-efficiency zone, flow rate 280 L/s~320 L/s, are in good agreement with the outcomes of the numerical simulation. In the range of calculated flow rate conditions 200 L/s~400 L/s, the maximum relative head error is 7.6 and the maximum absolute efficiency error is 2.5, all of which are within acceptable bounds. Indicating that the numerical calculation results are realistic and reliable and can accurately reflect the internal flow characteristics of the pump device, the numerical calculation predicts the overall agreement between the energy performance results of the pump device and the physical model test results. For the purpose of analysis, three characteristic flow rate conditions were selected, namely, 1.0Q_d (Q = 300 L/s) for the design flow rate condition, 1.2 Q_d (Q =

TABLE 3 Systematic uncertainty of the test equipment.

Item	Equipment	Model	Systematic uncertainty
Flow rate	Electromagnetic flowmeter	E-mag DN400	±0.22%
Head	Velocity torque sensing differential pressure transmitter	EJA110A	±0.015%
Torque	Speed and torque sensor	ZJ 500	±0.10%
Rotational speed			±0.05%

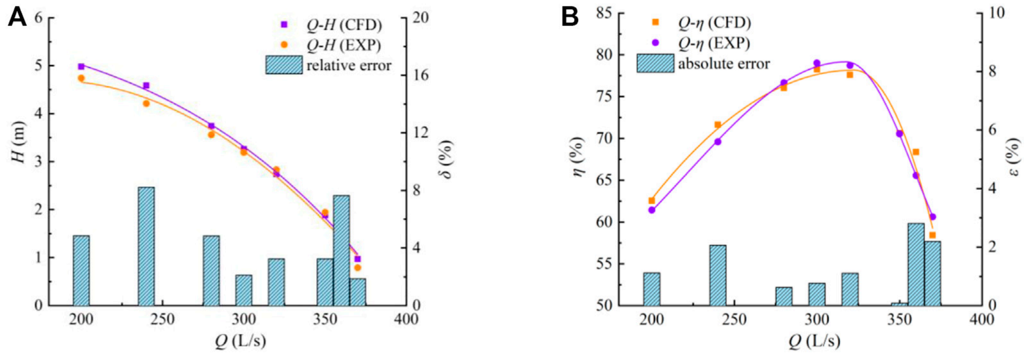

Flow rate ~ Head

Flow rate ~ Efficiency

FIGURE 5
Comparison between numerical simulation and test results of energy performance parameters of the pump device.

360 L/s) for the high flow rate condition, and 0.8 Q_d ($Q = 280$ L/s) for the low flow rate condition.

4 Results of calculations and analyses

4.1 Analysis of the internal flow characteristics of the pump device

Omega criterion has a low perception of moderate threshold change compared to traditional vortex identification methods, and it is able to precisely capture the intricate weak and strong vortices inside each overflow part of the pump device (Liu et al., 2016; Wang et al., 2019b). In this study, the omega criterion was used to analyze the vortex structure of the guide vane domain at $1.0Q_d$ operating conditions, and the vortex structure inside the guide vane is shown in Figure 6, using turbulent kinetic energy (TKE) for a threshold value of 0.68 equivalent surface coloring to reflect the intensity of the vortex structure (Hunt et al., 1988; Jeong and Hussain, 1995). The vortex structure of the guide vane body at three different characteristic moments in one rotational period *(T)* under the low flow rate condition mainly exists at the position where the hub, rim, and blade are connected, and the influence of the guide vane on the fluid flow pattern is easy to form a vortex at the edge of the blade. The number of vortex structures from the guide vane body inlet to the outlet direction shows a gradual increase in the trend. With the same rotational period at different moments, the change in size and scale of the vortex structure is small, the shape of the vortex structure overall is a long strip, and there is obvious continuity. The guide vane body's exit rim is where the high turbulence energy area is concentrated, and its value is primarily between 0.5 and 0.8.

The guide vane body of the submersible tubular electric pump device plays a role in changing the flow direction and recovering kinetic energy, and the vane blade of the guide vane body has a great influence on the flow pattern of water. Bulb body support is an important over-flow component inside the submersible tubular electric pump device, and a reasonable shape of the support can improve the flow pattern, reduce the amount of water circulation, and improve the efficiency of the pump device. The water flow at the outlet of the guide vane has a certain residual velocity circulation, which induces the spiral operation of the water flow inside the flow conduit and affects the hydraulic loss of the outlet conduit. The tail of the bulb body increases the radial velocity due to the increase in the flow area, the water flow is disordered, and the velocity distribution is uneven. The flow field of the characteristic section of the bulb body is analyzed by selecting three

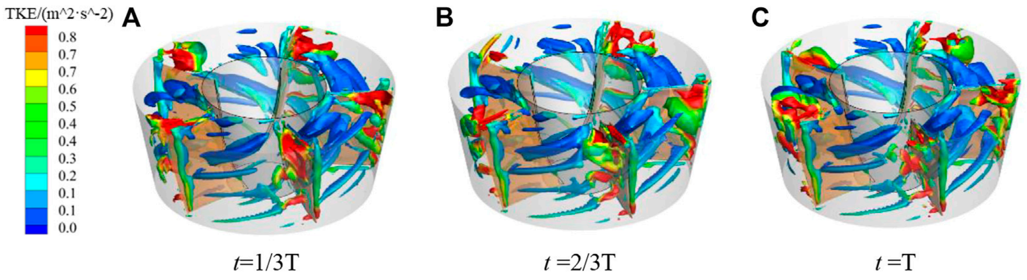

FIGURE 6
Structure of the vortex of the guide vane body at different moments (1.0Q_d).

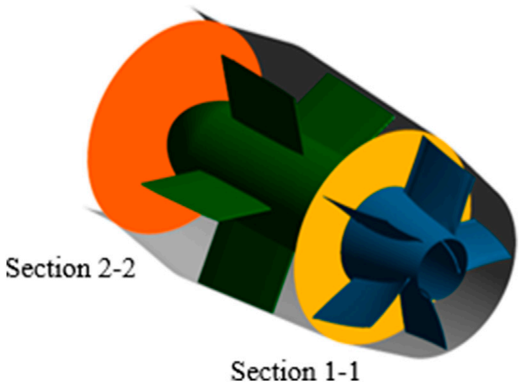

FIGURE 7
Diagram of each section position of the bulb body.

characteristic moments in one rotational period, and the location of the characteristic section is shown in Figure 7. The distance of section 1-1 from the center line of the impeller is 0.61D and the distance of section 2-2 from the center line of the impeller is 2.3D. The relative velocity distribution of section 1-1 at different moments of the guide vane body (v_i is the instantaneous velocity at this point and v_a is the average velocity of the section) is shown in Figure 8. There are five similar areas at the outlet all showing obvious high-velocity and low-velocity areas, and the low-velocity area is mainly at the position of the guide vane because the water flow at the suction surface and the hub of the guide vane has a bad flow pattern. The flow velocity distribution of section 2-2 at different moments is shown in Figure 9. The overall flow velocity value at the exit of the bulb body is small, basically the low-velocity zone. In the tail area of the bulb body, due to the sudden expansion of the overflow section, resulting in complex flow patterns such as deluge and vortex, the size distribution position of the flow velocity in the same cycle is relatively unchanged in periodic changes.

The deflection of the flow velocity at the guide vane body and bulb body outlet needs to be statistically analyzed. The deflection angles of the flow at the two characteristic sections of the guide vane body outlet and the bulb body outlet at 0.8 Q_d, 1.0 Q_d, and 1.2 Q_d operating conditions were analyzed (Yan et al., 2016), and the calculated equation is shown below.

$$\gamma = \arctan \frac{v_t}{v_z},$$

where v_t is the transverse velocity and v_z is the axial velocity.

Figure 10 shows the deflected flow angle of section 1-1 at all three characteristic flow rate conditions, and the flow at the outlet

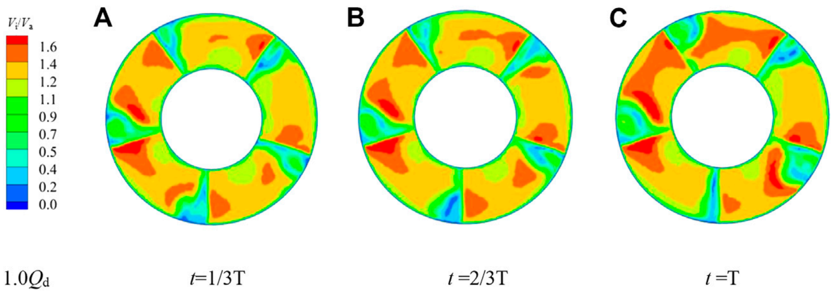

FIGURE 8
Outlet velocity cloud contour of section 1-1 guide vane at different moments (1.0Q_d).

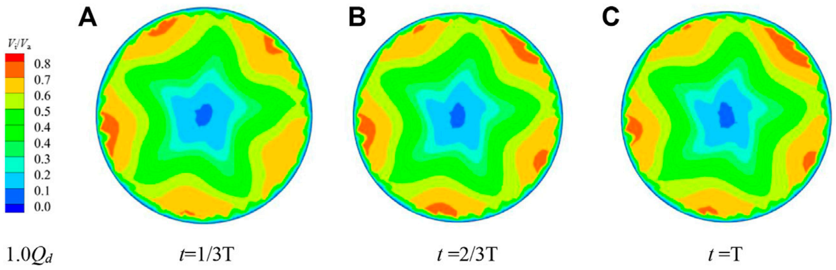

FIGURE 9
Velocity cloud contour of section 2-2 bulb body outlet at different moments (1.0Q_d).

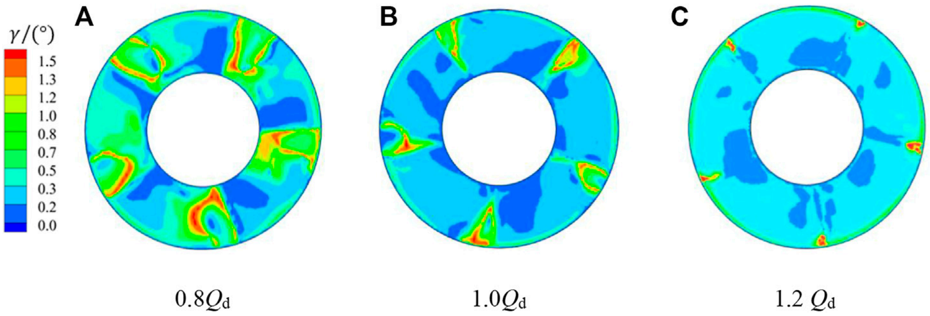

FIGURE 10
Distribution diagram of the deflected flow angle of section 1-1 under different conditions.

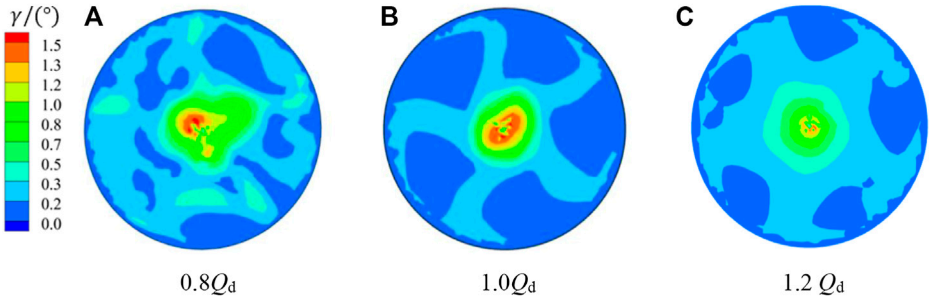

FIGURE 11
Distribution diagram of the deflected flow angle of section 2-2 under different conditions.

of the guide vane body has a certain circumferential flow velocity, among which the deflected flow angle is larger at the low flow rate condition of 0.8 Q_d, mainly due to the larger remaining ring volume at the outlet of the guide vane body at the low flow rate condition. Figure 11 shows a cloud diagram of the deflection angle of the bulb body outlet of section 2-2 at different flow rate conditions; the larger deflection area is concentrated in the tail center of the bulb body. With the increase in flow rate, the bulb body inlet to the bulb body outlet angle of deflection is gradually decreasing trend. In the high flow rate condition of 1.2 Q_d, section 1-1 and section 2-2 deflected flow angle below 0.3°, the largest region, indicating that in the high flow rate condition, the bulb body outflow pattern is better and the flow line is relatively smoother.

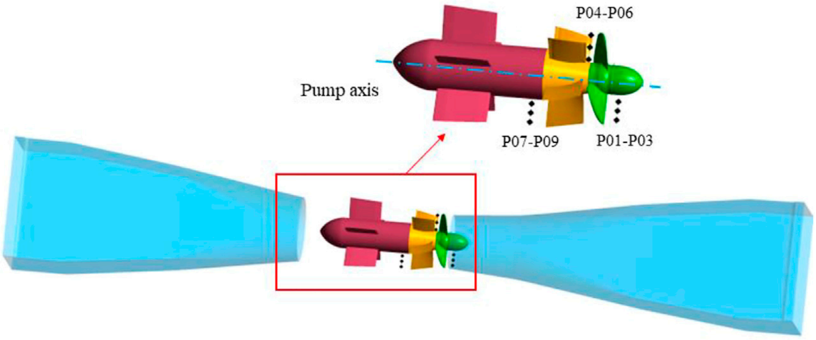

FIGURE 12
Schematic diagram of the pressure pulsation monitoring point.

4.2 Pressure pulsation characteristic analysis

Considering the unsteady sequential interference between the impeller and the guide vane, the pressure in the pump will change rapidly with time; that is, the pressure pulsation is generated. Monitoring points are set up at the inlet and outlet of the impeller and between the impeller and the guide vane to analyze the variation of pressure pulsation. Due to the sealing characteristics of the submersible tubular electric pump device and the limitation of the test method, the monitoring points of the model test can only be arranged on the wall surface of the pump device. In order to facilitate the comparison between the numerical simulation results and the pulsation test results, three pressure pulsation monitoring points were arranged near the wall surface. At three different flow rate conditions (0.8 Q_d, 1.0 Q_d, and 1.2 Q_d), pressure pulsation in the zone of the impeller and guide vane body was analyzed spectrally and in the temporal domain. Three pressure pulsation monitoring points were set separately at the impeller inlet, impeller outlet, and guide vane body outlet, and the location of each monitoring point is shown in Figure 12. Three monitoring points are set at the impeller inlet: the distance from monitoring points P01–P03 to the pump axis is 0.092D, 0.117D, and 0.143D, respectively. Between the impeller and the body of the guiding vane, the distance from monitoring points P04–P06 to the pump axis is 0.078D, 0.112D, and 0.149D, respectively. Three monitoring points are set at the guide vane body outlet: the distance from monitoring points P07–P09 to the pump axis is 0.078D, 0.112D, and 0.149D, respectively. The distance from P07–P09 to the pump axis is 0.242D, 0.256D, and 0.272D, respectively.

4.3 Time domain analysis of pressure pulsation

Frequency domain and time domain techniques are frequently used in pressure pulsation analysis. In the process of time domain analysis, in order to eliminate disturbances, the instantaneous pressure needs to be dimensionless, and the pressure coefficient C_P is calculated as shown below (Widmer et al., 2011):

$$C_P = \frac{P - \bar{P}}{0.5\rho u_2^2},$$

where P is the instantaneous pressure, $\bar{P}$ is the average pressure, and u_2 is the circumferential velocity of the impeller outlet. Figure 13 shows the time domain diagram of pressure pulsation at monitoring points P01–P03 of impeller inlet at different flow rate conditions. From Figure 13, it can be seen that the pressure pulsation at each monitoring point is more regular. In one rotational period, the three peaks and three troughs at the low flow rate condition 0.8 Q_d and the high flow rate condition 1.2 Q_d are consistent with the number of impeller blades of the pump device, demonstrating that the number of impeller blades affects the impeller inlet pressure pulsation and that the peaks and troughs are generated roughly at the same time, which is caused by the alternating pressure fluctuations when the impeller rotates. From the impeller hub to the wheel rim, the amplitude of pressure pulsation grows. At 0.8 Q_d working condition, the pressure pulsation amplitude at each monitoring point of the impeller inlet is the largest, and as the flow rate increases, the water flow is more and pressure pulsation amplitude fluctuation is smaller. Figure 14 depicts the time domain diagram of the pressure pulsation between the impeller and the guide vane body at monitoring points P04–P06 under various flow rate conditions. The vane of the guide vane body restrains the flow in the axial direction to better recover the circumferential kinetic energy of the flow. Under the constraint of the guide vane, the maximum value of the pressure pulsation amplitude between the impeller and the guide vane body is greatly decreased. The pressure fluctuation amplitude of the maximum monitoring point at the distance from the pump

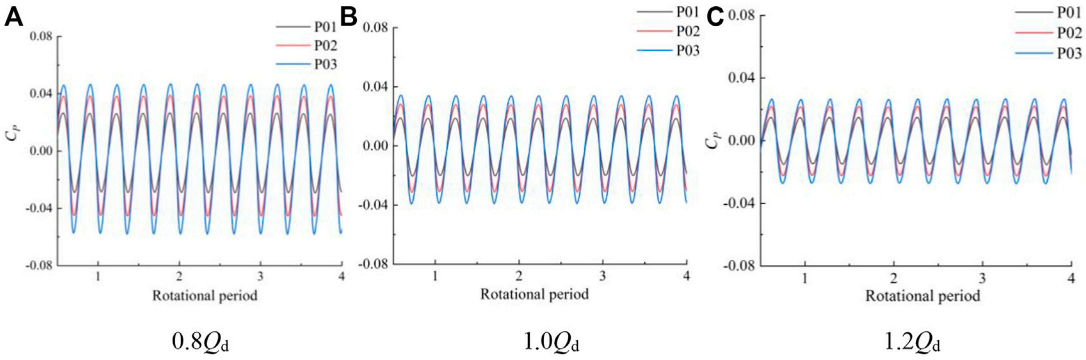

FIGURE 13
Time domain diagram of the impeller inlet monitoring points at different flow rate conditions.

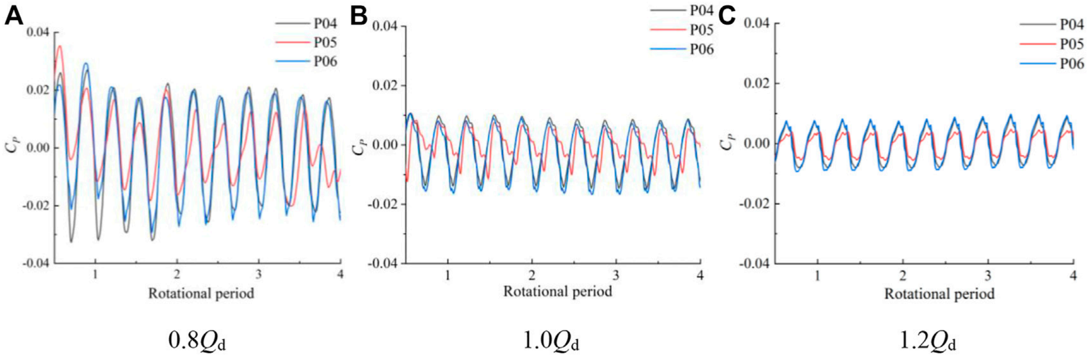

FIGURE 14
Time domain diagram of pressure pulsation at the monitoring point between the impeller and guide vane body at different flow rate conditions.

axis decreases by about 69.1% from 0.8 Q_d to 1.2 Q_d. The pressure pulsation amplitude increases with the distance from the pump axis, due to the influence of static and dynamic interference, which results in an unsteady flow at the impeller outlet, and at low flow rate condition, due to the existence of backflow, deliquescence and other undesirable flow patterns make pressure pulsation fluctuation more obvious. In the 1.2 Q_d working condition, the pressure pulsation law is more similar to the 1.0 Q_d working condition, and the pressure pulsation fluctuation is smaller. Figure 15 shows the time domain diagram of pressure pulsation at monitoring points P07–P09 of the guide vane body outlet. The pressure pulsation at the guide vane body's exit varies by about 0.01 for each flow rate condition, and the difference in amplitude is not large. At 0.8 Q_d, the pressure pulsation at the outlet of the guide vane body decreases significantly compared with that at the impeller inlet; there are irregular fluctuations, and the fluctuations at the monitoring points of the wheel rim and hub are larger than those at the middle point. At 1.2 Q_d, the pressure pulsation at the outlet of the guide vane body shows obvious periodic changes, and the pattern of pulsation fluctuation at each monitoring location is consistent.

After the initial analysis of the data with obvious features in the time domain, it is found that some signals with the same time domain parameters have differences in other parameters, so the concept of frequency domain is introduced here for further analysis of the signal. FFT can characterize the overall nature of the signal, but when it is necessary to understand the local characteristics of the signal, FFT is used to select a window function of limited length and divide the signal into many small intervals, and Fourier analysis is performed on the signal at each time interval. In this study, the FFT is used to convert the pressure pulsation time domain signal into frequency domain signal, and the pressure pulsation spectrum of each pressure pulsation monitoring point is obtained. In Figure 16, Figure 17, and Figure 18, the *X*-axis is the ratio of frequency to rotational

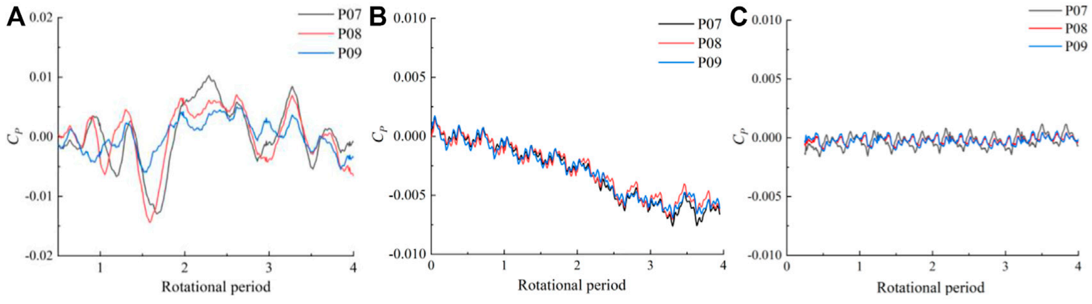

0.8Q_d 1.0Q_d 1.2Q_d

FIGURE 15
Time domain diagram of pressure pulsation at the outlet of the guide vane body at different flow rate conditions.

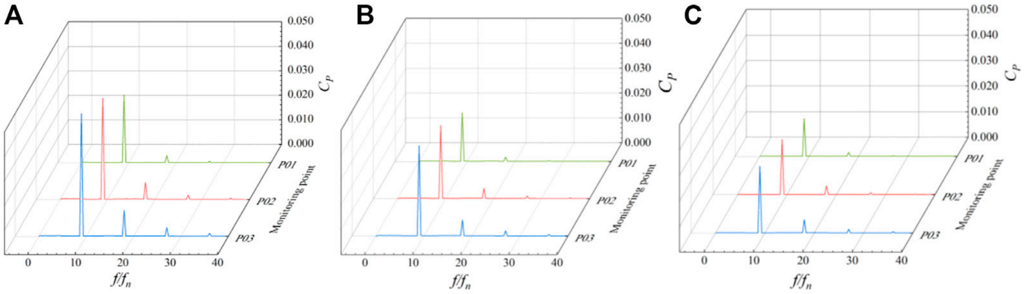

0.8Q_d 1.0Q_d 1.2Q_d

FIGURE 16
Pressure pulsation spectrum of impeller inlet monitoring points 1–3 at different flow rate conditions.

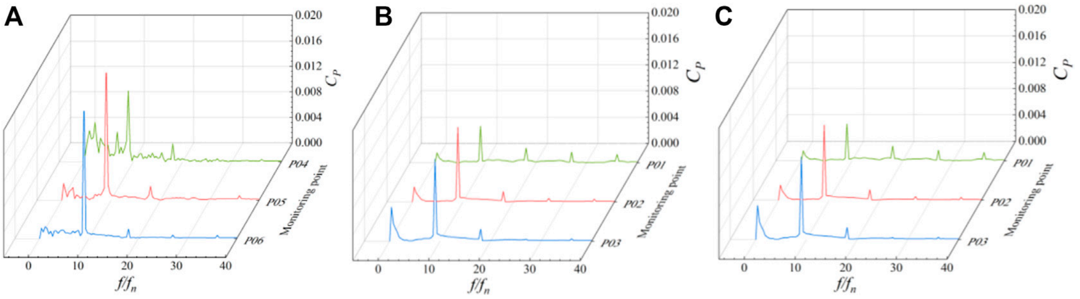

0.8Q_d 1.0Q_d 1.2Q_d

FIGURE 17
Pressure pulsation spectrum of monitoring points 4–6 between the impeller and guide vane body at different flow rate conditions.

frequency (rotational frequency $f_n = 67.6$ Hz), the Y-axis is the monitoring points of different sections, and the Z-axis is the amplitude of the pressure pulsation coefficient.

The frequency spectrum of pressure pulsation at monitoring points P01–P03 of the impeller inlet under various flow rate conditions is shown in Figure 16. The pressure pulsation

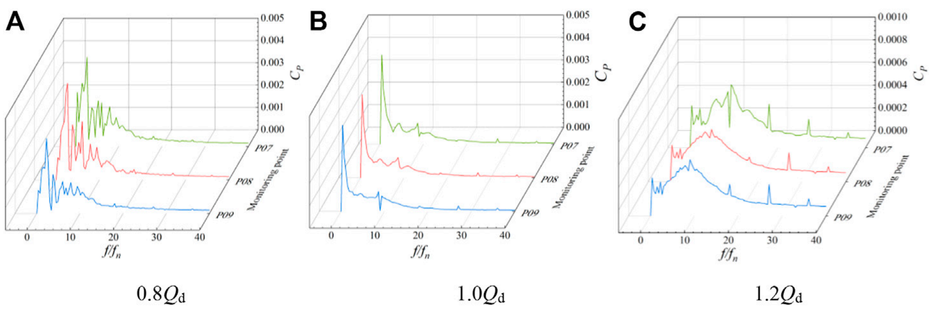

0.8Q_d 1.0Q_d 1.2Q_d

FIGURE 18
Pressure pulsation spectrum of monitoring points 7–9 between guide vane body outlets at different flow rate conditions.

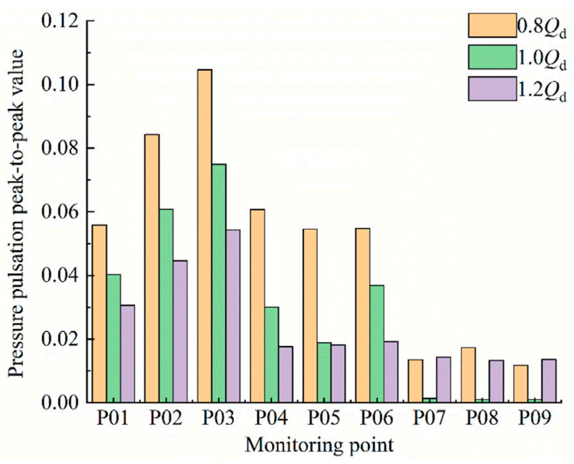

FIGURE 19
Pressure pulsation peak-to-peak.

amplitude increases from the hub to the rim, and the main frequency of each monitoring point is situated at three times the rotating frequency. Under various flow rate conditions, the pressure pulsation frequency at the impeller's input section is identical, indicating that the inlet section of the impeller domain is significantly influenced by the rotation of the impeller. With a rise in flow rate, each monitoring point's pressure pulsation amplitude reduces to varying degrees, and the pressure pulsation amplitude at the wheel edge at 1.2 Q_d operating condition decreases about 34 compared with the small flow rate at 0.8 Q_d operating condition. The main frequency amplitude of each monitoring point is P03, P02, and P01 in descending order, which indicates that the pressure fluctuation at the wheel edge of the impeller domain is greater. Figure 17 shows the pressure pulsation spectrum of monitoring points P04–P06 between the impeller and guide vane body. The main frequency is still visible at three times the rotational frequency, and the number of impeller blades has no effect on the pulsation at any monitoring point. In the 1.2 Q_d condition, the difference of the pressure pulsation amplitude at the hub and the wheel rim is not large, and the pressure pulsation amplitude value increases from the hub to the wheel rim and the overall value decreases. Figure 18 shows the pressure pulsation spectrum of monitoring points P07–P09 between the guide vane body outlets. In 0.8 Q_d and 1.0Q_d conditions, the pressure pulsation coefficient of each monitoring point dominates the corresponding frequency multiplier in the leaf frequency, and the spectrum of each monitoring point has no obvious similarity compared with other sections.

The highest pressure that can be obtained at that monitoring point in the calculation cycle is reflected by the pressure pulsation peak-to-peak value, which describes the pulsation pattern of the pulsation signal in one rotational period. Using 97% confidence interval for pressure pulsation peak value (Li et al., 2017; Yang et al., 2019), remove the first 1.5 and after 1.5 of the data samples; the maximum and minimum values of the remaining data are used to find the difference to obtain the peak pressure pulsation for further analysis of the impeller inlet, impeller and guide body, and guide body outlet pressure pulsation fluctuations; the monitoring points P01–P09 have been calculated for the peak. Figure 19 shows the peak values of pressure pulsation at each monitoring point under different working conditions. At the impeller inlet, due to the influence of the impeller blade rotation, the flow pattern is unstable and generates large fluctuations, and the peak value of pressure pulsation gradually increases from the wheel edge to the wheel hub. Due to the guide body rectification recovery effect, the water flows through the guide body, the pulsation pressure is reduced, the pressure gradient is reduced, and the corresponding peak value is reduced. At 0.8 Q_d working condition, pressure pulsation reaches its maximum at the impeller's intake wheel edge, where it reaches a peak value of 0.112, and at the guide body's exit wheel edge, where it reaches a peak value of 0.015, which is reduced by 88.46.

5 Conclusion

The reliability and validity of the numerical calculation were verified by physical model tests, and the variation law of the transient characteristics of the internal flow of the impeller and guide vane of the submersible tubular electric pump device was studied. By establishing monitoring points and conducting a time–frequency domain analysis of pressure pulsation, the features of this pump device's pressure pulsation under various flow rate conditions are better explored, and the following results are drawn.

1) The long strip vortex structure inside the guide vane body is mainly divided into the hub and guide vane body outlet area. As the flow rate increases, the size and number of vortex structures gradually decrease at different moments, and the number of vortex structures gradually increases from the inlet to the outlet of the guide vane, but the volume of the vortex structures gradually decreases, and the turbulence energy is significantly reduced. The deflected flow angle of the guide vane body outlet is mainly concentrated in the edge area of the guide vane. Thus, for each flow rate condition, there is a specific transverse flow velocity at the guide vane body's exit surface. The relative velocity at the exit of the guide vane body and bulb body does not change significantly in one rotational period.
2) Each monitoring point at the impeller inlet is in a rotational period, and the number of peaks and troughs of the pressure fluctuation time domain curve is three. The number of peaks and troughs is consistent with the number of impeller blades. The pressure fluctuation has strong periodicity and large fluctuation amplitude. The pressure fluctuation amplitude gradually increases with the increase of the distance between the monitoring point and the pump axis. With the increase of flow rate, the pressure fluctuation amplitude of each monitoring point at the impeller outlet decreases obviously. The pressure pulsation value of the farthest monitoring point from the pump shaft decreased by about 62.3%, and the pressure pulsation fluctuation is more obvious in the case of small flow rate, and the pressure pulsation fluctuation tends to be regular as the flow rate increases. The pressure pulsation amplitude at each monitoring point of the guide vane body outlet differs less, and the section mainly bears low-frequency pulsation and appears with more obvious irregular fluctuations. As the flow rate increases, the pressure pulsation amplitude at each section from the impeller inlet to the guide vane body outlet monitoring points obviously appears in different degrees of reduction.
3) The pressure pulsation peak value is greatest under the influence of impeller rotation at each monitoring point of the impeller inlet under the same flow rate conditions. Water flows through the guide vane body; because of the guide vane body rectification and diffusion effects, the pressure pulsation peak values at the guide vane body outlet monitoring points are lower than those of the guide vane body inlet monitoring points. Each monitoring point on the section surface shows a diminishing trend as the flow rate rises in terms of the peak value of pressure pulsation, and the peak value of pressure pulsation at each monitoring point of the impeller exit section is more influenced by the flow rate change. At the low flow rate 0.8 Q_d, the peak value of pressure pulsation at the monitoring point of the hub is 3.5 times higher than that at the high flow rate 1.2 Q_d.

Data availability statement

The raw data supporting the conclusions of this article will be made available by the authors, without undue reservation.

Author contributions

Conceptualization: FY; software, writing original draft: YL; formal analysis: YL and PD; methodology: PD and YL; funding: FY and JL; investigation: JL and HG; resources: FY and FT; supervision: FY and FT; visualization: YL and PD; writing–review and editing: HG and FT. All authors have read and agreed to the published version of the manuscript.

Funding

This research was funded by the National Natural Science Foundation of China (Grant No. 51609210), the Major Projects of the Natural Science Foundation of the Jiangsu Higher Education Institutions of China (Grant No.20KJA570001), the Technology Project of the Water Resources Department of Jiangsu Province (Grant No. 2022074), the Science and Technology Plan Project of Yangzhou City (Grant No. YZ2022192), and the Scientific Research Program of Jiangsu Hydraulic Research Institute (Grant No. 2021).

Conflict of interest

HG was employed by the company Yangzhou Surveying and Design Institute Co., Ltd. FY was employed by the Yangzhou University.

The remaining authors declare that the research was conducted in the absence of any commercial or financial relationships that could be construed as a potential conflict of interest.

Publisher's note

References

Al-Obaidi, A. R. (2020). Investigation of the influence of various numbers of impeller blades on internal flow field analysis and the pressure pulsation of an axial pump based on transient flow behavior. *Heat. Transf.* 49 (4), 2000–2024. doi:10.1002/htj.21704

Arocena, V. M., Abuan, B. E., Reyes, J. G. T., Rodgers, P. L., and Danao, L. A. M. (2021). Numerical investigation of the performance of a submersible pump: Prediction of recirculation, vortex formation, and swirl resulting from off-design operating conditions. *Energies* 14 (16), 5082. doi:10.3390/en14165082

Chalghoum, I., Elaoud, S., Kanfoudi, H., and Akrout, M. (2018). The effects of the rotor-stator interaction on unsteady pressure pulsation and radial force in a centrifugal pump. *J. Hydrodyn.* 30 (4), 672–681. doi:10.1007/s42241-018-0073-y

Choi, Y. D., Lim, J. I., Kim, Y. T., and Lee, Y. H. (2008). Effect of blade angle on the performance of a cross-flow hydro turbine. *J. Korean Soc. Mar. Eng.* 32 (3), 413–420. doi:10.5916/jkosme.2008.32.3.413

Chu, S., Dong, R., and Katz, J. (1995). Relationship between unsteady flow, pressure fluctuations, and noise in a centrifugal pump - part B: Effects of blade-tongue interactions. *J. Fluids Eng.* 117 (1), 30–35. doi:10.1115/1.2816814

Hunt, J. C., Wray, A. A., and Moin, P. (1988). “Eddies, streams, and convergence zones in turbulent flows,”. Studying turbulence using numerical simulation databases.Proceedings of the summer program, Stanford, CA.

Jeong, J., and Hussain, F. (1995). On the identification of a vortex. *J. Fluid Mech.* 285, 69–94. doi:10.1017/s0022112095000462

Ji, L., Li, W., Shi, W., Zhou, L., and Agarwal, R. (2020). Experimental study of pressure pulsation in a mixed-flow pump with different tip clearances based on wavelet analysis. *Shock Vib.* 2020, 1–15. doi:10.1155/2020/9041686

Ji, D., Lu, W., Lu, L., Xu, L., Liu, J., Shi, W., et al. (2021). Study on the comparison of the hydraulic performance and pressure pulsation characteristics of a shaft front-positioned and a shaft rear-positioned tubular pump devices. *J. Mar. Sci. Eng.* 10 (1), 8. doi:10.3390/jmse10010008

Jin, Y., He, X., Zhang, Y., Zhou, S., Chen, H., and Liu, C. (2019). Numerical and experimental investigation of external characteristics and pressure fluctuation of a submersible tubular pumping system. *Processes* 7 (12), 949. doi:10.3390/pr7120949

Khalifa, A. E., Al-Qutub, A. M., and Ben-Mansour, R. (2011). Study of pressure fluctuations and induced vibration at blade-passing frequencies of a double volute pump. *Arab. J. Sci. Eng.* 36 (7), 1333–1345. doi:10.1007/s13369-011-0119-8

Li, W., Zhou, L., Shi, W. D., Ji, L., Yang, Y., and Zhao, X. (2017). PIV experiment of the unsteady flow field in mixed-flow pump under part loading condition. *Exp. Therm. Fluid Sci.* 83, 191–199. doi:10.1016/j.expthermflusci.2017.01.009

Li, W., Zhang, Y., Shi, W., Ji, L., Yang, Y., and Ping, Y. (2018). Numerical simulation of transient flow field in a mixed-flow pump during starting period. *Int. J. Numer. Methods Heat. Fluid Flow.* 28 (4), 927–942. doi:10.1108/hff-06-2017-0220

Li, W., Li, S., Ji, L., Zhao, X., Shi, W., Agarwal, R. K., et al. (2021). A study on the cavitation and pressure pulsation characteristics in the impeller of an LNG submerged pump. *Machines* 10 (1), 14. doi:10.3390/machines10010014

Liu, C., Wang, Y., Yang, Y., and Duan, Z. (2016). New omega vortex identification method. *Sci. China Phys. Mech. Astron.* 59 (8), 684711–684719. doi:10.1007/s11433-016-0022-6

Lu, Z., Wang, C., Qiu, N., Shi, W., Jiang, X., Feng, Q., et al. (2018). Experimental study on the unsteady performance of the multistage centrifugal pump. *J. Braz. Soc. Mech. Sci. Eng.* 40 (5), 1–10. doi:10.1007/s40430-018-1157-x

Miyabe, M., Maeda, H., Umeki, I., and Jittani, Y. (2006). Unstable head-flow characteristic generation mechanism of a low specific speed mixed flow pump. *J. Therm. Sci.* 15 (2), 115–120. doi:10.1007/s11630-006-0115-6

Munih, J., Hočevar, M., Petrič, K., and Dular, M. (2020). Development of CFD-based procedure for 3d gear pump analysis. *Eng. Appl. Comput. Fluid Mech.* 14 (1), 1023–1034. doi:10.1080/19942060.2020.1789506

Shi, L., Yuan, Y., Jiao, H., Tang, F., Cheng, L., Yang, F., et al. (2021). Numerical investigation and experiment on pressure pulsation characteristics in a full tubular pump. *Renew. Energy* 163, 987–1000. doi:10.1016/j.renene.2020.09.003

Smirnov, P. E., and Menter, F. R. (2009). Sensitization of the SST turbulence model to rotation and curvature by applying the Spalart–Shur correction term. *J. Turbomach.* 131 (4), 041010. doi:10.1115/1.3070573

Sun, Z., Yu, J., and Tang, F. (2021). The influence of bulb position on hydraulic performance of submersible tubular pump device. *J. Mar. Sci. Eng.* 9 (8), 831. doi:10.3390/jmse9080831

Tao, R., Xiao, R., Yang, W., and Wang, F. (2014). A comparative assessment of Spalart-Shur rotation/curvature correction in RANS simulations in a centrifugal pump impeller. *Math. Problems Eng.* 2014, 1–9. doi:10.1155/2014/342905

Wang, C., Hu, B., Zhu, Y., Wang, X., Luo, C., and Cheng, L. (2019). Numerical study on the gas-water two-phase flow in the self-priming process of self-priming centrifugal pump. *Processes* 7 (6), 330. doi:10.3390/pr7060330

Wang, L., Zheng, Z. Y., Cai, W. H., and Li, W. Y. (2019). Extension Omega and Omega-Liutex methods applied to identify vortex structures in viscoelastic turbulent flow. *J. Hydrodyn.* 31 (5), 911–921. doi:10.1007/s42241-019-0045-x

Wang, F. J. (2020). *Analysis method of flow in pumps and pumping stations*. Beijing, China: China Water & Power Press.

Widmer, C., Staubli, T., and Ledergerber, N. (2011). Unstable characteristics and rotating stall in turbine brake operation of pump-turbines. *J. Fluids Eng.* 133 (4), 041101. doi:10.1115/1.4003874

Xiao, Z., Tan, J., Wang, S., Yu, Z., and Wu, W. (2019). PIV experimental study on the flow field characteristics of axial flow blood pump under three operating conditions. *J. Eng. (Stevenage).* 13, 155–158. doi:10.1049/joe.2018.9003

Xie, W. D., Fang, G. L., Liu, J. L., and Liu, R. H. (2010). Study on the hydraulic characteristics of submersible tubular pumping device in Gubei and Shannan pumping stations. *China Water Resour.* 2010(16), 13–15.

Yan, H., Liu, M. Q., Zhao, W. S., Lin, P., and Wu, Y. W. (2016). Effect of velocity loop volume on hydraulic performance of large axial flow pumping station. *J. Central South Univ. Nat. Sci. Ed.* 47 (6), 2125–2132.

Yang, J., Liu, J., Liu, X., and Xie, T. (2019). Numerical study of pressure pulsation of centrifugal pumps with the compressible mode. *J. Therm. Sci.* 28 (1), 106–114. doi:10.1007/s11630-018-1071-7

Yang, F., Zhang, Y., Yuan, Y., Liu, C., Li, Z., and Nasr, A. (2021). Numerical and experimental analysis of flow and pulsation in hump section of siphon outlet conduit of axial flow pump device. *Appl. Sci.* 11 (11), 4941. doi:10.3390/app11114941

Yang, F., Li, Z., Yuan, Y., Liu, C., Zhang, Y., and Jin, Y. (2021). Numerical and experimental investigation of internal flow characteristics and pressure fluctuation in inlet passage of axial flow pump under deflection flow conditions. *Energies* 14 (17), 5245. doi:10.3390/en14175245

Yang, X., Tian, D., Si, Q., Liao, M., He, J., He, X., et al. (2022). Flow loss analysis and optimal design of a diving tubular pump. *Machines* 10 (3), 175. doi:10.3390/machines10030175

Yang, F., Li, Z., Fu, J., Lv, Y., Ji, Q., and Jian, H. (2022). Numerical and experimental analysis of transient flow field and pressure pulsations of an axial-flow pump considering the pump–pipeline interaction. *J. Mar. Sci. Eng.* 10 (2), 258. doi:10.3390/jmse10020258

Yang, F., Chang, P., Jian, H., Lv, Y., Tang, F., and Jin, Y. (2022). Numerical analysis of unsteady internal flow characteristics of impeller-guide vane in a vertical axial flow pump device. *Front. Energy Res.* 1002, 935888. doi:10.3389/fenrg.2022.935888

Zhang, Y., Wang, X., Ding, P., and Tang, X. (2014). Numerical analysis of pressure fluctuation of internal flow in submersible axial-flow pump. *J. Drain. Irrig. Mach. Eng.* 32, 302–307. doi:10.3969/j.issn.1674-8530.13.0207

Zhang, N., Yang, M., Gao, B., Li, Z., and Ni, D. (2015). Experimental investigation on unsteady pressure pulsation in a centrifugal pump with special slope volute. *J. Fluids Eng.* 137 (6), 061103. doi:10.1115/1.4029574

frontiers | Frontiers in Energy Research

TYPE Original Research
PUBLISHED 13 January 2023
DOI 10.3389/fenrg.2022.1097729

OPEN ACCESS

EDITED BY
Leilei Ji,
Jiangsu University, China

REVIEWED BY
Xiaojun Li,
Zhejiang Sci-Tech University, China
Zihan Zhou,
Singapore University of Social Sciences, Singapore
Xiao Li,
Hangzhou Dianzi University, China

*CORRESPONDENCE
Yixuan Lu,
✉ yxluyzu@outlook.com

SPECIALTY SECTION
This article was submitted to Process and Energy Systems Engineering, a section of the journal Frontiers in Energy Research

RECEIVED 14 November 2022
ACCEPTED 28 November 2022
PUBLISHED 13 January 2023

CITATION
Xu J and Lu Y (2023), Operation optimization study of water pump production model based on low-carbon economy concept.
Front. Energy Res. 10:1097729.
doi: 10.3389/fenrg.2022.1097729

Operation optimization study of water pump production model based on low-carbon economy concept

Jing Xu[1] and Yixuan Lu[1,2]*

[1]Business School, Yangzhou University, Yangzhou, China, [2]Ningbo Jushen Pumps Industry Co., Ltd., Ningbo, China

The inventory and delivery rate of water pump are affected largely by the production mode. In order to improve the operation optimization of water pump production model, the simulation test method and system dynamics model were selected in the manuscript. Three different production modes, namely traditional make-to-order (MTO) model, make-to-stock (MTS) mode, and MTO & MTS model, were compared in terms of the indicators such as the inventory, productivity and delivery rate of water pump. Moreover, the three above production modes were also assessed by using the fuzzy comprehensive evaluation method. The results show that it is not well adapted in practical applications for the MTS production model with an intermediate level of inventory and customer demand satisfaction. The MTO production model is appropriate when it's easy to predict the customer demand that fluctuates scarcely. The MTO & MTS production model should be selected when it's difficult to predict the customer demand that fluctuates sharply. After comprehensive evaluation, the MTO & MTS production model is the best choice for pump.

KEYWORDS

pump, optimization, make to order, make to stock, production model

1 Introduction

Water pumps are a kind of general machine with many types and extremely wide applications. It can be said that wherever the liquid flows, there is almost always a pump at work. According to the statistics of different countries, the power consumption of pumps is about 20% of the total power generation, so pumps are, of course, big energy consumers. Therefore, it's important to reduce the energy consumption of pumps to achieve a low-carbon economy. As the largest consumer of pump products in the world, China accounts for 61% of the Asian region and nearly 25% of the world's market. As a powerful manufacturing country, China has globally advanced manufacturing technology and product development capability. Due to bottleneck limitation of pump design level and production capacity, it's rather difficult to significantly optimize the pump by developing new products, improving production processes and saving materials. Therefore, from the perspective of management, it's of positive significance to explore the scientific pump production models to improve pump productivity and reduce pump cost.

In 1984, Spencer (Smith, 1984) published Make-to-stock (MTS) and its combination mode of assembly problems in the Journal of Operations Management. Immediately afterwards, a number of studies were carried out by numerous scholars around the issue (Auberger and Ramsauer, 2020). Li et al. (2008) proposed a revenue management model for make-to-order (MTO) production in manufacturing. This is a useful guide for companies with random demand and fixed capacity. Modrak and Soltysova (2020) put forward the MTO mode optimization method in order to reduce cost and shorten the delivery time as much as possible. Subsequently, the mixed production mode of MTS and MTO became increasingly mature in management research. Scholars generally thought that the combination of the two modes could achieve good results in shortening delivery time and reducing production cost. However, the correlation analysis was still mainly focused on the theoretical level. Zhang et al. (2008) compared the application of MTO and MTO & MTS production organization modes in iron and steel enterprises. The results demonstrated that the MTO & MTS organizational model is able to hedge the risk of inaccurate demand forecasts. Not only is the conflict between fast delivery and reduced stock reconciled, but the trend towards more variety and smaller batches of customer demand can also be accommodated. Specifically in the pump industry, despite the wide range and usefulness of pump products. However, there has been very little research on the production management of pumps. Pump design and manufacturing technology is the main area of research focused on by academics (Xu, 2017; Ye et al., 2019). Only a small number of issues are related to pump operation cost-effectiveness (Muszynski and AndrzejczykJakubowska, 2019; Wang et al., 2019; Salakhov et al., 2020); total efficiency of a pump assembly line (Alvarado et al., 2020), design and improvement of pump model (Ji et al., 2021; Xi et al., 2022; Zhu et al., 2022), pump accessory market analysis (Wang et al., 2013); and supply chain management of pump enterprises, such as the discussion on the purchase of multi-variety and small-batch castings (Zhu, 2017), selection and evaluation of the pump suppliers (Liu, 2017; Bi, 2018), optimization of the regional logistics center system (Xu, 2015), and evaluation of the supply chain response ability of the pump valve industry (Zhang et al., 2012). In response to the many product categories, high demand and wide range of applications, as well as the vulnerability of the pump market to seasonal and climatic changes, and other characteristics. In addition, the requirement of supply chain is relatively high. Therefore, there is an urgent need to expand the production management research content of MTO, MTS and MTO & MTS hybrid models in pump manufacturing companies. The refinement of pump industry production management is the future development trend (Sun, 2018). Based on this context, this paper discusses the production organization mode of pump order and its management optimization scheme from the angle of management. And system dynamics simulations were carried out to investigate the effects of different production organization models on the inventory and customer delivery rates of pump companies. In order to better guide the production practices of pump enterprises.

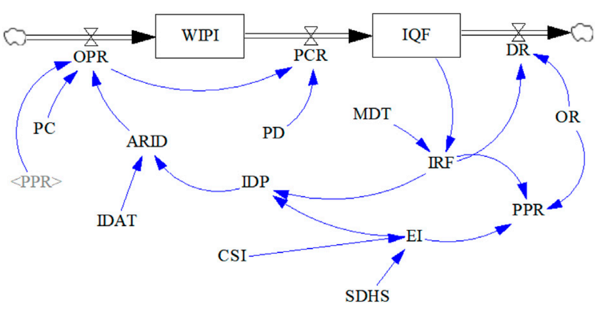

FIGURE 1
SD chart based on the combined MTO and MTS.

2 Comparison of production modes of water pump

Pumps are classified according to the fluid medium and include different types such as oil pumps, water pumps and vacuum pumps (air pumps). Water pumps are the most common and most widely used type of pump. It includes both the large pumps used in pumping stations and the small pumps commonly found in agricultural irrigation. Among them, the former products have high unit value, most of which are make-to-order (MTO) in the actual operation, represented by the axial flow pumps produced by Jushen Pumps Industry. Whereas the latter products have low unit value, most of which are make-to-stock (MTS) in the actual operation, represented by the small agricultural pumps produced by Shimge Pumps Industry. The different production models vary considerably in terms of customer responsiveness and level of capital employed. This also makes a clear difference to the requirements of corporate supply chain management.

2.1 Make-to-order

Manufacturing on an MTO basis, a pump manufacturer starts organizing the production after receiving the customer's order. At the same time, the company purchases raw materials from upstream suppliers and organizes delivery after production is complete. Inventory costs have been significantly reduced, and

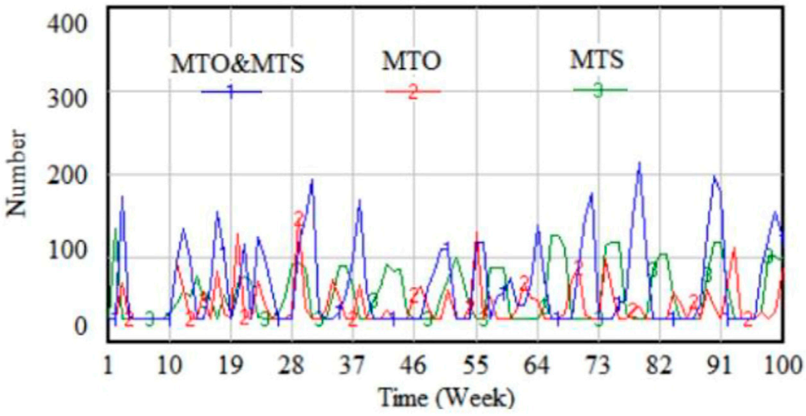

FIGURE 2
Changes in WIPI of pump enterprises.

orders required by the government can be customized. However, water pump enterprises that produce MTO are mostly in a relatively traditional hand-workshop management state due to their small production batches. They have a low level of production automation and a high dependence on key technicians for production.

2.2 Make-to-stock

Manufacturing on an MTS basis, a pump manufacturer checks the inventory after receiving the customer's order. If the inventory is sufficient, the goods can be delivered immediately. When stocks fall below the desired level, the company starts to organize production to replenish stocks and order response times are significantly reduced. However, owing to the need for maintenance of a certain amount of inventory, the capital and the actual operating costs of enterprises will increase.

2.3 Symbol description

To compare the two different production modes, the symbols of this pump manufacturing system are described as follows. DR, Delivery rate; IRF, Inventory rate of pump finished products; OR, Order rate; PPR, Planned production rate; OPR, Order production rate; PC, Production capacity; IDP, Inventory deviation of pump products; EI, Expected inventory; ARID, Adjustment rate of inventory deviation; IQF, Inventory quantity of finished pump; IDAT, Inventory deviation adjustment time; SDHS, Standard deviation of historical sales quantity; CSI, Coefficient of safety inventory; MDT, Minimum delivery time; WIPI, Work-in-process inventory; PCR, Production completion rate; PD, Production delay.

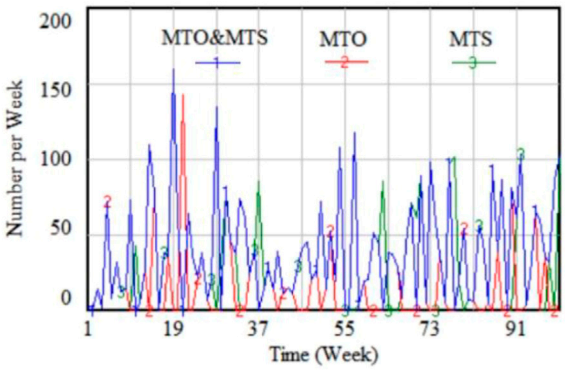

FIGURE 3
Changes in order delivery.

3 Constructing system dynamics model of production modes of water pump

3.1 Benchmark model

Depending on the different characteristics of MTO and MTS, the corresponding SD model is constructed. On the basis of the enterprises management practice obtained from the field investigation, two different modes of order production management mechanism are designed.

Production management mechanism on an MTO basis: DR = IF THEN ELSE (IRF > OR, OR, 0); PPR = IF THEN ELSE (IRF > OR, OR, 0, OR-IRF); OPR = IF THEN ELSE (PPR < PC, PPR, 0). Production management mechanism on an MTS basis: DR = IF THEN ELSE (IRF > OR, O); IDP = IF THEN ELSE (EI > IRF, EI-

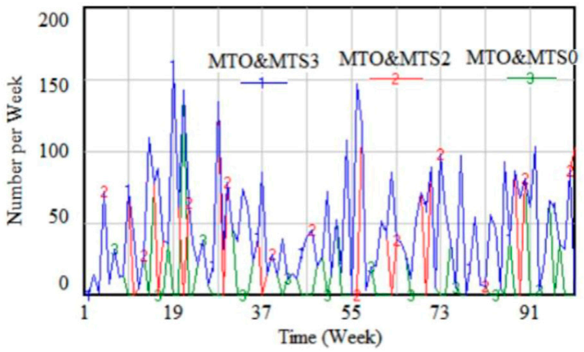

FIGURE 4
Influence of CSI on DR in the case of the MTO & MTS combined mode.

IRF, 0), that is, when IRF is lower than EI, IDP is equal to EI deducted inventory rate of pump products; otherwise, the inventory level will not be adjusted, unit: set/week); OPR = IF THEN ELSE (ARID < PC, ARID, 0).

3.2 Operation optimization

Considering manufacturing on an MTO basis, in the event of a sudden, high-volume emergency order, companies may be overwhelmed. Thereby necessitating an appropriate amount of buffer inventory. The MTS model, on the other hand, requires consistently high stock levels and temporary stock-outs are also difficult to avoid. Therefore, on the basis of MTO and MTS, an order production organization mode of combining MTO and MTS is designed. Figure 1 shows the system dynamics (SD) chart based on the above mode. The order production management mechanism is DR = IF THEN ELSE (IRF > OR, OR, 0). If the stock is greater than the current order quantity, immediate dispatch will be arranged, otherwise no dispatch will be made. Delays in delivery are negotiated with the company depending on the volume of the specific order, unit: set/week; PPR = IF THEN ELSE (IRF−EI>OR, 0, OR + EI−IRF), that is, if the IQF deducting the expected (safety) inventory is more than the order rate, then, the order production will not be prepared, and the products are delivered immediately. Otherwise, the order production is organized according to the order rate; plus, the expected inventory deducts the quantity of finished pump inventory. Unit: set/week; OPR = IF THEN ELSE (PPR + ARID < PC, PPR + ARID, 0), unit: set/week.

3.3 Construction of system basic equation

TABLE 1 Proportional scale.

Degree	Description
1	Two factors are equally preferred
3	One factor is moderately preferred over another
5	One factor is strongly preferred over another
7	One factor is very strongly preferred over another
9	One factor is extremely preferred over another
2, 4, 6, 8	The intermediate values

TABLE 2 Judgment matrix of production management mode in pump manufacturing enterprises.

Index	In	ORT	EU	TC	CSD
IN	1	1/3	5	1/7	1/4
ORT	3	1	7	1/5	1/2
EU	1/5	1/7	1	1/9	1/6
TC	7	5	9	1	3
CSD	4	2	6	1/3	1

The system simulates the initial time as 1, the end time as 100, and the time step as 1. The basic variables and descriptions are explained as follows. The SDHS = 52, which is calculated according to the historical sales data of a certain type of pump from January to November in 2019 of JS pump company, unit: set/week; Customer service level can be reflected by the CSI, the supply satisfaction of enterprises can reach nearly 98% when CSI is two; IDAT = 1, unit: set/week, that is, when the inventory is lower than the safety inventory, 1 week is required to recover to the safety inventory. ARID = DELAY FIXED (IDP, IDAT, 0), and it reflects the level of inventory deviation that requires adjustment, unit: set/week; MDT = 1, unit: set/week; EI = SDHS * CSI, which is a buffer inventory for enterprises to deal with demand uncertainty, which is synonymous with safety inventory, unit: set/week; WIPI = INTEG (OPR-PCR, 28), unit: set/week; IQF = INTEG (PCR−DR, 118), the initial value of inventory is 118, unit: set/week; IRF = IQF/MDT, unit: set/week; PCR = DELAY FIXED (OPR, PD, 0), some production delay from order to finished product is reflected, unit: set/week; Production delay = 1, unit: weeks; Production capacity = 200, unit: weeks.

4 Analysis of the results

4.1 Model testing

The test in the SD model includes theoretical test and historical tests. Of which, the theoretical test includes three aspects: the consistency test of model structure and actual system, the consistency test of equation and dimension, and robustness test of model structure. As this paper was actually communicated with the

TABLE 3 Degree of membership.

Mode	Index	Huge advantage (V_1)	Slight advantage (V_2)	General (V_3)	Slight disadvantage (V_4)	Huge disadvantage (V_5)
MTS	IN	0.0	0.1	0.2	0.3	0.4
MTS	ORT	0.6	0.2	0.1	0.1	0.0
MTS	EU	0.2	0.5	0.1	0.1	0.1
MTS	TC	0.1	0.2	0.1	0.2	0.4
MTS	CSD	0.0	0.0	0.2	0.2	0.6
MTO	IN	0.6	0.2	0.1	0.1	0.0
MTO	ORT	0.1	0.1	0.1	0.3	0.4
MTO	EU	0.2	0.2	0.3	0.1	0.2
MTO	TC	0.4	0.2	0.2	0.2	0.0
MTO	CSD	0.7	0.2	0.1	0.0	0.0
MTO&MTS	IN	0.4	0.4	0.1	0.1	0.0
MTO&MTS	ORT	0.3	0.4	0.1	0.1	0.1
MTO&MTS	EU	0.2	0.3	0.2	0.2	0.1
MTO&MTS	TC	0.6	0.2	0.2	0.0	0.0
MTO&MTS	CSD	0.6	0.3	0.1	0.0	0.0

TABLE 4 Weight calculation results.

Mode	V_1	V_2	V_3	V_4	V_5
MTS	0.153	0.157	0.130	0.189	0.371
MTO	0.428	0.184	0.157	0.161	0.070
MTO&MTS	0.524	0.273	0.154	0.030	0.019

TABLE 5 Scores of the evaluation factor sets.

Mode	MTS	MTO	MTO & MTS
Score	0.506	0.748	0.851

company prior to the modelling. The feedback structure and equations are fitted to the main characteristics of the actual system and the relevant data are derived from the actual data of the enterprise. Therefore, the model is consistent with the actual production management theoretical model of the enterprise. The equation and magnitude check functions that come with the Vensim software are used. The results all passed, indicating that the model is valid.

4.2 Numerical simulation

In order to simulate the variation in order production at JS Pumps, the order rate = INTEGER [RANDOM NORMAL (0, 200, 24, 52, 20)] is set. Which reflects the transformation of each variable in the case of random change in customer demand. Where 24 is the mean, 52 is the standard deviation, 0 is the minimum and 200 is the maximum. Notably, these data are calculated on the bases of the data of JS Pump Company from January to November 2019. The noise was set as a function of a random normal distribution of 20 as the customer order rate, due to the highly volatile demand, unit: unit/week.

Variations of a pump company's inventory over time. Figure 2 depicts the change in the WIP inventory of a pump company under three different production organization modes. Obviously, the MTO inventory is the smallest. The combined MTO & MTS model has a relatively larger inventory, but the overall difference is not significant.

Variations in a pump company's order productivity and delivery rate over time. As can be observed from Figure 3, companies with a combined MTO and MTS type order management model have higher shipment rates. This indicates a higher level of order delivery for pump customers under this model. Through further inspection of the data, the number of out-of-stock orders under the MTO, MTS, and MTO & MTS order management modes are respectively found to be 48, 25, and 11 during the 100 simulation periods. Evidently, the enterprise production organization and customer service level of the MTO & MTS combined order production organization mode are more optimal.

The influence of the CSI on delivery rate under the MTO & MTS combined order production organization mode. Figure 4 compares the changes in the pump companies' delivery rates of pump companies when the CSIs are 0, 2, and 3. It is clear that as safety has improved, so has the satisfaction rate of pump companies ordering services. The numbers of out-of-stocks in 100 periods respectively are 48, 11, and 2. The validity of the model is further validated in terms of the correspondence between safety stock factors and service levels.

4.3 Fuzzy comprehensive evaluation of three organizational modes

The fuzzy comprehensive evaluation method (FCE) is an evaluation method based on fuzzy mathematics. In this paper, FCE is used to compare and evaluate the MTO, MTS, and MTO & MTS combined production management mode and to verify the accuracy of the previous numerical simulation results.

According to expert consultation and literature review, the FCE method is used to first set up the evaluation index set. Build the index set U = {U1, U2, U3, U4, U5} = {Inventory (IN), Order response time (ORT), Equipment utilization (EU), Total cost (TC), Customer satisfaction with diversified demand (CSD)}, then, build the evaluation set V = {V1, V2, V3, V4, V5} = {Huge advantage, Slight advantage, General, Slight disadvantage, Huge disadvantage}, and the grading level set $F = (1, 0.8, 0.6, 0.4, 0.2)^T$.

In order to determine the weights of each evaluation indicator of the production management model using the hierarchical analysis method (AHP). First, the judgment matrix is constructed, and the corresponding importance level of the two schemes is expressed in the form of the ratio of two importance levels. Table 1 shows the proportional scale.

Afterwards, experts in the relevant fields are invited and consulted on the actual operation of the companies using the three models. The importance of the indicators is assigned for comparison, so the weighting judgment matrix is constructed. Table 2 presents the judgment matrix.

With the help of SPSSAU18.0, weight set of the indexes can be calculated: W = [IN, ORT, EU, TC, CSD] = [0.08,0.16,0.03,0.51,0.22]. When CR < 0.1, the consistency of the judgment matrix is generally believed to be acceptable; otherwise, the judgment matrix is considered to have not met the requirements, thereby requiring rectification. In this paper, the maximum eigenvalue of judgment matrix $\lambda_{\max} = 5.345$, and the consistency index CI = 0.086. The random consistency index RI = 1.12, and the consistency ratio CR = 0.077 < 0.1. Thus, the result passes the consistency test of the judgment matrix.

A panel of experts judged each of the five evaluation factors in the three production organization models. The affiliation degrees of each indicator were obtained, as depicted in Table 3. The results of the weighting calculations for the three production organization models were calculated using SPSS 18.0 and are depicted in Table 4.

Finally, the final composite score was obtained according to the points corresponding to the rubric levels ($V_1 = 1$, $V_2 = 0.8$, $V_3 = 0.6$, $V_4 = 0.4$, $V_5 = 0.2$), as depicted in Table 5. According to the table, the order of comprehensive scores is MTS<MTO<MTO & MTS. Therefore, the MTO & MTS mode is the best choice of production mode for pump.

5 Conclusion

The comparison reveals that the MTO model has the lowest inventory levels, but a higher number of stock-outs. This indicates an uneven production pattern and low production efficiency. Customer service requirements are often difficult to meet when demand is volatile. The optimized MTO & MTS combined order management model not only improves inventory, but also presents a better customer demand response to huge changes in demand and higher production utilization. Therefore, the MTO model is suitable for use when the pump company's customer demand is relatively smooth and predictable. The combined MTO & MTS production organization model is used when customer demand is volatile and unpredictable. Under MTS order management mode, the inventory level and customer demand satisfaction level are in the middle, which can cope with certain demand disturbance, but the adaptability is poor in practical application. The combined MTO & MTS production organization model is a superior order management model as the pump market is sensitive to seasonal factors and natural climate change being taken into account. A fuzzy comprehensive evaluation of the three production organization models was found by combining expert references and practical application in enterprises. The combined MTO and MTS production management model is a better improvement on the MTO and MTS models. It effectively reduces the total cost of ownership, balancing reduced inventory management pressure with shorter order response times. In this way the total cost of doing business is reduced while meeting the needs of the customer, and pump manufacturers can have more funds to control pollutant emissions.

Data availability statement

The original contributions presented in the study are included in the article/supplementary material, further inquiries can be directed to the corresponding author.

Author contributions

Conceptualization, JX; methodology, JX; software, YL; formal analysis, YL; investigation, JX; resources, JX; writing—original draft preparation, JX; writing—review and editing, JX; funding acquisition, JX. All authors have read and agreed to the published version of the manuscript.

Funding

This research was funded by the National Natural Science Foundation of China (51779215). This research was funded by the Jiangsu Provincial Social Science Foundation Project (19EYB020).

Conflict of interest

Author YL was employed by the company Ningbo Jushen Pumps Industry Co., Ltd.

The remaining author declares that the research was conducted in the absence of any commercial or financial relationships that could be construed as a potential conflict of interest.

Publisher's note

References

Alvarado, L. W., Quijada, J., and Lopez Ontiveros, M. (2020). Analysis of the dynamic behavior of efficiency at the bottleneck station of a water pump assembly line. *Dyna (Medellin).* 95 (4), 354. doi:10.6036/9753

Auberger, E., and Ramsauer, C. (2020). Integration of tactical aspects into strategic production network planning. *Teh. Glas.* 14 (3), 281–287. doi:10.31803/tg-20200718171824

Bi, M. (2018). Zhuzhou, China: Hunan University of Technology. MA. Dissertation, *Research on supplier selection and eval-uation optimization of X Pump Company*

Ji, L., Li, W., Shi, W., Tian, F., and Agarwal, R. (2021). Effect of blade thickness on rotating stall of mixed-flow pump using entropy generation analysis. *Energy* 236, 121381. doi:10.1016/j.energy.2021.121381

Li, L., Chen, R., and Li, Y. (2008). A revenue management model for MTO manufacturing. *Industrial Eng. Manag.* 13 (3), 26–28. doi:10.19495/j.cnki.1007-5429.2008.03.008

Liu, J. (2017). Shanghai, China: Shanghai Jiao Tong University. MA. Dissertation, *Study on selection of pump company's supplier based on AHP and fuzzy synthetic evaluation*

Modrak, V., and Soltysova, Z. (2020). Batch size optimization of multi-stage flow lines in terms of mass customization. *Int. J. Simul. Model.* 19 (2), 219–230. doi:10.2507/IJSIMM19-2-511

Muszynski, T. (2019). Andrzejczyk, R., and Jakubowska, B., The impact of environmentally friendly refrigerants on heat pump efficiency. *J. Power Technol.* 99 (1), 40–48.

Salakhov, R., Ermakov, A., and Gabdulkhakova, E. (2020). Numerical and experimental study of the impeller of a liquid pump of a truck cooling system and the development of a new open-type impeller. *Teh. Glas.* 14 (2), 135–142. doi:10.31803/tg-20200309115417

Smith, S. B. (1984). The subassemblies problem: Make to stock or combine? *J. Operations Manag.* 5 (1), 1–17. doi:10.1016/0272-6963(84)90003-2

Sun, W. (2018). On lean management of equipment manufacturing industry. *China Nonferrous Met.* 35 (1), 189–193.

Wang, B., Liang, Y., and Yuan, M. (2019). Water transport system optimisation in oilfields: Environmental and economic benefits. *J. Clean. Prod.* 237, 117768. doi:10.1016/j.jclepro.2019.117768

Wang, C., Xu, J., and Shi, W. (2013). Market analysis of plastic impeller manufacturers based on the six-power interactive model. *Energy Educ. Sci. Technol. Part B Soc. Educ. Study.* 5 (4), 567–575.

Xi, B., Wang, C., Xi, W., Liu, Y., Wang, H., and Yang, Y. (2022). Experimental investigation on the water hammer characteristic of stalling fluid in eccentric casing-tubing annulus. *Energy* 2022, 124113. doi:10.1016/j.energy.2022.124113

Xu, Y. (2017). Multi-parameter optimizing the impellers in mixing-flow pump. *J. Irrigation Drainage.* 36 (5), 79–83. doi:10.13522/j.cnki.ggps.2017.05.014

Xu, Z. (2015). Guangzhou, China: South Chi-na University of Technology. MA Dissertation, *Area logistic center's system of optimization for G pump company*

Ye, D., Li, H., Ma, Q., Han, Q., and Sun, X. (2019). Opti-mal design of vortex pump using approximate model and the non-dominated sorting genetic algorithm. *J. Irrigation Drainage.* 38 (7), 76–83. doi:10.13522/j.cnki.ggps.20190018

Zhang, T., Cheng, H., and Zhang, Y. (2008). A method based on MTO-MTS for the order planning of the steel plant. *Syst. Engineering-Theory Pract.* 28 (11), 85–93.

Zhang, Y. C., Shen, F. P., and Guo, N. (2012). Research on evaluation of supply chain quick response ability in enterprise cluster environment based on grounded theory—taking pump and valve industry in yongjia county, wenzhou as an example. *Prod. Res.* 26 (12), 211–213.

Zhu, X. (2017). Jiangsu, China,: Nanjing University. MA. Dissertation, *Research on the procurement of multi-variety small batch castings of F Pump Company*

Zhu, Z., Lin, Y., Li, X., Zhai, L., and Lin, T. (2022). Axial thrust instability analysis and estimation theory of high speed centrifugal pump. *Phys. Fluids* 34, 075118. doi:10.1063/5.0098194

frontiers | Frontiers in Energy Research

TYPE Original Research
PUBLISHED 23 January 2023
DOI 10.3389/fenrg.2022.1095854

OPEN ACCESS

EDITED BY
Kan Kan,
College of Energy and Electrical Engineering, China

REVIEWED BY
Wei Jiang,
Northwest A&F University, China
Xiaojun Li,
Zhejiang Sci-Tech University, China
Shi Lijian,
Yangzhou University, China

*CORRESPONDENCE
Erfeng Zhang,
✉ 2222006046@stmail.ujs.edu.cn

SPECIALTY SECTION
This article was submitted to Process and Energy Systems Engineering, a section of the journal Frontiers in Energy Research

RECEIVED 11 November 2022
ACCEPTED 28 November 2022
PUBLISHED 23 January 2023

CITATION
Tian F, Zhang E, Yang C, Sun D, Shi W and Chen Y (2023), Influence of installation height of a submersible mixer on solid–liquid two–phase flow field.
Front. Energy Res. 10:1095854.
doi: 10.3389/fenrg.2022.1095854

Influence of installation height of a submersible mixer on solid–liquid two–phase flow field

Fei Tian[1], Erfeng Zhang[1]*, Chen Yang[1], Dehua Sun[1], Weidong Shi[2] and Yonghua Chen[3]

[1]School of Energy and Power Engineering, Jiangsu University, Zhenjiang, China, [2]School of Mechanical Engineering, Nantong University, Nantong, China, [3]Yatai Pump & Valve Co., Ltd, Taixing, Jiangsu, China

With the increasingly severe situation of water pollution control, optimal design of the mixing flow field of submersible mixers and improving the mixing uniformity of activated sludge have become key research issues. At present, the research on the submersible mixer is mostly focused on water as the medium, and the flow field characteristics of solid-liquid two-phase flow, which is closer to the actual scene, still need more systematic research. This paper presented numerical simulations of the solid–liquid two–phase flow problem at various installation heights based on the coupled CFD–DEM method in the Euler–Lagrange framework. The velocity distribution, dead zone distribution, particles' velocity development, particles' mixing degree, and particles' aggregation of the flow field were compared and analyzed for different installation heights. The results show that the flow field has two flow patterns: single– and double–circulation, due to different installation heights, in which the velocity and turbulent kinetic energy of the flow field of the double–circulation flow pattern are more uniform. The installation height affects the moment particles enter the impeller and the core jet zone, thus affecting the degree of particle mixing and the mixing time. The adjustment of the installation height also has an impact on particle aggregation. These findings indicate that the installation height significantly affects the flow field characteristics and the particle motion distribution. The coupled CFD–DEM method can analyze the macroscopic phenomenon of the solid–liquid two–phase flow field of the submersible mixer from the scale of microscopic particles, which provides a theoretical approach for the optimal design of the mixing flow field. It can provide better guidance for engineering practice.

KEYWORDS

submersible mixer, CFD-DEM, two-phase, distribution uniformity method, grey relation analysis

1 Introduction

Submersible mixer is an efficient mixing machinery and pushing device, which plays an essential role in the wastewater treatment process. The impeller of submersible mixer rotates at a high speed driven by the motor, and energy is transferred to the surrounding fluid through the impeller to generate a rotating jet. The jet pushes and reels the surrounding fluid together with low–speed motion, thus effectively ensuring the suspension of the mixture and promoting sufficient contact and reaction between the sewage and activated sludge.

The flow field inside the pool is exceptionally complicated during the operation of submersible mixer, and experimental studies on it are challenging due to the measurement difficulty and other factors (Tian et al., 2022a). Chen et al. analyzed the effect of impeller diameter on the hydraulic characteristics of a submersible mixer based on STAR–CCM + simulation software. It was found that the mixer had the best pushing effect when the impeller diameter was 3.7 m in the square pool (Chen et al., 2018). Shi et al. analyzed the mixing flow field of submersible mixers under different pool shapes from the perspective of power consumption. They developed a more suitable pool shape for engineering applications (Shi et al., 2009). Zhang et al. found that by adjusting the placement angle of the submersible mixer, the number and scale of vortices could reduce, which improved the flow pattern at the bottom of the pool and prevented the sedimentation of activated sludge (Zhang et al., 2020). Xu et al. studied the effect of the blade gap on the shaft power, outlet flow rate, and mixing effect of a submersible mixer (Xu and Yuan, 2011). Chen et al. realized the optimal design of the blade airfoil by changing the outlet placement angle of a submersible mixer impeller. It was also verified using numerical simulation to obtain the best airfoil design (Chen et al., 2020a).

To simplify the study, the above studies have used clear water as the study medium. However, the practical application scenario of submersible mixer is sewage–activated sludge solid–liquid two–phase flow. The flow process of sludge particles in the pool is very complex, and the movement is affected by various factors. In studying of the flow field characteristics of submersible mixer, the action of fluid and medium should also be considered, namely, the solid–phase problem. Therefore, the research on the solid–liquid two–phase flow of submersible mixer is of great significance to improve the effect of sewage purification, enhance the purification efficiency and reduce energy consumption.

Currently, two main approaches are used for the study of multiphase flows in fluid mechanics: one is the Euler–Euler model, which treats both the solid particle phase and liquid phase as continuous phases (Li et al., 2021). The Mixture model based on Euler–Euler model was primarily adopted for the simulation of the solid–liquid two–phase of submersible mixer in the early days (Jin and Zhang, 2014; Tian et al., 2014). The other is Euler–Lagrange model, which treats solid particles as discrete phase and liquids as continuous phase. Compared with the two–fluid model, Euler–Lagrange model successfully introduces particle dynamics, which has the advantages of both macro and micro. It can simulate the actual situation of particle movement in the sewage treatment pool more accurately. The coupled CFD–DEM (Cundall and Strack, 1979) numerical simulation method based on Euler–Lagrange framework is now widely used in multiphase simulations in many fields. The model can realistically track the motion of each particle and calculate the collision process between particles by hard or soft sphere model, and the particle rotation can also be captured. With the development of CFD–DEM technology in recent years, the contact model of particles also introduces rolling friction model for strongly rotating systems, JKR Cohesion model for adhesion and agglomeration between particles containing moisture, and Bonding model for simulating problems such as crushing and fracture, which can analyze the interaction between continuous and discrete phases more accurately. Zhao et al. designed an orthogonal test using a coupled CFD–DEM method and an integrated Qt–based simulation platform to investigate the effect of various parameters of the impeller of the stirred kettle on the blending effect of the mixing system (Zhao, 2021). Xia et al. based on the CFD–DEM coupling method, discussed the flow characteristics of particles in the mixed–flow pump, the collision form between particles and impeller, and the severe wear area (Xia et al., 2021). Song et al. investigated particle concentration and size effects on the operational performance and wear performance of transfer pumps using coupled CFD–DEM (Song et al., 2021a). Li et al. used the DEM-CFD coupling method to analyze the internal flow field and particle motion law of a two-stage deep-sea lifting pump at different speeds and studied the secondary flow phenomenon (Yuanwen et al., 2022). Tian et al. studied the solid–liquid two–phase flow field of a submersible mixer by using the CFD–DEM coupling method. They found that the distribution of particles was affected by the vortices in the pool. The particle group easily accumulated around the vortices and near the dead zones of the flow field (Tian et al., 2022b).

In summary, this paper compared and analyzed the motion features of two phases at different installation heights based on the unresolved CFD–DEM coupled numerical simulation method. At the same time, the mixing degree of activated sludge particles inside the pool is comprehensively evaluated and analyzed using the distribution uniformity method and grey relation analysis method. In addition, the aggregation of particles at different installation heights and the occurring causes are discussed, which has good guidance significance for engineering practice.

2 Calculation model

2.1 Physical model

The pool model and the arrangement of the submersible mixer studied in this paper are shown in Figure 1. The model and

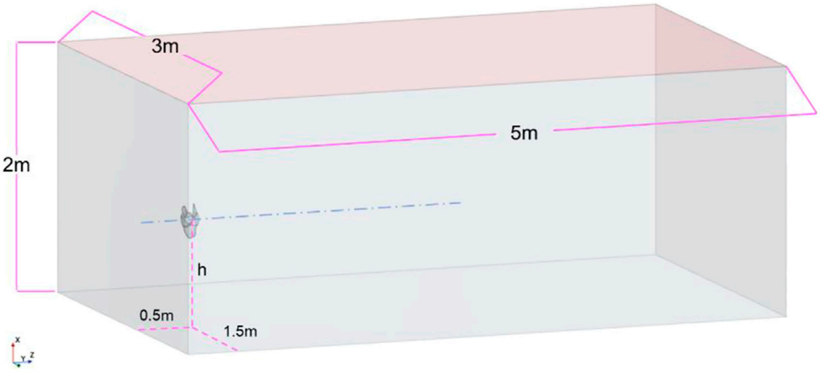

FIGURE 1
Arrangement of pool and submersible mixer.

TABLE 1 Installation height of submersible mixer.

Scheme	1	2	3	4
h (m)	0.3	0.5	0.8	1

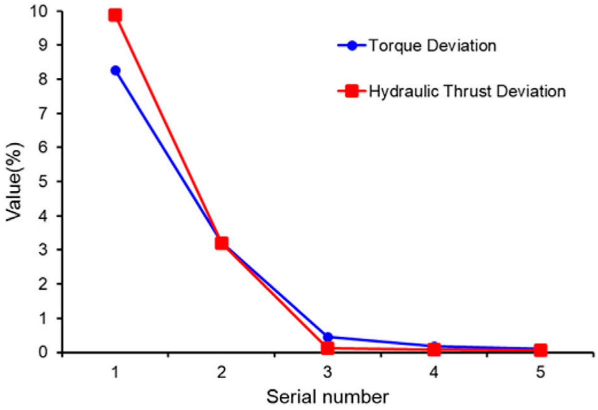

FIGURE 2
Grid independence verification.

arrangement refer to the actual model of a wastewater treatment plant. The size of the pool is the length $L = 5$ m, width $W = 3$ m, and effective water depth of $H = 2$ m. The model of the submersible mixer is simplified for the impeller water body, impeller diameter $D = 315$ mm, hub diameter $d = 105$ mm, impeller speed $n = 1{,}600$ rpm. The submersible mixer is installed parallel to the bottom of the pool, equal distance from the left and right walls, and the height from the bottom of the pool is h. To study the influence of the installation height of the submersible mixer on the solid–liquid two–phase flow field, four schemes are designed, as shown in Table 1.

2.2 Mathematical model

2.2.1 Continuous phase mathematical model

In this paper, the continuity equation and momentum equations (Navier–Stokes equations) are used for the solution

TABLE 2 Discrete phase parameters.

D_p/mm	Number	ρ_p/kg/m^3	Poisson's ratio	Young's modulus/MPa
6	396,500	1,004	0.45	0.21

FIGURE 3
Y = 0 plane.

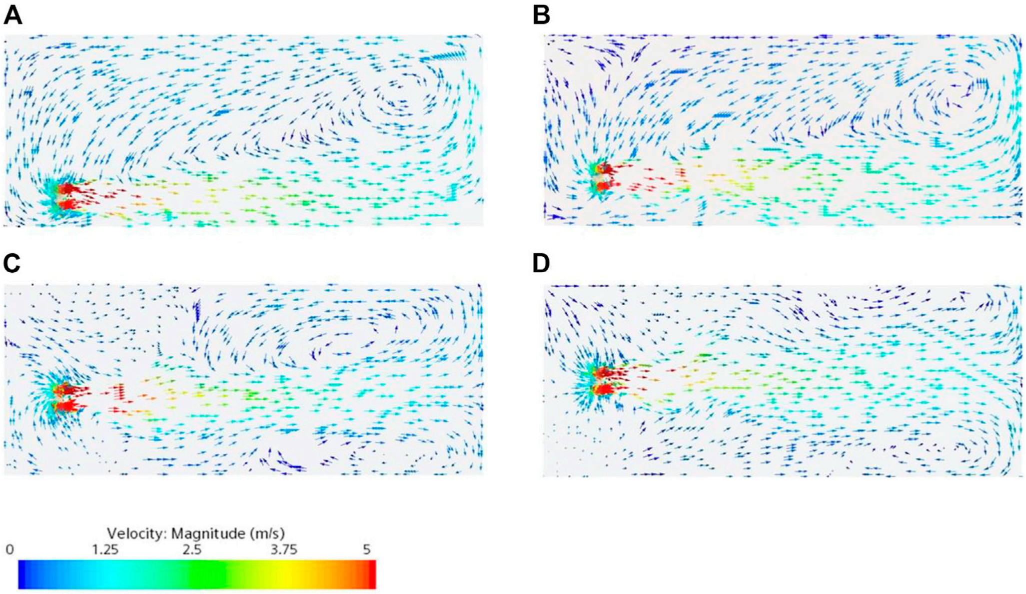

FIGURE 4
Velocity contour maps of Y = 0 plane at 36 s:**(A)** Scheme 1; **(B)** Scheme 2; **(C)** Scheme 3; **(D)** Scheme 4.

of continuous phase. The standard $k-\varepsilon$ turbulence model is chosen for the turbulence model.

1) Continuity equation

$$\frac{\partial u_j}{\partial x_j}=0 \tag{1}$$

2) Navier–Stokes equations

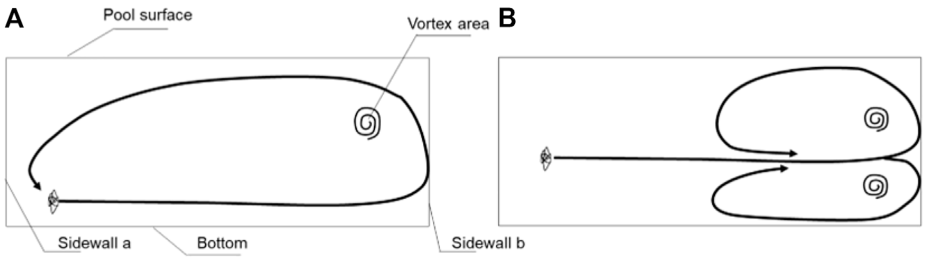

FIGURE 5
Schematic generalization of flow contours: **(A)** Single cycle; **(B)** Double cycle.

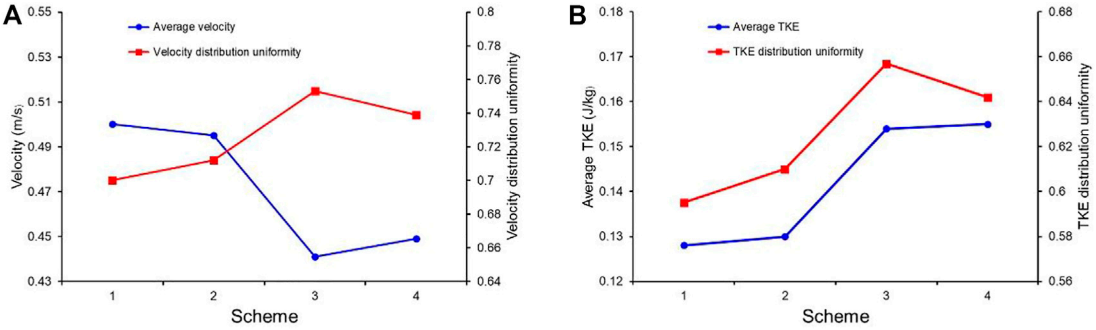

FIGURE 6
(A) Flow field average velocity and velocity distribution uniformity; **(B)** Flow field average TKE and TKE distribution uniformity.

FIGURE 7
X = 0.01 m plane.

$$\frac{\partial u_i}{\partial t}+u_j\frac{\partial u_i}{\partial x_j}=f_i-\frac{1}{\rho_f}\frac{\partial p}{\partial x_j}+\frac{\mu_f}{\rho_f}\frac{\partial^2 u_i}{\partial x_j} \tag{2}$$

where ρ_f is the density of fluid, u is the velocity of fluid, μ_f is the dynamic viscosity of fluid, p is the pressure, and f is the volume force.

3) Turbulence model

In the numerical simulation of submersible mixers, the turbulence model that is currently used is the standard k-ε model (Chen et al., 2016; Gong et al., 2017; Chen et al.,

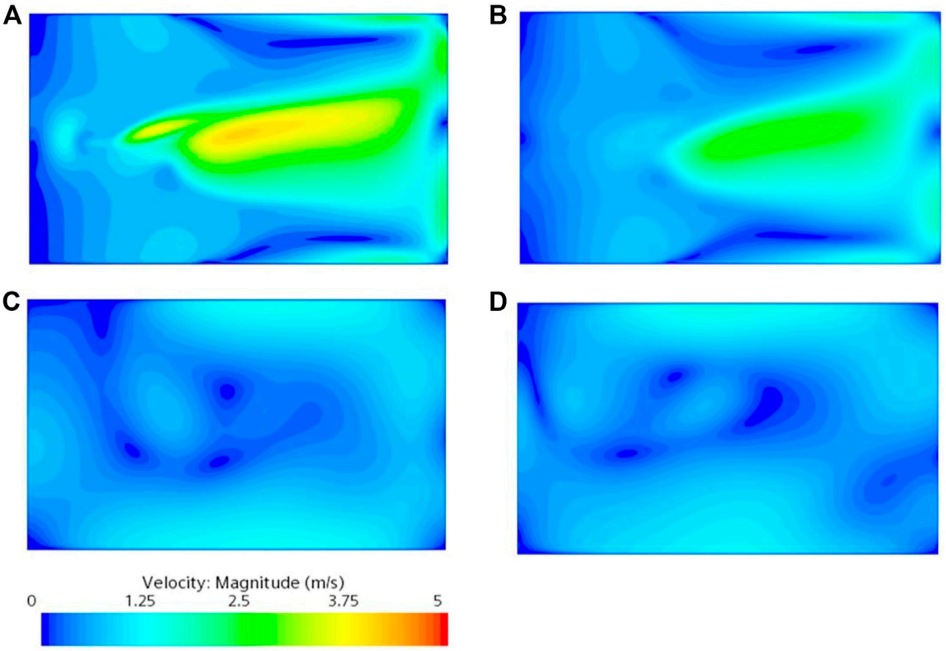

FIGURE 8
Velocity contour maps of X = 0.01 m plane:**(A)** Scheme 1; **(B)** Scheme 2; **(C)** Scheme 3; **(D)** Scheme 4.

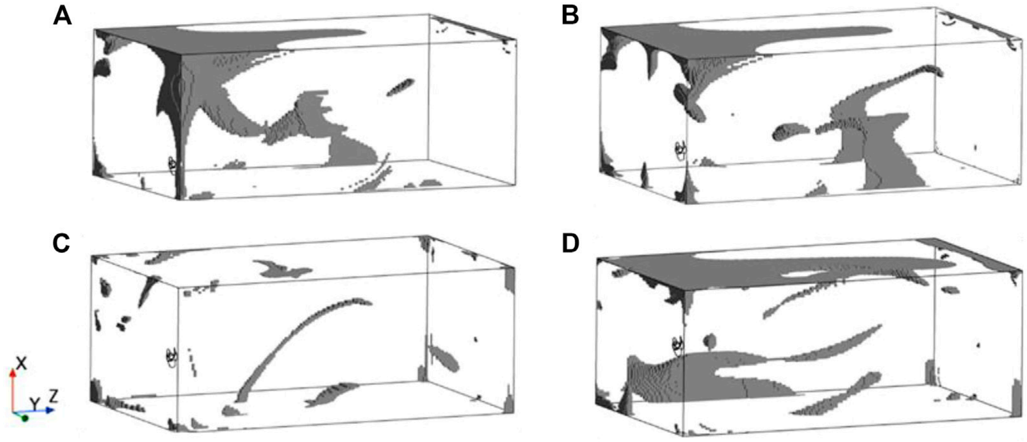

FIGURE 9
Dead zone distribution:**(A)** Scheme 1; **(B)** Scheme 2; **(C)** Scheme 3; **(D)** Scheme 4.

2020a; Zhang et al., 2020). Li compared the difference between the standard k-ε, RNG k-ε, SST, and RSM four turbulence models in the numerical simulation of the stirred kettle with the experimental results. It was found that the results of the pressure and velocity fields predicted using the RSM model and the RNG k-ε model deviated significantly from the actual situation. While the results using the SST model and the standard k-ε model were closer to the actual situation (Li, 2020). In this paper, the standard $k-\varepsilon$ turbulence model is used to determine the turbulent viscosity coefficient μ_t using the turbulent energy transport k equation and the energy dissipative transport ε equation. The equations are as follows.

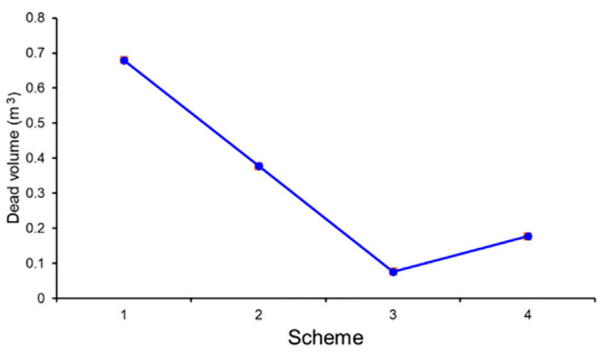

FIGURE 10
Dead zone volume.

$$\begin{cases} \mu_t = \rho_f C_\mu \dfrac{k^2}{\varepsilon} \\ \dfrac{\partial}{\partial t}(\rho_f k) + \dfrac{\partial}{\partial x_i}(\rho_f k u_i) = \dfrac{\partial}{\partial x_j}\left[\left(\mu_f + \dfrac{\mu_t}{\sigma_k}\right)\dfrac{\partial k}{\partial x_j}\right] + G_k - \rho_f \varepsilon \\ \dfrac{\partial}{\partial t}(\rho_f \varepsilon) + \dfrac{\partial}{\partial x_i}(\rho_f k u_i) = \dfrac{\partial}{\partial x_j}\left[\left(\mu_f + \dfrac{\mu_t}{\sigma_\varepsilon}\right)\dfrac{\partial \varepsilon}{\partial x_j}\right] + C_{1\varepsilon}\dfrac{\varepsilon}{k}G_k - C_{2\varepsilon}\rho_f \dfrac{\varepsilon^2}{k} \\ G_k = \mu_t\left(\dfrac{\partial u_i}{\partial x_j} + \dfrac{\partial u_j}{\partial x_i}\right)\dfrac{\partial u_i}{\partial x_j} \\ C_\mu = 0.09, \sigma_k = 1.0, \sigma_\varepsilon = 1.44, C_{1\varepsilon} = 1.44, C_{2\varepsilon} = 1.92 \end{cases} \tag{3}$$

where G_k is the turbulent kinetic energy term generated by the average velocity gradient; σ_k and σ_ε are the Prandtl numbers corresponding to turbulent kinetic energy and turbulent dissipation rate, respectively; C_μ, $C_{1\varepsilon}$ and $C_{2\varepsilon}$ are empirical constants.

2.2.2 DEM mathematical model

The motion of discrete phase is described by discrete element method (DEM). The motion equations of particles under translation and rotation are as follows (Song et al., 2021b):

$$\begin{cases} m_p \dfrac{dv_p}{dt} = F_{drag} + F_p + F_g + F_{LR} + F_{LS} + F_c \\ I_p \dfrac{d\omega_p}{dt} = M_b + M_c \end{cases} \tag{4}$$

where m_p is the particle mass, v_p is the instantaneous particle velocity, M_d is the drag torque, M_c is the contact torque, $F_{drag}, F_p, F_g, F_{LR}, F_{LS}$ and F_c are the surface and volume forces acting on particle, I_p is the rotational inertia of particle, ω_p is the angular velocity of particle.

1. Surface forces
1) Drag force

F_{drag} is drag force of continuous relative discrete phase, defined as follows:

$$\begin{cases} F_{drag} = \dfrac{1}{2} C_d \rho_f A_p \left|v_f - v_p\right|\left(v_f - v_p\right) \\ C_d = \begin{cases} \dfrac{24}{\mathrm{Re}_p}\left(1 + 0.15\mathrm{Re}_p^{0.687}\right) Re_p \leqslant 10^3 \\ 0.44 \quad Re_p > 10^3 \end{cases} \\ \mathrm{Re}_p = \dfrac{\rho_f \left|v_f - v_p\right| D_p}{\mu_f} \end{cases} \tag{5}$$

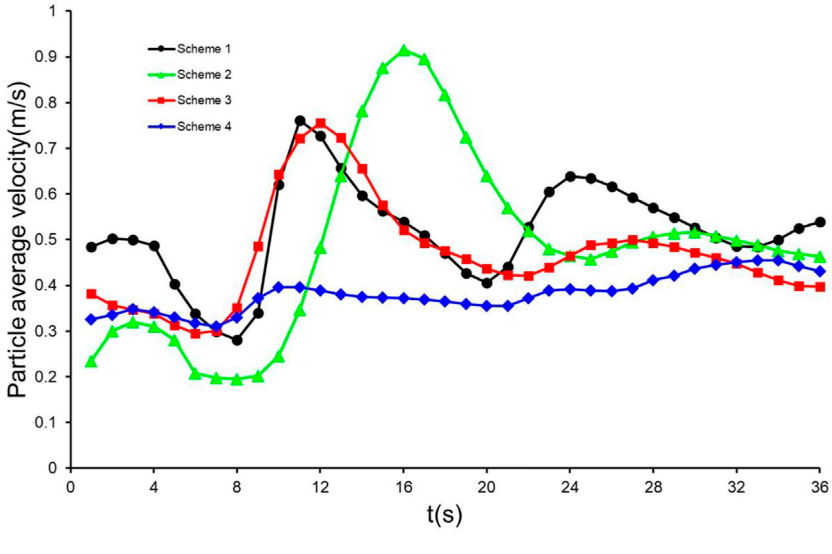

FIGURE 11
0 s–36 s particle average velocity.

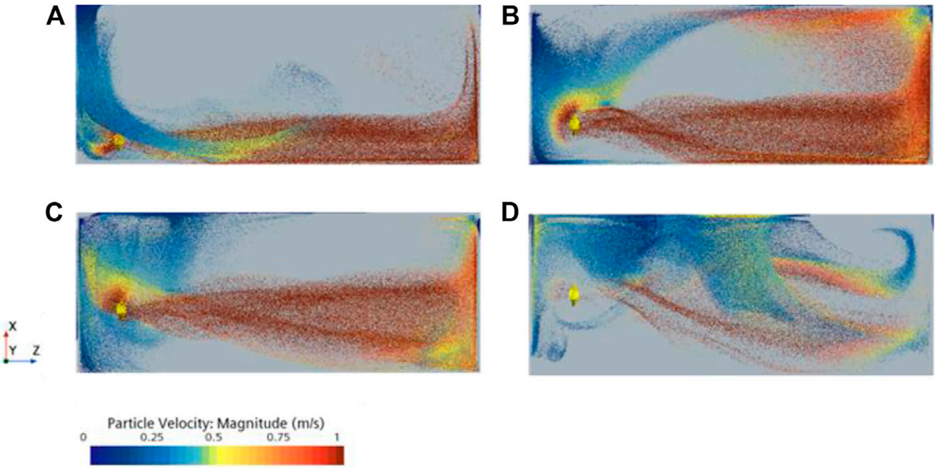

FIGURE 12
Particle distribution and velocity at peak time:**(A)** Scheme 1:11 s; **(B)** Scheme 2:16 s; **(C)** Scheme 3:12 s; **(D)** Scheme 4:10 s.

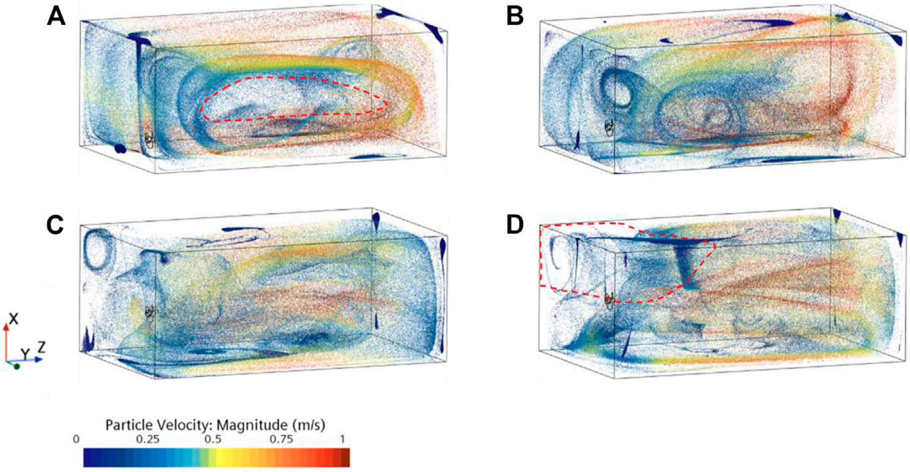

FIGURE 13
Particle position and velocity at 36 s:**(A)** Scheme 1; **(B)** Scheme 2; **(C)** Scheme 3; **(D)** Scheme 4.

where, C_d is the drag coefficient (Schiller, 1933), v_f is the instantaneous fluid velocity, Re_p is the particle Reynolds number, and D_p is the particle diameter.

2) Pressure gradient force

F_p is the pressure gradient force, defined as follows:

$$F_p = -V_p \nabla p_{static} \tag{6}$$

where V_p is the particle volume and ∇p_{static} is the gradient of the static pressure in continuous phase.

2. Volume forces
1) Gravitational force

F_g is the gravitational force of particle, defined as follows:

$$F_g = m_p g \tag{7}$$

2) Rotational lift force

F_{LR} is the particle rotational lift force, which is the lift due to the change in the flow field's velocity gradient caused by the particles' rotation (Oesterlé and Dinh, 1998). The jet of the

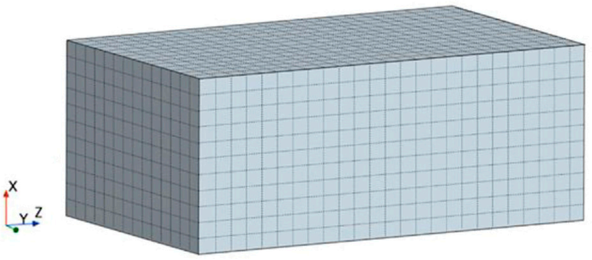

FIGURE 14
Cells of pool.

submersible mixer is rotational, and the particles acquire a large angular velocity after being ejected from the impeller, making the particles still have a high angular velocity in the low Reynolds number regions (Tian et al., 2022b). In these areas, the rotational lift's influence on the particles' motion is greater. Therefore, rotational lift should not be neglected in mixing systems with high impeller speeds (Shao et al., 2013). It is defined as follows:

$$\begin{cases} F_{LR} = \frac{\rho\pi}{8} D_p^2 C_{LR} \left| v_f - v_p \right| \frac{\Omega\left(v_f - v_p\right)}{|\Omega|} \\ C_{LR} = 0.45 + \left(\frac{\mathrm{Re}_R}{\mathrm{Re}_p} - 0.45\right) e^{-0.5684 \mathrm{Re}_R^{0.4} \mathrm{Re}_p^{0.3}} \end{cases} \tag{8}$$

where Ω is the angular velocity of the particle relative to the fluid and C_{LR} is the rotational lift coefficient.

3) Shear lift force

F_{LS} is the particle shear lift force, which is generated by the velocity gradient perpendicular to the main flow direction (Saffman, 1965). In the flow field of the submersible mixer, a very distinct central jet region exists, and there is a large velocity gradient between this region and the surrounding flow field, so the shear lift force should not be neglected (Zhang et al., 2009; Ren et al., 2021). It is defined as follows:

$$\begin{cases} F_{LS} = C_{LS} \frac{\rho\pi}{8} D_p^3 \left(v_f - v_p\right) \omega \\ C_{LS} = \frac{4.1126}{\mathrm{Re}_S^{0.5}} \\ \omega = \nabla \times u \end{cases} \tag{9}$$

Where $\boldsymbol{\omega}$ is the curl of fluid velocity, and C_{LS} is the shear lift coefficient.

4) Contact force

F_c is the contact force. In this paper, the Hertz–Mindlin no–slip contact model is chosen, defined as follows (Xia et al., 2021):

$$\begin{cases} F_c = F_{cn} + F_{ct} \\ F_{cn} = 1.5 \frac{Y}{1 - \mu^2} \sqrt{R_{ab}} \sqrt{u_n^3} \\ F_{ct} = 12\left(G_{ab} \sqrt{R_{ab} u_n}\right) \sqrt{u_t^3} \end{cases} \tag{10}$$

where F_{cn} and F_{ct} are normal and tangential contact forces respectively, Y is the equivalent modulus of elasticity, μ is the Poisson's ratio, R_{ab} is the equivalent contact radius, u_n is the normal displacement, u_t is the tangential displacement, and G_{ab} is the equivalent shear modulus.

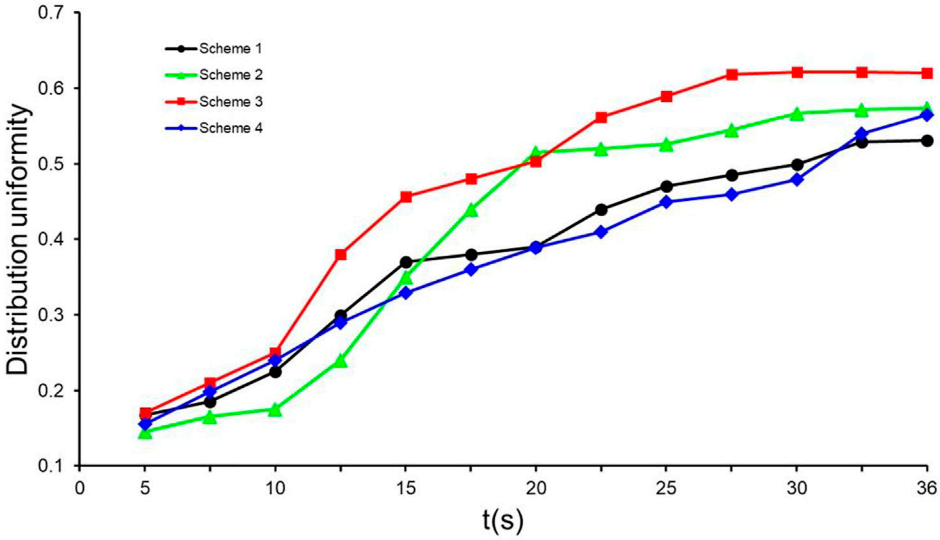

FIGURE 15
Particle distribution uniformity.

TABLE 3 Percentage of cells number in each particle bin.

Particle bin	ξ_1/%	ξ_2/%	ξ_3/%	ξ_4/%
0–80	69.89	62.35	62.32	69.31
80–150	15.71	20.40	19.52	16.00
150–300	4.48	5.89	6.99	5.25
300–500	7.07	8.59	9.63	7.47
500–100	2.00	1.79	1.07	1.23
>1,000	0.85	0.99	0.48	0.75

The normal activated sludge MLSS, concentration range is 1,500–4,000 mg/L, and the corresponding particle number range is 95–280. Therefore, the maximum value of 80–150, 150–300, and the minimum value of the remaining intervals are selected to form an ideal sequence. The ideal sequence is.

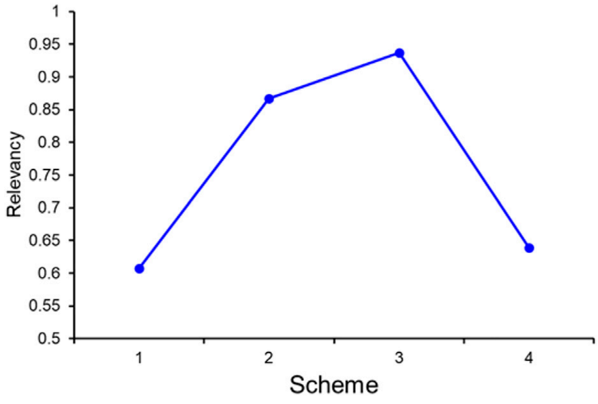

FIGURE 16
Relevancy.

3 Numerical calculation

3.1 Grid

In the simulation calculation, increasing the number of cells can improve the computational accuracy, but the computational time will increase significantly. In addition, the improvement in computational accuracy is not noticeable when the number of cells reaches a specific number. In addition, grid independence verification is required to achieve guaranteed computational accuracy while minimizing the number of cells and improving the quality of the grid. This paper selected the commercial software STAR–CCM + for grid generation. The pool region was divided by the hexahedral grid, and the impeller region was divided by the polyhedral grid. The polyhedral grid originated from the honeycomb conjecture that the same area can be

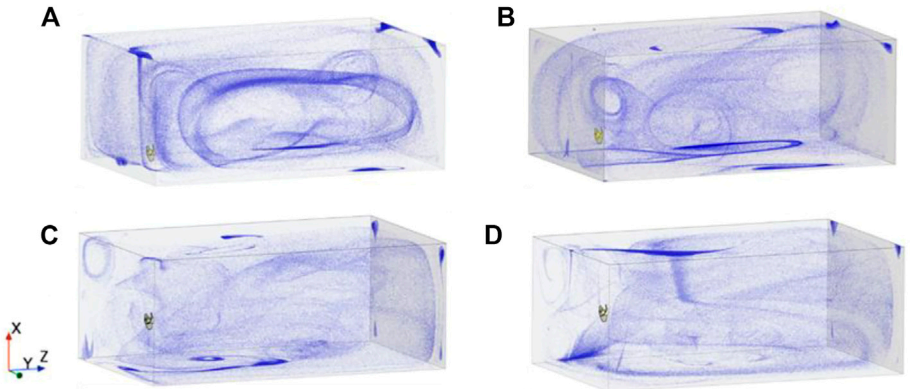

FIGURE 17
Particle distribution at 36 s:**(A)** Scheme 1; **(B)** Scheme 2; **(C)** Scheme 3; **(D)** Scheme 4.

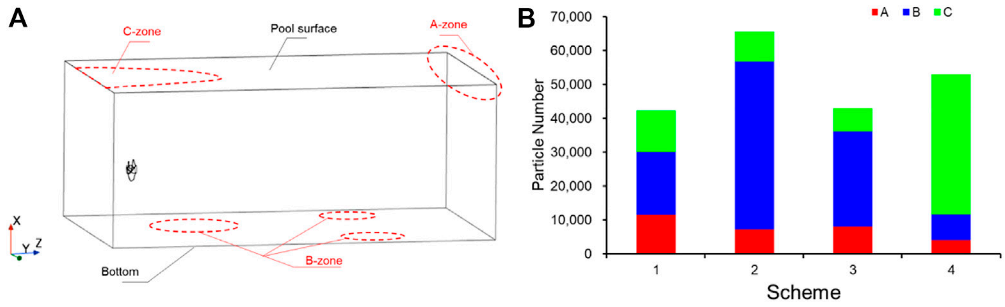

FIGURE 18
(A) Position of particle accumulation zones; **(B)** Number of particles in the particle accumulation zones.

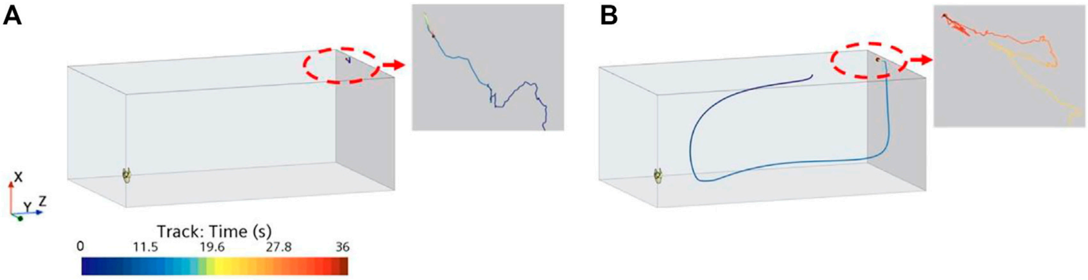

FIGURE 19
Particle track in the A–zone: **(A)** Particle track 1; **(B)** Particle track 2.

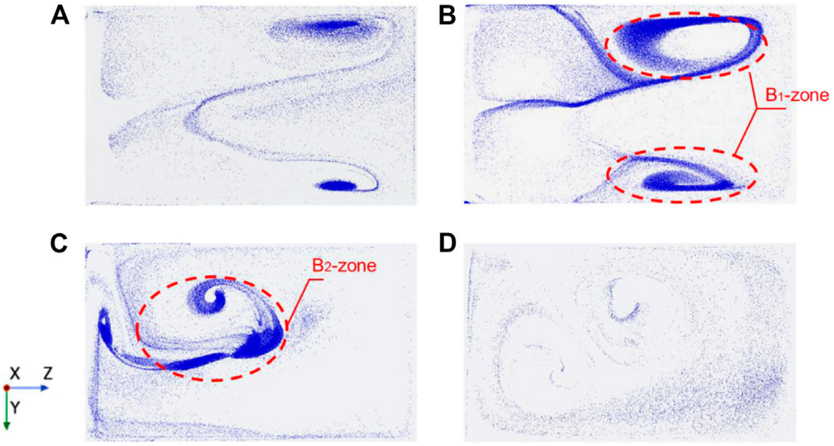

FIGURE 20
Particle distribution in the B–zone at 36 s **(A)** Scheme 1; **(B)** Scheme 2; **(C)** Scheme 3; **(D)** Scheme 4.

divided using the least number of perimeters. Compared with the traditional grid, the polyhedral grid has more adjacent cells, and the calculation of gradient and local flow conditions are predicted more accurately. Chen et al. studied the flow field of a submersible mixer using the polyhedral grid for research. They concluded that the polyhedral grid could reduce the

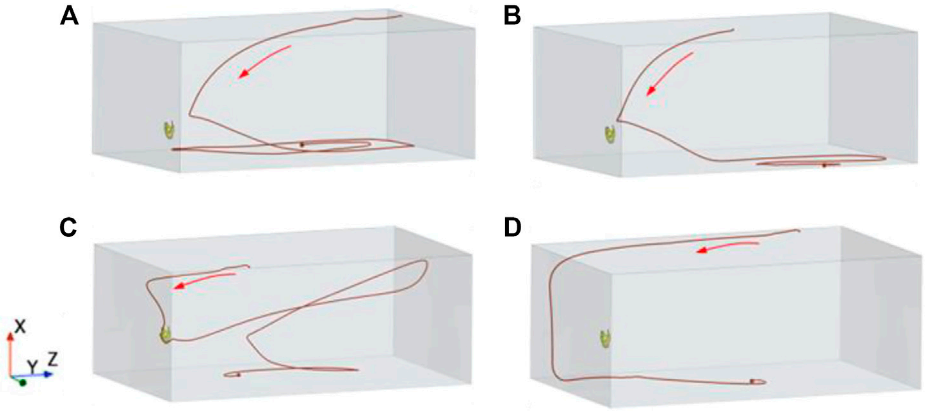

FIGURE 21
Particle track in the B–zone. **(A)** Particle track one in the B_1–zone; **(B)** Particle track two in the B_1–zone; **(C)** Particle track one in the B_2–zone; **(D)** Particle track two in the B_2–zone.

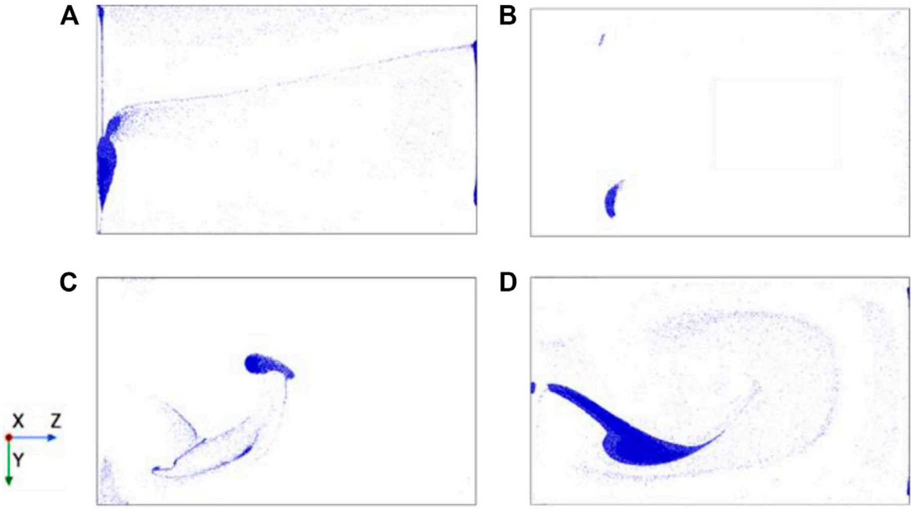

FIGURE 22
Particle distribution in the C–zone at 36 s **(A)** Scheme 1; **(B)** Scheme 2; **(C)** Scheme 3; **(D)** Scheme 4.

computational time and ensure computational accuracy (Chen et al., 2020b; Xu et al., 2021).

Five sets of grids are established, which are 320,438, 621,211, 1,542,649, 2,186,086, and 4,030,726. The grid independence verification was performed by comparing the deviations of the hydraulic thrust and torque of the five sets of models with the actual model (Lin et al., 2021; Zhu et al., 2022). The water thrust of this actual model is 2284 N, and the torque is 109 Nm. The deviation of the numerical simulation results from the actual model parameters under five different sets of grid models is shown in Figure 2. The deviation between the numerically simulated torque and hydraulic thrust and the actual model gradually decreases as the number of cells increases, and the deviation tends to be stable from the third group of models. Taking into account the issues of calculation accuracy and computing capacity, this paper selects the third grid as the simulated object.

3.2 Other settings

The initial conditions of the continuous phase were calculated by the MRF method, and then the sliding grid method was used for the coupling calculation. The impeller

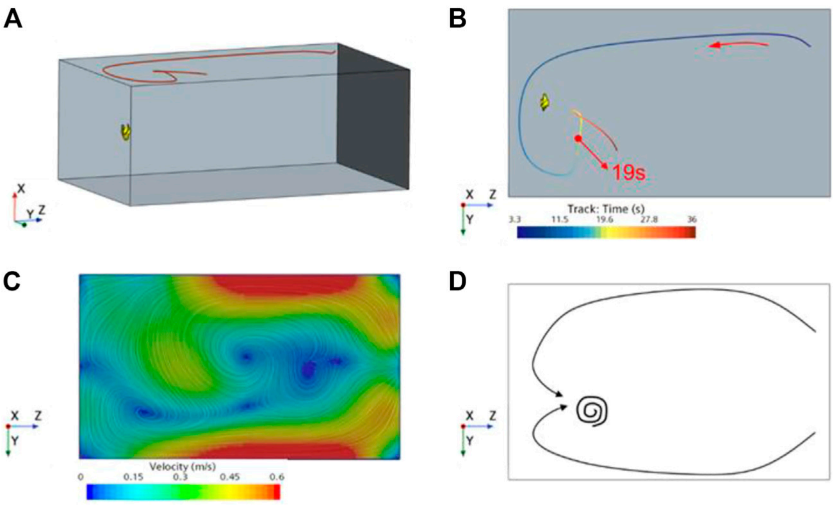

FIGURE 23
(A) Particle track in the C–zone; **(B)** Vertical view of particle track; **(C)** Flow field diagram of C–zone; **(D)** Schematic diagram of vortex formation.

area was the rotational domain, and the interface between the pool and the impeller region was set to interface. The free surface of the pool was set by the rigid–lid assumption, and the remaining walls were set to non-slip walls. The standard $\kappa - \varepsilon$ turbulence model was chosen for the turbulence model. The wall treatment was high y + wall treatment, y + > 30, and the continuous convergence residual was set to 10^{-4}.

The discrete phase was solved using the DEM model. The ejector of particles was located near the water surface, and the particles entered the pool vertically downward from the vicinity of the water surface after the convergence of the continuous phase. The injection time was 4 s. The particles were activated sludge particles and the specific parameters are shown in Table 2. The water surface was set to "phase impermeable" to avoid particles escaping from the water surface, and the rest of the walls were selected to "DEM mode". The DEM time step was set to 0.000497 s, and the time step of the continuous phase was 0.00497 s. The second–order implicit unsteady solver was adopted to perform the solution, and the total solution time was 36 s.

4 Result and discussion

4.1 Distribution of the pool flow field

4.1.1 Distribution of velocity

The cross–section (Y = 0 m plane) along the axis of the impeller and perpendicular to the pool bottom is selected for flow field analysis. The plane's position is shown in Figure 3. Figure 4 shows the velocity vector of the Y = 0 m plane in the four schemes at 36 s. With the increase in the submersible mixer's installation position, the jet's adsorption on the surrounding fluid inhibits the backflow. The vortex above gradually decreases, and the vortex below gradually forms. The jet zone of Scheme 1 and Scheme 2 scour the pool bottom, climb along the pool wall after impacting the wall, and begin to backflow near the pool surface. In scheme 3 and scheme 4, the jet zone is far from the pool bottom, and the development of the jet is less affected by the bottom. It is inferred that the pool has two approximate macroscopic flow patterns due to the different installation heights. Schemes 1 and 2 can be approximated as a single cycle, as shown in Figure 5A, and schemes 3 and 4 can be approximated as a double cycle, as shown in Figure 5B. The single–cycle flow field has a large vortex, and the double–cycle flow field has a vortex on each side of the jet.

To evaluate the flow field under the two flow patterns, the average velocity, average turbulent kinetic energy (TKE), velocity distribution uniformity, and turbulent kinetic energy distribution uniformity of the flow field at 36 s were counted. The calculation formula is as follows:

$$\begin{cases} \bar{v} = \dfrac{\sum_c v_c V_c}{\sum_c V_c} \\ \bar{k} = \dfrac{\sum_c k_c V_c}{\sum_c V_c} \\ \Upsilon_v = 1 - \dfrac{\sum_c |v_c - \bar{v}| V_c}{2\bar{v} \sum_c V_c} \\ \Upsilon_k = 1 - \dfrac{\sum_c |k_c - \bar{k}| V_c}{2\bar{k} \sum_c V_c} \end{cases} \tag{11}$$

where v_c is the velocity of the fluid in the grid cell, V_c is the volume of the grid cell, $\bar{k}$ is the turbulent kinetic energy of the fluid in the grid cell, and $\bar{v}$, $\bar{k}$, Υ_v and Υ_k are the average velocity, velocity distribution uniformity, average turbulent kinetic energy, and turbulent kinetic energy distribution uniformity of the flow field, respectively.

The statistical results are shown in Figure 6. Scheme 1 and scheme 2 under the single–cycle flow pattern have higher average velocities, but the uniformity of the velocity distribution, average turbulent kinetic energy, and turbulent kinetic energy distribution are smaller than those of scheme 3 and scheme 4 under the double–cycle flow pattern. Combined with the vector diagram in Figure 4, it can be analyzed that although the velocity in the flow field of the single–cycle flow pattern is significant, the velocity direction tends to be consistent, and the turbulence intensity is low. The velocity direction of the flow field in the double cycle flow pattern is chaotic, and the turbulence intensity is high. Its overall velocity and turbulent kinetic energy distribution are uniform, and thus, the mixing performance is better.

The flow field distribution at the pool bottom usually significantly influences the solid phase distribution at the bottom (Zhang et al., 2020). Therefore, the flow field on the horizontal cross–section (x = 0.01 m plane) at 0.01 m from the pool bottom was analyzed, and its location is shown in Figure 7. The velocity contour maps in the x = 0.01 m plane at 36 s for the four schemes are shown in Figure 8. It can be seen that there is a sizeable high–speed region at the pool bottom for scheme 1 and scheme 2. This region is caused by the effective diffusion radius (ChineseStandard.net, 2007) of the submersible mixer's rotational jet along the axial development being greater than the installation height and causing the jet to scour the pool bottom. In Schemes 3 and 4, the overall velocity at the pool bottom is lower but more uniformly distributed.

4.1.2 Distribution of dead zones

The purpose of mixing is to transport more kinetic energy to more regions of the flow field. However, due to various factors, there will always be regions with good fluidity and adequate mixing and regions with too low flow velocity, also known as dead zones (Monteith and Stephenson, 1981). The distribution of the dead zone is an important indicator to evaluate the distribution of the flow field. In the field of submersible mixers, the flow field region where the velocity is less than 0.05 m/s is called the dead zone (Tian et al., 2014). Figure 9 shows the distribution of dead zones in the four schemes. The dead zones of the flow field are consistently located, mainly at the pool's corners, the water surface above the submersible mixer, and the vortex's core. Figure 10 shows the value of the dead zone volume. The volume size of the dead zone changes with the installation height of the mixer. The dead zone volume of program three is significantly smaller, with a dead zone volume of 0.0765 m^3, accounting for 0.25% of the total volume.

4.2 Motion analysis of particles

4.2.1 Particle velocity analysis

Figure 11 shows the variation in the average velocity of particles with time. The average velocity of the particles in schemes 1, 2, and three fluctuates considerably with time, while the average velocity of scheme 4 changes more gently throughout the period. Schemes 1, 2, and three all show one significant decrease in the average velocity of the particles after t = 4 s. The main reason is that 0–4 s is the generation period of the particles. The particles have a vertical downward initial velocity, while the velocity component in the vertical direction of the flow field in this region is low. There is a large slip velocity between the two phases, which leads to a decrease in the average velocity of the particles. Subsequently, the average velocity of particles in schemes 1, 2, and three increased rapidly and gradually reached the peak, but scheme 4 did not show a significant peak. Figure 12 shows the position and velocity distribution of particles at the peak time of each scheme. It can be seen that a large number of particles in schemes 1, 2, and three are inhaled by the impeller and move with the jet, and the particles obtain a large amount of energy. At this time, the particle group moves like a jet in the flow field. In Scheme 4, due to the high installation position, many particles are entrained by the jet and not into the impeller, so there is no prominent velocity peak. After the first peak, the change in the average particle velocity of scheme 2 and scheme 3 gradually stabilized. In contrast, scheme 1 showed a significant peak again, indicating that more particles entered the impeller again. At 36 s, it can be seen that the average velocity of particles in schemes 2, 3, and 4 has reached a relatively stable state, while the average velocity of scheme 1 has a significant increasing trend. Figure 13 shows the velocity and position distribution of the particles in the four schemes at 36 s. Combined with Figure 5, it can be concluded that since scheme 1 is an apparent single–cycle flow field, a large number of particles move along the wall of the pool, while fewer particles move to the middle of the pool, as shown in the dashed area of Figure 13A Scheme 4 is an apparent double–cycle flow field. A large number of particles do not enter the impeller, and kinetic energy is obtained mainly through the entrainment of the jet. The particles mainly circulate downstream of the pool, so a sizeable sparse particle area and a low–speed particle aggregation area appear in the upper area of the impeller, as shown in the dashed area of Figure 13D.

4.2.2 Particle mixing analysis

In this paper, the distribution uniformity method and the grey relation analysis (Zhang et al., 2020) are used to evaluate the mixing degree of particles in pool.

Divide the pool evenly into 3,750 parts. Define each part as a cell, as shown in Figure 14. The number of particles in each cell was counted to calculate the uniformity of particle distribution in the pool. The calculation formula is as follows (Tian et al., 2022b):

$$\Upsilon_p = 1 - \frac{\sum_c |n_c - \bar{n}|}{2|\bar{n}|C} \tag{12}$$

where n_c is the number of particles in the cell, $\bar{n}$ is the average number of all cells, and C is the number of cells. The value of Υ_p is larger, indicating that the distribution of particles is more uniform, and the maximum value is 1.

The variation in particle distribution uniformity with time for the four schemes is shown in Figure 15. The uniformity of the particle distribution of schemes 1, 2, and three is close to stable at t = 33 s, t = 30 s, and t = 27 s, respectively, indicating that the distribution of particles has reached the dynamic equilibrium state at this time, while the distribution of particles of scheme 4 still has not reached the stable state until 36 s. It can be seen that the mixing time for the particles of scheme 3 to reach the stable state is the shortest, and the mixing time of scheme 4 is the longest. At t = 36 s, the particles of scheme 3 had the highest uniformity of distribution with 0.62; scheme 1 had the worst uniformity of distribution with 0.53. The installation height of the submersible mixer has a significant impact on the degree of mixing of particles and mixing time.

The grey relation analysis method is used to evaluate the mixing of particles in the pool (Zhang et al., 2020). The percentage of cells number in different particle number bins constitute a set of sample sequences, with a total of four sets of characteristic sequences. Each group of sequences is recorded as:

$$X = \begin{cases} \xi_l \mid l \in M, M = 1, 2\cdots, mm \geqslant 1 \\ \xi_l = (\xi_l(1), \xi_l(2), \cdots, \xi_l(n)) \\ \xi_l(k) \in \xi_l, k \in K, K = 1, 2\cdots, n, n \geqslant 2 \end{cases} \tag{13}$$

where, l is the l-th scheme and k is the k-th particle number bin, m is the number of schemes and n is the number of particle bins. The details are shown in Table 3.

$$\xi_0 = \{62.32,\ 20.40,\ 13.60,\ 7.07,\ 1.07,\ 0.48\} \tag{14}$$

The formula for calculating the relevance coefficient (Υ) is as follows:

$$\xi_{0l}(k) = \frac{\min\limits_{l\in M}\min\limits_{k\in K}|\xi_0(k) - \xi_l(k)| + 0.5\max\limits_{l\in M}\max\limits_{k\in K}|\xi_0(k) - \xi_l(k)|}{|\xi_0(k) - \xi_l(k)| + 0.5\max\limits_{l\in M}\max\limits_{k\in K}|\xi_0(k) - \xi_i(k)|} \tag{15}$$

The formula for calculating the relevancy (Υ_i) is as follows:

$$\Upsilon(\xi_0, \xi_l) = \frac{1}{n}\sum\nolimits_{k=1}^{n}\xi_{0l}(k) \quad l = 1, 2, \cdots, m \tag{16}$$

where $\Upsilon(\xi_0, \xi_l)$ is the relevancy of ξ_l to ξ_0, its value ranges from 0 to 1, with 0 indicating no correlation and one indicating complete correlation.

Figure 16 shows the relevancy between the characteristic and ideal sequences at different installation heights. From the figure, it can be seen that the highest distribution correlation is 0.936 for scheme 3 and the lowest distribution correlation is 0.607 for scheme 1. The particle distribution inside the pool is closest to the ideal situation when the installation height is 0.8 m as evaluated by the grey relation analysis. The result is consistent with the conclusion reached using the distribution uniformity method, so it can be concluded that the grey relation analysis method can be used to analyze the degree of particle mixing. The grey relation analysis method considers the existence of multiple concentration ranges of solid phase distribution inside the pool. It is suitable for evaluating the mixing of solid phases in the flow field where there are significant core jet zones or high concentration zones.

4.2.3 Particle aggregation analysis

Figure 17 shows the distribution of particles inside the pool at 36 s, and the location where particle aggregation occurs can be seen from the figure. The location of particle aggregation changes with the change in installation height, and there are three prominent locations where aggregation occurs, as shown in Figure 18A. These three areas are named the A–zone, B–zone, and C–zone. The number of particles in these three areas is counted, as shown in Figure 18B. It can be found that the least number of particles with aggregation occurs in scheme 1, but the number of particles with aggregation in the A–zone is more significant than that in the other schemes. Scheme 2 has the highest number of particles with aggregation, and the aggregation of particles mainly occurs in the B–zone. The number of particles aggregated in Scheme 3 is close to that of Scheme 1, and the particles aggregated mainly in the B–zone. Scheme 4 has a higher number of aggregated particles, and the main aggregation area of particles is the C–zone. It is the scheme with the highest number of aggregated particles in the C–zone among the four groups of schemes.

Figure 19 shows the tracks of the two particles aggregated in the A–zone during 0–36 s. From Figure 9, it can be seen that the A–zone of all four schemes is the dead zone of the flow field. Due to the inability to obtain enough kinetic energy, the particles that enter this region directly from the beginning cannot leave and gradually accumulate, as shown in Figure 19A. Some particles enter this region during the backflow process. Due to the large slip velocity between the particles and the flow field in this region, the kinetic energy of the particles decreases and gradually aggregates, as shown in Figure 19B.

Figure 20 shows the particle distribution of the B–zone in the four schemes. It can be seen that schemes 1 and 2 have similar particle aggregation areas downstream of the pool, named the B_1–zone. Schemes 3 and 4 have no particle aggregation in this area, but Scheme 3 has a lot of particle aggregation in the middle of the pool bottom, which is named the B_2–zone. Several particle tracks in Scheme 2, where particle aggregation is more pronounced in the B_1–zone, are selected, as shown in Figures 21A, B. Combined with Figure 4, it can be seen that the radial disturbance radius of the rotational jet of the submersible mixer gradually increases along the axial direction, and the jet area scours the pool bottom because the installation position is closer to the bottom. Some of the particles carried by the jet will impact the pool bottom together with the jet. After the collision with the pool bottom, the vertical particle velocity decreases to zero, and the particles move forward along the wall of the pool bottom. Combined with the flow field analysis of the bottom area of the pool in Figure 8, the particles moving in the bottom area of the pool eventually gathered in the low–speed area on both sides of the high–speed area. The installation position of the submersible mixer in scheme 3 and scheme 4 is higher from the pool bottom, and the particles will not hit the pool bottom with the jet, so no aggregation is formed in the B_1–zone. The particles in Scheme 3 mainly accumulate in the B_2–zone, as Figures 21C, D show the tracks of the particles in the B_2–zone. The particles in Figure 21C are impacted by the jet to the pool bottom and move forward along the wall, and due to the double circulation of the flow field in Scheme 3, the particles are pushed by the return flow below and finally accumulate in the middle of the pool bottom. Figure 21D shows that some particles sink to the pool bottom along the low–velocity zone near the pool wall and eventually aggregate in the B_2–zone.

Figure 22 shows the particle distribution in the C–zone of the four schemes. It can be found that the clustering of scheme 4 is most evident in the region. The 0–36 s track of an aggregated particle in the region of Scheme 4 is selected, as shown in Figures 22A, B is its vertical view. The particle was generated downstream at 3.3 s, reached the aggregation area at 19 s, and then moved at a low speed in this area. Figure 23C shows the flow field in this area. Due to the submersible mixer's high installation position, a plurality of backflows is formed after the swirling jet impacts the wall surface, in which the two backflows meet upstream to form some low–speed vortices. Figure 22D is a schematic diagram of vortex formation. Therefore, the particles moving along this path eventually accumulate in the C–zone.

Based on the above analysis, it can be seen that the installation height of the submersible mixer greatly influences the movement of the particles. When the installation height is too close to the pool bottom (scheme 1 and scheme 2), the average velocity of particles is high, but the distribution uniformity of particles is poor, and the jet will carry some particles to impact and scour the local area of the pool bottom, resulting in the aggregation of particles. When the installation height is far from the pool bottom (scheme 4), there is no particle aggregation at the pool bottom. Nevertheless, a large amount of particle aggregation occurs upstream of the water surface, and the mixing time and uniformity of the particles are not ideal. Among the four schemes in this paper, scheme 3 is the best because of its ideal mixing time and degree, and the number of particles gathered is less. Therefore, the installation height of the submersible mixer should be greater than the radius of its core jet zone, that is, the effective radial disturbance radius, to avoid the jet zone directly scouring the pool bottom. At the same time, it should not be too far away from the pool bottom to avoid causing the pool surface upstream area of a large number of particles to gather.

5 Conclusion

In this paper, the solid–liquid two–phase flow field of submersible mixer installed at different heights is studied by coupled CFD–DEM. From the perspective of particles, the motion features of particles under different installation heights, the extent of mixing and the reasons for aggregation are analyzed, which has good engineering guidance. The following conclusions can be drawn:

1) With the different installation height of submersible mixer, the flow field inside the pool has single–cycle and double–cycle two flow patterns. The double–cycle flow pattern's average velocity of the flow field is lower. Still, the average turbulent kinetic energy is higher, and the distribution of velocity and turbulent kinetic energy is better, so the mixing ability of the flow field is stronger.
2) Variations in the installation height of the submersible mixer will affect the time for particles to access the impeller and core jet area and significantly impact the degree of particle mixing, mixing time, and the aggregation intensity of particles. The installation height of the submersible mixer should be greater than its effective jet area's radius to avoid scouring the pool's bottom, but it should not be too far from the pool bottom.
3) The method based on the coupling of CFD–DEM can perform the simulation and study of the solid–liquid two–phase flow of submersible mixer effectively. Adjusting the installation position of submersible mixer by using the simulation results can improve the flow pattern inside the pool, improve the mixing uniformity of activated sludge, promote the purification of wastewater, and improve energy utilization efficiency.

Data availability statement

The original contributions presented in the study are included in the article/supplementary material further inquiries can be directed to the corresponding author.

Author contributions

Conceptualization, FT; methodology, FT; software, CY; formal analysis, EZ; investigation, YC and DS; writing—original draft preparation, EZ; writing—review and editing, FT; supervision, WS. All authors have read and agreed to the published version of the manuscript.

Funding

This research was funded by the National Key R&D Program Project (No. 2020YFC1512405), the National Natural Science Foundation of China (No. 51979125), and the Six Talent Peaks Project of Jiangsu Province (JNHB–192).

Acknowledgments

The authors would like to acknowledge the support received from the National Key R&D Program Project (No.2020YFC1512405), the National Natural Science Foundation of China (No.51979125), Six Talent Peaks Project of Jiangsu province (JNHB–192).

Conflict of interest

Author YC was employed by the Yatai Pump & Valve Co., Ltd.

The remaining authors declare that the research was conducted in the absence of any commercial or financial relationships that could be construed as a potential conflict of interest.

Publisher's note

References

Chen, B., Wang, B. Q., Zhang, H., Wang, Q., and Wang, Z. (2016). Effects of propeller layout position on flow characteristics in oxidation ditch. *J. Drain. Irrig.* 34 (3), 227–231. doi:10.3969/j.issn.1674-8530.15.0257

Chen, B., Zhuang, Y. F., Chen, K. M., Chen, X. J., and Yang, J. L. (2018). Influence of impeller diameter on hydraulic characteristics of submersible propeller. *China Water & Wastewater* 34 (5), 57–60.

Chen, Y. F., Cai, X., Zhang, H., Yang, C., Wang, Y., and Xu, Y. F. (2020a). Calculation and analysis of airfoil optimization in artificial flow. *J. J. Drainage Irrigation Mach. Eng.* 38 (2), 170–175. doi:10.3969/j.issn.1674-8530.19.0185

Chen, Y. F., Yang, Chen., and Zhang, H. (2020b). Influence and optimization of mixer's arrangement of flow field of anoxic pool. *J. Drain. Irrig. Mach. Eng.* 38, 1045–1050. doi:10.3969/j.issn.1674-8530.19.0210

ChineseStandard.net (2007). *Cj/T 109-2007.* Submersible Agitator. S.

Cundall, P. A., and Strack, O. D. L. (1979). A discrete numerical model for granular assemblies. *Géotechnique* 29, 47–65. doi:10.1680/geot.1979.29.1.47

Gong, F. Y., Pan, M. Z., and Tang, L. (2017). Numerical simulation of submersible agitator inside two-dimensional flow field. *J. J. Hubei Univ. Technol.* 32 (1), 93–96.

Jin, J. H., and Zhang, H. W. (2014). A numerical simulation of submersible mixer in three-dimensional flow with sewage-sludge two-phase. *China Rural. Water Hydropower* 10, 159–162. doi:10.3969/j.issn.1007-2284.2014.10.0

Li, Q. Y. (2020). Flow field numerical simulation of different turbulent models in miniature reactor based on CFD. *J. Contemp. Chem. Ind.* 49 (7), 1483–1487. doi:10.3969/j.issn.1671-0460.2020.07.05

Li, W., Wang, L., Shi, W. D., Chang, H., and Wu, P. (2021). Numerical simulation and performance prediction of solid-liquid two-phase flow of alkaline pump based on full factor test. *J. Drain. Irrig. Mach. Eng.* 39, 865–870. doi:10.3969/j.issn.1674-8530.19.0331

Lin, Y. P., Li, X. J., Li, B. W., Jia, X. Q., and Zhu, Z. C. (2021). Influence of impeller sinusoidal tubercle trailing-edge on pressure pulsation in a centrifugal pump at nominal flow rate. *J. Fluids Eng.* 143 (9). doi:10.1115/1.4050640

Monteith, H. D., and Stephenson, J. P. (1981). Mixing efficiencies in full-scale anaerobic digesters by tracer methods. *J. Water Pollut. Control Fed.* 53 (1).

Oesterlé, B., and Dinh, B. (1998). Experiments on the lift of a spinning sphere in a range of intermediate Reynolds numbers. *Exp. Fluids* 25, 16–22. doi:10.1007/s003480050203

Ren, X. X., Tang, F. P., Xu, Y., Shi, L. J., and Shang, X. J. (2021). Performance analysis of blade angle of submersible agitator. *J. South-to-North Water Transfers Water Sci. Technol.* 19, 805–813. doi:10.13476/j.cnki.nsbdqk.2021.0084

Saffman, P. G. (1965). The lift on a small sphere in a slow shear flow. *J. Fluid Mech.* 22, 385–400. doi:10.1017/s0022112065000824

Schiller, V. L. (1933). Uber die Grundlegenden Berechnungen bei der Schwerkraftaufbereitung. *Z. Vernes Dtsch. Inge* 77, 318–321.

Shao, T., Hu, Y. Y., Wang, W. T., Jin, Y., and Cheng, Y. (2013). Simulation of solid suspension in a stirred tank using CFD-DEM coupled approach. *Chin. J. Chem. Eng.* 10, 1069–1081. doi:10.1016/s1004-9541(13)60580-7

Shi, W. D., Tian, F., Cao, W. D., Chen, B., and Zhang, D. S. (2009). Numerical simulation of mixer power consumptions in different ponds. J. *J. Drainage Irrigation Mach. Eng.* 27 (3), 140–144.

Song, L. B., Teng, S., Cao, Q., Kang, C., Ding, K. J., and Li, C. J. (2021a). Wear of large solid particles on the impeller of solid-liquid two-phase flow pump. *J. Drain. Irrig. Mach. Eng.* 39, 987–993.

Song, L. B., Teng, S., Cao, Q., Kang, C., Ding, K. J., and Li, C. J. (2021b). Solid-liquid two-phase flow characteristics in pipe during large solid particles lifting. *J. Drain. Irrig. Mach. Eng.* 39, 1111–1117. doi:10.3969/j.issn.1674-8530.20.0278

Tian, F., Shi, W., Jiang, H., and Zhang, Q. (2014). A study on two-phase flow of multiple submersible mixers based on rigid-lid assumption. *Adv. Mech. Eng.* 2014, 531234. doi:10.1155/2014/531234

Tian, F., Zhang, E. F., Yang, C., Shi, W. D., and Zhang, C. H. (2022a). Review of numerical simulation research on submersible mixer for sewage. *Front. Energy Res.* 9. doi:10.3389/fenrg.2021.818211

Tian, F., Zhang, E. F., Yang, C., Shi, W. D., and Chen, Y. H. (2022b). Research on the characteristics of the solid-liquid two-phase flow field of a submersible mixer based on CFD-DEM. *Energies* 15 (16), 6096. doi:10.3390/en15166096

Xia, C., Zhao, R. J., and Shi, W. D. (2021). Numerical investigation of particle induced erosion in a mixed pump by CFD-DEM coupled method. *J. Eng. Thermophys.* 42, 357–369.

Xu, D. E., Yang, C. X., Cai, J. G., Han, Y., and Ge, X. F. (2021). Numerical simulation of solid-liquid two-phase in tubular turbine. *J. Drain. Irrig. Mach. Eng.* 39, 910–916. doi:10.3969/j.issn.1674-8530.20.0152

Xu, W. X., and Yuan, S. Q. (2011). Optimization design of submersible mixer based on a simulation study of agitated and engineering application. *China Rural. Water Hydropower* 06, 32–35.

Yuanwen, L., Zhiming, G., Liu, S., and Xiaozhou, H. (2022). Flow field and particle flow of two-stage deep-sea lifting pump based on DEM-CFD. *Front. Energy Res.* 10, 10. doi:10.3389/fenrg.2022.884571

Zhang, Y., Jin, B. S., Zhong, W. Q., Ren, B., and Xiao, H. (2009). DEM simulation of particle mixing in flat-bottom spout-fluid bed. *Chem. Eng. Res. Des.* 88 (5), 757–771. doi:10.1016/j.cherd.2009.11.011

Zhang, Z., Zheng, Y., Jiang, J. Q., and Li, C. Y. (2020). Influence of wastewater mixer setting angle on flow field in sewage treatment pool. *J. Drain. Irrig. Mach. Eng.* 38, 271–276. doi:10.3969/j.issn.1674-8530.18.0143

Zhao, L. J. (2021). *Numerical simulation for stirred mixing based on CFD-DEM and development of integrated simulation platform*. Hangzhou, China: Zhejiang University of Technology.

Zhu, Z. C., Lin, Y. P., Li, X. J., Zhai, L. L., and Lin, T. (2022). Axial thrust instability analysis and estimation theory of high speed centrifugal pump. *Phys. Fluids (1994).* 34 (7), 075118. doi:10.1063/5.0098194

frontiers | Frontiers in Energy Research

TYPE Original Research
PUBLISHED 24 January 2023
DOI 10.3389/fenrg.2022.1106789

OPEN ACCESS

EDITED BY
Yongfei Yang,
Nantong University, China

REVIEWED BY
Qiang Pan,
Jiangsu University, China
Weixuan Jiao,
Yangzhou University, China
Linwei Tan,
Nantong University, China

*CORRESPONDENCE
Congxin Yang,
ycxwind@163.com

SPECIALTY SECTION
This article was submitted to Process and Energy Systems Engineering, a section of the journal Frontiers in Energy Research

RECEIVED 24 November 2022
ACCEPTED 08 December 2022
PUBLISHED 24 January 2023

CITATION
Guo Y, Yang C, Mo Y, Wang Y, Lv T and Zhao S (2023), Numerical study on the mechanism of fluid energy transfer in an axial flow pump impeller under the rotating coordinate system.
Front. Energy Res. 10:1106789.
doi: 10.3389/fenrg.2022.1106789

Numerical study on the mechanism of fluid energy transfer in an axial flow pump impeller under the rotating coordinate system

Yanlei Guo[1,2], Congxin Yang[1,2]*, Yingxiang Mo[1,2], Yan Wang[3], Tianzhi Lv[1,2] and Sen Zhao[1,2]

[1]School of energy and power engineering, Lanzhou University of Technology, Lanzhou, China, [2]Key Laboratory of Fluid Machinery and Systems, Lanzhou, China, [3]Pump and Valve Research Department, Nuclear Power Institute of China, Chengdu, China

It is a necessary condition to obtain the fluid movement law and energy transfer and loss mechanism in the impeller of the axial pump for achieving an efficient and accurate design of the axial flow pump. Based on the shear stress transport k-ω turbulence model, a three-dimensional unsteady numerical simulation of the whole flow field of an axial flow pump was presented at different flow rates. Combined with the Bernoulli equation of relative motion, the flow field structure in the impeller under design condition was studied quantitatively in the rotating coordinate system. The fluid movement law and energy transfer and loss mechanism in the impeller of the axial flow pump was described in detail. In the relative coordinate system, the mechanical energy of the fluid on the same flow surface conserves. The dynamic energy is continuously transformed into pressure energy from the leading edge to the trailing edge and the dynamic energy is continuously transformed into pressure energy from the leading edge to the trailing edge. The energy conversion is mainly completed in the front half of the blade. The friction loss and the mixing loss are the basic sources of losses in the impeller flow passage. Most hydraulic losses of impeller flow passage are caused by friction and the hydraulic losses near the trailing edge are dominated by mixing loss. This research has certain reference significance for further understanding the flow field structure in the impeller of the axial flow pump, improving its design theory and method, and then realizing its efficient and accurate design of the axial flow pump.

KEYWORDS

axial flow pump, rotating coordinate system, energy transfer mechanism, friction loss, wake mixing loss

1 Introduction

The deteriorating climate has made energy conservation and emission reduction a common goal of all countries in the world. Climatologists pointed out that only if the emissions of greenhouse gas must be close to the peak by 2025 at the latest and reduce by 43% before 2050, can the earth's temperature rise be controlled by 1.5°C (Skea, et al., 2022). As one of three subtypes of blade pumps that consume 10% of global power generation each year, the others being mixed flow pump and centrifugal pump, axial flow pumps, also known as propeller pumps, are used in applications requiring very high flow rates and low pressures, such as long-distance water transfer, flood dewatering, and irrigation systems and pumped storage. Improving the efficiency of the axial flow pump is very important for achieving the carbon peak. However, mastering the movement law and energy transfer and loss mechanism of the fluid in the axial flow pump, especially in the impeller is the premise to improve the efficiency of axial flow pump.

In 1755, the Swiss mathematician Euler first proposed the constitutive equation of ideal fluid motion (Euler equation). It gave the law of fluid energy transfer in the pump theoretically and provided a theoretical basis for the design of blade pumps for the first time, but could not explain the cause of fluid energy loss in the pump. In 1785, John Skeys applied for and registered the structural patent of the axial flow pump, which is the earliest prototype of the axial flow pump in the world; In 1850, British scientist James Thomson installed guide vanes at the downstream of the impeller to improve the efficiency of the axial flow pump; In 1875, British scientist Osborne Reynolds designed the front guide vane for the axial flow pump for the first time, which further improved the efficiency of axial flow pump; In 1904, Prandtl put forward the boundary layer theory creatively, which was the first time to combine theoretical fluid mechanics and engineering fluid mechanics closely. It is a milestone in the history of fluid mechanics and fluid machinery. The boundary layer theory provided a theoretical basis for explaining the cause of fluid energy loss in the axial flow pump (Lazarkiewicz.and Troskolanski, 1965).

The boundary layer theory was applied rapidly to the study of the mechanism of fluid energy loss in the axial flow pumps. Generally speaking, hydraulic losses in the axial flow pump include inlet passage loss, impeller loss, guide vane loss and outlet pipe loss. The loss of the inlet and outlet channels is proportional to the square of the absolute velocity at the corresponding position. The loss of the axial flow pump impeller and guide vane is mainly in two forms: airfoil loss (blade surface friction loss and wake mixing loss) and non-airfoil loss due to limited wingspan (secondary flow loss in impeller channel and leakage loss due to the tip clearance). Professor Staritzky et al. (Srinivasan, 1966; Staritski, 1958; Staritski, 1964; Stefanovski, 1940) believed that the non-airfoil loss at the design operating point could be negligible compared with the airfoil loss (it accounted for about 5% of the total loss), and relevant tests also confirmed this argument (Csanady, 1964).

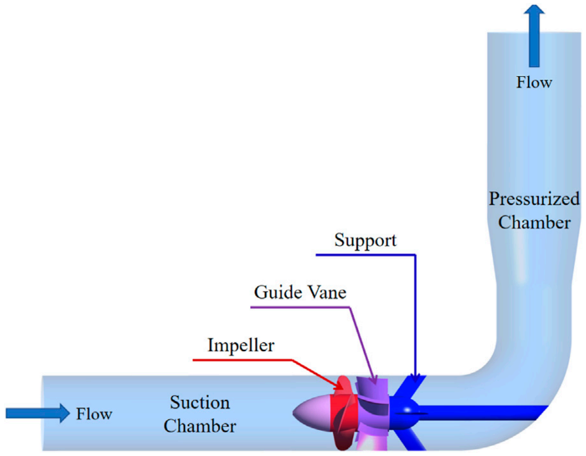

FIGURE 1
Axial flow pump model.

Some scholars tried to calculate the airfoil loss through the thickness of the boundary layer (Loitsanski, 1959; Srinivasan, 1968; Mac-Gregor, 1952; Markoff, 1948; Stepanoff, 1962; Proscura, 1954; Schlichting, 1979), and they gave the calculation methods of airfoil loss in several cascade systems. Some methods only considered the airfoil loss in the cascade, while some methods also considered the loss caused by wake mixing; Among them, the calculation method of Professor Loitsanski, (Proscura, 1954; Schlichting, 1979) is more accurate than other calculation methods.

Since the 21st century, CFD has been gradually applied in various industrial fields including the axial flow pump. It makes a big difference in studying the flow field structure of the axial flow pump such as cavitation (Wang, et al., 2021), tip leakage flow (Shen, et al., 2021; Zhang, et al., 2012), and pressure fluctuation (Shen, et al., 2019; F. Yang, et al., 2022). At the same time, it makes it possible to carry out quantitative research on the mechanism of flow loss in pumps. (Kan, et al., 2022) investigated the influences of the tip leakage vortex on the axial flow pump as turbine through numerical simulations, where the energy loss mechanism due to tip leakage flow was revealed K. (Pu, et al., 2022) studied the influence of vortex on steady flow and pressure fluctuation of circulating axial pump through numerical simulations, where energy loss caused by the low-speed vortex was analyzed quantitatively and the structure position of the low-speed vortex can be predicted Li et al. (Li, et al., 2021) studied the energy loss mechanism of a mixed-flow pump under stall condition with the numerical method. Especially, the combination of entropy generation theory and numerical simulation can well conduct quantitative research on the hydraulic loss of the pump (Zhou, et al., 2022; Xin, et al., 2022; Li, et al., 2020; Cui and Zhang, 2020) in recent years, which can describe the proportion of hydraulic loss of each flow passage component of the pump under different working conditions.

The Bernoulli equation of relative motion has given the mechanism of the energy transfer from the impeller inlet to the outlet in the view of theory. An unsteady numerical simulation of the whole flow field of an axial flow pump was carried out in this study based on the *SST k- ω* turbulence model. Combined with the Bernoulli equation of the relative motion and the numerical calculation results of the flow field structure in the impeller, the mechanism of energy transfer and loss in the impeller was revealed, which could provide a certain reference for the enrichment of the design theory of the axial flow pump.

2 Research project and method

2.1 Pump model

An axial flow pump with a design volume flow rate of 0.35 m^3/s, head of 6.7m, and rotation speed of 1450 rpm was chosen as the research object. The 3D model of the axial flow pump is shown in Figure 1. The whole pump section consists of five flow passage parts, namely the suction chamber, impeller, guide vane, support, and pressurized chamber. In addition, the diameter of pump impeller is 300 mm, the hub ratio is 0.5, the tip clearance is 0.2 mm, the impeller has four blades and the guide vane has seven blades.

2.2 Governing equations

Three governing equations, mass conservation equation, momentum conservation equation, and energy conservation equation, dominate the motion in the axial flow pump. For a general axial flow pump, its working pressure is low and the amplitude of the temperature change is small, so the density of the fluid medium could be considered constant and the heat transfer can be ignored. Eqs. 1, 2 show the tensor forms of the mass conservation equation and momentum conservation equation of the viscous incompressible medium.

$$\frac{\partial u_i}{\partial x_i} = 0 \tag{1}$$

$$\frac{\partial u_i}{\partial t} + u_j \frac{\partial u_i}{\partial x_j} = F_i - \frac{1}{\rho}\frac{\partial p}{\partial x_i} + \upsilon \frac{\partial^2 u_i}{\partial x_j \partial x_j} \tag{2}$$

where,

u_i is the velocity component in the x, y, and z directions

F_i is the mass force

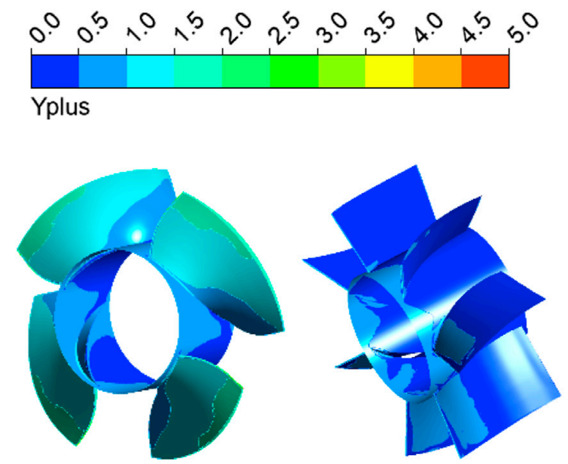

FIGURE 2
The y + distribution of grids near the wall.

p is the pressure

ρ is the medium density

υ is the medium kinematic viscosity.

SST k- ω turbulence model was selected for this study, which can predict effectively the fluid separation point under the condition of reverse pressure. At the same time, when solving the low Reynolds number flow near the wall area, the *SST k- ω* turbulence model has higher accuracy. Its basic equations are as follows:

$$\frac{\partial(\rho k)}{\partial t} + \frac{\partial(\rho u_j k)}{\partial x_j} = \frac{\partial}{\partial x_j}\left[\left(\mu + \frac{\mu_t}{\sigma_k}\right)\frac{\partial k}{\partial x_j}\right] + \tau_{ij}\frac{\partial u_i}{\partial x_j} - \beta^{*}\rho\omega k \tag{3}$$

$$\frac{\partial(\rho\omega)}{\partial t} + \frac{\partial(\rho u_j \omega)}{\partial x_j} = \frac{\partial}{\partial x_j}\left[\left(\mu + \frac{\mu_t}{\sigma_\omega}\right)\frac{\partial k}{\partial x_j}\right] + \frac{\gamma}{\nu_t}\tau_{ij}\frac{\partial u_i}{\partial x_j} - \beta\rho\omega^2 + 2(1 - F_1)\rho\sigma_{\omega^2}\frac{1}{\omega}\frac{\partial k}{\partial x_j}\frac{\partial \omega}{\partial x_j} \tag{4}$$

where, σ_k=1.176, σ_ω=2, β=0.075, β^{*}=0.09, κ=0.41, $\gamma_1 = \beta/\beta^{*} - \sigma_\omega \kappa^2/\sqrt{\beta^{*}}$.

$$F_1 = \tanh\left(\arg_1^4\right) \tag{5}$$

$$\arg_1 = \min\left(\max\left(\frac{\sqrt{k}}{\beta^{*}\omega y};\frac{500\nu}{y^2\omega}\right);\frac{4\rho k}{CD\sigma_{\omega 2}y^2}\right) \tag{6}$$

$$CD = \max\left(2\rho\frac{1}{\sigma_{\omega 2}\omega}\frac{\partial k}{\partial x_j}\frac{\partial \omega}{\partial x_j}, 1.0 \times 10^{-10}\right) \tag{7}$$

where, F_1 is a mixed function. $F_1 = 1$ in the area near the wall, which means that the whole area uses the *k- ω* turbulence model, and $F_1 = 0$ in the area far always from the wall, which means that the whole area uses the standard *k- ε* turbulence model, y is the distance from the first layer of the grid to the wall, $\sigma_{\omega 2}$= 1.168. The limiting equation of eddy viscosity is as follows:

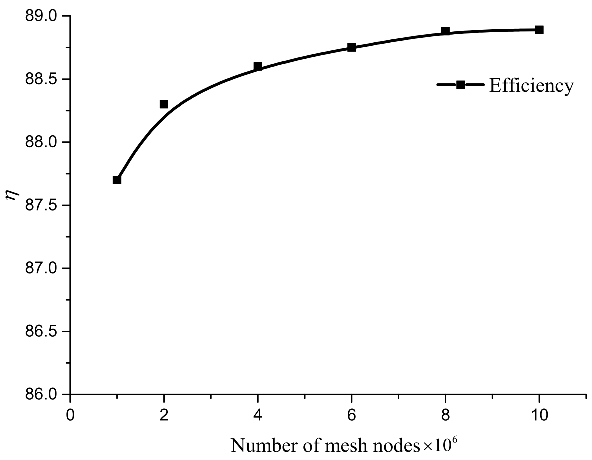

FIGURE 3
Results of grid independence.

TABLE 1 Mesh details for each domain.

Domain	Nodes/Million
Suction Chamber	0.87
Impeller	14.98
Guide Vane	15.98
Support	2.62
Pressurized Chamber	1.51

$$\nu_t = \frac{a_1 k}{\max(a_1\omega, SF_2)} \tag{8}$$

$$\nu_t = \mu_t/\rho \tag{9}$$

where, μ_t is turbulent viscosity, S is an invariant measure of strain rate, F_2 is also a mixed function, which is equal to 1 in the boundary layer and 0 in the shear layer, and a_1 is a constant, equal to 5/9.

$$\begin{aligned} F_2 &= \tanh\left(\arg_2^2\right) \\ \arg_2 &= \max\left\{2\frac{\sqrt{k}}{0.09\omega y};\frac{500\nu}{y^2\omega}\right\} \end{aligned} \tag{10}$$

2.3 Computational setup

As a kind of low Reynolds number turbulence model, the *SST k-ω* turbulence model requires that $y+\le 1$, which will ensure that at least one layer of grid exists within the viscous sublayer. However, it is a requirement that is almost impossible to meet unless a large number of grids that ordinary servers cannot afford are adopted. It has been shown in relevant research (Tao, 2001)that the first layer of the grid near the wall will also fall in the viscous sublayer when $y+\le 5$. The y+ near the wall of the impeller and guide vane is shown in Figure 2, where all the y+ near the blades is small than five and the final average of y+ is 1.1, and the growth rate of the grids off the wall is 1.1.

All the flow passage components of the axial flow pump were meshed by hexahedral structured grids. The grid independence was judged by the change of pump efficiency with the increasing of the number of grids. When the efficiency change amplitude did not exceed 2% with the increase of the number of grids, it could be considered that the grid independence verification was passed, which was shown in Figure 3. In addition, the grid independence verification was carried out under the condition that y+ meets the requirements of the *SST k-ω* turbulence model. The final grids of the computing domain verified by grid independence were shown Table. 1 and Figure 4.

The whole numerical calculation was completed by ANSYS-CFX 20.1 The medium is water with a density of 998.2 kg/m^3 and a dynamic viscosity of 0.000889 Pas. The rotating speed of the impeller was set to 1450rpm and all the other flow passages were stationary. A mass flow boundary (350 kg/s) with a turbulent intensity of 5% was adopted at the inlet of the computational domain and a pressure boundary (1 atm) was set at the outlet of the computational domain. All walls were subject to non-slip-wall boundary condition. Since the accuracy of the unsteady calculation results is higher than that of the steady calculation results, the unsteady calculation results were used in this study. However, the unsteady calculation requires the steady calculation results as the initial condition to accelerate convergence. The interfaces between the rotating region and the stationary region adopted the interface of the frozen rotor in the steady calculation, while the sliding grids were used in the unsteady calculation. The time-step size was set as 0.000115 s, which is the time for the rotor to turn for one degree to obtain sufficient flow field solution accuracy (Lin, et al., 2021). By changing the flow rate at the inlet boundary of the computational domain, the numerical calculation of the flow field structure in the axial flow pump under different flow rate conditions was completed. In addition, to weaken the influence of the inlet and outlet boundary conditions on the calculation results of the flow field in the axial flow pump, it is necessary to keep a sufficient distance between the inlet and outlet boundary and the axial flow pump. The distance between the inlet of the suction chamber and the impeller inlet was set as 8 R_t, and the distance between the end of the diffusion section and the outlet of the pressurized chamber was set as 6 R_t.

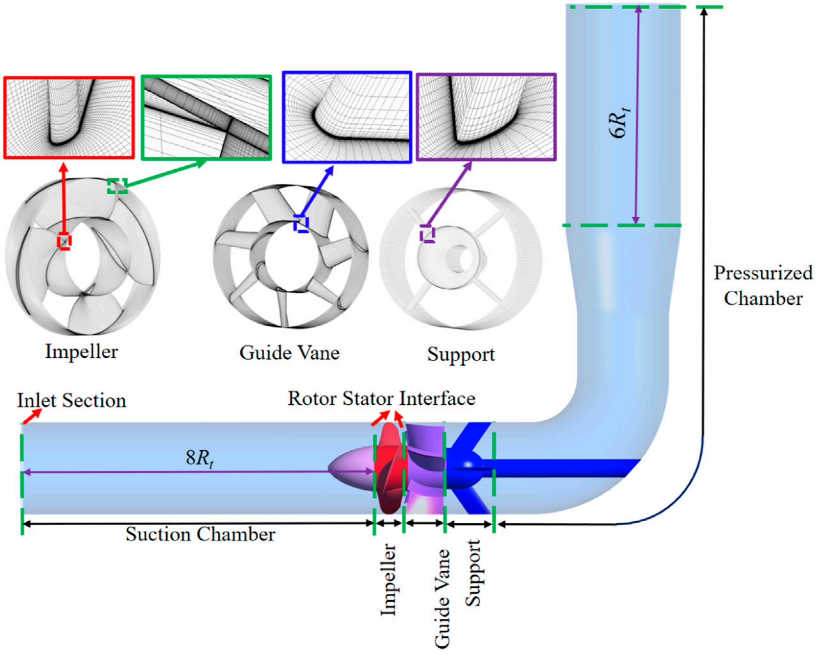

FIGURE 4
Flow domains and grids.

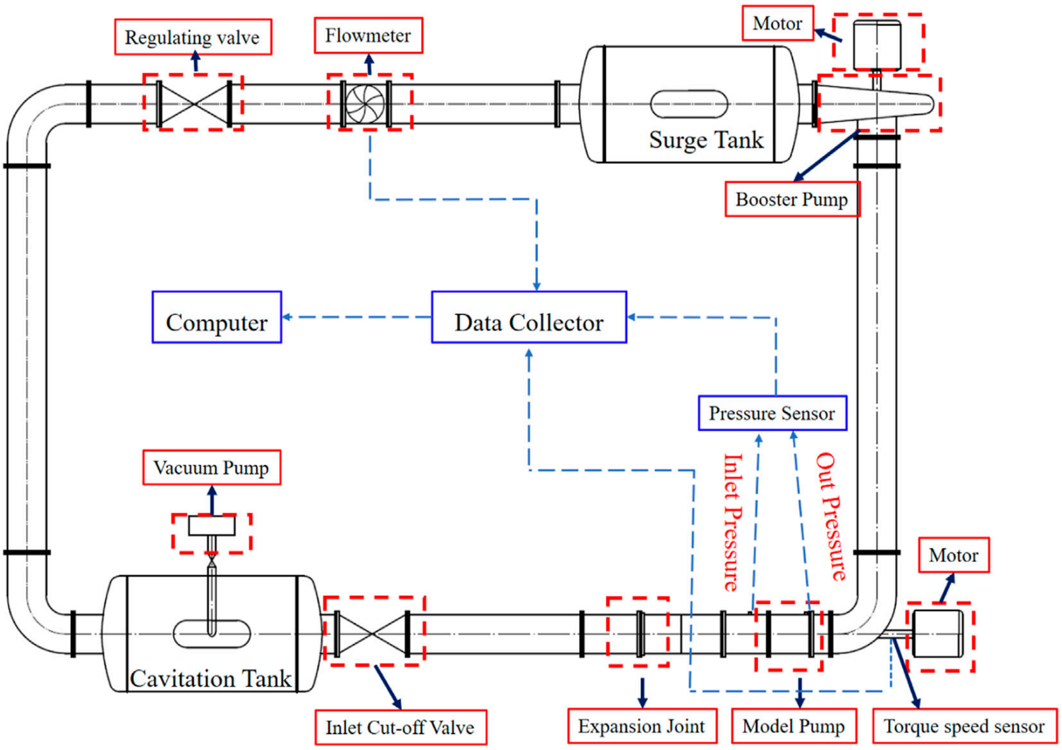

FIGURE 5
Schematic map of the hydraulic test rig.

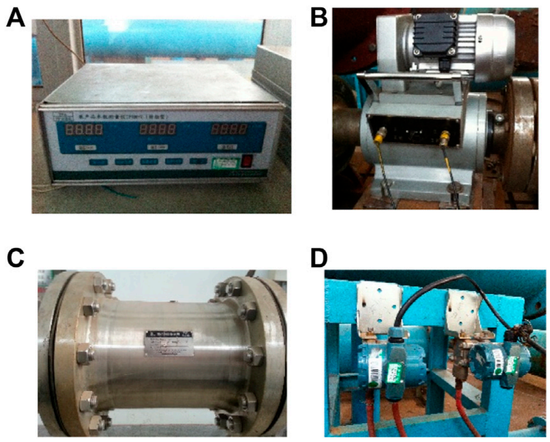

FIGURE 6
Measuring instruments: **(A)** data collector, **(B)** torque speed sensor, **(C)** flowmeter and **(D)** pressure sensor.

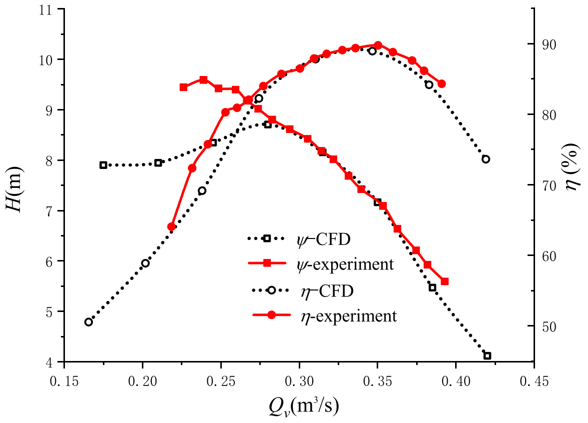

FIGURE 7
External characteristic analysis.

2.4 Numerical calculation accuracy verification

In order to verify the accuracy of numerical simulation, we completed the external characteristic test of the axial flow pump on the closed test bench. The schematic diagram of the test bench is shown in Figure 5 and the experimental instruments are shown in Figure 6, in which the uncertainty of the flowmeter is lower than 1.5%, the speed uncertainty of the torque speed sensor is less than 0.2% and the torque uncertainty of that is less than 1.5%, and the uncertainty of the pressure sensors is less than 1%. The external characteristic test at different flow rate was completed by adjusting the regulating valve opening. All the data were converted to digital form and stored in a computer database.

The numerical calculation results of the external characteristic curves, the head, and efficiency, of the axial flow pump were compared with the test results as shown in Figure 7. The simulation results are in good agreement with the test results near the design mass flowrate (0.35 m^3/s) condition. However, when the deviation from the design mass flow rate condition is too large, there is an obvious difference between the test value and the CFD value. Especially under the condition of small flow rate, the difference between the test results and the CFD results is the most obvious, which has lost reference value to the engineering practice. So, the turbulence model *SST k-ω* has sufficient accuracy in predicting the flow field structure under the design mass flow rate condition of the axial flow pump.

3 Results and discussion

3.1 Energy transfer mechanism in the impeller of the axial-flow pump

As we know, in the circumferential direction of specific axial and radial coefficient positions, the pressure, velocity, liquid flow angle, and other physical parameters in the impeller passage of the axial flow pump are periodically and symmetrically distributed. However, only the average value in space is taken as the design value in the design process of the axial flow pump. It also has been confirmed that the average value of the impeller inlet flow field structure in space is in good agreement with the theoretical design value under the design condition (Guo, et al., 2022) which proved that it is feasible to study the energy transfer and loss mechanism in the impeller passage using the weighted average treatment of the flow field structure in the impeller passage. The energy transfer and loss mechanism in the axial flow pump impeller was studied by using the method of the weighted average of mass flow rate in the circumferential direction in this study.

$$x_{MCA} = \frac{\sum (\Delta m \cdot x)}{m} \tag{11}$$

where x is the physical variable, x_{MCA} is the weighted average value of x in the circumferential direction based on the mass flow rate at the position of the specific streamwise location and radius coefficient. So, the weighted average value based on the mass flow of the parameters at different streamwise locations and different radius coefficients could be studied on the meridional surface. The data processing diagram is shown in Figure 8.

Equation 11 is the Bernoulli equation for the ideal fluid in the relative coordinate system. For a horizontal axial flow pump, the impeller inlet height is as same as the outlet center height, namely, $z_1 = z_2$. And so are the diameter of the impeller inlet and outlet. Then the circumferential velocity is the same, that is, Eq. 11 is transformed into Eq. 12, from which, it could be

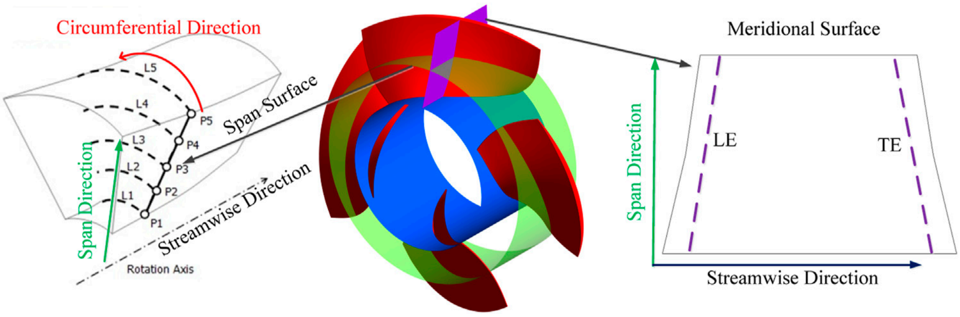

FIGURE 8
The diagram of the weighted average of parameters based on mass flow.

deduced that fluid maintains conservation of the mechanical energy from the impeller inlet to the outlet in the relative coordinate system and the dynamic energy is continuously transformed into the pressure energy.

$$z_1 + \frac{p_{1-t}}{\rho g} + \frac{V_{1-re}^2 - U_1^2}{2g} = z_2 + \frac{p_{2-t}}{\rho g} + \frac{V_{2-re}^2 - U_2^2}{2g} \tag{12}$$

$$\frac{p_{1-t}}{\rho g} + \frac{V_{1-re}^2}{2g} = \frac{p_{2-t}}{\rho g} + \frac{V_{2-re}^2}{2g} \tag{13}$$

The pressure coefficients are defined as follows to represent visually the energy change at the impeller inlet to a higher degree.

$$C_p = \frac{p - \overline{p_{\text{in}}}}{0.5\rho V_{in}^2}, C_d = \frac{0.5\rho V^2}{0.5\rho V_{in}^2}, C_{tot} = C_p + C_d \tag{14}$$

where, $\overline{p_{in}}$ is the average pressure at the pump inlet, C_p is the static pressure coefficient, C_d is the dynamic pressure coefficient, C_{tot} is the total pressure coefficient.

The flow surface of radius 0.5 was taken as the research object. The energy coefficients on the flow surface were processed by weighted average based on the mass flow. Equation 12 is changed into Eq. 13.

$$C_{1t-tot-rel-MCA} = C_{2t-tot-rel-MCA} \tag{15}$$

$$C_{1t-p-MCA} + C_{1-d-rel-MCA} = C_{2t-p-MCA} + C_{2-d-rel-MCA} \tag{16}$$

$$C_{1-tot-rel-MCA} = C_{2-tot-rel-MCA} + \Delta C_{(1-2)-tot-rel-MCA} \tag{17}$$

The coefficients are defined as follows to represent the energy change visually in the impeller passage to a higher degree.

$$C_p = \frac{p - p_{\text{in}}}{0.5\rho V_{in-re}^2}, C_d = \frac{0.5\rho V_{re}^2}{0.5\rho V_{in}^2}, C_{tot} = C_p + C_d \tag{18}$$

where,

p_{in} is the pressure at the pump inlet

V_{in-re} is the relative velocity at the pump inlet

C_p is the pressure coefficient

C_d is the dynamic pressure coefficient

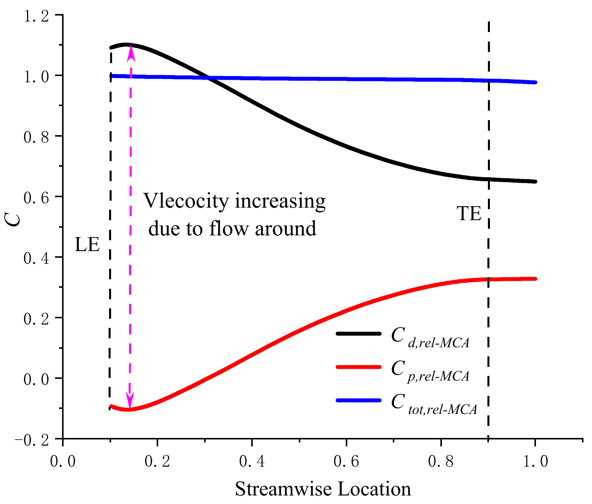

FIGURE 9
The distribution curve of the weighted average of the energy head coefficient based on the mass flow on the flow surface of R* = 0.5.

C_{tot} is the total pressure coefficient.

As shown in Figure 9, the total pressure coefficient in the relative coordinate system decreases slowly from the impeller inlet to the outlet and the decreasing range is very small, which proves the correctness of the theoretical analysis. That is, the mechanical energy of the fluid on the same flow surface in the impeller channel is conserved. The reason why the total pressure coefficient decreases slowly from the impeller inlet to the outlet is the hydraulic loss caused by the viscosity as shown in Eq. 15. The hydraulic loss consists of the friction loss caused by friction and the mixed loss caused by the boundary layer separation. The dynamic energy is constantly converted into pressure energy from the impeller inlet to the outlet as a whole in the relative coordinate system, which is the source of the pressure head of the axial flow pump.

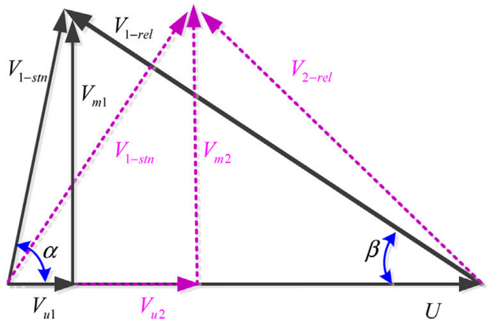

FIGURE 10
The velocity triangle at the impeller inlet and outlet.

However, it is easy to be noticed that the fluid dynamic pressure coefficient increases slightly before decreasing rapidly. On a specific flow surface of the impeller passage, it can be regarded as an infinite plane cascade. The aerodynamic theory has pointed out that a high speed and low pressure region will appear at the suction surface of the airfoil near the leading edge due to flow around the airfoil, so is the cascade in the impeller passage as shown in Figure 11C.

The theoretical head of the pump is defined as the sum of the dynamic head and the theoretical static head in the absolute coordinate system, in which, the theoretical static head is the difference between the theoretical pressure head from the impeller outlet to the inlet (Eq. 17), and the dynamic head is the difference of the velocity head in the absolute coordinate system between the impeller outlet and the inlet (Eq. 18). According to the relative Bernoulli equation, the theoretical pressure head difference between the impeller outlet and the inlet is equal to the velocity head difference between the impeller inlet and the outlet in the relative coordinate system, as shown in Eq. 17. The inlet and outlet velocity triangles of the impeller are shown in Figure 10. From the impeller inlet to outlet, the relative velocity gradually decreases and the dynamic energy is converted into the pressure energy. The reverse pressure gradient always exists in the whole impeller channel. The reverse pressure gradient will increase the thickness of the boundary layer and then, lead to its separation, which will cause great mixing loss. It is also the fundamental reason why the efficiency of the axial flow pump is lower than that of the axial flow turbine.

$$H_t = H_{P-t} + H_d \tag{19}$$

$$H_{p-t} = \frac{p_{2-t}}{\rho g} - \frac{p_{1-t}}{\rho g} = \frac{V_{1-re}^2}{2g} - \frac{V_{2-re}^2}{2g} \tag{20}$$

$$H_d = \frac{V_{2-stn}^2 - V_{1-stn}^2}{2g} \tag{21}$$

According to the velocity triangle, the relative velocity can be expressed as Eq. 19.

$$V_{re}^2 = V_m^2 + (U - V_u)^2 \tag{22}$$

The normal inlet is always adopted in the design of the axial flow pump, that is, $V_{u1} = 0$ m/s and the impeller inlet and outlet of the axial flow pump have the same diameter, that is, $V_{m1} = V_{m2}$ and $U_1 = U_2$, The theoretical static head Eq. 22 can be derived from Eqs. 20, 21.

$$V_{1-re}^2 = V_{m1}^2 + (U_1 - V_{u1})^2 = V_{m1}^2 + U_1^2 \tag{23}$$

$$V_{2-re}^2 = V_{m2}^2 + (U_2 - V_{u2})^2 = V_{m2}^2 + U_2^2 + V_{u2}^2 - 2U_2V_{u2} \tag{24}$$

$$H_{p-t} = \frac{2U_2V_{u2} - V_{u2}^2}{2g} \tag{25}$$

Equation 23 could be derived from the further derivation of Eq. 17.

$$H_d = \frac{V_{u2}^2}{2g} \tag{26}$$

The dynamic head is completely determined by the circumferential velocity component at the impeller outlet. Equation 24 is the theoretical head expression for the axial flow pump.

$$H_t = \frac{U_2V_{u2}}{g} \tag{27}$$

The actual head of the impeller could be calculated by Eqs. 25, 26. The theoretical head can also be expressed by Eq. 27. The actual head must be less than the theoretical head due to the hydraulic loss. It is not difficult to find out that the actual head and the theoretical head have the same dynamic head by comparing Eqs. 26, 27. The difference between them mainly exists in the static head. It has been described that the total energy in the relative coordinate system will decrease slowly because of the hydraulic loss in Eq. 15. The dynamic energy in the relative coordinate system could not be completely converted into the pressure energy without any hydraulic loss. During the flow process, the dynamic energy must be partially converted into internal energy in the form of friction and mixing caused by boundary layer separation, and then lost. The hydraulic loss is equal to the relative total energy reduction.

$$H = H_p + H_d \tag{28}$$

$$H = \frac{p_2}{\rho g} - \frac{p_1}{\rho g} + \frac{V_{2-stn}^2}{2g} - \frac{V_{1-stn}^2}{2g} = \frac{p_2}{\rho g} - \frac{p_1}{\rho g} + \frac{V_{u2}^2}{2g} \tag{29}$$

$$H_t = \frac{p_{2-t}}{\rho g} - \frac{p_{1-t}}{\rho g} + \frac{V_{u2}^2}{2g} = \frac{V_{1-rel}^2 - V_{1-rel}^2}{2g} + \frac{V_{u2}^2}{2g} \tag{30}$$

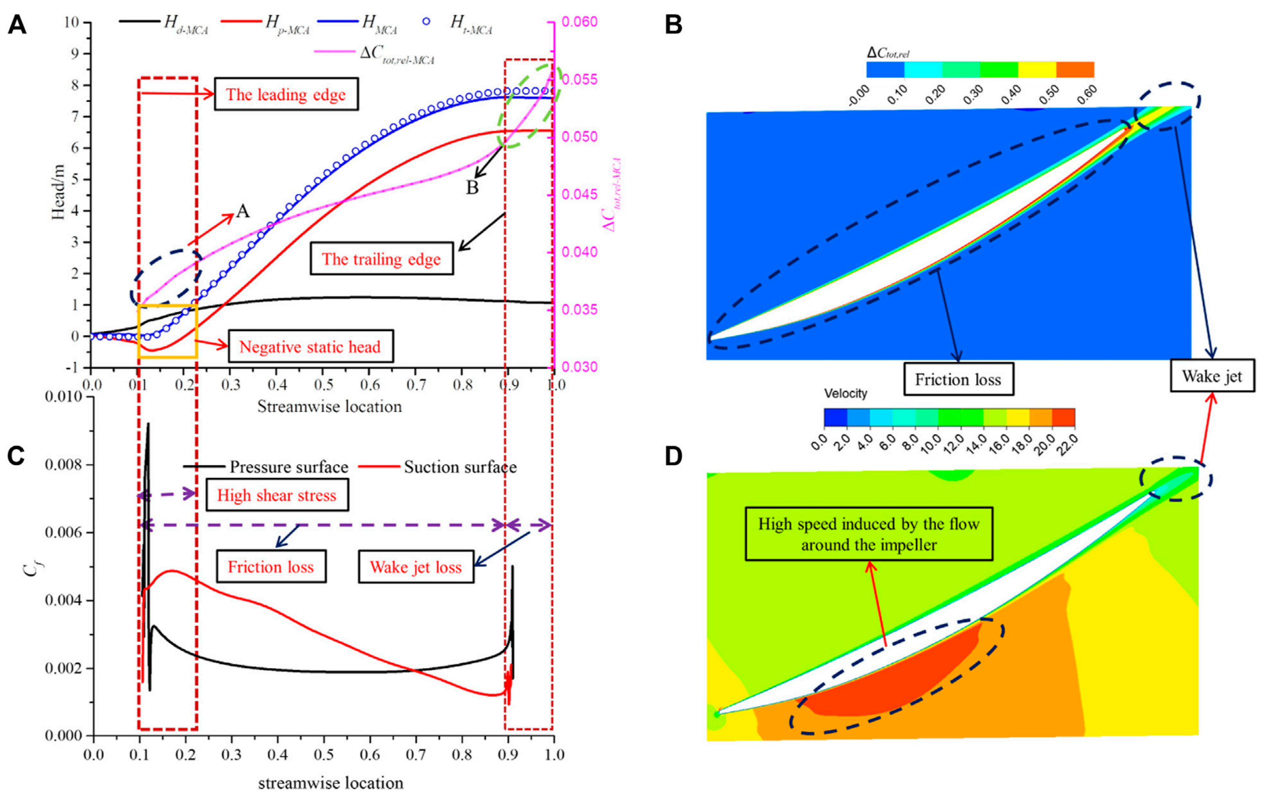

FIGURE 11
The energy transfer and loss mechanism on the surface of R* = 0.5: **(A)** The distribution curve of the coefficients of the head and relative total pressure loss with the flow direction coefficient; **(B)** The distribution curve of the friction coefficient; **(C)** The relative total pressure loss coefficient contour; **(D)** The relative velocity contour.

3.2 Energy transfer mechanism in the impeller of the axial-flow pump

The weighted average value of the performance characteristics such as H_d, H_p, H, H_t and $\Delta C_{tot-rel}$ on the flow surface of R^* 0.5 based on mass flow were taken as shown in Figure 11A and were recorded as $H_{d\text{-}MCA}$, $H_{p\text{-}MCA}$, H_{MCA}, $H_{t\text{-}MCA}$ and $\Delta C_{tot-rel-MCA}$ ($\Delta C_{tot-rel-MCA} = H_{t\text{-}MCA\text{-}}\ H_{MCA}$).

The static head is the main part of the axial flow pump head. It is mainly obtained by converting the relative dynamic energy into the pressure energy and the transformation is completed in the front half of the blade. The static head shows a trend of decreasing at first and then increasing on the whole flow surface, which is consistent with the changing trend of the static pressure coefficient in Figure 9. The negative static head exists near the leading edge, which is caused by that the flow around the blade will increase the relative velocity of the flow field near the leading edge of the suction surface (Figure 11D). This area is also the place most prone to cavitation. For the axial flow pump with a specific size, the key to improving its cavitation performance is to control the relative velocity at the suction surface of the leading edge. The dynamic head increases rapidly at the leading edge of the blade and then tends to be flat. It is also obtained mainly in the front half of the blade.

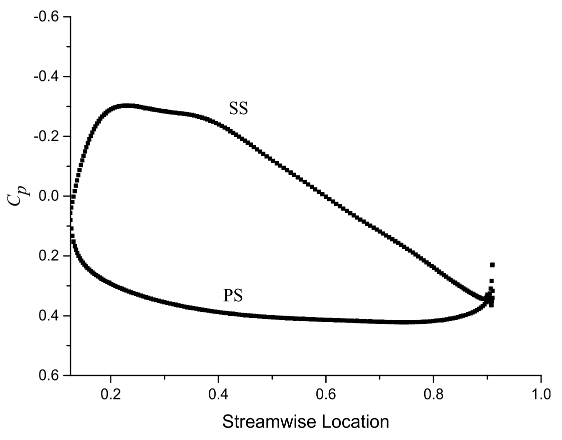

FIGURE 12
The distribution of the pressure coefficient on the blade surface at the radial coefficient of 0.5.

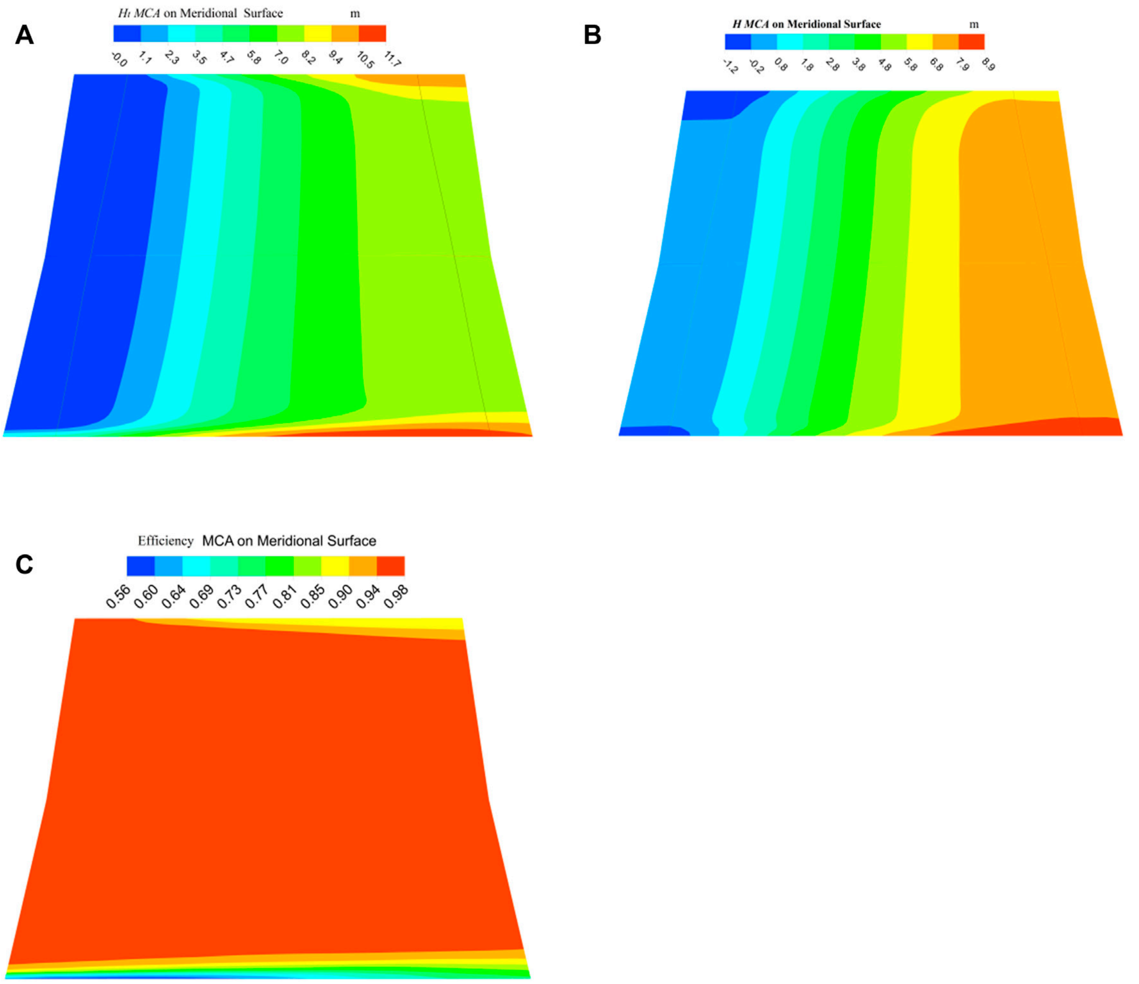

FIGURE 13
The contour of the weighted average of the head and efficiency coefficients based on mass flow: **(A)** The theoretical head; **(B)** The head; **(C)** The efficiency.

It is not difficult to infer that the actual head of the impeller is also mainly obtained in the front half flow passage. From the perspective of energy transmission, the torque formed by the pressure difference between the pressure surface and the suction surface is the fundamental source of the fluid energy. As shown in Figure 12, the pressure coefficient increases slowly from the leading edge to the trailing edge, while the pressure coefficient of the suction surface decreases rapidly near the leading edge and then up to be the same as that of the trailing edge gradually. The negative pressure coefficient at the front half of the whole blade is maintained on the suction surface of the blade. Therefore, the pressure difference between the pressure surface and the suction surface at the front half of the blade is far larger than that at the second half of the blade, which means that the torque on the front half of the blade is far larger than that on the second half. That is the reason why the actual head of the impeller is mainly obtained in the front half flow passage.

The friction loss caused by the velocity gradient in the boundary layer and the mixing loss caused by the separation of the boundary layer is the basic source of losses in the impeller flow passage. It can be seen from the distribution of the relative total pressure loss coefficient from the impeller inlet to the impeller outlet in Figure 11A that the gradient of the relative total pressure loss coefficient near the leading edge (Area A) and the trailing edge (Area B) is larger than that in the area between them, while the gradient near the trailing edge is greater than that near the leading edge. The relative velocity of the fluid near the leading edge at the suction surface of the blade will increase significantly due to the flow around the blade, which will result in a corresponding increase in the friction shear stress coefficient at this location as shown in Figure 11B. The greater the shear stress coefficient, the greater the friction loss gradient. Then, as the relative velocity decreases, the shear stress coefficient decreases, and the gradient of the relative total pressure loss coefficient decreases. The impeller passage of the axial flow pump, as we know, is basically under the adverse pressure gradient, and the adverse pressure gradient at the suction surface is obvious larger than that at the pressure surface. The thickness of the boundary layer on the suction surface increases gradually under the action of the adverse pressure gradient and reaches the maximum at the trailing edge as shown in Figure 11D. For the turbulent boundary layer, there is violent mixing movement in its interior. The thicker the boundary layer, the more mixing loss and therefore it can be seen that the relative total pressure loss coefficient gradient increases significantly at the trailing edge. In addition, the wake jet is formed after the fluid leaves the blade and it will result in more severe mixing loss. The gradient of the relative total pressure loss coefficient will also further increase.

Overall, on the one hand, friction loss is the main form of hydraulic loss in most areas of the impeller flow passage except the trailing edge, and the gradient of the relative total pressure loss coefficient is obviously greater because of the flow around the blade. On the other hand, the mixing loss inside the boundary layer and wake is the main form of hydraulic loss at the trailing edge. The gradient of the relative total pressure loss coefficient caused by mixing loss in the wake is the largest in the whole impeller flow passage. The point to improve pump efficiency is to avoid boundary layer separation in the flow channel and to eliminate the wake as soon as possible to prevent it from spreading in the downstream channel.

Figure 13 shows the distribution of the weighted average value of H_t, H and η based on the mass flow on the meridional surface of the impeller flow passage. The trend of the theoretical head (Figure 13A) and the actual head (Figure 13B) in the main flow area (Radial coefficient between 0.05 and 0.95) are basically consistent. They gradually increase from the impeller inlet to the outlet and the impeller has high hydraulic efficiency. However, the circumferential velocity component, V_u, of the fluid near the hub (Radial coefficient between 0 and 0.05) is large due to the rotation of the hub. According to the Euler equation, the increase of the circumferential velocity component means the increase of the theoretical head. The rotation of the blade tip makes the fluid near the rim (Radial coefficient between 0.95 and 1) maintain a high circumferential velocity component, while the flange wall makes the axial velocity in the tip area attenuate rapidly. Therefore, the absolute velocity of the fluid in this area is dominated by the circumferential direction. According to the Euler equation, this area will have a high theoretical head.

The actual head is the difference between the theoretical head and the hydraulic loss head. The fluid in the pressure surface will return to the suction surface of the blade through the clearance between the tip and the rim under the effect of the pressure difference between the pressure surface and the suction surface, which is called tip leakage flow. The tip leakage flow will cause complex leakage vortex, which will damage the flow field structure at the rim seriously and cause a lot of hydraulic loss. As a result, the actual head in this area also decreases. The actual head in the rim is obviously lower than that in other locations with the same streamwise location as shown in Figure 13B.

Efficiency is the ratio of the actual head to the theoretical head as shown in Figure 13C. It has been analyzed that the fluid in the main flow area has higher hydraulic efficiency because of that the main losses in this area are caused by the friction loss of the airfoil surface and the wake mixing loss of the trailing edge, which are small, while the hydraulic efficiency drops rapidly near the hub and rim. The fluid near the hub area is mainly affected by the corner separation, that near the rim area is mainly affected by the leakage vortex.

4 Conclusion

In this study, we made a three-dimensional unsteady numerical simulation of the whole flow field of an axial flow pump at the design operating point. The flow field structure in the impeller passage was analyzed quantitatively and the fluid movement law and energy transfer and loss mechanism were revealed from the perspective of the relative coordinate system. The main conclusions are as follows:

1) In the relative coordinate system, the mechanical energy of the fluid on the same flow surface conserves. The dynamic energy is continuously transformed into pressure energy from the leading edge to the trailing edge and the whole flow surface is under the adverse pressure gradient, which is the fundamental reason why the boundary layer separation is prone to occur near the trailing edge of the axial flow pump and the efficiency is lower than that of the axial flow turbine as the prime mover;
2) The flow around the blade inlet will cause the relative velocity of the fluid at the leading edge near the suction surface of the blade to increase and the pressure to decrease, which will result in a negative static head in this area. That is the basic reason why cavitation is prone to occur at the leading edge near the suction surface of the blade rim. The point to improve the cavitation performance of the axial flow pump is to reduce the maximum the relative velocity at the leading edge near the suction surface of the blade;
3) On the axial flow pump impeller, the pressure difference between the pressure surface and the suction surface in the front half of the blade is far greater than that in the back half of the blade, so the blade torque is mainly provided by the front half of the blade, and the energy conversion is mainly completed in the front half of the blade;

4) The friction loss and the mixing loss are the basic sources of losses in the impeller flow passage. On the one hand, there will not be boundary layer separation in most areas of the impeller flow passage except near the trailing edge under the design condition, therefore, the hydraulic loss here is mainly in the form of friction loss. On the other hand, the mixing loss inside the boundary layer and wake is the main form of hydraulic loss at the trailing edge. The gradient of the relative total energy loss coefficient caused by mixing loss in the wake is the largest in the whole impeller flow passage. The point to improve pump efficiency is to avoid boundary layer separation in the flow channel and to eliminate the wake as soon as possible to prevent it from spreading in the downstream channel;
5) The flow in the axial flow pump is obviously affected by the end wall effect of the hub and the rim. The rotation of the hub and the blade tip makes the theoretical head at the corresponding position obviously higher than that in the main flow area. In addition, the efficiency of the end wall area is significantly lower than that of the main flow area, the reason is that the flow near the hub is affected by the corner separation, and the flow near the rim is affected by the tip leakage flow.

Data availability statement

The original contributions presented in the study are included in the article/supplementary material, further inquiries can be directed to the corresponding author.

Author contributions

Conceptualization, CY; software, YG, SZ and TL; validation, YG; formal analysis, CY and YW;investigation, YG; data curation, YG; writing—original draft preparation, YG, YM; writing—review and editing, YG, YM and CY; visualization, YM, SZ and TL. All authors have read and agreed to the published version of the manuscript.

Funding

This research was funded by the National Science Fund Project (China) “Unsteady flow and its excitation mechanism in stator and rotor cascades of nuclear main pump” (51866009).

Acknowledgments

We thank Jiangsu YaTai pump and valve Co., Ltd. for its strong support of our experiment. The company was not involved in the study design, collection, analysis, interpretation of data, the writing of this article or the decision to submit it for publication.

Conflict of Interest

The authors declare that the research was conducted in the absence of any commercial or financial relationships that could be construed as a potential conflict of interest.

Publisher’s note

References

Csanady, G. T. (1964). *Theory of turbo machines*. New York: McGraw-Hill.

Cui, B., and Zhang, C. (2020). Investigation on energy loss in centrifugal pump based on entropy generation and high-order spectrum analysis. *J. Fluids Eng.* 142. doi:10.1115/1.4047231

Guo, Y., Yang, C., Wang, Y., Lv, T., and Zhao, S. (2022). Study on inlet flow field structure and end-wall effect of axial flow pump impeller under design condition. *Energies* 15, 4969. doi:10.3390/en15144969

Kan, K., Zhang, Q., Xu, Z., Zheng, Y., Gao, Q., and Shen, L. (2022). Energy loss mechanism due to tip leakage flow of axial flow pump as turbine under various operating conditions. *Energy* 255, 124532. doi:10.1016/j.energy.2022.124532

Lazarkiewicz, S., and Troskolanski, A. (1965). *Impeller pumps*. London: Pergamon Press.

Li, J., Meng, D., and Qiao, X. (2020). Numerical investigation of flow field and energy loss in a centrifugal pump as turbine. *Shock Vib.* 2020, 1–12. doi:10.1155/2020/8884385

Li, W., Ji, L., Li, E., Shi, W., Agarwal, R., and Zhou, L. (2021). Numerical investigation of energy loss mechanism of mixed-flow pump under stall condition. *Renew. Energy* 167, 740–760. doi:10.1016/j.renene.2020.11.146

Lin, Y. P., Li, X. J., Li, B. W., Jia, X. Q., and Zhu, Z. C. (2021). Influence of impeller sinusoidal tubercle trailing-edge on pressure pulsation in a centrifugal pump at nominal flow rate. *J. Fluid Eng-T Asme.* 143. doi:10.1115/1.4050640

Loitsanski, L. G. (1959). *Mechanics of liquids and gases*. Moscow: Government Technical Publishing House.

Mac-Gregor, G. A. (1952). Two dimensional losses in turbine blades. *J. Aero Sci.* 19, 332.

Markoff, N. M. (1948). Calculation of Profile losses in compressor cascades under non-separated flow of gas. *J. energy*, 32422.

Proscura, G. F. (1954). *Hydrodynamics of turbo machines*. Moscow: Moscow Publishing House.

Pu, K., Huang, B., Miao, H., Shi, P., and Wu, D. (2022). Quantitative analysis of energy loss and vibration performance in a circulating axial pump. *Energy* 243, 122753. doi:10.1016/j.energy.2021.122753

Schlichting, H. (1979). *Boundry layer theory*. 7th edition. New York: McGraw-Hill.

Shen, X., Zhang, D., Xu, B., Jin, Y., and Gao, X. (2019). Experimental and numerical investigation on pressure fluctuation of the impeller in an axial flow pump. *ASME-JSME-KSME 2019 8th Jt. Fluids Eng. Conf.* 55, 105562.

Shen, X., Zhang, D., Xu, B., Ye, C., and Shi, W. (2021). Experimental and numerical investigation of tip leakage vortex cavitation in an axial flow pump under design and off-design conditions. *Proc. Institution Mech. Eng. Part A J. Power Energy* 235, 70–80. doi:10.1177/0957650920906295

Skea, J., Priyadarshi, R., Shukla, A. R. R., and Slade, P. M. (2022). *Climate change 2022: mitigation of climate change*. New York: Intergovernmental Panel on Climate Change.

Srinivasan, K. M. (1966). *Comparative analysis of design of axial flow pumps*. Leningrad USSR: Leningrad PolytechnicPH.D.

Srinivasan, K. M. (1968). *Losses in axial flow pumps*. Coimbatore, India: Journal of PSG College of Technology.

Staritski, V. G. (1958). *Investigation of unequalness of flow parameters very near to diffusers of Axial flow pumps*. Moscow: Moscow Pub. House.

Staritski, V. G. (1964). *Selection of Fundamental parameters of Axial flow pumps*. Leningrad: Construction RoLPHMRussian.

Stefanovski, V. A. (1940). *Investigation of Axial diffusers of Propeller Pumps*, 11. Moscow: Machines RoMIoHReport of Moscow Institute of Hydro Machines Russian.

Stepanoff, G. U. (1962). Hydro dynamics of turbo machinery cascades moscow: Go. *Izd. Phy. Math. Lit.* 83, 2919.

Wang, L., Tang, F. P., Chen, Y., and Liu, H. Y. (2021). Evolution characteristics of suction-side-perpendicular cavitating vortex in axial flow pump under low flow condition. *J. Mar. Sci. Eng.* 9, 1058. doi:10.3390/jmse9101058

Xin, T., Wei, J., Qiuying, L., Hou, G., Ning, Z., Yuchuan, W., et al. (2022). Analysis of hydraulic loss of the centrifugal pump as turbine based on internal flow feature and entropy generation theory. *Sustain. Energy Technol. Assessments* 52, 102070. doi:10.1016/j.seta.2022.102070

Yang, F., Chang, P., Li, C., Shen, Q., Qian, J., and Li, J. (2022). Numerical analysis of pressure pulsation in vertical submersible axial flow pump device under bidirectional operation. *AIP Adv.* 12, 779.

Zhang, D., Shi, W., Zhang, H., Li, T., and Zhang, G. (2012). Numerical simulation of flow field characteristics in tip clearance region of axial-flow impeller. *Trans. Chin. Soc. Agric. Mach.* 43, 73–77.

Zhou, L., Hang, J., Bai, L., Krzemianowski, Z., El-Emam, M. A., Yasser, E., et al. (2022). Application of entropy production theory for energy losses and other investigation in pumps and turbines: A review. *Appl. Energy* 318, 119211. doi:10.1016/j.apenergy.2022.119211

Glossary

g Gravitational Acceleration, 9.8 m/s

C coefficient

H Head, m

p Pressure

$\mathbf{Q}_v$ Volume flow rate m^3/s

R Radius m

D Diameter, m

R* Radial coefficient

V Velocity, m/s

η Efficiency

ρ Density, kg/m^3

U Circumferential velocity, m/s

Subscripts

f friction

h Hub

t Tip

u Circumferential component

1 Impeller inlet

2 Impeller outlet

p Pressure

d Dynamic

tot Total

in Inlet of the pump

MCA Mass flow circle average

Superscript

\- Average

Frontiers in Energy Research

TYPE Methods
PUBLISHED 09 March 2023
DOI 10.3389/fenrg.2023.1147069

OPEN ACCESS

EDITED BY
Yang Yang,
Yangzhou University, China

REVIEWED BY
Maria Grazia De Giorgi,
University of Salento, Italy
Bin Xu,
Jiangsu University, China
Yandong Gu,
Yangzhou University, China

*CORRESPONDENCE
Wei Zhang,
✉ zhangwei@zime.edu.cn

SPECIALTY SECTION
This article was submitted to Process and Energy Systems Engineering, a section of the journal Frontiers in Energy Research

RECEIVED 18 January 2023
ACCEPTED 27 February 2023
PUBLISHED 09 March 2023

CITATION
Liu Y, Zhang J, Sun L, An L, Wang X, Cai J, Zhang W and Chen F (2023), Numerical study on flow separation and force evolution in liquid nitrogen cavitating flow.
Front. Energy Res. 11:1147069.
doi: 10.3389/fenrg.2023.1147069

Numerical study on flow separation and force evolution in liquid nitrogen cavitating flow

Yi Liu[1], JinLing Zhang[1], Lilong Sun[1], LiLi An[1], XunMing Wang[2], Jie Cai[2], Wei Zhang[2]* and Feng Chen[2]

[1]Hangzhou New-Asia Cryogenic Science and Technology Co., Ltd., Hangzhou, Zhejiang, China, [2]School of Intelligent Manufacturing, Zhejiang Institute of Mechanical and Electrical Engineering, Hangzhou, Zhejiang, China

In this paper, a two-phase flow model and the improved thermal cavitation model are used to study the flow characteristics and the evolution of vorticity force for liquid nitrogen cavitation flow. The results are validated against the experimental data from NASA, which shows that the flow re-attachment occurs in the area where the boundary vorticity flux begins to decrease from its positive value. Alternatively, the flow separation occurs near the area with low boundary vorticity fluxes. Besides, the boundary vorticity flux changes typically from negative to positive around the cavity. The development of the cavity affects the surrounding vortex structure, which leads to the evolution of vorticity force and the fluctuations of lateral force and drag force. The results show that the drag force is magnified by the cavitation, and it first decreases and then increases in a typical cycle of cavity evolution. The negative resistance unit is mainly produced in the front of the cavity, and the positive resistance unit is also made in the rear of the cavity. When the attached cavity is shed, the positive drag elements decrease, and the drag force drops to its minimum. When the attached cavity is growing, the positive resistance elements behind the cavity increase, making the resistance force gradually increase. For the lateral force, the existence of the cavity produces lift elements pointing out of the surface outside the cavity, and the unsymmetrical distribution of the cavity leads to the fluctuation of the lateral force.

KEYWORDS

thermo-sensitive cavitating flow, flow separation, boundary vorticity flux, vorticity force, force element

1 Introduction

Cavitation is a sudden phenomenon. When the local static pressure is lower than the saturated vapor pressure, the liquid evaporates and produces bubbles (Li et al., 2018). Cavitation involves complex flow phenomena, such as phase transition, multi-scale turbulence and compressibility, which may lead to vibration, noise and performance degradation in the fluid (Joseph, 1995; Li X et al., 2021). Cavitation flow is usually predicted as a phenomenon without considering the changes in liquid temperature and physical properties (Xu et al.,2022; Chen et al., 2023). However, the physical and thermodynamic properties of thermo-sensitive fluids would significantly change when cavitation occurs, affecting the cavitation characteristics and invalidating the constant temperature assumption. In recent decades, due to the wide application of thermal fluids in industrial applications, this phenomenon has attracted extensive research attention (Merouani et al., 2016; Abderrezzak and Huang, 2016; Li et al.,2023). For example, liquid hydrogen and oxygen are commonly used to fuel space launch vehicles. However, these fuels are prone to cavitation in the turbopump of space engines (Smirnov et al., 2014; Zhao et al., 2016), which directly affects the thrust level of the rocket engine and the success of the rocket launch. Since the cavitation of thermo-sensitive fluids is often accompanied by strong energy conversion and mass transfer (Long et al., 2017; Zhang BC et al., 2020), it is necessary to understand the flow characteristics and potential mechanisms.

A series of experiments on cryogenic cavitation were performed to explore its characteristics. For instance, Kikuta et al. (2008) studied the thermodynamic effects of cavitation performance and cavitation instability in the inducer by comparing the cavitation flow of thermal fluid and cold water. Franc et al. (2001) experimentally studied the cavitation flow of freon R114 in the inducer at three temperatures. They found that the length of the cavity near the inlet blade of the inducer decreased with the increase of the reference temperature. Kelly and Segal (2015) studied the cavitation flow of fluorone around the NACA 0015 hydrofoil under different free flow conditions, and observed the transition from classical cavitation to thermal cavitation at 318 k. Cervone et al. (2006) found that the length of the water chamber in the NACA 0015 hydrofoil is positively correlated with temperature. Šarc et al. (2017) found that the cavity size of water becomes larger at 313 k than at 273 K and 343 K. Zhang et al. (2018), Zhang et al. (2019) optimized and used the Zwart-Gerber-Belamri (ZGB) model to simulate the thermal cavitation flow on 2D and 3D hydrofoils. They found that when the temperature in the cavity decreased by 1 K–3 K, the thermal effect inhibited the growth of the cavity. Therefore, temperature fluctuation should be considered in thermal cavitation flow. Visualization experiments on cryogenic cavitation were also performed. For instance, Gopalan and Katz (2000) focused on the cavity structure of lamellar cavitation at different free flow temperatures. They found that a slight increase in temperature would slightly increase the size of the lamellar cavitation, which in turn significantly affects turbulence and kinetic energy in the closed region.

Liquid nitrogen is one of the most commonly applied thermo-sensitive fluids whose cavitation has been widely investigated. Holl et al. (1975) studied the variation of temperature and pressure in the cavitation region around ogive bodies with different diameters and established a connection between cavitation number and thermodynamic effects. Chen et al. (2017), Chen et al. (2019a), Chen et al. (2019b) studied the unsteady dynamic evolution of cavitating flow of liquid nitrogen at different temperatures and free flow rates, revealing the transient characteristics in the flow. De Giorgi et al. (2020) investigated cavitating flows of water, liquid hydrogen, and nitrogen on hydrofoils numerically using Eulerian homogeneous mixture approach. Thermal effects have been introduced by means of the activation of energy equation and latent heat source terms plus convective heat source term. Ohira et al. (2012) studied the instability of supercooled fluid nitrogen cavitation flow at different temperatures. They found that when the liquid temperature decreased, the cavitation model changed from a continuous model to an intermittent model. In addition, the oscillation pressure of the continuous model is much smaller than that of intermittent model. Shi and Wang (2020) used the improved Merkle cavitation model and the filter-based turbulence model to numerically analyze the influencing factors of the thermal effect produced by the cavitation flow of liquid nitrogen and hydrogen. Niiyama et al. (2012) studied the thermal effect of liquid nitrogen hollow flow and confirmed that such product inhibited the development of cavitation. However, the cavitation characteristics in thermosensitive fluids deserve further study.

The whole cavity evolution is accompanied by the change of eddy current, especially for thermal fluid. The purpose of this study is to establish the relationship between force evolution, flow separation, cavity growth, shedding and collapse (including corresponding connections through vortices).The flow separation in the cavitating flow field is influenced by cavity development and exacerbates flow instability. In addition, the flow separation due to cavitation is significantly influenced by vortices. Chen J et al. (2017) found that the cavity oscillates under the influence of the surrounding vortex flow field. Wang et al. (2019) theoretically studied the instability of non-Newtonian liquid jets with cavitating bubbles and found that the compressibility of the liquid led to flow instability. Li LM et al. (2021) studied the tip leakage cavitation flow and found that the cavitation characteristics were affected by the tip leakage vortex and the tip separation vortex. Kumar et al. (2018) simulated the separated flow in the laminar boundary layer, studied the flow separation mechanism, and proposed a separation model of steady-state flow.

Cavitation would cause force fluctuations in devices. Hsu and Chen, (2020) found that the amplitude of lift and drag increased along the standard slit in the cylinder. Zhu et al. (2015b) studied the cavitation flow of liquid hydrogen on ogive using the compressible Schnerr-Sauer cavitation model. In addition, they calculated the unsteady evolution of steam content, temperature and pressure fields in the cavity, and extended the schnerr Sauer model to simulate cavitation in cryogenic fluids (Zhu et al., 2015a). Keller (2001) experimentally studied the lift and drag coefficients under different cavitation numbers by testing other objects. Their experimental results show that lift is closely related to cavitation. Liu et al. (2020) studied the lift and drag fluctuations caused by the vortex structure caused by the evolution of the cavity on the hydrofoil. Seif et al. (2009) proposed a non-constant algorithm to simulate the cavitation problem in practical engineering applications, and determined the time-varying characteristics of the resistance coefficient during cavitation. They found that a certain degree of cavitation changed the mechanical properties and energy distribution, so the lift and resistance of the rotating body head fluctuated within a specific range. Ehara et al. (2019) conducted experimental research on lift and drag, and found that lift and drag move reasonably with the development of cavitation. Jafari and Rad, (2009) simulated the cavitation flow on the cylinder surface and observed the relationship between the cavitation number and lift and drag. De Giorgi et al. (2019) studied the relationship between lift and drag and three cavitation States, namely, cavitation, cloud cavitation and super cavitation. Shen et al. (2020) studied the relationship between hydrofoil surface lift resistance and cavity development. They found that with the increased cavitation number, the time average lift and drag coefficients first increased and then decreased. In addition, the downward trend of the drag coefficient is greater than that of the lift coefficient.

In thermal cavitation flow, the evolution of the cavity leads to the change of flow state. Flow separation and reattachment also occur frequently. At the same time, the development of cavity is inseparable from the evolution of the force. In the current work, we focus on analyzing of flow separation and detail change to reveal the detailed interaction between cavitation and flow characteristics. The improved ZGB cavitation model is realized and combined with the uniform mixing model to simulate the cavitation flow of liquid nitrogen around the oval structure. This paper first introduces the numerical model and its verification, then analyzes the transient flow field caused by cavitation, the influence of cavitation on flow separation, and the evolution of force with the development of cavitation. Finally, some conclusions are given. The conclusions obtained can provide theoretical support for the internal flow of cryogenic cavitation.

2 Thermo-sensitive cavitating flow model

Base on the ZGB cavitation model, the thermodynamic benefits are considered for correction.

2.1 Governing equations

Both the gas and liquid phases are considered homogeneous mixtures during the simulation, and the governing equations are formulated as

$$\frac{\partial \rho_m}{\partial t} + \frac{\partial}{\partial x_j}\left(\rho_m u_j\right) = 0 \tag{1}$$

$$\frac{\partial}{\partial t}\left(\rho_m C_{pm} T\right) + \frac{\partial}{\partial x_j}\left(\rho_m C_{pm} T u_j\right) = \frac{\partial}{\partial x_j}\left[(\lambda_m + \lambda_t)\frac{\partial T}{\partial x_j}\right] - \dot{m}L \tag{2}$$

$$\frac{\partial (\rho_m u_i)}{\partial t} + \frac{\partial\left(\rho_m u_i u_j\right)}{\partial x_j} = -\frac{\partial p}{\partial x_i} + \frac{\partial}{\partial x_j}\left[(\mu_m + \mu_t)\left(\frac{\partial u_i}{\partial x_j} + \frac{\partial x_j}{\partial x_i} - \frac{2}{3}\frac{\partial u_k}{\partial x_k}\delta_{ij}\right)\right] \tag{3}$$

$$\dot{m} = \frac{\partial (\rho_v \alpha_v)}{\partial t} + \frac{\partial\left(\rho_v \alpha_v u_j\right)}{\partial x_j} \tag{4}$$

where u and p are the velocity and pressure, x and the subscripts, i, j, and k represent the axes, μ_{m} and μ_t are the dynamic and turbulent viscosities of the mixture, λ_m and λ_t denote thermal conductivity and turbulent thermal conductivity, T denotes temperature, C_{pm} and L denote specific and latent heat, $\dot{m}$ is the mass transfer source term, a is the volume fraction, and δ_{ij} is a Kronecker Symbol.

$$\dot{m}^{+} = F_{vap}\frac{3\alpha_{nuc}(1-\alpha)\rho_g}{R_B}\left[\sqrt{\frac{2}{3}\frac{\max\left(p_v(T) - p, 0\right)}{\rho_l}} - \frac{C_0 h_b}{\sqrt{K_l \rho_l C_l}}\right] \tag{5}$$

$$\dot{m}^{-} = -F_{cond}\frac{3\alpha\rho_g}{R_B}\left[\sqrt{\frac{2}{3}\frac{\max\left(p - p_v(T)\right)}{\rho_l}} - \frac{C_0 h_b}{\sqrt{K_l \rho_l C_l}}\right] \tag{6}$$

where $R_B = 1 \times 10^{-6}\ m$ is the bubble diameter, $\alpha_{nuc} = 5 \times 10^{-4}$ is the volume fraction of the nucleation point, K_l is the thermal conductivity of the liquid, C_l is the specific heat capacity, h_b is the convective heat transfer coefficient, C_0 is the empirical coefficient, and $C_0 h_b$ is the recommended as $1\ W/(m^2K)$.

Since the saturation vapor pressure of liquid nitrogen $p_v\ (T)$ varies with temperature, a polynomial fit is used to represent the saturation vapor pressure:

$$p_v(T) = \sum_{i=-1}^{4} a_i T^i \tag{7}$$

where

$$a_{-1} = 7.9627702861 \times 10^9;\ a_0 = -4.7960049172 \times 10^8$$
$$a_1 = 1.1544023560 \times 10^7;\ a_2 = -1.3860791270 \times 10^5$$
$$a_3 = 8.2752103303 \times 10^2;\ a_4 = -1.9511544848 \times 10^0$$

The temperature field in cavitating flows, usually has thermal effects, is mainly determined by the heat transfer between the gas and liquid phases. Therefore, the results of compressibility and viscous dissipation in the energy equation are not considered for the time being. The density, dynamic viscosity, and enthalpy are calculated as

$$\rho_m = \rho_v \alpha_v + (1 - \alpha_v)\rho_l \tag{8}$$

$$\mu_m = \alpha_v \mu_v + (1 - \alpha_v)\mu_l \tag{9}$$

$$h_m = \frac{\rho_l h_l (1 - \alpha_v) + \rho_v h_v \alpha_v}{\rho_m}, h_l = C_l T, h_v = C_v T + L_{ev} \tag{10}$$

where T is the temperature of the liquid nitrogen, C_l and C_v represent the liquid and vapor heat capacities.

2.2 Model validation and mesh independency

The turbulence model SST k- ω is used in this paper. Numerical results are obtained by simulating the cavitating flow of liquid nitrogen in an axisymmetric body with a radius of 0.357 inches. The experimental values were obtained from Hord (1973), who performed sub-scale experiments on the cavitating flow of thermo-sensitive liquids with funding from NASA. The main body consists of a cylinder with a quarter-circular radius bend and is placed inside a transparent plastic tube. Five pressure and temperature sensors are arranged on the upper and lower surfaces of the ogive. Strictly follow the experimental conditions to confirm the accuracy of the numerical method.

Figure 1 shows the structure used in the numerical simulation. The boundary condition without a sliding wall is imposed on the oval surface (Liu et al. (2021)). The conditions of numerical simulation are set according to the experiment to ensure the reliability of the simulation results.

In the present study, The RMS residual is reduced to 10^{-4}, and 20 iterations are selected in each time step to balance computing resources and accuracy. The simulation of unsteady thermal cavitation flow begins with the results of steady-state cavitation flow. In the simulation process, the time-dependent governing equations are discretized in the space and time domains. The diffusion term is solved by the second-order central difference scheme. The time-dependent second-order implicit algorithm is used for the transient term.

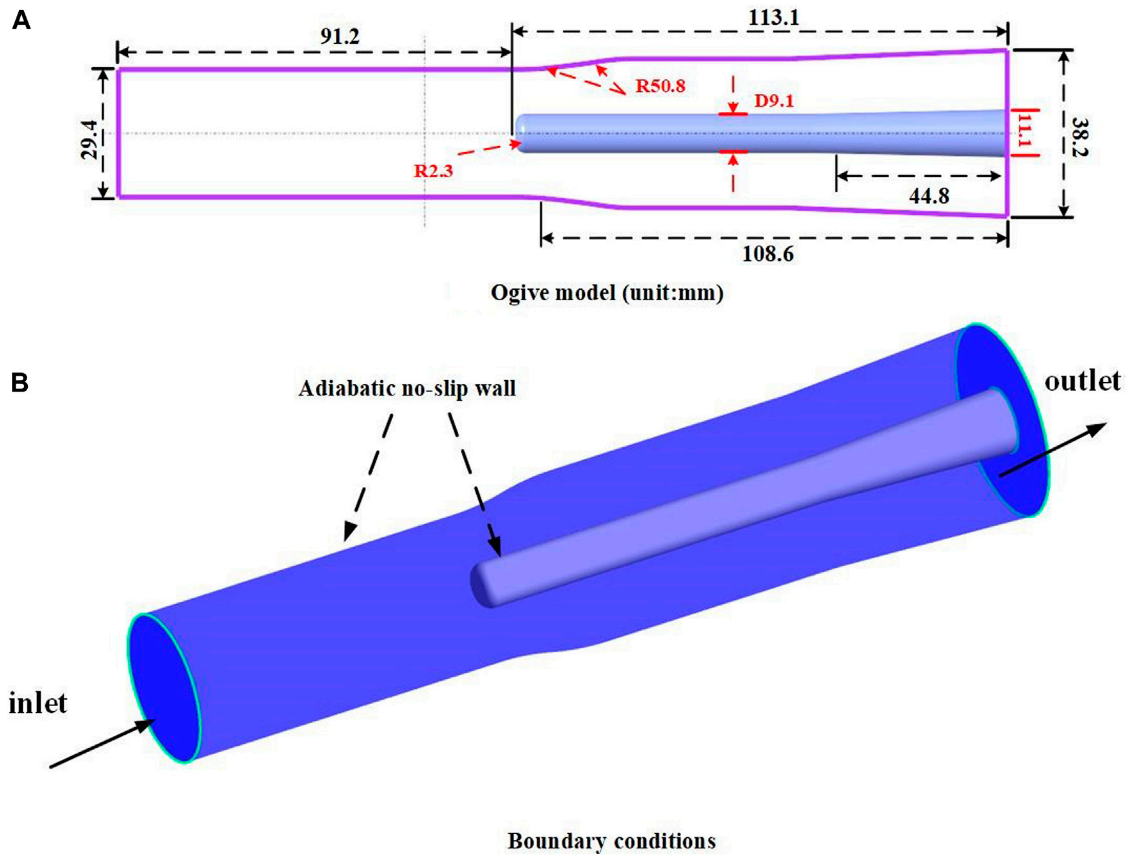

FIGURE 1
Computational domain and boundary conditions.

TABLE 1 Conditions for simulation.

Case	Inlet temperature T_{∞}/K	Inlet velocity u_{∞}/m · s^{-1}	Cavitation number σ_{∞}	Re/10^6
312 D	83.06	23.5	0.46	9
322 E	88.56	26.8	0.44	12

The computational domain of numerical simulation is discretized by structural hexahedral mesh. The mesh close to the wall is refined to improve the quality of the whole mesh and ensure the simulation accuracy. The conditions for the numerical simulation are obtained from Hord's experiments (Hord, 1973), and the details are given in Table 1. The mesh independence analysis is performed in Figure 2, and it can be seen that the calculation results are relatively consistent for all three meshes. Therefore, mesh 2 (4403880 nodes and 4505476 elements) is adopted in the following calculations due to the limitation of computational resources. Figure 3 shows some details of mesh 2. The mesh is refined near the head and wall to ensure the accuracy of the calculation.

The accuracy of numerical simulation is validated using the pressure and temperature distributions for the two conditions. Figure 4 shows the comparison between simulation and experimental data (hord, 1973), which agrees well with experimental data. Therefore, the simulation is reliable. In addition, there are temperature and pressure drop at the large curvature of the head. Then it gradually stabilized with the flow of liquid nitrogen and the development of the cavity.

In Figure 4, we can see that the low temperature and pressure areas are located around the cavitation area near the head, which is due to the sudden change of the leading edge of the oval structure, resulting in a large amount of vaporization. Meanwhile, the development of the cavity will also change the flow field. Once cavitation occurs, reentrant jets, flow separation and reattachment will frequently occur around the cavity. Such complex and variable flow phenomena will in turn affect the growth and shedding of cavities. Therefore, the following sections will analyze the interaction between cavitation development and flow field, as well as the impact on the temperature field and pressure field. By comparing between the two conditions, the cavitation number of condition 322 E is a bit

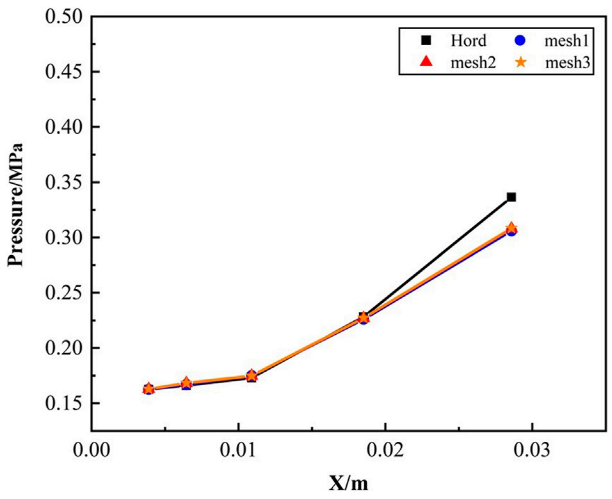

FIGURE 2
Mesh independence verification.

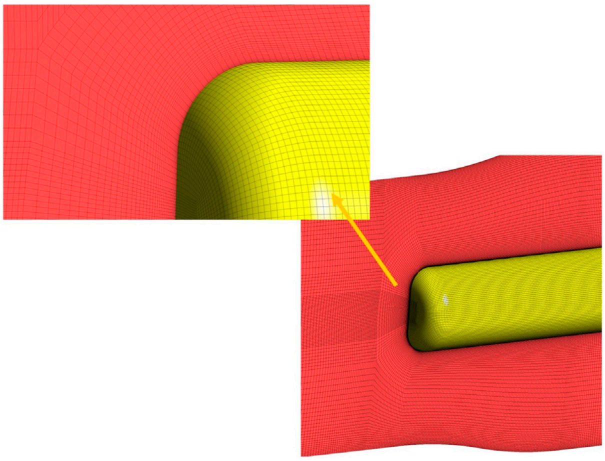

FIGURE 3
Mesh details of the computational domain.

smaller, indicating stronger cavitation, and thus the temperature drop is more significant.

3 Results and discussion

3.1 Unsteady cavitation features

To further analyze the flow field characteristics in the process of cavity development, the cavitation shedding cycle under 312 days condition is used to explain. The temperature and pressure distribution during the different periods of cavitation are shown in Figure 5. At the beginning of cavitation, the generation of cavitation will lead to changes in temperature and pressure. The low temperature and low-pressure area are mainly in the cavity. As the cavities gradually cover the surface, a few shedding cavities appear in the flow channel. It is caused by the unstable shedding of cavities. The low temperature and pressure areas are mainly in the head, which is consistent with Figure 4.

In temperature-sensitive cavitating flow, the pressure and temperature in the cavity are lower than those in other regions, resulting in a more severe cavitation phase transition. When the cavity is steadily covered by the surface, the re-entrant jet caused by the cavity development will have a better chance to enter the interior of the cavity. The free fluid flowed easily into the cavity as described by (Sun et al., 2019), because the liquid/vapor density ratio of liquid nitrogen under low temperatures would generate large cavity bubbles according to the conservation of mass ($4\pi r^3/3 = V_v = V_l\rho_l/\rho_v$). Therefore, increasing the temperature of the free fluid would gradually reduce the bubbles inside the cavity by lowering the density ratio. The reduction of bubbles would also accelerate their movement, which in turn would accelerate the cavity collapse. Therefore, in the thermo-sensitive cavitating flow, the vapor usually concentrates at the center of the vortex.

3.2 Characteristics of flow separation

In Figure 6, four moments in a cavitation shedding cycle are shown at the 312 D operating condition. In the figure, the growth and shedding of cavities severely disturb the flow state. In Figure 6A, the flow state at A is disturbed. Around the shedding cavity, the flow state is constantly being altered. At the rear, significant re-attachment can be seen where the cavities are shedding. In Figures 6A, B, flow separation and re-attachment around the cavity frequently occur. In Figure 6B, the re-entrant jet, flow separation and re-attachment phenomena occur frequently around the cavity. Such complex and variable flow phenomena will in turn affect the growth and shedding of cavities. Thus the development of the cavity leads to a change in the flow state, which in turn destabilizes the cavity and accelerates the cavity shedding Figure 6D.

The development of the cavity will affect the flow state, and then affect the falling off and growth of the cavity. The BVF can be used to describe the flow state, so the BVF needs to be introduced to investigate the interaction between flow and cavity. This section uses the 312 D operating condition as an example. Without considering compressibility, the root of all vortex generation and diffusion is boundary vorticity flux (BVF), which is the core theory of boundary vorticity dynamics. The BVF proposed by Lighthill, (1963) consists of the following components:

$$\sigma = \sigma_\alpha + \sigma_P + \sigma_\tau \tag{11}$$

$$\sigma_\alpha = \vec{n}\times \vec{\alpha}_B \tag{12}$$

$$\sigma_{\prod} = \frac{1}{\rho_m}\vec{n}\times\Delta\prod, \prod = p - (\lambda + 2\mu)\vartheta \tag{13}$$

$$\sigma_\tau = \upsilon(\vec{n}\times\nabla)\times\vec{\omega} \tag{14}$$

where σ_α, σ_P, and σ_τ represent the BVF induced by wall acceleration *a*, the normal stress $\prod$ of the tangential gradient, and the BVF caused by the boundary vortex (shear stress).

Besides BVF, vorticity lines are also used to study flow separation from cavitation effects (Liu et al., 2021). According to

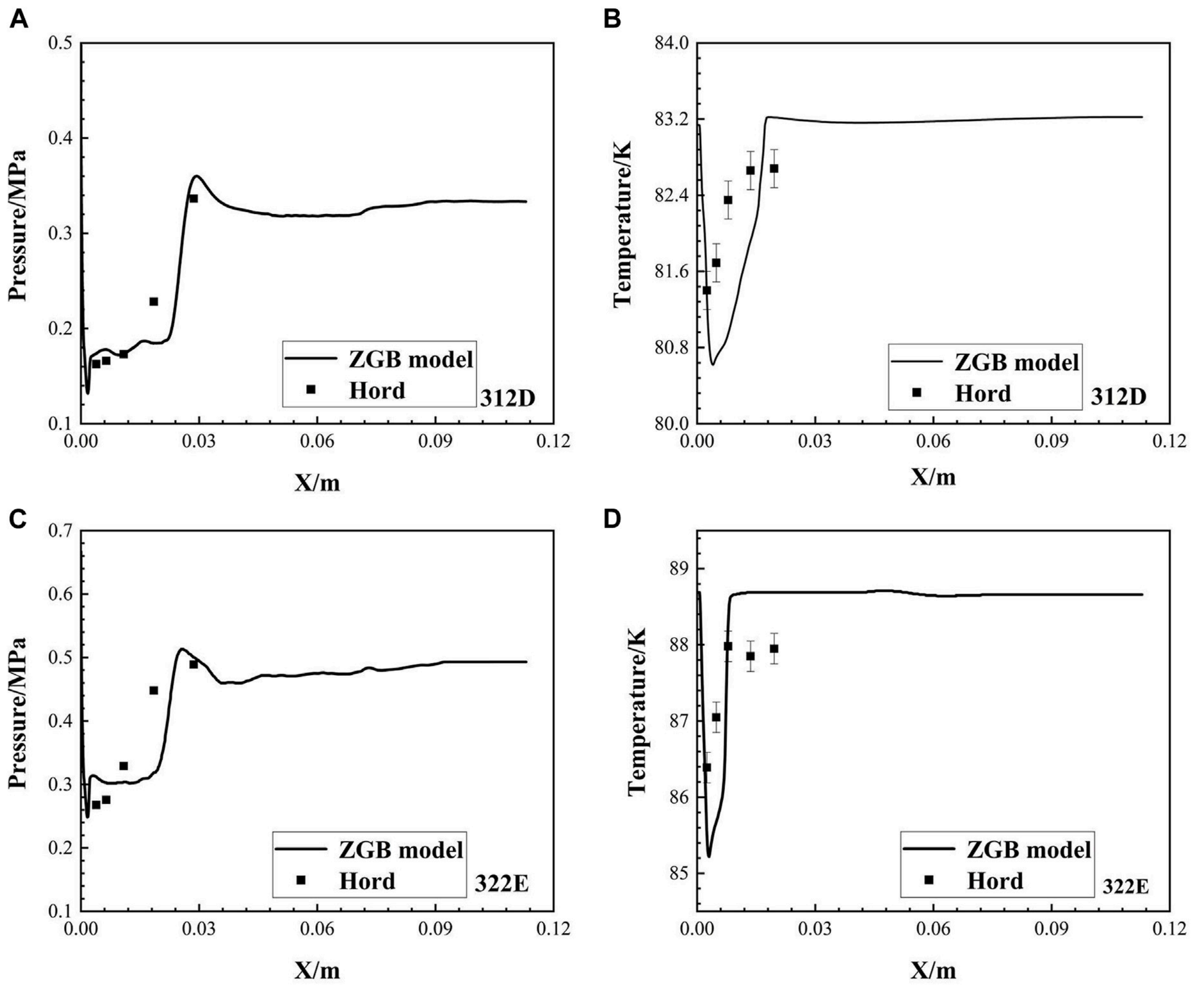

FIGURE 4
Comparison of pressure and temperature results between experiment and simulation.

the boundary vortex dynamics theory, the flow separation is manifested by the formation of a shear layer and the separation of fluid from the wall. The vortex dynamics is particularly critical in the separation zone, which connects the attached boundary layer and the separated shear layer, and exhibits the same properties as both layers. Generally, in the flow separation region, the vorticity line has a highly pronounced bend and high curvature. The peak of the BVF is usually found in this region.

In temperature-sensitive cavitation flow, the evolution of cavitation is closely related to the change of flow state. Figures 7, 8 illustrate the vortex structure around the cavity and the variation of BVF during a cavitation shedding cycle. Figure 9 shows the change in the vorticity line.

In Figures 7, 8, it can be seen that the BVF varies significantly at the large curvature of the head. A rapid increase in BVF indicates that the flow state has changed dramatically. Then, at 1/8 T the shed cavities are randomly distributed on the surface. Therefore, the flow state becomes irregular and the BVF fluctuates (Figure 8A). It shows that the change in flow state at this point is mainly influenced by the shedding cavity. As the cavity shed, a stable area of peak BVF is created around it and the BVF changes significantly at this point (Figure 8B). A negative peak in the BVF and a significant bend in the vorticity line (Figure 9B) indicate that flow separation occurs at this point (Figure 6A). Also, when the cavity is shedding, the values of BVF increase rapidly from negative to positive. It shows that the flow separation and re-attachment around the cavity occur at the same time. In Figure 9, it can be noticed that the large curvature vorticity lines often appear with large values of the BVF. Combined with Figure 7, it can be seen that the changes in vortex structure caused by the shedding cavity can also lead to the appearance of large curvature vorticity lines. Therefore, the difference in fluid state is mainly influenced by the cavity in the cavitating flow.

When the attached cavity appears at the head of the structure, a reentrant jet will be generated and enter the cavity, as shown in Figures 6B, C. Colliding with the incident flow, the flow state inside the cavity will be changed. However, as shown in Figure 8, the change in BVF is not significant at this time (Figures 8C–F). This is because the change in internal flow state being suppressed by the attached cavity. It can be seen in Figure 9 that in the area with an additional cavity, there is only a tiny curvature vorticity line. This indicates that the flow in the cavity is relatively stable. At the same time, in the tail of the cavity, with the development of the additional

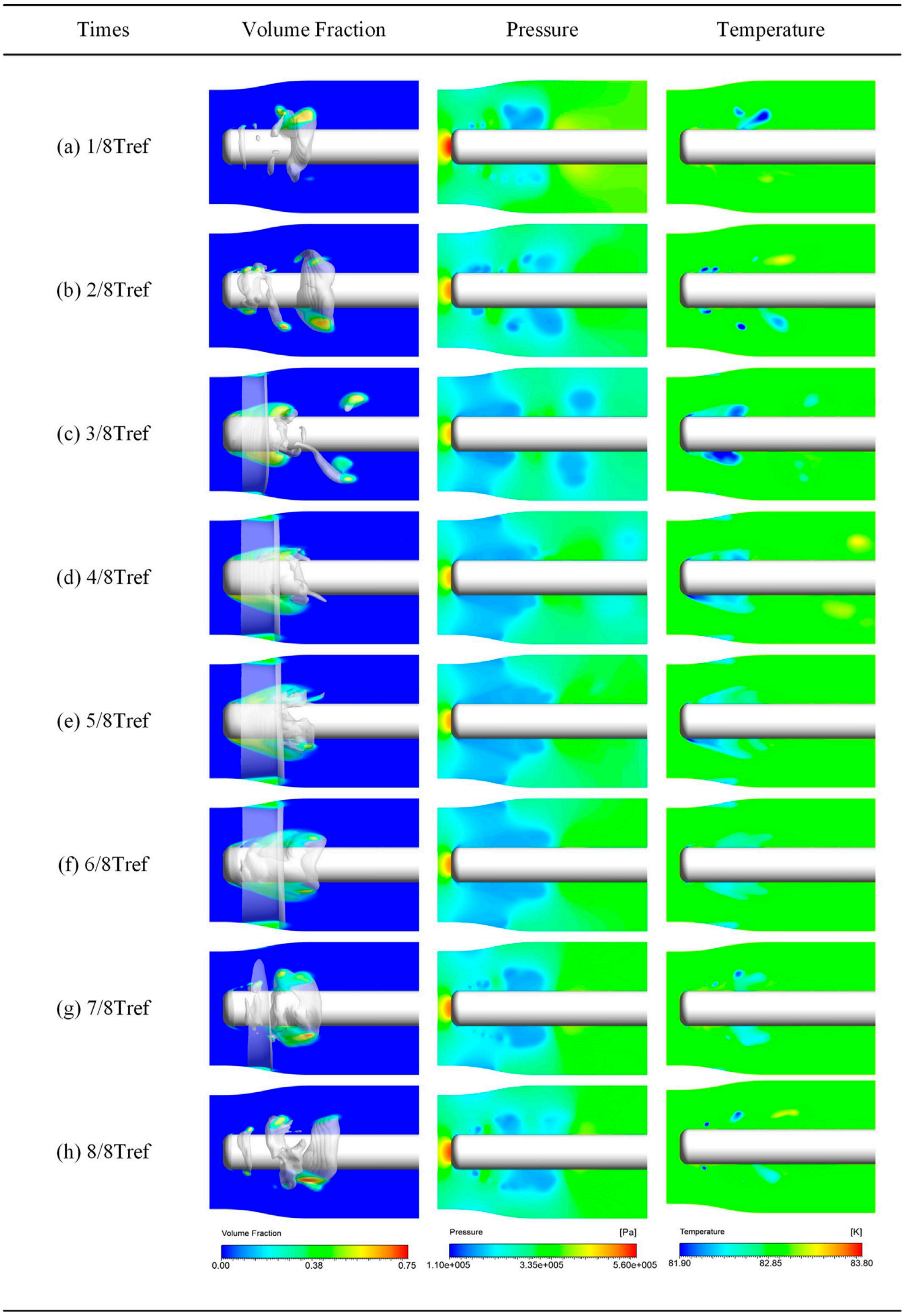

FIGURE 5
Changes in cavity, temperature and pressure in a cavitation shedding cycle.

cavity and the emergence of the falling cavity, the vortex structure will change. At this time, the BVF value rapidly increases from negative to positive. At 4/8Tref, a typical U-shaped vortex structure is formed. This shows that the reentrant jet is not only produced at the end of the cavity, but also the flow state becomes turbulent with the change of the flow direction. So reentry, flow separation and

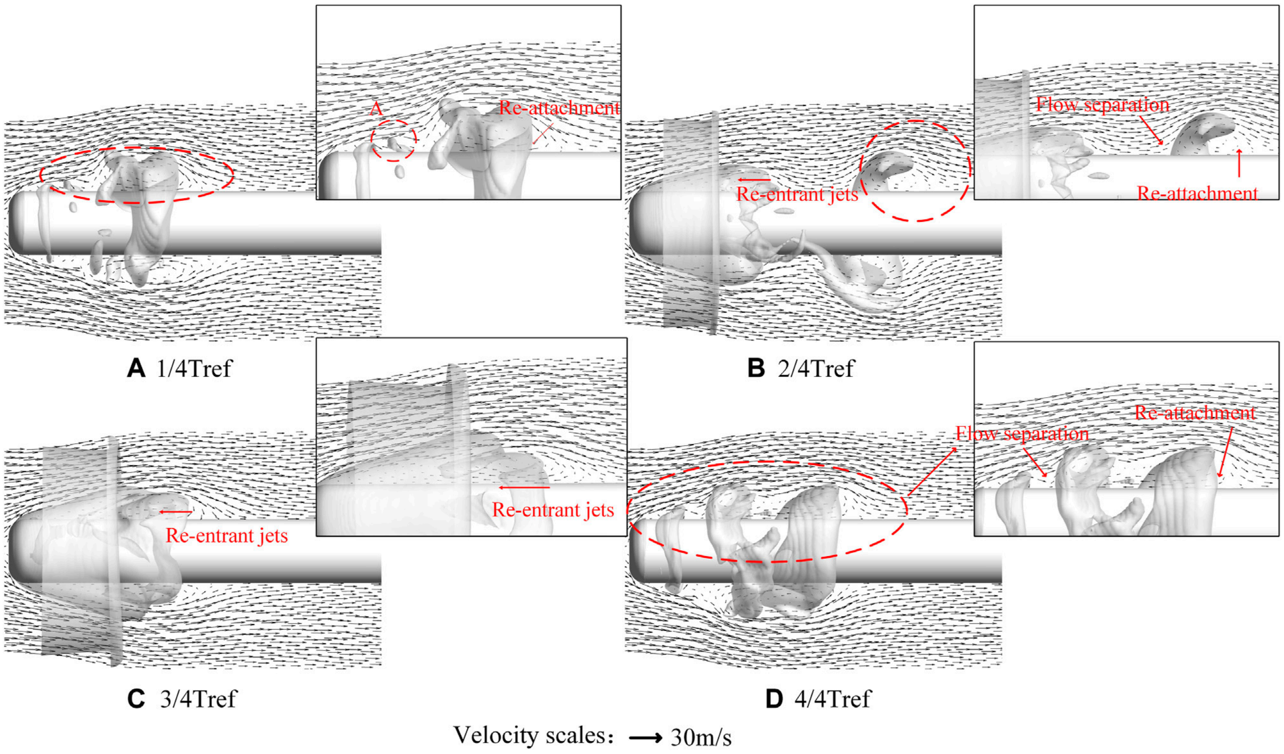

FIGURE 6
Cavity development and velocity streamlines.

reattachment phenomena will occur frequently around the cavity. And this complex and variable flow phenomenon will in turn affect the growth and shedding of cavities.

When the shedding of the attached cavity starts, the flow state gradually changes around the head of the structure. In Figures 7G, H, the values of BVF change rapidly around the shedding cavity. We can find that the BVF around the shedding cavity decreases quickly from positive to negative values, while large curvature vorticity lines appear (Figure 9H). This indicates that significant flow separation occurs at the front of the opening and flow the reattachment occurs at the rear. Therefore, the combination of BVF and vorticity line can well reveal and predict the flow state.

In summary, the development of the cavity seriously affects the flow state. The production of the reentrant jets is the main reason for the complexity of the flow state in the additional cavity. The production of the reentry jet also accelerates the falling off of the cavity. Cavity shedding causes the BVF value to increase from negative to positive. Combined with the changes in BVF and vorticity line, they can predict the phenomena of flow separation and reattachment.

3.3 Characteristics of vorticity force evolution

This section will analyze the variation of lateral force and drag during cavity development. Lee et al. (2012) examined the fluid to finite wing up lateral force and drag, and found that the forces applied on the wing surface can be classified into surface and volume forces. The equations for lateral force and drag forces are

$$F_L = -\int_V \vec{v}\times\vec{\omega}\cdot\nabla\phi_L \mathrm{d}V + \frac{1}{\mathrm{Re}}\int_S \vec{n}\times\vec{\omega}\cdot(\nabla\phi_L + j)dA \tag{15}$$

$$F_D = -\int_V \vec{v}\times\vec{\omega}\cdot\nabla\phi_D \mathrm{d}V + \frac{1}{\mathrm{Re}}\int_S \vec{n}\times\vec{\omega}\cdot(\nabla\phi_D + i)dA \tag{16}$$

where $\vec{n}\times\vec{\omega}\cdot(\nabla\phi_D + i/j)/Re$ is the hydrofoil surface force element created by surface vorticity, $-\vec{v}\times\vec{\omega}\cdot\nabla\phi$ is the volume element caused by vorticity in the flow, ϕ Is the velocity potential function, and n is the normal vector inward from the hydrofoil surface. According to the force element theory, the surface velocity potential function of the hydrofoil meets the conditions $-\vec{n}\cdot\nabla\phi = \vec{n}\cdot e$ at the hydrofoil surface. The numerical results also show that the lateral force and resistance components caused by surface vorticity are significantly smaller than those caused by flow vorticity. Zhang K et al. (2020) also confirmed this conclusion. Therefore, the study of hydrofoil surface force elements only analyzes the distribution of volume lift and drag.

The forces and the moments on the arbitrarily shaped objects can be expressed as integrals of the BVF, for arbitrary wall surface ∂_B, the combined force $F = F_s + F_l$ is calculated as

$$F_s = -\int_{\partial_B} \rho x \times \left(\frac{1}{2}\sigma\prod + \sigma_\tau\right)\mathrm{ds} \tag{17a}$$

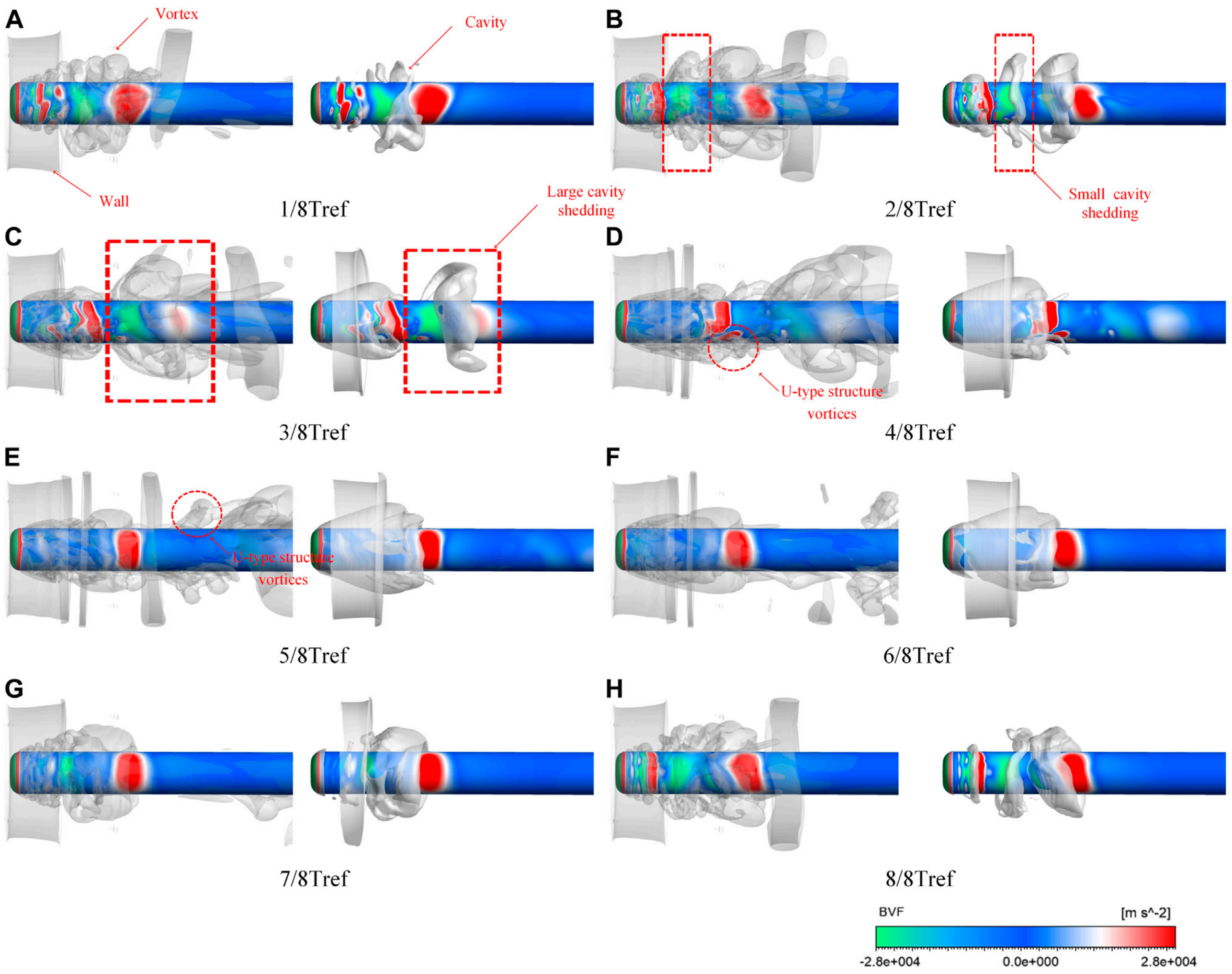

FIGURE 7
Vortices, cavities and BVF distributions.

$$F_l = \oint_C x \times \left(\frac{1}{2}\prod \mathrm{d}x + \mu_\omega \times \mathrm{d}x\right) \qquad (17b)$$

The x is the position vector and establishes the relationship between BVF and force.

In the case of large Reynolds numbers, σ_τ is much smaller than $\sigma_\prod$ and can usually be ignored. Ignoring the small contribution of surface friction to the combined force, then at this point its lateral force F_L and drag F_D can be simply expressed by BVF as

$$F_L = \oint_C \rho x \sigma_p \mathrm{d}s \qquad (18a)$$

$$F_D = -\oint_C \rho y \sigma_p \mathrm{d}s \qquad (18b)$$

Because the oval surface changes little in the X direction, the influence of BVF in the force element can be concentrated on the resistance. This can better explain the changes of force elements in the process of cavity development.

Figure 10 is selected from one cycle of the 322 E operating condition and describes the detailed vortex structures. In Figure 10A, it can be seen that in the middle stage of the cavity development, more U-type structures appear on the surface, which means that at this time, there is more cavity shedding to create disturbances. During the cavity development, cavity shedding and a fracture of structures are observed on the cloud cavities attached to the cylinder surface, enhancing vorticity and the 3D nature of velocity gradients in the corresponding regions. In the instantaneous 2/8Tref, 4/8Tref, 6/8Tref, and 8/8Tref moments, the multiscale nature of vorticity and its three-dimensional structure become more obvious with the significant enhancement of its intensity. The unstable vortex extends further into the wake, and a small-scale cylindrical vortex appears in the spanwise vortex. At this point, the wake becomes more complex. Therefore, in this paper, we will focus on the cavity development caused by the change of resistance and lateral force.

Figure 11 shows the variation of lateral forces on the ogive surface for the two operating conditions. The points a - h are the moments for further investigation in the following words in a cavitation shedding cycle for a better understanding. In Figure 11, the fluctuation of 322 E is higher compared to

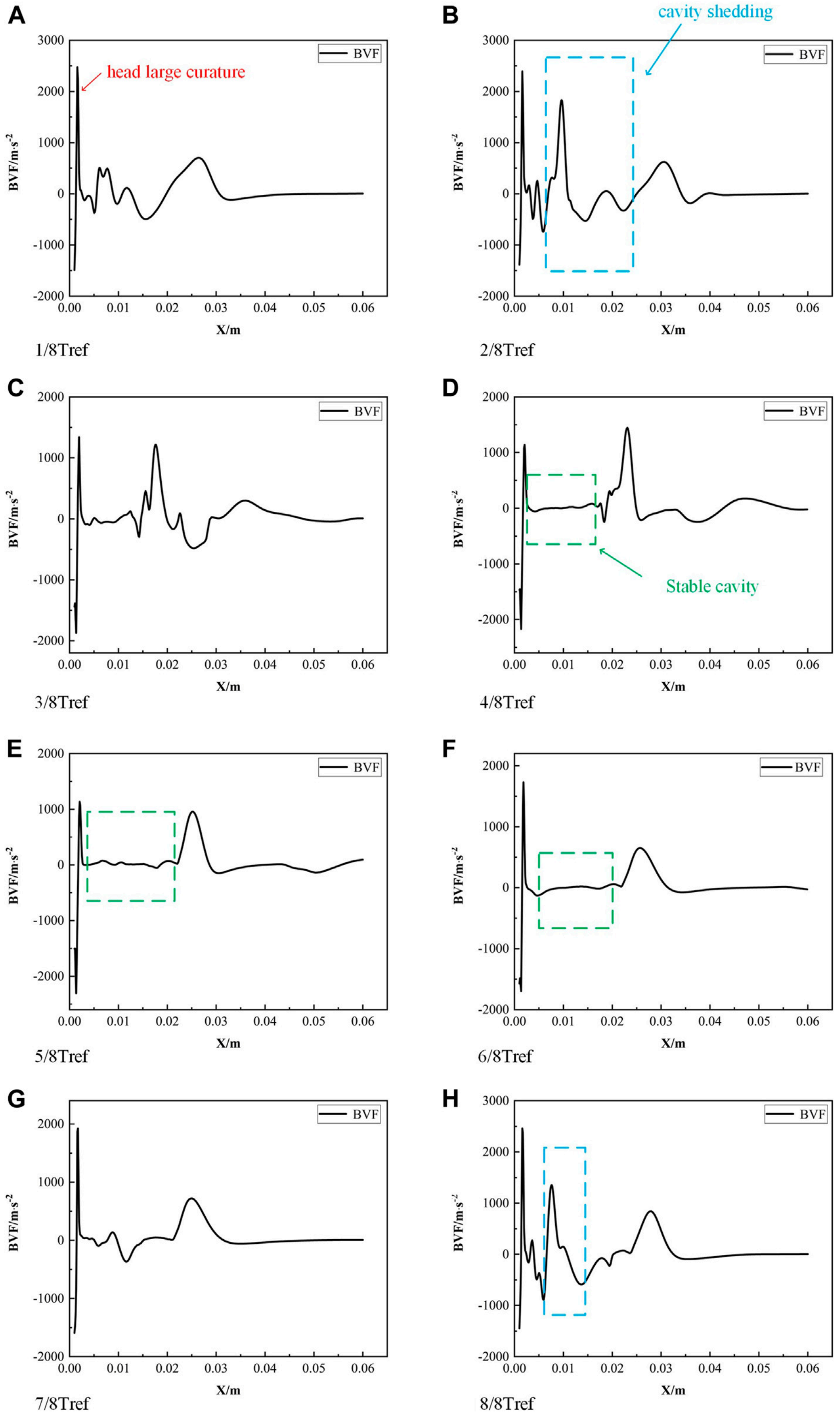

1/8Tref

2/8Tref

3/8Tref

4/8Tref

5/8Tref

6/8Tref

7/8Tref

8/8Tref

FIGURE 8
Changes in BVF.

312 D conditions. Figure 12 shows the change in drag for the two states. The shift in drag can be seen to be cyclical, with the drag first decreasing and then increasing during a cavitation shedding cycle. The 322 E condition shows a larger drag value, and this is due to the more significant cavity generated by the increased temperature.

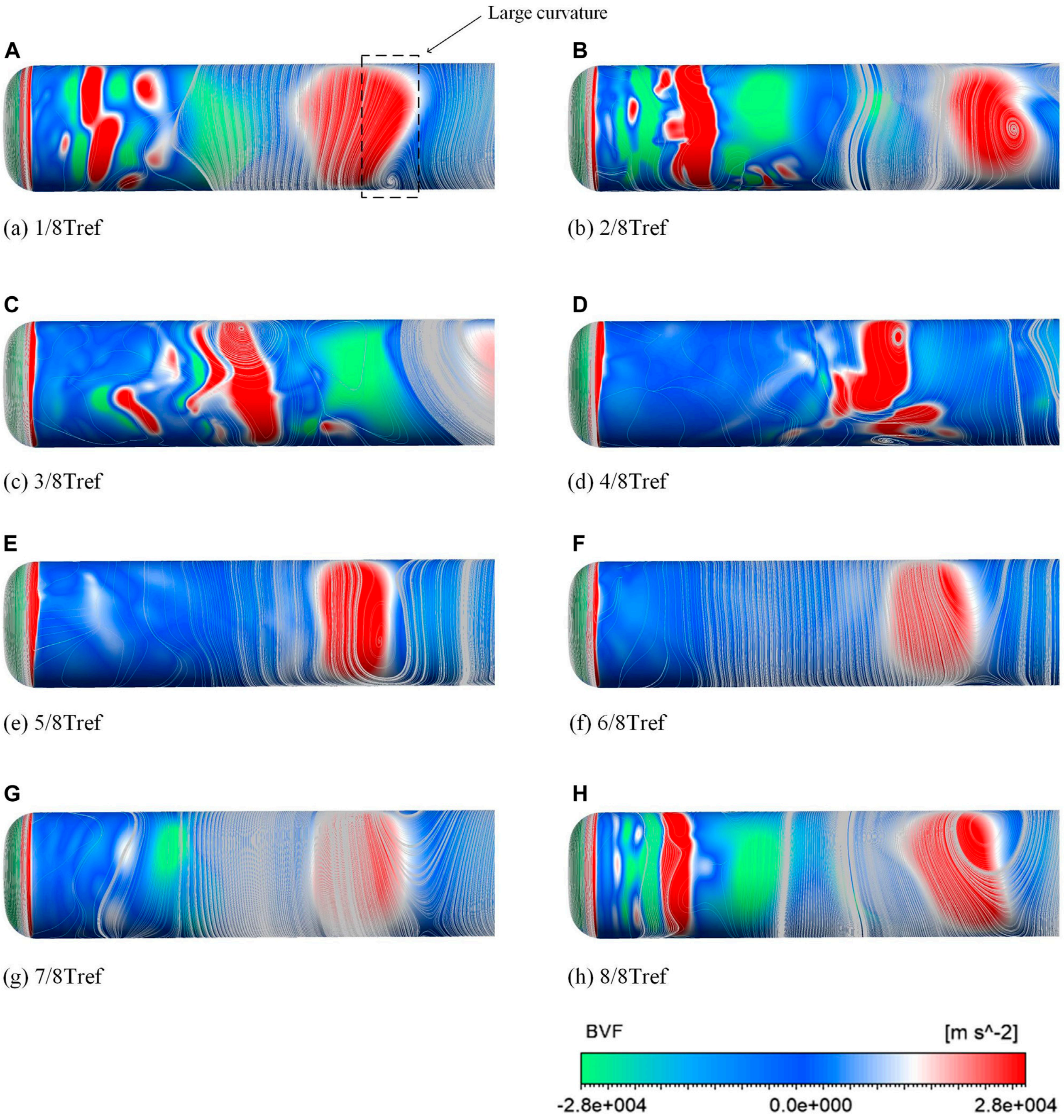

(a) 1/8Tref (b) 2/8Tref (c) 3/8Tref (d) 4/8Tref (e) 5/8Tref (f) 6/8Tref (g) 7/8Tref (h) 8/8Tref

FIGURE 9
Vorticity line and BVF on the ogive surface.

According to the above, the flow state on the ogive surface is influenced by the development of the cavity. Combined with the changes of lateral force and resistance operating conditions in Figures 11, 12, it can be seen that under a series of conditions, the lateral force changes less with the increase of temperature. In contrast, the resistance increases with the rise in temperature. Also, the asymmetry of cavity development can lead to oscillations in the variation of lateral forces and drags. Therefore it is necessary to analyze the changes in lateral force and drags in connection with the cavitation shedding cycle.

The change in vorticity force is explained by selecting a cycle in the 322 E condition. In Figure 13A, the drag decreases and increases as the cavity develops. The reason for this change can be explained as follows: at the beginning of the stage, the falling cavity leads to a reduction in resistance. With the progress of cavitation, the falling cavity gradually collapses, and the generation of the attached cavity leads to the increase of resistance. In the later

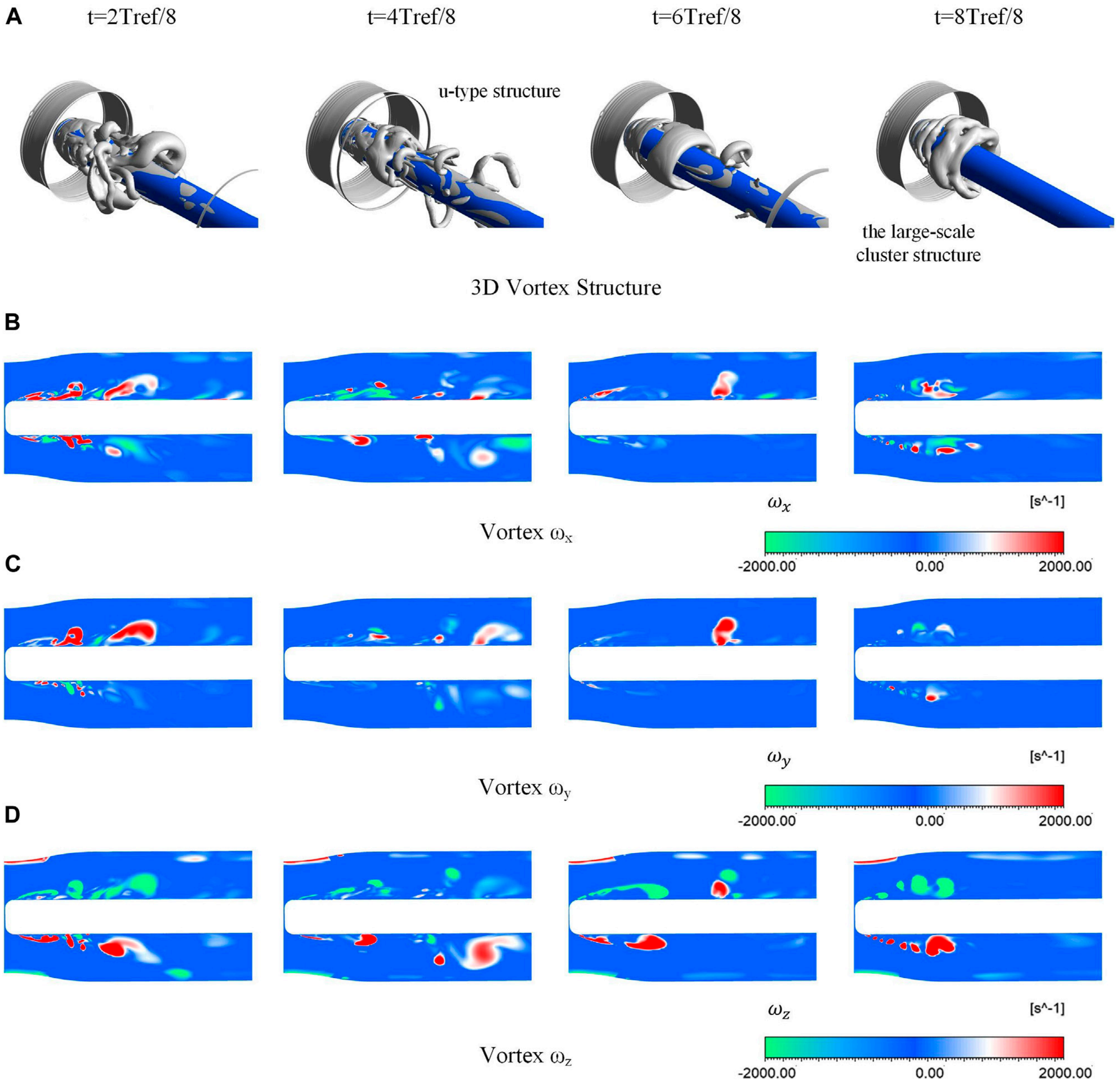

FIGURE 10
Distribution of vorticity.

stages of cavitation, the attached cavity begins to shed, and the drag decreases again as many negative drag elements are generated. The lateral forces, on the other hand, fluctuate in the development of the cavity due to the asymmetrical characteristics of the growth and shedding of the cavity. In the next section, the cavity development is divided into eight moments according to Figure 13 to explain the detailed effects of cavity development on drag and lateral forces.

Figures 14, 15 show the vorticity forces and the corresponding BVF distributions at eight moments in a typical cycle. In Figure 14, the positive lateral force elements point to the *y* direction, and the negative lateral force elements point to the reverse *y* direction, which means that the cavitation makes the force elements point out of the surface around the cavity. As the cavity and vapor cloud distributions are unsymmetrical, the numbers of positive and negative lateral force elements are different, which makes the lateral force fluctuate. As seen from Figures 14G, H, the negative lateral force elements are more than the positive lateral force elements, which makes the total lateral force negative.

In Figure 15, negative resistance elements are generated in front of the open cavity and around the additional cavity. In contrast, positive resistance elements are concentrated behind the cavity pointing in the *y* direction. Cavity development can be divided into three stages: cavity falling off stage, different cavity generation stage and additional cavity falling off stage. The cavity

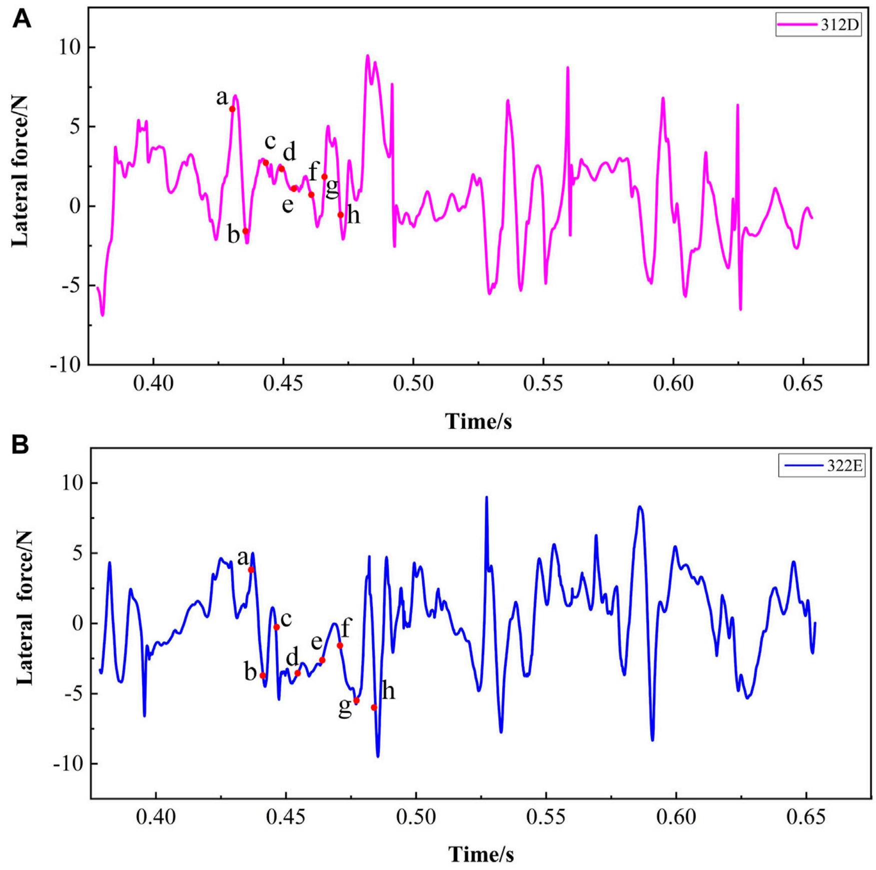

FIGURE 11
Periodic variation of ogive surface lateral force under two conditions.

falling off stage is shown in Figures 15A, B, in which the cavity falls off. The negative resistance element appears in front of the falling off cavity, which is significantly larger than the positive resistance element, so the resistance decreases at this stage. Then, the shed cavity collapses and the attached cavity grows (Figure 15C). At the back of Figure 15C, the negative resistance element decreases with the collapse of the falling cavity. In contrast, around the attached cavity, the positive resistance element gradually increases, and the resistance begins to increase. Then, in Figures 15D–F, the negative resistance elements decrease with the development of the other cavity, and more positive resistance elements appear at the end of the additional cavity. It can be seen that the positive resistance elements are more than the negative resistance elements, so the resistance increases at this stage. In Figure 15C, since there is still a falling cavity, the resistance rises slowly at this stage. In Figure 15F, when only an attached cavity exists, the resistance increases rapidly. In Figure 15H, the attached cavity begins to fall off, producing negative resistance elements. At this time, the negative resistance elements are more than the positive ones, and the resistance starts to decrease.

In summary, the lateral force element points out of the surface around the cavity under the effect of cavitation. As the distribution of cavities and vapor clouds is asymmetrical, the amount of positive and negative lateral forces are different, which leads to fluctuations in lateral forces. The resistance decreases first and then increases with the development of cavitation. Negative resistance units are distributed in front of the open cavity and around the additional cavity, while positive resistance units are distributed behind the cavity.

4 Summary

The thermal cavitation model based on the ZGB model is used to simulate the thermal cavitation flow of liquid nitrogen on the oval surface. The BVF is used to study the flow separation under the influence of cavitation, and force element analysis is used to reveal the force evolution mechanism caused by cavitation shedding. Through cavitation flow and mechanical analysis, the internal flow mechanism of fluid machinery can be revealed, which can provide theoretical guidance for the design of fluid machinery. The main research results are summarized as follows.

(1) The reentrant jet generated by cavity growth will enter the cavity and collide with the incident flow to produce flow separation. At this time, the reentrant jet in the cavity is the main reason for flow separation. However, a stable cavity will inhibit the change

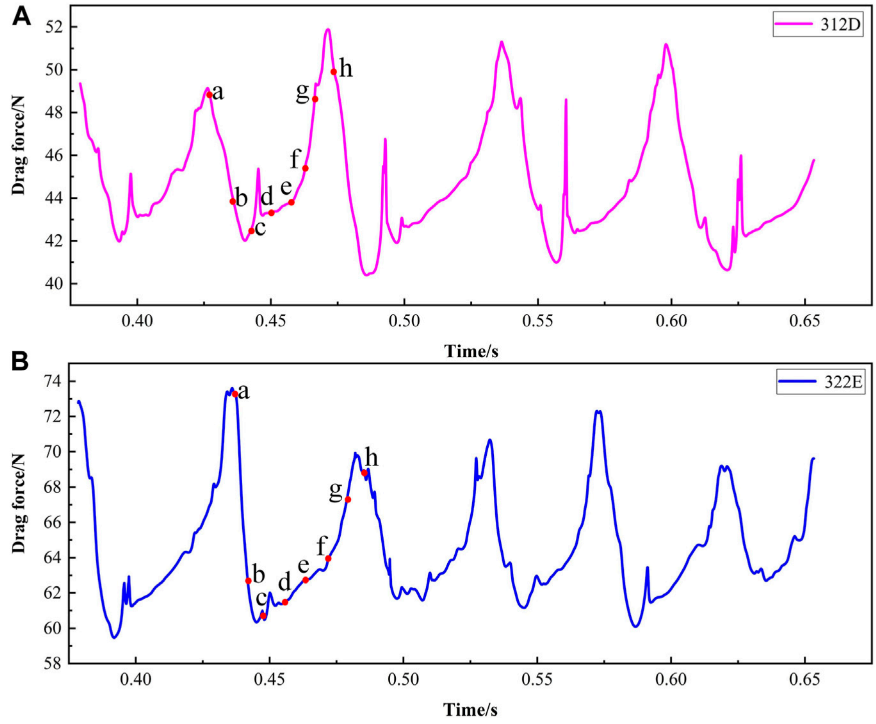

FIGURE 12
Periodic variation in ogive surface drag under the two conditions.

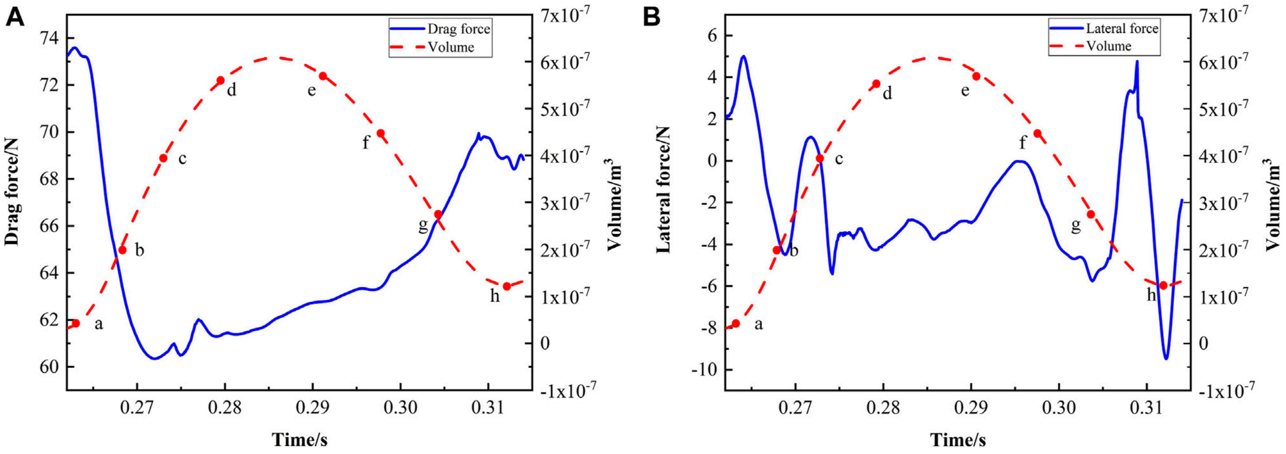

FIGURE 13
Lateral force-drag variation in cavity development and streamlines in the flow field.

of flow state, and the change of flow state in the cavity will accelerate the cavity falling off.

(2) The re-attachment usually occurs in the region where BVF decreases rapidly from positive values to negative values, while flow separation usually occurs where there are negative values. And in vorticity force studies, it has been shown that the distribution of drag usually shows the same trends as the value of BVF.

(3) The force element method can provide the distribution of force elements in the process of cavitation development, and can well reveal the evolution mechanism of force in cavitation flow. For lateral forces, the existence of cavities makes lift force elements point out of the surface. The random cavity shedding induced by the turbulence makes the distribution of the vapor cloud asymmetrical, which leads to fluctuations in the lateral force.

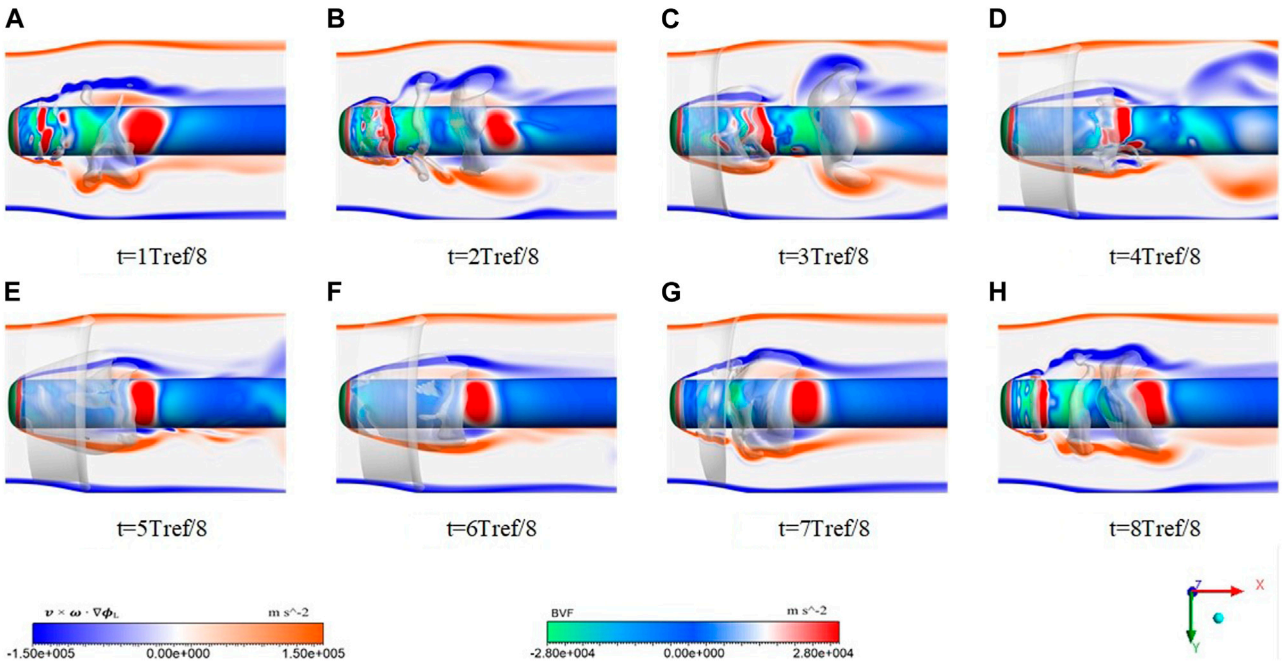

FIGURE 14
Evolution of lateral force element and BVF in a cavitation shedding cycle.

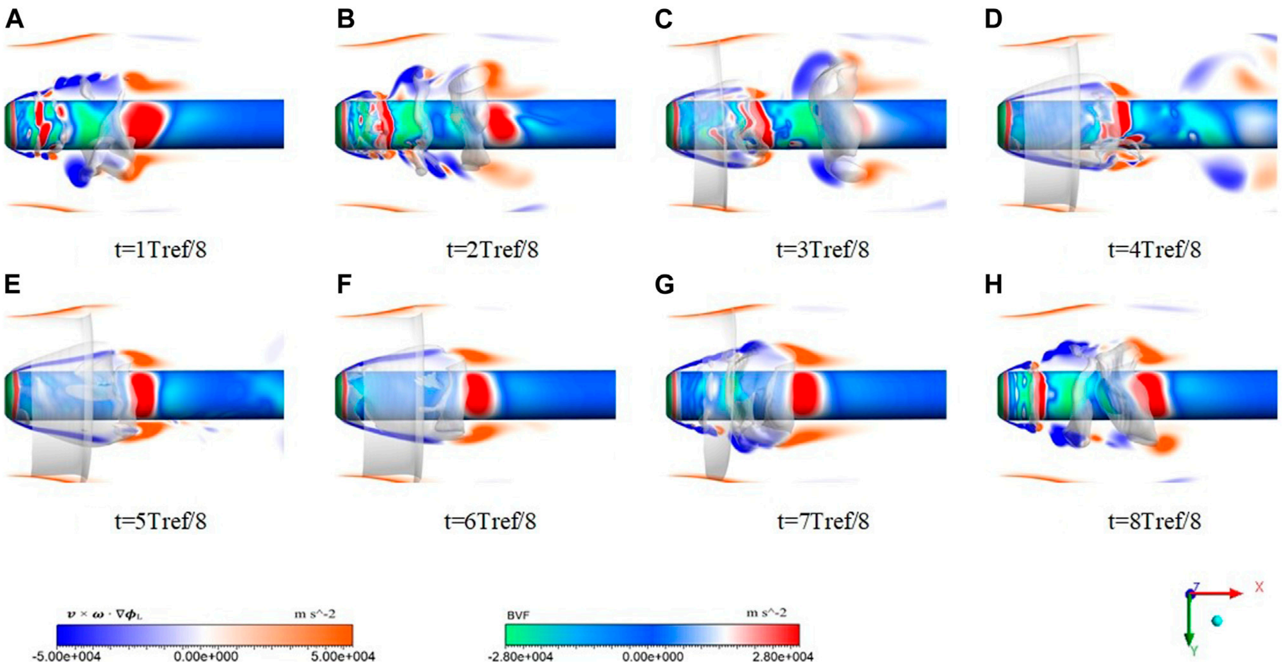

FIGURE 15
Evolution of drag force element and BVF in a cavitation shedding cycle.

(4) In the process of cavitation development, negative resistance units are produced at the front of the cavity, while positive resistance units are made at the end of the cavity. In the early stage of cavitation, the falling off of the attached cavity and the appearance of a large number of negative resistance elements lead to reduced resistance. With the gradual formation of the attached cavity and the gradual increase of positive resistance elements, the resistance will increase.

Data availability statement

The raw data supporting the conclusion of this article will be made available by the authors, without undue reservation.

Author contributions

YL proposed the overall idea and experimental framework of this study, JZ, LS, and LA designed and implemented specific implementation methods of the research, the other authors carried out the specific steps of numerical simulation research and reviewed the results.

Funding

The authors are grateful to the support by the National Natural Science Foundation of China (Grant Nos. 52006197, 52076196), the Natural Science Foundation of Zhejiang Province (Grant Nos. LGG21E060002, LR20E090001), the Key Research and Development Program of Zhejiang Province (Grant Nos. 2021C05006, 2021C01156).

Conflict of interest

Authors YL, JZ, LS, and LA was employed by the company Hangzhou New-Asia Cryogenic Science and Technology Co., Ltd.

The remaining authors declare that the research was conducted in the absence of any commercial or financial relationships that could be construed as a potential conflict of interest.

Publisher's note

References

Abderrezzak, B., and Huang, Y. (2016). A contribution to the understanding of cavitation effects on droplet formation through a quantitative observation on breakup of liquid jet. *Int. J. Hydrogen Energy* 41 (35), 15821–15828. doi:10.1016/j.ijhydene.2016.04.209

Cervone, A., Bramanti, C., Rapposelli, E., and d'Agostino, L. (2006). Thermal cavitation experiments on a NACA 0015 hydrofoil. *J. Fluids Eng.* 128, 326–331. doi:10.1115/1.2169808

Chen, J., Lin, F. Y., and Zou, J. (2017). Experimental investigation of vortex-ring cavitation. *J. Zhejiang University-SCIENCE A* 18 (7), 545–552. doi:10.1631/jzus.a1600537

Chen, T. R., Chen, H., Liang, W. D., Huang, B., and Xiang, L. (2019a). Experimental investigation of liquid nitrogen cavitating flows in converging-diverging nozzle with special emphasis on thermal transition. *Int. J. Heat Mass Transf.* 132, 618–630. doi:10.1016/j.ijheatmasstransfer.2018.11.157

Chen, T. R., Chen, H., Liu, W., Huang, B., and Wang, G. (2019b). Unsteady characteristics of liquid nitrogen cavitating flows in different thermal cavitation mode. *Appl. Therm. Eng.* 156, 63–76. doi:10.1016/j.applthermaleng.2019.04.024

Chen, T. R., Huang, B., Wang, G., Zhang, H., and Wang, Y. (2017). Numerical investigation of thermo-sensitive cavitating flows in a wide range of free-stream temperatures and velocities in fluoroketone. *Int. J. Heat Mass Transf.* 112, 125–136. doi:10.1016/j.ijheatmasstransfer.2017.04.023

Chen, Z. D., Yang, S. D., Li, X. J., Li, Y., and Li, L. (2023). Investigation on leakage vortex cavitation and corresponding enstrophy characteristics in a liquid nitrogen inducer. *Cryogenics* 129, 103606. doi:10.1016/j.cryogenics.2022.103606

De Giorgi, M. G., Fontanarosa, D., and Ficarella, A. (2019). Characterization of unsteady cavitating flow regimes around a hydrofoil, based on an extended Schnerr–Sauer model coupled with a nucleation model. *Int. J. Multiph. Flow* 115, 158–180. doi:10.1016/j.ijmultiphaseflow.2019.03.025

De Giorgi, M. G., Ficarella, A., and Fontanarosa, D. (2020). Numerical investigation of nonisothermal cavitating flows on hydrofoils by means of an extended schnerr–sauer model coupled with a nucleation model. *ASME. J. Eng. Gas. Turbines Power* 142 (4), 041003. doi:10.1115/1.4044352

Ehara, Y., Kitamura, S., Tsuru, W., Watanabe, S., and Tsuda, S. I. (2019). Unsteady forces and moments acting on a cantilevered rectangular hydrofoil with tip clearance in cavitating conditions. *IOP Conf. Ser. Earth Environ. Sci.* 240 (6), 062054. doi:10.1088/1755-1315/240/6/062054

Franc, J. P., Janson, E., and Morel, P. (2001). Visualizations of leading edge cavitation in an Inducer at different temperatures. Fourth International Symposium on Cavitation. Canada: 124-130. Available at: https://resolver.caltech.edu/CAV2001:sessionB7.002.

Gopalan, S., and Katz, J. (2000). Flow structure and modeling issues in the closure region of attached cavitation. *Phys. fluids* 12 (4), 895–911. doi:10.1063/1.870344

Holl, J. W., Billet, M. L., and Weir, D. S. (1975). Thermodynamic effects on developed cavitation. *J. Fluids Eng.* 97 (4), 507–513. doi:10.1115/1.3448095

Hord, J. (1973). *Cavitation in liquid cryogens. 3: Ogives*. Washington, D. C: National Aeronautics And Space Administration.

Hsu, L. C., and Chen, C. L. (2020). The drag and lift characteristics of flow around a circular cylinder with a slit. *Eur. J. Mech. - B/Fluids* 82, 135–155. doi:10.1016/j.euromechflu.2020.02.009

Jafari, G. I., and Rad, M. (2009). Experimental analysis of cavitation effects on drag force and back pressure of circular cylinder with free turbulence. *Sci. Iran.* 16 (4), 221–225.

Joseph, D. D. (1995). Cavitation in a flowing liquid. *Phys. Rev. E* 51 (3), R1649–R1650. doi:10.1103/PhysRevE.51.R1649

Keller, A. P. (2001). Cavitation scale effects - empirically found relations and the correlation of cavitation number and hydrodynamic coefficients. Fourth International Symposium on Cavitation. Available at: https://resolver.caltech.edu/CAV2001:lecture.001.

Kelly, S., and Segal, C. (2015). Characteristics of thermal cavitation on a two-dimensional hydrofoil. *J. Propuls. Power* 29 (2), 410–416. doi:10.2514/1.B34707

Kikuta, K., Yoshida, Y., Watanabe, M., Hashimoto, T., Nagaura, K., and Ohira, K. (2008). Thermodynamic effect on cavitation performances and cavitation instabilities in an inducer. *J. Fluids Eng.* 130 (11), 111302. doi:10.1115/1.2969426

Kumar, D., Sourav, K., Sen, S., and Yadav, P. K. (2018). Steady separation of flow from an inclined square cylinder with sharp and rounded base. *Comput. Fluids* 171, 29–40. doi:10.1016/j.compfluid.2018.05.020

Lee, J. J., Hsieh, C. T., Chang, C. C., and Chu, C. C. (2012). Vorticity forces on an impulsively started finite plate. *J. Fluid Mech.* 694, 464–492. doi:10.1017/jfm.2011.563

Li, D., Liu, S., Wei, Y., Ren, T., and Tang, Y. (2018). A turbulent two-phase model for predicting cavitating flow based on homogenous nucleation theory. *Int. Commun. Heat Mass Transf.* 97, 17–29. doi:10.1016/j.icheatmasstransfer.2018.06.001

Li, L. M., Wang, Z. D., Li, X. J., and Zhu, Z. (2021). Multiscale modeling of tip-leakage cavitating flows by a combined volume of fluid and discrete bubble model. *Phys. Fluids* 33, 062104. doi:10.1063/5.0054795

Li, W. G., Yu, Z. B., and Kadam, S. (2023). An improved cavitation model with thermodynamic effect and multiple cavitation regimes. *Int. J. Heat Mass Transf.* 205, 123854. doi:10.1016/j.ijheatmasstransfer.2023.123854

Li, X. J., Liu, Y. Y., Zhu, Z. C., Lin, P., and Li, P. (2021). Boundary vorticity analysis and shedding dynamics of transient cavitation flow around a twisted hydrofoil. *J. Fluids Eng.* 143 (7), 071501. doi:10.1115/1.4050135

Lighthill, M. J. (1963). Introduction boundary layer theory. *Laminar Bound. Layers* 46, 113.

Liu, Y. Y., Li, X. J., Lin, Z., Li, L., and Zhu, Z. (2021). Numerical analysis of thermo-sensitive cavitating flows with special emphasises on flow separation and enstrophy conversion. *Int. Commun. Heat Mass Transf.* 125, 105336. doi:10.1016/j.icheatmasstransfer.2021.105336

Liu, Y. Y., Li, X. J., Wang, W. J., Li, L., and Huo, Y. (2020). Numerical investigation on the evolution of forces and energy features in thermo-sensitive cavitating flow. *Eur. J. Mech. - B/Fluids* 84, 233–249. doi:10.1016/j.euromechflu.2020.06.011

Long, X. P., Liu, Q., Ji, B., and Lu, Y. (2017). Numerical investigation of two typical cavitation shedding dynamics flow in liquid hydrogen with thermodynamic effects. *Int. J. Heat Mass Transf.* 109, 879–893. doi:10.1016/j.ijheatmasstransfer.2017.02.063

Merouani, S., Hamdaoui, O., Rezgui, Y., and Guemini, M. (2016). Computational engineering study of hydrogen production via ultrasonic cavitation in water. *Int. J. Hydrogen Energy* 41 (2), 832–844. doi:10.1016/j.ijhydene.2015.11.058

Niiyama, K., Yoshida, Y., Hasegawa, S., Watanabe, M., and Oike, M. (2012). “Experimental investigation of thermodynamic effect on cavitation in liquid nitrogen,” in Proceeding of the Eighth International Symposium on Cavitation, Singapore, 153–157.

Ohira, K., Nakayama, T., and Nagai, T. (2012). Cavitation flow instability of subcooled liquid nitrogen in converging-diverging nozzles. *Cryogenics* 51 (1), 35–44. doi:10.1016/j.cryogenics.2011.11.001

Šarc, A., Stepinik-Perdih, T., Petkovek, M., and Dular, M. (2017). The issue of cavitation number value in studies of water treatment by hydrodynamic cavitation. *Ultrason. Sonochemistry* 34, 51–59. doi:10.1016/j.ultsonch.2016.05.020

Seif, M., Asnaghi, A., and Jahanbakhsh, E. (2009). Drag force on a flat plate in cavitating flows. *Pol. Marit. Res.* 16 (3), 18–25. doi:10.2478/v10012-008-0028-2

Shen, T. J., Li, X. J., Li, L. M., Wang, Z., and Liu, Y. (2020). Evaluation of vorticity forces in thermo-sensitive cavitating flow considering the local compressibility. *Int. Commun. Heat Mass Transf.* 120, 105008. doi:10.1016/j.icheatmasstransfer.2020.105008

Shi, S. G., and Wang, G. Y. (2020). Numerical analysis of factors influencing thermal effects generated by cavitation flow of cryogenic fluids. *Mod. Phys. Lett. B* 34 (17), 2050184. doi:10.1142/S0217984920501845

Smirnov, N. N., Betelin, V. B., Shagaliev, R. M., Nikitin, V., Belyakov, I., Deryuguin, Y., et al. (2014). Hydrogen fuel rocket engines simulation using LOGOS code. *Int. J. Hydrogen Energy* 39 (20), 10748–10756. doi:10.1016/j.ijhydene.2014.04.150

Sun, T. Z., Wei, Y. J., Zou, L., Jiang, Y., Xu, C., and Zong, Z. (2019). Numerical investigation on the unsteady cavitation shedding dynamics over a hydrofoil in thermo-sensitive fluid. *Int. J. Multiph. Flow* 111, 82–100. doi:10.1016/j.ijmultiphaseflow.2018.11.014

Wang, X. T., Ning, Z., and Lü, M. (2019). Linear temporal instability analysis of a non-Newtonian liquid jet containing cavitation bubbles. *Eur. J. Mech. - B/Fluids* 77, 118–124. doi:10.1016/j.euromechflu.2019.04.014

Xu, B., Yang, K., Chen, Q. X., and Wang, H. (2022). Influence of thermal effects on the cavitation of orifices in nuclear power plants. *Nucl. Eng. Des.* 398 (2022), 111942. ISSN 0029-5493. doi:10.1016/j.nucengdes.2022.111942

Zhang, B. C., Li, Q. L., Wang, Y., Zhang, J. q., Song, J., and Zhuang, F. c. (2020). Experimental investigation of nitrogen flow boiling heat transfer in a single mini-channel. *J. Zhejiang University-SCIENCE A* 21 (2), 147–166. doi:10.1631/jzus.a1900468

Zhang, K., Hayostek, S., Amitay, M., He, W., and Theofilis, V. (2020). On the formation of three-dimensional separated flows over wings under tip effects. *J. Fluid Mech.* 895, A9. doi:10.1017/jfm.2020.248

Zhang, S. F., Li, X. J., Hu, B., Liu, Y., and Zhu, Z. (2019). Numerical investigation of attached cavitating flow in thermo-sensitive fluid with special emphasis on thermal effect and shedding dynamics. *Int. J. Hydrogen Energy* 44 (5), 3170–3184. doi:10.1016/j.ijhydene.2018.11.224

Zhang, S. F., Li, X. J., and Zhu, Z. C. (2018). Numerical simulation of cryogenic cavitating flow by an extended transport-based cavitation model with thermal effects. *Cryogenics* 92, 98–104. doi:10.1016/j.cryogenics.2018.04.008

Zhao, Y., Wang, G., Jiang, Y., and Huang, B. (2016). Numerical analysis of developed tip leakage cavitating flows using a new transport-based model. *Int. Commun. Heat Mass Transf.* 78, 39–47. doi:10.1016/j.icheatmasstransfer.2016.08.007

Zhu, J. K., Chen, Y., Zhao, D. F., and Zhang, X. (2015a). Extension of the Schnerr–Sauer model for cryogenic cavitation. *Eur. J. Mech. B/fluids* 52, 1–10. doi:10.1016/j.euromechflu.2015.01.008

Zhu, J. K., Zhao, D. F., Xu, L., and Zhang, X. (2015b). Interactions of vortices, thermal effects and cavitation in liquid hydrogen cavitating flows. *Int. J. Hydrogen Energy* 41 (1), 614–631. doi:10.1016/j.ijhydene.2015.10.042

Nomenclature

C heat capacity
c velocity of sound
C_p pressure coefficient
h_b convection heat transfer coefficient
k turbulent kinetic energy
K thermal conductivity
L latent heat
M mach number
p pressure
p_v saturated vapor pressure
R_B single spherical bubble radius
R constant
T temperature
V volume
u velocity
x subscripts
ρ density
μ dynamic viscosity
σ cavitation number
α volume fraction
ε turbulent eddy dissipation
λ thermal conductivity
ΔT temperature drop
$\dot{m}^+$ condensation rate
$\dot{m}^-$ evaporation rate

Subscripts

c empirical coefficient
$i,\ j,k$ directions of the cartesian coordinates
l liquid phase
tur turbulence
v vapor phase
∞ reference

frontiers | Frontiers in Energy Research

TYPE Original Research
PUBLISHED 17 March 2023
DOI 10.3389/fenrg.2023.1170123

OPEN ACCESS

EDITED BY
Leilei Ji,
Jiangsu University, China

REVIEWED BY
Xiangyuan Zhu,
shandongjianzhudaxue, China
Fei Tian,
Jiangsu University, China

*CORRESPONDENCE
Yajing He,
✉ 15529038421@163.com

SPECIALTY SECTION
This article was submitted to Process and Energy Systems Engineering, a section of the journal Frontiers in Energy Research

RECEIVED 20 February 2023
ACCEPTED 06 March 2023
PUBLISHED 17 March 2023

CITATION
Cheng K, Jiang T, He Y and Wang X (2023), Volute clapboard and clearance of wear-ring effect on the operation characteristics of canned motor pump. *Front. Energy Res.* 11:1170123.
doi: 10.3389/fenrg.2023.1170123

Volute clapboard and clearance of wear-ring effect on the operation characteristics of canned motor pump

Ke Cheng[1], Ting Jiang[2], Yajing He[3]* and Xiulan Wang[4]

[1]Sinopec Luoyang Company, Luoyang, China, [2]Innovation Institute of Shaanxi Aerospace Power High Tech Co.,LTD., Xi'an, China, [3]Guangdong University of Petrochemical Technology, Maoming, China, [4]Hefei Huasheng Pumps & Valves CO., LTD., Hefei, China

Canned Motor Pump (CMP) is widely used in petroleum, chemical, electric power, aerospace engineering, and military manufacturing industries due to its good sealing performance. In the structure of canned motor pump, the rotor of the motor and the impeller of the pump are fixed on the same shaft. Therefore, balancing the axial force and the radical force of the rotor is a key task for its reliable operation. The numerical simulation study of CMP is carried out in this paper, aiming to improve the pump efficiency and balance the axial force and radial force. The internal flow and rotor force characteristics of CMP under different radial clearances of front or back wear-rings and different volute partitions are studied. The results show that with the increase of wear-ring gap, external performances decline, and the front wear-ring gap contributed the largest influence. Under the working conditions of $0.6Q_{BEP}$ and $0.8Q_{BEP}$, front wear-rings contributed the largest influence to axial force, and the degree of influence decreases with the rate of flow increase. Radial clearances of front or back wear-rings have less impact on the radial force of the impeller. Adding clapboard for volute has a greater impact on the value and direction of radial force, and it can promote the balance of radial force. However, the effectiveness value will decrease. The research in this paper can provide theoretical basis and reference for performance prediction and hydraulic optimization of CMP.

KEYWORDS

canned motor pump, numerical simulation, radial clearance of wearrings, rotor stress, steady calculation

1 Introduction

As general machinery, centrifugal pumps are widely used in aerospace, navigation, petrochemical, refrigeration, medical, environmental protection, agricultural irrigation and other fields (Rzentkowski and Zbroja, 2000; Cdina, 2003; Choi et al., 2003; Alfayez et al., 2005). However, when centrifugal pumps are used for medium transfer or pressurization, due to the characteristics of the medium, such as flammable, explosive, volatile, corrosive, and highly toxic, its tightness and reliability often failed to reach the standard. The canned motor pump does not have the shaft sealing device of the traditional centrifugal pump, which makes it leak-free. It is suitable for transporting valuable or radioactive media. Canned motor pump is widely used for medium transfer as its advantages of no leakage, small size and high reliability (Author Anonymous, 1996; Zhu et al., 2020). In the design, manufacture and operation of canned motor pump, axial and radial forces are one of important factors that must be considered (Zhou and Wang, 2016; Arndt et al., 1989; ye Jin et al., 2022; Qianyan et al., 2018). If axial and radial forces are not reduced, the rotor shaft will be deflected by alternating stresses during operation. So that the bearing rotor shielding sleeve and even impeller motor cause serious damage (Launder and Spalding, 1974; Author Anonymous, 2019; Jin et al., 2022a). At the same time, the canned motor pump is not easy to disassemble and later maintenance is difficult. Therefore, in the early design, the accuracy of the shaft and radial forces calculation will directly affect the safety and reliability of the unit (Wang et al., 2001; Zhu and Kamemoto, 2005).

At present, the research on canned motor pump mainly includes theoretical analysis, experimental study, empirical analysis and numerical study (Arndt et al., 1990; Dawes, 1994; Qin and Tsukamoto, 1997; Guan et al., 2020a; Guan et al., 2020b; Hongyu et al., 2021; Song et al., 2021). Cabrera et al. (2005) experimentally measured the magnitude of the radial force on the impeller of canned motor pump. And also carried out theoretical research on the force characteristics at both ends of the canned motor pump bearing by means of calculation simulation software. Gertzos et al. (2008) used the Bingham fluid model in the FLUENT software to perform a three-dimensional numerical calculation of the canned motor pump bearing ends, analyzed the influence of different bearing width-diameter ratios on the pressure distribution of the liquid film and studied the load carrying capacity and cooling performance of the motor bearing end. Friedrich et al. (Benra et al., 2006) carried out bi-directional fluid-structure coupling calculation on the vibration of a single canned motor pump blade, and obtained the influence of static pressure distribution on the pump blade under fluid transient state. The calculated results were compared with the experimental results, which proved that the bi-directional fluid-structure coupling calculation results were more consistent with the experimental values. Fortes et al. (Hirsch, 1988; Qu et al., 2010) calculated the transient pressure fluctuation in canned motor pump by using the periodic boundary condition of the overlapping network and phase lag. Koji Ikuta et al. (Jameson et al., 1981; Koji, 1991; Rasmussen et al., 2005) of Japan also proposed the application of contactless permanent magnet shielded pump in non-industrial fields. The research on the unsteady flow field characteristics of the impeller end of the canned pump and the force characteristics of the rotor at medium and high specific speeds is still relatively small at home and abroad, and some calculation formulas are quite different, which makes it difficult to follow. At present, the research papers on canned motor pump in international journals mainly focus on bearing cooling circuit, fluid-structure coupling calculation, *etc.* At the same time, a new canned motor pump with special structure and special purpose is also studied.

The research on the unsteady flow field at the impeller end and the rotor force characteristics of canned motor pump at medium and high specific speed is still less at home and abroad, and some calculation formulas are quite different, which makes it difficult for people to adapt to it (Jin et al., 2022b). Therefore, it is not only extremely important to study the accurate calculation and balance method of axial and radial forces of canned motor pump at medium and high specific speed, but also of great practical significance to the safety production of enterprises.

During the operation of canned motor pump, the internal flow is a complex three-dimensional unsteady turbulent flow. Up to now, the understanding of the fluid flow characteristics in the rotor components of the canned motor pump at medium and high specific speeds is not clear enough in engineering, especially the research on the leakage flow characteristics under the clearance between the front and rear rings of the canned motor pump is lacking. This paper takes the analysis of the details of the clearance flow and studies the influence of the clearance and the volute diaphragm on the external characteristics, internal flow field, and rotor force of the canned motor pump.

2 Numerical model and method

2.1 The governing equations

In this study, the transport medium of the canned motor pump is water, without considering compressibility, and the influence of gravity is weak. In the inertial coordinate system, the Naiver-Stokes equation can be written as:

$$\frac{\partial \rho}{\partial t} + \frac{\partial}{\partial x_j}\left(\rho u_j\right) = 0 \qquad (2-1)$$

$$\frac{\partial}{\partial t}\left(\rho u_i\right) + \frac{\partial}{\partial x_j}\left(\rho u_i u_j\right) = -\frac{\partial p}{\partial x_i} - \frac{\partial \tau_{ij}}{\partial x_j} + \rho f_i \qquad (2-2)$$

where the τ_{ij} can be expressed as:

$$\tau_{ij} = -\frac{2}{3}\mu\delta_{ij}\frac{\partial u_l}{\partial x_l} - \mu\left(\frac{\partial u_i}{\partial x_j} + \frac{\partial u_j}{\partial x_i}\right) \qquad (2-3)$$

For the canned motor pump in this paper, the internal flow of its impeller is three-dimensional viscous incompressible unsteady flow. The continuity equation and the momentum equation are shown as follows:

$$\frac{\partial \rho}{\partial t} + \nabla \cdot \rho \vec{u} = 0 \qquad (2-4)$$

$$\frac{\partial u_i}{\partial t} + u_j \frac{\partial u_i}{\partial x_j} = -\frac{1}{\rho}\frac{\partial p}{\partial x_j} + \nu \frac{\partial^2 u_i}{\partial x_i \partial x_j} + f_i \qquad (2-5)$$

$$f_i = 2\bar{\omega} \times \bar{\omega} + \bar{\omega} \times \bar{\omega} \times r \qquad (2-6)$$

Where: u_i is instantaneous velocity, p is the instantaneous pressure, ν is the viscosity coefficient of fluid molecular motion. When the impeller selects the rotating non-inertial coordinate system to describe the relative motion, u_j is the relative velocity, f_i is the volume force, indicating the influence of Coriolis force and centrifugal force, respectively.

There are significant differences between temporal and spatial characteristic scales in turbulent flow, and there are still many difficulties in solving the N-S equations directly to study the actual flow problems. Moreover, in engineering projects, the average flow on the time scale of turbulent flow is often considered, and in current engineering applications, the Reynolds time-averaged equation is usually used to simulate the canned motor pump. The Reynolds-averaged equation is expressed as follows:

$$\frac{\partial u_i}{\partial t} + u_j \frac{\partial u_i}{\partial x_j} = f_i - \frac{1}{\rho}\frac{\partial p}{\partial x_i} + \frac{\partial}{\partial x_i}\left(\nu \frac{\partial u_i}{\partial x_i} - \overline{u_i^{`} u_j^{’}}\right) \qquad (2-7)$$

TABLE 1 Geometric dimensions of the CMP.

	Unit	Value
Impeller outlet diameter	mm	249
Impeller inlet diameter	mm	175
Width of impeller outlet	mm	44
Hub diameter	mm	59
Base circle diameter of volute	mm	255
Number of blades		7
Volute tongue radius	mm	143/144.5
Balance hole diameter	mm	15
Balance hole center radius is located	mm	55
Number of balance holes		7

where the $u_i{}'$ and $u_j{}'$ are the velocity fluctuation.

Incompressible and without considering the volume force, Eq. 2-7 is changed into the following equation for steady calculation.

$$u_j \frac{\partial u_i}{\partial x_j} = f_i - \frac{1}{\rho}\frac{\partial p}{\partial x_i} + \frac{\partial}{\partial x_i}\left(v\frac{\partial u_i}{\partial x_i} - \overline{u_i`u_j`}\right) \quad (2-8)$$

Because of the characteristics of governing equations and turbulent flow in the canned motor pump, Reynolds time-averaged equations are used to analyze the internal flow field of canned motor pump.

2.2 Design schemes and computational grid

Model HP300-175E/62 (3) canned motor pump is taken as the research object in this study. The design parameters are as follows, the flow rate is Q = 300 m^3/h, the design head is H = 18.8m, the rotational speed is n = 1,500 r/min, and the specific is speed n_s = 175. The system pressure is less than 0.6MPa, and the temperature of the conveying medium is less than 40 °C. The main geometric dimensions are shown in Table 1.

The 3D model of the canned motor pump is established by the Pro/E software (As shown in Figure 1A). The calculation domain consists of impeller, volute, front pump chamber, back pump chamber, inlet pipe, and outlet pipe. The model is meshed hexahedrally using ICEM. The tetrahedral unstructured grid is used for the water body at the impeller and volute, and the impeller surface and the volute tongue are densified to ensure the accuracy of the computation. The grid of each flow passage area is shown in Figure 1. For the small-size gap flow in the fluid domain of the front and rear pump chambers, the hexahedral structured grid is

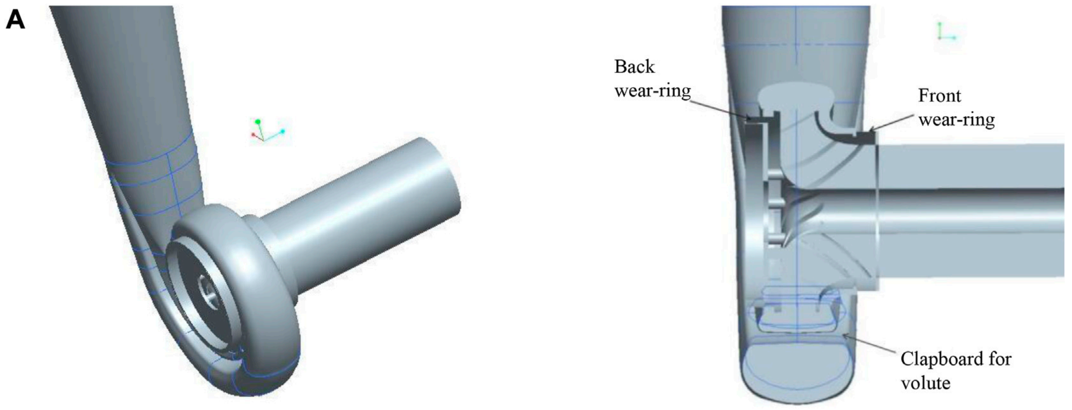

Three-dimensional computational model of the CMP

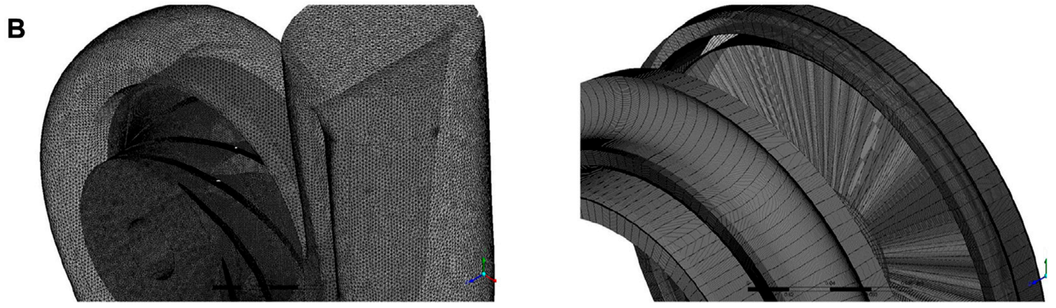

The grid of the impeller and volute

The grid of the front and rear cover plates

FIGURE 1
Three-dimensional computational model and grid of the CMP. **(A)** Three-dimensional computational model of the CMP. **(B)** The grid of the impeller and volute and the grid of the front and rear cover plates

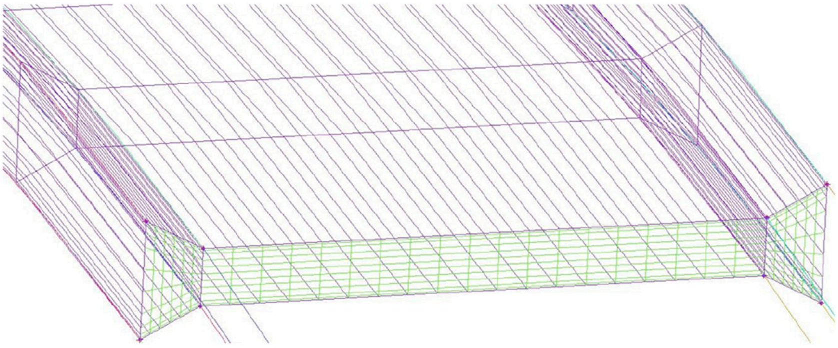

FIGURE 2
Mesh details at wear-ring.

TABLE 2 Grid independence analysis.

Parameter	Number of grids (10,000)				
	197	348	478	546	761
Efficiency η/%	80.21	78.45	77.65	77.72	77.63
Head H/m	20.42	19.53	18.96	18.87	19.03

used in this paper to ensure that there are more grid layers to meet the calculation requirements when the gap thickness is small, as shown in Figure 2.

The grid independence of the centrifugal pump is verified at a flow rate of 300 m^3/h. In theory, the more the number of grid, the smaller the error caused by the grid. In this paper, five different mesh sizes are selected to simulate the internal flow of the model pump, and the simulation results are shown in Table 2. It can be seen that when the number of grids is greater than 4.78 million, with the increase of the number of grids, the head and efficiency values fluctuate slightly, which can be considered to meet the grid-independent conditions. Considering the calculation cost, the number of grids selected in the future calculation is 4.78 million.

The front and back wear-rings have a great influence on the axial force balance of the canned motor pump, and the volute diaphragm has a great influence on the radial force balance of the canned motor pump. In order to study the influence of each component on the performance of the canned motor pump in detail, three groups of schemes are set up in this paper. The detailed information of each group is shown in Table 3. The b_1 and b_2 represent the unilateral radial clearance size of the front and rear rings respectively.

2.3 Computational setup and experimental validation

The ANSYS CFX software is chosen to simulate the internal flow of the canned motor pump. The *RNG k-ε* turbulence model has high accuracy in calculating high-speed flow and vortex flow, so it is used to analyze the internal flow field of the canned motor pump in this paper. The inlet boundary condition is set to total pressure inlet and medium turbulence (intensity = 5%). The mass flow outlet is adopted as the outlet boundary condition. All walls are set to have no-slip walls, and the standard wall function is used in the near-wall region. The convergence criterion is that the root means square is less than 10^{-5}. In order to verify the numerical simulation results, external characteristics experiments were conducted on the CMP model. The comparison curve of numerical simulation results and test results are shown in Figure 3. It can be seen from the curves, the trend of the two basically agrees, and the computation error is

TABLE 3 Simulation grouping and related experimental scheme.

	Prototype pump	Scheme 1	Scheme 2	Scheme 3
Front ring size (mm)	b_1 = 0.3	b_1 = 0.8	b_1 = 0.3	b_1 = 0.3, b_2 = 0.3; redesign the volute size (remove the volute diaphragm)
		b_1 = 1.3		
		b_1 = 1.8		
		b_1 = 2.3		
Back ring size (mm)	b_2 = 0.3	b_2 = 0.3	b_2 = 0.8	
			b_2 = 1.3	
			b_2 = 1.8	

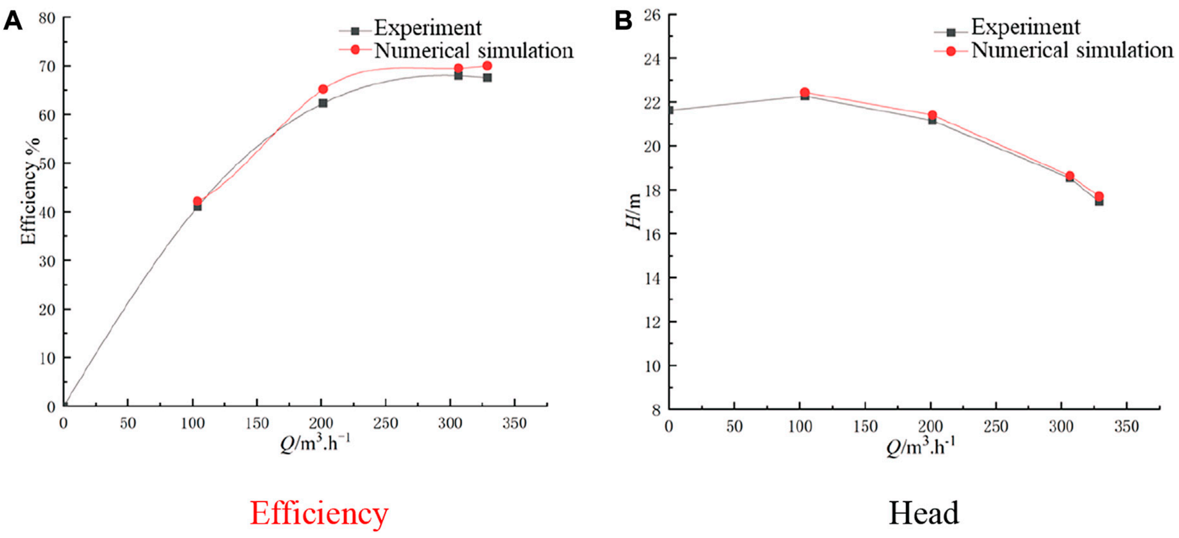

FIGURE 3
Comparison of hydraulic characteristics between numerical simulation and experiment. **(A)** Efficiency; **(B)** Head.

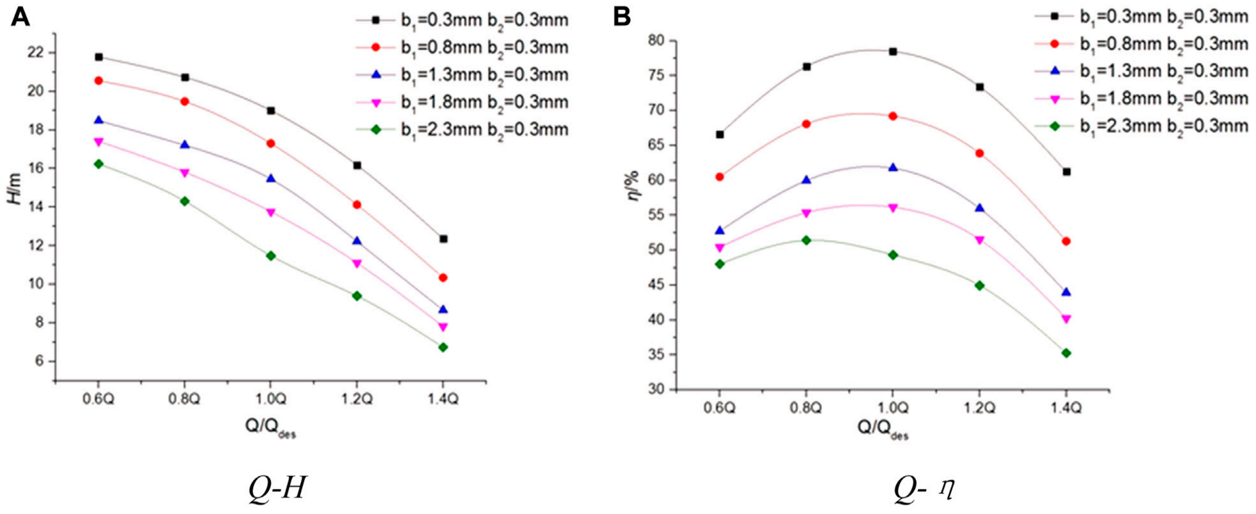

FIGURE 4
The performance curves of Scheme 1. **(A)** *Q-H*; **(B)** *Q-η*.

within 4%. This indicates that the accuracy of the numerical computation is high and meets the research requirements.

3 Results and discussion

3.1 Influence of wear-ring clearance on operating characteristics

3.1.1 Effects on the external characteristics

Figure 4 is the performance curve of the canned motor pump when the clearance of the front wear-ring is changed. It can be seen that the change of the clearance of the front wear-ring has a great influence on the external characteristics of the canned motor pump. The *Q-H* curve shows that the head decreases with the increase of flow. Under various working conditions, compared with the prototype pump head, with the increase of the clearance of the front wear-ring, the flow rate decreases regardless of its size. The *Q-η* curve shows that with the increase of flow rate, the efficiency value decreases first and then increases, and reaches the maximum value near the 1.0*Q* operating point. Compared with the efficiency of the prototype pump, the efficiency also decreases with the increase of the clearance of the front wear-ring under various working conditions. The efficiency decreases

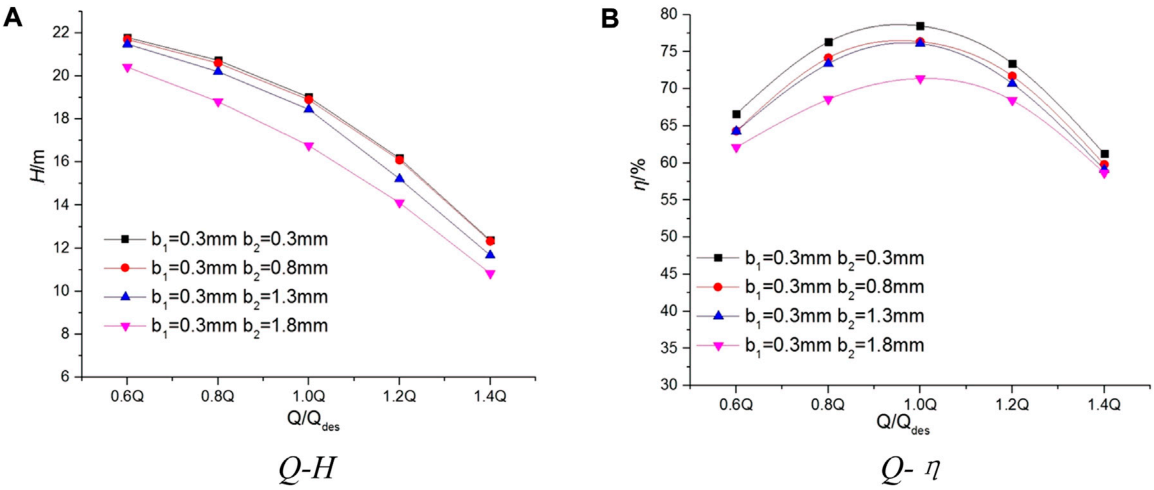

FIGURE 5
The performance curves of Scheme 2. **(A)** *Q-H*; **(B)** *Q-η*.

by 5% with the increase of the radial gap of 0.5 mm at 0.6*Q* and 1.4*Q*, and decreases by 10% at 1.0*Q*.

Figure 5 is the performance curve of the canned motor pump when the clearance of the back wear-ring is changed. It can be seen from the Fig that the change of the clearance of the back wear-ring has little effect on the external characteristics of the canned motor pump. Among them, with the increase of flow, the head will show a downward trend. Compared with the prototype pump, the head and efficiency under all working conditions show a downward trend with the increase of the clearance of the rear wear-ring. In addition, the impact of scheme 2 is less than that of scheme 1.

3.1.2 Effects on the internal flow field

The internal flow fields of Scheme 1 and Scheme 2 under standard conditions are compared and analyzed in this section. For the convenience of observation, the X = 0 section is take n as the observation object. This section is located at the section position shown in Figure 1A.

Figure 6 shows the static pressure cloud image under different front wear-ring clearances in Scheme 1. As shown in Figure 6A, with the work done by the impeller, the static pressure of the water body increases significantly along the flow passage and reaches the maximum value at the outlet of the volute. With the increase of the clearance of the front wear-ring, the static pressure in the front cavity decreases significantly, while the static pressure in the rear cavity does not decrease significantly. The static pressure at the outlet of the front cavity increases to a certain extent, which affects the distribution of static pressure inside the whole impeller. At the same time, from the static pressure distribution in the figure, it is not difficult to find that with the increase of the radial clearance of the front wear-ring, the outlet pressure of the canned motor pump decreases significantly, and the head at the design operating point decreases. Traditionally, it is believed that the larger the clearance of the front wear-ring is, the easier it is to accumulate high-pressure and high-speed liquid in front of the impeller inlet, which reduces the necessary net positive suction head (NPSH) and improves the anti-cavitation ability of the canned motor pump.

Figure 7 shows the static pressure cloud image under different back ring clearances in Scheme 2. When the back ring clearance increases from 0.3 mm to 1.8 mm, the static pressure of the water in the front pump chamber and the impeller does not change significantly, while the static pressure of the water in the rear chamber increases slightly. At the same time, with the increase of the clearance of the rear ring, the leakage from the back pump chamber to the balance hole becomes larger, which affects the static pressure distribution at the back position of the shielding pump impeller.

Figure 8 is the absolute velocity cloud image under different front wear-ring clearances in Scheme 1. With the work done by the impeller, the absolute velocity increases significantly along the flow passage and reaches the maximum value at the impeller outlet. With the increase of the gap size of the front wear-ring of the canned motor pump, the flow velocity increases at the same time, the absolute velocity near the inlet of the impeller changes significantly, and the absolute velocity in the impeller increases significantly, which makes the velocity distribution in the impeller uneven and the flow stability worse.

Figure 9 is the absolute velocity cloud image under different back wear-ring clearances in Scheme 2. When the back wear-ring clearance changes (0.3 mm–1.8 mm), the absolute velocity of the water in the front pump cavity of the canned motor pump does not change much. When the gap of the rear ring is from 0.3 mm to 1.5 mm, the absolute velocity change is still not obvious. With the further increase of the ring leakage to 1.8 mm, the absolute velocity in the pump cavity behind the canned motor pump increases significantly. In addition, the change of the size of the rear mouth ring also affects the distribution of the velocity in the balance hole. When the

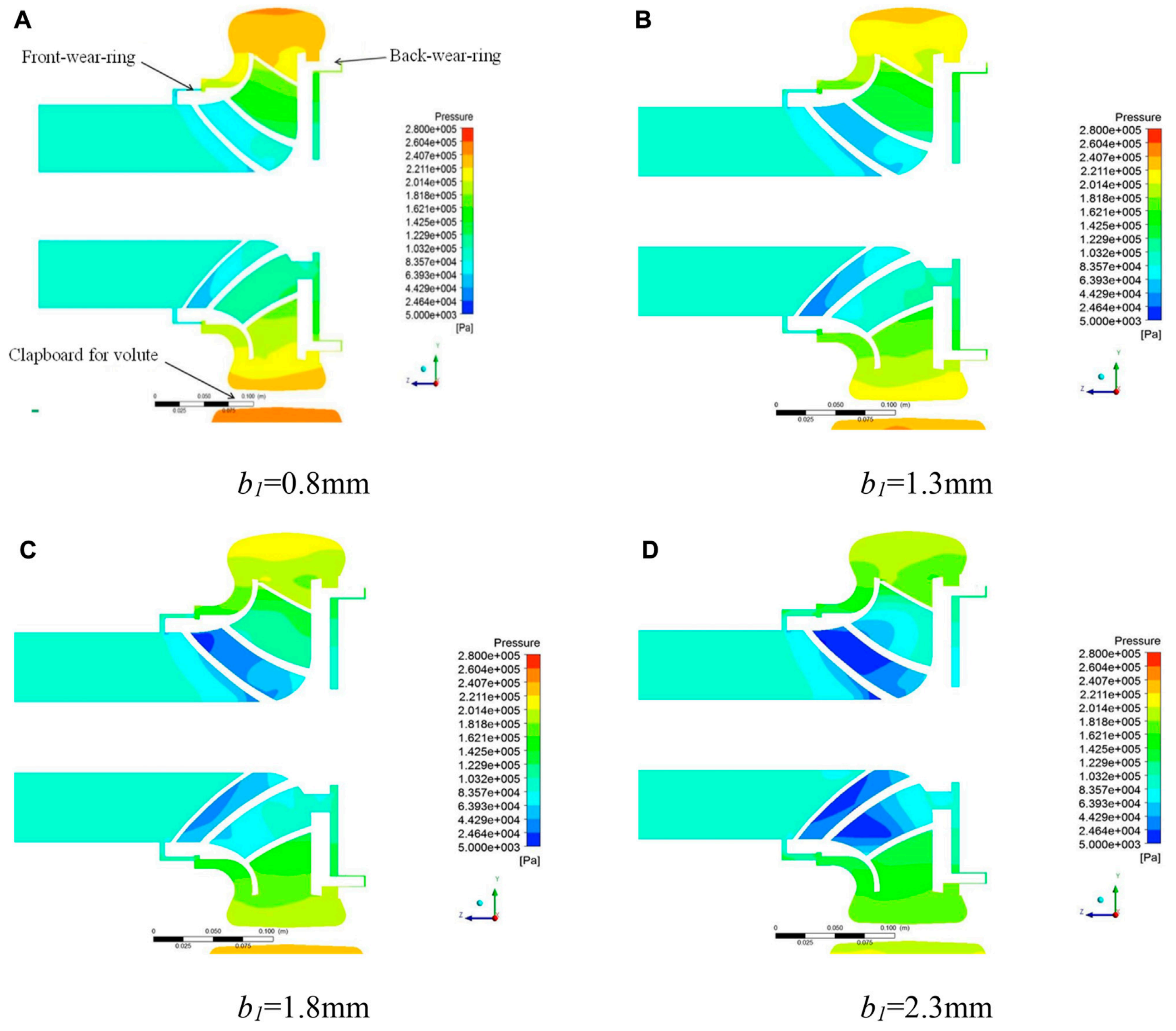

b_1=0.8mm b_1=1.3mm

b_1=1.8mm b_1=2.3mm

FIGURE 6
The static pressure distribution of X = 0 section under different clearance of front wear-ring. **(A)** b_1 = 0.8 mm; **(B)** b_1 = 1.3 mm; **(C)** b_1 = 1.8 mm; **(D)** b_1 = 2.3 mm.

clearance leakage decreases, the liquid flowing into the balance hole from the impeller outlet through the rear pump chamber decreases, and the vortex in the balance hole is obvious. With the increase of clearance leakage, the amount of liquid flowing into the balance hole from the rear pump chamber increases significantly, and there is no obvious vortex in the balance hole, which affects the velocity of main flow and the external characteristics of the canned motor pump.

3.1.3 Effects on the force of the rotor

Change the radial clearance value of the front and back wear-rings according to the previous scheme 1 and scheme 2, draw the following curve, and observe the change trend of the axial and radial forces. The positive direction of axial force is specified as the inlet direction of the impeller.

As shown in Figure 10, the size and direction of the axial force on the rotor components of the canned motor pump are determined by keeping the clearance of the rear ring unchanged and increasing the clearance of the front wear-ring. Under the standard working condition, the axial force increases with the increase of the front wear-ring clearance, and the axial force increases significantly when the front ring radial clearance increases from 0.3 mm to 2.3 mm, and the increment slows down from 2.3 to 10.3 mm. Under the condition of low flow rate (0.6Q), the axial force increases by 300 N when the clearance of the front orifice ring increases from 0.3 mm to 0.8 mm, and the direction does not change. With the further increase of the clearance of the front orifice ring, the axial force increases significantly. In the small flow range, the canned motor pump runs under the positive axial force, which affects the operation reliability of the canned motor pump. Under the

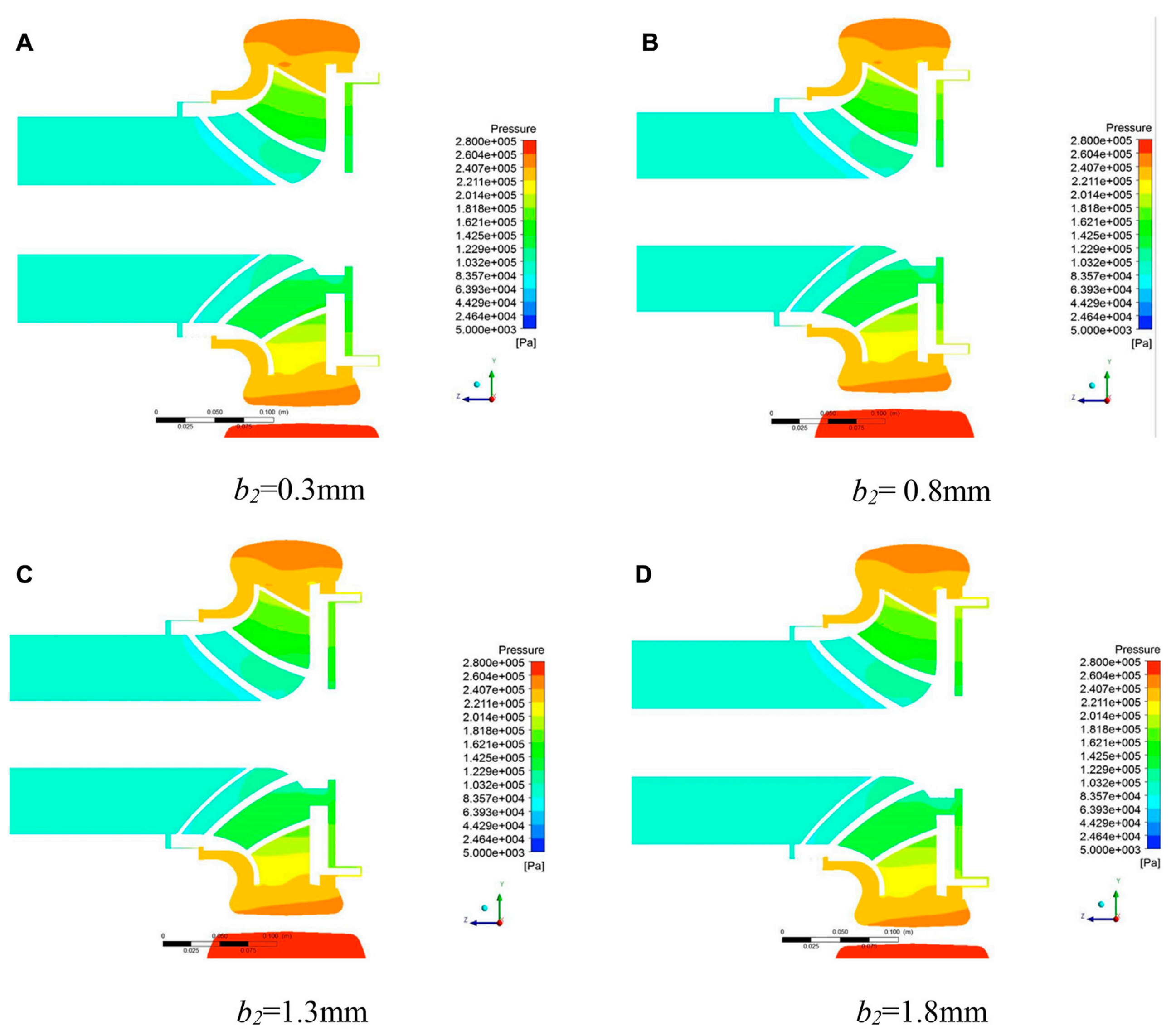

b_2=0.3mm

b_2= 0.8mm

b_2=1.3mm

b_2=1.8mm

FIGURE 7
The static pressure distribution of X = 0 section under different clearance of back wear-ring. **(A)** b_2 = 0.3 mm; **(B)** b_2 = 0.8 mm; **(C)** b_2 = 1.3 mm; **(D)** b_2 = 1.8 mm.

condition of large flow rate (1.4Q), the direction of axial force changes from positive to negative, and the magnitude changes but is not obvious.

As shown in Figure 11, keep the clearance of the front wear-ring unchanged and increase the clearance of the back wear-ring. In the whole flow range, the axial force decreases gradually with the increase of the clearance of the back wear-ring. Under the standard working condition, the axial force direction changes from positive to negative with the increase of the clearance of the ring, and its magnitude decreases first and then increases. Under the condition of small flow, the direction of axial force is not changed, and the magnitude of axial force decreases but not obviously, only decreases 50N at the point of 0.8 mm–1.3 mm. Under the overload condition, the axial force increases by 200N in the reverse direction when the clearance of the back wear-ring increases from 0.3 mm to 0.8 mm. And with the increase of the clearance of the rear grinding ring, the change is more obvious.

Figures 12, 13 are the curves showing the change of the meridional force on the canned motor pump rotor with the working condition after changing the clearance between the front and back wear-rings. Through the comparison of the first and second schemes, it is found that the wear-rings of the front and back clearances has little effect on the radial force of the canned motor pump. Because the magnitude of the radial force is closely related to the absolute velocity of the impeller outlet, and the clearance of the wear-ring has little effect on the flow of the liquid in the impeller, and the absolute velocity of the impeller outlet changes little, so the change of the front and back wear-rings has little effect on the radial force on the impeller.

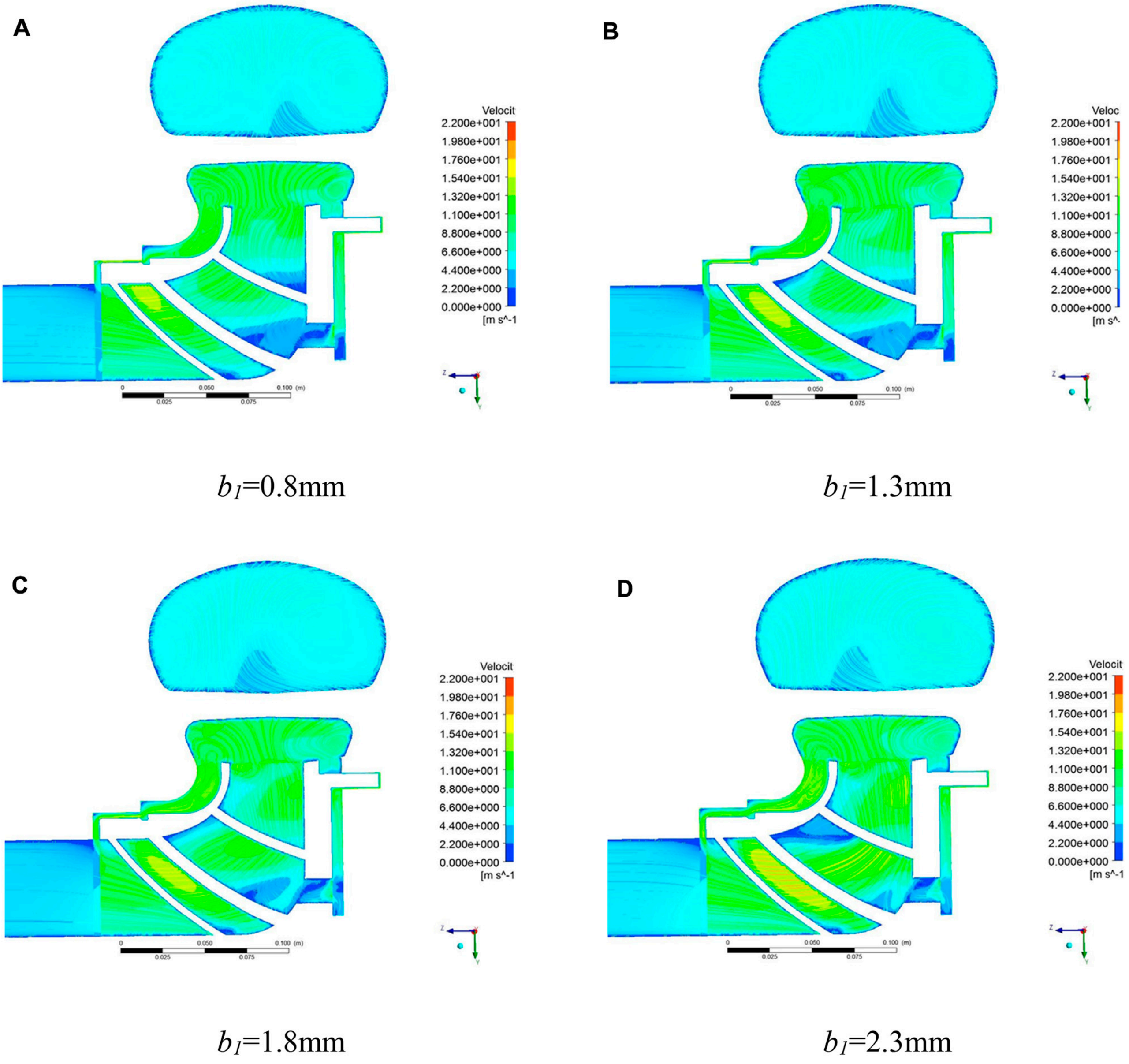

b_1=0.8mm

b_1=1.3mm

b_1=1.8mm

b_1=2.3mm

FIGURE 8
The absolute velocity distribution of X = 0 section under different clearance of front wear-ring. **(A)** b_1 = 0.8 mm; **(B)** b_1 = 1.3 mm; **(C)** b_1 = 1.8 mm; **(D)** b_1 = 2.3 mm.

3.2 Influence of volute diaphragm on operating characteristics

3.2.1 Effects on the external characteristics

As shown in Figure 14, there are two external characteristic curves of different volute forms under variable working conditions. It can be seen from the *Q-H* curve that when the flow rate is less than 0.6*Q*, the head of the prototype canned pump is higher than that of the third scheme, and with the increase of the flow rate, the head of the prototype canned pump decreases significantly, while the head curve in the third scheme is relatively flat as a whole, and the heads of the two models are basically close from 0.8*Q* to 1.0*Q*. The head value of the third scheme is greater than that of the prototype canned pump, and the difference is greater with the increase of flow. It can be seen from the *Q-η* curve that the highest efficiency point of the prototype canned motor pump and the third scheme both appears at the design working condition value, and the highest efficiency point of the third scheme is higher than that of the prototype pump under different working conditions. The main reason for this observation is that the addition of shell clapboard makes the flow passage of the pumping chamber blocked, the highest efficient point deviates to a small flow rate, and the high efficiency area narrows.

3.2.2 Effects on the internal flow field

As shown in Figure 15, the static pressure distribution in the impeller flow passage of the third scheme is not much different from

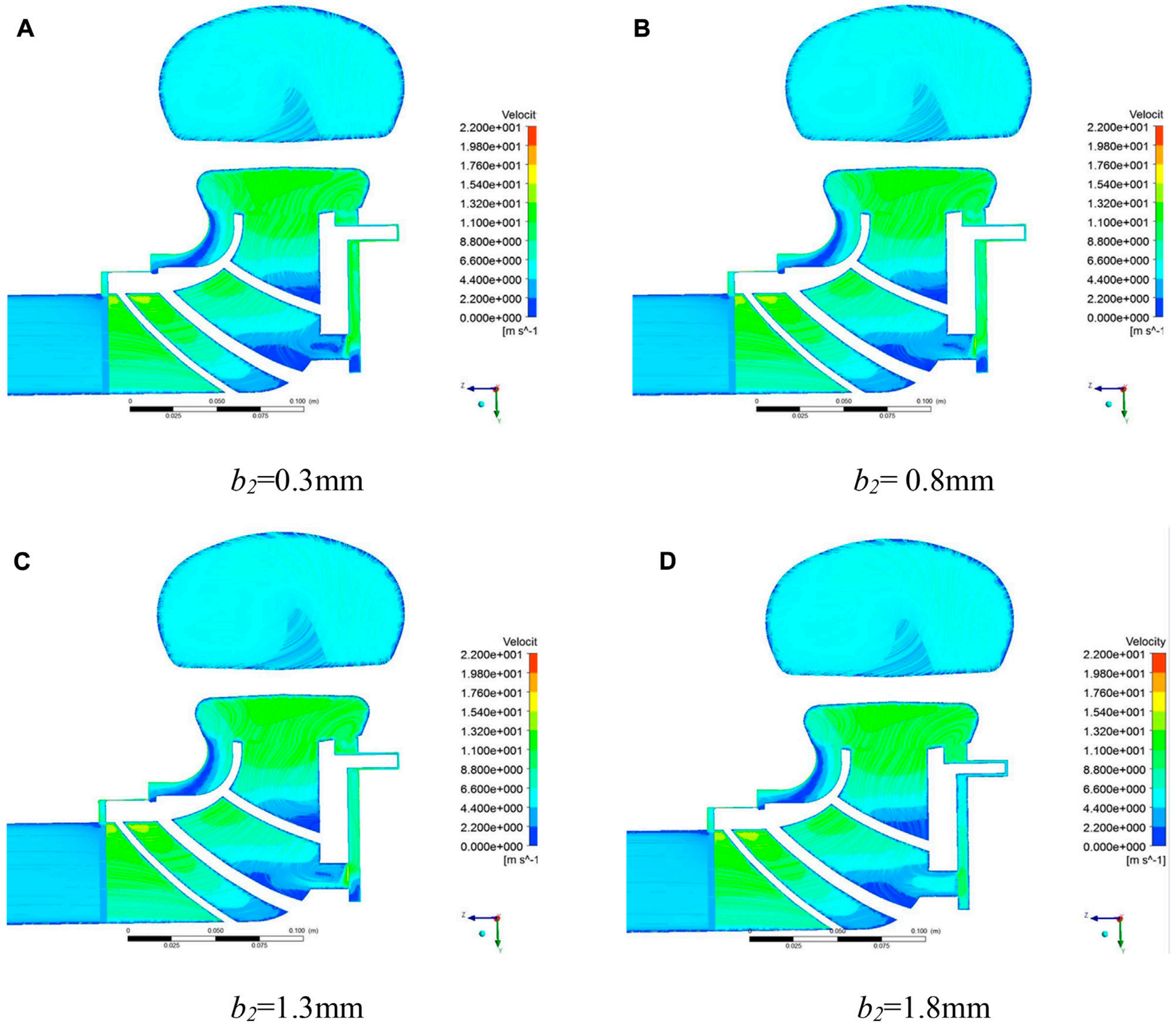

b_2=0.3mm b_2= 0.8mm

b_2=1.3mm b_2=1.8mm

FIGURE 9
The absolute velocity distribution of X = 0 section under different clearance of back wear-ring. **(A)** b_2 = 0.3 mm; **(B)** b_2 = 0.8 mm; **(C)** b_2 = 1.3 mm; **(D)** b_2 = 1.8 mm.

that of the prototype canned motor pump, and the pressure diffusion in the volute is obvious. It can be seen from Figures 16,17 that the liquid flow in the volute without the diaphragm in Scheme 3 is smooth, and there is no impact blocking between the liquid flow and the diaphragm, which reduces the energy loss of the water body and improves the head and efficiency compared with the prototype. In the prototype shell, although the liquid flow is blocked, the radial force of the impeller can be effectively balanced by the dynamic reaction force of the water on both sides of the baffle.

3.2.3 Effects on the force of the rotor

In order to analyze the influence of volute models with different structures on the axial and radial force of canned motor pump impeller, numerical analysis was carried out under five working conditions of 0.6*Q*, 0.8*Q*, 1.0*Q*, 1.2*Q*, and 1.4*Q*. Considering that the volute diaphragm is symmetrically distributed about the *Z* axis, the influence on the axial force is negligible. This section will mainly study the influence of the diaphragm on the magnitude and direction of the rotor radial force.

Figure 18 shows the magnitude and direction of the radial force of two types of volute under different working conditions. The *X*-axis direction in Figure 2 is set to 0°. It can be seen from Figure 18A that the radial force curve of the prototype pump is relatively flat with the change of flow, while the radial force in Scheme 3 decreases first and then increases with the increase of flow. In the whole flow range, the radial force in Scheme 3 is greater than that in the prototype pump, especially at the non-design operating point. In the vicinity of the design condition, the radial force (absolute value) on the impeller of the canned motor pump is the smallest.

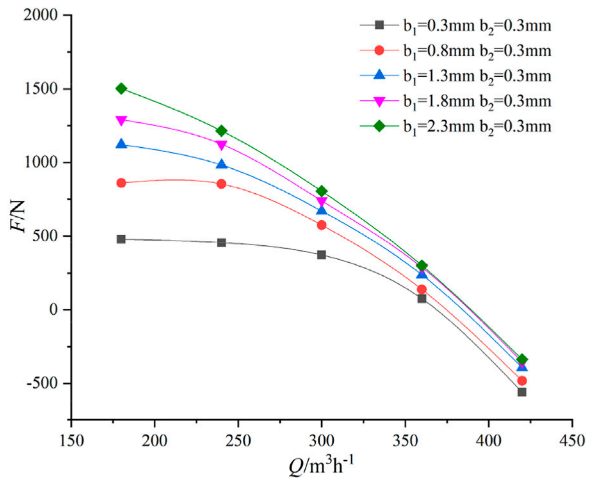

FIGURE 10
Axial force change of the CMP under different front wear-ring clearances.

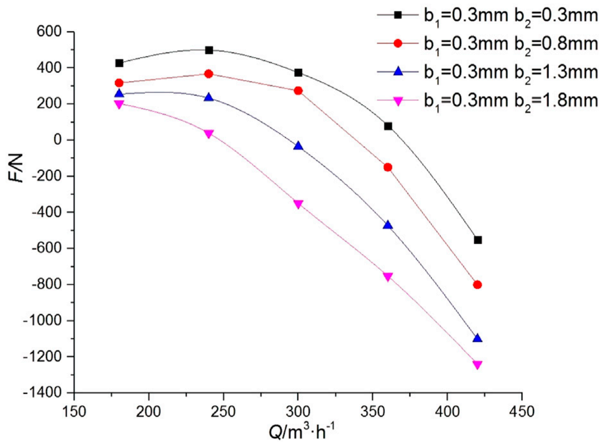

FIGURE 11
Axial force change of the CMP under different back wear-ring clearances.

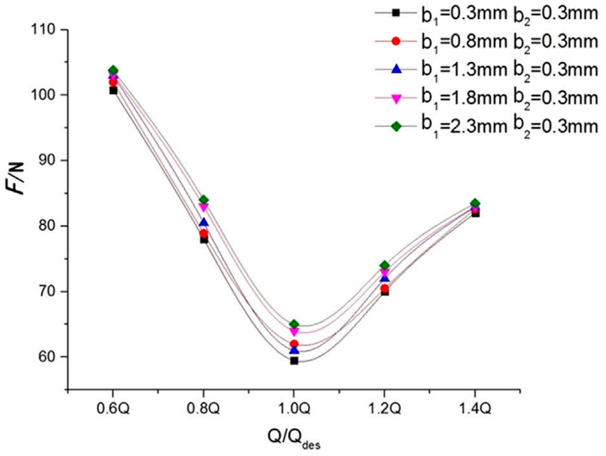

FIGURE 12
Radial force change of the CMP under different front wear-ring clearances.

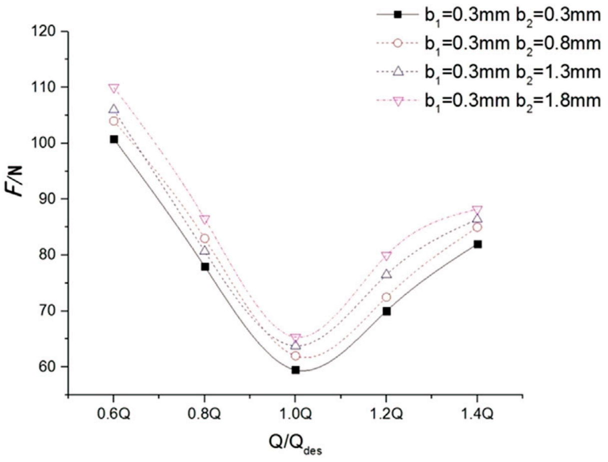

FIGURE 13
Radial force change of the CMP under different back wear-ring clearances.

It can be seen from Figure 18B that in Scheme 3, with the increase of water flow in the canned motor pump, the angle value of the radial force on the impeller of the canned motor pump changes greatly; However, the direction vector of radial force on the impeller of double volute pump changes little from 0.6*Q* to 1.0*Q* and from 1.2*Q* to 1.4*Q*, and changes greatly from 1.0*Q* to 1.2*Q*. This is mainly due to the fact that when the actual flow is less than the design flow, the outflow velocity in the volute is small, resulting in a continuous increase in pressure from the tongue; when the actual flow is greater than the design flow, the static pressure in the volute decreases from the tongue. Therefore, the radial force direction of the impeller in the prototype canned motor pump and the third scheme moves from the vicinity of the downstream of the tongue to the direction of the tongue outlet with the increase of flow.

Under the design condition of single volute, the surrounding pressure distribution is uniform and the radial force is small, but under the off-design condition, there is a large radial force. The double volute type consists of two single volute chambers arranged symmetrically, so that the radial force can be kept relatively balanced under any working condition. The experiment shows that the radial force decreases obviously even if the inner and outer flow channels are not completely symmetrical. The efficiency of the double volute is close to that of the single volute. The efficiency of the double volute is about 1%–2% lower than that of the single volute at the design operating

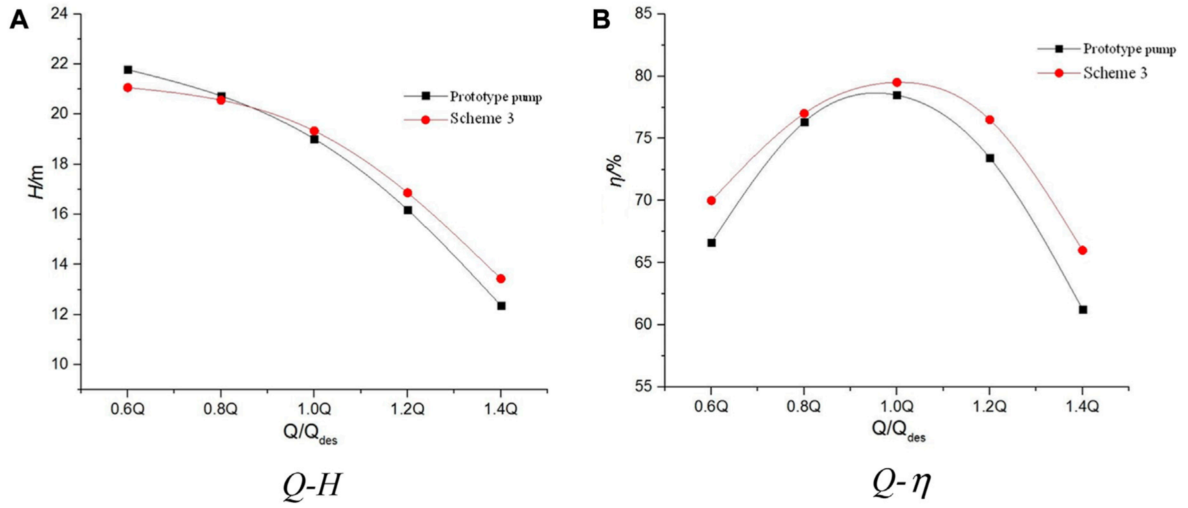

FIGURE 14
The performance curves of Scheme 3. **(A)** *Q-H*; **(B)** *Q-η*.

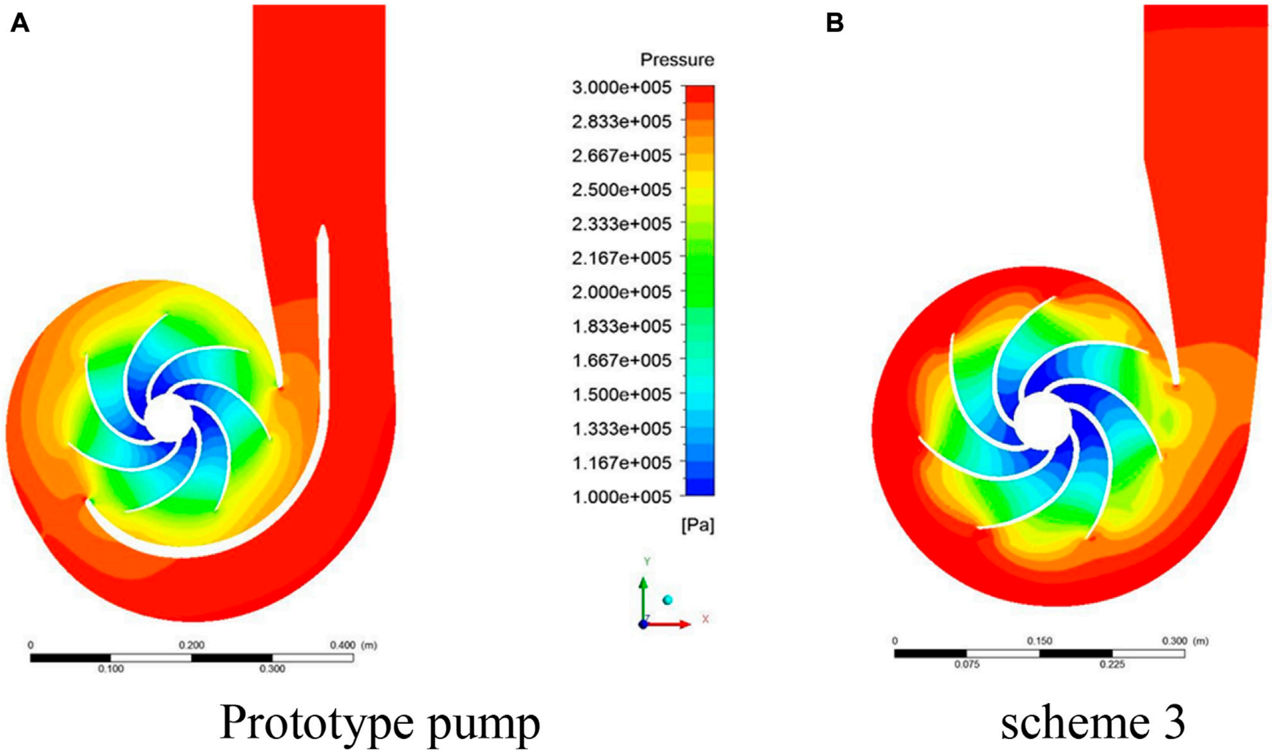

FIGURE 15
The static pressure distribution in the *Z*-axis direction under design conditions. **(A)** Prototype pump; **(B)** Scheme 3.

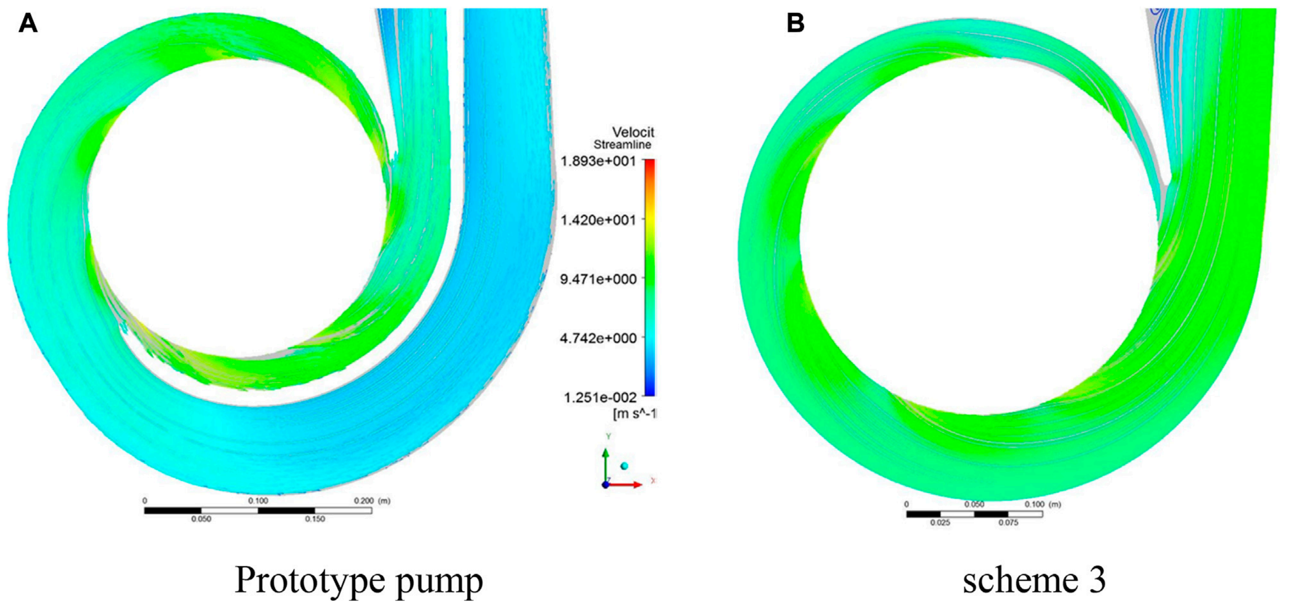

Prototype pump

scheme 3

FIGURE 16
The absolute velocity distribution in the volute under design condition. **(A)** Prototype pump; **(B)** Scheme 3.

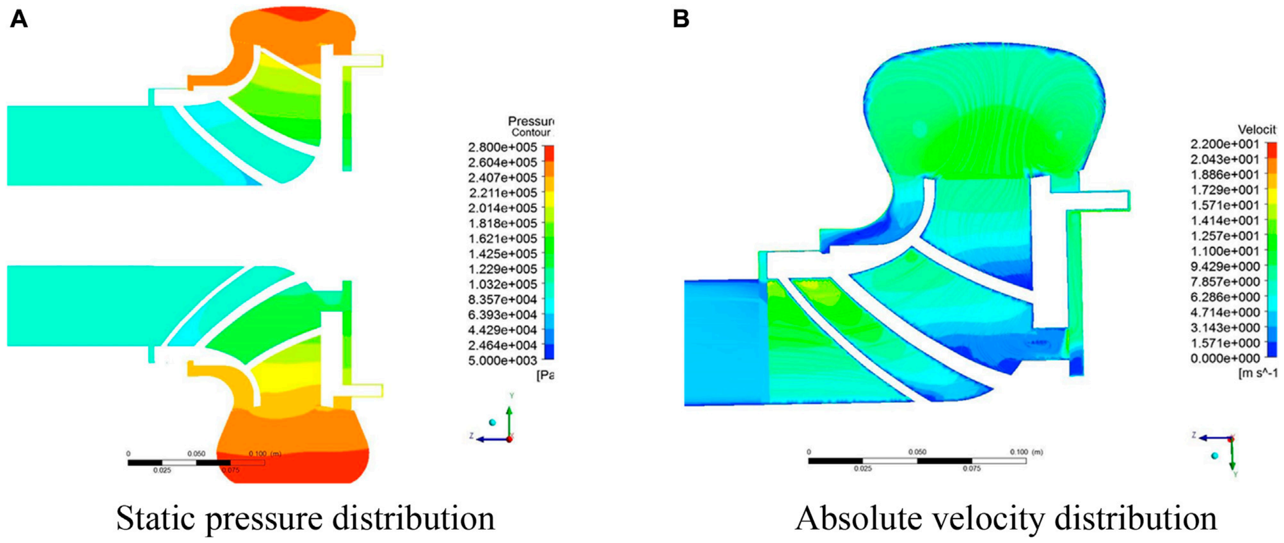

Static pressure distribution

Absolute velocity distribution

FIGURE 17
The static pressure and absolute velocity distribution on the X = 0 section in Scheme 3. **(A)** Static pressure distribution; **(B)** Absolute velocity distribution.

point, and about 2.5% lower at the off-design operating point. Therefore, the double volute chamber has a wider range of high efficiency and is suitable for operation under variable conditions. In addition, the strength of the double volute chamber is better than that of the single volute chamber, and the radial force is effectively reduced by more than 30%.

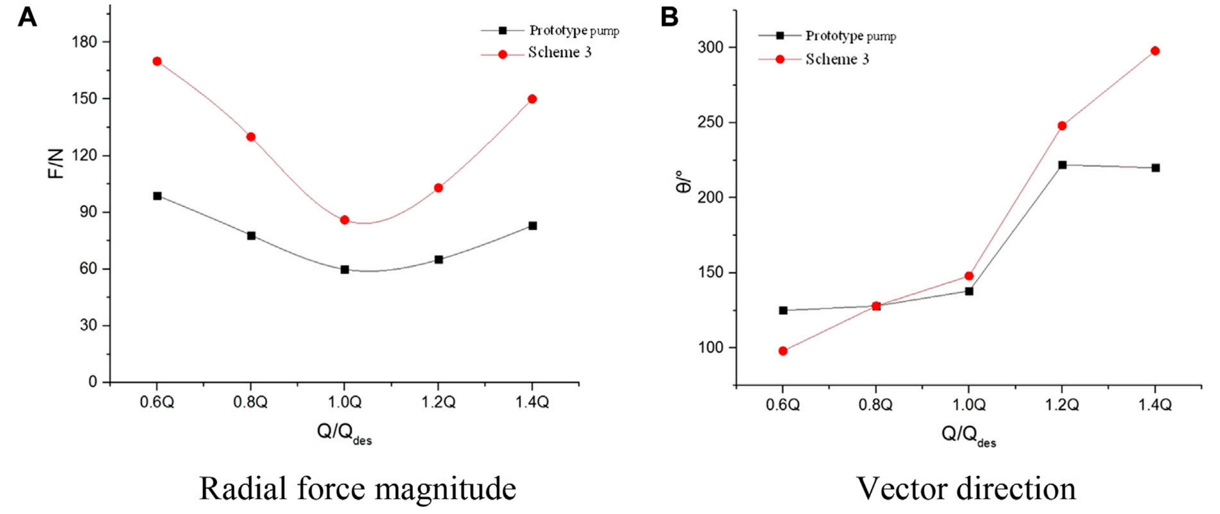

FIGURE 18
The magnitude and direction of radial force under different conditions. **(A)** Radial force magnitude; **(B)** Vector direction.

4 Conclusion

Based on the CFD technology, the internal flow field of the flow components, the external characteristic curve of the canned motor pump, the balance shaft, and the radial force are analyzed in this paper. The influence of the geometric parameters of the wear-ring clearance and the form of the volute diaphragm on the performance of the canned motor pump is investigated. The conclusion can be drawn from the above analysis as follows:

1. By comparing the prototype pump with the values in the first and second schemes, it can be found that changing the clearance of the front and back wear-rings has an impact on the external characteristics, rotor force and internal flow field of the canned motor pump. The external characteristics of the prototype pump are better than those of the first and second schemes, and the efficiency decreases significantly with the increase of the front ring gap, while the efficiency does not decrease significantly with the increase of the clearance of the back wear-ring. The efficiency of the prototype pump and the third scheme decreased under different flow rates. Therefore, in the process of machining, the machining accuracy of the front wear-ring should be ensured. If there is no requirement for the radial force of the impeller, the diaphragm can be removed.
2. The change of the clearance of the wear-ring and the volute diaphragm affects the internal flow of the impeller, and the change of the front wear-ring clearance affects the flow characteristics in the front pump chamber and at the inlet end of the impeller, and then has a greater impact on the internal flow characteristics of the impeller; The baffle has a great influence on the flow field distribution in the volute.
3. Under the condition of small flow rate, the clearance of the front wear-ring has a great influence on the axial force, and the influence becomes smaller with the increase of flow rate. The influence of the rear wear-ring clearance on the axial force is the opposite. The clearance of the mouth ring has little effect on the radial force of the canned motor pump. In addition, the addition of volute diaphragm helps to balance the radial force of the canned motor pump, but at the same time, the efficiency decreases.

Data availability statement

The raw data supporting the conclusion of this article will be made available by the authors, without undue reservation.

Author contributions

KC (First Author): conceptualization, methodology, software, investigation, formal analysis, writing original draft; TJ: data curation, writing original draft; YH (Corresponding Author): conceptualization, funding acquisition, resources, supervision, review, editing; XW: data curation, writing original draft.

Funding

This work was supported by the Quantitative evaluation and process optimization of aeration conditions in biochemical tank based on multi-sensor fusion (grant number 202203a05020026), the Research on key technologies of *in-situ* detection of marine microplastics (grant number YZJJ202203-CX).

Conflict of interest

Author KC was employed by Sinopec Luoyang Company; Author TJ was employed by Innovation Institute of Shaanxi Aerospace Power High Tech Co., LTD; Author XW was employed by Hefei Huasheng Pumps & Valves CO., LTD.

The remaining author declares that the research was conducted in the absence of any commercial or financial relationships that could be construed as a potential conflict of interest.

Publisher's note

References

Alfayez, L., Mba, D., and Dyson, G. (2005). The application of acoustic emission for detecting incipient cavitation and the best efficiency point of a 60kW centrifugal pump: Case study[J]. *NDT E Int.* 38 (5), 354–358. doi:10.1016/j.ndteint.2004.10.002

Arndt, N., Acosta, A. J., Brennen, C. E., and Caughey, T. K. (1990). Experimental investigation of rotor-stator interaction in a centrifugal pump with several vaned diffusers. *J. Turbomach.* 112, 98–108. doi:10.1115/1.2927428

Arndt, N., Acosta, A. J., Brennen, C. E., and Caughey, T. K. (1989). Rotor-Stator interaction in a diffuser pump. *J. Turbomach.* 111, 213–221. doi:10.1115/1.3262258

Author Anonymous (1996). *Canned motor pumps offer reliability and safety in industrial applications[J].* England: World Pumps, 30–34.

Author Anonymous (2019). *Engineering - power engineering; findings from shanghai jiao tong university provides new data about power engineering (numerical and experimental research on the fluid-induced forces of clearance flow in canned motor reactor coolant pump)[J].* Atlant, Georgia: Energy Weekly News.

Benra, F-K., Josef Dohmen, H., and Wan, B. (2006). *ASME joint.* United States: U.S.-European Fluids Engineering Summer Meeting.

Cabrera, D. L., Woolley, N. H., and AllansonTridimas, D. R. (2005). Film pressure distribution in water-lubricated rubber journal bearing[J]. *Mech. E* 219, 125–132. doi:10.1243/135065005X9754

Cdina, M. (2003). Detection of cavitation phenomenon in a centrifugal pump using audible sound[J]. *Mech. Syst. signal Process.* 17 (6), 1335–1347. doi:10.1006/mssp.2002.1514

Choi, J. S., McLaughlin, D. K., and Thompson, D. E. (2003). Experiments on the unsteady flow field and noise generation in a centrifugal pump impeller[J]. *J. Sound Vib.* 263 (3), 493–514. doi:10.1016/S0022-460X(02)01061-1

Dawes, W. N. (1994). A simulation of the unsteady interaction of a centrifugal impeller with its vaned diffuser: Flows analysis. *Proc. ASME Turbo Expo* 117, 213–222. doi:10.1115/1.2835649

Gertzos, K. P., Nikolakopoulos, P. G., and Papadopoulos, C. A. (2008). CFD analysis of journal bearing hydrodynamic lubrication by Bingham lubricant. *Tribol. Int.* 41 (12), 1190–1204. doi:10.1016/j.triboint.2008.03.002

Guan, H., Jiang, W., Wang, Y., Hou, G., Zhu, X., Tian, H., et al. (2020a). Effect of vaned diffuser clocking position on hydraulic performance and pressure pulsation of centrifugal pump. *Instituion Mech. Eng.* 235, 7247. doi:10.1177/0957650920967247

Guan, H., Jiang, W., Yang, J., Wang, Y., Zhao, X., and Wang, J. (2020b). Energy loss analysis of the double-suction centrifugal pump under different flow rates based on entropy production theory, *J. Mech. Eng. Sci.* 234 4009–4023. doi:10.1177/0954406220919795

Hirsch, C. (1988). Numerical computation of internal and external flows, in *Fundamentals of numerical discretization* (Chichester: Wiley).

Hongyu, G., Wei, J., Yuchuan, W., Hui, T., Ting, L., and Diyi, C. (2021). Numerical simulation and experimental investigation on the influence of the clocking effect on the hydraulic performance of the centrifugal pump as turbine. *Renew. Energy* 168, 21–30. doi:10.1016/j.renene.2020.12.030

Jameson, A., Schmidt, W., and Turkel, E. (1981). Numerical solutions of the Euler equations by finite volume methods using Runge-Kutta time-stepping schemes[J]. *AIAA Pap.* 81, 9. doi:10.2514/6.1981-1259

Jin, F., Li, N., Tao, R., and Xiao, R. (2022). Investigation of the self-balance impeller of a canned motor pump for axial force reduction. *Proc. Inst. Mech. Eng. C J. Mech. Eng. Sci.* 22, 3735. doi:10.1177/09544062221133735

Jin, F., Tao, R., and Xiao, R. (2022). Study on axial clearance size and leakage of canned motor pump under axial force self-balance state. *J. Phys. Conf. Ser.* 2160, 012082. doi:10.1088/1742-6596/2160/1/012082

Koji, I. (1991). "Non-contact magnetic gear for micro transmission mechanism[C]," in Proceedings of the 1991 IEEE Micro Electro Mechanical Systems-MEM'91[J], Nara Japan, 30-02 January.

Launder, B., and Spalding, D. (1974). The numerical computation of turbulent flows [J]. *Comput. Methods Appl. Mech. Eng.* 3 (2), 269–289.

Qu, L. X., Wang, F. J., and Liu, Z. Q., (2010). Numerical analysis of unsteady flow in a large double-suction centrifugal pump[J]. *ASME Fluid Mach.*, 31: 81–84. doi:10.1115/FEDSM-ICNMM2010-30441

Qianyan, T., Fanyu, K., Yuxing, B., and Xin, Y. (2018). Research on axial forces balance of stamping-welding canned motor pump. *IOP Conf. Ser. Earth Environ. Sci.* 168, 012026. doi:10.1088/1755-1315/168/1/012026

Qin, W., and Tsukamoto, H. (1997). Theoretical study of pressure fluctuations downstream of a diffuser pump impeller—Part 1: Fundamental analysis on rotor-stator interaction. *J. Fluids Engineering-Transactions Asme* 119, 647–652. doi:10.1115/1.2819293

Rasmussen, P. O., Andersen, T. O., and Frank, T. (2005). Development of a high-performance magnetic gear. *IEEE Trans. Industry Appl.* 41, 764–770. doi:10.1109/TIA.2005.847319

Rzentkowski, G., and Zbroja, S. (2000). Experimental characterization of centrifugal pumps as an acoustic source at the blade-passing frequency[J]. *J. Fluids Struct.* 14 (4), 529–558. doi:10.1006/jfls.1999.0280

Song, X., Yu, W., Pan, X., and Luo, X. (2021). Energy balance analysis for a canned motor pump used for heat supply system. *J. Phys. Conf. Ser.* 1909, 012072. doi:10.1088/1742-6596/1909/1/012072

Wang, H., Student, G., and Tsukamoto, H. and Professor (2001). Fundamental analysis on rotor-stator interaction in a diffuser pump by vortex method[J]. *J. fluids Eng.* 123 (1), 737–747. doi:10.1115/1.1413242

ye Jin, F., Tao, R., Zhu, D., and fu Xiao, R. (2022). Stability of the axial-auto-balanced impeller of centrifugal pump. *J. Hydrodynamics* 34, 665–680. doi:10.1007/s42241-022-0060-1

Zhou, F. M., and Wang, X. F. (2016). Effects of staggered blades on the hydraulic characteristics of a 1400-MW canned nuclear coolant pump. *Adv. Mech. Eng.* 8, 168781401665794–21. doi:10.1177/1687814016657944

Zhu, B., and Kamemoto, K. (2005). Numerical simulation of unsteady interaction of centrifugal impeller with its diffuser using Lagrangian discrete vortex method[J]. *Acta Mech. Sin.* 21 (1), 40–46. doi:10.1007/s10409-004-0005-7

Zhu, X., Shahat, S. A. E., Lai, F., Jiang, W., and Li, G. (2020). Numerical investigation of rotor–stator interaction for canned motor pump under partial load condition[J]. *Mod. Phys. Lett. B* 34 (03), 18. doi:10.1142/S0217984920500396

frontiers | Frontiers in Energy Research

TYPE Original Research
PUBLISHED 17 March 2023
DOI 10.3389/fenrg.2023.1135543

OPEN ACCESS

EDITED BY
Yang Yang,
Yangzhou University, China

REVIEWED BY
Yue Jiang,
Jiangsu University, China
Weixuan Jiao,
Yangzhou University, China
Linwei Tan,
Nantong University, China

*CORRESPONDENCE
Qingjiang Xiang,
✉ xiang_qj@163.com

SPECIALTY SECTION
This article was submitted to Process and Energy Systems Engineering, a section of the journal Frontiers in Energy Research

RECEIVED 01 January 2023
ACCEPTED 07 February 2023
PUBLISHED 17 March 2023

CITATION
Qureshi WA, Xiang Q, Xu Z and Fan Z (2023), Study on the irrigation uniformity of impact sprinkler under low pressure with and without aeration.
Front. Energy Res. 11:1135543.
doi: 10.3389/fenrg.2023.1135543

Study on the irrigation uniformity of impact sprinkler under low pressure with and without aeration

Waqar Ahmed Qureshi, Qingjiang Xiang*, Zhengdian Xu and Zhizun Fan

Research Center of Fluid Machinery Engineering and Technology, Jiangsu University, Zhenjiang, Jiangsu, China

The distribution of water deteriorates when the operating pressure of an impact sprinkler (IS) decreases to some level. The aeration jet method is utilized to form an aeration impact sprinkler (AIS), aiming to improve the uniformity of water distribution under low pressure. Based on the structures of a 20PY$_2$ impact sprinkler, an IS and AIS with the same sprinkler discharge were studied under operating pressures range between 150 and 250 kPa. A square test zone was formed by the four sprinklers, and the combined irrigation experiment was conducted under windless conditions. The results showed that the water loss ranged from 3% to 9.5% in all 18 test schemes. The coefficient of uniformity (CU) and distribution uniformity (DU) were used to quantify the degree of uniformity. The AIS had an approximately 3%–7% greater CU than the IS, which resulted in the CU reaching the specified value in the IS standard when the sprinkler functioned under low operating pressure. A linear relationship was found between the CU and DU$_{lq}$. The uniformity of water distribution clearly changed with the operating pressure (150 kPa, 200 kPa, and 250 kPa) but decreased slightly with the increase in combination spacing (1 R, 1.1 R, and 1.2 R). In addition, the results of field experiment were compared with those of the simulation developed from a single sprinkler indoor experiment based on the water distribution radial curve. The simulated coefficient of uniformity was highly consistent with the experimental data and had an error of <7%. A sprinkler water jet with the aeration method was proven to be a feasible solution to reduce the operating pressure.

KEYWORDS

sprinkler irrigation, impact sprinkler, water distribution uniformity, aeration water jet, low pressure irrigation

1 Introduction

Irrigation techniques have been used to increase agricultural productivity in dry regions, as well as where rainfall is the leading source for growing crops. Moreover, irrigation engineering can control the amount of irrigation applied and render a more convenient schedule (Montazar and Sadeghi, 2008). Owing to the convenience of operational function, sprinkling irrigation systems are used as part of the applications of irrigation systems throughout the world. In addition, this type of irrigation offers the precise combination of water distribution, precision control in the depth of irrigation, and high applied irrigation efficiency for various types of soil and topographical conditions (Cai et al., 2020). There are many types of rotating sprinklers used in irrigation systems based on driving principles, such as reacting force, impact, impeller and fluidic element sprinklers (Zhu et al., 2018). Irrigation sprinklers are ranked as high pressure, medium pressure, and micro-sprinklers based on their working pressure. An impact sprinkler (IS) is a type of irrigation sprinkler that is commonly and widely used for field crops, such as orchards, tea gardens, and lawns. This type of sprinkler has an advantage of ensuring a circular wetted area or sector under stable working performance over an extensive range of working pressures. The original horizontal action impact-driven sprinkler was invented by a citrus grower in Glendora, California, United States, and Orton Englehardt first introduced its patent in 1933 (Tarjuelo et al., 1999).

To date, the performance of impact sprinklers is continuously improving to address different requirements, such as precise irrigation, energy and water-saving irrigation, uniform irrigation, and sloped or hilly land sprinkler irrigation among others (Xu et al., 2018). Many researchers have improved the performance of impact sprinklers by modifying its structures, such as the secondary nozzle (Liu et al., 2011), water split needle (Zakaria et al., 2018), non-circular nozzle (Li et al., 1994; Li and Kawano, 1995) and the other auxiliary structures (Wang et al., 2019). Some research has shown that the decrease in working pressure leads to savings in energy for sprinkler irrigation (Schneider, 2000). However, decreasing the operating pressure produces two problems. The first is that the irrigation time increases under the same conditions of crop water requirement because the flow discharge of sprinkler decreases with respect to working pressure. The other problem is that the distribution of water is severely uneven when the pressure is reduced to below normal pressure (Huffman et al., 2013, 407 pp.). Less water scatters near the area of the nozzle of a stationary rotating single impact sprinkler and at the middle range, whereas too much water concentrates at the end of the jet. This means that the jet dispersal effect is not effective when the working pressure decreases to some degree. We considered a new method of jet to solve this problem. Swirl, oscillation, and pulsed jets are usually used in the industry. In this study, we focused on an aeration jet proposed by Lefebvre and Wang, 1988, who conducted the research on firefighting sprinklers. The phenomena were observed that the jet would break near the outlet of the nozzle even with a small amount of gas-induced in, and excellent water distribution would be obtained. The aeration jet was also studied in the research area of hydraulic structure discharge jet. For example, the jet atomization characteristics were changed, and the scour prevention ability was enhanced for the spillway (Deng et al., 2002). Based on the structure of impact sprinkler, an aeration impact sprinkler (AIS) was invented. It has self-suction ability, and the second fluid (air, chemical gas or liquid fertilizer) can be mixed with the main jet. The droplet diameter and suction capability of the AIS were measured by Xiang et al. (2016) and Xiang et al. (2021) who found that the peak value of water distribution radial curve and the d_{50} droplet diameter were reduced at the end of the jet when the sprinkler was functioning under lower pressure.

Sprinkler irrigation uniformity is an essential indicator in the design of sprinkler irrigation systems (Louie and Selker, 2000). In this study, the low-pressure irrigation of the AIS was studied and compared with the IS in terms of intensity of irrigation and distribution of water. The research objective is energy saving. Moreover, the water distribution of a combination sprinkler irrigation was simulated and compared with the experimental data. Based on a sprinkler experiment under open-air conditions conducted by Sanchez et al. (2011), a wind velocity threshold value of 0.6 ms^{-1} was adopted to reliably determine the radial water distribution curves. Thus, the water distribution experiment was conducted under windless conditions to ensure that the results are comparable. A normal operating pressure of $20PY_2$ IS specified from 250 kPa to 450 kPa for standard usages, but the range from 150 kPa to 250 kPa was utilized in this study.

2 Materials and methods

2.1 Newly designed aeration structural and working principal

Generally, an IS consists of the main nozzle and a smaller auxiliary nozzle that is used to improve the water distribution near the sprinkler. An aeration structure was designed based on a type of $20PY_2$ impact sprinkler. The schematics of the IS and AIS structures are shown in Figure 1. A gas suction pipe was coaxially inserted in the sprinkler spray tube, with one end of the gas suction pipe connected to a plastic hose to intake air or gas, and the other end was near the outlet of the main nozzle. The reference $20PY_2$ IS had a sprinkler inlet diameter of 20 mm, an auxiliary nozzle diameter of 3.5 mm, a main nozzle diameter of 7 mm, and a spray tube angle of 28°. The inlet diameter, auxiliary nozzle diameter, and angle of spray tube should maintain the same sizes for the design of AIS. The size of the gas suction pipe was selected based on the existing brass pipe, with a wall thickness of 1 mm and an inner diameter of 2 mm. The performance of the AIS and IS should be compared with the same discharge under each testing pressure. Therefore, the main nozzle diameter of the AIS was designed to be slightly larger than that of the IS because the flow passage was partially blocked by the gas suction pipe. However, it is difficult to know the precise size because the exact hydraulic loss in flow passage is unknown. The main nozzle diameter of the AIS was 8.06 mm according to the equivalent area of the IS outlet (7 mm diameter). A flow rate measurement experiment was conducted with manufactured nozzles whose diameter ranged from 8.1 mm to 8.5 mm with an increment of 0.1 mm. However, the operating pressure increased from 150 kPa to 400 kPa under the pressure increment of 50 kPa. Finally, the main nozzle diameter of the AIS was determined to be 8.3 mm at which the sprinkler flow rate met this requirement, that is to say, the annulus cross section of AIS main nozzle has the same flow rate as the IS does. The end of the gas suction pipe was set to 2 mm outside of the main nozzle since the AIS is better able to suck (Xiang et al., 2016). The sketch of the main nozzle is shown in Figure 1C, the nozzle has a contract contour line with an angle in which θ is of 45°.

The driving mechanism for the rotation of AIS was the same as that of the IS. The driving force originates from the water jet impinging on the spoon of rocker arm, and the rotation effect was small when the sprinkler functioned under low pressure. Thus, the spring of the rocker arm needs to be tightened to prevent a

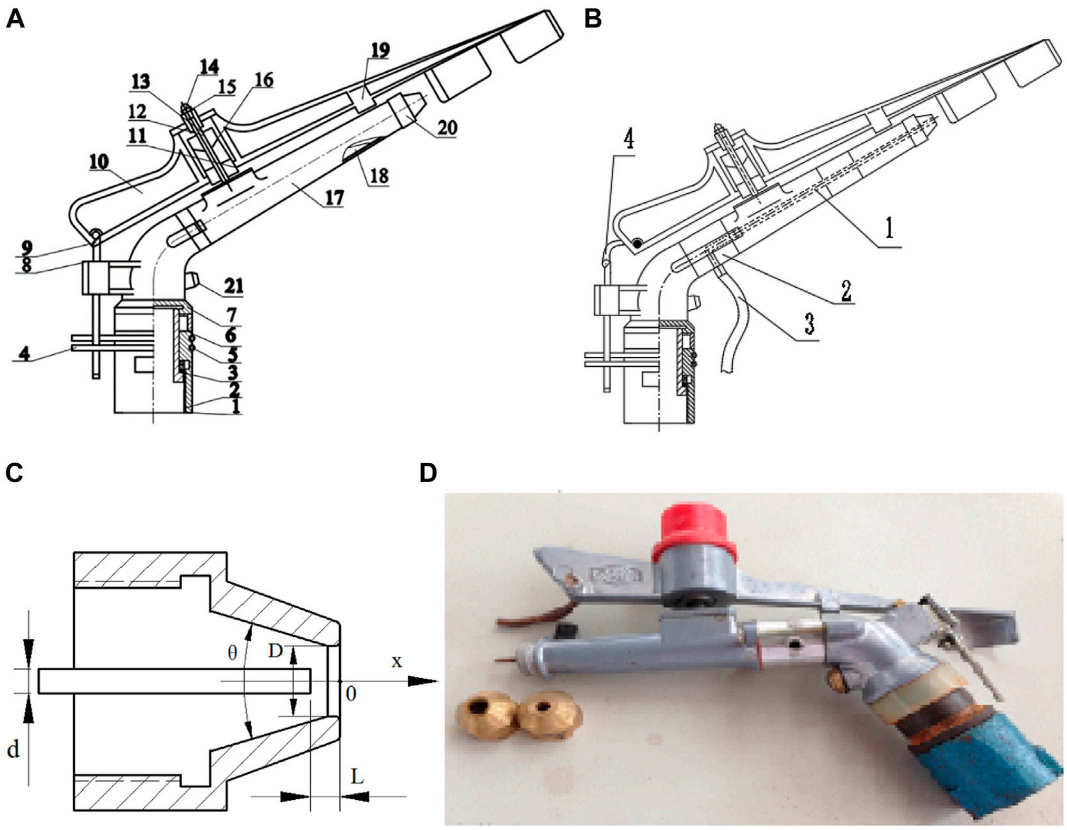

FIGURE 1
The schematics of the IS and AIS structures. **(A)** Schematic diagram of the IS (1 Hollow bushing, 2 hollow shaft, 3 Antifriction seal, 4 Limit ring, 5 Sand-proof spring, 6 Spring cover, 7 Base, 8 Commutator, 9 Reverse hook, 10 Rocker arm, 11 Rocker arm Bushing, 12 Spring seat, 13 Rocker shaft bushing, 14 Position screw, 15 Rocker Shaft, 16 Rocker arm Spring, 17 Spray tube, 18 stabilizer, 19. Strike block, 20 Main nozzle, and 21 Auxiliary nozzle), **(B)** Schematic diagram of the AIS (1 Gas suction pipe; 2 Joint; 3 Plastic hose; 4 Extension rod), and **(C)** Schematic diagram of the main nozzle (D, diameter of the primary nozzle; d, Diameter of the suction pipe; L, The adjusting length of the suction pipe, ϴ Degree of nozzle curve). **(D)** A prototype of the Aeration sprinkler.

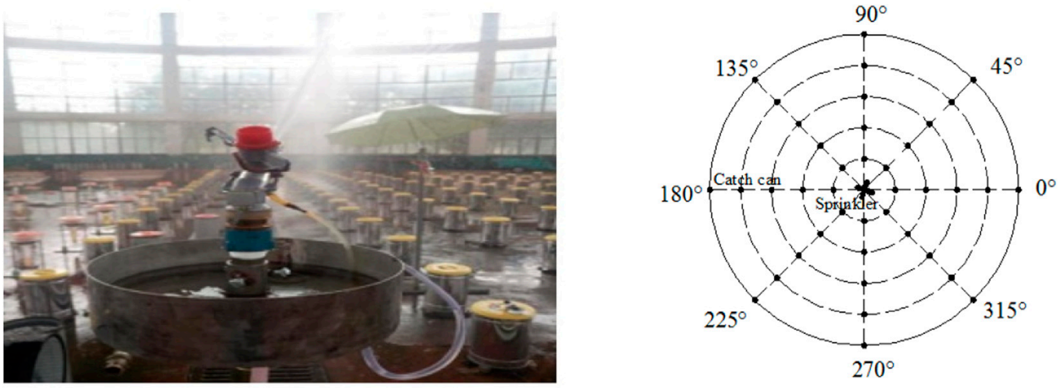

FIGURE 2
Schematic and pictorial view of sprinkler test.

rotating speed that is too slow. The principle of the AIS gas suction is that the pressure difference between two ends of the suction tube formed when an annular water jet passed through the main nozzle. Furthermore, the gas was taken away because of the effect of fluid viscosity. The spray of the AIS is the gas-liquid two-phase jet flow.

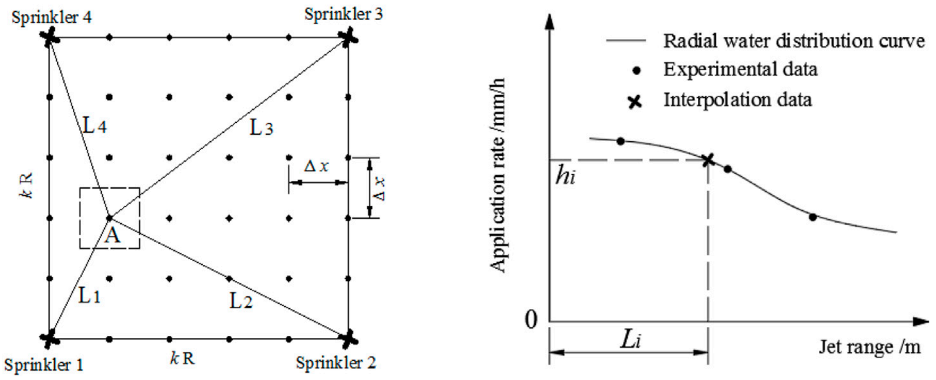

FIGURE 3
Schematic diagram of combined irrigation simulation.

2.2 Single sprinkler test plan and the simulation of combined irrigation

All experiments were performed based on the following standards: GB/T2299, 2008 and ISO 7749-2, 1990. The hydraulic performance test of the single sprinklers was performed at the Jiangsu University Sprinkler Irrigation Experiment Hall, Zhenjiang, China. The test site was an indoor facility, which avoided wind resistance for the rotation (Sourell et al., 2003). The irrigation depth was measured by the 152 catch cans that were 20 cm in diameter and 60 cm high and placed in a cylindrical shape. However, the arrangement of the catch cans was placed in eight radial lines around the sprinkler as shown in Figure 2, and each catch can was spaced 1 m along the line. In a single sprinkler test, the discharges under different operating pressures, the jet ranges (wetted radius of throw), and the sprinkler rotating speeds were measured. It took each sprinkler about 99–104 s to turn a circle when the operating pressure is 150 kPa, 86–92 s as the pressure is 200 kPa, 75–79 s when the pressure increase to 250 kPa. Four IS and four AIS prepared for outdoor experimentation were tested.

The schematic diagram of the square combined irrigation simulation is shown in Figure 3. The steps to calculate the distributions of water are as follows.

(1) The test data of application rate on the eight radial lines of a single sprinkler were averaged into one water distribution radial curve by the arithmetic average method.
(2) The side length of the square was determined by multiplying the sprinkler jet range R with the combination spacing coefficient k. The grid points for each catch can had the same spacing Δx when the outdoor experiment was conducted. Where the parameter k and Δx was selected according to the scheme of research and the standards respectively.
(3) The irrigation depth of each grid point was calculated based on to the sprinkler rotating speed ω_i, rpm, the distance from the corner of square L_i, m, and the interpolation value on the radial water distribution curve h_i, mm/h. The subscript i (1, 2, 3, 4) represents the combined sprinklers. For the grid point A, the irrigation depth h_a was calculated by the following equation:

$$h_a = \sum_{i=1}^{4} h_i \cdot \omega_i / \bar{\omega} \tag{1}$$

Where is the average rotating speed of four IS or AIS. Different rotating speeds are caused by an effect of the impact arm through the different twisting force of spring and different friction forces at the hollow shaft under the same values of working pressure (Figure 1A).

(4) The amount of water that fell into the square test zone must have been calculated. The water in the cell zone can be regarded as $h_a \cdot (\Delta x)^2 \cdot t$, where t is the irrigation time.
(5) The average value of irrigation depth and the uniformity coefficient of water distribution must have been calculated.
(6) The grid data must be saved and can be used to show the contour map.

2.3 The outdoor experimental test

The experimental test site for field sprinkler irrigation was selected at Jintan City, Jiangsu Province (31°33′ N, 119°17’ E, 15 m altitude), as shown in Figure 4. Plastic buckets with 20 cm in diameter were used as catch cans. The layout arrangement of catch cans was in the square with an area of 1.5 × 1.5 m. Four impact sprinklers, or aeration impact sprinklers, were established at the corner of the test square. During the experiment, the following parameters were recorded, including the total flow rate, operating pressure of every sprinkler, wind velocity, air temperature and humidity, and irrigation depth among others. The combined uniformity coefficient was affected by various factors, including primary sprinkler type, lateral arrangement, environmental conditions, and pressure (Branscheid and Hart, 1986; Vories et al., 1987; Playán et al., 2006). The operating pressure was controlled by the valve opening, which was installed near the inlet of the system. The side length of the square test zone was changed from 1 R, 1.1 R and 1.2 R to meet the test requirement, in which R represents the jet range of sprinkler.

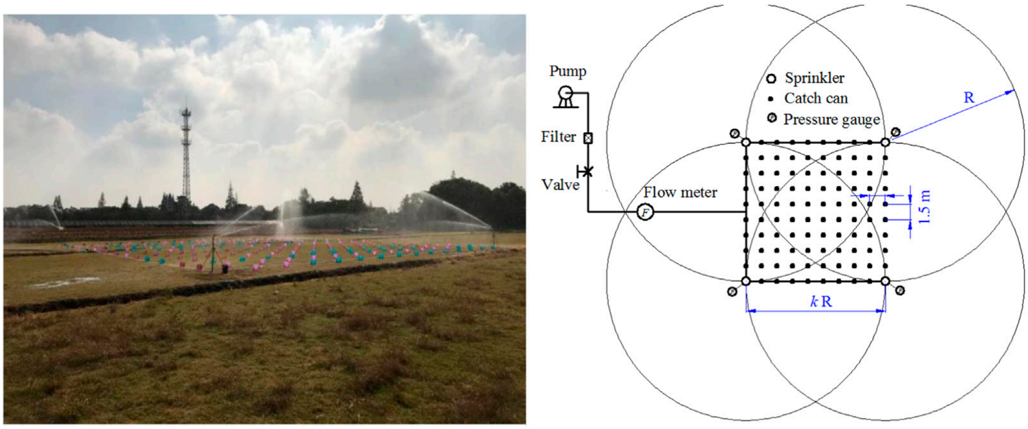

FIGURE 4
Schematic and pictorial view of sprinkler area.

2.4 Sprinkler irrigation intensity and water distribution uniformity coefficient

At the sampling point where the catch can was placed, the collected irrigation depth was calculated using Eq. 2. The mean sprinkler irrigation depth can be defined as the average value of all the irrigation depths collected over the duration of the test.

$$x_i = \frac{4V_i}{\pi D^2} \times 10 \tag{2}$$

$$\mathrm{TsID} = \frac{1}{\mathrm{N}} \sum_{i=1}^{\mathrm{N}} x_i \tag{3}$$

Where x_i is the collected irrigation depth, mm/h; V_i is the volume of a waterfall in each catch can in 1-h, cm^3/h, and D is the opening diameter of the catch can (20 cm). N is the total number of catch cans for the experiment; TsID is the experimental value of mean sprinkler irrigation depth, and the theoretical value was defined as the following formula:

$$\mathrm{ThID} = \frac{Qt}{4(k \cdot R)^2} \times 1000 \tag{4}$$

Where ThID is the water depth in the wetted square test zone, mm/h; Q is the total discharge measured by an electromagnetic flow meter, m^3/h, and it was installed near the inlet of the sprinkler irrigation system. t is the experiment irrigation time, h; Qt represents the amount of waterfall in the test square zone, and k is the combination spacing coefficient (CSC) 1, 1.1, and 1.2, respectively.

The evaporation and drift losses (water loss) for the combined sprinkler irrigation were calculated using the following formula.

$$\eta = \left(1 - \frac{\mathrm{TsID}}{\mathrm{ThID}}\right) \times 100\% \tag{5}$$

Where η is the water loss, including evaporation and wind drift. There are two problems in Eq. 5 that merit attention.

(1) Four solid set sprinklers tested had almost the same speed of rotation, which was confirmed by the indoor experiment.

(2) Four sprinklers had little pressure difference (hydraulic loss) caused by the pipe system. The pressure difference increased with the operating pressure. The outdoor experimental result showed that the pressure difference was no more than 12 kPa, which indicates that the discharge of four test sprinklers was almost the same. If the pressure difference was greater, the following equation was adopted to calculate the discharge of a single sprinkler (Tarjuelo et al., 1999; Stambouli et al., 2014).

$$Q_s = C_D \times A \times (2gp)^{0.5} \tag{6}$$

Where Q_s is the single sprinkler discharge, m^3/h, and C_D is the discharge coefficient. A is the area of the nozzle's openings, mm^2; g is the gravitational acceleration, $\mathrm{m/s}^2$, and p is the operating pressure of sprinkler, kPa. It can be observed from Eq. 6 that the coefficient C_D can be obtained by an indoor flow rate measurement experiment, and p can be obtained by the field test.

The water distribution uniformity coefficient of the sprinkler irrigation system was calculated by the widely used Christiansen's Uniformity coefficient (CU) (Christiansen, 1942), which are the important parameters used to determine whether an irrigation system is acceptable or not.

$$\mathrm{CU} = \left(1 - \frac{\Delta \mathrm{h}}{\mathrm{N} \cdot \bar{\mathrm{h}}}\right) \times 100\% \tag{7}$$

Where $\Delta \mathrm{h} = \sum_{i=1}^{\mathrm{N}} |\mathrm{x}_i - \bar{\mathrm{x}}|$ is the sum of deviation of all the collected irrigation depths, mm/h. CU shows the overall deviation of the whole field irrigation depth from the average value, but it is challenging to show how many collection points were close to or away from the average value. Thus, the collected irrigation depths were sorted from high to low and divided equally into four parts, as suggested by Criddle (1956).

$$\mathrm{DU}_{\mathrm{lq}} = 4\sum_{i=1}^{\mathrm{N_{lq}}} \mathrm{x}_{\mathrm{lq}i} \Big/ \sum_{i=1}^{\mathrm{N}} \mathrm{x}_i \tag{8}$$

$$\mathrm{DU}_{\mathrm{hq}} = 4\sum_{i=1}^{\mathrm{N_{hq}}} \mathrm{x}_{\mathrm{hq}i} \Big/ \sum_{i=1}^{\mathrm{N}} \mathrm{x}_i \tag{9}$$

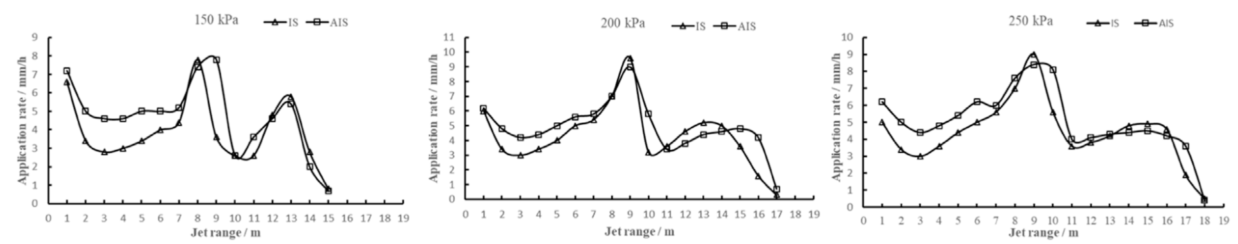

FIGURE 5
Radial water distribution curve between the AIS and the IS with different pressure. AIS, aeration impact sprinkler; IS, impact sprinkler.

Where DU_{lq} and DU_{hq} are water distribution uniformity coefficients in respect to the 25% lowest and highest parts of the data; N_{lq} and N_{hq} are a quarter of the total number catch can, and x_{lq} and x_{hq} are the collected irrigation depth that represents the highest part and lowest part, respectively. Similarly, Beale (1964) defined the water distribution uniformity coefficient DU by dividing the collected irrigation depth into two parts.

$$DU_{lh} = 2\sum_{i=1}^{N_{lh}} x_{lhi} \Big/ \sum_{i=1}^{N} x_i \tag{10}$$

$$DU_{hh} = 2\sum_{i=1}^{N_{hh}} x_{hhi} \Big/ \sum_{i=1}^{N} x_i \tag{11}$$

Where DU_{lh}, DU_{hh} is 50% low and the high water distribution uniformity coefficient, and N_{lh}, N_{hh} is half of the total number of the catch can.

3 Results and discussion

3.1 Water distribution radial curves of the single sprinkler test

The water distribution radial curves of the AIS and the IS were compared in Figure 5. It is apparent that when the operating pressure was increased, the jet range (wetted radius of throw) also increased. These two types of sprinklers have approximately the same jet range under the same operating pressure. The jet range is defined by the wetted boundary where the application rate is <0.25 mm/h (GB/T2299, 2008). The curves in Figure 5 were more uneven when the operating pressure was lower than the normal pressure, particularly at 150 kPa. There were three peaks on each curve that occurred near the sprinkler, at the middle jet range, and near the end of the jet range, respectively. Along with the radial direction, the three peak values were primarily caused by the strike movement of the impact sprinkler rocker arm, the auxiliary nozzle, and the main nozzle, respectively. The radial water distribution improved as the operating pressure increased, which was the reason why the range of normal operating pressure was specified in the IS standard. It can be observed from Figure 5 that the application rate of the AIS was a little lower than that of the IS near the end of jet range (the third peak value). This result showed that the jet breakup from the main nozzle differed when the aeration method was adopted. The auxiliary nozzle was designed for the original $20PY_2$ impact sprinkler that works under the specified pressure. With the increase in operating pressure, the peak value at the middle range tended to be reduced, as can be deduced from the 200 kPa −250 kPa in Figure 5. Moreover, some exceptional improvement is merited to render the auxiliary nozzle suitable for the AIS when the operating pressure is decreased.

The radial water distribution curve was used to simulate the sprinkler combined irrigation. It was convenient to change the parameters, such as the sprinkler interval distance or the layout forms (square, rectangular, and triangular among others) of the sprinkler in simulation method. The calculations were analyzed using a workstation that was programmed with FORTRAN, and the calculations of the water distribution were shown using TECPLOT software (Tecplot, Inc., Bellevue, WA, United States). The basic idea of simulation was to convert the discrete experiment points in Figure 5 into a continuous curve using the interpolation method, and then add the irrigation depth together at the location where the data overlapped. The researchers used simulation methods that had been previously described by Montero et al. (2001), Playán et al. (2006) and Li et al. (2015). The simulated results were compared with those of the outdoor experiment in this study.

3.2 Combined solid set sprinkler irrigation test

Combined sprinkler irrigation tests were conducted in a grassy field, which had a low wind velocity. The solid set sprinkler combination effect of technical, meteorological and agronomical factors were utilized as described Sanchez et al. (2010a), Sanchez et al. (2010b). The results of water losses are presented in Table 1.

As shown in Table 1, four AIS and four IS had nearly the same total flow rate under the same operating pressure, which is consistent with their experimental design. Based on Eq. 5, the water loss changed from 3% to 9.5% (Table 1). When the combination spacing coefficients became more significant, the ThID value decreased, and the TsID value also decreased, while the relationship between the CSC and the water loss was unclear. When the arithmetic means of water loss were compared, the AIS was found to have a smaller average value than that of the IS. Therefore, it can be concluded that the two types of sprinklers performed differently. Environmental parameters, such as humidity and air temperature, do not contribute much to water losses since they primarily affect water evaporation. The sprinkler water losses affected by weather factors primarily refer to the wind speed and slight

TABLE 1 Outdoor operational and metrological parameters of the solid set experiment with different pressures and lateral spacing.

Type of sprinkler	D + d (mm)	P kPa	Q m^3h^{-1}	Range (m)	CSC	Temp C ^{0}	RH (%)	U m/s	Th ID (mm/h)	Ts ID (mm/h)	Water loss η%
AIS	8.3 + 3.5	150	12.3	16	1	20.3	82	0.6	11.29	10.74	4.87
					1.1	28.5	65	1.3	9.33	8.73	6.43
					1.2	30.1	32	1.3	7.84	7.23	7.78
	8.3 + 3.5	200	13.3	17.5	1	27.3	65	1.6	10.85	9.89	8.85
					1.1	28.3	45	0.84	8.97	8.45	5.80
					1.2	30.2	24	0.4	7.54	7.01	7.03
	8.3 + 3.5	250	15.9	18.5	1	19.8	86	0.3	11.61	11.26	3.01
					1.1	19.1	89	0.3	9.5	8.79	7.47
					1.2	19.2	88	0.5	7.9	7.36	6.84
IS	7 + 3.5	150	12.4	16	1	24.8	54	0.7	11.38	10.54	7.38
					1.1	23.9	82	1.7	9.41	8.52	9.46
					1.2	30.3	45	0.7	7.91	7.39	6.57
	7 + 3.5	200	13.3	17.5	1	30.3	67	1.4	10.85	9.98	8.02
					1.1	26.7	72	1.03	8.97	8.24	8.14
					1.2	28.4	66	1.17	7.53	6.99	7.17
	7 + 3.5	250	15.8	18.5	1	27.5	64	0.95	11.39	10.82	5.00
					1.1	25.8	79	1.2	9.47	8.76	7.50
					1.2	30.6	31	1.14	8.06	7.49	7.07

Type of sprinkler, Diameter of the main and auxiliary nozzles (D, d, mm), Operating pressure (P, kPa), Combination spacing coefficient (CSC), Average sprinkler discharge (Q, m^3/h), Average air temperature (T, C°), Average air relative humidity (RH, %) Wind speed (U m/s), Theoretical irrigation depth (Th ID), Test irrigation depth (Ts ID) and Water loss (η%).

differences in the speed of rotating sprinklers, which causes slightly different rainfall in the studied test zone. In the outdoor test conditions, a hand-held anemometer was used to average three measurements every 15 min. The maximum value was 1.97 m/s, and the average value was 0.9 m/s, which was owing to the breeze. Thus, the drift loss was minor. Another reason for the small loss is that the test was conducted at a lower pressure, indicating that the droplets generated by low-pressure jet breakup are vulnerable to wind resistance. The results of water loss also indicated that the open-air test data of the AIS and IS were comparable.

3.3 Water uniformity affected by operating pressure

The spacing was set to 1R to compare the water uniformity under different pressures. The experimental data of water distribution were plotted in Figure 6, in which the x- and y-coordinates represented the side lengths of the square test zone. The difference in operating pressure led to differences in the sprinkler jet range, as well as the edge length of the test zone. The legend H represents the intensity of sprinkler irrigation. When the operating pressure increased from 150 kPa to 250 kPa, the total flow rate of the irrigation system increased, as indicated by the maximal legend value. It is apparent in the figure that the higher irrigation depth area was concentrated in the central (overlapped) region as shown in Figure 4, and the lower area of irrigation depth was distributed at the corner region near the sprinklers. Judging from the 2-D contour map in Figures 6A,B, the water distribution at the lowest test pressure of 150 kPa differed slightly from the others, so that some high irrigation depth areas occurred near the edges. The reason could be that the rotation speed of the sprinkler became slow and uneven at 150 kPa or was caused by the curve pattern of the single sprinkler radial water distribution curves as shown in Figure 5. When the water distribution of the two types of sprinklers was compared, the blue color area of the AIS was smaller than that of the IS, which indicates the lower irrigation depth was enhanced from using the aeration impact sprinkler and were verified by following uniformity coefficients.

The results of the coefficients calculated using Eqs (7–11) are shown in Table 2 to more clearly evaluate the uniformity.

Table 2 indicates that CU increased with the operating pressure for the two types of sprinklers. At the same operating pressure, the AIS had a 3.09%–5.25% larger CU value than that of the IS. Thus, this proved that the jet aeration method could improve the water distribution uniformity to some degree under the low pressure for solid set sprinkler irrigation. Since the wind velocity was low during the experiment, the operating pressures became the primary factors that affected the uniformity of the distribution of water. It is difficult to show the influence of massive deviation on water uniformity using the CU coefficient, and thus, the DU coefficient was adopted to compare the performance of combined sprinkler irrigation. As

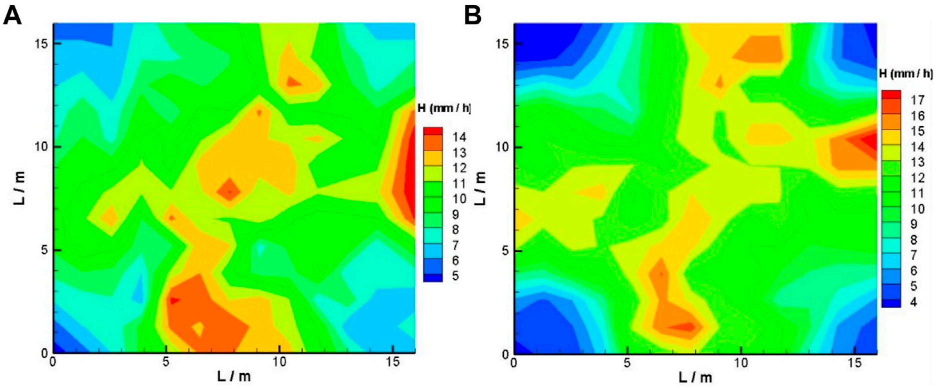

150 kPa AIS

150 kPa IS

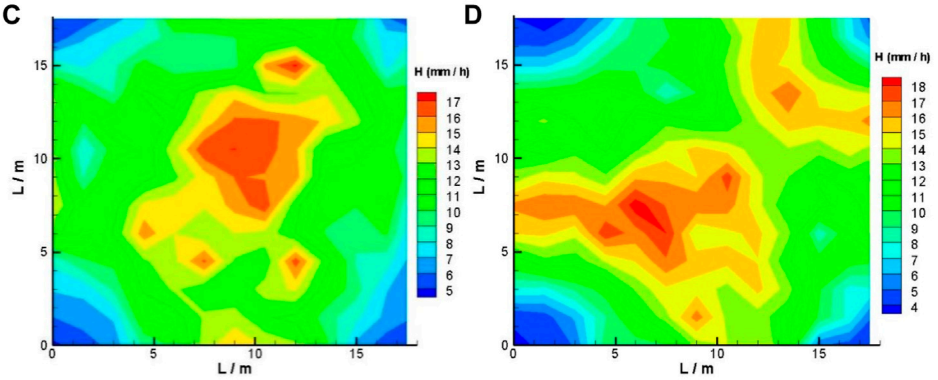

200 kPa AIS

200 kPa IS

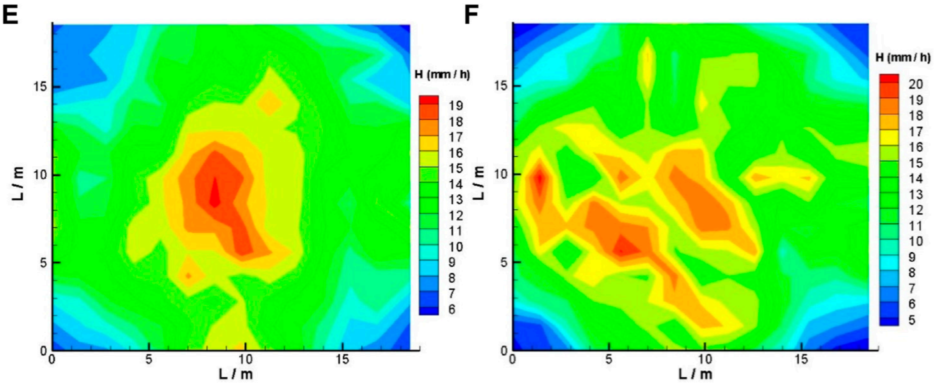

250 kPa AIS

250 kPa IS

FIGURE 6
Contour map of the experimental data with 1R lateral spacing and at different operating pressures. A, C, E for the AIS at 150, 200, and 250 kPa, and B, D, and F for the IS at the same pressure. AIS, aeration impact sprinkler; IS, impact sprinkler. **(A)**: 150 kPa AIS **(B)**: 150 kPa IS **(C)**: 200 kPa AIS **(D)**: 200 kPa IS **(E)**: 250 kPa AIS **(F)**: 250 kPa IS.

shown in Table 2, the coefficients DU_{lq} and DU_{lh} were <1. In addition, it could be observed that the DU_{lh} was slightly larger than that of the DU_{lq}. If these two coefficients are closer to 1, then the experimental data of lower irrigation depth is much less common, which indicates the uniformity of water distribution is good. Alternatively, if they are significantly >1, the results indicated that the irrigation was much less uniform. As shown in Table 2, when the operating pressure increased, the lower part of the DU coefficient also increased, and the upper part of DU decreased. This was similar to the tendency as indicated by the CU. The DU coefficients showed that the AIS was more effective than the IS. In the impact sprinkler standard (GB/T2299, 2008), the CU coefficient is specified as > 75% for the combined solid set sprinkler irrigation. When the combination spacing was 1 R in Table 2, and the operating pressure was 200 kPa, the CU coefficient of the AIS was larger than the specified value, while that of the IS was below the level. The jet aeration method can decrease approximately 50 kPa degrees of the operating pressure

TABLE 2 Results of water uniformity coefficients with a 1R combination spacing coefficient.

Operating pressure (kPa)	Sprinkler	CU%	DU_{lq}	DU_{hq}	DU_{lh}	DU_{hh}
150	AIS	71.37	0.605	1.360	0.721	1.279
	IS	68.28	0.530	1.452	0.649	1.350
200	AIS	78.59	0.688	1.283	0.774	1.227
	IS	73.34	0.629	1.381	0.730	1.269
250	AIS	80.67	0.711	1.257	0.826	1.174
	IS	76.85	0.662	1.353	0.795	1.205

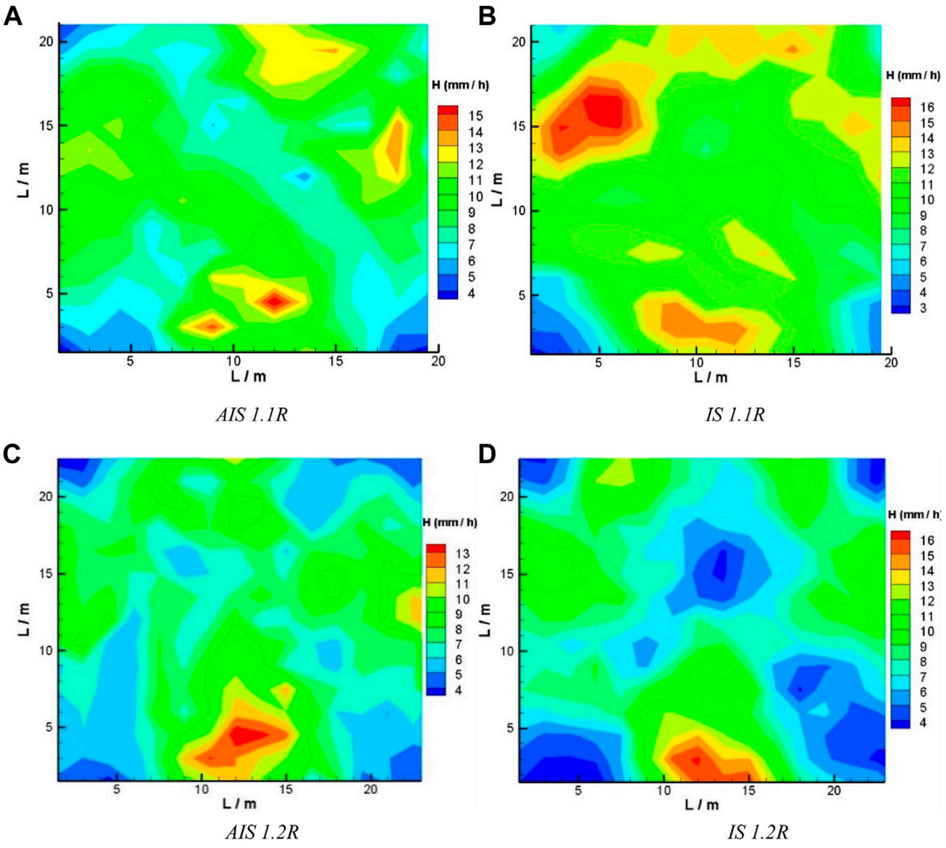

AIS 1.1R

IS 1.1R

AIS 1.2R

IS 1.2R

FIGURE 7
Contour map of the experimental data with an operating pressure of 250 kPa with different lateral spacing. AIS, aeration input sprinkler; IS, input sprinkler. **(A)**: AIS 1.1R **(B)**: IS 1.1R **(C)**: AIS 1.2R **(D)**: IS 1.2R.

for the $20PY_2$ impact sprinkler. At 150 kPa of pressure, the CU coefficients of both the IS and AIS did not reach the specified value. Furthermore, there is still room to enhance the water uniformity at even lower pressure using the aeration method. Research by Zhang et al. (2013) shows that substantial energy savings were achieved, and the CO_2 emissions were reduced as the low-pressure pipeline irrigation was adopted. Thus, it is safe to conclude that reducing the operating pressure of the sprinkler will lead to a decrease in the pressure of sprinkler irrigation system.

3.4 The uniformity of water distribution was affected by different combinations of spacing

The operating pressure was set as 250 kPa to compare the uniformity of water distribution with different spacing. The outdoor experiment was conducted under the CSC set as 1, 1.1, and 1.2. The results of 1R are plotted in Figures 6E,F, and the results of 1.1R and 1.2R are plotted in Figure 7. It is apparent that the peak value of irrigation depth decreased when the

TABLE 3 Results of water uniformity coefficients with 250 kPa operating pressure.

Sprinkler	CSC	CU/%	DU_{lq}	DU_{hq}	DU_{lh}	DU_{hh}
AIS	1.1	80.54	0.696	1.343	0.769	1.231
IS	1.1	73.32	0.640	1.379	0.733	1.267
AIS	1.2	75.13	0.629	1.36	0.733	1.267
IS	1.2	72.93	0.593	1.398	0.729	1.271

combination spacing coefficient increased. This is consistent with the trends shown in Table 1 that indicated that the average irrigation depth decreased. With the same CSC, the peak value of the AIS was slightly lower than that of the IS, suggesting that the water distribution uniformity differed for the two types of sprinklers. The overlap zone changed when the CSC increased, so the peak value did not occur in the center area of the test zone as shown in Figure 7.

The calculated uniformity coefficients are shown in Table 3 to evaluate the water distribution uniformity that changed with CSC.

It is apparent from Tables 2, 3 at 250 kPa operating pressure that with different CSC, the uniformity coefficients of the AIS are better than those of the IS. In particular, when the CSC was 1.1, the AIS had a CU value that was 7.22% larger than that of the IS. The purpose of increasing the lateral spacing was to find a suitable combination to optimize the irrigation performance of sprinklers. When the sprinkler was applied during the actual engineering application, the number of sprinklers could be reduced by increasing the lateral spacing, and the cost of irrigation system would be reduced under the premise that the water uniformity meets the requirement. As shown in Table 3, the CU decreased slightly with the increase in CSC, so that the 1R arrangement can obtain the best uniformity coefficients. If the requirement of the water uniformity was established as the standard value of >75% at an operating pressure of 250 kPa, the AIS can still meet the requirements when the CSC increased to 1.2, but the IS cannot meet them even at a CSC value of 1.1. The differences in sprinkler performance were shown when the CSC increased. Based on the conclusions from previous researchers, the irrigation water distribution follows the laws of a normal distribution when the CU > 70%, and the relationship between the CU and DU is approximately linear. There were 18 data samples in this study, including three levels of operating pressure, three types of CSC, and two types of sprinklers under a low wind speed. The fitting curve between DU_{lq} and CU also shows a linear relationship as indicated in Eq. 12.

$$DU_{lq} = 1.01 \cdot CU - 10.9 \left(r^2 = 0.92, n = 18\right) \tag{12}$$

Where r^2 is the correlation coefficient, and n is the sample number. The CU changed from 61% to 81% in Eq. (12), and this relationship coincided with that of Li and Kawano (1995).

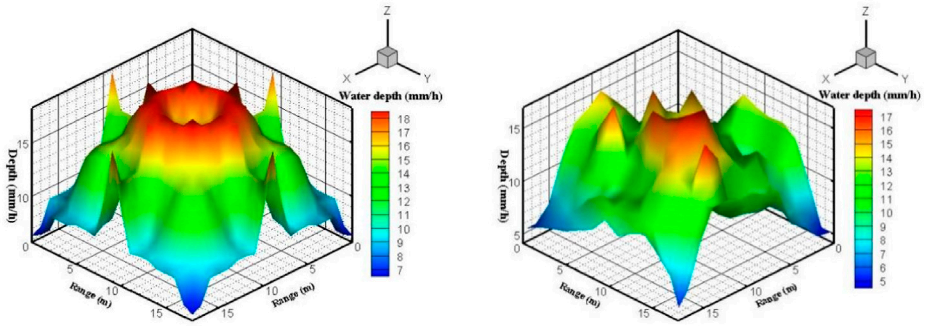

200 kPa AIS Simulate   *200 kPa AIS Experiment (Fig. 6c)*

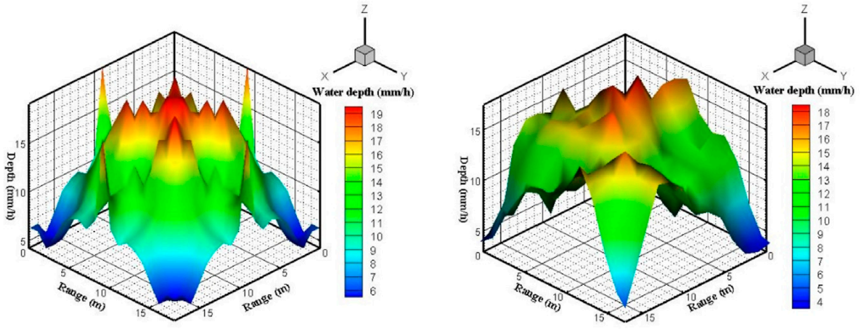

200 kPa IS Simulation   *200 kPa IS Experiment (Fig. 6d)*

FIGURE 8
Simulated 3-D graph of the AIS and the IS and compared with experimental data. AIS, aerated impact sprinkler; IS, impact sprinkler. 200 kPa AIS Simulate 200 kPa AIS Experiment (Figure 6C) 200 kPa IS Simulation 200 kPa IS Experiment (Figure 6D).

TABLE 4 The Comparison of the simulated sprinkler irrigation with the outdoor experimental results.

Type of sprinkler	Pressures (kPa)	CSC	Sim. ID (mm/h)	ID error%	CU	Sim. CU	CU error%	DU_{lq}	Sim. DU_{lq}	DU_{lq} error %
AIS	150	1	10.9	3.5	71.3	73.3	2.8	0.605	0.625	3.4
		1.1	8.1	13.2	69.4	72.1	4.0	0.613	0.639	4.2
		1.2	7.0	10.7	63.4	66.6	5.1	0.552	0.593	7.5
	200	1	11.7	7.8	78.5	78.4	0.2	0.688	0.729	6.0
		1.1	9.6	7.0	78.4	76.3	2.6	0.692	0.701	1.4
		1.2	7.5	0.5	74.7	76.9	3.0	0.654	0.66	0.9
	250	1	10.9	6.1	80.6	80.2	0.4	0.711	0.734	3.3
		1.1	8.8	7.3	80.5	82.7	2.7	0.696	0.71	2.1
		1.2	7.2	8.8	75.1	78.6	4.6	0.629	0.682	8.4
IS	150	1	10.2	10.3	68.2	70.0	2.5	0.530	0.568	7.2
		1.1	7.7	18.1	66.5	69.5	4.5	0.553	0.59	6.7
		1.2	6.5	17.8	61.2	65.5	6.9	0.504	0.533	5.9
	200	1	11.1	2.3	73.3	75.1	2.3	0.629	0.656	4.3
		1.1	9.3	3.6	72.6	76.2	4.9	0.617	0.655	6.2
		1.2	7.1	5.7	69.3	73.5	6.0	0.576	0.621	7.8
	250	1	10.7	6.0	76.8	79.8	3.8	0.662	0.669	1.1
		1.1	8.4	11.3	73.3	78.1	6.5	0.640	0.687	7.4
		1.2	7.0	13.1	72.9	77.1	5.7	0.593	0.622	5.0

3.5 Comparison of the uniformity of water distribution of the AIS and IS using simulated and experimental data

To illustrate the effect of simulation, The operation condition results of Figures 6C,D were plotted in 3-D, as shown in Figure 8.

As indicated from the graph of simulated water distribution, the peaks and valleys of the AIS and the IS occur in pairs because the radial water distribution curves in Figure 5 are similar. The simulated result of the AIS near the square center is more uniform than that of the IS. A side peak value appeared near the middle edge position of the square that is consistent with the experiment. The simulated maximal water depth is shown in the legend, which was consistent with the experimental data. The simulated water distribution graph was similar to the experimental results when the CSC was 1R. However, when the CSC increased, the simulated graph began to differ from that of the experimental water distribution.

Based on Eq. 1, the simulated collected irrigation depths were obtained. The simulated mean irrigation depth (Sim. ID) can be obtained as Eq. 3, and the simulated water uniformity coefficients can be calculated as Eqs 7–11. The results are shown in Table 4 and analyzed with the outdoor experimental data.

All the experimental results of CU are shown in Table 4, which changed from 61% to 81%. The maximal error between the simulation CU and experimental results was approximately 7%. Therefore, the error of DU_{lq} was acceptable. Since the low wind speed had little effect on water droplets flying in the air in the outdoor experimental conditions, the sprinkler irrigation intensity in the test zone was barely influenced. Thus, the results of simulated water distribution uniformity provide a useful reference for the comparison of the AIS and the IS performances. In all the test schemes, both the experiment and simulation show that the AIS have higher values of average CU and average DU_{lq} than the IS, proving that the aeration method could improve the water uniformity under the low operating pressure. The results of simulated water distribution uniformity were primarily affected by the pattern of the radial water distribution curve in the combined sprinkler irrigation. The results of these simulations could be useful for the optimal design of the sprinkler and for determining the optimal combination parameters, such as layout or lateral spacing.

In Table 4, the simulation results of the mean irrigation depth deviated far from the theoretical ThID that was listed in Table 1. That indicates that there is high error between the total calculations of the amount of water that fell in the test zone and the water measured by the electromagnetic flow meter. This error could be caused by the sprinkler step rotation speed, by the fitted curves of radial water distribution and by the meteorological parameters.

4 Conclusion

In this study, the structure of an aeration impact sprinkler is introduced, which functions as a liquid-gas two-phase jet spray. The performance of $20PY_2$ impact sprinkler and the aerated sprinkler were compared by a combination of sprinkler irrigation experiments conducted under low operating pressures. The outdoor experiment was conducted on a flat lawn and under breezy environmental conditions. The water distribution was simulated based on indoor experiment results of the single sprinkler. Operating pressure and combination spacing were found to be the primary factors that affect the irrigation performance. The main conclusions are presented as follows.

1) The water loss measured from the two types of sprinklers ranged from 3% to 9.5%, which means that the open-air test data of the AIS and the IS are comparable. Thus, only a small influence was generated by the environmental conditions.
2) The water distribution uniformity coefficient of the AIS is higher than that of the IS under lower operating pressure. The coefficient of CU improved by approximately 3%–7% in all 18 test schemes, and the DU_{lq} was approximately 0.5 using the AIS. There is a linear relationship between CU and the DU_{lq}.
3) The simulation method developed in this study is reliable at predicting the water uniformity but is difficult to predict the water loss. Moreover, the simulation work is useful for studying the flexible pattern of the radial water distribution curve.
4) A sprinkler water jet with the aeration method was proven to be a feasible solution to decrease the sprinkler operational pressure owing to the improvement in water uniformity coefficient. In addition, it met the requirements for the specified value in standard as the AIS functions at low pressure.

Data availability statement

The original contributions presented in the study are included in the article/Supplementary Material, further inquiries can be directed to the corresponding author.

Author contributions

WQ conceived and designed the study and completed the paper in English. QX and ZX revised it critically for important intellectual content and gave good research advice and revised the manuscript. All authors have read and agreed to the published version of the manuscript.

Funding

This work was supported by the National Natural Science Foundation of China (Grant No 51939005). The artical was supported by Key R&D Project of Jiangsu Province (Modern Agriculture), No. BE2022351.

Conflict of interest

The authors declare that the research was conducted in the absence of any commercial or financial relationships that could be construed as a potential conflict of interest.

Publisher's note

References

Beale, J. G. (1964). *Distribution uniformity of sprinkler irrigation systems*. Sydney: University of NSW.

Branscheid, V. O., and Hart, W. E. (1986). Predicting field distribution of sprinkler systems. *Trans. ASAE* 11, 801–803.

Cai, D. Y., Yan, H. J., and Li, L. H. (2020). Effects of water application uniformity using a center pivot on winter wheat yield, water and nitrogen use efficiency in the North China Plain. *J. Integr. Agric.* 19 (9), 2326–2339. doi:10.1016/S2095-3119(19)62877-7

Christiansen, J. E. (1942). *Irrigation by sprinkling. California agricultural experiment station bulletin*, 670. Berkeley: University of California.

Criddle, W. D. (1956). Method for evaluating irrigation systems. *Agric. Handb.* 82, 2–11.

Deng, J., Xu, W. L., and Qu, J. X. (2002). Influence of aeration on scouring. *J. Hydraulic Eng.* (10), 8–13. (in Chinese).

GB/T2299. 2008. Rotating sprinkler. National standard of people's republic of China. (in Chinese).

Huffman, R. L., Fangmeter, D. D., and William, J. E. (2013). "Sprinkler irrigation," in *Mich. Soil and water conservation engineering* Editor St. Joseph 7th Edition (ASABE), 403–435. Chapter 17 doi:10.13031/swce.2013.17

ISO 7749-2 (1990). *Irrigation equipment - rotating sprinklers - Part 2: Uniformity of distribution and test methods. British standard.*

Lefebvre, A. H., Wang, X. F., and Martin, C. A. (1988). Spray characteristics of aerated-liquid pressure atomizers. *J. Propuls. Power* 4 (4), 293–298. doi:10.2514/3.23066

Li, J., Kawano, H., and Yu, K. (1994). Droplet size distributions from different shaped sprinkler nozzles. *Trans. ASAE* 37, 1871–1878. doi:10.13031/2013.28278

Li, J. S., and Kawano, H. (1995). Simulating water-drop movement from noncircular sprinkler nozzles. *J. Irrigation Drainage Eng.* 121 (2), 152–158. doi:10.1061/(asce)0733-9437(1995)121:2(152)

Li, Y. C., Bai, G., and Yan, H. J. (2015). Development and validation of a modified model to simulate the sprinkler water distribution. *Comput. Electron. Agric.* 111, 38–47. doi:10.1016/j.compag.2014.12.003

Liu, J. P., Yuan, S. Q., Li, H., and Zhu, X. (2011). Combination uniformity improvement of impact sprinkler. *Trans. Chin. Soc. Agric. Eng.* 27 (7), 107–111. doi:10.3969/j.issn.1002-6819.2011.07.018

Louie, M. J., and Selker, J. S. (2000). Sprinkler head maintenance effects on water application uniformity. *J. Irrigation Drainage Eng.* 126, 142–148. doi:10.1061/(asce)0733-9437(2000)126:3(142)

Montazar, A., and Sadeghi, M. (2008). Effects of applied water and sprinkler irrigation uniformity on alfalfa growth and hay yield. *Agric. Water Manag.* 95, 1279–1287. doi:10.1016/j.agwat.2008.05.005

Montero, J., Tarjuelo, J., and Carrión, P. (2001). Sirias: A simulation model for sprinkler irrigation. *Irrigation Sci.* 20, 85–98. doi:10.1007/s002710000032

Playán, E., Zapata, N., Faci J, M., Tolosa, D., Lacueva, J., Pelegrin, J., et al. (2006). Assessing sprinkler irrigation uniformity using a ballistic simulation model. *Agric. Water Manag.* 84, 89–100. doi:10.1016/j.agwat.2006.01.006

Sanchez, I., Faci, J. M., and Zapata, N. (2011). The effects of pressure, nozzle diameter and meteorological conditions on the performance of agricultural impact sprinklers. *Agric. Water Manag.* 102 (1), 13–24. doi:10.1016/j.agwat.2011.10.002

Sanchez, I., Zapata, N., and Faci, J. M. (2010b). Combined effect of technical, meteorological and agronomical factors on solid-set sprinkler irrigation: II. Modifications of the wind velocity and of the water interception plane by the crop canopy. *Agric. Water Manag.* 97 (10), 1591–1601. doi:10.1016/j.agwat.2010.05.013

Sanchez, I., Zapata, N., and Faci, J. M. (2010a). Combined effect of technical, meteorological and agronomical factors on solid-set sprinkler irrigation: I. Irrigation performance and soil water recharge in alfalfa and maize. *Agric. Water Manag.* 97 (10), 1571–1581. doi:10.1016/j.agwat.2010.05.012

Schneider, A. D. (2000). Efficiency and uniformity of the lepa and spray sprinkler methods: A review. *Trans. Am. Soc. Agric. Eng.* 43 (4), 937–944. doi:10.13031/2013.2990

Sourell, H., Faci, J. M., and Playán, E. (2003). Performance of rotating spray plate sprinklers in indoor experiments. *J. Irrigation Drainage Eng.* 129 (5). doi:10.1061/(asce)0733-9437(2003)129:5(376)

Stambouli, T., Zapata, N., and Faci, J. M. (2014). Performance of new agricultural impact sprinkler fitted with plastic nozzles. *Biosyst. Eng.* 118, 39–51. doi:10.1016/j.biosystemseng.2013.11.002

Tarjuelo, J. M., Montero, J., Valiente, M., Honrubia, F. T., and Ortiz, J. (1999). Irrigation uniformity with medium size sprinklers Part I: Characterization of water distribution in no-wind conditions. *Trans. Am. Soc. Agric. Eng.* 42, 665–676. doi:10.13031/2013.13228

Vories, E. D., Von Bernuth, R. D., and Mickelson, R. H. (1987). Simulating sprinkler performance in wind. *J. irrigation drainage Eng.* 113 (1), 119–130. doi:10.1061/(asce)0733-9437(1987)113:1(119)

Wang, Z. J., Hui, X., and Li, Y. J. (2019). Optimization of nozzle structure and investigation on hydraulic performance of impact sprinkler. *J. Hydraulic Eng.* 50 (4), 488–496. (in Chinese). doi:10.13243/j.cnki.slxb.20180660

Xiang, Q. J., Qureshi, W. A., Tunio, M. H., Solangi, K. A., Xu, Z., and Lakhiar, I. A. (2021). Low-pressure drop size distribution characterization of impact sprinkler jet nozzles with and without aeration. *Agric. Water Manag.* 243, 106458. doi:10.1016/j.agwat.2020.106458

Xiang, Q. J., Xu, Z. D., Chen, C., and Li, H. (2016). Experiment on aeration water jet applied to low pressure impact sprinkler irrigation. 32 (16), 54–58. (in Chinese). doi:10.11975/j.issn.1002-6819.2016.16.008

Xu, Z. D., Xiang, Q. J., and Qureshi, W. A. (2018). Field combination experiment on impact sprinklers with aerating jet at low working pressure. *J. drainage irrigation Mach. Eng. (JDIME)* 36 (9), 841–845. (in Chinese).

Zakaria, I., Li, H., Jiang, Y., Tang, P., and Chao, C. (2018) Influence of fixed water dispersion devices on water distribution uniformity under different spacing and layouts for impact sprinkler *ASABE 2018 Annu. Int. Meet.* doi:10.13031/aim.201800020

Zhang, Q. T., Xia, Q., Clark, C. K., and Geng, S. (2013). Technologies for efficient use of irrigation water and energy in China. *J. Integr. Agric.* 12 (8), 1363–1370. doi:10.1016/S2095-3119(13)60544-4

Zhu, X. Y., Fordjour, A., Yuan, S. Q., Dwomoh, F., and Ye, D. (2018). Evaluation of hydraulic performance characteristics of a newly designed dynamic fluidic sprinkler. *Water* 10, 1301. doi:10.3390/w10101301

frontiers | Frontiers in Energy Research

TYPE Original Research
PUBLISHED 06 April 2023
DOI 10.3389/fenrg.2023.1177437

OPEN ACCESS

EDITED BY
Yongfei Yang,
Nantong University, China

REVIEWED BY
Bing Qi,
Lanzhou University of Technology, China
Yonghai Yu,
Hohai University, China
Banglun Zhou,
Guizhou Institute of Technology, China

*CORRESPONDENCE
Mengcheng Wang,
✉ jdwmc2018@163.com

SPECIALTY SECTION
This article was submitted to Process and Energy Systems Engineering, a section of the journal Frontiers in Energy Research

RECEIVED 01 March 2023
ACCEPTED 22 March 2023
PUBLISHED 06 April 2023

CITATION
Chen J, Wang M, Bao Y, Chen X and Xia H (2023), Mixed-flow pump performance improvement based on circulation method.
Front. Energy Res. 11:1177437.
doi: 10.3389/fenrg.2023.1177437

Mixed-flow pump performance improvement based on circulation method

Jiaqi Chen[1], Mengcheng Wang[2]*, Yonghao Bao[2], Xiao Chen[3] and Hepeng Xia[4]

[1]National Research Center of Pumps, Jiangsu University, Zhenjiang, China, [2]College of Electrical, Energy and Power Engineering, Yangzhou University, Yangzhou, China, [3]Anhui Ding Yuan Engineering Construction Co., Hefei, China, [4]Jiangsu Province Water Engineering Sci-tech Consulting Co., Nanjing, China

Mixed-flow pumps have been extensively employed in daily life, improving their energy characteristics contribute to the reduction of energy consumption worldwide. In this study, to overcome the decrease of optimization upper limit caused by using a single type of parameter as the design parameter, a typical mixed-flow pump was chosen for study, and its impeller was parameterized by five geometric and eight hydrodynamic parameters. With head and efficiency as the constraint and optimization objective respectively, 27 schemes were constructed by the Taguchi method. The influence of design factors to the objective and constraint was analyzed based on range and regression analysis. The optimization mechanism was elucidated using the entropy production method. The result reveals that the geometric and hydrodynamic parameters have a significantly impact on the mixed-flow pump's energy characteristics. The optimized model head is 12.43m, which meets the constraints, while the efficiency increases by 3.2%–88.51%. Therefore, considering both geometric and hydrodynamic parameters in the mixed-flow pump optimization is workable and necessary. This paper can provide practical instructions on the optimal design of different turbomachines.

KEYWORDS

pump, coupling optimization, circulation method, geometric and hydrodynamic parameters, numerical simulation

1 Introduction

As a general-purpose machine, pumps have been extensively employed in daily life, especially mixed-flow pumps with moderate head and large flow rates, which are highly sought after (Kim et al., 2019; Wang et al., 2021a). However, the energy consumption of pumps is also staggering, with recent studies showing that their share of total energy consumption exceeds 22%, and is set to increase further to over 30% in the next decade (Gu et al., 2022a). Hence, improving the energy conversion efficiency of mixed-flow pumps is very important.

Among the many in-depth studies on turbomachinery design optimization, Zangeneh (1991) creatively proposed the circulation method, which uses hydrodynamic parameters (circulation, pressure and loading, etc) as design parameters in the blade parameterization. The greatest advantage of the circulation method is the close connection between parameters and hydraulic performance (Lu et al., 2018; Zhang and Zhao, 2020), as well as easier access to innovative solutions (Yin and Wang, 2014; Fallah-Ardeshir et al., 2020). More importantly, the design results obtained by the circulation method represents the optimal flow field distribution rather than the best combination of geometric parameters, which can provide designers with more valuable references in future optimization studies (Leguizamon and Avellan, 2020; Gu et al., 2022b).

The effectiveness of the circulation method was extensively demonstrated in previous study. Zangeneh et al. (1996) successfully suppressed the secondary flow within a mixed flow pump using the circulation method in an optimization study. In subsequent work, Goto et al., 1996) verified the validity of this work through experiments. Huang et al. (2015) using blade loading as design parameters carried out a parametric optimization for the impeller of a mixed-flow pump, and found that changing the position of the first loading point can effectively inhibit the blade suction surface flow separation. Bonaiuti et al. (2010) investigated the effectiveness of the circulation method in mixed-flow water-jet pumps by varying impeller outlet circulation distribution. They found that the hydraulic mixing losses near the diffuser outlet and the secondary flow losses in the diffuser can be effectively balanced by adjusting the value of the diffuser outlet residual circulation. In another study (Bonaiuti and Zangeneh, 2009), they investigated the compressor diffuser and impeller coupling optimization by changing the loading pattern at the hub and shroud. Ma et al. (2019) performed a performance improvement for a turbine runner by circulation method, and investigated the effect of several key hydrodynamic factors on the Francis turbine runner by model comparison. Yang and Xiao (2014) conducted a similar study on a Pump-Turbine impeller and successfully improved the model's efficiency in both turbine and pump mode. Lee et al. (2008) optimized an axial fan using the Taguchi method with blade leading edge loading and loading pattern as design parameters. According to the idea of Taguchi's method, Yang et al. (2017) investigated the impact of loading distribution to a submersible axial flow pump. Wang et al. (2022) compared the advantages and disadvantages of three different circulation distributions in mixed-flow pump design optimization by coupling Taguchi and circulation method.

An obvious similarity between the above studies is that only hydrodynamic parameters were used as design parameters. However, some studies have shown that geometric parameters also greatly influence the performance of turbomachinery. Using the control parameters of the meridional plane as design parameters, a mixed-flow pump overall performance have been successfully improved by Suh et al. (2019). By modifying the position of the shroud, the effect of overflow area on the impeller energy characteristics was investigated by Bing et al. (2013). Shim et al. (2018) improved a mixed-flow pump flow recirculation and cavitation performance by modifying the position of the blade inlet, as well as the hub and shroud profile. Si et al. (2020) completed the optimization of an automotive electronic pump with inlet and outlet diameter as design parameters, as well as blade number. Taking the arc radius and angle of the hub and shroud as design parameters, the cooling water pump used in nuclear plants was improved in its operational efficiency by Pei et al. (2016). Overall, it is necessary to take into account the presence of geometrical parameters in the optimized design, as they can effectively affect the turbomachinery's performance.

This work aims to research the impact of hydrodynamic and geometric parameters on mixed-flow pump performance in a bid to improve its performance further. Optimization based on the Taguchi method was adopted to improve the energy characteristics of the impeller by coupling its geometric and hydrodynamic parameters. The parameters' main and secondary effect were then determined by range analysis, and the equations between design parameters and objectives were established by regression variance analysis. Finally, the flow loss visualization technique was employed to clarify the optimization mechanism.

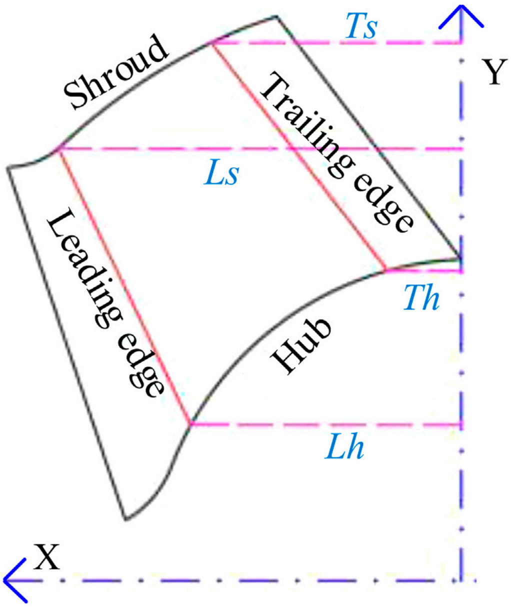

FIGURE 1
Meridional plane of the original model impeller.

TABLE 1 Original model design parameters.

Item	Symbols	Value
Design head	H_d	12.66 m
Design flow rate	Q_d	0.42 m^3/s
Impeller blade number	B	4
Impeller diameter	D	320 mm
Impeller hub radius	R_h	115 mm
Impeller shroud radius	R_s	195.3 mm
Rotating speed	N	1,450 rpm
Specific speed	n_s	511

2 Methodology

2.1 Calculation setup and validation

2.1.1 Original model and geometric parameter definition

The original model chosen for this investigation is a mixed-flow pump used in coastal pumping stations. Figure 1 is the impeller

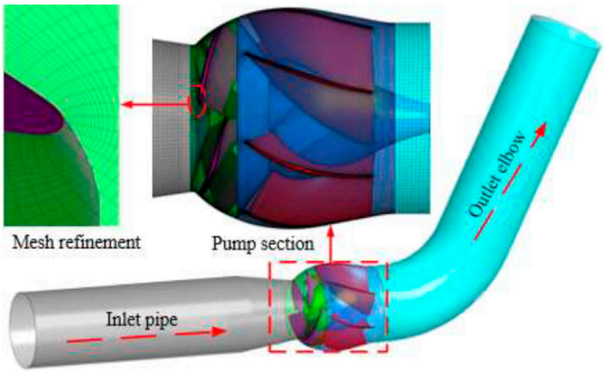

FIGURE 2
Mesh division.

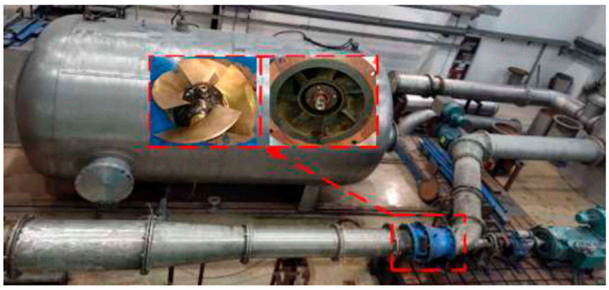

FIGURE 3
Test bench.

TABLE 2 Mesh-independence analysis results.

Scheme	1	2	3	4	5
Inlet pipe $(\times 10^6)$	0.19	0.43	0.83	1.18	1.67
Impeller $(\times 10^6)$	0.31	0.63	1.40	1.72	2.41
Diffuser $(\times 10^6)$	0.39	0.70	1.42	1.87	2.69
Outlet elbow $(\times 10^6)$	0.41	0.48	0.95	1.33	1.72
Overall $(\times 10^6)$	1.30	2.34	4.60	6.10	8.49
Efficiency (%)	83.72	84.53	85.11	85.12	85.11
Head (m)	12.03	12.13	12.11	12.11	12.11

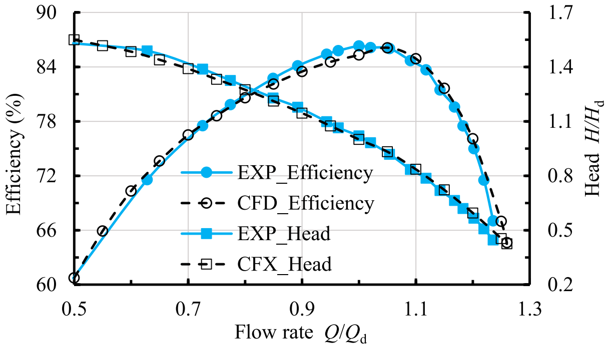

FIGURE 4
Comparison between experimental and predicted performance.

meridional plane, where the X-axis indicates the rotation axis, and the intersection of the Y-axis and X-axis is the circle center of the shroud and hub profile. *Ls* and *Lh* are the distances from the intersection of the blade leading edge with shroud and hub to the Y-axis, respectively. Similarly, *Ts* and *Th* are the distances from the intersection of the blade trailing edge with shroud and hub to the Y-axis, respectively. Table 1 lists the model's major design parameters.

2.1.2 Original model and geometric parameter definition

A calculation domain (Figure 2), consisting of four components—the output elbow, diffuser, impeller and inlet pipe—was constructed to ensure that the numerical simulation accurately reflects the experimental condition. To improve the computational convergence and accuracy, structured meshes with O-type topology were used to mesh the outlet elbow and inlet pipe in ANSYS-ICEM, and hexahedral structured meshes with H/C-type and O-type topologies were used to mesh the impeller and diffuser in ANSYS-Turbogrid. For the same purpose, all the meshes near the walls were refined.

The mesh-independence analysis results are presented in Table 2. When the number of grids is greater than 4.6 million, the calculated values of head and efficiency almost not change with the number of grids. Therefore, after taking into account the cost and accuracy of the calculation, scheme 3 was adopted for meshing the computational domain in this study, and the maximum Y+ near the wall is 46.

2.1.3 Original model and geometric parameter definition

The commercial software ANSYS-CFX was employed in this study to perform the full-channel numerical simulation of mixed-flow pumps with the help of k–ω shear stress transport turbulence model. "Opening" and "Mass flow rate" were employed in the outlet and inlet, respectively. The interface between the rotating and fixing parts is "Frozen rotor". The convective term was discretized by "High resolution". "Automatic wall function" and "No slip wall" were employed for all walls (Menter, 1994; Menter et al., 2003; Hieninger et al., 2021). The number of iterative steps was set to 1,000 and the convergence criterion was set to 10^{-5}.

2.1.4 Experimental verification

A closed test stands at Jiangsu University (Figure 3) with comprehensive uncertainty of 0.28% was used to test the performance of the original model to check the numerical simulation accuracy. The following is the description of the main equipments and their accuracy: EJA intelligent differential pressure transmitters with 0.1% accuracy, JCL1 intelligent torque-speed sensor with 0.1% accuracy, OPTIFLUX 2000F intelligent electromagnetic flowmeter with 0.2% accuracy, CY200 pressure sensors with 0.1% accuracy.

Figure 4 gives the comparison of the original model prediction results with the experimental results. The predicted performance can be seen highly consistent with the experimental performance in the range of $0.5Q_{\mathrm{des}}$ to $1.3Q_{\mathrm{des}}$, and the largest error between them does not exceed 2.5%. Hence, it can be considered that the numerical simulation has adequate precision to guarantee the credibility of this study.

2.2 Circulation method and validity verification

2.2.1 Governing equation

The proved circulation method based on the inviscid assumption was adopted to parameterize the blade (Zangeneh et al., 1998). To save space, only a brief description of the core computation was given here; for more details, please refer to the original literature (Zangeneh, 1991). In flow field calculation, velocity was divided into circumferential average and periodic velocity, which can be calculated by the following equations.

$$\frac{\partial}{\partial r}\left(\frac{1}{rB_f}\frac{\partial \varphi}{\partial r}\right)+\frac{\partial}{\partial z}\left(\frac{1}{rB_f}\frac{\partial \varphi}{\partial z}\right)=\frac{\partial r\bar{V}_\theta}{\partial z}\frac{\partial f}{\partial r}-\frac{\partial r\bar{V}_\theta}{\partial r}\frac{\partial f}{\partial z} \tag{1}$$

$$\begin{aligned}\frac{\partial^2\Phi_m}{\partial r^2}+\frac{1}{r}\frac{\partial\Phi_m}{\partial r}+\frac{\partial^2\Phi_m}{\partial z^2}-\frac{m^2B^2}{r^2}\Phi_m\\ =\frac{e^{-imBf(r,z)}}{imB}\left(\nabla^2 r\overline{V_\theta}\right)-e^{-imBf(r,z)}\left(\frac{\partial f}{\partial r}\frac{\partial r\overline{V_\theta}}{\partial r}+\frac{\partial f}{\partial z}\frac{\partial r\overline{V_\theta}}{\partial z}\right)\end{aligned} \tag{2}$$

where φ represents the stream function; Φ_m represents the potential function; z represents the axial coordinate; r represents the radial coordinate; i represents the imaginary unit; i represents the wrap angle; m represents the number of Fourier expansion terms; B represents the blade number; B_f represents the blocking factor; $\overline{V_\theta}$ represents the circumferential-averaged tangential velocity.

The blade shape was calculated by Eq. 3

$$\left(\overline{V_z}+v_z\right)\frac{\partial f}{\partial z}+\left(\overline{V_r}+v_r\right)\frac{\partial f}{\partial r}=\frac{r\overline{V_\theta}}{r^2}+\frac{v_\theta}{r}-\omega \tag{3}$$

where ω represents the angular velocity; v represents the periodic velocity; $\bar{V}$ represents the circumferential-averaged velocity.

2.2.2 Hydrodynamic parameter definition

From the control equation, it is clear that the parameter $r\overline{V_\theta}$ has a decisive influence on the calculation results of the circulation method. Hawthorne et al. (1984) and Nahon et al. (2021) pointed out that $r\overline{V_\theta}$ and blade pressure were related by Eq. 4:

$$\Delta p=p^{+}-p^{-}=\frac{2\pi}{B}W_s\frac{\partial r\overline{V_\theta}}{\partial s} \tag{4}$$

where W_s represents the relative velocity on the meridional plane; p^- represents the suction surface static pressure; p^+ represents the pressure surface static pressure.

Therefore, to facilitate the blade pressure control, blade loading ($\partial r\overline{V_\theta}/\partial s$) at shroud and hub was controlled by the segmented curve in the circulation method (Figure 5), where LE denotes the preloading, ND denotes the second loading point, NC denotes the first loading point, K denotes the straight line slope. It should be noted that only the blade loading at the hub and shroud was controlled by the above segmented curve, while the blade loading at other positions on the meridional plane was obtained by linear interpolation.

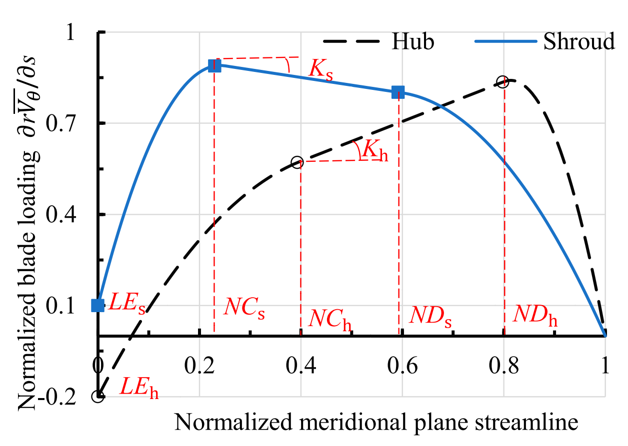

FIGURE 5
Hydrodynamic parameters definition schematic.

3 Optimization design based on Taguchi method

3.1 Optimization targets and test factors

To make the optimized mixed-flow pump have better energy characteristics and similar head, the head and efficiency at $1.0Q_{\mathrm{des}}$ were taken as the constraint and optimization target in this study.

The hub ratio was maintained during the optimization process to provide a better match between the diffuser and the optimized impeller (Wang et al., 2021b). Thus, in the parameterization of the impeller, the geometric parameters Lh, Ls, Th and Ts shown in Figure 1 were used for the parametrization of the meridional plane, and the hydrodynamic parameters LE_h, NC_h, ND_h, K_h, LE_s, NC_s, ND_s and K_s shown in Figure 5 were used for the blade parametrization. Zhu et al. (2018) indicated that the inclination angle at blade trailing edge (ST) has a large influence on the calculation results of the circulation method; therefore, ST was also selected as a test factor in this study. To facilitate the subsequent range analysis, the level of each factor was set to 3, as shown in Table 3.

3.2 Experimental scheme and calculation result

Taguchi method (Yang et al., 2021; Bai et al., 2022) has the advantages of reasonable experimental arrangement, short cycle and low cost, making it wise to be used for the experimental scheme construction in this study. From the above analysis, the number of factors and their levels were 13 and 3 respectively, therefore, the L27 (3^{13}) standard orthogonal table was employed for the construction of

TABLE 3 Relationship between the test factors true value and level.

Factors		Geometric parameters					Hydrodynamic parameters							
		Lh/mm	*Ls*/mm	*Th*/mm	*Ts*/mm	*ST*/°	LE_h	NC_h	ND_h	K_h	LE_s	NC_s	ND_s	K_s
Levels	1	85.5	126	14	76	-20	-0.2	0.1	0.5	-1.6	-0.2	0.1	0.5	-1.6
	2	90	133	16	80	0	0	0.3	0.7	0	0	0.3	0.7	0
	3	94.5	140	18	84	20	0.2	0.5	0.9	1.6	0.2	0.5	0.9	1.6

TABLE 4 Experimental scheme and calculation results.

Item no.	Factors													Targets	
	Lh	*Ls*	*Th*	*Ts*	*ST*	LE_h	NC_h	ND_h	K_h	LE_s	NC_s	ND_s	K_s	η/%	*H*/m
1	1	1	1	1	1	1	1	1	1	1	1	1	1	83.43	13.07
2	2	2	2	2	2	1	1	1	1	2	2	2	2	86.69	13.00
3	3	3	3	3	3	1	1	1	1	3	3	3	3	87.96	12.49
4	2	3	3	3	2	2	1	2	2	2	1	1	1	86.86	13.38
5	3	1	1	1	3	2	1	2	2	3	2	2	2	86.57	13.12
6	1	2	2	2	1	2	1	2	2	1	3	3	3	85.98	11.26
7	3	2	2	2	3	3	1	3	3	3	1	1	1	86.52	12.62
8	1	3	3	3	1	3	1	3	3	1	2	2	2	85.51	11.26
9	2	1	1	1	2	3	1	3	3	2	3	3	3	84.59	11.11
10	3	2	1	3	2	3	2	1	2	1	1	2	3	87.07	12.87
11	1	3	2	1	3	3	2	1	2	2	2	3	1	87.62	13.17
12	2	1	3	2	1	3	2	1	2	3	3	1	2	85.91	12.50
13	1	1	3	2	3	1	2	2	3	2	1	2	3	83.86	12.01
14	2	2	1	3	1	1	2	2	3	3	2	3	1	85.81	11.96
15	3	3	2	1	2	1	2	2	3	1	3	1	2	85.54	12.63
16	2	3	2	1	1	2	2	3	1	3	1	2	3	87.69	12.67
17	3	1	3	2	2	2	2	3	1	1	2	3	1	86.27	12.60
18	1	2	1	3	3	2	2	3	1	2	3	1	2	87.37	12.30
19	2	3	1	2	3	2	3	1	3	1	1	3	2	86.65	12.53
20	3	1	2	3	1	2	3	1	3	2	2	1	3	84.81	12.22
21	1	2	3	1	2	2	3	1	3	3	3	2	1	85.96	12.90
22	3	2	3	1	1	3	3	2	1	2	1	3	2	87.50	12.79
23	1	3	1	2	2	3	3	2	1	3	2	1	3	87.08	13.18
24	2	1	2	3	3	3	3	2	1	1	3	2	1	86.52	12.14
25	1	1	2	3	2	1	3	3	2	3	1	3	2	85.01	12.31
26	2	2	3	1	3	1	3	3	2	1	2	1	3	85.52	12.08
27	3	3	1	2	1	1	3	3	2	2	3	2	1	87.18	12.13

the experimental scheme, and a total of 27 different schemes were created.

Table 4 is the factors and targets of each scheme. In contrast to the original model efficiency (85.31%) and head (12.42 m), there were 21 schemes with improved efficiency, 16 schemes with the required head, and 15 schemes with both head and efficiency. Furthermore, scheme 4 has the highest head of 13.38 m, while scheme 3 has the highest efficiency of 87.96%.

TABLE 5 Range analysis results.

Item factors	Efficiency					Head				
	$\overline{K_1}$	$\overline{K_2}$	$\overline{K_3}$	R^*	Rank	$\overline{K_1}$	$\overline{K_2}$	$\overline{K_3}$	R^*	Rank
Lh	85.76	86.25	86.60	0.84	3	12.38	12.37	12.61	0.23	10
Ls	85.22	86.49	86.90	1.68	1	12.34	12.42	12.60	0.26	9
Th	86.19	86.26	86.15	0.11	12	12.47	12.45	12.45	0.03	13
Ts	86.05	86.24	86.32	0.28	9	12.62	12.43	12.33	0.29	8
ST	85.98	86.12	86.51	0.53	6	12.21	12.66	12.50	0.46	4
LE_h	85.67	86.46	86.48	0.81	4	12.41	12.55	12.40	0.15	12
NC_h	86.01	86.35	86.25	0.34	8	12.37	12.52	12.48	0.16	11
ND_h	86.23	86.19	86.18	0.05	13	12.75	12.50	12.12	0.63	1
K_h	86.72	86.41	85.47	1.25	2	12.69	12.54	12.14	0.56	2
LE_s	85.83	86.28	86.50	0.67	5	12.27	12.46	12.64	0.37	7
NC_s	86.07	86.21	86.33	0.27	10	12.69	12.51	12.16	0.53	3
ND_s	85.89	86.34	86.38	0.48	7	12.66	12.46	12.25	0.42	6
K_s	86.24	86.31	86.06	0.24	11	12.66	12.49	12.21	0.45	5

3.3 Range analysis

The influence order of factors on the target, and the trend of the target with the level of factors is defined by extreme analysis (Ahmad and Prakash, 2021). The range R^* was calculated by the following equations:

$$K_i = \sum_{j=1}^{9} Y_{ij} \tag{5}$$

$$\overline{K_i} = \frac{K_i}{9} \tag{6}$$

$$R^* = \max\left(\bar{K}_1, \bar{K}_2, \bar{K}_3\right) - \min\left(\bar{K}_1, \bar{K}_2, \bar{K}_3\right) \tag{7}$$

where i is the level; Y_{ij} is the target value of a factor with level i; K_i is the sum of the Y_{ij}.

Table 5 is the efficiency and head range analysis results. The effect order of factors on efficiency is Ls, K_h, Lh, LE_h, LE_s, ST, ND_s, NC_h, T_s, NC_s, K_s, Th and ND_h, while the effect order of factors on head is ND_h, Kh, NC_s, ST, K_s, ND_s, LE_s, Ts, Ls, Lh, NC_h, LE_h and Th. Therefore, both hydrodynamic and geometric parameters should be considered simultaneously in the mixed-flow pump optimization design to maximize the energy characteristics improvement, since both of them have a large influence on the efficiency. To show the trend of the target with the level of factors more intuitively, geometric and hydrodynamic parameters' main effects on the target were plotted in Figure 6 according to Table 5.

3.4 Regression analysis of variance

To obtain the response relationship between the factors and the objectives, the data in Table 4 were subjected to a regression analysis of variance (Chiranjeevi et al., 2022). It is generally accepted that the correlation between the test factors and the optimization objectives is statistically significant when the p-value is less than 0.05. Therefore, according to the results of variance analysis in Table 6, parameters Ls, K_h, Lh, LE_h and LE_s were significant factors for efficiency, and parameters ND_h, K_h, NC_s, K_s, ND_s and LE_s were significant factors for head. The results of the p-value analysis once again show that both the geometric and hydrodynamic parameters have significant influence on the mixed-flow pump energy characteristics. Equation 8 and Equation 9 are the efficiency and head regression equations, respectively.

$$\begin{aligned}\eta_D = {} & 81.924 + 0.422Lh + 0.840Ls - 0.022Th + 0.139Ts + 0.265ST \\ & + 0.407LE_h + 0.118NC_h - 0.024ND_h - 0.626K_h + 0.334LE_s \\ & + 0.134NC_s + 0.242ND_s - 0.089K_s\end{aligned} \tag{8}$$

$$\begin{aligned}H_D = {} & 14.118 + 0.112Lh + 0.131Ls - 0.014Th - 0.145Ts + 0.144ST \\ & - 0.002LE_h + 0.054NC_h - 0.315ND_h - 0.278K_h - 0.278K_h \\ & + 0.184LE_s - 0.266NC_s - 0.209ND_s - 0.227K_s\end{aligned} \tag{9}$$

3.5 Optimal model determination and performance comparison

To make the optimized mixed-flow pump with better energy characteristics and suitable head, the levels of the test factors Lh, Ls, Th, Ts, ST, LE_h, NC_h, ND_h, K_h, LE_s, NC_s, ND_s and K_s were set to 3, 3, 2, 3, 3, 3, 2, 1, 1, 3, 3, 3 and 2, respectively, based on the results of the range and regression analyses.

Figure 7 shows the impeller shape comparison between the original and optimized model. Compared to the original model

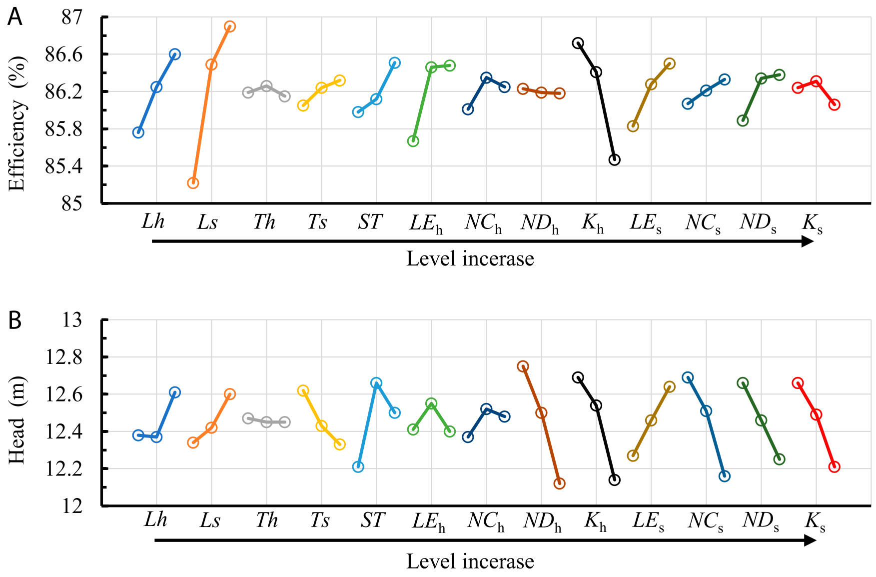

FIGURE 6
Main effect of hydrodynamic and geometric parameters on the objectives: **(A)** Efficiency; **(B)** Head.

TABLE 6 Results of the variance regression analysis.

Source	Freedom degree	Efficiency				Head			
		Adj SS	Adj SS	F- value	*p*-value	Adj SS	Adj SS	F- value	*p*-value
Regression	13	31.345	2.411	8.781	0.000	8.112	0.624	7.598	0.000
Lh	1	3.209	3.209	11.687	0.005	0.224	0.224	2.733	0.122
Ls	1	12.701	12.701	46.255	0.000	0.309	0.309	3.767	0.074
Th	1	0.009	0.009	0.032	0.860	0.004	0.004	0.046	0.834
Ts	1	0.347	0.347	1.265	0.281	0.378	0.378	4.608	0.051
ST	1	1.264	1.264	4.604	0.051	0.376	0.376	4.572	0.052
LE_h	1	2.977	2.977	10.841	0.006	0.000	0.000	0.001	0.974
NC_h	1	0.250	0.250	0.909	0.358	0.052	0.052	0.636	0.439
ND_h	1	0.011	0.011	0.039	0.846	1.786	1.786	21.745	0.000
K_h	1	7.044	7.044	25.653	0.000	1.389	1.389	16.910	0.001
LE_s	1	2.013	2.013	7.332	0.018	0.609	0.609	7.411	0.017
NC_s	1	0.325	0.325	1.185	0.296	1.275	1.275	15.519	0.002
ND_s	1	1.051	1.051	3.829	0.072	0.785	0.785	9.562	0.009
K_s	1	0.144	0.144	0.524	0.482	0.925	0.925	11.259	0.005
Error	13	3.570	0.275			1.068	0.082		
Total	26	34.914				9.180			

the optimized model has an increased overflow area at the hub and a reduced overflow area at the shroud. In addition, the optimized model blade trailing edge inclination angle is also increased. Figure 8 is the energy characteristics comparison between the optimized and original model. The optimized model efficiency and head at design condition are 88.51% and 12.43 m respectively, representing a 3.2% increase in efficiency and almost no change in head. The improved efficiency and nearly unchanged head indicate that the geometric and hydrodynamic parameters adopted in this study are reasonable.

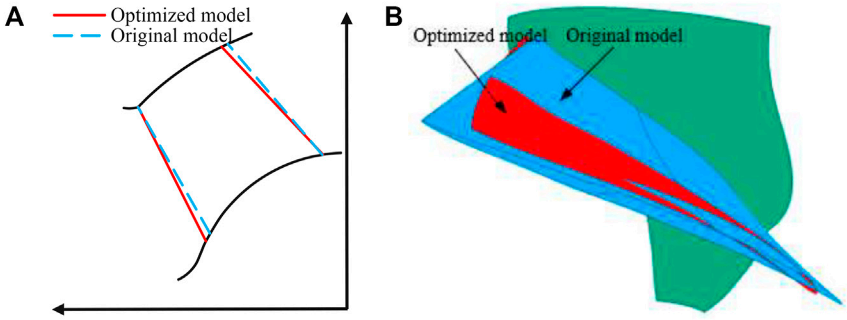

FIGURE 7
Comparison of original and optimized model impeller shapes: **(A)** Meridional plane; **(B)** blade shape.

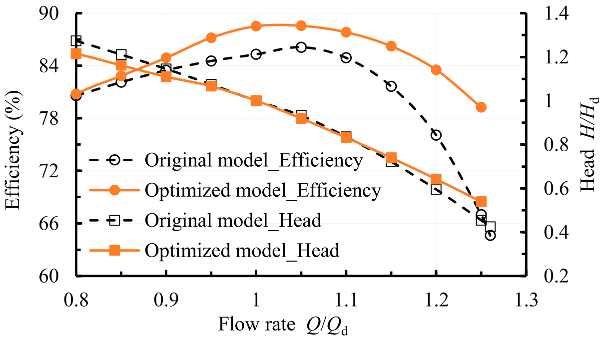

FIGURE 8
Comparison of original and optimized model energy characteristic.

4 Energy loss analysis

4.1 Entropy production theory

To elucidate the optimization mechanism, the energy loss of the optimized model was comparatively analyzed with that of the original model using entropy production theory. Similarly, only a brief introduction to the main computational equations of entropy production theory was given here; for more details, please refer to the original literature (Kock and Herwing, 2004; Qi et al., 2022).

For turbulent flow of viscous fluids, the entropy is largely induced by viscous dissipation, turbulent kinetic energy dissipation and wall effects, and are respectively calculated using the following equations.

$$E_V = \frac{\mu}{T}\left\{2\left[\left(\frac{\partial \bar{u}}{\partial x}\right)^2 + \left(\frac{\partial \bar{v}}{\partial y}\right)^2 + \left(\frac{\partial \bar{w}}{\partial z}\right)^2\right] + \left(\frac{\partial \bar{u}}{\partial y} + \frac{\partial \bar{v}}{\partial x}\right)^2 + \left(\frac{\partial \bar{v}}{\partial z} + \frac{\partial \bar{w}}{\partial y}\right)^2 + \left(\frac{\partial \bar{u}}{\partial z} + \frac{\partial \bar{w}}{\partial x}\right)^2\right\} \tag{10}$$

$$E_T = 0.09\frac{\rho\varepsilon}{T} \tag{11}$$

$$E_W = \frac{\vec{\tau}\cdot\vec{v}}{T} \tag{12}$$

where E_V represents the viscous dissipation induced direct entropy production rate; E_T represents the turbulent kinetic energy dissipation induced indirect entropy production rate; E_W represents the wall effects induced wall entropy production rate; ρ represents fluid density; ε represents the turbulent dissipation rate; T represents the thermodynamic temperature; $\vec{v}$ represents the first grid node velocity; $\vec{\tau}$ represents the shear stress; μ represents the dynamic viscosity; u, v and w represent the flow velocity components of x, y and z axis, respectively.

ΔE is calculated by the following equation:

$$\Delta E = \Delta E_V + \Delta E_T + \Delta E_w = T\left(\int_V E_V \mathrm{d}V + \int_V E_T \mathrm{d}V + \int_S E_W \mathrm{d}S\right) \tag{13}$$

where ΔE, ΔE_V, ΔE_T and ΔE_w represent the total, direct, indirect and wall entropy production, respectively.

4.2 Analysis of energy loss

The comparison of different types of entropy production distributions for the optimized and original models can be found in Figure 9. The total entropy production of the optimized model was significantly reduced in comparison to the original model, especially in the impeller, diffuser and outlet pipe, where total entropy production was reduced by 104.31, 389.66 and 308.61 W, respectively. When specific to the different types of entropy production, the variation of total entropy production in the impeller was mainly caused by both indirect and wall entropy production, while the variation of total entropy production in the diffuser and outlet pipe was mainly induced by indirect entropy production.

To better clarify how the mixed flow pump's energy loss characteristics are affected by internal flow patterns, the energy dissipation caused by the fluid motion was defined as the fluid entropy production rate (FEPR), whose value is equal to the sum of the direct and indirect entropy production rate.

The distribution of FEPR for the optimized and original models at impeller different spans is shown in Figure 10. The optimized and

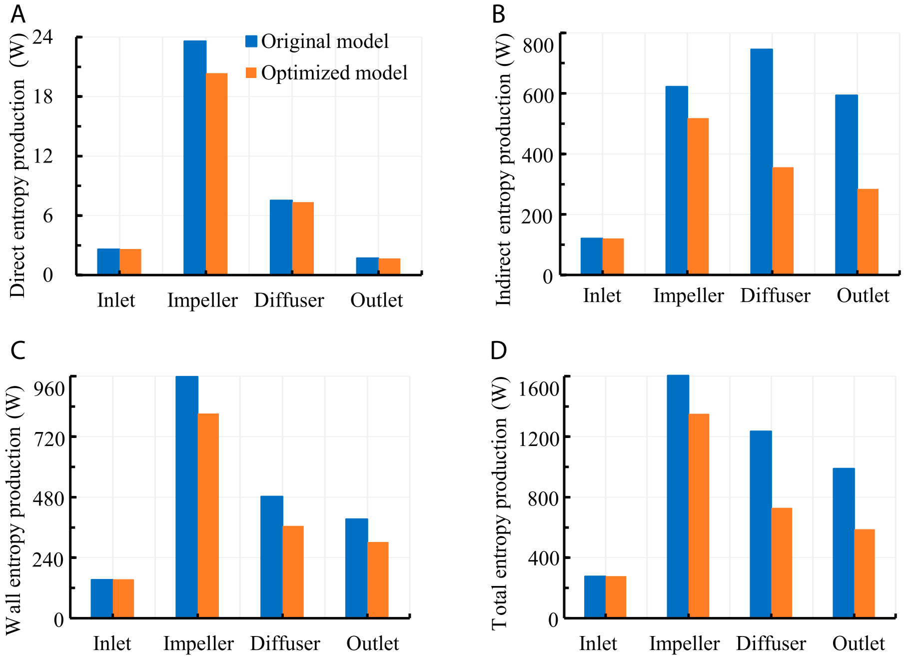

FIGURE 9
Comparison of different types of entropy production distribution: **(A)** ΔE_V; **(B)** ΔE_T; **(C)** ΔE_w; **(D)** ΔE.

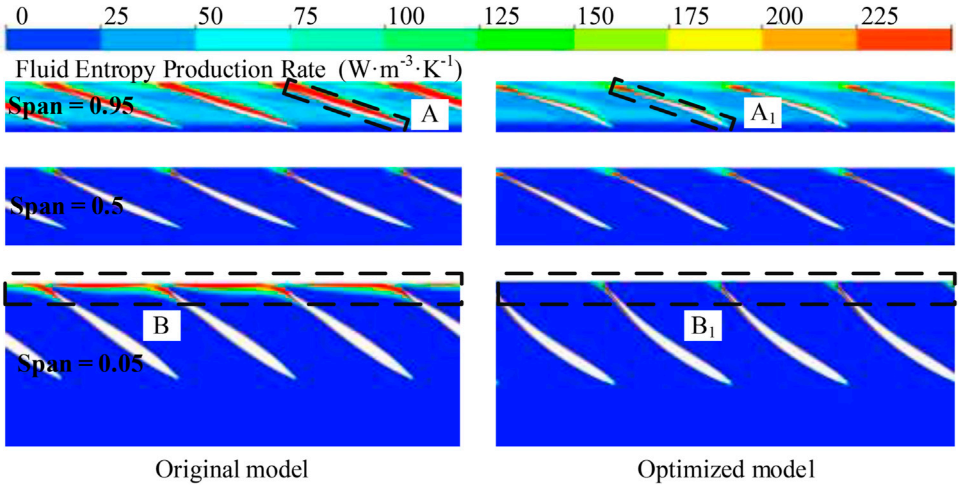

FIGURE 10
Impeller FEPR distribution comparison.

original model mid-span FEPR distribution was basically the same, and a larger FEPR caused by the jet-wake (Wu et al., 2021) was observed at blade trailing edge. However, compared to the original model, the FEPR in the optimized model shroud was markedly decreased, especially near the pressure surface. Also, near the hub of the impeller, the FEPR of the optimized model at the blade trailing edge was markedly decreased compared to the original model.

Although the diffuser is the same for the optimized and original models, the FEPR distribution in the two diffusers is quite different due to the difference of impeller outlet flow regime. Figures 11, 12 are the impeller outlet axial velocity distribution and diffuser different spans FEPR distribution respectively. The axial velocity at the outlet of the original model impeller increases progressively from the hub to shroud, and backflow was generated in a small region near the hub due to the boundary layer detachment

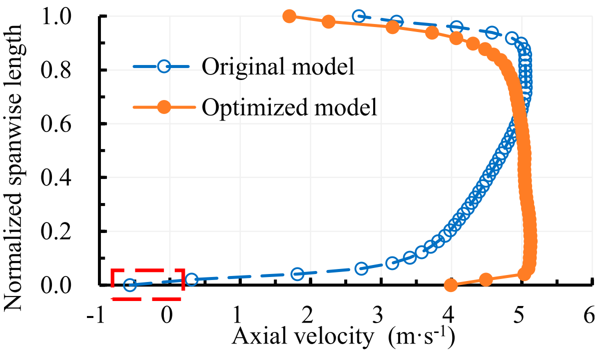

FIGURE 11
Impeller outlet axial velocity distribution comparison.

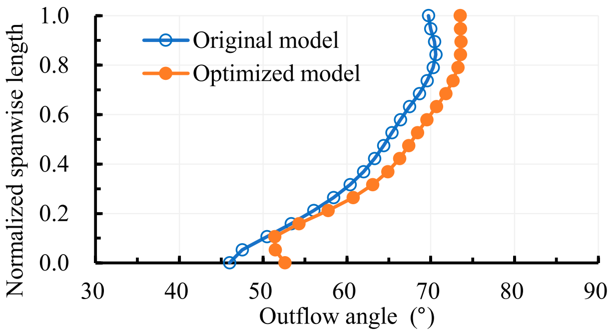

FIGURE 13
Diffuser outlet outflow angle distribution comparison.

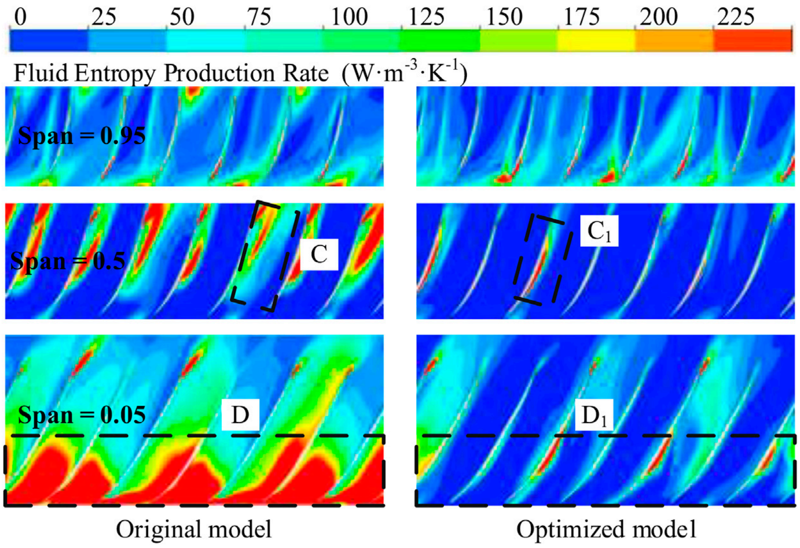

FIGURE 12
Diffuser FEPR distribution comparison.

(Kim et al., 2020). Due to the adverse flow pattern at the outlet of the original model impeller, a large FEPR was produced near the hub at the inlet of the diffuser, as shown in region D of Figure 12. After optimization, the axial velocity at impeller outlet near the hub was significantly increased, which effectively prevents the boundary layer detachment caused by the accumulation of low-momentum fluid. Accordingly, the FEPR near the hub at the inlet of the diffuser is markedly reduced.

A similar analysis was performed on the outlet pipe. Figure 13 is the distribution of the outflow angle θ at the diffuser outlet, which is calculated by Eq. 14. The optimized model has a larger outflow angle throughout the diffuser outlet than the original model, which means that the fluid residual rotational kinetic energy at the diffuser outlet is smaller for the optimized model. Lu et al. (2018) indicated that the fluid residual rotational kinetic energy at diffuser outlet is the outlet pipe energy loss primary

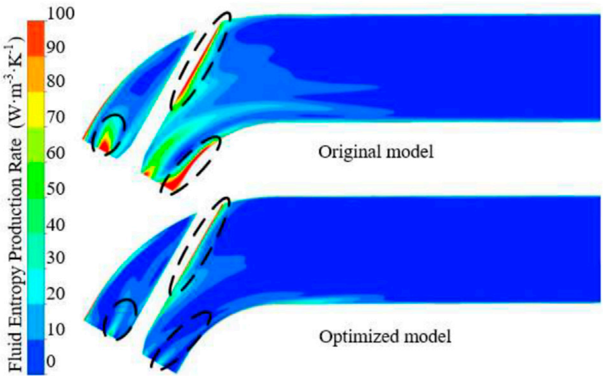

FIGURE 14
Outlet pipe FEPR distribution comparison.

cause. Therefore, the optimized model outflow pipe FEPR was remarkably lower than that of the original model, as shown in Figure 14.

$$\theta = \arcsin \frac{V_Z}{V} \tag{14}$$

where V represent the velocity, V_Z represent the z-axial component of velocity.

5 Conclusion

In this work, a typical mixed-flow pump was numerically simulated and experimentally verified. Then, its impeller was parameterized by five geometric and eight hydrodynamic parameters and optimized using the Taguchi method. Finally, the main and minor order of the parameters were determined using range and regression analysis, and the optimization mechanism was revealed by the energy loss visualization technique. The following conclusions were drawn:

(1) The geometric parameters Ls and Lh, as well as the hydrodynamic parameters LE_h, LE_s and K_h have a great influence on the mixed-flow pump efficiency. To maximize the energy characteristics of the mixed-flow pump, both geometric and hydrodynamic parameters need to be considered in its optimization design.
(2) The efficiency and head of the optimized model at the design condition are 88.51% and 12.43 m respectively, which represents a 3.2% increase in efficiency and almost no change in head compared to the original model. The improved efficiency and nearly unchanged head indicate that the geometric and hydrodynamic parameters adopted in this study are reasonable.
(3) The reduction of energy loss in the impeller downstream components induced by the improved flow pattern at impeller outlet contributes more than 87% to the performance improvement. Therefore, in the optimization of mixed-flow pump impeller, not only the improvement of impeller energy characteristics should be concerned, but also the change of its outlet flow pattern.

Data availability statement

The original contributions presented in the study are included in the article/supplementary material, further inquiries can be directed to the corresponding author.

Author contributions

JC: Writing–original draft, Software, Methodology. YB: Writing–review and editing. MW: Supervision, Guidance. HX: Supervision. XC: Data curation.

Conflict of interest

Author XC was employed by Anhui Ding Yuan Engineering Construction Co., HX was employed by Jiangsu Province Water Engineering Sci-tech Consulting Co.

The remaining author declares that the research was conducted in the absence of any commercial or financial relationships that could be construed as a potential conflict of interest.

Publisher's note

References

Ahmad, S., and Prakash, O. (2021). Optimization of ground heat exchanger of the ground source heat pump system based on exergetic analysis using Taguchi technique. *P I Mech. Eng. C-J Mec.* 235 (21), 5892–5901. doi:10.1177/0954406221991183

Bai, L., Yang, Y., Zhou, L., Li, Y., Xiao, Y., and Shi, W. (2022). Optimal design and performance improvement of an electric submersible pump impeller based on Taguchi approach. *Energy* 252, 124032. doi:10.1016/j.energy.2022.124032

Bing, H., Cao, S., Tan, L., and Zhu, B. (2013). Effects of meridional flow passage shape on hydraulic performance of mixed-flow pump impellers. *Chin. J. Mech. Eng-en* 26 (3), 469–475. doi:10.3901/cjme.2013.03.469

Bonaiuti, D., Zangeneh, M., Aartojarvi, R., and Eriksson, J. (2010). Parametric design of a waterjet pump by means of inverse design, CFD calculations and experimental analyses. *J. Fluid Eng-T Asme* 132 (3), 031104. doi:10.1115/1.4001005

Bonaiuti, D., and Zangeneh, M. (2009). On the coupling of inverse design and optimization techniques for the multiobjective, multipoint design of turbomachinery blades. *J. Turbomach.* 131 (2), 021014. doi:10.1115/1.2950065

Chiranjeevi, P., Ashok, V., Srinivasan, K., and Sundararajan, T. (2022). Performance analysis of single-phase space thermal radiators and optimization through taguchi-neuro-genetic approach. *J. Therm. Sci. Eng. Appl.* 14 (6), 061012. doi:10.1115/1.4052897

Fallah-Ardeshir, H., Ehghaghi, B., and Nill-Ahmadabadi, M. (2020). Inverse design of a centrifugal pump on the meridional plane using ball-spine algorithm. *Sci. Iran.* 27 (5), 2478–2488.

Goto, A., Takemura, T., and Zangeneh, M. (1996). Suppression of secondary flows in a mixed-flow pump impeller by application of three-dimensional inverse design method: Part 2-experimental validation. *J. Turbomach.* 118 (3), 544–551. doi:10.1115/1.2836701

Gu, Y., Cheng, J., Wang, P., Cheng, L., Si, Q., Wang, C., et al. (2022). A flow model for side chambers of centrifugal pumps considering radial wall shear stress. *P I Mech. Eng. C-J Mec.* 236 (13), 7115–7126. doi:10.1177/09544062211073023

Gu, Y., Li, J., Wang, P., Cheng, L., Qiu, Y., Wang, C., et al. (2022). An Improved one-dimensional flow model for side chambers of centrifugal pumps considering the blade slip factor. *J. Fluid Eng-T Asme* 144 (9), 091207. doi:10.1115/1.4054138

Hawthorne, W., Wang, C., and McCune, J. (1984). Theory of blade design for large deflections: Part I-two-dimensional cascade. *J. Eng. Gas. Turb Power* 106 (2), 346–353. doi:10.1115/1.3239571

Hieninger, T., Schmidt-Vollus, R., and Schlucker, E. (2021). Improving energy efficiency of individual centrifugal pump systems using model-free and on-line optimization methods. *Appl. Energ* 304, 117311. doi:10.1016/j.apenergy.2021.117311

Huang, R., Luo, X., Ji, B., Wang, P., Yu, A., Zhai, Z., et al. (2015). Multi-objective optimization of a mixed-flow pump impeller using modified NSGA-II algorithm. *Sci. China Technol. S. C.* 58 (12), 2122–2130. doi:10.1007/s11431-015-5865-5

Kim, S., Kim, Y., Kim, J., and Choi, Y. (2020). Design optimization for mixed-flow pump impeller by improved suction performance and efficiency with variables of specific speeds. *J. Mech. Sci. Technol.* 34 (6), 2377–2389. doi:10.1007/s12206-020-0515-7

Kim, S., Kim, Y., Kim, J., and Choi, Y. (2019). Three-objective optimization of a mixed-flow pump impeller for improved suction performance and efficiency. *Adv. Mech. Eng.* 11 (12), 168781401989896. doi:10.1177/1687814019898969

Kock, F., and Herwing, H. (2004). Local entropy production in turbulent shear flows: A high-Reynolds number model with wall functions. *Int. J. Heat. Mass Tran* 47 (10), 2205–2215. doi:10.1016/j.ijheatmasstransfer.2003.11.025

Lee, K., Choi, Y., Kim, Y., and Yun, J. (2008). Design of axial fan using inverse design method. *J. Mech. Sci. Technol.* 22 (10), 1883–1888. doi:10.1007/s12206-008-0727-8

Leguizamon, S., and Avellan, F. (2020). Open-Source implementation and validation of a 3D inverse design method for Francis turbine runners. *Energies* 13 (8), 2020. doi:10.3390/en13082020

Liang, J., Lu, L., Xu, L., Chen, W., and Wang, G. (2012). Influence of flow velocity circulation at guide vane outlet of axial-flow pump on hydraulic loss in outlet condition. *CSAE* 28 (01), 55–60.

Lu, Y., Wang, X., Wang, W., and Zhou, F. (2018). Application of the modified inverse design method in the optimization of the runner blade of a mixed-flow pump. *Chin. J. Mech. Eng-en* 31 (1), 105. doi:10.1186/s10033-018-0302-x

Ma, Z., Zhu, B., Rao, C., and Shangguan, Y. (2019). Comprehensive hydraulic improvement and parametric analysis of a Francis turbine runner. *Energies* 12 (2), 307. doi:10.3390/en12020307

Menter, F., Ferreira, J., and Esch, T. (2003). *The SST turbulence model with improved wall treatment for heat transfer predictions in gas turbines*. Tokyo, Japan: International Gas Turbine Congress.

Menter, F. (1994). Two-equation eddy-viscosity turbulence models for engineering applications. *AIAA J.* 32 (8), 1598–1605. doi:10.2514/3.12149

Nahon, J., Zangeneh, M., Nohmi, M., Watanabe, H., and Goto, A. (2021). A robust inverse design solver for controlling the potential aggressiveness of cavitating flow on hydrofoil cascades. *Int. J. Numer. Meth Fl* 93 (7), 2291–2310. doi:10.1002/fld.4974

Pei, J., Wang, W., and Yuan, S. (2016). Multi-point optimization on meridional shape of a centrifugal pump impeller for performance improvement. *J. Mech. Sci. Technol.* 30 (11), 4949–4960. doi:10.1007/s12206-016-1015-7

Qi, B., Zhang, D., Geng, L., Zhao, R., and Van Esch. (2022). Numerical and experimental investigations on inflow loss in the energy recovery turbines with back-curved and front-curved impeller based on the entropy generation theory. *Energy* 239 (E), 122426. doi:10.1016/j.energy.2021.122426

Shim, H., Kim, K., and Choi, Y. (2018). Three-objective optimization of a centrifugal pump to reduce flow recirculation and cavitation. *J. Fluid Eng-T Asme* 140 (9), 091202. doi:10.1115/1.4039511

Si, Q., Lu, R., Shen, C., Xia, S., Sheng, G., and Yuan, J. (2020). An intelligent CFD-based optimization system for fluid machinery: Automotive electronic pump case application. *Appl. Sci-basel* 10 (1), 366. doi:10.3390/app10010366

Suh, J., Yang, H., Kim, Y., Lee, K., Kim, J., Joo, W., et al. (2019). Multi-objective optimization of a high efficiency and suction performance for mixed-flow pump impeller. *Eng. Appl. Comp. Fluid* 13 (1), 744–762. doi:10.1080/19942060.2019.1643408

Wang, M., Li, Y., Yuan, J., and Osman, F. (2021). Influence of spanwise distribution of impeller exit circulation on optimization results of mixed flow pump. *Appl. Sci-basel* 11 (2), 507. doi:10.3390/app11020507

Wang, M., Li, Y., Yuan, J., and Osman, F. (2021). Matching optimization of a mixed flow pump impeller and diffuser based on the inverse design method. *Processes* 9 (2), 260. doi:10.3390/pr9020260

Wang, M., Li, Y., Yuan, J., and Yuan, S. (2022). Effects of different vortex designs on optimization results of mixed-flow pump. *Eng. Appl. Comp. Fluid* 16 (1), 36–57. doi:10.1080/19942060.2021.2006091

Wu, C., Li, Q., Zheng, F., Wu, P., Yang, S., Ye, H., et al. (2021). Improve of unsteady pressure pulsation based on jet-wake suppression for a low specific centrifugal pump. *J. Fluid Eng-T Asme* 143 (11), 111202. doi:10.1115/1.4051402

Yang, W., Lei, X., Zhang, Z., Li, H., and Wang, F. (2017). Hydraulic design of submersible axial-flow pump based on blade loading distributions. *CSAM* 48 (11), 179–187.

Yang, W., and Xiao, R. F. (2014). Multiobjective optimization design of a pump-turbine impeller based on an inverse design using a combination optimization strategy. *J. Fluid Eng-T Asme* 136 (1), 014501. doi:10.1115/1.4025454

Yang, Y., Zhou, L., Hang, J., Du, D., Shi, W., and He, Z. (2021). Energy characteristics and optimal design of diffuser meridian in an electrical submersible pump. *Renew. Energ* 167, 718–727. doi:10.1016/j.renene.2020.11.143

Yin, J., and Wang, D. (2014). Review on applications of 3D inverse design method for pump. *Chin. J. Mech. Eng-en* 27 (3), 520–527. doi:10.3901/cjme.2014.03.520

Zangeneh, M. (1991). A compressible three-dimensional design method for radial and mixed flow turbomachinery blades. *Int. J. Numer. Meth Fl* 13, 599–624. doi:10.1002/fld.1650130505

Zangeneh, M., Gota, A., and Takemura, T. (1996). Suppression of secondary flows in a mixed-flow pump impeller by application of three-dimensional inverse design method: Part 1-design and numerical validation. *J. Turbomach.* 118 (3), 536–543. doi:10.1115/1.2836700

Zangeneh, M., Goto, A., and Harada, H. (1998). On the design criteria for suppression of secondary flows in centrifugal and mixed flow impellers. *J. Turbomach.* 120 (4), 723–735. doi:10.1115/1.2841783

Zhang, R., and Zhao, X. (2020). Inverse method of centrifugal pump blade based on Gaussian process regression. *Math. Probl. Eng.* 2020, 1–10. doi:10.1155/2020/4605625

Zhu, B., Tan, L., Wang, X., and Ma, Z. (2018). Investigation on flow characteristics of pump-turbine runners with large blade lean. *J. Fluid Eng-T Asme* 140 (3), 031101. doi:10.1115/1.4037787

Frontiers | Frontiers in Energy Research

TYPE Original Research
PUBLISHED 13 April 2023
DOI 10.3389/fenrg.2023.1183086

Analysis of internal flow characteristics and entropy generation of low head bulb tubular pump

Xinyi Tian, Li Cheng*, Weixuan Jiao, Yuqi Wang* and Can Luo

College of Hydraulic Science and Engineering, Yangzhou University, Yangzhou, China

EDITED BY
Yongfei Yang,
Nantong University, China

REVIEWED BY
Xinyang Liu,
North China University of Water Resources and Electric Power, China
Haoru Zhao,
Tsinghua University, China
Shibiao Fang,
Shenzhen University, China

*CORRESPONDENCE
Li Cheng,
✉ chengli@yzu.edu.cn
Yuqi Wang,
✉ wyq20000524@163.com

SPECIALTY SECTION
This article was submitted to Process and Energy Systems Engineering, a section of the journal Frontiers in Energy Research

RECEIVED 09 March 2023
ACCEPTED 17 March 2023
PUBLISHED 13 April 2023

CITATION
Tian X, Cheng L, Jiao W, Wang Y and Luo C (2023), Analysis of internal flow characteristics and entropy generation of low head bulb tubular pump.
Front. Energy Res. 11:1183086.
doi: 10.3389/fenrg.2023.1183086

To study the internal flow characteristics and energy characteristics of a large bulb perfusion pump. Based on the CFX software of the ANSYS platform, the steady calculation of the three-dimensional model of the pump device is carried out. The numerical simulation results obtained by SST k-ω and RNG k-ε turbulence models are compared with the experimental results. Finally, SST k-ω is selected for subsequent calculation. With the help of the flow line diagram and turbulent kinetic energy table of the whole flow channel of the pump device, the flow components of the pump device under different working conditions are analyzed, and the pressure and velocity distribution at the impeller and guide vane are analyzed by pressure cloud diagram and velocity cloud diagram. It is found that there are three high-pressure areas in the impeller and guide vane section, and the high-pressure regions are mainly distributed in the middle of the impeller channel. As the head decreases, the pressure at the impeller and guide vane positions decreases gradually, and the flow rate increases. Based on the entropy production principle, the wall entropy production and the distribution of mainstream entropy production at the impeller and guide vane parts are analyzed.

KEYWORDS

bulb tubular pump, numerical simulation, turbulence model, internal flow characteristics, entropy production

1 Introduction

In the middle and lower reaches of the Yangtze River along the Yangtze River in China, due to the low-lying and flat terrain, there are many low-head axial flow pumping stations in these places. These pumping stations have the characteristics of large flow, low head, and a high degree of automation. The common types of low-head axial flow pumping stations along the Yangtze River are vertical, oblique, tubular, and bidirectional (channel). The bulb tubular pumping station has been widely used in the Yangtze River Delta (Liu, 2009) and the Pearl River Delta due to its simple structure, shallow excavation depth, slight hydraulic loss, and excellent performance. Therefore, the study of internal flow characteristics and entropy generation analysis of low-head bulb tubular pumps play an essential role in the practical design of the flow components in the bulb tubular pump, the economy, and the safety of the pumping station operation.

At present, most of the domestic and foreign scholars' research on tubular pump station focuses on the analysis of pump station's internal and external characteristics and model optimization. Yang et al. (Yang et al., 2020) studied the effect of adjustable inlet guide vane Angle on hydraulic performance of axial-flow pump and impeller by numerical simulation technique, and concluded that the pump efficiency first increased and then decreased with decreasing installation Angle. Zhang et al. (Zhang et al., 2017) artificially analyzed the wear characteristics of the axial-flow pump with sewage as the medium, and the research results showed the relationship between the solid volume fraction and the sweep Angle of the pressure/suction surface and the particle diameter. In order to reveal the influence of tip clearance on the flow characteristics and pressurization performance of spiral axial flow pump, Kan et al. (Kan et al., 2021) analyzed the flow characteristics and energy characteristics of spiral axial flow pump and found that tip clearance increased the possibility of cavitation and had a great influence on the pressurization performance of spiral axial flow pump. The damage of axial flow pump impeller in sandy water was predicted and analyzed by Hua (Hua et al., 2018). Guo et al. (Guo et al., 2022) conducted a quantitative study on the flow field structure at the inlet of axial flow pump and found that there are obvious impeller rotation effect and end wall effect in the inlet flow field of axial flow pump. Zhang et al. (Zhang et al., 2022) tested the hydrodynamic characteristics of the bidirectional axial flow pump on the high-precision hydraulic mechanical test bench, and revealed the energy characteristics and pressure pulsation propagation law of the bidirectional axial flow pump during positive and negative operation. Ji et al. (Ji et al., 2021) studied the difference between the lowest saddle head of the axial flow pump and the axial flow pump device and applied it correctly. They conducted energy performance tests on the hydraulic model TJ04-ZL-06 and the corresponding pump device, and obtained that the first saddle head of the axial flow pump or the saddle head of the corresponding pump device can be used as the control value of the highest lift of the pump station. Wei et al. (Shi et al., 2020b) studied the pressure pulsation law of impeller guide vane under different working conditions of a rear bulb tubular pump calculated and analyzed the pressure pulsation in impeller guide vane area under partial working conditions, and believed that the number of impeller blades had a certain influence on the primary and secondary frequency of pressure pulsation. Wang et al. (Wang and Dai, 2010) used RNG k-ε turbulence model and slip grid technology to study the unsteady flow inside the transect pump and analyzed it in the frequency domain. The results show that the disturbance between impeller and tongue is the main source of pressure pulsation. Wang et al. (Wang et al., 2008) artificially accurately captured the unsteady flow field characteristics of axial flow pump, and used Reynolds time-mean method and large eddy simulation method to numerically simulate the unsteady turbulence of axial flow pump. Zheng et al. (Zheng et al., 2017) and Ran et al. (Ran et al., 2012) respectively studied the pressure pulsation characteristics of axial flow pump and turbine under different working conditions. Ma (Ma, 2021) carried out acceptance tests on the model device of bulb flow pump in Sihong Station, trial operation of real machine and other tests at different stages. Qin et al. (Qin et al., 2009) introduced the structural characteristics and hydraulic characteristics of bulb flow pump units with different structure types.

Mu et al. (Mu et al., 2020) proposed a new groove flow control technique for axial-flow pumps, which can be used to improve the rotating stall problem that is prone to occur when the tubular pump has a small flow rate. Shi et al. (Shi et al., 2020a) designed an axial-flow pump impeller based on the surface element method, and studied the influence of the impeller rotor on the hydraulic performance of the all-tube pump, and found that the reduction of the maximum running head of the all-tube pump was greater than that of the axial flow pump. Pan et al. (Pan et al., 2021) proposed a method to optimize the hydrodynamic characteristics of axial piston pumps and the structural parameters of the distribution zone considering the evolution of cavitation bubbles. Liang et al. (Liang et al., 2018) used CFD numerical simulation technology to optimize the design of the impeller and guide vane body of the tubular pump in order to deeply study the performance of the tubular pump device with rear bulb. In the process of analysis, the operation range of the traditional tubular pump was broken through, and the hydraulic model of the tubular pump with low specific speed and high efficiency was obtained.

At present, entropy generation theory is also the focus of domestic and foreign scholars. Zhang et al. (Zhang et al., 2008) in order to study shaft tubular pump flow dynamic damage characteristics of the shaft tubular pump internal flow field in the unsteady calculation, and using the theory of entropy production of shaft tubular pump under different traffic conditions flow loss characteristics of components, the results show that the impeller is the main source of energy loss turbulent dissipation, the entropy production rate of up to 92%. Song et al. (Wu et al., 2011) analyzed the flow loss characteristics of the duct propeller from the perspective of energy and revealed the characteristics of the flow loss during the operation of the duct propeller. Yang et al. (Yang et al., 2018a) entropy Generation Rates in two-dimensional Rayleigh-Taylor (RT) mixing are investigated by Numerical Calculation. Hddad et al. (Haddad et al., 2004) focused on the generation of forced convective entropy of laminar flow in the entryway of concentric rings. Finally, it is found that thermal entropy generation is relatively dominant over viscous entropy generation. Osman et al. (Koranteng Osman et al., 2019) investigated the energy losses of LNG two-stage cryogenic submersible pumps and two-stage axially split centrifugal pumps based on entropy production theory, respectively, and showed that turbulent dissipation and wall friction were the primary sources for generating hydraulic losses. David et al. (David et al., 2012) evaluated the feasibility of optimization methods for electric heat pumps with the help of entropy production dissipation theory. An et al. (Yu et al., 2022) conducted a numerical study of the energy characteristics of pumped storage pumping stations based on entropy production dissipation theory.

In summary, there are relatively affluent domestic and foreign studies on the internal and external characteristics and model optimization of the bulb perforation pump device, but few studies on the entropy generation analysis of the bulb perforation pump device. This paper uses a large low-head bulb perforation pump device as the research object based on computational fluid dynamics methods and model tests. The internal flow characteristic curve and the entropy generation characteristic of the main parts of the bulb penetration pump without a distinct head are analyzed to help study the fluid characteristics of the bulb irrigation pump.

2 Calculation model

2.1 Establishment of calculation model

The calculation model is a low-head bulb tubular pumping station. The designed flow rate of a single pump station is 37.5 m^3/s, the diameter of the pump impeller is 3,350 mm, and the rotational speed is $n = 115.4$ r/min. There are three impeller blades and five guide blades. The designed head of the low-head bulb perfusion pump is 2.45 m, the highest head is 2.75 m, the average

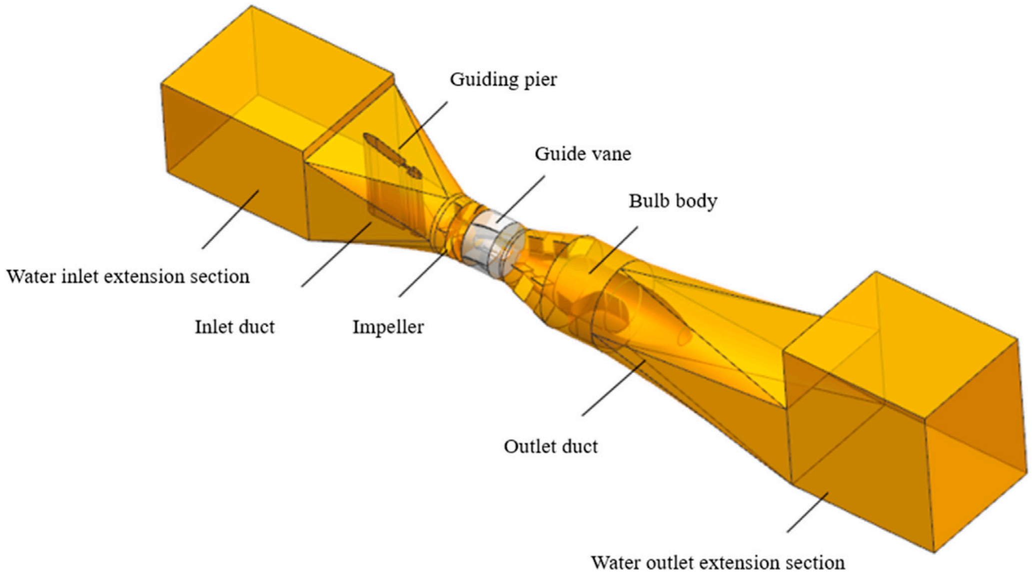

FIGURE 1
Flow channel structure of bulb tubular pump device.

head is 2.10 m, and the lowest head is 1.25 m. Taking a single unit of a pumping station as the calculation model for numerical simulation to better simulate the inflow and outflow forms of inlet and outlet channels, according to the design water level, the inlet extension section and the outlet extension section are set before and after the inlet channel. In order to ensure that the size and shape of the calculation channel model are completely geometrically similar to those of the prototype pump station channel model, the overall calculation domain includes the inlet extension section, inlet conduit and diversion pier, impeller, guide vane, bulb body, outlet conduit, and outlet extension section. Figure 1 is the flow channel structure diagram of the bulb tubular pump.

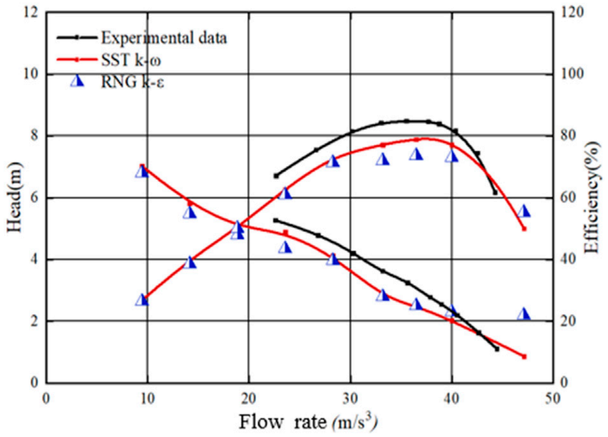

FIGURE 2
Comparison of numerical and experimental results from different turbulence models.

2.2 Turbulence model selection

In this paper, based on the continuity equation of three-dimensional incompressible turbulence and the Reynolds time-averaged N-S equation, the internal flow characteristics and hydraulic performance of the bulb tubular pump device are numerically calculated, ignoring the heat exchange effect and ignoring the energy conservation equation. For the selection of turbulence model, SST *k*-*ω* and RNG *k*-*ε* turbulence models are usually used to simulate the water flow inside the low-lift bulb tubular pump in the present study (Zhang et al., 2012; Ahn et al., 2018; Yang et al., 2018b; Xie et al., 2018; Ma et al., 2019). In order to compare the simulation authenticity of turbulence model, this paper selects these two turbulence models based on CFX platform, carries out numerical calculation respectively, and compares the calculation results with the model test values (Figure 2). The model test is carried out on the experimental equipment of Hitachi Industrial Equipment Technology Tupu Research Institute. The impeller diameter used in the model test is 315 mm, the rotational speed is 1223 r/min, the number of impeller blades is 3, the number of guide vane blades is 5, and the blade placement angle is 0°.

The pump performance data measured by the test bench are converted according to "SL140-2006"pump model and device model acceptance test procedure prototype pump performance conversion method. Numerical simulation results of prototype pump the conversion formula of model pump characteristics:

$$\frac{Q_P}{Q_M} = \frac{N_P D_P^3}{N_M D_M^3} \tag{1}$$

$$\frac{H_P}{H_M} = \frac{N_P^2 D_P^2}{N_M^2 D_M^2} \tag{2}$$

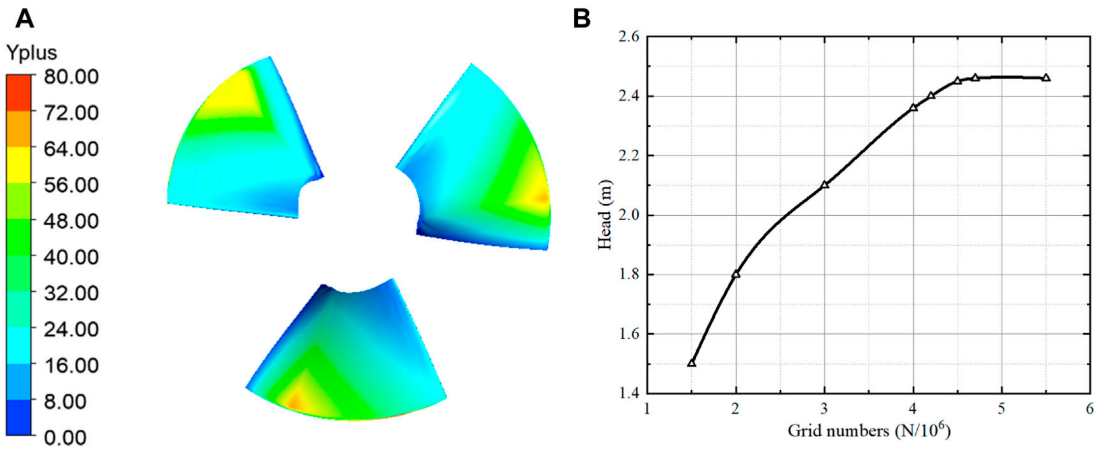

Distribution of y+ on impeller

Grid independence verification

FIGURE 3
Model grid analysis. **(A)** Distribution of y + on impeller. **(B)** Grid independence verification.

In the above calculations:

Q_p、Q_m—Flow rate of original and model pumps.

H_p、H_m—Original and model pump head.

N_p、n_m—Rotational speed of original and model pumps.

D_p、D_m—Impeller diameter of original and model pumps.

It can be seen from the curves that the numerical simulation results obtained by the two turbulence models are similar to the overall trend of the experimental data, but there is a deviation between some data points near the design condition and the experimental data points using the RNG k-ε model data. Relatively speaking, the consistency between the results obtained by SST k-ω model and the data is better than that of the RNG k-ε model. Therefore, the SST k-ω turbulence model is comprehensively considered for subsequent steady calculation.

2.3 Grid division

In order to consider the later calculation efficiency and accuracy, the ICEM CFD software under the ANSYS platform is used to generate a hexahedral mesh for the impeller part of the calculation model. By controlling the nodes on each topological line, the degree of mesh refinement of the impeller part is ensured. The other parts use the Mesh software of ANSYS platform to generate tetrahedral mesh. For meshing, the smaller the grid size and the higher the number of grids, the higher the computational accuracy. The number of grids will also directly affect the computational time. It is necessary to analyze the irrelevance of the computational grid to save computational resources as much as possible to satisfy sure computational accuracy. In this paper, the grid independence test of the impeller part of the large bulb tubular pump is carried out under the design condition of stable operation (Figure 3A). On the premise of not reducing the quality, the number of grids is changed, and the number of grids at the impeller is gradually increased to verify the rationality of grid subdivision. After analysis, it is found that when the number of grids in the computational domain reaches about 2 million, the control range of hydraulic loss change is within ±5%, which meets the requirements of grid independence test. Therefore, the total number of grid cells in the fluid region is set to 4.5 million. In order to verify the quality of the grid, the y + analysis of the grid of the impeller blade position is carried out in this paper. Because the turbulence model SST k-ω selected in this paper is a high Reynolds number model, it is considered that the y + value is between 30 and 300 in the case of this model. The grid quality is better. It can be seen from Figure 3B that the y + value of the blade does not exceed 100, so the grid quality is considered to be better.

2.4 Boundary condition setting

The inlet boundary adopts the quality inlet condition, which is set as 37,500 kg/s, and is imported on the section of the extended section at a certain distance from the inlet port. The outlet boundary adopts the pressure outlet condition, taking 1 atm, set in the distance of the outlet channel. There is no slip condition and no heat transfer at the solid side wall, and the wall function is used in the near wall region. The blade surface is set as a moving wall. For the pump station, it includes rotating impeller, stationary guide vane and inlet and outlet channels, wherein the inlet channel and impeller, impeller and guide vane have mutual flow coupling effect, and the dynamic and static interface treatment is set as frozen rotor other interfaces are static interfaces, which are set as general interfaces. The calculation scheme is set as first-order upwind, and the convergence accuracy is 10–^{4}.

3 Internal flow characteristics of flow passage components under different head conditions

3.1 Full flow pattern of pump unit

In order to comprehensively study the flow pattern of the whole flow channel of the pump device, four schemes are selected

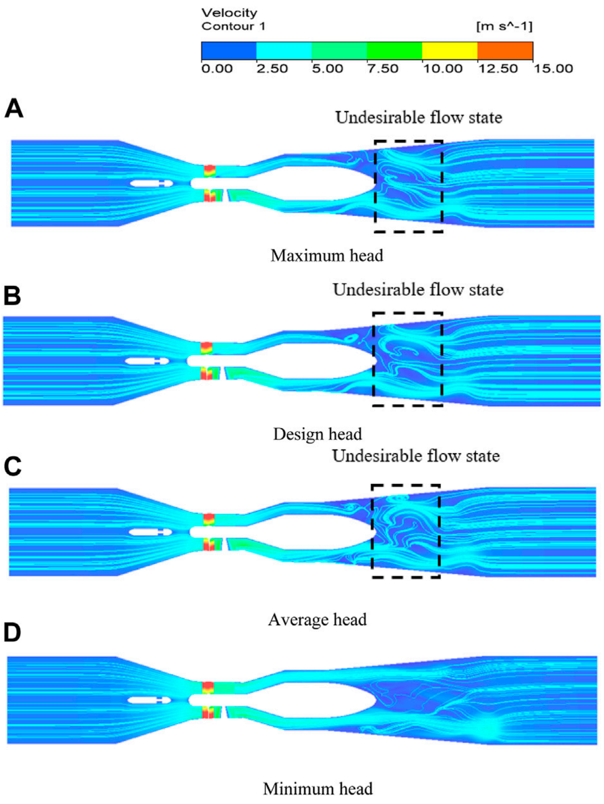

FIGURE 4
Full flow channel flow chart and velocity distribution contour chart. **(A)** Maximum head. **(B)** Design head. **(C)** Average head. **(D)** Minimum head.

TABLE 1 The change of turbulent kinetic energy under different characteristic head conditions.

Head/m	Turbulent kinetic energy/m^2/s^2
2.59	0.71
2.48	0.82
2.03	0.83
0.87	0.97

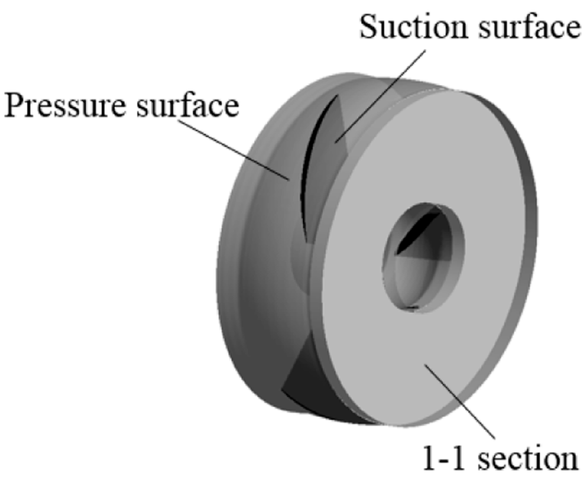

FIGURE 5
Characteristic section diagram of impeller.

according to the characteristic head. The characteristic head is 2.45 m in design, 2.75 m in maximum, 2.10 m in average, and 1.25 m in minimum. The corresponding flow rates are 37.5 m^3/s, 36.2 m^3/s, 40.0 m^3/s, and 47.13 m^3/s, respectively.

The flow line diagram of the entire flow path of the pump device axis surface is shown in Figure 4. It can be seen that the flow line of the inlet channel position is smooth in the impeller position due to the rotation of the blade to produce ring volume, so the flow speed in this position is accelerated, after the guide vane rectification flow line to restore smooth, but due to the bulb body tail end of the over-flow cross-section changes dramatically in making the region appeared obvious destructive flow pattern. By comparing different working conditions, we can see that the flow line diagram at the end of the bulb body can be seen, the maximum head, design head, and average head working conditions all appear to have evident vortex distribution in this location, the minimum head working conditions in this area of the vortex distribution is less, but in the bulb body at the end of the apparent off-flow phenomenon.

Water disturbance will cause flow disorder and increase the turbulent kinetic energy. Turbulent kinetic energy is the kinetic energy of unit mass fluid due to turbulent fluctuation. The greater the turbulent kinetic energy is, the higher the turbulent degree of the flow field is, and the instability of the flow increases. As shown in Table 1, the turbulent kinetic energy of each characteristic head is compared. It can be seen that with the rise of the head, the flow rate decreases, resulting in the decrease of the turbulent kinetic energy. However, the change of the turbulent kinetic energy is small in the range from the average head to the design head. At this time, the flow state of the whole pump device is relatively stable in the high-efficiency area. When the head increases to the maximum head, the turbulent kinetic energy decreases rapidly, and the decline rate in this section reaches 45% of the total decline. This is because, with the increase of the head, the flow rate decreases correspondingly, the disturbance between the water particles falls, and the guide vane has a better rectification effect for the water body under the condition of a small flow rate under the condition of constant rotational speed.

3.2 Internal flow characteristics at impeller

The impeller rotation work provides energy for water flow, and its structural parameters and motion state play a decisive role in the overall pump device. In order to further analyze the flow pattern in the impeller area, the impeller inlet section 1–1 and the impeller pressure surface are analyzed. The impeller inlet section 1-1 is 0.284*D* away from the impeller center line. The section diagram is shown in Figure 5.

The pressure contours of impeller cross-sections 1–1 are shown in Figure 6A. The distribution of cross-section pressure under different head conditions is the same. There are three

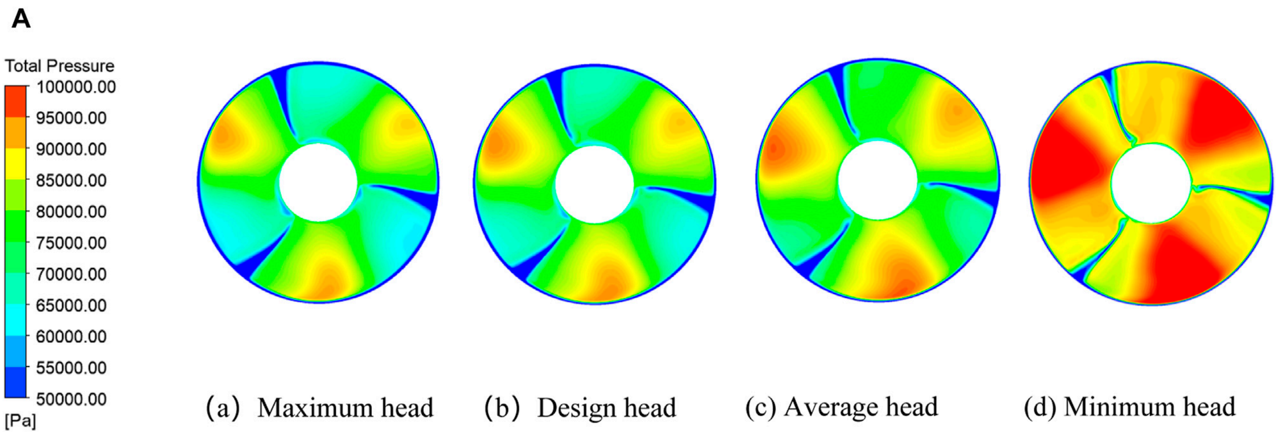

(a) Maximum head (b) Design head (c) Average head (d) Minimum head

Impeller cross-section 1-1 section

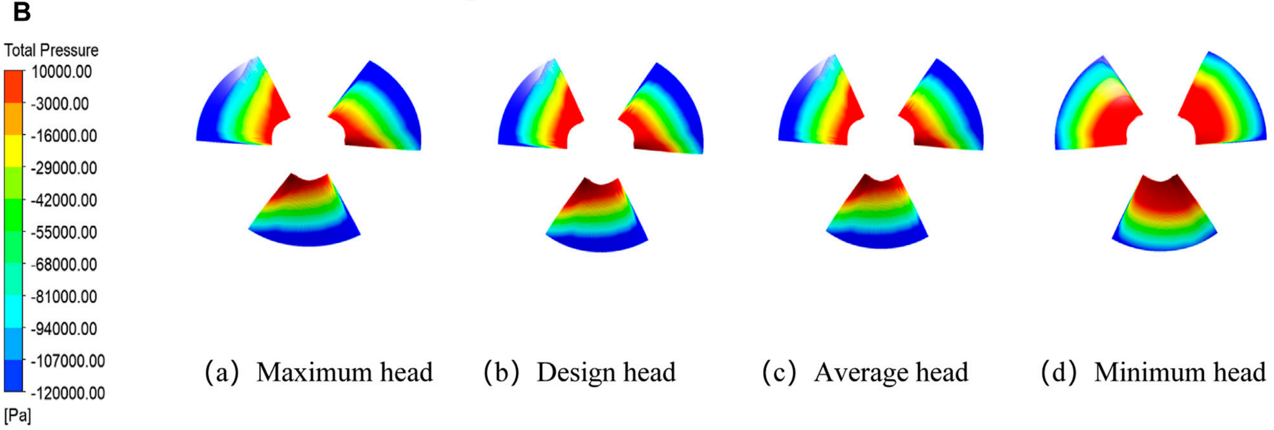

(a) Maximum head (b) Design head (c) Average head (d) Minimum head

Impeller blade (suction surface)

FIGURE 6
Impeller domain pressure contour. **(A)** Impeller cross-section 1-1 section (a) Maximum head. (b) Design head. (c) Average head. (d) Minimum head. **(B)** Impeller blade (suction surface). (a) Maximum head. (b) Design head. (c) Average head. (d) Minimum head.

high-pressure zones and three low-pressure zones, the high-pressure zone and the low-pressure zone interval distribution, and the number of blades is consistent. The high-pressure area is mainly concentrated in the impeller head, and the low-pressure zone is focused primarily in the impeller tail. The center of the high-pressure site is close to the rim, and the pressure decreases from the periphery to the hub. The center of the low-pressure zone is also located at the boundary, gradually increasing to the hub. It can be seen that with the decrease of the head, the pressure gradient at the cross section gradually decreases, and the range of the high-pressure area expands. At the minimum head, the high-pressure area is close to the hub part.

The pressure contours of the impeller pressure surface are shown in Figure 6B. When the impeller runs in a rotating state, the flow pattern at the impeller is complex, so the pressure on the blade surface is also problematic. The high-pressure zone of the blade is mainly distributed in the root of the blade, which is due to the existence of lousy flow patterns such as off-flow and secondary reflux at the basis of the blade. The high-pressure zone gradually decreases to the outer edge of the impeller, and the low-pressure area is located at the outer edge of the blade, and the range is enormous. When the head decreases from the average head to the design head, the area of the high-pressure zone of the blade increases significantly, which is because the increase of the water flow velocity at the impeller will increase the impact pressure on the blade, increasing the area of the high-pressure zone.

3.3 Inflow characteristics of guide vane

The guide vane is located at the outlet of the impeller domain, which mainly acts as a rectifier. Through the guide vane, the flow direction is changed, and the energy loss caused by the circumferential flow of water is reduced, so that it flows into and out of the water pipeline in a relatively stable flow state. In order to further understand the influence of guide vane on water flow, the characteristic section is taken for analysis. The characteristic section 1–1 is the interface between the inlet of the guide vane and the outlet

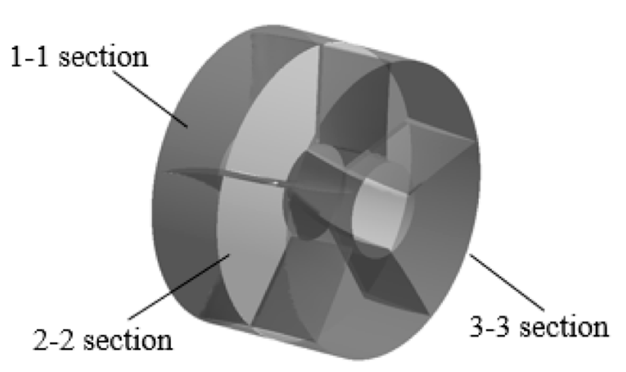

FIGURE 7
Characteristic section diagram of guide vane.

of the impeller, 0.322*D* away from the center line of the impeller. In order to find out the law of internal pressure and flow velocity in the guide vane domain, a 2-2 section is set inside the guide vane domain. Section 2–2 is located in the middle of the guide vane, 0.597*D* away from the center line of the impeller. Section 3–3 is located at the outlet of the guide vane. The schematic diagram of section 1.018*D* away from the center of the impeller is shown in Figure 7.

The pressure contours of the 1–1 section of the guide vane body is shown in Figure 8A The 1–1 section is located at the junction of the guide vane and the impeller domain. The pressure contour of this section mainly shows the distribution of large water pressure before entering the guide vane body. Due to the rotation of the impeller in the front of the section, there are three main high-pressure areas in the 1–1 section. However, due to the rectification effect of the guide vane body on the water body, there are also small-scale high-pressure areas in the position of the guide vane of the section. The high-pressure area is mainly distributed in the edge of the wheel to gradually reduce the pressure in the direction of the hub, and the low-pressure area is mainly concentrated in the hub. With the decrease of head, the flow rate increases gradually, the range of high-pressure area in the section cloud image decreases, the pressure gradient increases, and the section pressure is gradually uniform.

The pressure contours of the 2–2 section of the guide vane body is shown in Figure 8B. Section 2–2 is located in the middle of the guide vane body, which mainly shows the internal pressure change of the guide vane body. The guide vane body of the section is divided into five parts, but the high-pressure area is still concentrated in the projection position of the impeller blade, but it is smaller than the range of section 1–1. There is a low-pressure zone under each head condition, and the low-pressure zone is mainly distributed in the pressure surface of the guide vane. With the decrease of the head, the range of the high-pressure zone and the low-pressure zone of the section decreases, and the pressure change trend is consistent with that of section 1–1, and gradually tends to be uniform.

The pressure contours of the 3–3 section of the guide vane is shown in Figure 8C After the rectification of the guide vane, the water flow ahead of the spiral is blocked by the guide vane blade, and the direction of movement is changed, so that the flow pattern of the guide vane outlet is more stable, and the range of the high-pressure area and the low-pressure area of the section are reduced compared with those of the 1–1. The pressure variation trend of each head working condition is basically consistent with that of 1–1 section and 2–2.

The velocity contours of the 1–1 section of the guide vane is shown in Figure 9A. When the maximum head reaches the average head, there are three high velocity regions in the section and the position corresponds to the position of the blade. This is because the rotation of the blade makes the flow have a large velocity at this position. However, at the minimum flow rate, due to the mismatch between the blade speed and the flow rate, the flow is limited affected by the rotation of the blade. Therefore, the flow velocity at the cross section is relatively chaotic and there is no obvious division of high flow velocity area, and the overall flow velocity at the cross section is large.

The velocity contours of the 2-2 section of the guide vane are shown in Figure 9B. Due to the speed loop generated by the impeller rotation, three high velocity zones are generated at the corresponding position of the guide vane, and they are mainly distributed at the rim position and decrease to the hub. However, the range of high flow velocity area is large and the distribution is still relatively chaotic under the minimum head condition due to the mismatch between blade speed and flow. The velocity contour of the 3-3 section of the guide vane body is shown in Figure 9C. By comparing with the velocity contour of the 2-2 section, it can be seen that after the rectification of the guide vane body, the area of the high velocity area and the low velocity area of each working condition section is reduced, and the velocity of the section water body is more uniform after the rectification of the guide vane body.

4 Analysis of entropy generation characteristics of overcurrent components

4.1 Entropy production theory

Due to the simple model experiment is difficult to measure the energy loss in the pump device, so calculating the pressure difference between the inlet and outlet of the flow components is often used to analyze the energy loss of the pump device. However, this method can only calculate the energy loss of the whole flow channel of the pump device, and it is difficult to analyze the energy change of each component and even each characteristic section in detail. Therefore, the entropy production theory is introduced in the hydraulic analysis. Entropy production is due to the dissipation effect caused by irreversible factors in the process so that the mechanical energy lost by the system is converted into internal energy. In the pump system, since the flow we studied is constant temperature and there is no form of heat transfer in the process of movement, the increase of water entropy is mainly caused by the negative flow patterns such as flow separation and vortex, and the influence of solid wall viscous force on the pump device during operation. In turbulent flow, the fluid velocity includes two parts: average velocity and fluctuating velocity, and the corresponding entropy production rate also consists of two parts: one is the entropy production rate produced by the average flow movement. Second, the entropy production rate caused by turbulent kinetic energy dissipation caused by turbulent fluctuating velocity. The analysis of energy loss in the flow channel of the pump device utilizing entropy

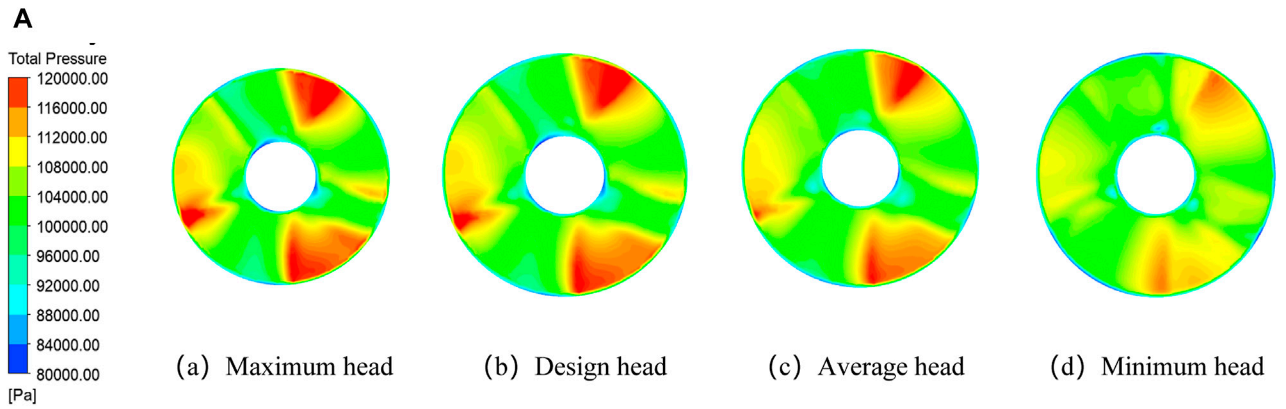

Guide vane 1-1 section

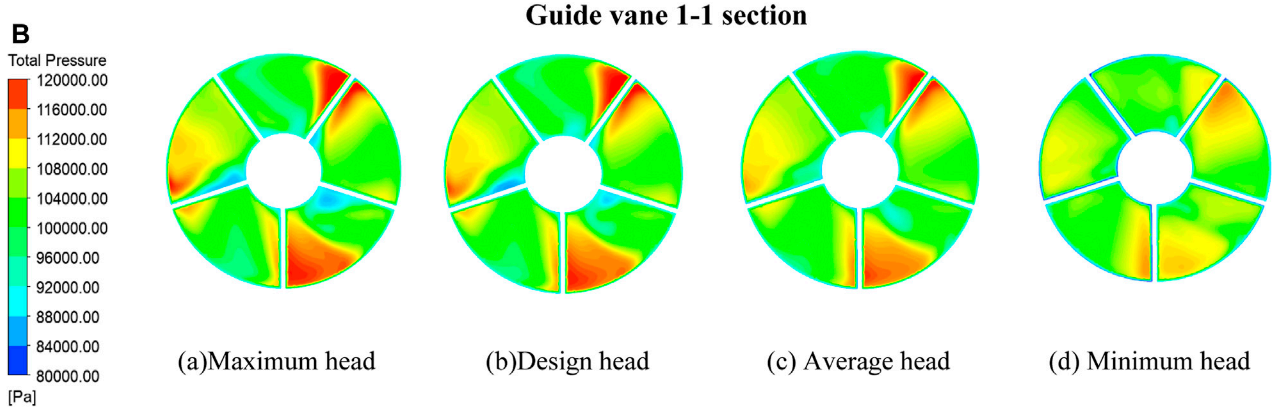

Guide vane 2-2 section

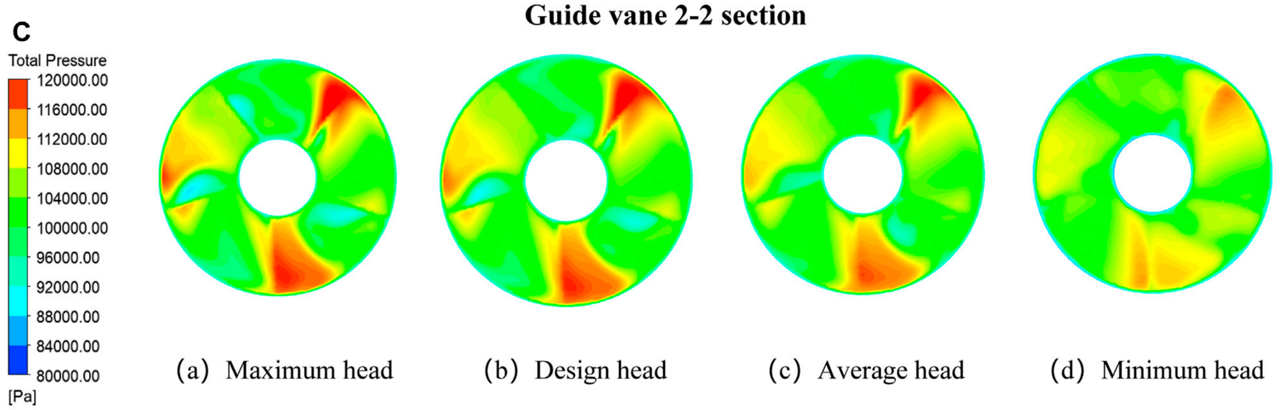

Guide vane 3-3 section

FIGURE 8
Guide vane domain pressure contour. **(A)** Guide vane 1-1 section. (a) Maximum head. (b) Design head. (c) Average head. (d) Minimum head. **(B)** Guide vane 2-2 section. (a) Maximum head. (b) Design head. (c) Average head. (d) Minimum head. **(C)** Guide vane 3-3 section. (a) Maximum head. (b) Design head. (c) Average head. (d) Minimum head.

generation theory can intuitively show the size and distribution of energy dissipation in the pump device. Therefore, when optimizing the structure of the pump device, we can focus on the intensive area of entropy generation and excess in the pump.

For turbulent flow, the entropy production dissipation based on the Reynolds time average can be divided into two parts: the viscous entropy production dissipation caused by fluid viscosity $\Delta S_{pro,\bar{D}}$ and the turbulent entropy production dissipation caused by turbulent pulsation $\Delta S_{pro,D'}$.In addition, the wall entropy production dissipation due to wall friction loss is $\Delta S_{pro,w}$.

The total entropy production dissipation of the whole device can be obtained from Equation 6 ΔS_{pro}.

$$\Delta S_{pro} = \Delta S_{pro,\bar{D}} + \Delta S_{pro,D'} + \Delta S_{pro,w} \tag{6}$$

The entropy production dissipation due to the time-averaged velocity can be calculated as follows.

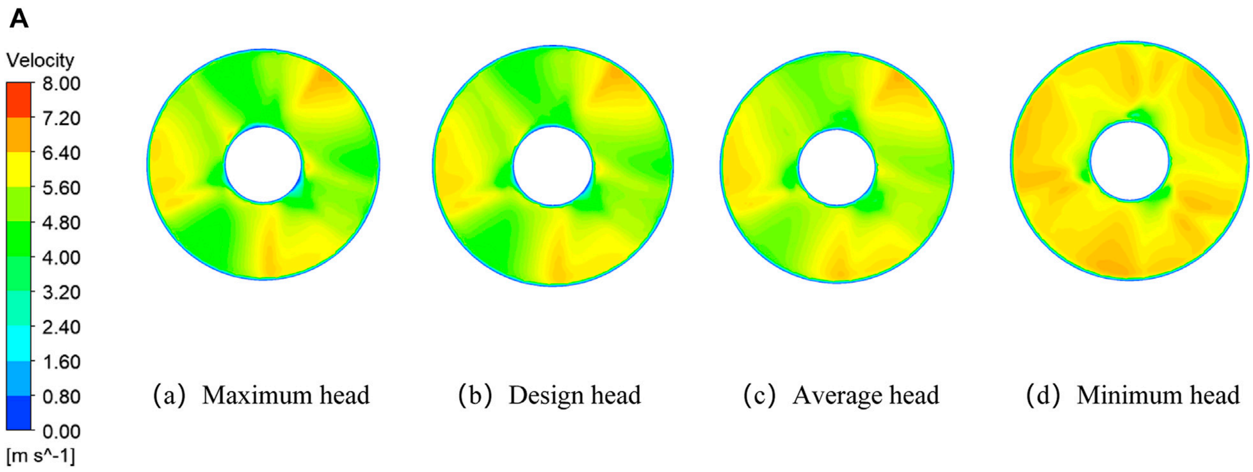

(a) Maximum head (b) Design head (c) Average head (d) Minimum head

Guide vane 1-1 section

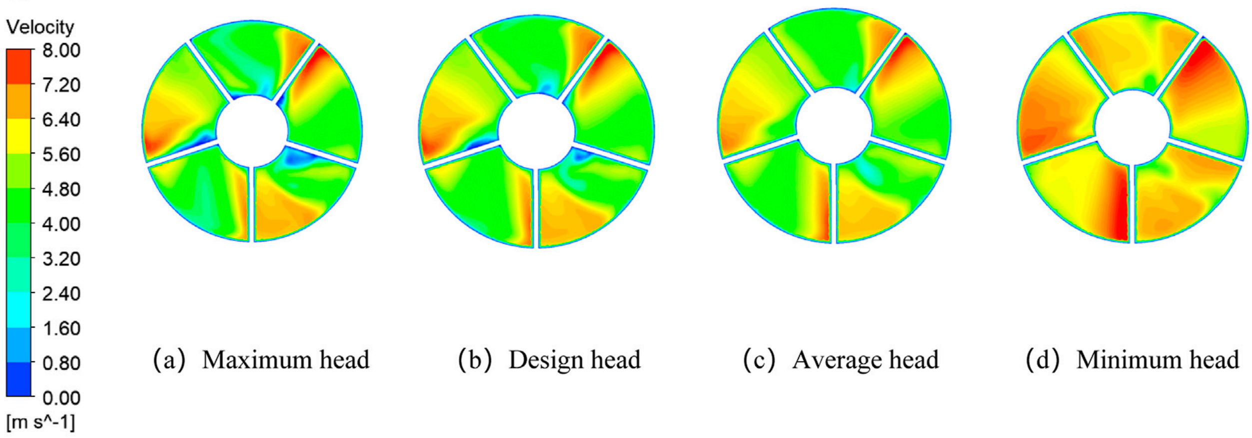

(a) Maximum head (b) Design head (c) Average head (d) Minimum head

Guide vane 2-2 section

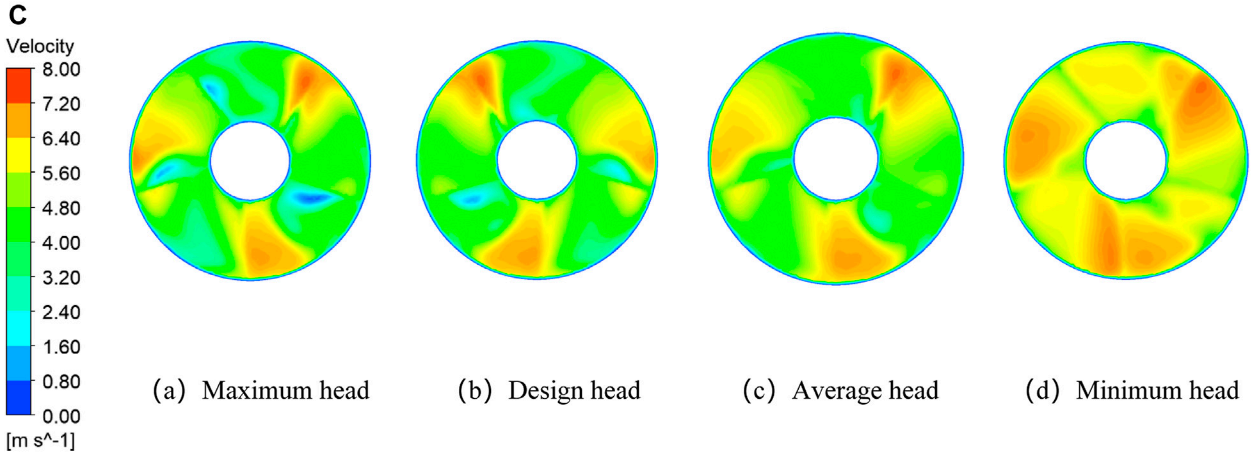

(a) Maximum head (b) Design head (c) Average head (d) Minimum head

Guide vane 3-3 section

FIGURE 9
Guide vane domain velocity contour. **(A)** Guide vane 1-1 section. (a) Maximum head. (b) Design head. (c) Average head. (d) Minimum head. **(B)** Guide vane 2-2 section. (a) Maximum head. (b) Design head. (c) Average head. (d) Minimum head. **(C)** Guide vane 3-3 section. (a) Maximum head. (b) Design head. (c) Average head. (d) Minimum head.

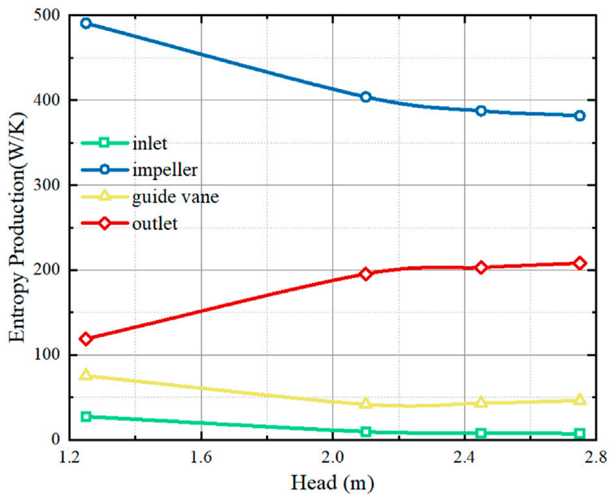

FIGURE 10
Total entropy production under different working conditions.

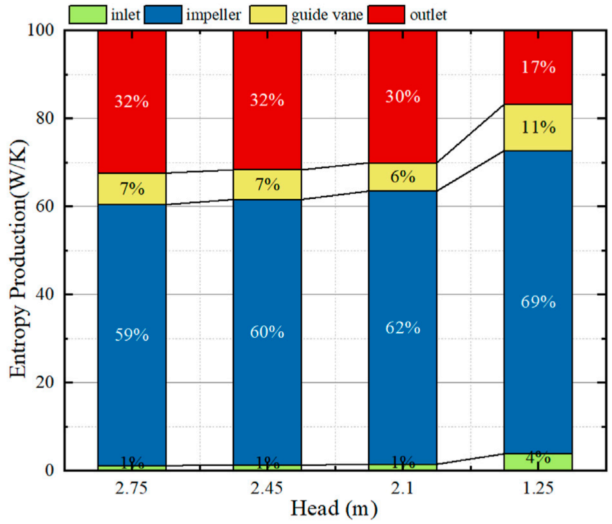

FIGURE 11
Percentage of entropy production per flow component.

$$\dot{S}_{\bar{D}}^{'''} = \frac{\mu_{eff}}{T}\left\{2\left[\left(\frac{\partial\bar{u}}{\partial x}\right)^2 + \left(\frac{\partial\bar{v}}{\partial y}\right)^2 + \left(\frac{\partial\bar{w}}{\partial z}\right)^2\right] + \left[\left(\frac{\partial\bar{v}}{\partial x} + \frac{\partial\bar{u}}{\partial y}\right)^2 + \left(\frac{\partial\bar{w}}{\partial x} + \frac{\partial\bar{u}}{\partial z}\right)^2 + \left(\frac{\partial\bar{v}}{\partial z} + \frac{\partial\bar{w}}{\partial y}\right)^2\right]\right\} \tag{7}$$

Where μ_{eff} is the dynamic viscosity (Pa-s). $\bar{u}$ 、 $\bar{v}$; $\bar{w}$ is the time-averaged velocity in the direction x, y, z components, (m/s).

The entropy production dissipation of turbulent dissipation due to velocity fluctuations can be calculated by the following Equation 8.

$$\dot{S}_{D}^{D'} = \beta\frac{\rho\omega k}{T} \tag{8}$$

Where $\beta = 0.09$. Ω is the turbulent eddy frequency (s^{-1}) and k is the turbulence energy (m^2/s^2).

The local entropy production dissipation integral of the computational domain is shown in Equations 9, 10.

$$\Delta S_{pro,\bar{D}} = \int_V \dot{S}_{\bar{D}}^{'''}\,\mathrm{d}V \tag{9}$$

$$\Delta S_{pro,D'} = \int_V \dot{S}_{D}^{D'}\,\mathrm{d}V \tag{10}$$

The wall entropy production dissipation can be calculated using the equation.

$$\Delta S_{pro,w} = \int_A \frac{\vec{\tau}\cdot\vec{v}}{T}\mathrm{d}A \tag{11}$$

Where, $\vec{\tau}$ is the wall shear stress (Pa), A is the area (m^2). $\vec{\tau}$ denotes the first grid velocity near the wall (m/s).

The entropy production of low head bulb perfusion pump under different characteristic head conditions is analyzed. Figure 10 is the total entropy production under other working conditions, and Figure 11 is the percentage of entropy production per flow component. The total entropy production of the impeller is the highest in the flow components, reaching more than 100,000 W/K, and has an increasing trend with the decrease of the head. The ratio of the entropy production of the impeller to the total entropy production increases significantly under the condition of a small head. The entropy production generated by the outflow channel ranked second and gradually decreased with the decrease of the head. Under the condition of a large head, the flow was small, and the flow was greatly affected by the velocity circulation, which was spiral forward. The flow pattern was disordered at the guide vane outlet, resulting in the entropy production reaching more than 40,000 W/K. When the head comes to the minimum head, the flow pattern in the outlet channel is improved, and the entropy production decreases sharply or even falls below the entropy output value of the inlet. When the head increases to the average head, the entropy production changes little. The entropy production at the guide vane decreases with the increase of the head, indicating that the recovery effect of kinetic energy increases with the addition of the flow rate. The total entropy production of the inlet decreases with the increase of the head but only accounts for 1% of the total entropy production. The channel has little effect on the entropy production loss of the pump device. The entropy production ratio at the impeller position increases gradually as the head decreases. When the head reduces from the complete head to the minimum head condition, the entropy production ratio at the impeller rises by 10%, the most apparent change among all overflow components.

4.2 Entropy production loss of each component

4.2.1 Entropy generation characteristics at impellers

The distribution of mainstream entropy production of impeller inlet 1–1 section is shown in Figure 12A. The mainstream entropy production around the flange and hub of impeller 1–1 section and

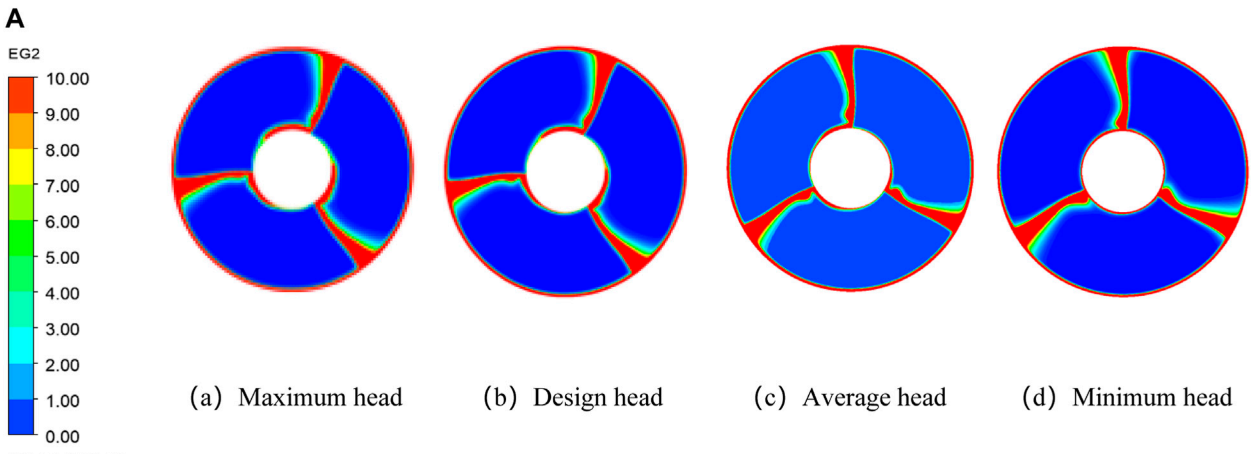

Impeller section 1-1 mainstream entropy production dissipation contour

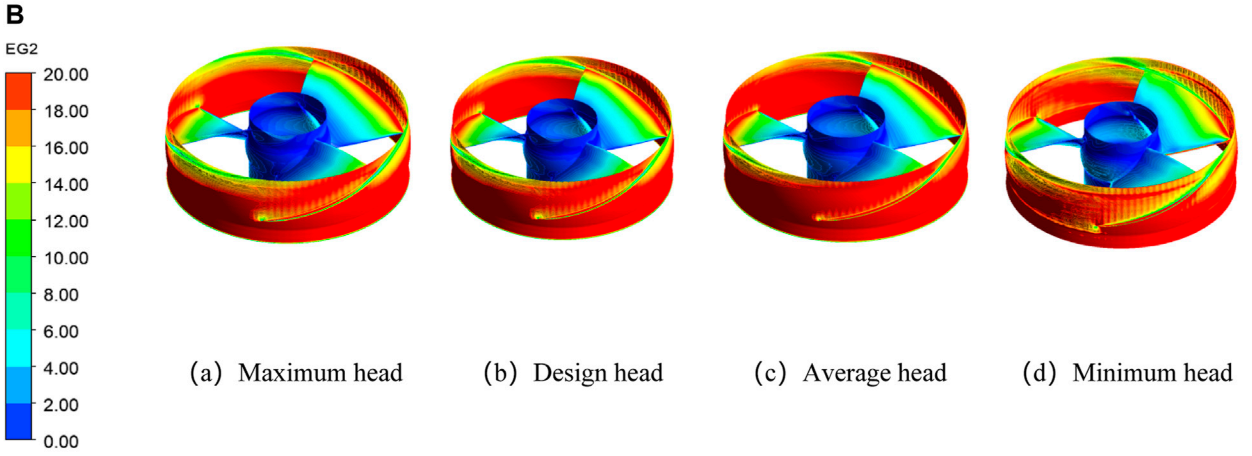

Impeller section wall entropy production dissipation contour

FIGURE 12
Entropy production dissipation contour in impeller domain. **(A)** Impeller section 1-1 mainstream entropy production dissipation contour. (a) Maximum head. (b) Design head. (c)Average head. (d) Minimum head. **(B)** Impeller section wall entropy production dissipation contour. (a) Maximum head. (b) Design head. (c) Average head. (d) Minimum head.

near the blade is relatively high. From the flange and hub, the entropy production gradually decreases to the center of the flow channel, and there is a very obvious change gradient at the edge wall of the section. The high value range of mainstream entropy production increases with the decrease of head. When head decreases, the flow rate increases with the increase of flow velocity, which increases the collision between water flow and wall and causes the increase of entropy production loss. In the mainstream region, the flow pattern is good, and there is no obvious energy conversion, so the entropy production loss is small.

The entropy production distribution at the impeller's overall wall is shown in Figure 12B. The entropy production of the impeller hub is significantly lower than that of the blade surface and the rim. The hub is selected for local amplification to analyze the distribution of entropy production. The rotation of the blade drives the flow to produce centrifugal force, which makes the flow and the pump shell have considerable friction. Therefore, the entropy production of the impeller rim and the wall of the blade domain is higher than that of the hub. The maximum entropy production rate on the blade is also at the rim. The entropy production rate decreases from the impeller rim to the hub, showing a gradient distribution.

4.2.2 Entropy generation characteristics at guide vane

The distribution of the main entropy production of the 1-1 section of the guide vane is shown in Figure 13A. Under different head conditions, the main entropy production has a high value area at the rim and hub. There are three high value areas of equal spacing around the hub, mainly due to the rotation of the blade at the impeller outlet section, which makes the water have a certain amount of circulation, resulting in the loss of entropy production caused by intense friction between the water and the wall. When the head is reduced, the high value distribution range of entropy production around the hub is further reduced, indicating that the entropy production distribution at the inlet of the guide vane is obviously affected by the impeller rotation under small flow conditions.

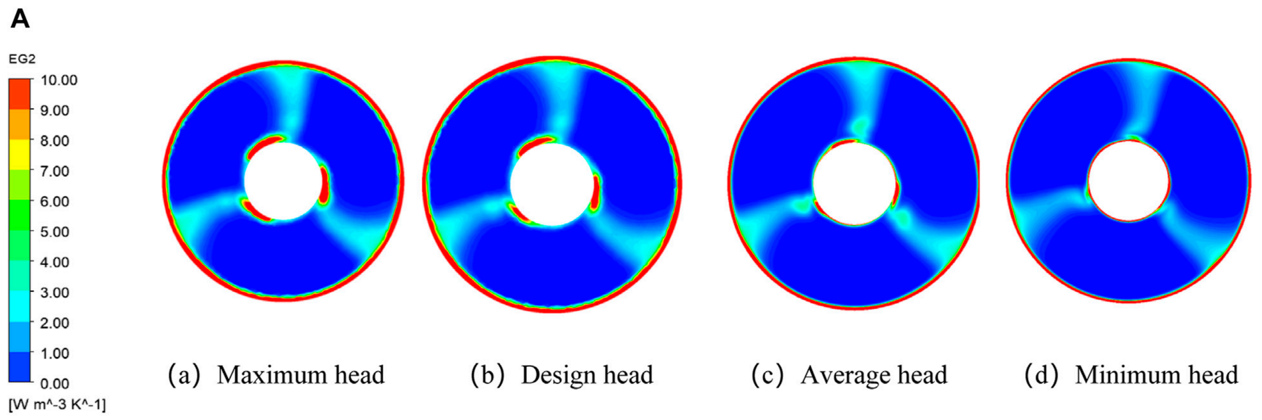

Guide vane 1-1 section

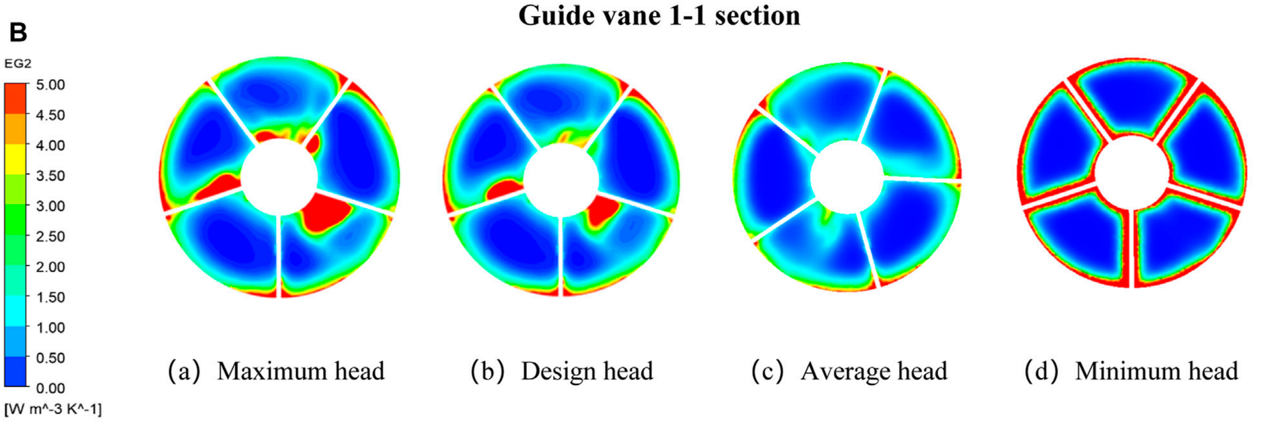

Guide vane 2-2 section

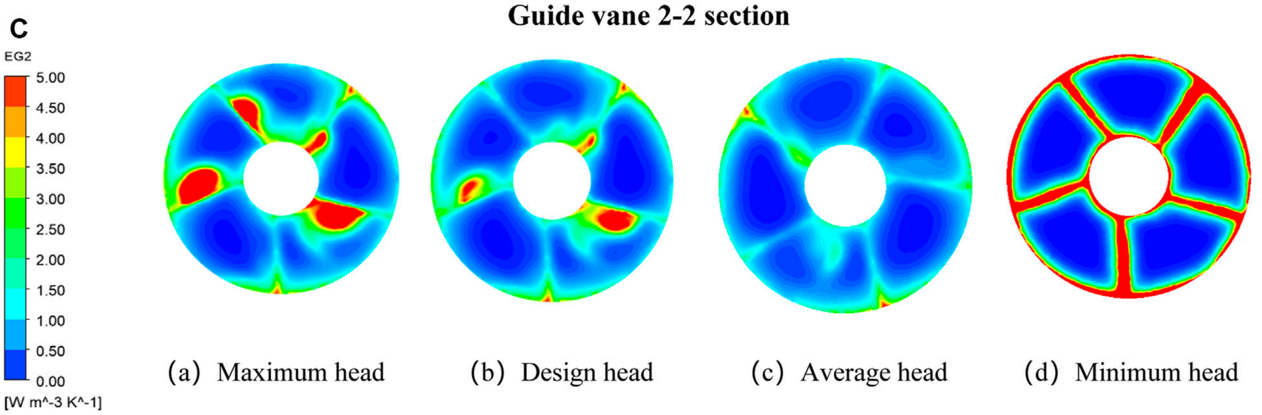

Guide vane 3-3 section

FIGURE 13
Mainstream entropy production dissipation in guide vane domain. **(A)** Guide vane 1-1 section. (a) Maximum head. (b) Design head. (c) Average head. (d)Minimum head. **(B)** Guide vane 2-2 section. (a) Maximum head. (b) Design head. (c) Average head. (d) Minimum head. **(C)** Guide vane 3-3 section. (a) Maximum head. (b) Design head. (c) Average head. (d) Minimum head.

The main entropy production distribution of guide vane 2-2 section is shown in Figure 13B. Due to the influence of guide vane, the section is divided into five channels, and the high value area of entropy production is still mainly distributed at the outer rim. However, at high lift, due to the small flow rate and low flow velocity, adverse flow patterns such as vortex or backflow are generated in the guide vane, which increases the entropy production loss. However, in the case of small head, the flow pattern of the water body is improved due to the increase of the flow velocity, but the friction between the water body and the wall increases, resulting in the increase of the high value area around the rim, hub and guide vane.

The mainstream entropy production distribution of the 3–3 section of the guide vane is shown in Figure 13C. The entropy production distribution of this section is still roughly divided into five parts with the same law. Under the high head condition, the bad flow pattern is improved after the guide vane rectifying the water body, and the range of high value area in the

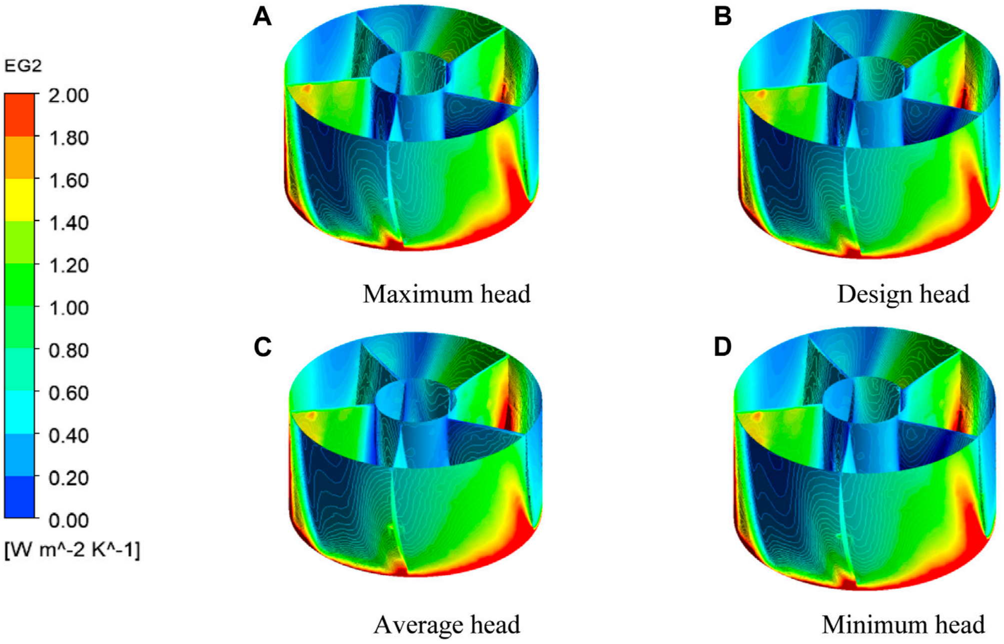

FIGURE 14
Guide vane section wall entropy production dissipation contour. **(A)** Maximum head. **(B)** Design head. **(C)** Average head. **(D)** Minimum head.

section is reduced. The high entropy production area under low head condition is still mainly located near the rim, hub and guide vane.

The wall entropy production contour of the guide vane computational domain is shown in Figure 14. The entropy production of the wall is lower than that of the mainstream entropy production, indicating that the mainstream entropy production is dominant at the guide vane. At the inlet of the guide vane body, the water has a certain amount of circulation due to the rotation of the impeller, and there is a strong impact and friction on the pump shell and the guide vane blade at the guide vane domain, resulting in a large loss of wall entropy production at this position. However, after the recovery of the water circulation by the guide vane, the wall entropy production of the water flow pattern gradually stabilized at the outlet of the guide vane decreases significantly, and there is a significant change gradient from the inlet to the outlet.

5 Conclusion

This paper mainly studies low-head bulb perfusion pumps' internal flow characteristics and analyzes essential components' entropy production.

(1) Firstly, through the comparative analysis of the numerical simulation experiment and the experimental data of the model machine, it is considered that the SST k-ω turbulence model can better match the experimental data in this paper.
(2) The streamline analysis of the pump device's whole flow channel shows that the inlet channel's streamline is usually good. After the impeller is rotated, the water body will have a certain amount of circulation. After the guide vane is recovered, the flow pattern is improved. The flow pattern is chaotic after the water flows through the bulb. The turbulent kinetic energy of water increases gradually with the decrease of the head.
(3) The high-pressure zone at the impeller is mainly located at the wheel rim, decreasing towards the hub, with a transparent gradient of variation, and the extent of the high-pressure zone gradually increases as the head decreases. The pressure variation in the impeller section also results in the water flow velocity at the impeller position being most excellent at the rim and reducing towards the hub. The guide vanes have a particular rectification effect on the water body. The cross-sectional analysis shows that the flow pattern of the water body through the guide vanes is improved to a certain extent and that the flow velocity of the water body at the guide vanes position gradually increases with decreasing head.
(4) The water entropy production head decreases and increases gradually, and the ratio of entropy production at the impeller to total entropy production is the largest. The mainstream entropy production at the impeller is mainly distributed around the blade because the impeller rotation reduces the water body. The entropy production of the wall is primarily located at the pump shell. The primary stream entropy production of the guide vane is under the non-design condition. Due to the instability of the water flow pattern, there is a lousy flow pattern inside the guide vane, which leads to a decrease in the turbulent entropy production. The wall entropy production at the inlet of the guide vane is more extensive, and there is a significant gradient change at the outlet.

Data availability statement

The raw data supporting the conclusion of this article will be made available by the authors, without undue reservation.

Author contributions

Software, WJ and YW Validation, LC and CL Writing-original draft preparation XT and YW Writing-review and editing, XT and LC Supervision, WJ, LC, and CL All authors have read and agreed to the published version of the manuscript.

Funding

This research was funded by the National Natural Science Foundation of China (grant no. 52279091), A Project Funded by the Priority Academic Program Development of Jiangsu Higher Education Institutions (PAPD). Water Conservancy Science and Technology Project of Jiangsu Province.

Conflict of interest

Publisher's note

References

Ahn, S. H., Xiao, Y., Wang, Z., Luo, Y., and Fan, H. (2018). Unsteady prediction of cavitating flow around a three dimensional hydrofoil by using a modified RNG k-ε model. *Ocean. Eng.* 158, 275–285. doi:10.1016/j.oceaneng.2018.04.005

David, B., Ramousse, J., and Luo, L. (2012). Optimization of thermoelectric heat pumps by operating condition management and heat exchanger design. *Energy Convers. Manag.* 60, 125–133. doi:10.1016/j.enconman.2012.02.007

Guo, Y., Yang, C., Wang, Y., Lv, T., and Zhao, S. (2022). Study on inlet flow field structure and end-wall effect of axial flow pump impeller under design condition. *Energies* 15 (14), 4969. doi:10.3390/en15144969

Haddad, O. M., Alkam, M. K., and Khasawneh, M. T. (2004). Entropy generation due to laminar forced convection in the entrance region of a concentric annulus. *Energy* 29 (1), 35–55. doi:10.1016/s0360-5442(03)00156-7

Hua, H., Zhang, Z., Liu, X., et al. (2018). Predictive analysis of the damage to axial-flow pump's impeller in sandy water. *Mechanics* 24 (3), 323–328. doi:10.5755/j01.mech.24.3.13854

Ji, D., Lu, W., Lu, L., Xu, L., Liu, J., Shi, W., et al. (2021). Comparison of saddle-shaped region of head-flow curve between axial-flow pump and its corresponding axial-flow pump device. *Shock. Vib.* 2021, 1–17. doi:10.1155/2021/9481822

Kan, N., Liu, Z., Shi, G., and Liu, X. (2021). Effect of tip clearance on helico-axial flow pump performance at off-design case. *Processes* 9 (9), 1653. doi:10.3390/pr9091653

Koranteng Osman, M., Wang, W., Yuan, J., Zhao, J., Wang, Y., and Liu, J. (2019). Flow loss analysis of a two-stage axially split centrifugal pump with double inlet under different channel designs. *Proc. Institution Mech. Eng. Part C J. Mech. Eng. Sci.* 233 (15), 5316–5328. doi:10.1177/0954406219843573

Liang, H., Dai, Q., Hua, X., and Wang, H. (2018). Optimization design and experimental research on low specific speed high efficiency cross-flow pump model. *People's Chang.* 49 (21), 84–89. doi:10.16232/j.cnki.1001-4179.2018.21.016

Liu, C. (2009). *Water pumps and pumping stations*. Beijing: China Water Conservancy and Hydropower Publishing House.

Ma, X., Liu, X., and Zhang, C. (2019). Analysis of internal flow field and optimal design of static vane of oil and gas mixing pump. *Fluid Mach.* 47 (7), 21–26. doi:10.16617/j.cnki.11-5543/TK.2021.06.11

Ma, Y. (2021). Analysis of operational performance of inverter-regulated bulb cross-flow pump at Sihong Station of South-North Water Transfer. *China Water Energy Electrification* 2021 (06), 47–51. doi:10.16617/j.cnki.11-5543/TK.2021.06.11

Mu, T., Zhang, R., Xu, H., Zheng, Y., Fei, Z., and Li, J. (2020). Study on improvement of hydraulic performance and internal flow pattern of the axial flow pump by groove flow control technology. *Renew. Energy* 160, 756–769. doi:10.1016/j.renene.2020.06.145

Pan, Y., Chen, A., and Wang, Z. (2021). Fluid dynamic characteristics and flow Distribution structure optimization of axial piston pump Considering cavitation bubble evolution. *J. Appl. Fluid Mech.* 14 (6), 1603–1616. doi:10.47176/jafm.14.06.32437

Qin, Z., Wu, J., and Zhang, R. (2009). Analysis of hydraulic performance and structure for linjiaba bulb tubular pump set. *J. Drainage Irrigation Mach. Engin* 27 (3), 177–180. doi:10.3969/j.issn.1674—8530.2009.03.010

Ran, H., Luo, X., Zhu, L., Zhang, Y., Wang, X., and Xu, H. (2012). Experimental study of the pressure fluctuations in a pump turbine at large partial flow conditions. *Chin. J. Mech. Eng.* 25 (6), 1205–1209. doi:10.3901/cjme.2012.06.1205

Shi, L., Zhang, W., Jiao, H., Tang, F., Wang, L., Sun, D., et al. (2020a). Numerical simulation and experimental study on the comparison of the hydraulic characteristics of an axial-flow pump and a full tubular pump. *Renew. Energy* 153, 1455–1464. doi:10.1016/j.renene.2020.02.082

Shi, W., Cai, R., Li, S., et al. (2020b). *Numerical simulation of pressure fluctuation characteristics of rear bulb tubular pump*. South-to-North water transfer and water conservancy technology, 1–11.

Wang, F., Zhang, L., Li, Y., and Zhang, Z. (2008). Some key issues in numerical simulation of non-constant turbulent flow in axial flow pumps. *J. Mech. Eng.* 2008 (08), 73–77. doi:10.3901/JME.2008.073

Wang, Y., and Dai, C. (2010). Analysis of pressure pulsation characteristics of unsteady flow field inside centrifugal pump. *J. Agric. Mach.* 41 (03), 91–95. doi:10.3969/j.issn.1000-1298.2010.03.019

Wu, Y., Liu, S., Yuan, H., and Shao, J. (2011). PIV measurement on internal instantaneous flows of a centrifugal pump. *Sci. China Technol. Sci.* 54, 270–276. doi:10.1007/s11431-010-4262-3

Xie, C., Wang, D., and Deng, X. (2018). "Application of SST turbulence model in high precision algorithms," in Proceedings of the 10th National Conference on Fluid Mechanics Abstracts, 52. [publisher unknown].

Yang, F., Hu, W., Li, C., Liu, C., and Jin, Y. (2020). Computational study on the performance improvement of axial-flow pump by inlet guide vanes at part loads. *J. Mech. Sci. Technol.* 34 (12), 4905–4915. doi:10.1007/s12206-020-2103-2

Yang, X., He, H., Xu, J., Wei, Y., and Zhang, H. (2018a). Entropy generation rates in two-dimensional Rayleigh–taylor turbulence mixing. *Entropy* 20 (10), 738. doi:10.3390/e20100738

Yang, X., Yu, Y., Liu, H., et al. (2018b). Research on the improvement of lateral inlet water flow pattern of pumping station based on SST k-ω turbulence model. *J. Three Gorges Univ. Nat. Sci. Ed.* 40 (03), 1–4.

Yu, A., Li, L., Ji, J., and Tang, Q. (2022). Numerical study on the energy evaluation characteristics in a pump turbine based on the thermodynamic entropy theory. *Renew. Energy* 195, 766–779. doi:10.1016/j.renene.2022.06.077

Zhang, D., Zhang, G., Shi, W., and Li, T. (2012). Performance prediction and experimental verification of axial flow pump based on CFD. *Appl. Mech. Mater.* 152, 1566–1571. doi:10.4028/www.scientific.net/AMM.152-154.1566

Zhang, R., Deng, D., Zhu, H., and Yao, L. (2008). Technical characteristics of different types of bulb cross-flow pumps. *South-North Water Divers. Water Conservancy Sci. Technol.* 6 (06), 6–9+15. doi:10.13476/j.cnki.nsbdqk.2008.06.030

Zhang, X., Tang, F., Chen, Y., Huang, C., Chen, Y., Wang, L., et al. (2022). Experimental study on the internal pressure pulsation characteristics of a bidirectional axial flow pump operating in forward and reverse directions. *Machines* 10 (3), 167. doi:10.3390/machines10030167

Zhang, D., Pan, Q., Hu, Z., Shi, W. D., Zhang, R. J., and Xing, J. (2017). Numerical simulation and optimization of solid-liquid two-phase flow in a back-swept axial-flow pump. *Therm. Sci.* 21 (4), 1751–1757. doi:10.2298/tsci160310064z

Zheng, Y., Chen, Y., Zhang, R., Ge, X., Lin, G., and Sun, A. (2017). A Study on non-constant flow characteristics of axial flow pump under stall conditions. *J. Agric. Mach.* 48 (07), 127–135. doi:10.6041/j.issn.1000-1298.2017.07.016

frontiers | Frontiers in Energy Research

TYPE Methods
PUBLISHED 18 May 2023
DOI 10.3389/fenrg.2023.1203801

OPEN ACCESS

EDITED BY
Yang Yang,
Yangzhou University, China

REVIEWED BY
Wei Zhao,
Northwest University, China
Shuang-Xi Guo,
Chinese Academy of Sciences (CAS),
China
Bo Chen,
Zhejiang Sci-Tech University, China

*CORRESPONDENCE
Xian Xu,
✉ xuxian@comac.cc

RECEIVED 11 April 2023
ACCEPTED 04 May 2023
PUBLISHED 18 May 2023

CITATION
Xu X, Chen Y, Han Z and Zhou F (2023), A total energy-based adaptive mesh refinement technique for the simulation of compressible flow.
Front. Energy Res. 11:1203801.
doi: 10.3389/fenrg.2023.1203801

A total energy-based adaptive mesh refinement technique for the simulation of compressible flow

Xian Xu*, Yingchun Chen, Zhirong Han and Feng Zhou

Shanghai Aircraft Design and Research Institute, Shanghai, China

In this paper, an adaptive mesh refinement technique is presented for simulation of compressible flows, which can effectively refine the mesh in the regions with shock waves and vortices. The present approach uses the total energy per unit volume as an indicator to capture the shock waves and vortical structures. In the approach, an h-refinement strategy is adopted. To save the computational effort, the flow variables on the new mesh are obtained from the previous step by interpolation, which ensures that the problem is always solved on the refined mesh. Both inviscid and viscous compressible flows are considered in this work. Their governing equations are, respectively, Euler equations and Navier–Stokes equations associated with the implementation of the Spalart–Allmaras turbulence model. The cell-centered finite volume method and Jameson scheme are chosen to carry out spatial discretization, and the five-stage Runge–Kutta scheme is applied to discretize the temporal derivative. The present approach is applied to simulate three test problems for its validation. Numerical results show that it can effectively capture the shock waves and vortices with improvement in solution accuracy.

KEYWORDS

adaptive technique, total energy per unit volume, shock wave, vortical structure, finite volume method

1 Introduction

To analyze the fluid characteristics, accurate simulation of the flow field is one of the main tasks in computational fluid dynamics (CFD). A high-quality mesh plays an important role in solution accuracy of the flow field. Generation of a good mesh usually requires some prior knowledge of the flow behavior in order to match the mesh point distribution to the essential features of the flow field. However, this prior knowledge may not always be available in advance. On the other hand, if the mesh is refined in the whole domain to guarantee the desired solution accuracy, the amount of computational time, effort, and resources may become excessive. How to balance the high-quality mesh and the computational effort is a critical issue. It seems that the solution-adaptive mesh refinement technique is an answer to this problem. It can effectively refine the mesh only in pivotal regions to improve the solution accuracy. In fact, research on this aspect is currently a hot topic in CFD (Harvey et al., 1992; Murayama et al., 2001; Yamazaki et al., 2007; Fossati et al., 2010).

One of the key issues in the solution-adaptive mesh refinement process is the identification of cells for refinement. Much effort has been devoted to this part (Murayama et al., 2001; Aftosmis and Berger, 2002; Jones et al., 2006; Yamazaki et al., 2007). The parameter used to identify the mesh refinement is generally called an adaptation function or indicator. Usually, the adaptation function is associated with some key physical variables such as density, entropy, kinetic energy, or a combination of them (Peraire et al., 1987). Some physical variables, such as helicity density and turbulent kinetic viscosity, are not always easy to derive, and the form of adaptation function may be complicated (Fossati et al., 2010). Under the premise of compressible flows, most adaptation functions are designed to resolve either shock waves or vortices (Pirzadeh, 1999; Ito et al., 2009). As the features of shock waves (high gradients for pressure and density) are quite different from those of vortices (high velocity gradients), a single adaptation function for compressible flows can usually only detect one feature of them. Wang et al. (2020) utilized adaptive mesh refinement (AMR) to capture vortices for improving the accuracy and efficiency of numerical simulation of the cavitation–vortex interaction. Steinthorsson et al. (1994) introduced a methodology based on the AMR algorithm of Berger and Colella (1989) for the accurate and efficient simulation of unsteady, compressible flows. Gou et al. (2018) introduced an accurate and robust AMR system suitable for turbomachinery applications and widely studied shock wave and tip leakage using the AMR method. Pantano et al. (2007) presented a methodology for the large-eddy simulation of compressible flows with a low-numerical dissipation scheme and structured adaptive mesh refinement (SAMR) used in turbulent flow regions while employing weighted essentially non-oscillatory order (WENO) to capture shocks. Papoutsakis et al. (2018) presented an adaptive mesh refinement (AMR) method suitable for hybrid unstructured meshes that allows for local refinement and de-refinement of the computational grid during the evolution of the flow to increase the order of accuracy in the region of shear layers and vortices. This paper takes this challenging issue and aims to present an indicator which can well detect both the shock waves and vortices in the compressible flow using h-type AMR.

This paper is organized as follows: in Section 2, the governing equations and methodologies for numerical discretization are briefly described. Section 3 depicts the solution-adaptive mesh refinement approach which involves the selection of the adaptation function and the h-refinement strategy (Pepper and Wang, 2007) based on body-fitted quadrilateral/hexahedral mesh. Section 4 presents three numerical examples to validate the present approach. We report conclusion in Section 5.

2 Governing equations and numerical discretization

The viscous, compressible flow of a perfect gas is governed by Navier–Stokes (N–S) equations (Blazek, 2001a). In a three-dimensional domain of volume Ω with boundary S, the integral form of the equations is expressed as

$$\frac{\partial}{\partial t}\int_{\Omega}\vec{W}\,d\Omega+\oint_{\partial\Omega}\left(\vec{F}_c-\vec{F}_v\right)dS=0. \tag{1}$$

Here, $\vec{W}$ is the vector of conservative variables which can be written in the three-dimensional form as

$$\vec{W}=\left[\rho\ \ \rho u\ \ \rho v\ \ \rho w\ \ \rho E\right]^T, \tag{2}$$

where ρ is the density of fluid; $u,\ v,\ w$ are the velocity components in x-, y-, and z-direction, respectively; and E is the energy. $\vec{F}_c$ is the vector of convective fluxes, which can be expressed as

$$\vec{F}_c=\begin{bmatrix}\rho V\\ \rho uV+n_x p\\ \rho vV+n_y p\\ \rho wV+n_z p\\ \rho HV\end{bmatrix}, \tag{3}$$

where p is the pressure and V is the velocity normal to the surface element dS, which is defined as the scalar product of the velocity vector and unit normal vector as follows:

$$V\equiv\vec{v}\cdot\vec{n}=n_x u+n_y v+n_z w. \tag{4}$$

The total enthalpy H is given by $E+p/\rho$. For the vector of viscous fluxes $\vec{F}_v$, we have

$$\vec{F}_v=\begin{bmatrix}0\\ n_x\tau_{xx}+n_y\tau_{xy}+n_z\tau_{xz}\\ n_x\tau_{yx}+n_y\tau_{yy}+n_z\tau_{yz}\\ n_x\tau_{zx}+n_y\tau_{zy}+n_z\tau_{zz}\\ n_x\Theta_x+n_y\Theta_y+n_z\Theta_z\end{bmatrix}, \tag{5}$$

where

$$\begin{aligned}\Theta_x&=u\tau_{xx}+v\tau_{xy}+w\tau_{xz}+k\frac{\partial T}{\partial x},\\ \Theta_y&=u\tau_{yx}+v\tau_{yy}+w\tau_{yz}+k\frac{\partial T}{\partial y},\\ \Theta_z&=u\tau_{zx}+v\tau_{zy}+w\tau_{zz}+k\frac{\partial T}{\partial z}\end{aligned} \tag{6}$$

are the terms describing the work of viscous stresses and the heat conduction in the fluid. T is the temperature. The thermal conductivity coefficient k is evaluated by

$$k=k_L+k_T=c_p\left(\frac{\mu_L}{Pr_L}+\frac{\mu_T}{Pr_T}\right). \tag{7}$$

Here, c_p is the specific heat coefficient at constant pressure, Pr_L and Pr_T are the laminar and turbulent Prandtl numbers, respectively; μ_L is the laminar viscosity; and μ_T is the turbulent eddy viscosity.

Generally, both Pr_L and Pr_T are assumed to be constant, i.e., $Pr_L=0.72$ and $Pr_T=0.9$. At the same time, the laminar viscosity can be calculated using the Sutherland formula: $\mu_L=10^{-6}\times 1.45T^{1.5}/(T+110)$, where the temperature T is in Kelvin degree. For the turbulent eddy viscosity, it can be determined with the aid of the turbulence model (Blazek, 2001b).

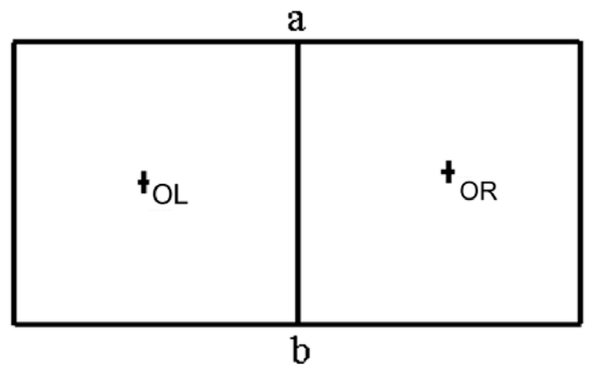

FIGURE 1
Cell-centered scheme of Jameson.

In this work, the Spalart–Allmaras (S–A) one-equation turbulence model (Spalart and Allmaras, 1992) is adopted. In this model, a transport equation is employed to calculate an eddy-viscosity variable $\tilde{\nu}$, and then the turbulent eddy viscosity μ_T is obtained from $\tilde{\nu}$.The S–A turbulence model allows for reasonably accurate predictions of turbulent flows with adverse pressure gradients. In this model, the solution at one point does not depend on the solution at other points. Therefore, it can be readily implemented on unstructured grids. It is also robust, converges fast to steady-state, and requires only moderate grid resolution in the near-wall region. The S–A model (Spalart and Allmaras, 1992) reads as follows:

$$\frac{\partial \tilde{\nu}}{\partial t} + \frac{\partial}{\partial x_i}(\tilde{\nu} u_i) = C_{b1}\tilde{S}\tilde{\nu} + \frac{1}{\sigma}\left\{\frac{\partial}{\partial x_j}\left[(\nu_L + \tilde{\nu})\frac{\partial \tilde{\nu}}{\partial x_j}\right] + C_{b2}\left(\frac{\partial \tilde{\nu}}{\partial x_j}\right)^2\right\} - C_{\omega 1} f_\omega \left(\frac{\tilde{\nu}}{d}\right)^2, \tag{8}$$

Here, $\nu_L = \mu_L/\rho$ is the laminar kinematic viscosity and $\sigma = 2/3$.

The terms controlling the destruction of the eddy viscosity read

$$f_\omega = g\left(\frac{1 + C_{\omega 3}^6}{g^6 + C_{\omega 3}^6}\right)^{1/6}, \quad g = r + C_{\omega 2}\left(r^6 - r\right), \quad r = \frac{\tilde{\nu}}{\tilde{S}\kappa^2 d^2}, \tag{9}$$

and the production term $\tilde{S}$ is evaluated using the following formulae:

$$\tilde{S} = S_{SA} + \frac{\tilde{\nu}}{\kappa^2 d^2} f_{\nu 2}, \quad f_{\nu 2} = 1 - \frac{\chi}{1 + \chi f_{\nu 1}}, \quad f_{\nu 1} = \frac{\chi^3}{\chi^3 + C_{\nu 1}^3}, \quad \chi = \frac{\tilde{\nu}}{\nu_L}. \tag{10}$$

Here, d is the distance to the closet wall and S_{SA} stands for the magnitude of the mean rotation rate, *i.e.*,

$$S_{SA} = \sqrt{2\Omega_{ij}\Omega_{ij}}, \quad \Omega_{ij} = \frac{1}{2}\left(\frac{\partial u_i}{\partial x_i} - \frac{\partial u_j}{\partial x_i}\right). \tag{11}$$

Finally, the constants in Eqs 8–10 are defined as

$$C_{b1} = 0.1355,\ C_{b2} = 0.622,\ C_{\nu 1} = 7.1,\ C_{\nu 2} = 7.1,$$
$$\kappa = 0.41,\ C_{\omega 1} = C_{b1}/\kappa^2 + (1 + C_{b2})/\sigma,\ C_{\omega 2} = 0.3,\ C_{\omega 3} = 2. \tag{12}$$

In current simulation, $\tilde{\nu} = 0.1\nu_L$ is set as the initial value of $\tilde{\nu}$ as well as the inflow boundary conditions. At outflow boundaries, $\tilde{\nu}$ is simply extrapolated from the interior of the computational domain. At solid walls, it is appropriate to set $\tilde{\nu} = 0$.

When the ideal gas is considered, we can simply neglect the viscous effect and get rid of $\vec{F}_v$; therefore, the N–S equations can be simplified to Euler equations.

To spatially discretize the governing equations, the finite volume method (FVM) is used in this study. FVM first divides the physical space into a number of control volumes and then integrates the governing equation (Eq. 1) over each control volume. In this work, the Jameson cell-centered scheme (Jameson et al., 1981) is used to define the location and shape of the control volume. The mean theorem is applied to approximate both the volume integral and the surface integral. The surface integral involves evaluation of fluxes at the interface between two neighboring control volumes. The flow quantities are stored at the centroids of each control volume which coincides with the grid cell. Note that with the mean theorem, the convective and the viscous fluxes are only evaluated at the center of each control surface using the flow information adjacent to two sides of the interface.

Two-dimensional grid is taken as an example. Using the cell-centered finite volume approach, in which the conserved variables $\vec{W}$ are located at the center of cells, the flux across the edge ab is calculated using the simple average of variables at the left cell center OL and right cell center OR (shown in Figure 1), e.g.,

$$\vec{W}_{ab} = \left(\vec{W}_{OL} + \vec{W}_{OR}\right)/2, \tag{13}$$

$$flux_{ab} = f\left(\vec{W}_{ab}\right). \tag{14}$$

Cell-centered schemes such as the one described previously would lead to odd–even decoupling of the solution, so that any errors are not damped and oscillations will be presented in the steady-state solution. Artificial dissipation terms D can eliminate these oscillations. Terms D are usually added to the convective fluxes in Eq. 8 and constructed as a blending of the second-order differences $d^{(2)}$ and the fourth-order differences $d^{(4)}$ of the conserved variables $\vec{W}$.

$$D = \sum_{i=1}^{kedges} d_i^{(2)} + \sum_{i=1}^{kedges} d_i^{(4)}, \tag{15}$$

$$d_i^{(2)} = \alpha_i \varepsilon_i^{(2)}\left(\vec{W}_{left} - \vec{W}_{right}\right)_i, \tag{16}$$

$$d_i^{(4)} = -\alpha_i \varepsilon_i^{(4)}\left(\nabla^2 \vec{W}_{left} - \nabla^2 \vec{W}_{right}\right)_i, \tag{17}$$

where the index i denotes the edges/faces delimiting the control volumes. $\vec{W}_{left}/\vec{W}_{right}$ denotes left/right cell conserved variables of the i^{th} edge/face. ∇^2 is defined for cell OL as

$$\nabla^2 \vec{W}_{OL} = \sum_{OA=1}^{OLedges}\left(\vec{W}_{OA} - \vec{W}_{OL}\right), \tag{18}$$

where OA stands for the cells around the cell OL.

Adaptive coefficients $\varepsilon_i^{(2)}$ and $\varepsilon_i^{(4)}$ are defined as

$$\varepsilon_i^{(2)} = kk^{(2)}\nu_i, \varepsilon_i^{(4)} = \max\left(0, kk^{(4)} - \varepsilon_i^{(2)}\right), \tag{19}$$

$$\nu_i = \frac{\left|p_{left} - p_{right}\right|}{\left|p_{left} + p_{right}\right|}, \tag{20}$$

where $kk^{(2)}$ and $kk^{(4)}$ are two empirical constants, which typically have values ranging between $0.5 < kk^{(2)} < 1.0$ and $kk^{(4)} = kk^{(2)}/32.0$. p_{left} in the shock sensor ν_i denotes the left cell pressure of the i^{th} edge/face. The scaling factor α_i is defined as

$$\alpha_i = (|V| + c)\Delta S, \tag{21}$$

where c and ΔS are the local speed of sound and the length of the edge/face, respectively.

After spatial discretization, the resultant ordinary differential equations can be solved using the explicit five-stage Runge–Kutta scheme of Jameson et al. (1981).

$$\begin{aligned}
\vec{W}^{(0)} &= \vec{W}^{n}, \\
\vec{W}^{(1)} &= \vec{W}^{(0)} - \frac{\alpha_1 \Delta t}{\Omega} \vec{R}^{n}\left(\vec{W}^{(0)}\right), \\
\vec{W}^{(2)} &= \vec{W}^{(0)} - \frac{\alpha_2 \Delta t}{\Omega} \vec{R}^{n}\left(\vec{W}^{(1)}\right), \\
\vec{W}^{(3)} &= \vec{W}^{(0)} - \frac{\alpha_3 \Delta t}{\Omega} \vec{R}^{n}\left(\vec{W}^{(2)}\right), \\
\vec{W}^{(4)} &= \vec{W}^{(0)} - \frac{\alpha_4 \Delta t}{\Omega} \vec{R}^{n}\left(\vec{W}^{(3)}\right), \\
\vec{W}^{n+1} &= \vec{W}^{(0)} - \frac{\alpha_5 \Delta t}{\Omega} \vec{R}^{n}\left(\vec{W}^{(4)}\right),
\end{aligned} \tag{22}$$

where $\vec{W}$ is the conservative variable in Eq. 1 and $\vec{R}$ is the corresponding residual. Δt is the time step, and Ω is the area of the cell. n is the current time level, $n+1$ is the new time level, and coefficients are taken as

$$\alpha_1 = 1/4, \alpha_2 = 1/6, \alpha_3 = 3/8, \alpha_4 = 1/2, \alpha_5 = 1. \tag{23}$$

3 Total energy-based adaptive mesh refinement approach

3.1 Selection of total energy per unit volume as the refinement indicator

After obtaining the basic solution of governing equations in the flow field, two important steps in any solution-adaptive mesh refinement technique must be followed. The first one requires an indicator to detect and locate the flow structures of interest, where the mesh refinement is needed. From a practical point of view, the adaptation function should indicate where the mesh must be refined to improve the accuracy. The adaptation function is usually selected from flow variables such as density, entropy, and turbulent kinetic energy. The flow considered in this paper is at high Reynolds number, and the Mach number ranges from low-compressible regime (Mach number < 0.3) to supersonic regime (Mach number > 1.0). In some cases, the viscous effect is very important. Thus, there is a practical demanding to select an adaptation function which can well capture both the features of shock waves and viscous effect.

It is known that any perturbation of flow must be followed by the perturbation of total energy per unit volume (ρE) in the flow field. For instance, when the air passes through the Mach wave, a perturbation of total energy per unit volume happens before and after the shock wave. ρE in the region with vortices is lower than that in other regions due to the effect of dissipation, and this is also a perturbation of total energy per unit volume. In this sense, ρE can be considered a universal adaptation variable. In this work, the adaptation function is constructed by the adaptation variable ρE as

$$\begin{aligned}
&\varphi_i = \frac{\Delta(\rho E)_i}{(\rho E)_\infty}, \quad \Delta(\rho E)_i = \max\left(\left|(\rho E)_i - (\rho E)_j\right|\right), \\
&\phi_i = \max\left(0, k_0 - \frac{(\rho E)_i}{(\rho E)_\infty}\right), \left\{ \begin{array}{l} \text{Euler Eq.} \;\; k_0 = 0, \\ \text{N} - \text{S Eq.} \;\; k_0 = 1, \end{array} \right.
\end{aligned} \tag{24}$$

where subscripts ∞, i, and j stand for the free stream, the i^{th} grid cell, and the cells adjacent to cell i, respectively. $(\rho E)_\infty$ is used to normalize ϕ_i and φ_i. Since there is a perturbation near the shock wave and in the region with vortices, ϕ_i is supposed to capture the shock waves and vortical structures. Furthermore, φ_i mainly contributes to locate the vortical structure when k_0 is taken as 1 in the viscous flow. The standard deviations (Zhang et al., 2001) of ϕ and φ are taken as

$$\sigma_\phi = \sqrt{\frac{1}{N}\sum_{i=1}^{N} {\phi_i}^2}, \quad \sigma_\varphi = \sqrt{\frac{1}{N}\sum_{i=1}^{N} {\varphi_i}^2}. \tag{25}$$

The summation is only performed for cells which satisfy $\phi_i > \varepsilon\phi_{\max}$, $\varphi_i > \varepsilon\varphi_{\max}$, where ε is an empirical threshold and is equal to 0.05 in this paper.

In the refinement process, the value of $\phi_i + \varphi_i$ for each cell depends on the value of $\sigma_\varphi + \sigma_\phi$. When $\phi_i + \varphi_i$ is greater than or equal to $\sigma_\varphi + \sigma_\phi$, the corresponding i^{th} grid cell is flagged for refinement. ρE, the last component of vector $\vec{W}$ in Eq. 2, is easy to be obtained from either N–S equations or Euler equations. From Eq. 24, we know that $\phi_i + \varphi_i$ has no effect on mesh configuration and is a non-dimensional number. Therefore, it is very convenient to set the threshold for mesh refinement.

3.2 Mesh refinement process

After determining the indicator, the process of mesh refinement, as the second step in adaptive technique, can be executed. In general, adaptive methods can be roughly classified into three categories (Pirzadeh, 2000; Pepper and Wang, 2007): grid movement (r-refinement), grid enrichment (h-refinement), and local solution enhancement (p-refinement). Each method has its own merits and shortcomings (Pepper and Wang, 2007; Li et al., 2010).

In the r-refinement method, the value of the adaptation function directly determines the mesh spacing. As described previously, the values of adaptation function in this work do not represent the

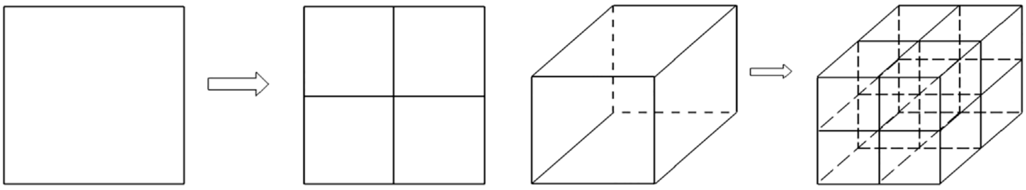

FIGURE 2
Refinement strategies.

magnitudes of estimated errors. Instead, they only indicate the location of dominant flow features. Therefore, r-refinement is not appropriate for this work. At the same time, although the p-refinement approach can obtain a solution with high order of accuracy in smooth flow regions, it is not effective in regions with discontinuity of flow variables. In addition, the coding of p-refinement is very complicated. In the methods based on h-refinement, however, an adaptation function only serves as a means to locate the regions which can be refined without considering the mesh spacing. Additionally, the h-refinement approach can be effectively applied in both the smooth flow and discontinuous flow regions. Due to these advantages, the h-refinement process is adopted in this work.

To reduce the number of cells, and in the meantime, to well capture the thin boundary layer, the structured mesh is taken as the background mesh. Grid cells are quadrilaterals for two-dimensional cases and hexahedra for three-dimensional cases. It should be indicated that as refinement process goes on, the overall unstructured mesh is formed.

During refinement, each quadrilateral/hexahedron is divided into four/eight sub-cells by joining the midpoints of opposite faces, as shown in Figure 2. For the two-dimensional case, to the initial coarse grid cell, a parent face is replaced by the current parent face and a new child face. This may form a hanging node (Spragle et al., 1995) between the initial coarse cell and the refined cells.

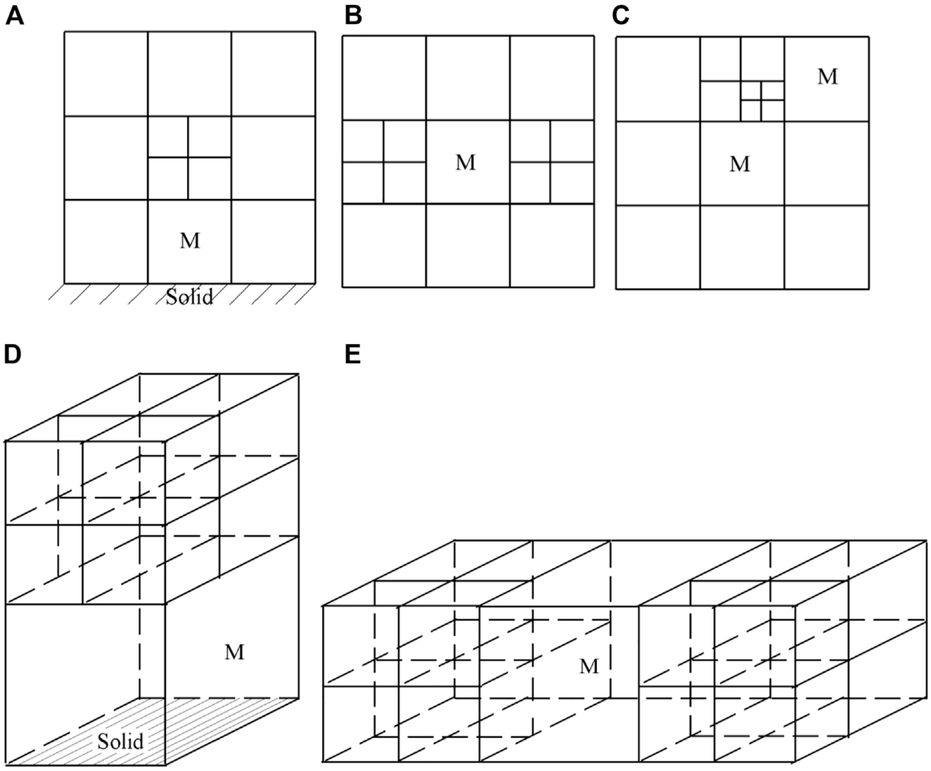

FIGURE 3
Unsmooth cells. **(A)** A two-dimensional cell has only one adaptive neighboring cell and its opposing neighboring cell is the wall. **(B)** A two-dimensional cell has two opposing adaptive neighboring cells. **(C)** A two-dimensional cell has a neighboring cell which has two or more adaptive levels. **(D)** A three-dimensional cell has only one adaptive neighboring cell and its opposing neighboring cell is the wall. **(E)** A three-dimensional cell has two opposing adaptive neighboring cells.

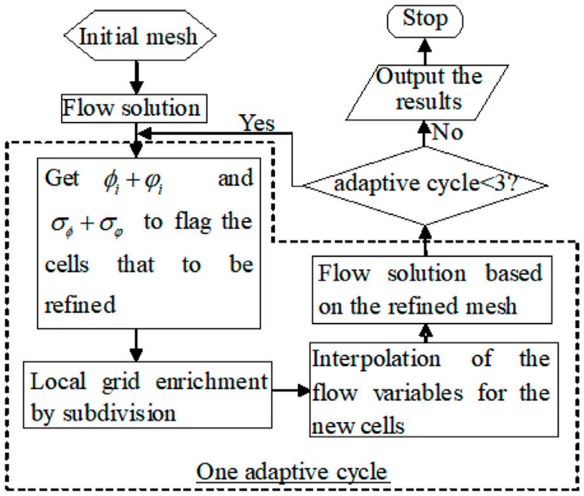

FIGURE 4
Flowchart of the process of the refinement strategy.

A node is a hanging node if it is not a vertex of all cells sharing one face. The hanging node grid adaptive scheme has the ability to efficiently operate on grids with a variety of cell shapes, including hybrid grids. However, the hanging node adaption scheme makes some solvers unusable, especially for the structured solvers. In contrast, the face-based unstructured solver presented by Li et al. (2010) provides an ideal environment for dealing with a hanging node adaption scheme. For the cell-centered scheme used in this work, as shown in Figure 1, the solver simply visits each face and then uses flow variables on its left and right grid cell to evaluate the face flux, and the contribution of the face flux is then sent to the two neighboring cells sharing the interface.

$$\begin{aligned} flux_{OL} &= flux_{OL} + flux_{ab}, \\ flux_{OR} &= flux_{OR} - flux_{ab}. \end{aligned} \tag{26}$$

Once the integration loop is performed along all face indexes, spatial discretization of the governing equations is completed.

To maintain a smooth variation of cell volume, additional cells are refined based on the relative position of neighboring cells or boundary conditions. There are three cases shown in Figure 3 in which cell M must be refined. One is that a cell has only one neighboring cell which is refined but its opposing neighboring cell is the solid wall (Figures 3A, D). The second is that a cell has two opposing neighboring cells (Figures 3B, E) or more than two neighboring cells are refined. If the initial grid needs more than one adaptation, then the third case (Figure 3C) arises: a cell has a neighboring cell which has two or more levels. For these cases, additional refinement is needed.

The flow field variables of new children cells can be interpolated from their parent cells. To carry out that, there are several different techniques. The simplest way, which is employed in this work, is to directly copy all physical variables of parent cells to their children cells. Such kind of implementation can improve the computational efficiency.

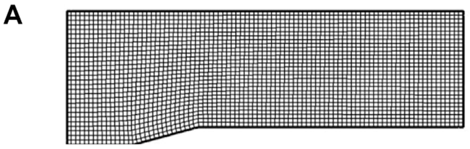

Initial mesh 89×29 for refinement case

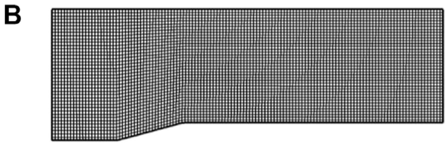

Uniform mesh with 5120 cells (without refinement)

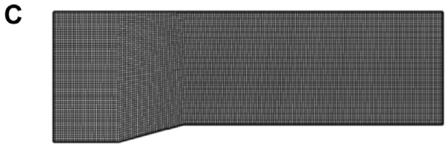

Uniform mesh 178×58 (without refinement)

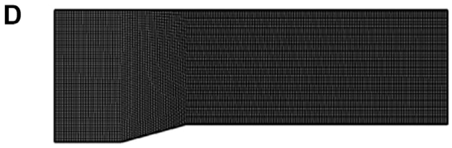

Uniform mesh 356×116 (without refinement)

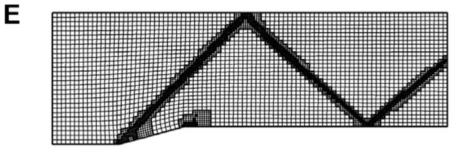

Final refined mesh with 5116 cells (refinement case)

FIGURE 5
Uniform meshes and final refined mesh after two levels of adaptation. **(A)** Initial mesh 89 × 29 for the refinement case. **(B)** Uniform mesh with 5,120 cells (without refinement). **(C)** Uniform mesh 178 × 58 (without refinement). **(D)** Uniform mesh 356 × 116 (without refinement). **(E)** Final refined mesh with 5,116 cells (refinement case).

The process of the refinement strategy is summarized in the flowchart as shown in Figure 4. On the other hand, it should be noted that the coarsening process, which is not required in this paper, can be easily implemented based on the obtained information during the refinement process.

4 Numerical examples

To validate the present approach and demonstrate its capability for effective simulation of inviscid/viscous compressible flows, three typical problems are selected. The first problem is a two-dimensional inviscid flow in a channel with a 15° ramp with the typical multi-channel shock wave and expansion wave, to demonstrate the capability to capture shock waves. The second problem is the three-dimensional inviscid flow around the ONERA M6 wing at a transonic speed resulting in a λ

TABLE 1 Comparison of computational cost among different meshes.

	Initial mesh cell number	Final mesh cell number	Time/s
Refinement (two adaption levels)	2,581	5,116	113
	5,120	5,120	37
Without refinement	10,324	10,324	104
	41,296	41,296	1,106

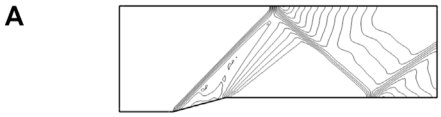

Mach number contours based on initial mesh of 89×29

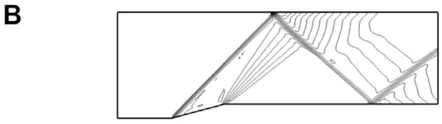

Mach number contours based on uniform mesh with 5120 cells

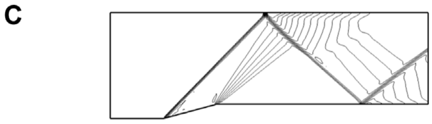

Mach number contours based on uniform mesh of 178×58

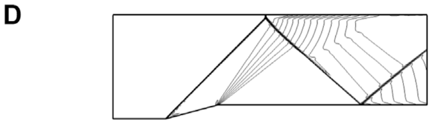

Mach number contours based on uniform mesh of 356×116

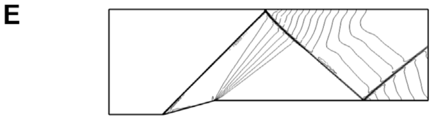

Mach number contours based on final refined mesh of refinement case

FIGURE 6
Mach number contours in the contracted channel based on uniform meshes and final refined mesh. **(A)** Mach number contours based on the initial mesh of 89 × 29. **(B)** Mach number contours based on the uniform mesh with 5,120 cells. **(C)** Mach number contours based on the uniform mesh of 178 × 58. **(D)** Mach number contours based on the uniform mesh of 356 × 116. **(E)** Mach number contours based on the final refined mesh of the refinement case.

shock wave on the upper surface of the wing, to show the capability of the algorithm to capture shock waves in a transonic flow. In the third problem, we hope to show the capability of the algorithm on simulating a detached vortex of a delta wing, especially the vortex core fragmentation, which is important in calculating the lift and drag coefficients.

4.1 Two-dimensional inviscid flow in a channel with a ramp

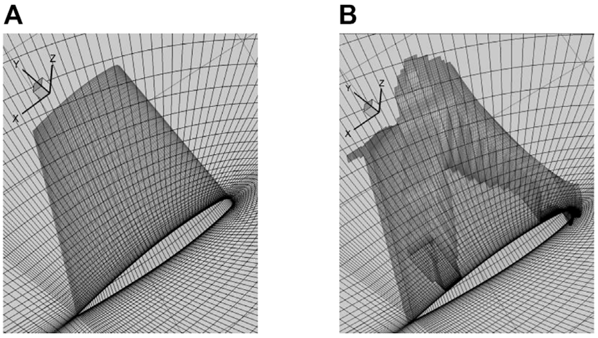

Initial mesh

Refined mesh

FIGURE 7
Initial and refined mesh for the ONERA M6 wing. **(A)** Initial mesh. **(B)** Refined mesh.

By solving Euler equations, the results for supersonic flow at a Mach number of 2 in a channel with a 15^0 ramp ranging from $x = 0.5$ to $x = 1.0$ can be obtained. The upper and bottom boundaries are solid walls, and the left and right boundaries are the inlet and outlet of the flow field, respectively.

The initial mesh is a uniform mesh containing 89 × 29 quadrilateral cells as shown in Figure 5A. Figure 6A shows the Mach number contour lines for the entire flow field based on the initial mesh. The shock wave emanating from the leading ramp and its reflection as well as the expansion wave can be clearly captured. After two levels of adaptation are implemented, the final refined mesh, as depicted in Figure 5E, contains 5,116 quadrilateral cells. The Mach contours on the final refined mesh are displayed in Figure 6E.

To compare the computational cost (cells and seconds) between cases with refinement and without refinement, numerical simulation of the same problem on the three uniform meshes without refinement is carried out. The three uniform meshes without refinement are shown in Figures 5B–D. The mesh in Figure 5B has 5,120 cells. The number of cells for this mesh is the same as the final refined mesh of the refinement case. The mesh in Figure 5C has 10,324 cells which are approximately two times the cells in the final refined mesh of the refinement case. The mesh spacing for this case is the same as the minimum mesh spacing of the refinement case when the initial mesh shown in Figure 5A is refined by one adaption level. The mesh in Figure 5D has 41,296 cells which are approximately eight times the cells in the final refined mesh of the refinement case. The mesh spacing for this case is the same as the minimum mesh spacing of the refinement case when the initial mesh in Figure 5A is refined by two adaption levels. All the results (Mach number contour) are demonstrated in Figure 6. The minimum and maximum levels of contours are 1.0 and 1.8 respectively, and the number of levels is 14. Figures 6A–D show that the shock wave becomes thinner and thinner with the increase in cell numbers. It is seen clear from the figure that the results of the uniform mesh of 41,296 cells are very close to those of the final refined mesh where two adaption levels are used to refine the mesh. This can be well understood as both cases have the same mesh spacing in the vicinity of the

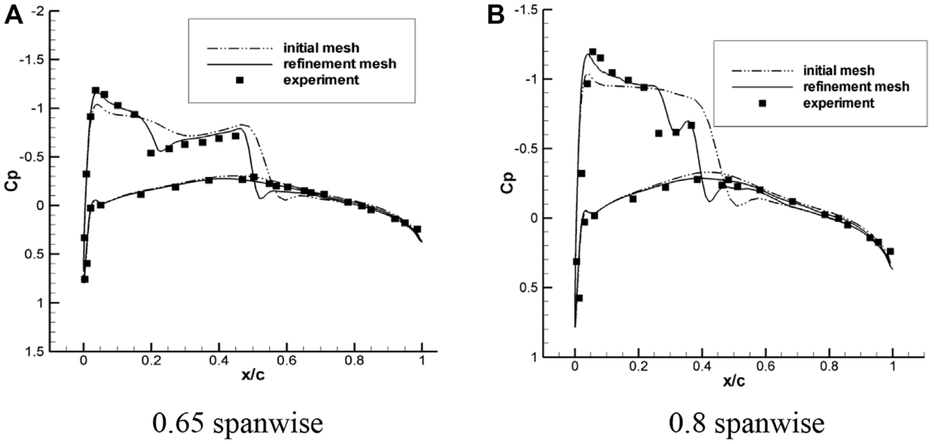

FIGURE 8
Pressure coefficient distributions at 0.65 and 0.8 spanwise locations for the ONERA M6 wing. **(A)** 0.65 spanwise. **(B)** 0.8 spanwise.

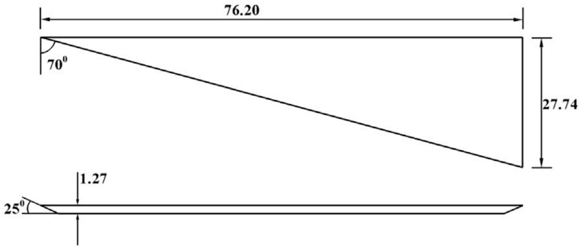

FIGURE 9
Flat-plate semispan delta wing model.

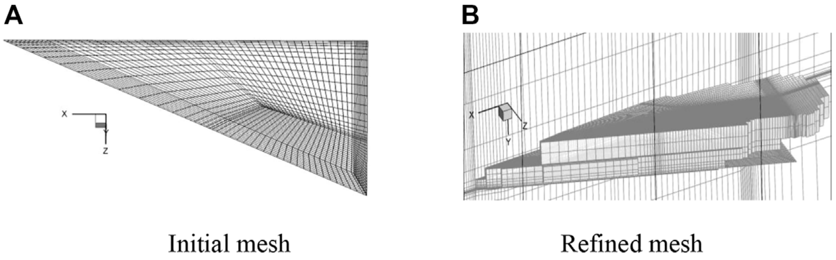

FIGURE 10
Initial mesh and refined mesh for the delta wing. **(A)** Initial mesh. **(B)** Refined mesh.

shock wave. The computational time required on the meshes shown in Figure 5 is listed in Table 1. It can be observed from Table 1 that the refinement case with two adaption levels only takes approximately 10% of the computational time of the uniform mesh case (without refinement) when the mesh spacing near the shock wave is kept the same. This well demonstrates high computational efficiency of the solution-adaptive approach.

4.2 Three-dimensional inviscid flow around the ONERA M6 wing

To further demonstrate the capability of the present solution-adaptive mesh refinement approach for capturing the shock wave, the inviscid flow around the ONERA M6 wing is considered. The Mach number is 0.84, and the incidence is 3.06°. Same as the case in Section 4.1, the governing equations are Euler equations.

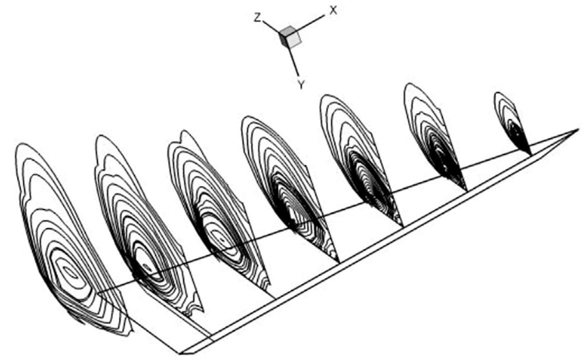

FIGURE 11
Contours of $\phi_i + \varphi_i$ at different cross sections.

A background mesh with a nearly uniform grid distribution is generated as shown in Figure 7A. The initial mesh contains 294,912 hexahedral cells. Figure 7B shows the final refined mesh which contains 440,365 hexahedral cells. Obviously, the majority of mesh refinement occurs in the shock wave regions, and the refined cells clearly outline the λ shock waves.

The surface pressure coefficient distributions at 0.65 and 0.8 spanwise locations obtained on the initial coarse mesh and the final refined mesh are compared in Figure 8 with the experimental data (Schmitt and Charpin, 1979). The comparison indicates that the shock wave is diffused due to the coarse mesh. The high resolution of shock waves by the refined mesh is evident as revealed by sharp discontinuity of the pressure distribution. There are some deviations between the numerical results and the experimental data. The reason may be due to the fact that the inviscid flow is assumed in the numerical computation, while the real flow always involves viscous effect.

Numerical simulations for two-dimensional inviscid flows in a channel with a ramp and three-dimensional inviscid flows around the ONERA M6 wing well demonstrate the capability of the present solution-adaptive mesh refinement approach for capturing shock waves and expansion waves. To illustrate the ability of the present approach for capturing vortices, numerical simulation of three-dimensional compressible viscous flows around a delta wing is considered in the following example. The prediction of leading-edge vortex breakdown on a delta wing at high angles of attack is made.

4.3 Three-dimensional viscous flow around a delta wing

The geometry chosen for this case is a flat-plate semispan delta wing with a leading-edge sweep of 70^0 and a 25^0 bevel on the lower surface along the leading and trailing edges (Agrawal et al., 1992) as shown in Figure 9. For this problem, N–S equations with the S–A turbulent model are taken as governing equations. Numerical simulation is carried out at a Mach number of 0.3 and an incidence of 30^0. The Reynolds number based on the root chord is taken as one million.

The initial mesh and the adaptive refined mesh are displayed in Figure 10. The corresponding adaptation function is shown in Figure 11. The initial mesh contains 320,624 hexahedral cells. After refinement, the final mesh contains 503,317 hexahedral cells.

Figure 12 shows some numerical results for this problem. The solution presented in Figure 12A shows the vortex core line without vortex breakdown, which is different from the solution based on the refined mesh presented in Figure 12B.

5 Conclusion

A solution-adaptive mesh refinement technique, which is based on the total energy per unit volume as the refinement indicator, is presented in this work. Different from previous adaptation indicator used, the present indicator can well detect both the shock waves and vortices. The technique is validated by applying it to simulate two-dimensional and three-dimensional steady compressible inviscid/viscous flows. The h-refinement approach by subdivision is adopted to perform the mesh refinement process.

The capability of the present solver is verified by applying it to handle three test problems. For inviscid/viscous flows, the Euler/

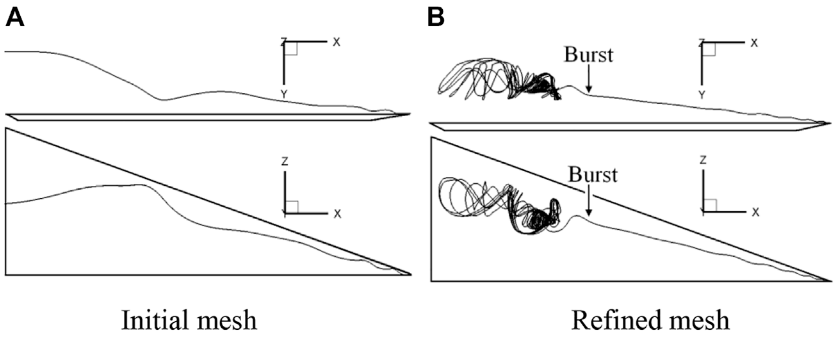

FIGURE 12
Vortex breakdown position indicated by the core line, $Ma_\infty = 0.3, \alpha = 30^0$, Re = 1.0E6. A vortex breakdown at approximately 0.6 root chord observed from the adaptive solution is supported by both experimental data and other numerical results (Agrawal et al., 1992; O'Neil et al., 1989). **(A)** Initial mesh. **(B)** Refined mesh.

Navier–Stokes (with the Spalart–Allmaras one-equation turbulence model) equations are employed. The cell-centered finite volume method is applied for spatial discretization, and an explicit five-stage Runge–Kutta scheme is used to implement time integration. Numerical results show that the proposed adaptation function can well capture the shock waves, expansion waves, and vortices in the flow field. As a consequence, a high-resolution solution of important flow features such as shock waves and vortices is obtained.

Data availability statement

The original contributions presented in the study are included in the article/Supplementary Material; further inquiries can be directed to the corresponding author.

Author contributions

Conceptualization and methodology, XX; methodology, YC; resources and data curation, ZH; writing—original draft preparation, XX; writing—review and editing, ZH; supervision, FZ; project administration, XX; funding acquisition, YC. All authors listed have made a substantial, direct, and intellectual contribution to the work and approved it for publication.

Funding

This research was funded by the National Key R&D Program of China (Project No. 2020YFA0712000).

Conflict of interest

The authors declare that the research was conducted in the absence of any commercial or financial relationships that could be construed as a potential conflict of interest.

Publisher's note

References

Aftosmis, M. J., and Berger, M. J. "Multilevel error estimation and adaptive h-refinement for Cartesian meshes with embedded boundaries," in Proceedings of the 40th AIAA Aerospace Sciences Meeting & Exhibit, Reno, NV, USA, January 2002. doi:10.2514/6.2002-863

Agrawal, S., Barnett, R. M., and Robinson, B. A. (1992). Numerical investigation of vortex breakdown on a delta wing. *AIAA J.* 30 (3), 584–591. doi:10.2514/3.10960

Berger, M. J., and Colella, P. (1989). Local adaptive mesh refinement for shock hydrodynamics. *J. Comput. Phys.* 82 (1), 64–84. doi:10.1016/0021-9991(89)90035-1

Blazek, J. (2001). *Computational fluid dynamics: Principles and applications.* Kidlington, England: Elsevier Science Ltd, 5–22.

Blazek, J. (2001). *Computational fluid dynamics: Principles and applications.* Kidlington, England: Elsevier Science Ltd, 225–265.

Fossati, M., Guardone, A., and Vigevano, L. (2010). A node-pair finite element/finite volume mesh adaptation technique for compressible flows. *Int. J. Numer. Methods Fluids* 70. doi:10.1002/fld.2728

Gou, J., Yuan, X., and Su, X. (2018). Adaptive mesh refinement method based investigation of the interaction between shock wave, boundary layer, and tip vortex in a transonic compressor. *Proc. Institution Mech. Eng. Part G J. Aerosp. Eng.* 232 (4), 694–715. doi:10.1177/0954410016687142

Harvey, A. D., Acharya, S., and Lawrence, S. L. (1992). Solution-adaptive grid procedure for the parabolized Navier-Stokes equations. *AIAA J.* 30 (4), 953–962. doi:10.2514/3.11014

Ito, Y., Shih, A., Koomullil, R., Kasmai, N., Jankun-Kelly, M., and Thompson, D. (2009). Solution adaptive mesh generation using feature-aligned embedded surface meshes. *AIAA J.* 47 (8), 1879–1888. doi:10.2514/1.39378

Jameson, A., Schmidt, W., and Turkel, E. "Numerical solutions of the Euler equations by finite volume methods using Runge-Kutta time-stepping schemes," in Proceedings of the 14th Fluid and Plasma Dynamics Conference, Palo Alto, CA, USA, June 1981. doi:10.2514/6.1981-1259

Jones, W. T., Nielsen, E. J., and Park, M. A. "Validation of 3D adjoint based error estimation and mesh adaptation for sonic boom prediction," in Proceedings of the 44th AIAA Aerospace Sciences Meeting and Exhibit, Reno, NV, USA, January 2006. doi:10.2514/6.2006-1150

Li, Y., Premasuthan, S., and Jameson, A. "Comparison of h- and p-adaptations for spectral difference methods," in Proceedings of the 40th Fluid Dynamics Conference and Exhibit, Chicago, IL, USA, June 2010.

Murayama, M., Nakahashi, K., and Sawada, K. (2001). Simulation of vortex breakdown using adaptive grid refinement with vortex-center identification. *AIAA J.* 39 (7), 1305–1312. doi:10.2514/2.1448

O'Neil, P. J., Roos, F. W., Kegelman, J. T., Barnett, R. M., and Hawk, J. D. (1989) NADC-89114-60. Canada: NRC.Investigation of flow characteristics of a developed vortex

Pantano, C., Deiterding, R., Hill, D. J., and Pullin, D. (2007). A low numerical dissipation patch-based adaptive mesh refinement method for large-eddy simulation of compressible flows. *J. Comput. Phys.* 221 (1), 63–87. doi:10.1016/j.jcp.2006.06.011

Papoutsakis, A., Sazhin, S. S., Begg, S., Danaila, I., and Luddens, F. (2018). An efficient Adaptive Mesh Refinement (AMR) algorithm for the Discontinuous Galerkin method: Applications for the computation of compressible two-phase flows. *J. Comput. Phys.* 363, 399–427. doi:10.1016/j.jcp.2018.02.048

Pepper, D. W., and Wang, X. (2007). Application of an h-adaptive finite element model for wind energy assessment in Nevada. *Renew. Energy* 32, 1705–1722. doi:10.1016/j.renene.2006.08.011

Peraire, J., Vadhati, M., Morgan, K., and Zienkiewicz, O. C. (1987). Adaptive remeshing for compressible flow computations. *J. Comput. Phys.* 72, 449–466. doi:10.1016/0021-9991(87)90093-3

Pirzadeh, S. Z. (2000). A solution-adaptive unstructured grid method by grid subdivision and local remeshing. *J. Aircr.* 37 (5), 818–824. doi:10.2514/2.2675

Pirzadeh, S. Z. "An adaptive unstructured grid method by grid subdivision, local remeshing, and grid movement," in Proceedings of the 14th Computational Fluid Dynamics Conference, Norfolk, VA, USA, November 1999. doi:10.2514/6.1999-3255

Schmitt, V., and Charpin, F. (1979). Pressure distributions on the ONERA M6-wing at transonic mach numbers. *AGARD Ar.* 138.

Spalart, S. R., and Allmaras, S. A. "A one-equation turbulence model for aerodynamic flows," in Proceedings of the 30th Aerospace Sciences Meeting and Exhibit, Reno, NV, USA, January 1992. doi:10.2514/6.1992-439

Spragle, G. S., Smith, W. A., and Weiss, J. M. "Hanging node solution adaption on unstructured grids," in Proceedings of the 33rd Aerospace Sciences Meeting and Exhibit, Reno, NV, USA, January 1995. doi:10.2514/6.1995-216

Steinthorsson, E., Modiano, D., and Colella, P. "Computations of unsteady viscous compressible flows using adaptive mesh refinement in curvilinear body-fitted grid systems," in Proceedings of the Fluid Dynamics Conference, Colorado Springs, CO, USA, June 1994. doi:10.2514/6.1994-2330

Wang, Z., Li, L., Cheng, H., and Ji, B. (2020). Numerical investigation of unsteady cloud cavitating flow around the Clark-Y hydrofoil with adaptive mesh refinement using OpenFOAM. *Ocean. Eng.* 206, 107349. doi:10.1016/j.oceaneng.2020.107349

Yamazaki, W., Matsushima, K., and Nakahashi, K. (2007). Drag decomposition-based adaptive mesh refinement. *J. Aircr.* 44 (6), 1896–1905. doi:10.2514/1.31064

Zhang, S. J., Liu, J., and Chen, Y. S. "Adaptation for hybrid unstructured grid with hanging node method," in Proceedings of the 15th AIAA Computational Fluid Dynamics Conference, Anaheim,CA,U.S.A, June 2001. doi:10.2514/6.2001-2657

frontiers | Frontiers in Energy Research

TYPE Original Research
PUBLISHED 24 May 2023
DOI 10.3389/fenrg.2023.1204300

OPEN ACCESS

EDITED BY
Leilei Ji,
Jiangsu University, China

REVIEWED BY
Jia Chen,
Jiangsu University, China
Yongfei Yang,
Nantong University, China

*CORRESPONDENCE
Yan Hao,
✉ yanying0708@126.com

RECEIVED 12 April 2023
ACCEPTED 09 May 2023
PUBLISHED 24 May 2023

CITATION
Liang C, Hao Y, Tengzhou X and Zhiguo L (2023), Identification of cavitation state of centrifugal pump based on current signal. *Front. Energy Res.* 11:1204300.
doi: 10.3389/fenrg.2023.1204300

Identification of cavitation state of centrifugal pump based on current signal

Chen Liang[1,2,3], Yan Hao[1,4]*, Xie Tengzhou[4] and Li Zhiguo[1]

[1]Hefei Institutes of Physical Science, Chinese Academy of Sciences, Hefei, China, [2]University of Science and Technology of China, Hefei, China, [3]Anhui High-Tech Development Center, Hefei, China, [4]School of Mechanical Engineering, Hefei University of Technology, Hefei, China

Centrifugal pump, which is widely used in water conservancy, electric power, petrochemical, ship, aerospace, and other technical fields, is the core equipment used to ensure all kinds of energy transfer. Cavitation not only affects the service life of the centrifugal pump but also seriously impacts the reliability of the process flow or device system. Due to the influence of the life, position and number of vibration sensors, the existing cavitation fault feature identification accuracy is not enough. The state analysis and characteristic recognition of the current signal under the cavitation state of the centrifugal pump are conducted in this paper based on soft sensing technology, and the signal component and judgment threshold representing the cavitation state are obtained. The following results are presented. Under different critical cavitation numbers, a small number of bubbles appeared near the suction surface of the inlet edge of the impeller, which verified the reliability of criterion for the critical cavitation number when the head coefficient decreased by 3%. The overall accuracy of binary classification cavitation recognition based on the current signal is 12.9% higher than that of three classification cavitation recognition. The recognition rate of VMD decomposition under different working conditions is higher than that of EMD, in design conditions, for example, overall accuracy improved by 7.3%, which also indicates that the obtained cavitation information of each component by VMD decomposition is richer than that obtained by EMD decomposition. Comparing different working conditions, a large flow rate easily leads to cavitation and high recognition current rate, compared with the flow of 0.75 Q and 1.25 Q, the overall accuracy is improved by 9.6%.

KEYWORDS

centrifugal pump, current signal, cavitation recognition, VMD, EMD

1 Introduction

As the main fluid conveying medium, centrifugal pump plays an important role in many industrial applications. Cavitation is one of the key factors affecting its performance. In traditional centrifugal pump cavitation monitoring, flow, and pressure data are measured, and a 3% drop in centrifugal pump head is taken as the occurrence standard of cavitation (ISO, 2010). However, in high and ultralow temperatures, conveying toxic and harmful or easy-to-wear medium and other extreme conditions and accurately measuring the centrifugal pump flow and pressure is difficult. Determining the centrifugal pump cavitation state using the head-down method is also complicated. Soft sensing technology uses relevant knowledge to build the mathematical relationship between the easy and difficult to measure quantities in the production process. The slightly measurable

TABLE 1 Parameters of the model pump.

Parameter	Numerical value
Diameter of impeller inlet D_1/mm	62
Diameter of impeller outlet D_2/mm	185
Width of blade outlet b_2/mm	10
Blade envelope angle θ/°	90
Number of blades Z	6
Diameter of volute Inlet D_s/mm	195
Diameter of volute outlet D_d/mm	50

quantities are then predicted and estimated through these easy to measure quantities. At present, the soft sensing technology of centrifugal pump cavitation monitoring mainly includes the pressure pulsation, vibration, noise, and current methods. Among them, the vibration method is the most widely used in monitoring the cavitation state of a centrifugal pump (Sánchez et al., 2018; Wang and Wang, 2018), which has the advantages of avoiding research object damage and high signal sensitivity. However, in a complex environment, the location and number of monitoring points have a direct impact on the accuracy of cavitation identification, thus failing to meet the needs of some remote real-time monitoring due to the impact of sensor life and operating cost. With the continuous development of fluid dynamics, the fault diagnosis technology based on motor current signal is characterized by its simple, feasible, low cost, and remote real-time monitoring, which has attracted considerable attention (Wang et al., 2021). However, the current signal processing methods in the cavitation state are insufficient and comparative analysis of different signal processing methods is lacking. Second, the low sensitivity of the current signal leads to the unsatisfactory monitoring of the cavitation state of the centrifugal pump in some special cases. Therefore, other signals are also needed for multi-information fusion monitoring. Overall, the current signal has considerable potential advantages in the soft sensing field of the cavitation state of centrifugal pumps. However, research and application in related fields are still lacking.

In the existing cavitation research and monitoring methods, Mouleeswaran et al. (Senthilkumar et al., 2015) used the LabVIEW program and DAQ card as the interface to obtain vibration amplitude and frequency, respectively, on different axes of the pump with the help of an accelerometer. The vibration spectrum is then analyzed and the cavitation state of the centrifugal pump is determined by identifying the frequency whose vibration amplitude is higher than the dangerous limit. LIU et al. (2020) used the VMD algorithm to process and analyze the acoustic signals of centrifugal pump cavitation. Their results showed that the signal energy value at 50 and 100 KHz frequency bands decreased first and then increased with the intensification of cavitation degree. Izadeh and Yari (2017) classified the vibration signal data under the pump cavitation state and extracted the probability of cavitation recognition as features to build a classifier. The classifier is then used to determine the cavitation state by using Bayesian theory. Nazarov et al. (2018) proposed a high-speed cavitation test method, which can significantly shorten the test cycle and improve the accuracy of specified cavitation characteristics.

The current was first used to detect motor faults. Nazarychev et al. (2020) proposed a method for monitoring the rotor winding state of the asynchronous motor based on the current variation. The numerical simulation was conducted on the digital model of the induction motor developed in the ANSYS software package, and then the test was performed on the test bench. The results show that the amplitude of the high harmonic component of the current, which is consistent with the number of pole pairs of the motor, increases sharply at low frequency when the rotor rod is broken. Skowron et al. (2020) used a convolutional neural network (CNN) to detect and classify stator winding faults of induction motors. The feasibility of applying CNN to stator early winding fault detection and classification is proven by an online test. Siegler et al. (2010) used the motor current to monitor the impeller of a marine centrifugal pump and found the relationship between the current signal and the cavitation degree of the impeller through research. Casada et al. (1999) studied rotor misalignment faults of pump units, used instantaneous power spectrum analysis of motor current to characterize rotor misalignment faults, and obtained corresponding time- and frequency-domain characteristics of current signals under such faults. Welch et al. (2002) monitored the operating conditions

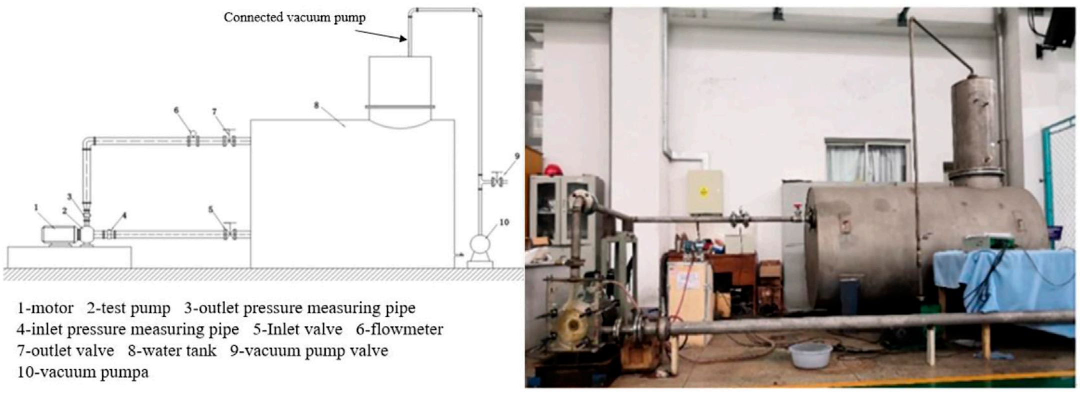

FIGURE 1
Schematic diagram and physical diagram of the test bed.

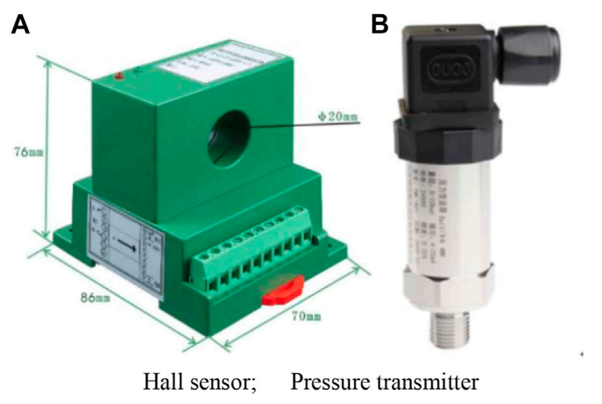

FIGURE 2
The physical picture of the sensor. **(A)** Hall sensor; **(B)** Pressure transmitter.

of equipment by measuring current and power and the test results can be applied to most electromechanical equipment, realizing remote analysis and continuous monitoring. Perovic (Perovic, 2000) proved through experiments that the energy value of a specific frequency range of current signals could be used as the judgment value due to pump outlet blockage, blade damage, and cavitation. Kenull et al. (2003) studied the cavitation and inversion faults of centrifugal pumps, extracted fault features by using the motor current spectrum and energy distribution curve, and established a diagnostic model. Their results showed that current signals can effectively monitor the cavitation state of centrifugal pumps under certain circumstances. Schmalz and Schuchmann (2004) used the energy distribution diagram of the low-frequency band signal of motor current to monitor the cavitation state of the centrifugal pump under different working conditions. Harihara and Parlos (2008) utilized the centrifugal pump monitoring algorithm to determine cavitation faults, blade damage, and bearing failure. However, the signal classification basis has not been provided. Hu and Zhao (2007) analyzed the motor current signal in the frequency domain and found a corresponding relationship between the motor current signal and the pump medium pulsation information in the frequency domain. They also established the pump unit model for verification, and their results were consistent with the experimental conclusions.

Overall, the current signal-based soft sensing technology can be extended from motor fault diagnosis to centrifugal pump cavitation operating condition monitoring and fault diagnosis due to the electromagnetic coupling between the rotor system and windings. This technology is characterized by its simplicity, feasibility, and low cost; it can also realize the function of remote monitoring. However, overall research on the application of current soft sensing technology to the monitoring of centrifugal pump working conditions is limited. Particularly, the processing methods related to the extraction of minimal information containing cavitation state in the current signal are insufficient. The low sensitivity of the current signal also leads to the unsatisfactory monitoring of the cavitation primary state of the centrifugal pump. Therefore, further research is necessary to build an accurate identification model of the cavitation state of the centrifugal pump. Therefore, first of all, the current signal of the centrifugal pump model is obtained in this paper. Two methods of Empirical Mode Decomposition (EMD) and singular value decomposition (SVD) are adopted to analyze and identify the current signal in the cavitation state of the centrifugal pump. The signal component and the judgment threshold representing the cavitation state are obtained. Cavitation signals under different working conditions were identified and their applicability to the soft sensing technology was compared. The research results can provide reference for the soft sensing technology in the fault diagnosis of centrifugal pump cavitation.

2 Physical model

2.1 Geometric model

The model pump of this test is a single-stage single-suction centrifugal pump with a specific speed of 62, a rated head of 10 m, a rated flow of 13 m^3/h, a motor power of 3.5 kw, and a speed of 1,450 r/min. The centrifugal pump in this test adopts a transparent plexiglass shell and impeller to facilitate the shooting of water conditions around the impeller during cavitation. The motor is a three-phase AC asynchronous motor. The parameters of the tested centrifugal pump are shown in Table 1 below.

2.2 Experimental platform

The test equipment mainly includes a closed test bench, a signal acquisition system, and high-speed photography equipment. The centrifugal pump test bed comprises the following: model pump, motor, water tank, flow meter, inlet pressure sensor, outlet pressure sensor, stainless steel tube, vacuum pump, valve, and bracket. The schematic and physical diagrams of the test are shown in Figure 1.

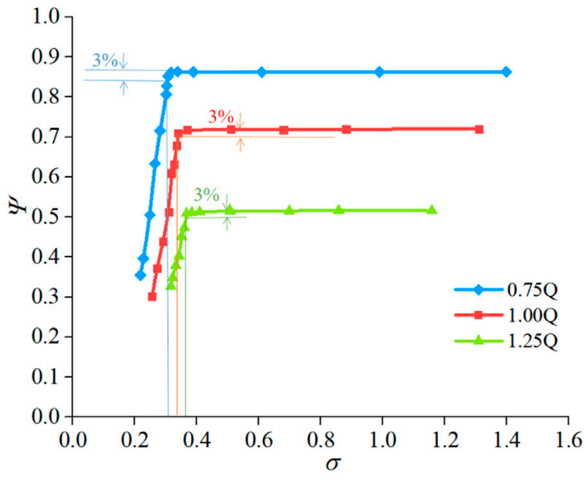

FIGURE 3
Cavitation performance curves of centrifugal pump under different working conditions.

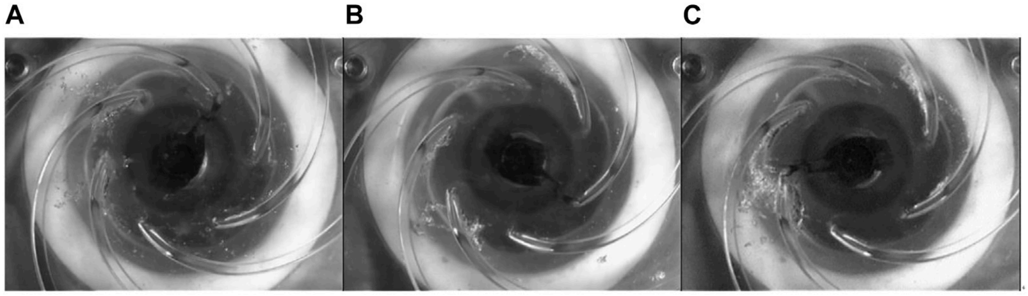

0.75Q, σ=0.305 1.0 Q, σ=0.34 1.25Q, σ=0.36

FIGURE 4
Birth of cavitation under the critical cavitation number in each working condition. **(A)** 0.75 Q, σ = 0.305 **(B)** 1.0 Q, σ = 0.34 **(C)** 1.25 Q, σ = 0.36.

2.3 Data acquisition system

Data acquisition for this test included flow rate, inlet and outlet pressures, motor current voltage, speed, and vibration signal. The data acquisition system comprises a Graphical User interface (GUI) data acquisition system based on MATLAB and an NI data acquisition system based on LabVIEW. The GUI data acquisition system mainly collects traffic, import and export pressures, and current and voltage signals. The current signal is collected by the Hall sensor, and the sensor adopts the principle of the Roche coil probe, which has a fast response speed and no waveform distortion. High reliability, can work in 10 KV high-pressure environment, anti-interference ability to reach the national standard level two or above, precision level of 0.1. The pressure transmitter uses a piezoresistive sensor as a signal-measuring element with an accuracy class of 0.2% FS, as shown in Figure 2.

2.4 Cavitation performance test analysis

The cavitation condition of the test aims to vacuum the tank. Two important parameters in the cavitation test, namely, cavitation number and head coefficient, are respectively expressed as $\psi = H/(u_0^2/2g)$ and $\sigma = (P - P_v)/(0.5\rho u_0^2)$, where ψ is the head coefficient, σ is the number of cavitation, H is the head of the centrifugal pump (the unit is m), $u0$ is the velocity of a fluid medium (the unit is m/s), P is the inlet static pressure (the unit is Pa), and Pv is the saturated vapor pressure of the medium at ambient temperature (the unit is Pa).

Using the above-closed test device, the cavitation performance curve as shown in Figure 3 is obtained. The figure shows that the head coefficient Ψ is unchanged at the beginning and then starts to decline with the decrease in the cavitation number. The reduction of the head coefficient by 3% is the critical cavitation point. When the pump cavitation occurs relatively early at high flow (1.25 Q), its corresponding critical cavitation σ is 0.36, the design condition (1.0 Q) critical cavitation σ is 0.34, and the low flow condition (0.75 Q) critical cavitation σ is 0.305. The cavitation state in each cavitation stage of a centrifugal pump is further accurately described and marked with cavitation σ to observe the changes in water flow in the cavitation stage of a centrifugal pump under different working conditions directly. Figure 4 shows that the high-speed camera technology was used to track and capture the internal cavitation of the pump to verify the accuracy of the above discrimination.

Figure 4 also shows the existence of relatively few vacuoles inside the blade in the low flow condition (0.75 Q) and cavitation σ = 0.305, and these vacuoles are mainly distributed near the suction surface at the blade inlet. Vacuoles collapse and disappear in the middle of the blade with the fluid flow. When σ = 0.34 in the design condition and σ = 0.36 in the large flow condition (1.25 Q), a small number of cavitation also appears near the suction surface at the inlet edge of the blade, representing the birth of cavitation, which further verifies the accuracy of the above critical cavitation determination.

TABLE 2 BIMF each characteristic part data table.

Classification pattern	Energy proportion	Variance	Kurtosis	Skewness	Root mean square value	Sample size	Class tag
Three-classification	0.882	0.0089	2.991	−0.131	0.097	125	Y1
	0.880	0.010	2.828	−0.122	0.095	125	Y2
	0.879	0.009	2.856	−0.197	0.094	175	Y3
Binary-classification	0.882	0.0084	2.996	−0.134	0.096	180	P1
	0.880	0.0092	2.853	−0.196	0.098	200	P2

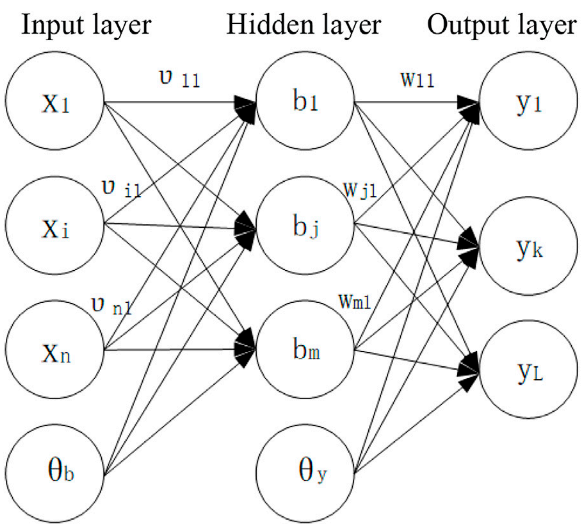

FIGURE 5
Multilayer feedforward (BP) neural network.

3 Identification of the cavitation state of the current signal

3.1 Current signal feature extraction

The empirical mode decomposition (EMD) method is used to decompose the signal according to the time scale characteristics of the data without setting any basis function in advance. This method can decompose complex signals into a finite number of intrinsic mode functions (IMFs), and each decomposed IMF component contains local characteristic information of the original signal at different time scales (Dragomiretskiy and Zosso, 2014; Li et al., 2021). Singular value decomposition (SVD) is similar considering the diagonalization of symmetric or Hermite matrices based on eigenvectors and is a generalization of spectral analysis theory on arbitrary matrices. In the scope of software filtering, SVD can remove strong interference signals and retain weak signals. Particularly, as a method of current power frequency filtering, the effect is satisfactory; thus, SVD is used to filter the current signal power frequency. Therefore, this paper mainly utilizes EMD and VMD to process and analyze current signals, respectively.

Each component of the current signal obtained by filtering can be effectively distinguished after the decomposition of EMD and VMD; particularly, the distinguishing effect of individual components is observed under the low flow condition. The obtained energy proportion of each component by different decomposition methods can also be used as a characteristic index to some extent. Therefore, in this paper, the energy ratio e_i, variance S_i, kurtosis k_i, skewness γ_i, and root mean square ε_i values of i components obtained by EMD and VMD decomposition are used in this paper as feature vectors T for current identification of cavitation state.

When current is used as the signal of cavitation state identification, the cavitation state can be divided into non-cavitation ($\sigma > 0.358$), cavitation birth ($0.358 > \sigma > 0.302$), severe cavitation ($\sigma < 0.257$), uncavitation ($\sigma > 0.358$), and

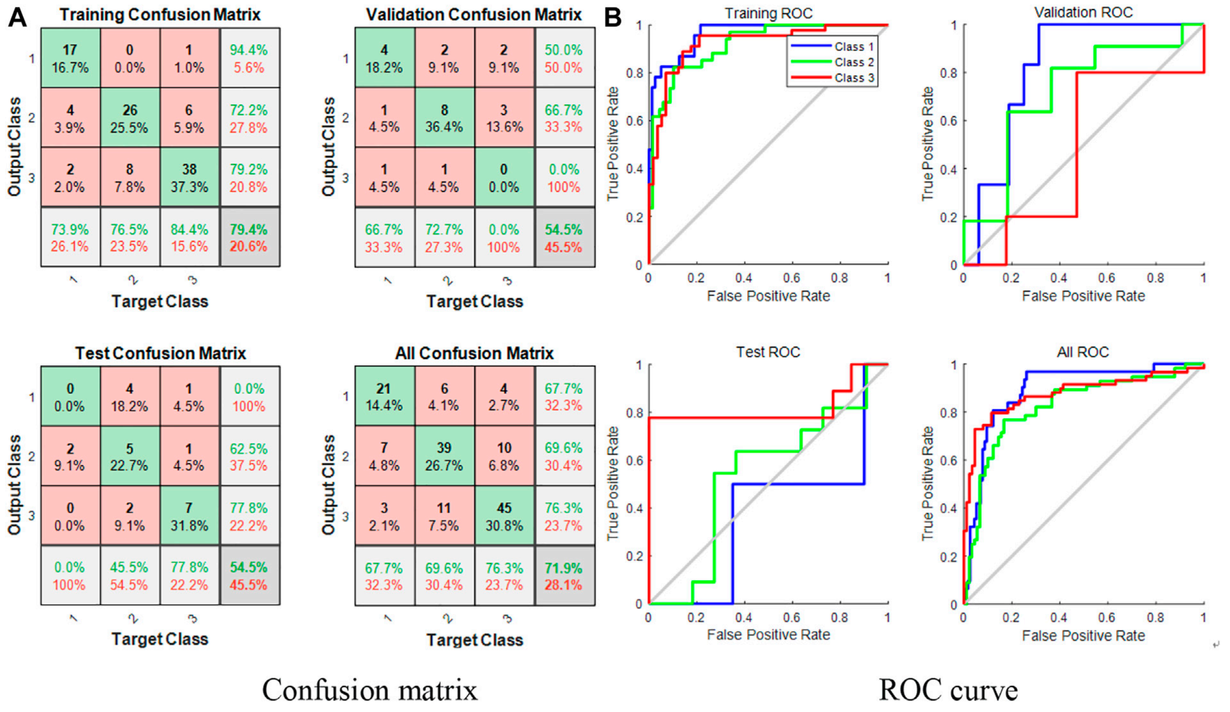

FIGURE 6
Three classification effects of EMD decomposition neural network cavitation state recognition. **(A)** Confusion matrix **(B)** ROC curve.

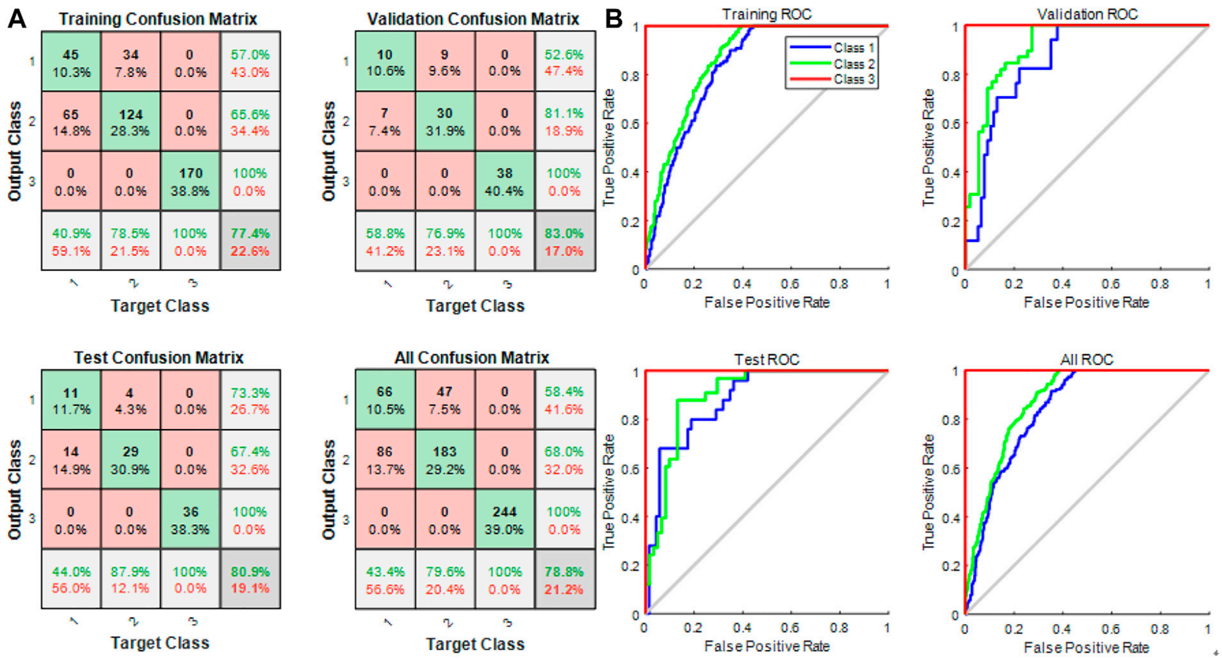

Training Confusion Matrix

Output Class	1	2	3	
1	45 10.3%	34 7.8%	0 0.0%	57.0% 43.0%
2	65 14.8%	124 28.3%	0 0.0%	65.6% 34.4%
3	0 0.0%	0 0.0%	170 38.8%	100% 0.0%
	40.9% 59.1%	78.5% 21.5%	100% 0.0%	77.4% 22.6%

Validation Confusion Matrix

Output Class	1	2	3	
1	10 10.6%	9 9.6%	0 0.0%	52.6% 47.4%
2	7 7.4%	30 31.9%	0 0.0%	81.1% 18.9%
3	0 0.0%	0 0.0%	38 40.4%	100% 0.0%
	58.8% 41.2%	76.9% 23.1%	100% 0.0%	83.0% 17.0%

Test Confusion Matrix

Output Class	1	2	3	
1	11 11.7%	4 4.3%	0 0.0%	73.3% 26.7%
2	14 14.9%	29 30.9%	0 0.0%	67.4% 32.6%
3	0 0.0%	0 0.0%	36 38.3%	100% 0.0%
	44.0% 56.0%	87.9% 12.1%	100% 0.0%	80.9% 19.1%

All Confusion Matrix

Output Class	1	2	3	
1	66 10.5%	47 7.5%	0 0.0%	58.4% 41.6%
2	86 13.7%	183 29.2%	0 0.0%	68.0% 32.0%
3	0 0.0%	0 0.0%	244 39.0%	100% 0.0%
	43.4% 56.6%	79.6% 20.4%	100% 0.0%	78.8% 21.2%

Confusion matrix

ROC curve

FIGURE 7
Effect of three classifications of VMD decomposition neural network cavitation state recognition. **(A)** Confusion matrix **(B)** ROC curve.

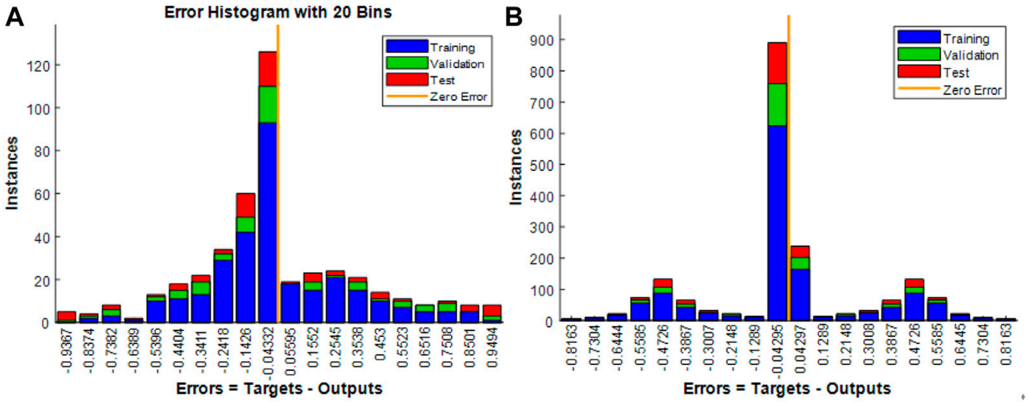

EMD decomposition

VMD decomposition

FIGURE 8
Error range distribution diagram of neural network training model based on current signal cavitation tri-classification. **(A)** EMD decomposition **(B)** VMD decomposition.

cavitation ($\sigma < 0.286$) of the binary category. The sensitivity of the current signal to cavitation is lower than that of the vibration signal; thus, low differentiation may occur in the discrimination between non-cavitation and cavitation initiation. Distinguishing between cavitation and non-cavitation states is important for some practical engineering applications. Therefore, three classification [Y1, Y2, and Y3] and binary classification [P1 and P2] cases are respectively used in this paper for cavitation state identification and comparative analysis. Table 2 shows the characteristic data of the first component of the current signal at 1.0 Q after VMD decomposition.

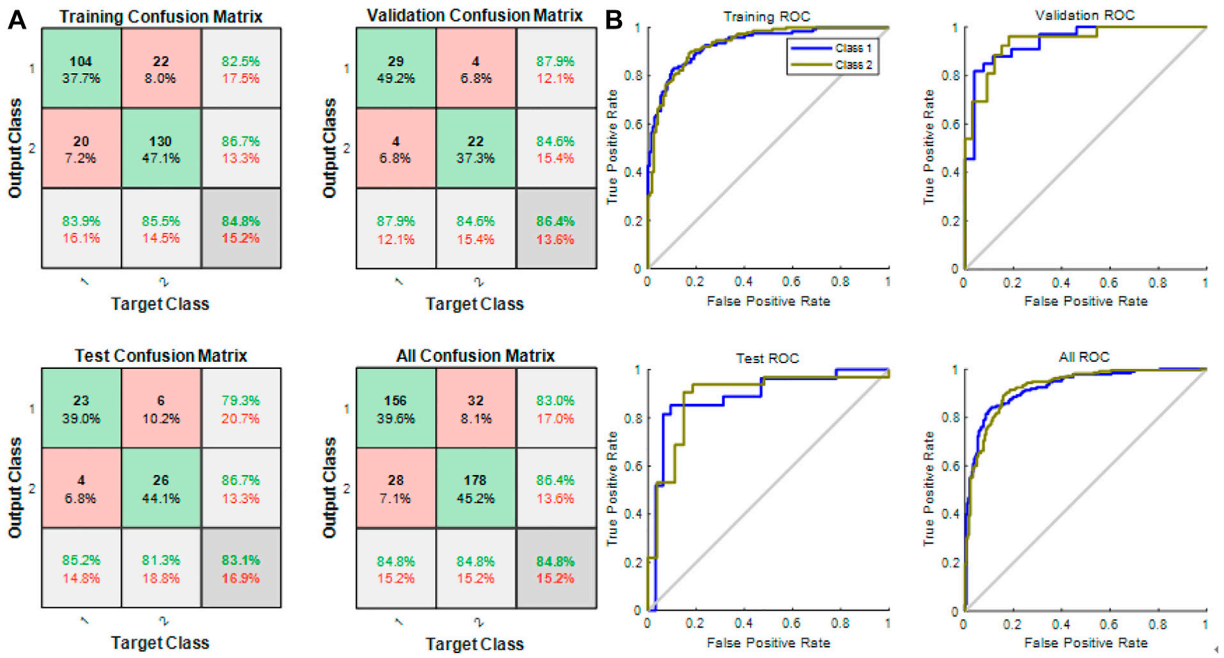

FIGURE 9
Effect of EMD binary classification. **(A)** Confusion matrix **(B)** ROC curve.

TABLE 3 Overall recognition accuracy table of current cavitation degree of the neural network under each decomposition method.

Classification method	Analytical method	0.75 Q (%)	1.0 Q (%)	1.25 Q (%)	Overall accuracy (%)
Three-classification	EMD	70.6	71.2	81.4	74.4
	VMD	79.2	85.5	88.9	84.5
Two-classification	EMD	77.8	84.8	87.4	83.33
	VMD	89.3	92.1	95.5	92.30

3.2 Cavitation state prediction and result analysis of neural network based on current

The back propagation (BP) neural network is a multilayer feed-forward neural network trained in accordance with an error back propagation algorithm (Haykin, 1994; Sain, 1997). The structure of the multilayer feed-forward BP neural network is shown in Figure 5. Firstly, the obtained mixed current signals are estimated, and the independent component estimates of the completely separated source signals are obtained. Secondly, genetic algorithm is used to optimize the weight and threshold of BP neural network. Finally, the normalized energy of multiple independent component estimates is isolated and used as the input of neural grid for the training and prediction of optimized BP neural network.

The number of nodes in the BP network is determined. The choice of the number of nodes in each layer has a considerable influence on the performance of the network. The selection for the output node depends on the representation of the output and the number of categories of input vectors to be identified (or classified). Therefore, the choice of hidden junction points should be determined in accordance with the actual situation and experience. Node selection generally follows the equation $m = \sqrt{n + l} + \alpha$, where n is the number of input nodes, l is the number of output nodes, and α is a number within 1–10.

After the decomposition of the filtered current signal by EMD and VMD, the cavitation representation components of different layers contain different cavitation information. This paper divides the sample data obtained under different decomposition methods of current signals into binary and triple classification and then establishes different neural network training models for cavitation pattern recognition to achieve the accuracy of sample classification and the comprehensiveness of comparative analysis to a considerable extent. EMD divides the filtered current signal into seven layers according to the analysis in Chapter 3. Therefore, the number of sample features is 5 × 7, and the number of hidden junctions of neural networks is 40. VMD was decomposed into seven layers; thus, the number of sample features is 5 × 7, and the number of hidden layer junctions of neural networks is 40. The

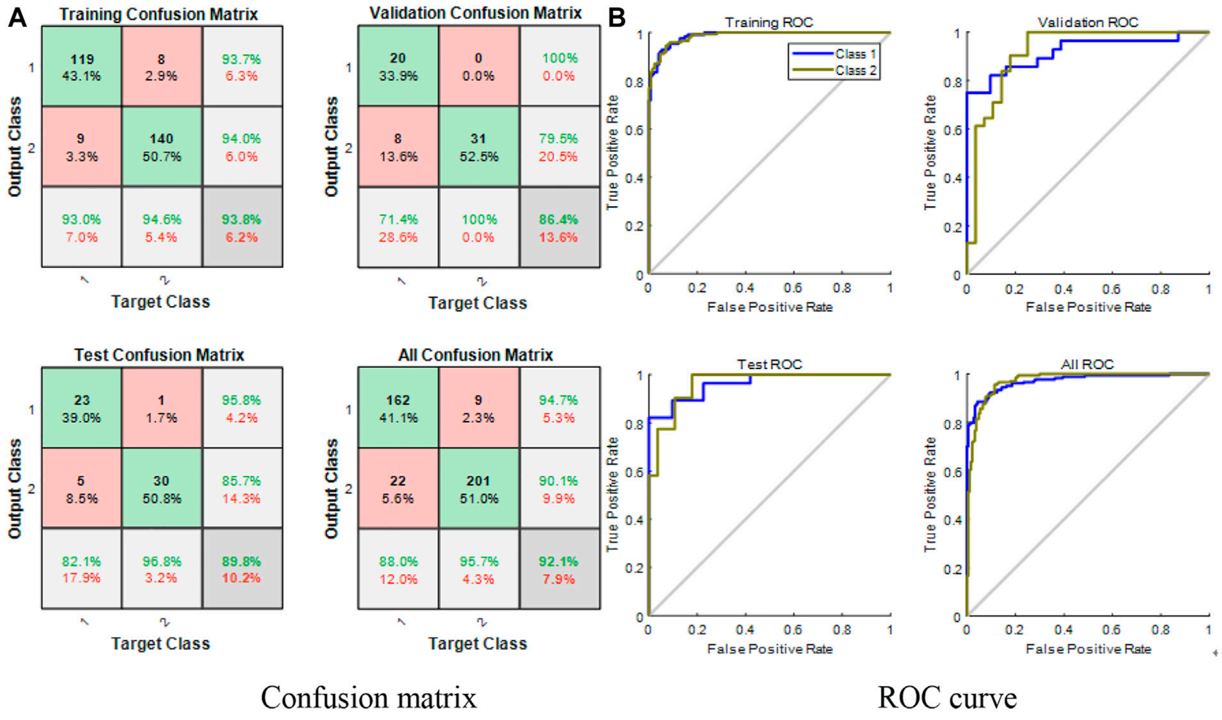

Training Confusion Matrix

Output Class	1	2	
1	119 43.1%	8 2.9%	93.7% 6.3%
2	9 3.3%	140 50.7%	94.0% 6.0%
	93.0% 7.0%	94.6% 5.4%	93.8% 6.2%

Target Class

Validation Confusion Matrix

Output Class	1	2	
1	20 33.9%	0 0.0%	100% 0.0%
2	8 13.6%	31 52.5%	79.5% 20.5%
	71.4% 28.6%	100% 0.0%	86.4% 13.6%

Target Class

Test Confusion Matrix

Output Class	1	2	
1	23 39.0%	1 1.7%	95.8% 4.2%
2	5 8.5%	30 50.8%	85.7% 14.3%
	82.1% 17.9%	96.8% 3.2%	89.8% 10.2%

Target Class

All Confusion Matrix

Output Class	1	2	
1	162 41.1%	9 2.3%	94.7% 5.3%
2	22 5.6%	201 51.0%	90.1% 9.9%
	88.0% 12.0%	95.7% 4.3%	92.1% 7.9%

Target Class

Confusion matrix

ROC curve

FIGURE 10
Effect of VMD binary classification. **(A)** Confusion matrix **(B)** ROC curve.

training times are set to 1,000 and the learning rate is 0.02. The training of this model is based on the MATLAB pattern recognition module. The training results are represented by a confusion matrix and ROC curve. The confusion matrix is a direct representation of the accuracy rate of classification results and the category where the current classification results belongs to. The abscissa typically represents the real target category, and the ordinate is the obtained category by model classification. The “receiver operating characteristic,” which is also known as ROC curve, is used to determine the quality of the classification model and test results. The ROC curve is an essential and common statistical analysis method.

3.2.1 Three classifications of cavitation states

The training, validation, and test matrices comprised 75%, 10%, and 15% of the sample data of each training model, respectively. The classification results are shown in Figure 6.

As shown in Figure 6, the accuracy of the neural network training set obtained by EMD decomposition is 79.4%, the verification set is 54.5%, the test set is 54.4%, and the overall accuracy is 71.9%. The ROC curve distribution is poor, the verification and test sets of the first and second classifications have a considerable uncertainty, and the recognition rate is the lowest. Overall, the accuracy of cavitation recognition and classification of the three classification neural network obtained by EMD decomposition is poor, and the classification model trained is not good.

As shown in Figure 7, the accuracy of the neural network training set obtained by VMD decomposition is 77.4%, the verification set is 83.0%, the test set is 80.9%, and the overall accuracy is 78.8%. In the ROC curve distribution diagram, the third classification has the best effect, while the first and second categories are partially confused. The current signal contains abundant cavitation information under serious cavitation. Overall, the classification accuracy of the three classification neural network obtained from VMD decomposition is universal, and the classification model is generally trained. The error distribution histogram of the recognition results is shown in the Figure 8.

As shown in Figure 8, the error range distribution of the neural network training model obtained by three classification EMD and VMD decomposition is wide but that of VMD decomposition is relatively concentrated. The classification effect is slightly higher than that of EMD decomposition.

3.2.2 Cavitation state dichotomy

The effect of the three classifications is average based on the above analysis. Model training and prediction are conducted considering the requirement of cavitation state binary classification in practical engineering applications. For the sample data of the training model, the training, validation, and test matrices accounted for 75%, 15%, and 15% of the samples, respectively. The classification results are shown in the figure below.

As shown in Figure 9, the accuracy of the binary neural network obtained by EMD decomposition is 84.8% for the training set, 86.4% for the verification set, 83.1% for the test set, and 84.8% for overall accuracy. The ROC curve distribution is vertical, the distribution of the verification and test sets is similar, the resolution of the first and second classifications is also high, and the test performance of the model is satisfactory. Overall, the binary neural network obtained by EMD decomposition has high cavitation recognition and classification accuracies and the trained classification model is superior.

Table 3 is overall recognition accuracy table of current cavitation degree of the neural network under each decomposition method, where the "Q" is the flow of centrifugal pump. As shown in Figure 10, the accuracy of the neural network training set obtained by VMD decomposition is 93.8%, the verification set is 86.4%, the test set is 89.8%, and the overall accuracy is 92.1%. Meanwhile, the ROC curve distribution is approximately vertical, and the first and second classification accuracies are both high. Test set accuracy is also higher than EMD decomposition. Overall, the binary neural network obtained from VMD decomposition has high cavitation recognition and classification accuracy and trained classification model is superior.

As shown in Table 3, the accuracy of binary cavitation recognition is generally higher than that of three-category cavitation recognition. Comparing the results under different working conditions, a large flow rate possibly leads to cavitation; therefore, the recognition rate of the current is high. The recognition rate of VMD decomposition under different working conditions is higher than that of EMD, indicating that each component obtained by VMD decomposition contains richer cavitation information than that obtained by EMD decomposition. Overall, in practical engineering applications, the neural network binary classification centrifugal pump cavitation recognition model based on VMD decomposition has high accuracy and has application value in general centrifugal pump cavitation monitoring applications when the cavitation state of the centrifugal pump is identified by current. This is consistent with the research conclusions obtained from the application of vibration signals in literature (Li et al., 2016) and literature (Ming et al., 2017). VMD decomposition can identify characteristic quantities with higher accuracy in centrifugal pump fault diagnosis. Therefore, the cavitation recognition technology based on current signal provided in this paper can still obtain the cavitation fault recognition rate of the same precision under complex and harsh environment. Therefore, the research results in this paper have obvious advantages, and also have significant value in the traditional centrifugal pump fault diagnosis application.

4 Conclusion

This paper mainly focuses on the soft sensing of the cavitation state of a centrifugal pump. In view of the difficulty of judging the cavitation state of centrifugal pump under complex working conditions, this paper analyzes the current and vibration signals in the cavitation state of centrifugal pump based on soft sensing technology. On this basis, based on the information fusion theory, a cavitation state recognition model combining the current and vibration signals is constructed to improve the cavitation state recognition rate and anti-interference performance, and the following conclusions are drawn:

(1) Testing results of the cavitation performance of the centrifugal pump showed that the head coefficient Ψ initially remains unchanged with the decrease in the cavitation number and the value of Ψ decreases rapidly when the cavitation number is reduced to a certain value. Comparison of the critical cavitation number under different conditions indicated the relatively early occurrence of cavitation under the high flow condition (1.25 Q). Thus, under the corresponding critical cavitation number, a small number of bubbles appear near the suction surface of the inlet edge of the impeller, which represents the beginning of cavitation.

(2) Comparison results of the neural network training obtained from EMD and VMD decompositions under the cavitation state classification revealed that the overall accuracy of EMD is 71.9%, which is lower than that of VMD (78.8%). The ROC curve distribution indicated that the first and second classifications of the verification and test sets obtained by EMD showed considerable uncertainty and the recognition rate was the lowest. The third classification obtained by VMD is the best, while the first and second categories are partially obscured.

(3) Comparison results of the neural network training obtained by EMD and VMD decompositions under cavitation state dichotomy demonstrated that the overall accuracy of the neural network training obtained by EMD decomposition is 84.8% while that of VMD can reach 93.8%. From the perspective of ROC curve distribution, the distribution obtained by VMD is approximately vertical, the resolution of the first and second classifications is high, and the accuracy of the test set is higher than that of EMD decomposition.

The current signal based centrifugal pump monitoring has a high application value for some low requirements of centrifugal pump cavitation state monitoring, especially for the monitoring equipment portability, low cost and accuracy has a great application demand. Therefore, the follow-up work can develop the corresponding portable monitoring equipment, focusing on the future 5G and Internet of things technology in the "cloud" development of the corresponding soft sensor model and database, to achieve the real-time monitoring of centrifugal pump cavitation state and pump operation stability.

Data availability statement

The original contributions presented in the study are included in the article/supplementary material, further inquiries can be directed to the corresponding author.

Author contributions

LC: Conceptualization, methodology, software; HY: Data curation, writing–original draft; TX: Visualization, investigation, supervision; ZL: Software, validation, writing–review editing. All authors listed have made a substantial, direct, and intellectual contribution to the work and approved it for publication.

Funding

This work was supported by the Fundamental Research Funds for the Central Universities (No: JZ2021HGTB0090), the University Synergy Innovation Program of Anhui Province under Grant No. GXXT-2019-004, the financial support provided by the National Natural Science Foundation of China (51806053).

Acknowledgments

The authors are grateful for the support of the National Natural Science Foundation of China.

Conflict of interest

The authors declare that the research was conducted in the absence of any commercial or financial relationships that could be construed as a potential conflict of interest.

Publisher's note

References

Casada, D., Tutterow, V., and Mckane, A. (1999). Screening pumping systems for energy savings opportunities. *Energy Eng.* 97 (2), 43–63.

Dragomiretskiy, K., and Zosso, D. (2014). Variational mode decomposition. *IEEE Trans. Signal Process.* 62 (3), 531–544. doi:10.1109/tsp.2013.2288675

Harihara, P. P., and Parlos, A. G. "Sensorless detection and isolation of faults in motor-pump systems," in Proceedings of the ASME International Mechanical Engineering Congress and Exposition, Boston, Massachusetts, USA, November 2008.

Haykin, S. (1994). "Neural networks:A comprehensive foundation," in *Neural networks A comprehensive foundation* (Upper Saddle River, NJ, United States: Prentice Hall PTR), 71–80.

Hu, H. Y., and Zhao, H. P. (2007). The analysis of stator harmonic current when piston pump is driven by asynchronous motor. *Ship Sci. Technol.* 29 (1), 55–57.

Iso (2010). ISO 13709:2009 (identical). Centrifugal pumps for petroleum, petrochemical and natural gas industries. https://www.iso.org/standard/41612.html.

Izadeh, S. A. .F., and Yari, B. (2017). Pump cavitation detection through fusion of support vector machine classifier data associated with vibration and motor current signature. *Insight - Non-Destructive Test. Cond. Monit.* 59 (12), 669–673. doi:10.1784/insi.2017.59.12.669

Kenull, T., Canders, W. R., and Kosyna, G. (2003). Formation of self-excited vibrations in wet rotor motors and their influence on the motor current. *Eur. Trans. Electr. Power* 13 (2), 119–125. doi:10.1002/etep.4450130207

Li, H., Yu, B., Qing, B., and Luo, S. (2016). Cavitation pulse extraction and centrifugal pump analysis. *J. Mech. Sci. Technol.* 31 (3), 1181–1188. doi:10.1007/s12206-017-0216-z

Li, Z., Jiang, W., Zhang, S., and Sun, Y. (2021). A hydraulic pump fault diagnosis method based on the modified ensemble empirical mode decomposition and wavelet kernel extreme learning machine methods. *Sensors* 21 (8), 2599. doi:10.3390/s21082599

Liu, Z., Zhang, X., Zou, S., and Li, Z. (2020). Feature extraction of cavitation acoustic emission signal of centrifugal pump based on improved variational mode decomposition. *J. Drainage Irrigation Mach. Eng.* 38 (12), 1196–1202.

Ming, Z., Jiang, Z., and Feng, K. (2017). Research on variational mode decomposition in rolling bearings fault diagnosis of the multistage centrifugal pump. *Mech. Syst. Signal Process.* 93, 460–493. doi:10.1016/j.ymssp.2017.02.013

Nazarov, V., Zuev, A., and Nazarov, L. (2018). Advancing methodology to specify cavitation characteristic of screw-type centrifugal pumps. *Iop Conf.* 450, 11–22.

Nazarychev, A. N., Novoselov, E. M., Polkoshnikov, D. A., Strakhov, A. S., and Skorobogatov, A. A. (2020). A method for monitoring the condition of rotor windings in induction motors during startup based on stator current. *Russ. J. Nondestruct. Test.* 56 (8), 661–667. doi:10.1134/s1061830920080070

Perovic, S. (2000). *Diagnosis of pump faults and flow regimes*. Brighton and Hove, England: University of Sussex.

Sain, S. R. (1997). The nature of statistical learning theory. *Technometrics* 38 (4), 409. doi:10.1080/00401706.1996.10484565

Sánchez, W., Carvajal, C., Poalacin, J., and Salazar, E. "Detection of cavitation in centrifugal pump for vibration analysis," in Proceedings of the 4th International Conference on Control, Automation and Robotics (ICCAR), Auckland, New Zealand, April 2018, 460–464.

Schmalz, S. C., and Schuchmann, R. P. (2004). "Method and apparatus of detecting low flow/cavitation in a centrifugal pump,". US6709240B1 (Alexandria, Virginia, United States: United States Patent and Trademark Office).

Senthilkumar, M., Yuvaraja, M., and Kok, M. (2015). fault diagnosis of centrifugal pump and vibration control using shape memory alloy based ATDVA. *Appl. Mech. Mater.* 787, 927–931. doi:10.4028/www.scientific.net/amm.787.927

Siegler, J. A., Sark, Ad Y. A. A., and Nemarich, C. (2010). Motor current signal analysis for diagnosis of fault conditions in shipboard equipment. *Nav. Eng. J.* 107 (1), 77–98. doi:10.1111/j.1559-3584.1995.tb02576.x

Skowron, M., Orlowska-Kowalska, T., and Wolkiewicz, M. (2020). Convolutional neural network-based stator current data-driven incipient stator fault diagnosis of inverter-fed induction motor. *Energies* 13 (6), 1–21.

Wang, C., Wang, M., Yang, B., Song, K., Zhang, Y., and Liu, L. (2021). A novel methodology for fault size estimation of ball bearings using stator current signal. *Measurement* 171 (3), 108723. doi:10.1016/j.measurement.2020.108723

Wang, J., and Wang, Y. (2018). Rotating corrected-based cavitation model for a centrifugal pump. *J. Fluids Eng. Trans. Asme* 140, 111301.

Welch, D. E., Haynes, H. D., and Cox, D. F. (2002). *Electrical signature analysis (ESA) as a diagnostic maintenance technique for detecting the high consequence fuel pump failure modes*. Oak Ridge, TN, United States: Oak Ridge National Laboratory.

frontiers | Frontiers in Energy Research

TYPE Original Research
PUBLISHED 12 June 2023
DOI 10.3389/fenrg.2023.1202914

OPEN ACCESS

EDITED BY
Kan Kan,
College of Energy and Electrical Engineering, China

REVIEWED BY
Zhaohan Li,
Lam Research, United States
Rui Guo,
Yanshan University, China

*CORRESPONDENCE
Jiansong Li,
✉ lijiansong@cumt.edu.cn

RECEIVED 09 April 2023
ACCEPTED 30 May 2023
PUBLISHED 12 June 2023

CITATION
Li J, Li S, Ji Z and Wang Y (2023), Design and energy analysis of a flywheel-based boom energy regeneration system for hydraulic excavators.
Front. Energy Res. 11:1202914.
doi: 10.3389/fenrg.2023.1202914

Design and energy analysis of a flywheel-based boom energy regeneration system for hydraulic excavators

Jiansong Li[1,2,3]*, Shaohui Li[1], Zhi Ji[4] and Yunfei Wang[2]

[1]Research and Development Center for Intelligent Manufacturing Technology of Engineering Equipment, Xuzhou College of Industrial Technology, Xuzhou, China, [2]School of Mechatronic Engineering, China University of Mining and Technology, Xuzhou, China, [3]Technology Center, Xuzhou Villead Heavy Industry Technology Co. Ltd., Xuzhou, China, [4]Jiangsu College of Safety Technology, Xuzhou, China

The global energy crisis and growing environmental concerns provide a strong impetus for the development of fuel-efficient hydraulic excavators (HEs). The boom potential energy of a conventional HE is consumed by throttling in a lowering process, which is a major reason for energy inefficiency. To solve the issue, this paper presents a flywheel-based boom energy regeneration system for HEs using load-sensing systems. The otherwise wasted boom potential energy is regenerated by a pump/motor and stored in a flywheel. The recaptured energy is reused in the form of pressure energy released to the pump outlet. The energy efficiencies of a conventional load-sensing system and the proposed system were analyzed. A control strategy was proposed to optimize the energy-saving procedure. To obtain a more reliable simulation model, a coasting experiment of the flywheel was carried out to obtain the key parameters related to the friction of the flywheel. A 4-t HE in our laboratory was selected as a study case to investigate the energy-saving effect of the flywheel-based boom energy regeneration system. Numeric simulations showed that compared with a conventional load-sensing system, the energy-saving rate was about 32.7% in a typical digging and dumping cycle. These findings indicated that the flywheel-based boom energy regeneration system is promising for developing energy-efficient HEs.

KEYWORDS

energy-saving, energy regeneration, flywheel, hydraulic excavator, load sensing

1 Introduction

The global energy crisis and growing environmental concerns provide a strong impetus for the development of fuel-efficient construction machinery. This task is particularly of great importance in the case of hydraulic excavators (HEs) because HEs are the most widely used construction machinery in engineering construction. Conventional HEs frequently move up and down heavy booms to complete related work. During the lowering of the boom, the gravitational potential energy is converted into heat energy, which will cause the oil temperature to increase. This not only leads to energy waste but also increases the fluid temperature and shortens the life of the hydraulic components. The boom gravitational potential energy reportedly accounts for 15% of the total output energy of the diesel engine for a typical medium-size HE (Triet and Ahn, 2011). Therefore, studying how to recover and reuse the boom gravitational potential energy is of great significance for improving the energy efficiency of HEs and reducing the discharge of pollutants. Adding an energy regeneration system (ERS) is an effective energy-saving approach. According to the form of recaptured energy, ERSs can be classified into three major categories: electric, hydraulic, and mechanical systems (Yu and Ahn, 2019).

Inspired by the technology used in the automotive industry, electric ERSs were first developed in the field of HEs. Electric ERSs adopt a hydraulic motor and a generator as an energy converter (Wang and Wang, 2014) and either a battery or an ultracapacitor as the energy storage device (Hussaini and Wang, 2022). The battery has the advantage of high energy density while the ultracapacitor has the characteristic of high specific power. Wang et al. (Lin et al., 2010) proposed a pressure-compensated ERS with a hydraulic motor and generator installed in the main return line. The corresponding tests showed that up to 60% of the potential energy could be recovered. The recovered energy could be reutilized by adding another motor to assist the engine (Xia et al., 2019). Compared with traditional HEs that use internal combustion engines as a power source, the electric ERS is preferable for electric excavators because the existing batteries will greatly reduce the manufacturing investment (Amirante et al., 2017). However, excessive energy conversion cycles in electric ERSs can lead to a decrease in energy utilization efficiency. The low specific power and cycle life of batteries (Wang et al., 2017) are barriers to the mass application of this technology. Although ultracapacitors have the advantage of high specific power and lifetime, their high manufacturing cost and low specific energy are disadvantages (Joo and Stangl, 2016).

Hydraulic ERSs use hydraulic accumulators as energy storage devices. Such systems are characterized by high specific power and low manufacturing costs. Considering the existing hydraulic system in HEs, fewer energy conversions are involved in the hydraulic ERS than others. Regarding energy reutilization, the recaptured energy either can be used to assist the engine when high power is required (Zhao et al., 2011); releasing the pressurized fluid to the pump suction port (Ho and Ahn, 2008; Casoli et al., 2016) is another choice to reutilize the recaptured energy. However, the pressure in the hydraulic accumulator changes dramatically in the energy recovery and release process. This character will impact the boom movement during the lowering process and lead to inefficiency and difficulty in reusing the recaptured energy when the pressure in the accumulator is low. This is the so-called "pressure coupling" issue. To solve this problem, hydraulic transformers (Bui et al., 2015; Ge et al., 2018) and asymmetric pumps (Wasbari et al., 2017) have been developed. However, both of the above are in the research stage and no commercial products are currently available. Another issue is that hydraulic accumulators require more installation space and tend to be bulky due to the low specific energy (Takahashi et al., 2002).

Mechanical ERSs using flywheels have the potential for use in a range of applications due to their many advantages. High-speed flywheels have a high specific energy of up to 200 Wh/kg (Hedlund et al., 2015). Compared with batteries, an almost unlimited service life (in the order of 10^7 cycles) is the most important advantage (Hadjipaschalis et al., 2009). Furthermore, the energy storage capacity of a flywheel is independent of time or discharge depth. Flywheels also have disadvantages. One distinguishing disadvantage of the flywheel-based ERS is the high self-discharge rate (Zhou et al., 2013). For long-term applications, this feature will lead to unacceptable energy loss. However, if a flywheel is used as a buffer, the energy loss could be negligible (Dhand and Pullen, 2015). Many studies have explored the energy-saving potential of mechanical ERSs in the vehicle field (Li and Zhao, 2021), but very few have focused on HEs. We previously analyzed the main advantages of a flywheel-based architecture and discussed the feasibility of using a flywheel-based energy recovery system to regenerate the boom potential energy (Li et al., 2020). Specifically, we introduced a flywheel-based ERS for HE (Mahato and Ghoshal, 2020) and investigated the energy recovery effect. However, that study did not discuss the interaction of the original system and the added ERS. For HEs with different hydraulic architecture, the energy-saving effect should differ, even when adopting the same ERSs.

Load-sensing systems are commonly used in HEs (Xu et al., 2017). In this paper, an energy-saving system composed of a load-sensing system and a flywheel-based ERS is analyzed and the energy-saving effect is discussed. The remainder of this paper is structured as follows. Section 2 describes and analyzes the newly proposed system configuration and working principles. Section 3 presents and analyzes the energy analysis methodology. Section 4 describes the control strategy. The coasting experiment of the flywheel is shown in Section 5. The simulation model is built in AMESim software and corresponding simulations are studied in Section 6. Finally, conclusions are drawn in Section 7.

2 System configuration

2.1 Original boom driving system

A conventional load-sensing system of a HE boom subsystem is shown in Figure 1 (left half). This hydraulic system is composed of a pump, a main valve, and a boom cylinder. The pump is load-sensing and can automatically adjust its displacement to exactly deliver flow as required by the main valve and keep the pressure above the load pressure by a preset value. The main valve is an electronic proportional valve. Two check valves and two secondary relief valves are used to set the maximum feedback pressure in the corresponding pipes. When the boom lowers, due to the boom gravity, the pump just provides low-pressure fluid to the rod side of the boom cylinder.

2.2 Load-sensing system with a flywheel-based ERS

Figure 1 shows the proposed load-sensing system with a flywheel-based ERS (LS-FERS). Compared with the original system, a flywheel-based ERS is added to regenerate and reutilize the potential energy of the boom. The flywheel-based ERS consists of a hydraulic pump/motor (PM), a clutch, a flywheel, a regeneration valve, an energy-releasing valve, and three check valves. The PM is the energy converter and the flywheel is the energy storage device. The swashplate of the PM can swing to a negative angle or a positive angle, so the PM can reverse its flow direction without auxiliary valves and switch its operation mode. The clutch is energized to connect the shafts of the PM and the flywheel when there is an energy exchange between them. If not, the clutch is de-energized to

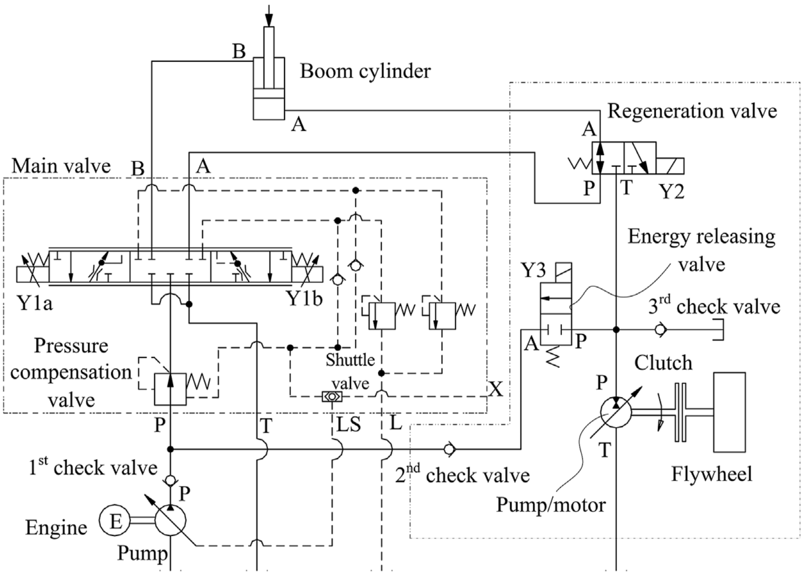

FIGURE 1
Proposed load-sensing system with a flywheel-based energy regeneration system.

avoid unnecessary friction loss. The regeneration valve is employed to control the operation of the flywheel-based ERS. The energy-releasing valve is activated when the ERS releases energy to the original system. The first and second check valves block any reverse fluid. The third check valve is employed to connect the inlet of the PM and the reservoir to avoid cavitation (Kan et al., 2022). The recaptured energy will be reutilized by releasing pressurized fluid to the inlet of the main valve.

The three modes for the ERS are the regeneration mode, the reutilization mode, and the standby mode. The operation principle of the proposed system is as follows:

(1) Regeneration mode. When the boom cylinder is lowered through the gravity force of the working device, the fluid discharged by the pump goes into the rod side of the boom cylinder. The regeneration valve shifts to its right position, and the fluid discharged from the cap side of the boom cylinder goes through the regeneration valve and the PM into the reservoir. The PM works in motoring mode and the pressure energy is converted into mechanical energy to accelerate the flywheel. As the name implies, the potential energy is regenerated and stored in the flywheel in the form of kinetic energy.
(2) Reutilization mode. When the boom is to be driven upwards, the fluid provided by the pump is directed by the main valve to the cap side of the boom cylinder. At the same time, the energy-releasing valve and the clutch are energized. The flywheel drives the PM at the cost of decreasing its rotational speed and the PM works in pumping mode. The fluid output from port P of the PM flows through the energy-releasing valve and the second check valve and joins the pump flow at the inlet of the main valve. Thus, the recaptured energy is used to drive the boom cylinder.
(3) Standby mode. When the boom is held in a certain position, the system enters the standby mode. In this mode, all valves return to their original positions and the clutch is de-energized. The flywheel remains rotating but its speed gradually decreases due to inevitable friction.

From the aforementioned description, it can be concluded that the LS-FERS consumes less energy than the conventional load-sensing system.

3 Energy distribution analysis

To better understand the energy distribution characteristics of the LS-FERS, the energy flow was compared between the original system and LS-FERS. The energy-saving effect of the LS-FERS was also analyzed. First, some assumptions were made.

- The tank pressure was always zero;
- The energy consumption caused by the pump control device was included in the energy loss of the pump;
- The dynamic of the clutch was negligible because a typical response time of an electromagnetic clutch was of the same order as that of an electromagnetic valve;
- The energy consumption of the pilot circuit was negligible;
- The energy losses of all check valves were negligible;
- The energy losses caused by the slippage of the clutch were negligible; and
- The internal and external leakages of the boom cylinder were negligible.

3.1 Energy analysis of the original system

For the original system, the mechanical energy absorbed by the pump was given as follows:

$$E_{pump\_in} = \int T_p n_p dt, \tag{1}$$

where T_p is the driving torque and n_p is the rotational speed of the pump.

The pressure energy output by the pump is described by

$$E_{pump\_out} = \int p_p q_p dt\,, \tag{2}$$

where p_p is the pressure and q_p is the flow rate at the pump outlet.

Hence, the energy loss of the pump is

$$\Delta E_{pump} = E_{pump\_in} - E_{pump\_out}\,. \tag{3}$$

The energy delivered to the boom cylinder is given by

$$E_{cylinder\_in} = \int p_{cylinder\_in} q_{cylinder\_in} dt, \tag{4}$$

where $p_{cyliner\_in}$ and $q_{cylinder\_in}$ represent the pressure and the flow rate at the boom cylinder inlet, respectively.

Since there is no flow loss at the main valve, the meter-in energy loss of the main valve is the throttling loss between the pump outlet and the boom cylinder inlet, which can be described by

$$\Delta E_{mv\_in} = \int \left(p_p - p_{cylinder\_in}\right) q_p dt\,, \tag{5}$$

In a load-sensing hydraulic system, the pressure difference between the pump outlet and the actuator (the boom cylinder inlet) should equal the setting pressure difference of the pump, which is

$$p_p - p_{cylinder\_in} = \Delta p_{ls}\,. \tag{6}$$

In a complete boom operation cycle, the energy equilibrium of the boom cylinder is

$$E_{cylinder\_in} = E_{cylinder\_out} + \Delta E_{cylinder}\,, \tag{7}$$

where $E_{\mathrm{cylinder\_out}}$ is the output energy at the boom cylinder outlet and $\Delta E_{cylinder}$ is the energy loss at the boom cylinder. The output energy can be expressed as

$$E_{cylinder\_out} = \int p_{cylinder\_out} q_{cylinder\_out} dt\,. \tag{8}$$

No matter whether the boom cylinder extends or retracts, the output energy of the boom cylinder is consumed at the main valve. This is the meter-out energy loss of the main valve,

$$\Delta E_{mv\_out} = E_{cylinder\_out}.$$

The total energy losses at the main valve can be calculated by

$$\Delta E_{mv} = \Delta E_{mv\_in} + \Delta E_{mv\_out}\,. \tag{9}$$

The inlet and outlet of the boom cylinder vary according to specific working conditions. When the boom is lifted, the pump flow enters the cap side chamber of the boom cylinder. That is,

$$\begin{cases} p_{cylinder\_in} = p_1 \\ q_{cylinder\_in} = q_1 \\ p_{cylinder\_out} = p_2 \\ q_{cylinder\_out} = q_2 \end{cases}. \tag{10}$$

When the boom is lowered, the pump flow enters the rod side chamber of the boom cylinder. That is,

$$\begin{cases} p_{cylinder\_in} = p_2 \\ q_{cylinder\_in} = q_2 \\ p_{cylinder\_out} = p_1 \\ q_{cylinder\_out} = q_1 \end{cases}, \tag{11}$$

where p_1 and q_1 are the pressure and flow rate of the cap side chamber of the boom cylinder and p_2 and q_2 are the pressure and flow rate of the rod side chamber of the boom cylinder, respectively.

According to Newton's Second Law, the force balance equation of the boom cylinder is as follows:

$$p_1 A_{cap} - p_2 A_{rod} = m\ddot{x} + B\dot{x} + F_{cylinder} + F_{Boom}, \tag{12}$$

where A_{cap} and A_{rod} represent the area of the cap side and the rod side of the boom cylinder, respectively; m is the equivalent mass of the working device; x is the piston displacement; B is the viscous friction coefficient, $F_{cylinder}$ is the coulomb friction force; and F_{Boom} is the output force of the boom cylinder.

The energy losses of the boom cylinder are caused by the coulomb friction force and the viscous friction forces. So,

$$\Delta E_{cylinder} = \int \left(B\dot{x}^2 + F_{cylinder}\right) dt\,. \tag{13}$$

According to the aforementioned equations, the energy efficiency from the engine to the boom can be described as

$$\eta_{total} = \frac{E_{cylinder\_in}}{E_{pump\_in}}. \tag{14}$$

3.2 Energy analysis of the proposed LS-FERS

The energy flow and losses of the LS-FERS can also be described by the aforementioned equations but based on the boom cylinder. The recoverable energy is the pressure energy output from the cap side chamber of the boom cylinder during lowering, while the energy output of the boom lifting process is not included, which can be concluded from the operation principle in Section 2. Therefore, the recoverable energy is as follows:

$$E_{recovrable} = \int_{t_3}^{t_4} p_{cylinder\_out} q_{cylinder\_out} dt, \tag{15}$$

where t_3 and t_4 are the start and end times of the boom-lowering process, respectively.

The regenerated energy E_{r} is the kinetic energy of the flywheel, which can be written as

$$E_r = \frac{1}{2} J \omega_{f\_max}^2, \tag{16}$$

where J is the moment of inertia of the flywheel and ω_{f_max} is the rotational speed just after the regeneration process is completed.

The ratio of the boom potential energy regeneration of the proposed system is calculated as follows:

$$\eta_r = \frac{E_r}{E_{recoverable}}. \tag{17}$$

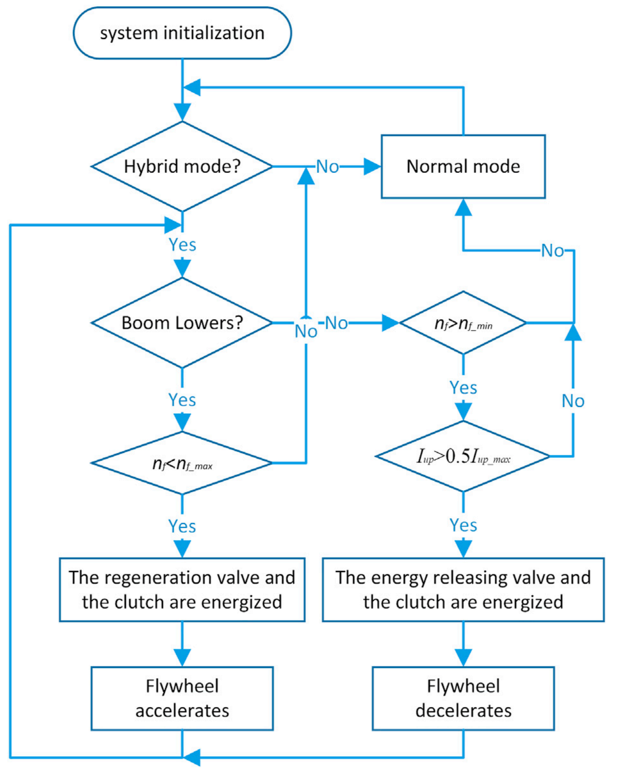

FIGURE 2
Flow chart of the control strategy.

3.3 Energy-saving effect analysis of LS-FERS

As illustrated in Section 2, during the lifting process, the flywheel drives the PM to provide pressurized fluid. So, in a complete boom operation cycle, the energy-saving rate of the proposed system can be described as

$$\eta_{energy\_saving} = 1 - \frac{E'_{pump\_in}}{E_{pump\_in}}, \tag{18}$$

where E'_{pump_in} is the mechanical energy absorbed by the pump in one cycle of the LS-FERS.

From the aforementioned analysis, one can conclude that the more energy the pump motor provides to the system, the less energy the hydraulic pump provides, and the better the energy-saving effects achieved by the system. To achieve the aforementioned goals, appropriate control strategies are required to improve the energy efficiency of the pump motor.

4 Control strategy

The two problems to be solved by the control strategy are how to regenerate the potential energy as much as possible and how to efficiently release the recaptured energy. When the boom goes down, the boom speed is regulated by adjusting the displacement of the PM. At the same time, the boom potential energy is converted to the kinetic energy of the flywheel. When the boom is lifted, the PM provides part of the fluid needed by the system to reduce the energy required by the engine. However, to efficiently use the recaptured energy, considering that the total efficiency of the PM is low when operating in a small displacement (Gong et al., 2019), only when the control signal of boom-up (I_{up}) is greater than its half-maximum value (I_{up_max}) can the PM provide fluid to the main valve. The control strategy is described in Figure 2.

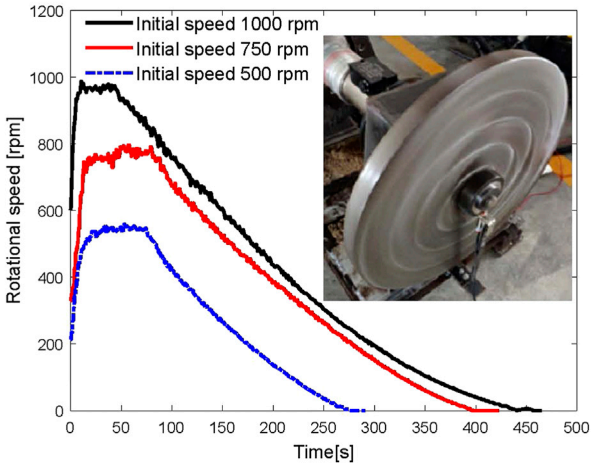

FIGURE 3
Flywheel rotational speed in terms of time.

5 Flywheel coasting experiment

The flywheel coasting experiment refers to the experimental process in which there is no energy exchange between the flywheel and the hydraulic motor, the flywheel rotates due to its own inertia, and its rotational speed gradually decreases because of air resistance and bearing friction. Since the current design used a low-speed metal flywheel with common deep groove ball bearings, the friction should not be ignored, especially when the flywheel is running in the atmospheric environment. For this reason, the self-discharging characteristics of the flywheel were tested. Figure 3 shows the coasting state of the flywheel used in the flywheel-based energy regeneration system. The relationship between the flywheel's rotational speed and time is also shown in Figure 3. In this figure, when the clutch is disconnected, the flywheel speed gradually decreases. At initial speeds of 500, 750, and 1,000 rev/min respectively, the flywheel requires approximately 200, 330, and 400 s from its initial state to stop. At the three initial speeds, it required approximately 8, 13, and 15 s to reduce the flywheel speed by 10% from the initial speed. These times are much longer than those for the boom lifting and landing cycle of the normal excavator, and more than the dwell time between boom lifting and landing actions during normal operation (about 1–2 s). These results showed that the energy loss of the flywheel itself could be ignored. In conclusion, the flywheel system had good self-discharging performance and could meet the requirements of the subsequent experiments.

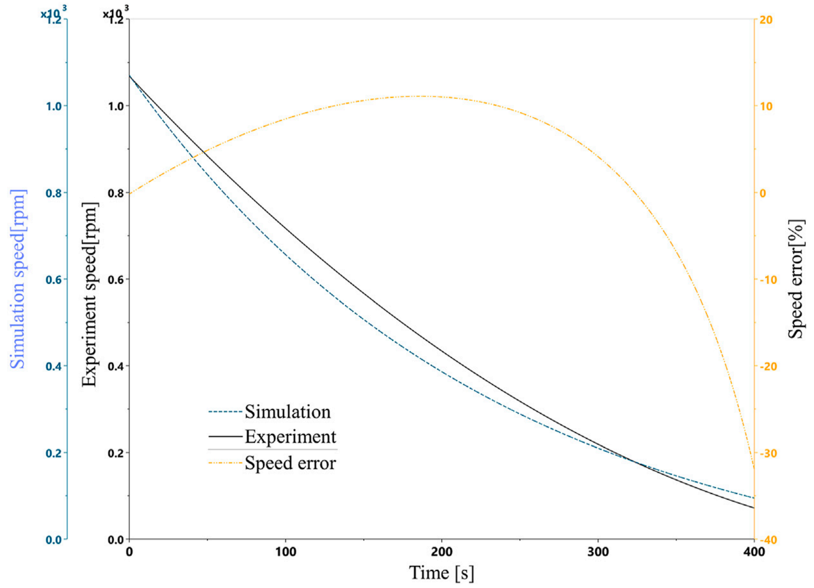

FIGURE 4
Experiment speed, simulation speed, and flywheel error in the coasting mode.

According to the experimental data, the speed curve of the flywheel under the coasting state was fitted, as shown in Figure 4. At the same time, based on these data, the relevant resistance parameters of the flywheel model were obtained, which were used for the following simulation. Figure 4 shows the speed curve of the flywheel model used for simulation under the self-energized state. Furthermore, the error was very small during most speed intervals, especially in the high-speed section. The figure demonstrates the high similarity of the simulation curve with the experimental data.

6 Simulation and discussion

To verify the energy regeneration and reutilization efficiency of the LS-FERS, Figure 5 shows a simulation model established in Amesim software.

The model was composed of two parts, the original load-sensing system, and the flywheel-based ERS. The original load-sensing system included a boom hydraulic cylinder, a main valve, and a load-sensing pump. Therefore, this model was also used to simulate the original load-sensing system. To regenerate the gravity potential energy, the flywheel-based ERS consisted of a flywheel, a PM, a clutch, a regeneration valve, an energy-releasing valve, and a check valve. As illustrated in Figure 1, the energy regeneration function can be achieved by deactivating the regeneration valve. An electric motor was used to simulate the commonly used internal combustion engine because the engine always works at a constant speed (Chen et al., 2019). In addition, some sensors, such as the power sensor and energy sensor, were used to obtain data for the corresponding components. The pertinent simulation parameters are given in Table 1. Regarding the LS pump and PM, the simulations were carried out assuming constant overall efficiencies. The pump displacement was controlled by the pressure compensator and flow compensator. Like previous studies, the load of the boom cylinder was constant (Wang and Wang, 2012; Chen et al., 2019) and the useful work in the simulation model was null (Xu et al., 2017).

6.1 Simulation results of the original load-sensing system

Figure 6 shows a complete operation cycle in which the boom is lifted and lowered. The initial displacement of the boom cylinder was 0.1 m and the final displacement was approximately 0.61 m. The maximum extending and retracting speeds of the boom cylinder were the same, at approximately 0.11 m/s.

The pressure curves of the boom cylinder and pump are illustrated in Figure 7.

In Figure 7, the initial pressure in the rodless chamber of the boom cylinder is approximately 46 bar due to the gravity of the boom. The pressure in the two chambers exhibited a sudden drop and resume at 8 s because the boom cylinder started to retract at this time. The pressure at the pump outlet was always 20 bar higher than the load-sensing pressure. These observations matched well with the characteristics of a load-sensing system. The load-sensing pressure was equal to the pressure in the cap side chamber when the boom was lifting and was equal to the pressure in the rod side chamber when lowering. Because all ports in the center position of the main valve were closed, the pressures in the cap side chamber after the boom cylinder reached the top position and retracted to the bottom position were 59 bar and 57 bar, respectively, which were higher than the initial value of 46 bar.

Figure 8 shows the energy curves of the original system, in which the motor outputs 30.7 kJ of energy to perform a lifting

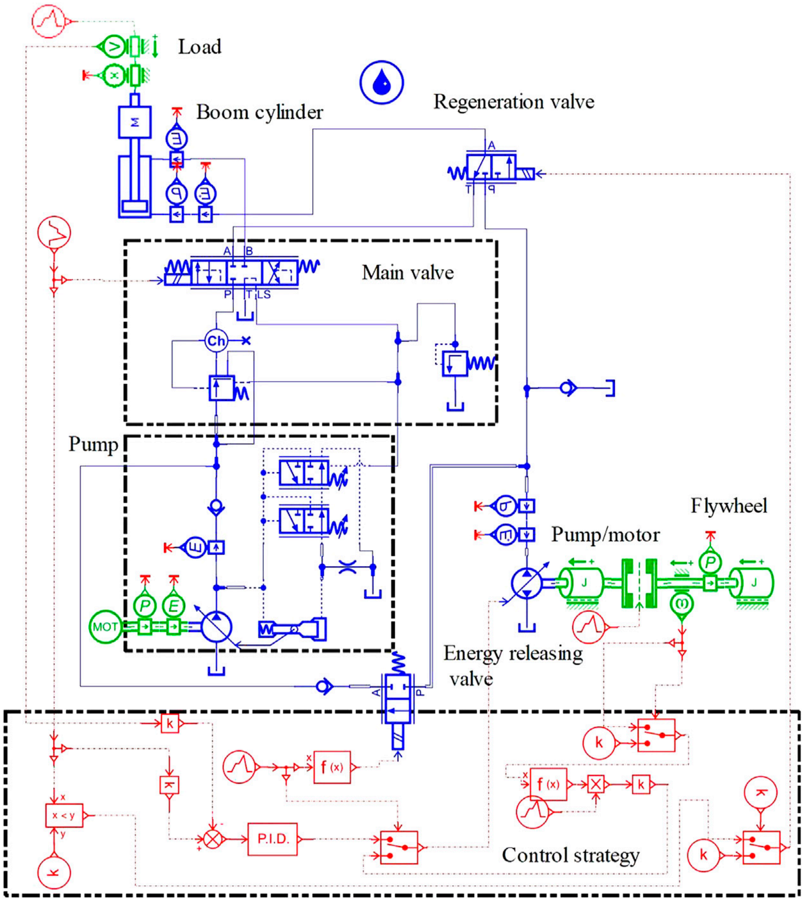

FIGURE 5
Simulation model established in Amesim.

motion and 13.3 kJ of energy to perform a lowering motion. Thus, the pump consumed 44 kJ of energy for one cycle. The difference between the motor output and pump output is due to hydro-mechanical and volumetric losses of the pump, which are described as the pump losses in Section 3. Similarly, the energy difference between the pump output and the boom cylinder input was generated by the pressure drop across the main valve. The energy entering the boom cylinder is greater in the boom-up phase than that in the boom-down phase, and the energy output by the boom cylinder has the opposite trend. The reason is that in the boom-up phase, most of the energy entering the boom cylinder is used to overcome the boom gravity. In addition, in the boom-down phase, the boom potential energy is converted to pressure energy accounting for a main part of the output energy. The energy difference between the input and output in a complete cycle is the friction losses of the boom cylinder, as described in equation (13).

6.2 Simulations of LS-FERS

With the same joystick signal, simulations of LS-FERS were carried out. However, to validate the energy reutilization effect, another lifting phase was added for LS-FERS. The resting time (13–14 s in Figure 9) of the boom between the lowering phase and the second lifting phase is 1 s, which is shorter than the actual operating time of the excavator. However, this was acceptable because this study only analyzed the recovery and reuse of the potential energy of the boom. The rod velocity and displacement of the boom cylinder are displayed in Figure 9. Compared with Figure 6, the boom cylinder in LS-FERS has the same displacement profile as the boom cylinder in the original system. The velocity in the lifting phases is the same as that in that original system. The velocity in the lowering phase differs from that of the original system because the system in the lowering phase is a displacement control system and it has a lower response than a throttling system. However, these two systems have the same mean velocity in the lowering phase since the retraction stokes are the same.

The boom cylinder and pump pressure curves of the proposed system are illustrated in Figure 10. These pressure curves highly resemble those in Figure 7. A pressure peak occurs at 8 s because the boom cylinder starts to retract during the low response of the combination of the flywheel and PM. The pressure drop across the main valve is always 20 bar, which is determined by the flow compensator of the load-sensing pump.

TABLE 1 Pertinent simulation parameter.

Component	Parameter	Value
Pump	Hydro-mechanical efficiency	0.93
	Volumetric efficiency	0.96
	Maximum displacement (mL/rev)	45
	Pressure difference set by the flow compensator (bar)	20
	Maximum pressure set by the pressure compensator (bar)	280
Pump/motor	Hydro-mechanical efficiency	0.93
	Volumetric efficiency	0.95
	Maximum displacement (mL/rev)	45
Boom cylinder	Piston diameter (mm)	90
	Rod diameter (mm)	53
	Stroke (m)	0.6
	Initial displacement (m)	0.1
	Viscous friction coefficient [N/(m/s)]	800
	Stiction force (N)	600
	Coulomb friction force (N)	600
Flywheel	Moment of inertia [$kg \cdot m^2$ ($kg{\cdot}m^2$)]	1.03
	Coulomb friction torque (Nm)	5.6×10^{-2}
	Viscous damping coefficient [Nm/(rev/min)]	4.6×10^{-4}

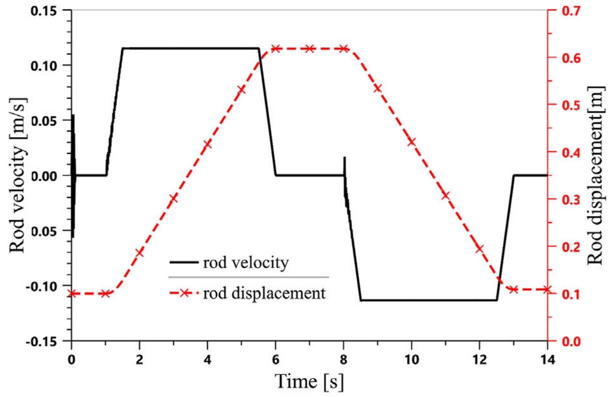

FIGURE 6
Boom cylinder rod velocity and displacement of the original system.

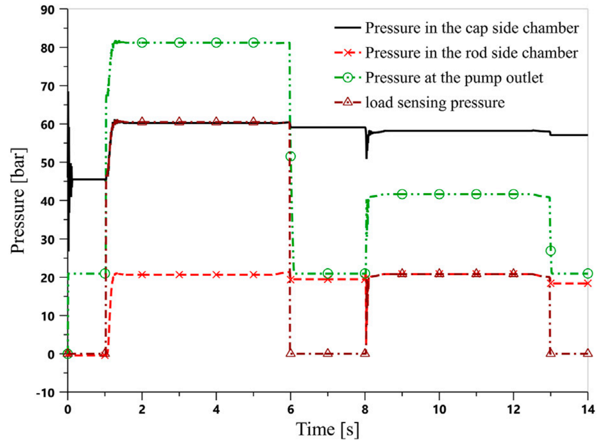

FIGURE 7
Boom cylinder and pump pressure curves of the original system.

Figure 11 shows the energy curves of LS-FERS. During the first lifting phase, the output energy of the motor is 30.7 kJ, which is the same as that in the original system. However, 14.1 kJ of energy is needed for the lowering phase, which is a little more than that of the original system. This energy and the potential energy of the boom are converted into mechanical energy by the PM and then transferred to the flywheel. This means that the flywheel energy is increasing as the boom lowers. When the boom reaches its bottom, the energy regeneration is finished and 16.5 kJ of energy is captured by the flywheel. The kinetic energy in the flywheel will gradually decrease due to windage and friction. In the second lifting phase, the flywheel drives the PM operating in pumping mode to provide fluid to the main valve at the cost of consuming the flywheel's kinetic energy. Therefore, the output

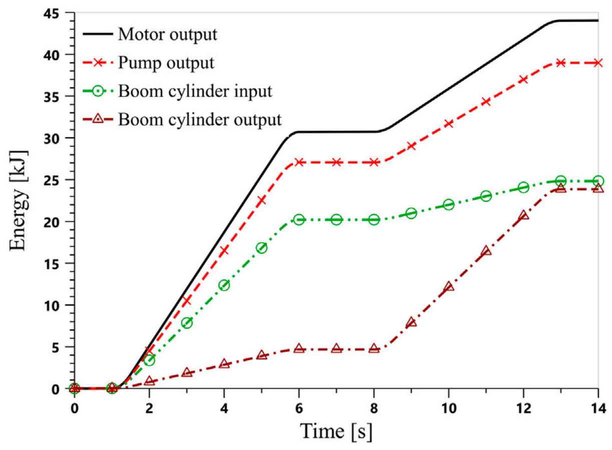

FIGURE 8
Energy consumption of the original system.

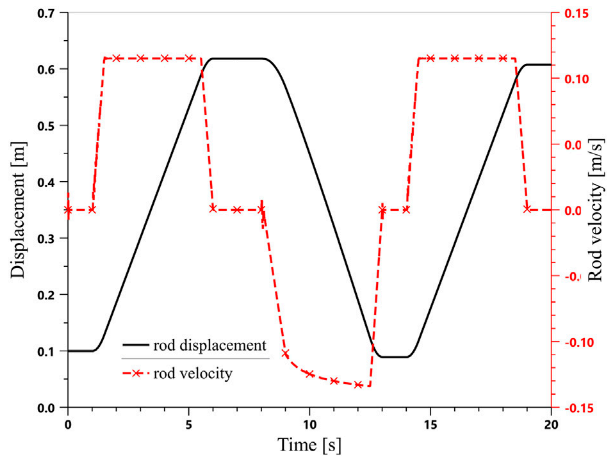

FIGURE 9
Boom cylinder rod velocity and displacement of the proposed system.

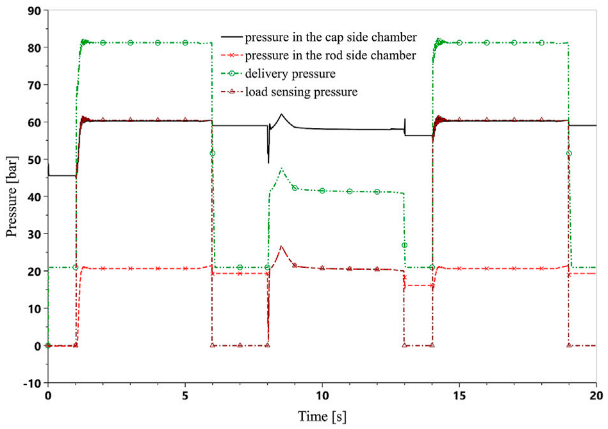

FIGURE 10
Boom cylinder and pump pressure curves of the proposed system.

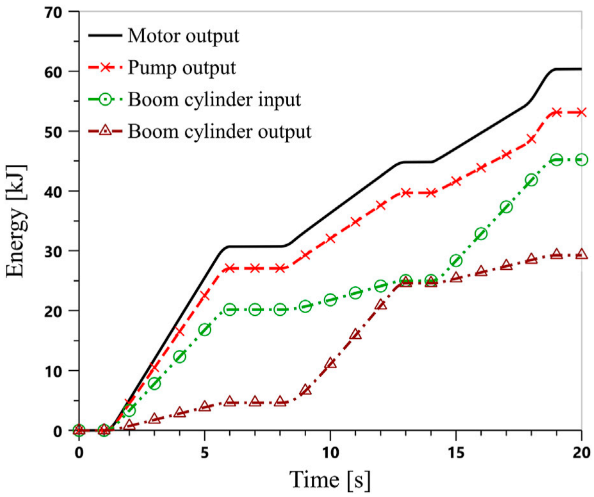

FIGURE 11
Energy consumption of the proposed system.

energy of the motor is only 15.5 kJ, which is much less than that of the original system. The pump in LS-FERS consumes 29.6 kJ in each cycle. Note that the energy amounts of the PM and flywheel differ by about 6.1 kJ. This is caused by the mechanical and volumetric loss of the PM and the windage and friction loss of the flywheel. The motor energy output curve in Figure 11 shows that the motor power is greater than that before from 17.7 s. This is because the flywheel and PM are not able to deliver enough energy, so the motor should output more to satisfy the system requirement. The pump output curve also shows a similar profile. The energy consumption is summarized in Table 2. Compared with a conventional load-sensing system, the energy-saving efficiency of the proposed system is 32.7% in a complete working cycle.

The power curves of the motor and flywheel are illustrated in Figure 12, in which positive and negative values indicate energy absorption and output by the flywheel, respectively. The motor is the only power source in the first lifting phase and the flywheel is at a standstill. The maximum power is approximately 6.8 kW. When the boom is lowered, the flywheel regenerates the output energy of the boom cylinder, which consists of the boom potential energy and the pressure energy entering the rod side chamber of the boom cylinder. This can explain why the power of the flywheel is greater than that of the motor from 9 s to 12 s. When the boom is lifted for the second time (from 14 s to 19 s), the motor is the only power source within the first 0.25 s. As described in Section 4, when the control signal exceeds its half-maximum valve, the flywheel starts to provide fluid. From 14.5 s to 17.7 s, the flywheel power is greater than the motor power. From 17.7 s, the flywheel cannot satisfy the power demand of the system and the motor will output more power to offset the gap. When the flywheel kinetic energy is exhausted, the motor again becomes the only power source.

TABLE 2 Summary of the energy-saving effects.

	Original system/kJ	Proposed system/kJ	Energy-saving rate/%
Motor energy needed to lift boom	30.7	15.5	49.5
Motor energy needed in one cycle	44	29.6	32.7

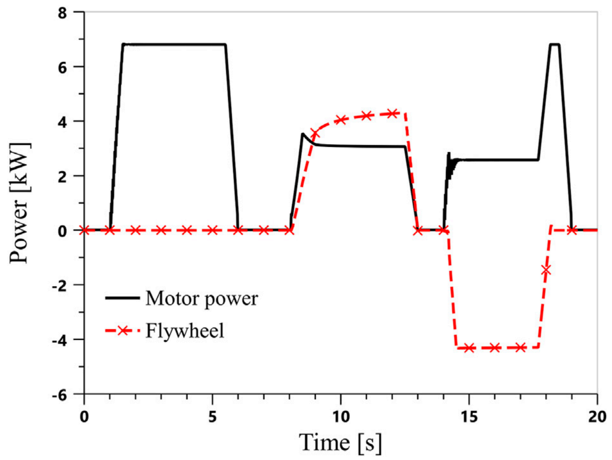

FIGURE 12
Power curves of the motor and flywheel.

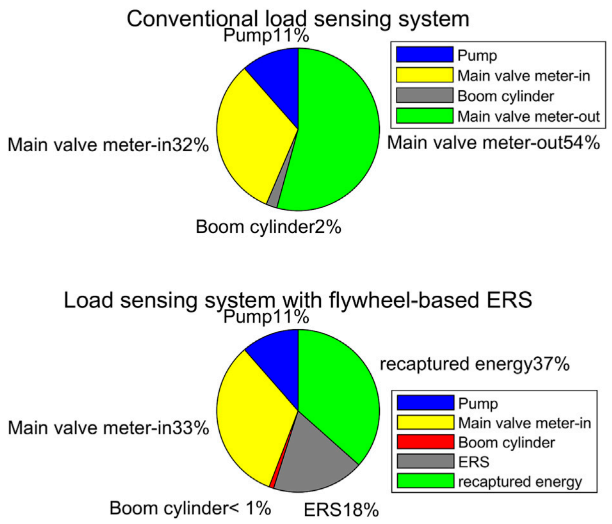

FIGURE 13
Comparison of energy loss distributions.

Figure 13 demonstrates the energy loss distributions in the boom-down condition of the conventional load-sensing system and LS-FERS. In the conventional load-sensing system, 86% of the total energy loss was caused by the main valve. By adding a flywheel-based ERS, 37% of the energy loss can be regenerated. Unfortunately, the main valve meter-in energy dissipation (33%) is still the largest contributor to the wasted energy. If it is needed to improve system energy efficiency, more attention should be paid to the main valve. The energy losses caused by components related to ERS accounted for 18% of the total energy, which was the second largest contributor. Therefore, employing components with higher efficiency, such as more efficient PM and flywheel, have the potential to reduce energy loss as all the recoverable energy will flow through the whole chain in both directions.

6.3 Further discussion of the energy-saving effect compared with other architecture

Our previous research reported a relatively higher energy-saving effect. The two main reasons for the decreased energy-saving effects in the present study are as follows.

- Based on the experiments illustrated in Section 5, compared with reference [], more accurate model parameters were obtained to describe the flywheel-based energy recovery system. However, the new model based on these parameters in the present study has a relatively low energy efficiency compared to that reported previously (Li et al., 2020).
- As shown in Figure 1, any fluid to the boom cylinder should go through the main valve. This will cause energy loss, as discussed in Section 6.2. In comparison, in the previous report (Li et al., 2020), the pressurized fluid provided by the PM was directly delivered to the boom cylinder without any significant throttling loss.

7 Conclusion

The main contributions of this paper can be summarized as follows:

1) A new load-sensing system with a flywheel-based ERS was proposed and analyzed. The boom potential energy is converted into kinetic energy of the flywheel by using a hydraulic PM when the boom goes down. The regenerated energy is reutilized by pumping fluid to the outlet of the pump to reduce the power demand of the original engine.
2) A simulation model was established in Amesim software, and simulation analysis was carried out to investigate the energy-saving effect. The results showed that the energy-saving efficiency of the proposed system was approximately 32.7% compared with a conventional load-sensing system.

These findings indicate that the flywheel-based scheme is promising for developing energy-efficient HEs. Although the data are not fuel-saving based, they provide a reference for evaluating the energy efficiency of the new system. In the future, it is worth building a full prototype to investigate its energy-saving effect.

Data availability statement

The original contributions presented in the study are included in the article/Supplementary Material. Further inquiries can be directed to the corresponding author.

Author contributions

JL and ZJ contributed to the study conception and design. JL and SL performed software simulation and the experiment. JL wrote the draft, and SL and YW revised the manuscript. JL and ZJ provided funding acquisition for this research. All authors contributed to the article and approved the submitted version.

Funding

This research was supported by the Jiangsu Overseas Visiting Scholar Program for the University Prominent Young and Middle-aged Teachers and Presidents 2018 (grant number 2018-3), the Jiangsu Qing Lan Project (grant numbers 2022-29 and RSC20201207), the China Postdoctoral Science Foundation (grant number 2022M722671), and the Xuzhou College of Industrial Technology Science and Technology Foundation (grant number XGY2022C006).

Acknowledgments

The authors would like to express our gratitude to the reviewers and friends who helped us in the process of completing this paper.

Conflict of interest

Author JL was employed by Xuzhou Villead Heavy Industry Technology Co., Ltd.

The remaining authors declare that the research was conducted in the absence of any commercial or financial relationships that could be construed as a potential conflict of interest.

Publisher's note

References

Amirante, R., Cassone, E., Distaso, E., and Tamburrano, P. (2017). Overview on recent developments in energy storage: Mechanical, electrochemical and hydrogen technologies. *Energy Convers. manage.* 132, 372–387. doi:10.1016/j.enconman.2016.11.046

Bui, N. M. T., Dinh, Q. T., Lee, S. Y., Lee, S. Y., and Ahn, K. K. (August 2015).Study on energy regeneration system for hybrid hydraulic excavator, Proceedings of the Int. Conf. Fluid Power Mechatronics, Harbin, China, 1349–1354. doi:10.1109/FPM.2015.7337331

Casoli, P., Gambarotta, A., Pompini, N., and Riccò, L. (2016). Hybridization methodology based on DP algorithm for hydraulic mobile machinery-Application to a middle size excavator. *Autom. Constr.* 61, 42–57. doi:10.1016/j.autcon.2015.09.012

Chen, Q., Lin, T., Ren, H., and Fu, S. (2019). Novel potential energy regeneration systems for hybrid hydraulic excavators. *Math. Comput. Simulat.* 163, 130–145. doi:10.1016/j.matcom.2019.02.017

Dhand, A., and Pullen, K. (2015). Review of battery electric vehicle propulsion systems incorporating flywheel energy storage. *Int. J. Auto. Tech-Kor.* 16 (3), 487–500. doi:10.1007/s12239–015–0051–0

Ge, L., Quan, L., Li, Y., Zhang, X., and Yang, J. (2018). A novel hydraulic excavator boom driving system with high efficiency and potential energy regeneration capability. *Energy Convers. manage.* 166, 308–317. doi:10.1016/j.enconman.2018.04.046

Gong, J., Zhang, D., Liu, C., Zhao, Y., Hu, P., and Quan, W. (2019). Optimization of electro-hydraulic energy-savings in mobile machinery. *Autom. Constr.* 98, 132–145. doi:10.1016/j.autcon.2018.08.011

Hadjipaschalis, I., Poullikkas, A., and Efthimiou, V. (2009). Overview of current and future energy storage technologies for electric power applications. *Renew. Sust. Energy. Rev.* 13 (6-7), 1513–1522. doi:10.1016/j.rser.2008.09.028

Hedlund, M., Lundin, J., Santiago, J., Abrahamsson, J., and Bernhoff, H. (2015). Flywheel energy storage for automotive applications. *Energies* 8 (10), 10636–10663. doi:10.3390/en81010636

Ho, T. H., and Ahn, K. K., A study on the position control of hydraulic cylinder driven by hydraulic transformer using disturbance observer, Proceedings of the Int. Conf. Control, Automation Syst. (October 2008). Seoul, Korea: COEX, 2634–2639. doi:10.1109/ICCAS.2008.4694301

Hussaini, H., and Wang, C. (2022). Battery energy storage system control and integration strategy for the more electric aircraft DC grid application. *Int. J. Hydromechatronics* 5 (3), 275–290. doi:10.1504/IJHM.2022.125093

Joo, C., and Stangl, M. (2016). "Application of power regenerative boom system to excavator," in Proceedings of the 10th international fluid power conference (Dresden, Germany), 175–184. Available at: https://tud.qucosa.de/api/qucosa%3A29389/attachment/ATT-0/.

Kan, K., Binama, M., Chen, H., Zheng, Y., Zhou, D., Su, W., et al. (2022). Pump as turbine cavitation performance for both conventional and reverse operating modes: A review. *Renew. Sustain. Energy Rev.* 168, 112786. doi:10.1016/j.rser.2022.112786

Li, J., and Zhao, J. (2021). Energy recovery for hybrid hydraulic excavators: Flywheel-based solutions. *Autom. Constr.* 125, 103648. doi:10.1016/j.autcon.2021.103648

Li, J., Zhao, J., and Zhang, X. (2020). A novel energy recovery system integrating flywheel and flow regeneration for a hydraulic excavator boom system. *Energies* 13 (2), 315. doi:10.3390/en13020315

Lin, T., Wang, Q., Hu, B., and Gong, W. (2010). Research on the energy regeneration systems for hybrid hydraulic excavators. *Autom. Constr.* 19 (8), 1016–1026. doi:10.1016/j.autcon.2010.08.002

Mahato, A. C., and Ghoshal, S. K. (2020). An overview of energy savings approaches on hydraulic drive systems. *Int. J. Fluid Power* 21 (1), 81–118. doi:10.13052/ijfp1439-9776.2114

Takahashi, K., Kitade, S., and Morita, H. (2002). Development of high speed composite flywheel rotors for energy storage systems. *Adv. Compos. Mat.* 11 (1), 40–49. doi:10.1163/156855102753613273

Triet, H. H., and Ahn, K. K. (2011). Comparison and assessment of a hydraulic energy-saving system for hydrostatic drives. *P. I. Mech. Eng. I-J. Sys.* 225 (1), 21–34. doi:10.1243/09596518jsce1055

Wang, H., Zhu, C., Chao, D., Yan, Q., and Fan, H. (2017). Nonaqueous hybrid lithium-ion and sodium-ion capacitors. *Adv. Mat.* 29 (46), 1702093. doi:10.1002/adma.201702093

Wang, T., and Wang, Q. (2012). Design and analysis of compound potential energy regeneration system for hybrid hydraulic excavator. *P. I. Mech. Eng. I-J. Sys.* 226 (10), 1323–1334. doi:10.1177/0959651812456642

Wang, T., and Wang, Q. (2014). Efficiency analysis and evaluation of energy-saving pressure-compensated circuit for hybrid hydraulic excavator. *Autom. Constr*. 47, 62–68. doi:10.1016/j.autcon.2014.07.012

Wasbari, F., Bakar, R. A., Gan, L. M., Tahir, M. M., and Yusof, A. A. (2017). A review of compressed-air hybrid technology in vehicle system. *Renew. Sust. Energy Rev*. 67, 935–953. doi:10.1016/j.rser.2016.09.039

Xia, L., Quan, L., Cao, D., and Yin, M. (2019). Research on energy saving characteristics of large hydraulic excavator boom driven by dual hydraulic-gas energy storage cylinder. *J. Mech. Eng.* 55 (20), 240–248. doi:10.3901/JME.2019.20.240

Xu, B., Hu, M., Zhang, J., and Mao, Z. (2017). Distribution characteristics and impact on pump's efficiency of hydro-mechanical losses of axial piston pump over wide operating ranges. *J. Cent. South Univ.* 24 (3), 609–624. doi:10.1007/s11771-017-3462-4

Yu, Y., and Ahn, K. K. (2019). Optimization of energy regeneration of hybrid hydraulic excavator boom system. *Energy Convers. manage.* 183, 26–34. doi:10.1016/j.enconman.2018.12.084

Zhao, D., Chen, M., Dai, Q., and Zhang, E. (2011). System of arm potential energy recovery in hybrid hydraulic excavators. *J. Jilin Univ. Eng. Tech.)* 41 (s1), 150–154. doi:10.13229/j.cnki.jdxbgxb2011.s1.064

Zhou, Z., Benbouzid, M., Charpentier, J. F., Scuiller, F., and Tang, T. (2013). A review of energy storage technologies for marine current energy systems. *Renew. Sust. Energy. Rev*. 18, 390–400. doi:10.1016/j.rser.2012.10.006

Frontiers in Energy Research

TYPE Original Research
PUBLISHED 19 June 2023
DOI 10.3389/fenrg.2023.1187558

Research on electro-hydraulic composite drive winch and energy recovery system for mobile crane

Xianggen Xu[1,2], Tianliang Lin[1,2]*, Haoling Ren[1,2], Tong Guo[1,2], Zhongshen Li[1,2] and Cheng Miao[1,2]

[1]College of Mechanical Engineering and Automation, Huaqiao University, Xiamen, China, [2]Fujian Key Laboratory of Green Intelligent Drive and Transmission for Mobile Machinery, Xiamen, China

OPEN ACCESS

EDITED BY
Yang Yang,
Yangzhou University, China

REVIEWED BY
Wang Hongliang,
Changzhou Institute of Technology, China
Weixuan Jiao,
Yangzhou University, China
Leilei Ji,
Jiangsu University, China

*CORRESPONDENCE
Tianliang Lin,
ltlkxl@163.com

RECEIVED 16 March 2023
ACCEPTED 01 June 2023
PUBLISHED 19 June 2023

CITATION
Xu X, Lin T, Ren H, Guo T, Li Z and Miao C (2023), Research on electro-hydraulic composite drive winch and energy recovery system for mobile crane. *Front. Energy Res.* 11:1187558. doi: 10.3389/fenrg.2023.1187558

Owing to the high power consumption and limited control precision of traditional hydraulic drive winch systems, this study proposes hydraulic and electric-type energy recovery systems. The accumulator used in the hydraulic type has low energy density, which makes it difficult to store a large amount of energy. Meanwhile, the electric motor/generator used in the electric type cannot solve the secondary slip because of oil leakage, which leads to low controllability and high-power consumption under near-zero speed and high torque conditions. Thus, based on electric construction machinery with high-pressure, energy-dense electric energy storage units, this study proposes an electro-hydraulic composite drive winch and energy recovery system and control strategy for mobile cranes. Considering the good control characteristics of the electric motor/generator and the high-power density of the hydraulic accumulator, this hydroelectric composite drive and energy recovery system may solve the secondary sliding challenge and ensure large torque output at near-zero speed. A simulation model of the mobile crane is established to verify the feasibility of the proposed system and control strategy. The research results showed that the system is more efficient at recovering energy when the weight is lowered by a greater distance.

KEYWORDS

winch system, engineering machinery, secondary slip, mobile crane, electro-hydraulic composite drive, energy recovery efficiency

1 Introduction

With global warming, rising oil prices, and the energy crisis, the importance of energy saving and emission reduction has been gradually increasing in numerous guiding frameworks (Zhang et al., 2017; Liu, 2019). Construction machinery often has a large amount of negative load during movement. Reducing carbon emissions and implementing electrification to achieve energy saving and environmental protection are of current interest worldwide (Lin et al., 2020). The types of winch energy-saving drives are divided according to their components into hydraulic drive, electro-hydraulic composite drive, and direct electric motor/generator drive. Similarly, according to the energy storage components, winch energy recovery can be divided into hydraulic recovery, electric recovery, and composite recovery.

The winch systems of traditional construction machinery are primarily hydraulic drives. Central South University proposed an energy-saving system for the recovery of the potential energy of the main lowering winch of rotating drilling rigs, in which the secondary element hydraulic pump/motor was mechanically connected to the engine in a coaxial manner, and the accumulator recovered the residual potential energy (Zhu et al., 2018). Fang at Central South University designed a hybrid oil-electric winch system based on the hydraulic system for the main winch of rotary drilling rigs, in which the hydraulic motor/generator was used to recover the potential energy into electric energy stored in the supercapacitor when the main winch was lowered (Fang et al., 2012). Bolonne, at the University of Molétouvo, proposed a hybrid system for RTG cranes that included a lithium battery, a supercapacitor, and a diesel generator, in which the supercapacitor and lithium battery worked together to recover the crane's regenerable energy (Bolonne and Chandima, 2019). Kim at the Korean Classification Society proposed a hybrid system using diesel generators in combination with supercapacitors and lithium-ion batteries and assessed energy recovery into lithium batteries and supercapacitors under different operating conditions. The results showed that the system could significantly reduce harmful emissions (Kim et al., 2019). Corral-Vega of the University of Cadiz proposed an RTG drive scheme using a fuel cell as the energy source and a supercapacitor as the energy storage system. The simulation results demonstrated the high energy efficiency of the hybrid system. Direct-drive winches are primarily used in stationary machinery, such as tower cranes, shovels, and elevators. Huang from Beijing Jiaotong University proposed a supercapacitor-based power compensation and energy recovery system for mine hoisting equipment, in which the energy of the shaft grid and the potential energy of the shaft repair machine were stored in the supercapacitor through a converter (Huang Pu, 2015). The results showed that the system was more practical at obtaining power and the load was lower. Li from ZOOMLION researched a purely electric truck crane energy recovery device and system strategy in unplugged and plugged operation conditions, and verified the effectiveness of the crane winch energy recovery device and control strategy (Li et al., 2022). Research on electric winches has focused on electrical control devices (Premkumar and Manikandan, 2014; Kodkin and Anikin, 2020). A control device was used to prevent backlash due to slack in the traction component (Lee et al., 2019; Caporali, 2021). In addition, there are control algorithms that compensate for the loss of torque in the low-speed area of the motors (Li and Wang, 2019; Roman et al., 2021), and mechanical methods to improve the structure and stability to provide ordered coiling of strings, etc. Electro-hydraulic composite drive winch systems have used electric motor-hydraulic pumps/motors to supplement the composite drive and the power regeneration system. Liu of the Taiyuan University of Technology proposed an electro-hydraulic hybrid drive winch potential energy recovery system, which used an electric motor as the main drive to reduce throttling losses, combined with a hydraulic pump/motor and accumulator as the energy recovery unit. The results showed that the electro-hydraulic composite drive winch system had good energy recovery (Liu et al., 2022). Zhao of the Taiyuan University of Technology applied the composite electric motor-hydraulic pump/motor composite drive system to an elevator system, which recovered energy from the traction machine's power generation state through the accumulator, and released the energy from the accumulator when the traction machine needed to be in the electric state for energy recovery (Zhao et al., 2016; Zhang et al., 2020). Wang Xthe at the Taiyuan University of Technology proposed a hybrid electro-hydraulic drive electric excavator hoist system, which utilized the engine as the main drive and the accumulator-hydraulic pump/motor as the auxiliary drive. The potential energy of the hoist system was mainly stored in the accumulator through the hydraulic pump/motor when the hoist system was lowered. The energy was released by the accumulator when it was lifted (Wang et al., 2020). The hydraulic pump/motor and the electric motor worked together to complete the lifting. The simulation results showed that the system reduced the power consumption by approximately 30% compared to the traditional system. Zhang of the Dalian University of Technology proposed a composite electro-hydraulic drive hoist system, in which the speed was controlled by a hydraulic system and the torque was controlled by an electric motor. The hydraulic motor was connected to the two ends of the bobbin to drag the load together. The results showed that the system energy recovery efficiency was approximately 60% (Zhang, 2019).

To recover the potential energy of the mobile crane winch system and reduce engine pollution, considering the good control characteristics of the electric motor/generator and the high power density of the hydraulic accumulator, this study proposes a hydro-electric composite drive and energy recovery system to solve the challenge of secondary sliding and ensure the large torque output at near-zero speed. A control strategy is also proposed to integrate energy recovery and regeneration for the proposed composite winch system.

2 Working principles of the winch system

The scheme of the proposed entity electro-hydraulic composite drive winch system is shown in Figure 1. The system mainly contains an electrical component, a hydraulic drive component, and a mechanical drive component.

2.1 Electric drive component

The pressure signal from the hydraulic system, the speed and torque signal from the motor controller, and the artificially desired weightlifting speed signal are collected by the vehicle control unit (VCU). The control unit in the hydraulic system, the electric motor controller unit (MCU), and the lithium battery management system (BMS) receive the control signals from the VCU via the controller area network (CAN) bus and input and output (IO) port. The closed-loop enables cooperative control in multiple quadrants of the electric motor/generator-variable displacement hydraulic pump/motor output speed, angle, torque, and other parameters. The weight is driven to lift and lower to achieve the desired movement.

2.2 Hydraulic drive component

The hydraulic drive component is shown in Figure 2. In addition to storing energy, the high-pressure and low-pressure accumulators provide hydraulic energy to the variable displacement hydraulic pump/motor. Each 2-position, 2-way electromagnetic valve receives control signals from the VCU depending on the different working conditions. Hydraulic oil in both the high-pressure and low-pressure accumulators is transferred to the variable displacement hydraulic pump/motor. The oil is pressurized or depressurized and then returned to the high-pressure and low-pressure

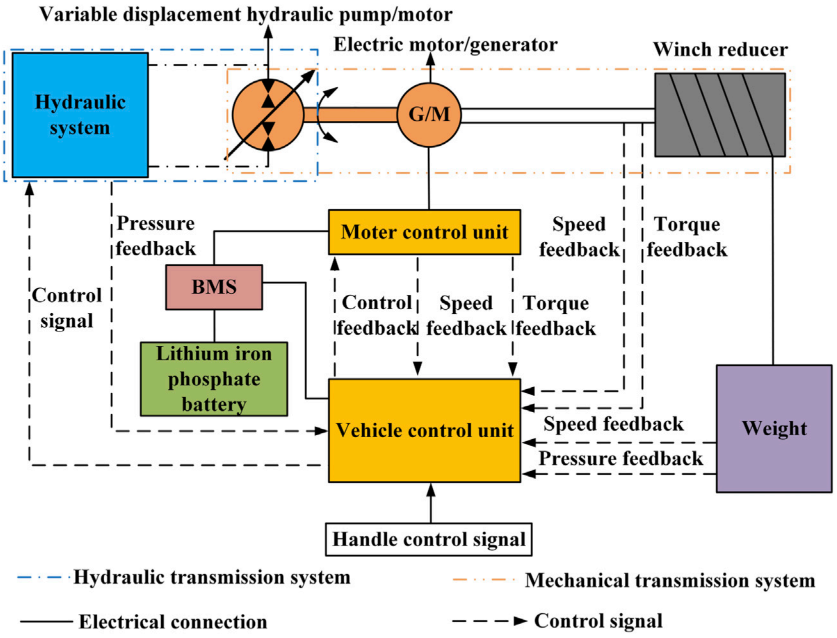

FIGURE 1
Schematic diagram of the proposed winch system.

accumulators via the 2-position, 2-way electromagnetic valve to complete the energy recovery. The differential pressure between the two ends of the variable-displacement hydraulic pump/motor changes continuously with changes in the pressure of the high-pressure and low-pressure accumulators. The variable-displacement hydraulic pump/motor receives control signals from the VCU to change the displacement to meet the required output torque, while the high-pressure and low-pressure accumulators satisfy the pressure conditions.

2.3 Mechanical drive component

The mechanical drive component consists of coaxial mechanical coupling among the variable-displacement hydraulic pump/motor, electric motor/generator, and winch reducer. The weight is wound onto the winch reducer using a wire string. The winch reducer is driven by the electric motor/generator-variable-displacement hydraulic pump/motor controlled by the VCU. The weightlifting and lowering motion is determined by the VCU.

3 Control strategy and implementation process of the winch system

3.1 Analysis of the winch system control strategy

The signals of the pressure, displacement, torque, and *SOC* are input to the VCU through various sensors. The weightlifting and lowering motion mode differs depending on the load weight, the pressure difference between the high-pressure and low-pressure accumulators, the low-pressure accumulator pressure, and the *SOC*. During the movement of the weight, the speed of the electric motor/generator is directly controlled by the handle opening. The displacement of the variable-displacement hydraulic pump/motor adapts itself to the speed. When a constant torque output of the variable-displacement hydraulic pump/motor is required, the VCU sends a corresponding control signal to each 2-position, 2-way electromagnetic valve and variable-displacement hydraulic pump/motor. The flow direction of the oil circuit and the displacement of the displacement hydraulic pump/motor change to achieve a constant torque output of the variable-displacement hydraulic pump/motor. The electric motor/generator for adaptive torque compensation and control strategy are shown in Figure 3, where Y_{P} is the handle opening (divided into positive and negative sides); $Y_{\min}$ is the positive and negative minimum handle opening; $Y_{\max}$ is the positive and negative maximum handle opening; *SOC* is the state of charge of the lithium battery; $S_{\max}$ is the maximum *SOC* value when potential energy recovery is performed; F is the negative load weight; $F_{\min}$ is the negative load weight when switching from purely electric motor/generator drive to electro-hydraulic composite drive; D_{17}, D_{18}, D_{19}, D_{20}, and D_{21} correspond to the first, second, third, fourth, and fifth 2-position, 2-way electromagnetic valve, respectively; Δp and $\Delta p_{\min}$ are the differential pressure and minimum differential pressure between the high-pressure and low-pressure accumulators, respectively; p_1 is the high-pressure accumulator pressure; p_2 is the low-pressure accumulator pressure; $p_{2\min}$ is the minimum threshold pressure of the low-pressure accumulator; and p_{BA} is the differential pressure between B-port pressure p_{B} and A-port pressure p_{A} of the variable-displacement hydraulic pump/motor, i.e., the differential pressure between the two ends of the variable displacement hydraulic pump/motor.

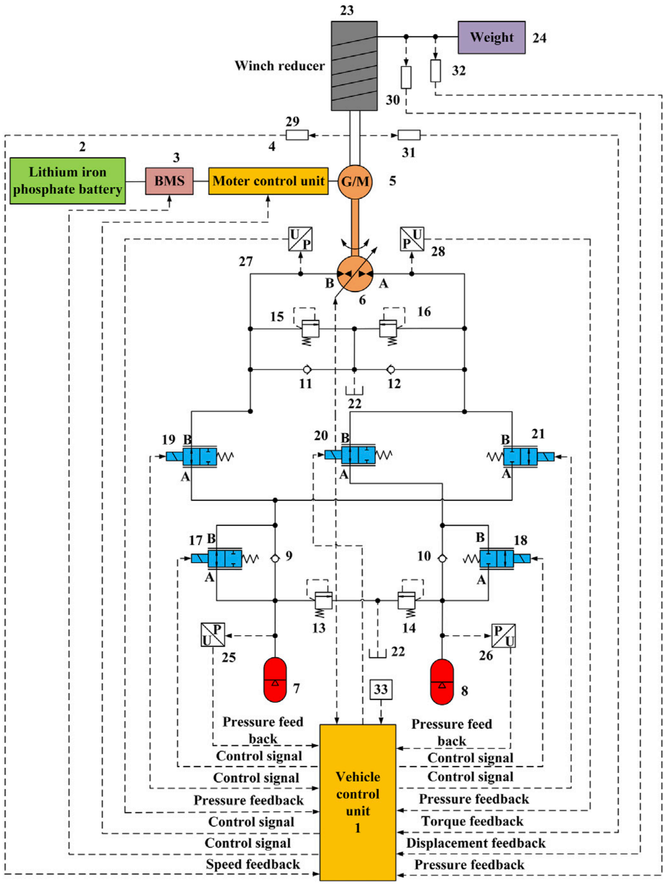

1. Vehicle control unit
2. Lithium iron phosphate battery
3. Battery management system
4. Machine controller
5. Electric motor/generator
6. The variable displacement hydraulic pump/motor
7, 8. High- and low-pressure accumulator
9, 10, 11, 12. The first, second, third, and fourth check valve
13, 14, 15, 16. The first, second, third, and fourth direct-acting relief valve
17, 18, 19, 20, 21. The first, second, third, fourth, and fifth 2-position 2-way electromagnetic valve
22. Oil box
23. Winch reducer
24. The weight
25, 26, 27, 28, 29, 30. The first, second, third, fourth, and fifth pressure sensor
31. Torque sensor
32. Displacement sensor
33. Handle control signal

FIGURE 2
Hydraulic schematic of the winch system.

According to the aforementioned, the control strategy is as follows:

(1) If the load weight satisfies $F < F_{\text{min}}$ or the battery satisfies $SOC \geq S_{\text{max}}$, the handle opening satisfies $Y_{\text{min}} < |Y_p| < Y_{\text{max}}$; the system is in the pure electric motor/generator drive and energy recovery mode. The electric motor/generator is in an electric motor state when the weight is lifting and in the electric generator state when it is lowering.
(2) If the load weight satisfies $F \geq F_{\text{min}}$ and the battery satisfies $SOC < S_{\text{max}}$, the handle opening satisfies $Y_{\text{min}} < Y_p < Y_{\text{max}}$ and the differential pressure between the high-pressure and low-pressure accumulators satisfies $\Delta p \geq \Delta p_{\text{min}}$; the system is in the electro-hydraulic composite drive mode. The electric motor/generator is working as the electrical motor. The variable-displacement hydraulic pump/motor is in a hydraulic motor state to allow the electro-hydraulic composite drive to lift the weight.
(3) If the load weight satisfies $F \geq F_{\text{min}}$ and the battery satisfies $SOC < S_{\text{max}}$, the handle opening satisfies $-Y_{\text{max}} < Y_p < -Y_{\text{min}}$ and the low-pressure accumulator pressure satisfies $p_2 \geq p_{2\,\text{min}}$; the system is in the recovery mode of the electro-hydraulic composite drive. The electric motor/generator is in the electric generator state. The variable-displacement hydraulic pump/motor is in the hydraulic pump state to allow the electro-hydraulic composite drive to lower the weight.

3.2 Implementation process for the winch system

If the load is light ($F < F_{\text{min}}$ or $SOC \geq S_{\text{max}}$), the winch drive system operates in a purely electric motor/generator drive mode with an energy recovery mode and the electric motor/generator in an electric motor or power production state.

If the load is heavy ($F \geq F_{\text{min}}$ and $SOC < S_{\text{max}}$), the winch drive system initially operates in electro-hydraulic composite drive mode, in which the electric motor/generator is in the electric motor state and the variable-displacement hydraulic pump/motor is in the hydraulic motor state. D_{17}, D_{19}, and D_{20} are energized and in a fully open state. D_{18} and D_{21} are de-energized. The hydraulic oil in the high-pressure accumulator reaches port B of the variable-displacement hydraulic pump/motor through D_{17} and D_{19}. The variable-displacement hydraulic pump/motor is then in the hydraulic-motor state. After depressurization, the oil is returned to the low-pressure accumulator from D_{20} and the second check valve. The pressures in both the high-pressure accumulator and the low-pressure accumulator, as well as the pressure at both ends of the

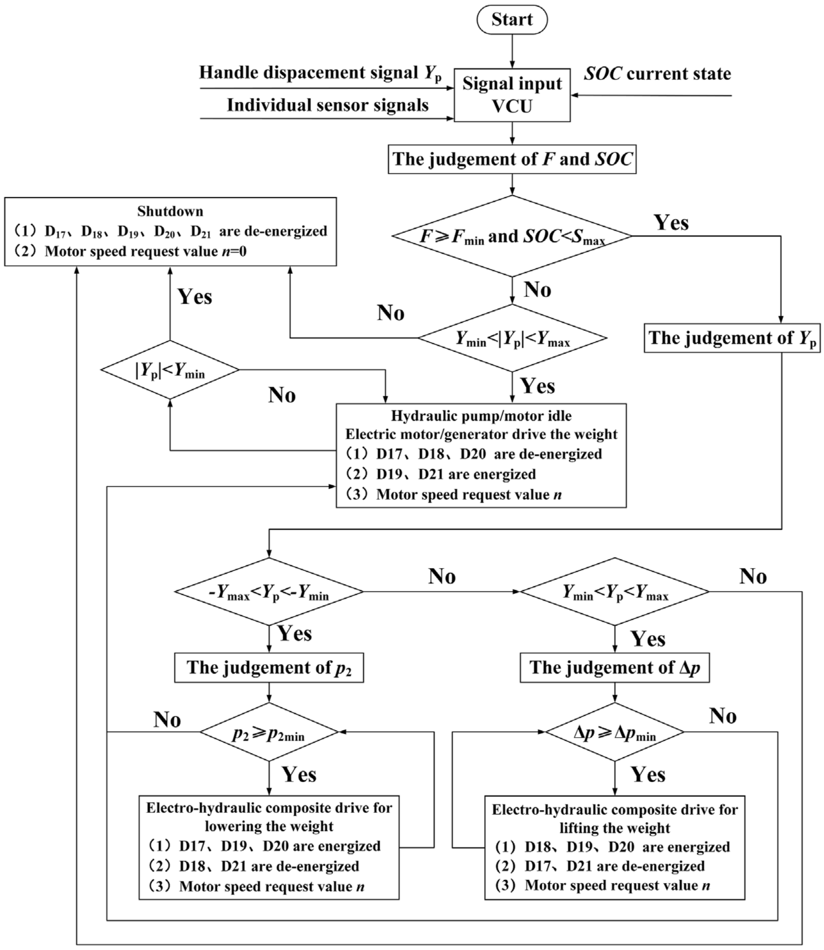

FIGURE 3
Control strategy for the winch system.

variable displacement hydraulic pump/motor, change with the above process. The displacement of the variable-displacement hydraulic pump/motor must be controlled to ensure that its output torque is constant and, thus, outputs a certain amount of power, as well as to control the motor controller to power the lithium battery to drive the electric motor/generator synergy to output the remaining power. If the differential pressure between the high-pressure and low-pressure accumulators cannot meet the constant torque output of the variable displacement hydraulic pump/motor; namely, $\Delta p < \Delta p_{\min}$ during the weight lifting, D_{17}, D_{18}, and D_{20} are de-energized and D_{19} and D_{21} are energized and in a fully open state. The electric motor/generator alone outputs power to drive the winch reduction gear to lift the weight and drive the variable-displacement hydraulic pump/motor in the idle state. The first and second check valves and all four direct-acting relief valves work as required. In the work process described earlier, the speed of the electric motor/generator is directly controlled by the handle opening to achieve the target velocity of the weightlifting and complete the lifting motion.

If the load is heavy ($F \geq F_{\min}$ and $SOC < S_{\max}$), the winch drive system initially operates in the electro-hydraulic composite drive mode. The electric motor/generator is in the electric generator state and the variable displacement hydraulic pump/motor is in the hydraulic pump state. D_{18}, D_{19}, and D_{20} are energized and in a fully open state. D_{17} and D_{21} are de-energized. The hydraulic oil in the low-pressure accumulator reaches port A of the variable displacement hydraulic pump/motor through D_{18} and D_{19}. After pressurization, the oil is returned to the high-pressure accumulator from D_{20} and the first check valve. The pressures in both the high-pressure and low-pressure accumulators, as well as the pressure at both ends of the variable displacement hydraulic pump/motor, change during the above process. The displacement of the variable-displacement hydraulic pump/motor is controlled by the VCU to ensure a constant power output of the variable-displacement hydraulic pump/motor. The lithium is treated as a power source to ensure the remaining power output of the electric motor/generator. If the fluid pressure in the low-pressure accumulator is insufficient to keep the reverse towing torque formed by the variable-displacement hydraulic pump/motor at a certain value during the weight lowering; namely, $p_2 < p_{2\min}$, D_{17}, D_{18}, and D_{20} will be de-energized. D_{19} and D_{21} will be energized and in a fully open state. The motor/generator alone outputs power to drive the winch reduction gear to lower the weight and make the variable-displacement hydraulic pump/motor in the idle state, and the first check valve, the second check valve, and all four direct-

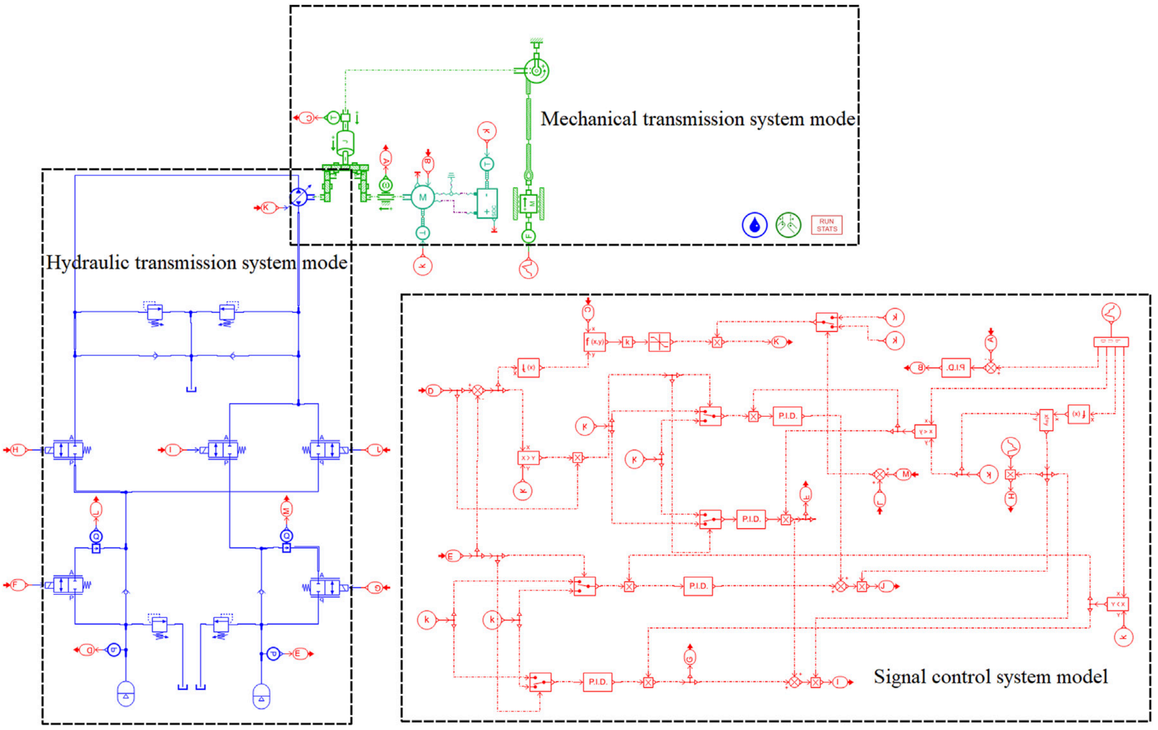

FIGURE 4
Simulation model of the winch system.

TABLE 1 Main simulation parameters of the winch system.

Parameter	Parameter value
Rated power of the motor	50 kW
Rated speed of the motor	3,600 r/min
Rated torque of the motor	130 N·m
Battery capacity	6.5 Ah
Initial battery charge	90% SOC
Winch gear ratio	55.2
Diameter of the winch reducer reel	0.44
Maximum velocity of the weight movement	1 m/s
Load weight range	1–4 t
Maximum displacement of the variable displacement hydraulic pump/motor	500 mL/r
Rated speed of the variable displacement hydraulic pump/motor	3,600 r/min
Opening pressure of the first direct-acting relief valve	20 MPa
Opening pressure of the second direct-acting relief valve	5 MPa
Opening pressure of the third direct-acting relief valve	20 MPa
Opening pressure of the fourth direct-acting relief valve	20 MPa

acting relief valves work as required. In the working process described above, the speed of the electric motor/generator is directly controlled by the handle opening to achieve the target lowering velocity of the weight.

When the winch must be stopped during the weight-lowering process, the handle opening should be reduced to below the minimum threshold. All the 2-position, 2-way electromagnetic valves are controlled in the de-energized state. The electric motor/generator is controlled by the VCU in the blocked condition to stop the movement of the weight. The first check valve, the second check valve, and all four direct-acting relief valves work as required.

The system makes full use of the high energy density of the electrical energy storage unit and the good control characteristics of the electric motor/generator. The system also provides a solution to the problem of secondary sliding of heavy loads as well as the low energy density of the accumulator. The proposed closed hydraulic system using the accumulator-variable displacement hydraulic pump/motor can achieve high power density and high torque output at near-zero speed and solve the problem of high energy consumption of the electric motor/generator drive winch and part of the energy loss in the balance and multiple directional control valves.

4 Winch system modeling and simulation model

4.1 Winch system modeling

After the load weight F and the desired lifting and lowering speed v have been determined, the output power of the electric motor/generator-variable displacement hydraulic pump/motor is determined using Eq. 1.

$$P = \frac{F \cdot v}{1000} = \frac{2\pi n \cdot T}{6000} \tag{1}$$

where P, n, and T are the output power, speed, and output torque of the electric/generator-variable hydraulic pump/motor, respectively.

The output power P includes two components: output torque T and output speed n. For the electric motor/generator-variable-displacement hydraulic pump/motor, the required output torque T is determined by the load weight F, the diameter of winch reducer reel D, and the winch reducer transmission ratio r, as shown in Eq. 2.

$$T = \frac{30F \cdot v}{\pi \cdot n} = \frac{F \cdot \mathrm{D}}{2\mathrm{r}} \tag{2}$$

In the case of the electric motor/generator-variable-displacement hydraulic pump/motor, the desired velocity n can be determined by the desired lift and lowering velocity v of the weight, the diameter of the winch reducer reel D, and the winch reducer transmission ratio r, as shown in Eq. 3.

$$n = \frac{60v \cdot \mathrm{r}}{\pi \mathrm{D}} \tag{3}$$

The variable-displacement hydraulic pump/motor is designed to deliver a constant proportional torque. The displacement V of the variable displacement hydraulic pump/motor can be determined by Δp, as shown in Eq. 4

$$V = \frac{2\pi T}{\Delta p \cdot k} \tag{4}$$

where V is the displacement of the variable displacement hydraulic pump/motor, and k is the displacement influencing factor, the value of which is directly related to the output power assumed by the artificially desired variable displacement hydraulic pump/motor. T/k denotes the amount of output torque that must be assumed by the variable-displacement hydraulic pump/motor.

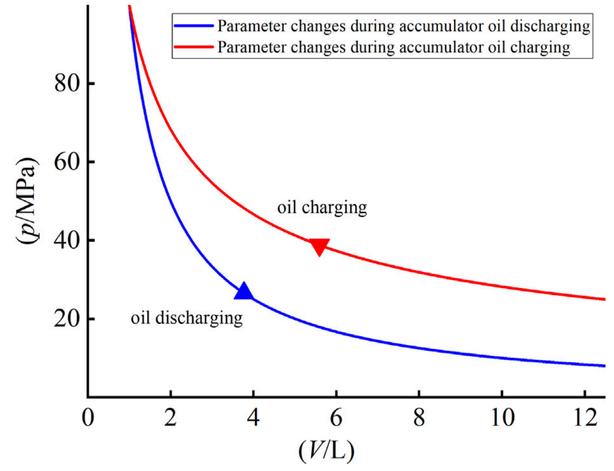

FIGURE 5
Variation in accumulator state parameters.

After the electric motor/generator speed has been controlled at the desired value and the displacement of the variable-displacement hydraulic pump/motor has been calculated, the required flow rate of the high-pressure accumulator q_1 and low-pressure accumulator q_2 can be calculated by Eq. 5.

$$q = n \cdot V \tag{5}$$

where q is the high-pressure and low-pressure accumulator flow rate.

The maximum pressures of the high-pressure and low-pressure accumulators are limited by the setting pressures of the first and second direct-acting relief valves, respectively. The setting pressures of the third and fourth direct-acting relief valves are determined by the system operating pressure. The first check valve, the second check valve, the first charge check valve, and the second charge check valve are not set to an initial pressure. Each 2-position 2-way electromagnetic valve has a fully open and a fully closed state. In the fully open state, the flow rate restriction or pressure drop at the inlet and outlet of the valve is as small as possible. Therefore, the differential pressure between the high-pressure and low-pressure accumulators can be approximated as that of the two ends of the variable displacement hydraulic pump/motor. The hydraulic system may not be capable of delivering constant proportional power due to the capacity limitations of the high-pressure and low-pressure accumulators. Thus, movement of the weight requires the electric motor/generator alone.

4.2 Winch system simulation model

According to the scheme presented in Figure 1 and the control strategy illustrated in Figure 3, the simulation model of the electro-hydraulic composite drive winch system is shown in Figure 4. The main components of the simulation model are the hydraulic system model, the signal control system model, and the mechanical system model.

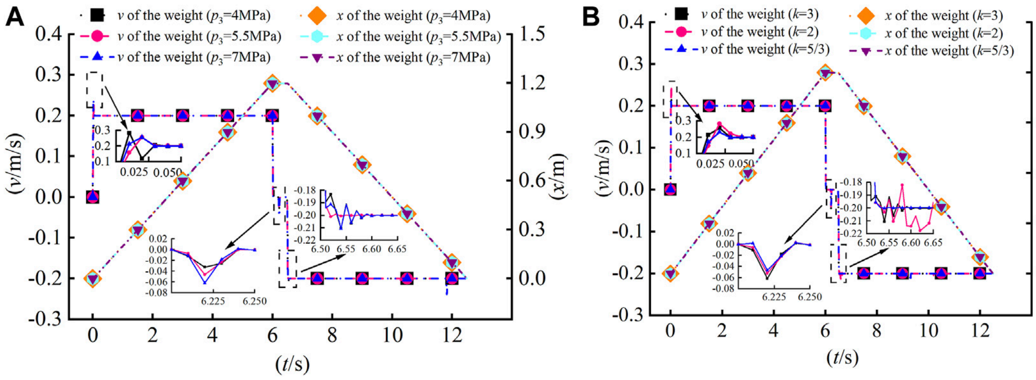

FIGURE 6
Dynamic characteristics of the system under different conditions. **(A)** Different p_3. **(B)** Different k.

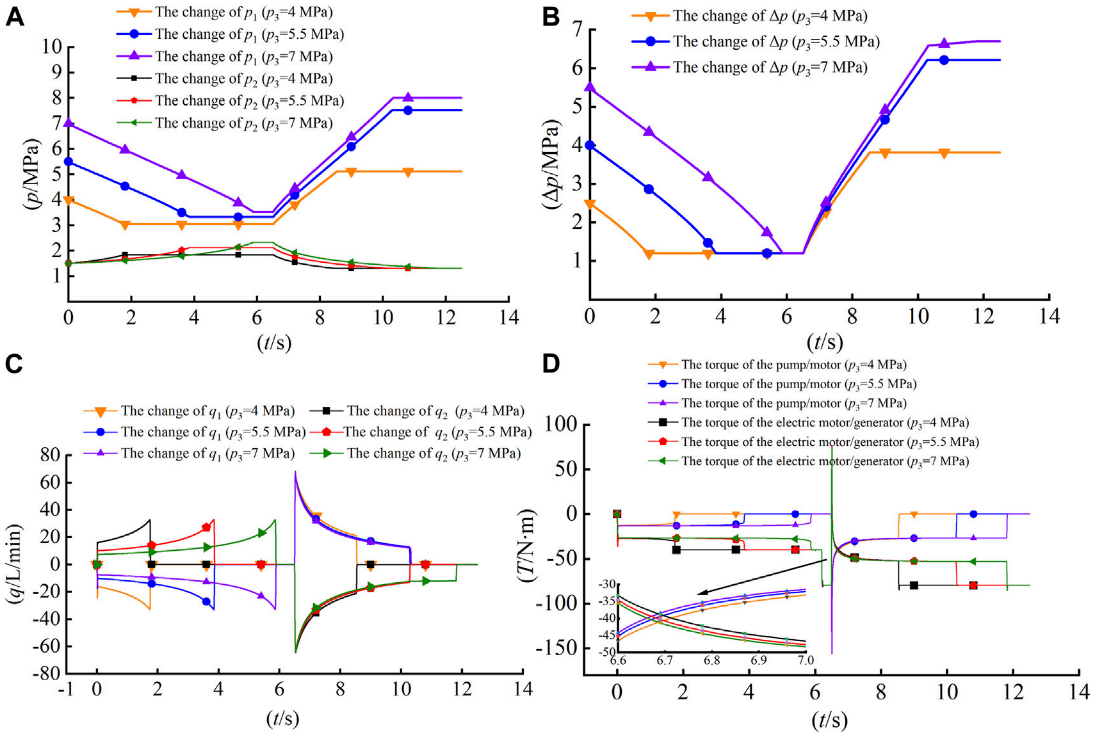

FIGURE 7
Pressure and flow rate characteristic of the system at different p_3. **(A)** High-pressure and low-pressure accumulator pressure variation. **(B)** Differential pressure variation of the high-pressure and low-pressure accumulators. **(C)** Flow rates of the high-pressure and low-pressure accumulators. **(D)** Variation in the output torque of the electric motor/generator-variable hydraulic pump/motor.

The heavy-load mass, the light-load mass, the winch reduction ratio r, the reel diameter, and the maximum lifting and lowering velocity of the weight are defined as 3 t, 1 t, 55.2, 0.44 m, and 1.5 m/s respectively.

Calculated using Eq. 1, the maximum output powers required by the electric motor/generator-variable-displacement hydraulic pump/motor for heavy and light loads are 45 kW and 15 kW, respectively.

Calculated using Eq. 2, the maximum output torques required by the electric motor/generator-variable-displacement hydraulic pump/motor for the heavy and light loads are 120 N·m and 40 N·m, respectively.

Calculated using Eq. 3, the maximum weight-lowering speed required by the electric motor/generator-variable-displacement hydraulic pump/motor is 3,594 r/min.

The $\Delta p_{\min}$ is controlled at around 1.2 MPa. The minimum k is set at 5/3, which means that 3/5 of the torque required by the system must be carried by the variable-displacement hydraulic pump/motor. The maximum V required by the variable-displacement hydraulic pump/motor for the heavy and light loads can be calculated using Eq. 4 as 450 mL/r and 150 mL/r, respectively.

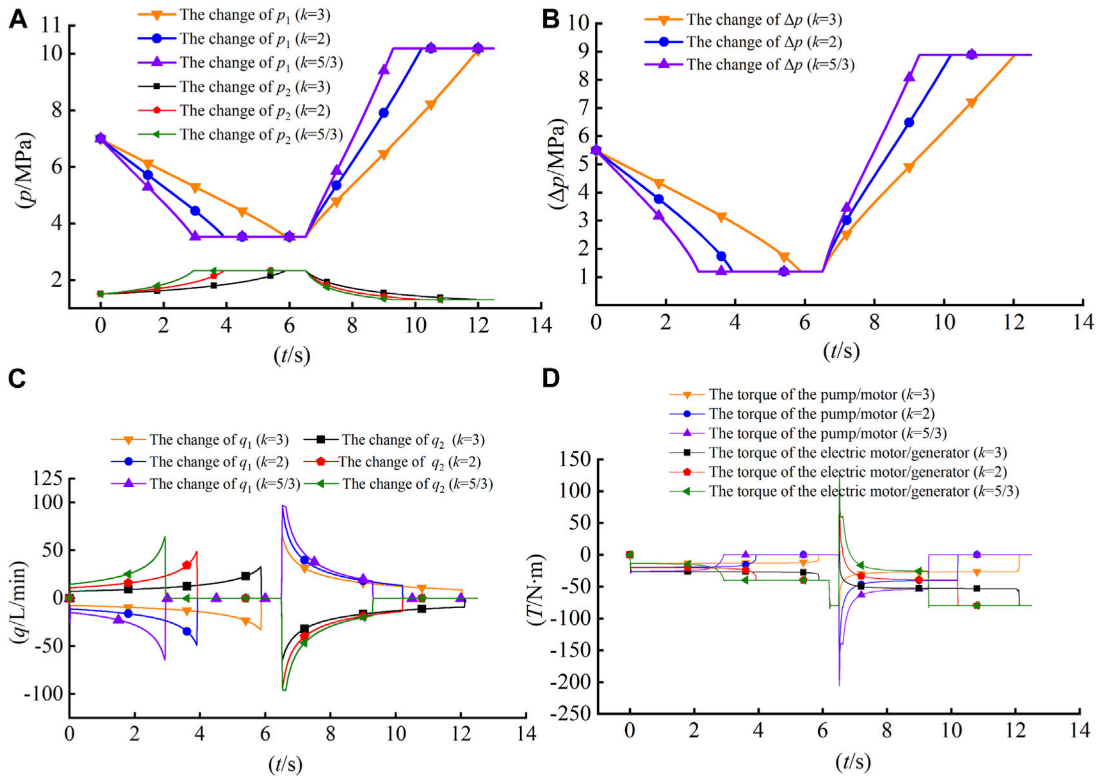

FIGURE 8
Pressure and flow rate characteristics of the system at different k values. **(A)** High-pressure and low-pressure accumulator pressure variation. **(B)** Differential pressure variation for high-pressure and low-pressure accumulators. **(C)** Flow rate for high-pressure and low-pressure accumulators. **(D)** Variation of the output torque of the electric motor/generator-variable-hydraulic pump/motor.

Therefore, the variable-displacement hydraulic pump/motor with a maximum V of 500 mL/r is used in the system.

The rated power, the rated torque, and the rated speed of the electric motor/generator should be greater than the values calculated above. The initial state of charge of the lithium battery is set to 90%, and the capacity of the lithium battery is set to 6.5 Ah.

The main technical parameters required for the simulation of the electro-hydraulic composite drive winch system are shown in Table 1.

5 System simulation analysis

The simulation analysis focuses on the dynamic characteristics of the lifting cycle of the weight at different variable-displacement hydraulic pump/motor output proportional torques and initial pressures of the high-pressure accumulator, as well as the energy recovery efficiency of the system during the lowering of the weight.

5.1 Dynamic characteristics of the weight under different conditions

The cycle time in the simulation is set to 12.5 s, where 0–6 s is the lifting condition, 6 s–6.5 s is the stop condition, and 6.5 s–12.5 s is the lowering condition. The expected lifting and lowering velocity is 0.2 m/s. The speed of the electric motor/generator-variable-displacement hydraulic pump/motor is controlled by the PID at 480 r/min. The dynamic characteristics of the weight lifting and lowering are studied under a different initial pressure of the high-pressure accumulator and output torque of the variable-displacement hydraulic pump/motor, respectively. As the Δp can be approximated as p_{BA}, it is set to Δp_{min} (1.2 MPa) when the weight is lifting (F = 1t) and to p_{2min} (1.3 MPa) when the weight is lowering (F = 2t). If the movement is not completed, the variable-displacement hydraulic pump/motor is put into an idle state by the VCU and no more power is outputted, while the remaining power is outputted by the electric motor/generator alone. During the simulation, SOC and F are set to $F \geq F_{min}$ and $SOC \geq SOC_{min}$, and the system in the electro-hydraulic composite drive and energy recovery mode.

Owing to the advantages of good oil and gas isolation, high specific volume, and tightness, airbag accumulators are used for both high-pressure and low-pressure accumulators in the system. The high-pressure accumulator is set to 5 L with a pre-charge pressure of 2 MPa, while the low-pressure accumulator is set to 10 L with a pre-charge pressure of 0.5 MPa. The relationship between the volume V_1 of the accumulator gas chamber and pressure is shown in Eq. 6.

$$pV_1^{\,m} = \mathrm{W} \tag{6}$$

where W is constant and m is the state index varying between 1 and 1.4.

The trend of the accumulator state parameters during the charging and discharging of the accumulator can be obtained from Figure 5. Where the charging and discharging process curves do not coincide, the general expansion process of the gas (discharging process) is faster than the compression process (charging process).

5.1.1 Different initial pressures of the high-pressure accumulator

The purpose of this study was to investigate the dynamic characteristics of weight lifting and lowering under different initial high-pressure accumulator pressures from p_3 to 4 MPa, 5.5 MPa, and 7 MPa. The initial pressure p_2 is the same 1.5 MPa under different conditions. Moreover, the lift condition is such that $k = 3$, i.e., 1/3 of the total torque at a constant output of the variable-displacement hydraulic pump/motor. As shown in Figure 6A, the weight can quickly and more stably reach the target velocity loaded from a stop condition ($t = 6.2$ s) and suddenly started from a stop condition to a lowering condition ($t = 6.5$ s) with different p_3. This indicates that the proposed winch system has good dynamic characteristics.

When the weight is in the lifting condition (0–6 s), the lower the p_3, the smaller the initial Δp and p_{BA} ends of the variable-displacement hydraulic pump/motor. In cases with the same required torque and speed, according to Eq. 4; Eq. 5, the larger the initial V required, the larger the initial q_1. Accordingly, a larger q will flow into the low-pressure accumulator with the same initial p_2 (1.5 MPa). For the system with lower p_3, as shown in Figures 5, 7A and Eq. 6 show that p_2 rises faster. The faster that p_{BA} falls, the faster that V will rise. As shown in Figure 7C, the q_1 will rise faster, the flow rate into the corresponding high-pressure and low-pressure accumulators will also rise, and the pressure will rise faster. As shown in Figures 7B, D, the faster the differential pressure reaches $\Delta p_{\min}$ (1.2 MPa), the faster the variable-displacement hydraulic pump/motor will be in an idle state without output torque, and the motor/generator will output torque separately during the lifting condition.

When the weight is in the stop condition (6 s–6.5 s), the load weight is lifted from 1 t to 2 t at 6.2 s and changed from the stop condition to the lower condition at 6.5 s. As shown in Figures 6A, 7B, D and Eq. 10, no sliding down of twice the weight occurs owing to the instantaneous high torque provided by the electric motor/generator and variable-displacement hydraulic pump/motor. The Δp is always 1.2 MPa during this period.

When the weight is in the lowering condition (6.5 s–12.5 s), for the system with a different p_3, the Δp is initially the same at 1.2 MPa. When the required torque and speed are the same, according to Eq. 4; Eq. 5, the required V and q_2 are also the same. For the system with higher p_3, as shown in Figure 7B shows that in the lowering condition, the faster that the Δp rises, the faster the pressure difference between the two ends of the variable-displacement hydraulic pump/motor rises, and the faster that V will fall. As shown in Figure 7C, q_2 will fall faster. It is reasonable to say that in the system with a higher p_3, the slower that the pressure of the corresponding high-pressure accumulator will rise and the slower that the pressure of the low-pressure accumulator will fall during the lowering process. For the system with a higher p_3, the initial p_1 and p_2 are higher. Combined with Figure 5; Figure 7B; Eq. 6 show that in the system with the higher p_3, the faster the Δp and the pressure difference between the two ends of the variable-displacement hydraulic pump/motor will rise during the entire lowering process. As shown in Figures 7A,D, the faster the p_2 reaches $p_{2\min}$ (1.3 MPa), the faster the variable-displacement hydraulic pump/motor will be in an idle state without output torque, and the motor/generator will output torque separately during the lowering condition.

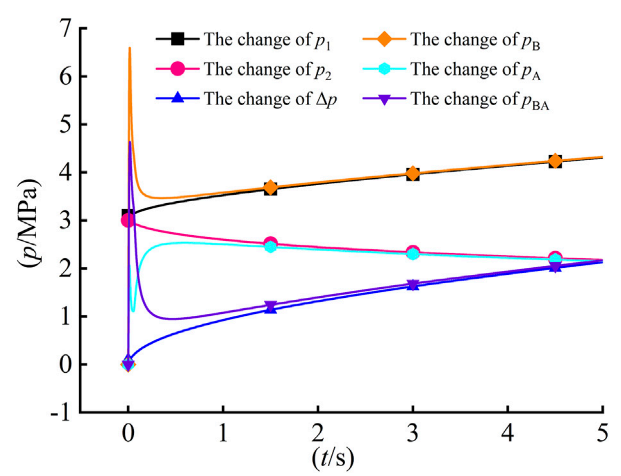

FIGURE 9
Variations in the pressures of the accumulators and hydraulic pump/motor.

5.1.2 Different variable-displacement hydraulic pump/motor output proportional torque

For $k = 3$, $k = 2$, and $k = 5/3$, we expect 1/3, 1/2, and 3/5 of the total torque at a constant output of the variable-displacement hydraulic pump/motor and observe the dynamic characteristics of the lifting and lowering of the mass. When p_3 is 7 MPa, the initial p_2 is 1.5 MPa. As shown in Figure 6B, the dynamic characteristics of this winch system are all good for different k values. The weight can quickly and more stably reach the target velocity when loaded from a stop condition ($t = 6.2$ s) and when suddenly starting from a stop condition to a down condition ($t = 6.5$ s).

When the weight is in the lifting condition (0–6 s), the initial pressures of the high-pressure and low-pressure accumulators are the same for systems with different k values. The initial Δp is the same. The initial differential pressure between the two ends of the variable-displacement hydraulic pump/motor is the same. For the system with larger proportional torque output, in the case of the same required speed according to Eq. 4, the larger the required initial V, the larger the initial q_1. According to Eq. 5 and as shown in Figure 5 and Eq. 6, the faster the p_1 falls and p_2 rises, the faster the pressure difference between the two ends of the variable-displacement hydraulic pump/motor falls and the faster the V will rise. As shown in Figure 8C, the q_1 will rise faster. The corresponding q_2 and p_2 will also rise faster. As shown in Figures 8B, D, the faster the differential pressure reaches $\Delta p_{\min}$ (1.2 MPa), the faster the variable displacement hydraulic pump/motor will be in

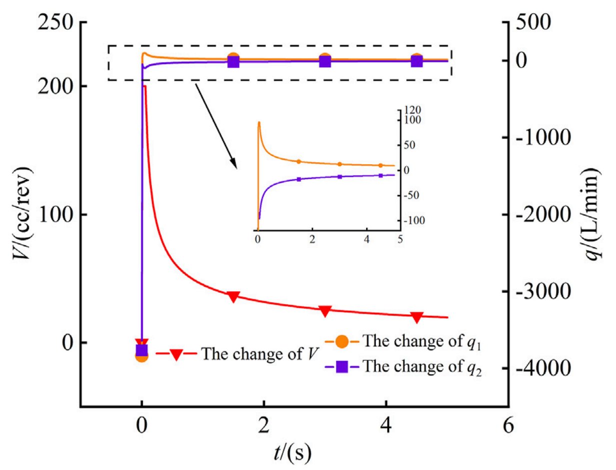

FIGURE 10
Variation in the displacement of the hydraulic pump/motor and the flow rate of the accumulators.

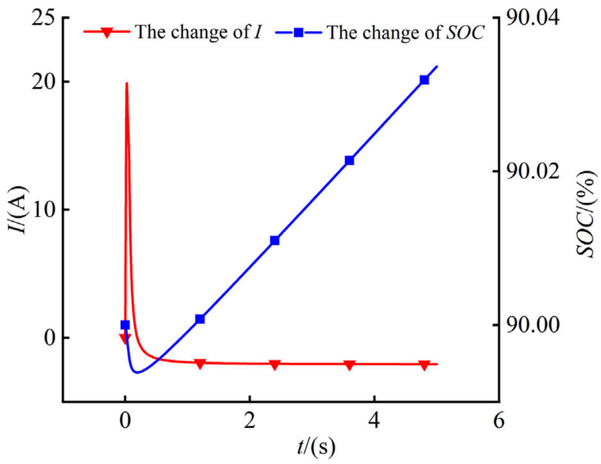

FIGURE 12
Variation in the busbar current of the electric motor/generator and the SOC of the battery.

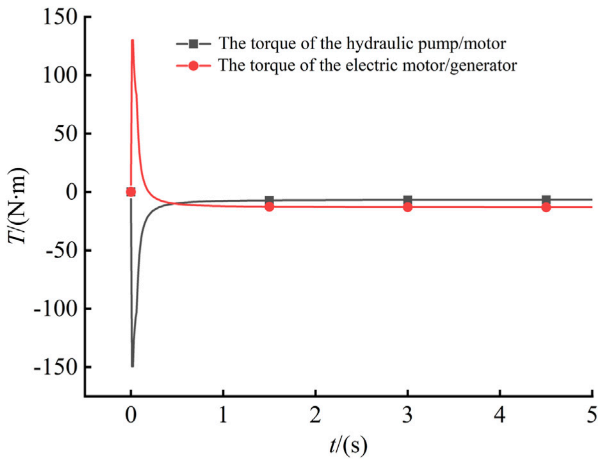

FIGURE 11
Variation in the torque of the hydraulic pump/motor and electric motor/generator.

an idle state without torque output and the motor/generator will separately output torque during the lifting condition.

When the weight is in the stop condition (6 s–6.5 s), the load weight is lifted from 1 t to 2 t at 6.2 s and changed from the stop condition to the lower condition at 6.5 s. As shown in Figures 6B, Figures 8B,D and Eq. 10, no sliding down of twice the weight occurs owing to the instantaneous high torque provided by the electric motor/generator and variable-displacement hydraulic pump/motor. The Δp is always 1.2 MPa during this period.

When the weight is in the lowering condition (6.5 s–12.5 s), for the different k in the system, the initial Δp is always 1.2 MPa. For the system with larger k, in the case of the same required speed according to Eq. 4; Eq. 5 shows that the required initial V and initial q_2 are larger. Figure 5 and Eq. 6 show that the faster the p_2 falls and the p_1 rises, the faster p_{BA} rises, and the faster the V will fall. As shown in Figure 8C, the q_2 will fall faster; thus, it is reasonable to say that the higher the k, the slower the corresponding p_1 will rise and the corresponding p_2 will fall during the lowering process. The system with the higher proportional torque output of the variable-displacement hydraulic pump/motor during the whole lower process can still rely on its higher torque required to maintain the q at a higher level even when the q falls, as shown in Figure 8C. The combination of Figures 5, 8A, B, and Eq. 6 shows that the higher the proportional torque of the variabledisplacement hydraulic pump/motor outputs during the whole lower process, the faster p_1 rises, the faster p_2 falls, and the faster Δp rises. As shown in Figures 8B, D, the faster that p_2 reaches $p_{2\min}$ (1.3 MPa), the faster the variable-displacement hydraulic pump/motor will be in an idle state without output torque, and the motor/generator will output torque separately during the lowering condition.

5.2 Analysis of the efficiency of the system energy recovery

The energy recovery efficiency of the winch system is discussed in terms of the power of the high-pressure accumulator, the power of the low-pressure accumulator, the power of the electric motor/generator, and the power consumption of the lowering weight. The energy can be obtained by integrating the corresponding power of each component. The system is in the recovery mode of the electro-hydraulic composite drive during the descent, i.e., $p_2 \geq p_{2\,min}$. The Δp in the simulation process can be treated as p_{BA}. The whole simulation system is first in the electro-hydraulic composite drive and energy recovery mode. The battery SOC and the load weight F are treated as $F \geq F_{\min}$ and $SOC \leq S_{\max}$, respectively.

The power of the high-pressure accumulator P_1 and the low-pressure accumulator P_2 are determined using Eq. 7 and Eq. 8.

$$P_1 = p_1 \cdot q \tag{7}$$

$$P_2 = p_2 \cdot q \tag{8}$$

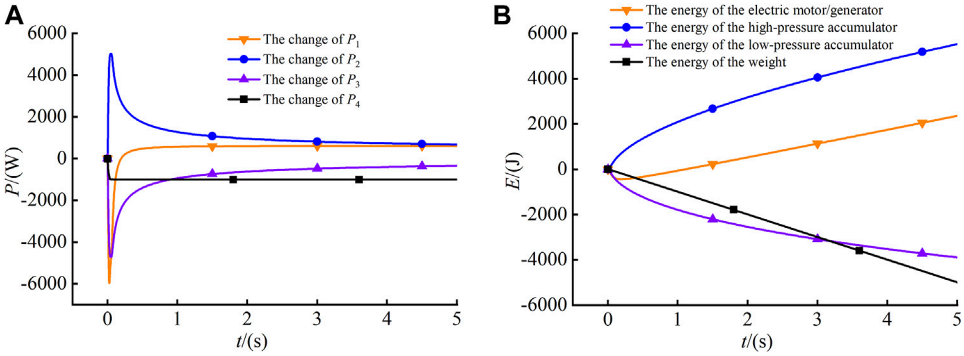

FIGURE 13
Variation in the power and energy of each component. **(A)** Variation in the power of each component. **(B)** Variation in the energy of each component.

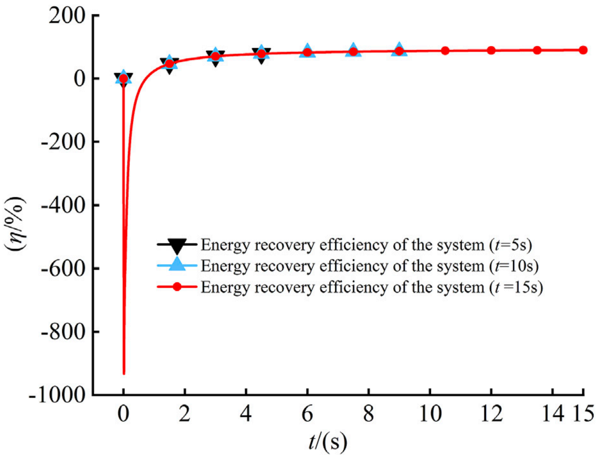

FIGURE 14
Energy recovery efficiency at different distances of weight descent.

The power of the electric motor/generator P_3 can be calculated from Eq. 9.

$$P_3 = U \cdot I \tag{9}$$

where U and I represent the busbar voltage and current of the electric motor/generator, respectively. The electric motor/generator is in the electric motor state when $I > 0$ and in the electric generator state when $I < 0$.

The power of the lowering weight P_4 can be determined by the weight lowering height s and F, as shown in Eq. 10.

$$P_4 = F \cdot s \tag{10}$$

The energy recovery efficiency of the system P_5 is determined using Eq. 11.

$$P_5 = \frac{P_1 - P_2 + P_3}{P_4} \cdot 100\% \tag{11}$$

After setting $F = 0.5\text{t}$, $k = 3$, and $v = 0.2\text{m/s}$, the energy recovery efficiency of the system is investigated for a weight-lowering height of 1 m ($s = 1\text{m}$). All the 2-position 2-way electromagnetic valves are controlled in the de-energized state before lowering the weight. As shown in Figure 9, no pressure is built up at the two ends of the variable-displacement hydraulic pump/motor, i.e., $p_{\text{BA}} = 0$ at $t = 0\text{s}$. Combined with Figure 10 and Eq. 4, these results show that the variable-displacement hydraulic pump/motor must adapt itself to rapidly increase V to deliver a certain torque when the weight suddenly starts to lower. As shown in Figure 10 and Eq. 5, the higher the V, the higher the q. As shown in Figure 13A, P_1 and P_2 both are large at the initial moment according to Eq. 7 and Eq. 8. The higher the q_1 and q_2, the greater the changes in the gas volumes of the high-pressure and low-pressure accumulators. As shown in Figure 5 and Eq. 6, the greater the changes in the gas volume of the high-pressure and low-pressure accumulators, the higher the changes in p_1 and p_2. As shown in Figure 9, p_1, Δp, and p_{BA} rise, while p_2 falls quickly after the weight has been lowered. As shown in Figure 10, V cannot be reduced in time due to the delay in system control after a rapid increase in p_{BA}. According to Eq. 4 and as shown in Figure 11, the variable-displacement hydraulic pump/motor output torque momentarily exceeds its required output by 1/3 proportional torque in the hydraulic pump state. At the same time, as shown in Figure 11, Figure 12, and Eq. 9, the positive torque output of the electric motor/generator ensures that the system outputs a constant torque; the busbar current I is > 0 meaning that the electric motor/generator is in the electric motor state; i.e., the *SOC* of the battery is consumed. Combined with Figure 13A, Figure 13B, Figure 14, and Eq. 11, the electric motor/generator is in the electric motor state, which means that $P_3 < 0$ is the main reason why $P_5 < 0$ at the initial moment. As shown in Figure 10, Figure 11, and Figure 12, the variable-displacement hydraulic pump/motor and the electric motor/generator can output a constant proportional torque respectively; $I < 0$ and $P_3 > 0$ means the electric motor/generator is in the electric generator state; i.e., the *SOC* of the battery is stored after V has returned to its normal range of variation. As shown in Figure 9, Figure 10, Figure 13A, Eq. 7, and Eq. 8, as p_1 increases, so does P_1; similarly, as p_2 increases, so does P_2. As shown in Figure 14 and Eq. 11, the longer the weight is lowered, the greater the P_5.

6 Conclusion

To recover the gravitational potential energy and avoid secondary sliding, this study proposed an electro-hydraulic composite drive winch and energy recovery system for mobile cranes. The problems of secondary sliding of the weight and the limited energy recovery of the accumulator can be solved effectively by the high energy density of the lithium batteries and the good control characteristics of the electric motor/generator. The problem of high energy consumption of the electric motor/generator drive winch and most of the energy consumption of the liquid drive winch in the balance and multiple directional control valves can be alleviated by instantaneous high-power density and large torque output at the near-zero speed of the accumulator-variable displacement hydraulic pump/motor.

The feasibility of the control strategy of the electro-hydraulic composite drive winch and potential energy recovery system was verified through the study of the dynamic characteristics of the weight lifting and lowering under different conditions. We studied the pressure variations of the high-pressure and low-pressure accumulators (p_1 and p_2), as well as the pressure difference (Δp), flow rate (q), and output torque of the electric motor/generator-variable displacement hydraulic pump/motor (T). When p_3 or k is at different values in this electro-hydraulic composite drive winch system, the weight lifting and lowering dynamic characteristics differ.

The energy recovery efficiency of the electro-hydraulic composite drive winch and potential energy recovery system control strategy was higher for weights lowered a greater distance. Although the energy recovery efficiency of the system was high in the final results, the magnitude of the final recovery efficiency could be influenced by changing the initial pressure and volume of the high-pressure and low-pressure accumulators as well as the fixed voltage of the lithium battery. The specific energy recovery efficiency is for reference only and must be considered in conjunction with the actual situation. The system control strategy is mainly based on the detection of load weight F, battery SOC, high-pressure and low-pressure accumulator pressure, etc., to determine the drive mode of the weight. The electro-hydraulic composite drive mode can reasonably use the motor speed active control to achieve variable-displacement hydraulic pump/motor adaptive speed. Automatic adjustment of the displacement of the variable-displacement hydraulic pump/motor is used to actively control the torque and, thus, achieve adaptive torque compensation of the electric motor/generator.

The energy recovery efficiency of the system in this study may vary considerably under different initial conditions. The basis for the high efficiency of the energy recovery of the system is the selection of suitable initial conditions in the actual working process. The efficiency of the energy recovery is not considered in this system when the initial pressure (p_1 and p_2) and volume of the high-pressure and low-pressure accumulators and the performance parameters of the lithium battery are changed. The results of this study lay a foundation for further experimental research.

7 Research ethics

The study does not involve animal or human subjects and does not contain identifiable human data.

Data availability statement

The raw data supporting the conclusion of this article will be made available by the authors, without undue reservation.

Author contributions

XX and TL contributed to the direction of the research content, study design, manuscript writing, data processing, and data analysis. HR and TG contributed to the literature searches and data collection. ZL and CM were mainly responsible for data analysis and project management. All authors contributed to the article and approved the submitted version.

Funding

This work was supported by the National Key Research and Development Program (2020YFB2009900), the National Natural Science Foundation of China (Grant No. 52275055), Key Projects of the Natural Science Foundation (Grant No. 2021J02013).

Acknowledgments

We thank all the authors for completing the study and acknowledge the valuable comments and constructive suggestions of the editor and reviewers.

Conflict of interest

The authors declare that the research was conducted in the absence of any commercial or financial relationships that could be construed as a potential conflict of interest.

Publisher's note

References

Bolonne, S. R. A., and Chandima, D. P. (2019). Sizing an energy system for hybrid Li-ion battery-supercapacitor RTG cranes based on state machine energy controller. *Ieee Access* 7, 71209–71220. doi:10.1109/access.2019.2919345

Caporali, R. P. L. (2021). Anti-sway method for reducing vibrations on a tower crane structure. *Int. J. Nonlinear Sci. Numer. Simul.* 24, 171–184. doi:10.1515/ijnsns-2021-0046

Corral-Vega, P. J., Garcia-Trivino, P., and Fernandez-Ramirez, L. M. (2019). Design, modelling, control and techno-economic evaluation of a fuel cell/supercapacitors powered container crane. *Energy* 186, 115863. doi:10.1016/j.energy.2019.115863

Fang, X., Zhao, H., and Liu, P. (2012). Simulation study of main winch system geopotential energy recovery in rotary driller. *Eng. J. Wuhan Univ.* 45, 241–245+272.

Huang Pu, H. (2015). *Study of ultracapicator-based power compensation and energy Rocovery system for mine lifting equipment*. Beijing: Beijing Jiaotong University.

Kim, K., An, J., Park, K., Roh, G., and Chun, K. (2019). Analysis of a supercapacitor/battery hybrid power system for a bulk carrier. *Appl. Sciences-Basel* 9. doi:10.3390/app9081547

Kodkin, V. L., and Anikin, A. S., (2020) The reflection mode of the moment loads by an asynchronous electric drive with vector control and the features of this mode in the rotation drive of the tower crane", in: International Ural Conference on Electrical Power Engineering, 22-24 September 2020, Russia.

Lee, J.-G., Yeo, H.-K., Jung, H.-K., Kim, T.-K., and Ro, J.-S. (2019). Electromagnetic and thermal analysis and design of a novel-structured surface-mounted permanent magnet motor with high-power-density. *Iet Electr. Power Appl.* 13, 472–478. doi:10.1049/iet-epa.2018.5322

Li, K., and Wang, Y. (2019). Maximum torque per ampere (MTPA) control for IPMSM drives using signal injection and an MTPA control law. *Ieee Trans. Industrial Inf.* 15, 5588–5598. doi:10.1109/tii.2019.2905929

Li, X., Cao, S., Luo, M., and Sun, L. (2022). Design and control strategy of energy recovery device for pure electric vehicle crane. *Constr. Mach. Equip.* 53, 104–108+113.

Lin, T., Lin, Y., Ren, H., Chen, H., Chen, Q., and Li, Z. (2020). Development and key technologies of pure electric construction machinery. *Renew. Sustain. Energy Rev.* 132, 110080. doi:10.1016/j.rser.2020.110080

Liu, H., Quan, L., Hao, Y., Huang, J., Li, Y., and Liu, Y. (2022). Fabrication of superhydrophobic coating based on waterborne silicone-modified polyurethane dispersion and silica nanoparticles. *Chin. Hydraulics Pneumatics* 46, 22–29. doi:10.3390/polym15010022

Liu, J. (2019). China's renewable energy law and policy: A critical review. *Renew. Sustain. Energy Rev.* 99, 212–219. doi:10.1016/j.rser.2018.10.007

Premkumar, K., and Manikandan, B. V. (2014). Adaptive neuro-fuzzy inference System based speed controller for brushless DC motor. *Neurocomputing* 138, 260–270. doi:10.1016/j.neucom.2014.01.038

Roman, R.-C., Precup, R.-E., and Petriu, E. M. (2021). Hybrid data-driven fuzzy active disturbance rejection control for tower crane systems. *Eur. J. Control* 58, 373–387. doi:10.1016/j.ejcon.2020.08.001

Wang, X., Ge, L., Zhao, B., Hao, Y., Quan, L., and Mu, X. (2020). Energy efficiency characteristics of cable shovel lifting system driven by hydraulic-electric hybrid system. *Trans. Chin. Soc. Agric. Mach.* 51, 418–426. [In Chinese].

Zhang, H. (2019). *Research on energy saving technology of hydraulic truck crane*. Dalian: Dalian Ligong University. [master's thesis].

Zhang, J., Zhao, B., Hao, Y., Yu, H., Wang, J., Lei, A., et al. (2020). Pluripotent stem cell-derived CAR-macrophage cells with antigen-dependent anti-cancer cell functions. *Chin. Hydraulics&Pneumatics* 13, 153–160. [In Chinese]. doi:10.1186/s13045-020-00983-2

Zhang, Y.-J., Peng, Y.-L., Ma, C.-Q., and Shen, B. (2017). Can environmental innovation facilitate carbon emissions reduction? Evidence from China. *Energy Policy* 100, 18–28. doi:10.1016/j.enpol.2016.10.005

Zhao, B., Quan, L., and Hao, Y. (2016). Research of operating characteristics and energy efficiency of traction elevator with hybrid electric-hydraulic drive. *J. Mech. Eng.* 52, 192–198. doi:10.3901/jme.2016.04.192

Zhu, J., Wang, P., Wu, H., and Zhu, Z. (2018). Guan (Care/Control): An ethnographic understanding of care for people with severe mental illness from shanghai's urban communities. *Mach. Des. Manuf.* 42, 92–111. doi:10.1007/s11013-017-9543-x

frontiers | Frontiers in Energy Research

TYPE Original Research
PUBLISHED 30 June 2023
DOI 10.3389/fenrg.2023.1184687

OPEN ACCESS

EDITED BY
Alexandre Presas,
Universitat Politecnica de Catalunya,
Spain

REVIEWED BY
Jingwei Cao,
Tsinghua University, China
Zhiyuan Cao,
Northwestern Polytechnical University,
China

*CORRESPONDENCE
Shuli Hong,
✉ hong_0815@163.com

RECEIVED 12 March 2023
ACCEPTED 01 June 2023
PUBLISHED 30 June 2023

CITATION
Hong S, Lu W, Xiang X and Qiu L (2023),
An unsteady flow control technique
based on negative circulation conception
and its application to a blade-divergent passage.
Front. Energy Res. 11:1184687.
doi: 10.3389/fenrg.2023.1184687

An unsteady flow control technique based on negative circulation conception and its application to a blade-divergent passage

Shuli Hong[1]*, Weiyu Lu[2], Xin Xiang[3] and Lei Qiu[1]

[1]College of Mechanical and Automotive Engineering, Ningbo University of Technology, Ningbo, China, [2]School of Physical and Mathematical Sciences, Nanjing Tech University, Nanjing, China, [3]School of Aeronautical Manufacturing Engineering, Nanchang Hangkong University, Nanchang, China

A two-dimensional vortex model is introduced in this paper in order to understand the characteristics of the shedding vortex in a blade-divergent passage and to mitigate or suppress it by appropriate methods. The performance of this model under the influence of three typical external factors is studied, namely, the main flow extrusion effect, viscous effect, and transport effect. Based on the analysis, a negative circulation unsteady flow control technique is proposed to compensate for the viscous effect, which is known as NCFC. Numerical simulation is performed to verify the effectiveness of the NCFC method. The results show that the NCFC method is superior to the conventional unsteady flow control for improving the performance of the blade-divergent passage in most cases. In addition, there is an optimum injection to suppress the shedding vortex with NCFC, which is about 0.2% of the main flow mass, and NCFC shows to be more efficient than conventional flow control in weakening the shedding vortex. Furthermore, NCFC can effectively inhibit separation flow and is shown to be insensitive to the injection flow mass. Finally, the NCFC method is highly recommended to adapt to the fact that the working conditions often change in practice.

KEYWORDS

unsteady flow control, vortex model, shedding vortex, flow control mechanism, compressor blade, negative circulation

1 Introduction

The compressor is an important part of the Brayton cycle system, which is widely used in military and civilian fields such as aircraft engines, gas turbines, and distributed energy systems. The development of these devices requires the compressor to have a higher pressure ratio. The improvement of the pressure ratio of the compressor can be achieved in two ways: one is to increase the linear speed of rotation, and the other is to increase the flow angle. The method of increasing the linear rotational speed to improve the compressor capacity has little room for manoeuvre due to the level of material technology. Therefore, the other way to improve the performance is to increase the flow angle of the compressor. The optimization design of the blade profile is the main way to improve the flow angle, but the accompanying large diffuser makes it easy to cause flow separation in the blade passage, which makes it difficult to significantly improve the performance of the compressor further.

Among these flow separations, the blade suction surface separation flow is one of the most typical complex separation flows in high-load compressors, which will lead to negative factors such as increasing losses, passage blockage, reducing efficiency, and even inducing stall or surge, which will seriously affect the stable operating range of the compressor (Gbadebo et al, 2005; Lei, 2006; Choi et al, 2008; Likiewicz et al, 2020). Therefore, based on the in-depth understanding of the separation flow mechanism of the blade suction surface, it is necessary to introduce an effective flow control technology to suppress or weaken the flow separation in the compressor so that the compressor can maintain a high load while having a wide stable working range and efficiency, which is one of the key research directions in the compressor field at present.

Up to now, a considerable amount of research has focused on the separation flow at the blade suction surface of the compressor or cascade, and some appropriate flow control techniques have also been used to achieve good results. Gbadebo et al (2008) used a suction flow control method with an inlet mass flow rate of 0.7% to weaken the flow separation at the blade suction surface, and the cascade experiment proves that this flow control method can increase the blade load and improve the average static pressure. Braunscheidel et al (2008) developed a synthetic jet system and applied it to the suction surface of stator blades in a low-speed axial compressor. The results showed a loss reduction of 5.5 percent for the entire passage. Yang et al (2021) studied the cascade-separated flow by numerical simulation and experimental methods. The flow control method of suction was used to control the separated flow at the blade suction surface, and various suction schemes were compared, including the suction position and suction capacity. The results showed that a suitable suction method was very effective in controlling the separated flow. Feng et al (2022) studied the influence of the separated vortex on the blade suction surface of the compressor and its propagation process to the adjacent blades at high angles of attack. It was found that the unsteady effect produced by the separated vortex had an important influence on the stable operation of the compressor, and it was considered that the study of the separated vortex was very important for predicting the stall of the compressor. Tang et al (2020) proposed a diagram to carry out the blade design by resisting the unfavourable pressure gradient near the suction surface and to determine a correct operating range.

Although these studies have made some progress and achieved good results, there are still many problems that cannot be solved. For example, the selection of the control location is very specific, whether the flow control is suction type or jet type (Matejka et al, 2008; Yousefi and Saleh, 2015; Chen et al, 2017; Abdolrahim et al, 2019). Now, the general conclusion is that the control position near the separation point is the best choice, but there is no final conclusion on such issues as where or within what range the specific position falls or what effect the change of position will have on the control effect. As another example, it is generally believed that the mechanism of suction is to eliminate the low-energy flow in the boundary layer (Liesner et al, 2010; Ma et al, 2018), and the jet can achieve the excitation effect by the principle of increasing momentum (Giorgi et al, 2015; Chen et al, 2022). However, the further problem is how these control methods specifically affect the coherent structures of turbulence and how they are coupled to the flow field to play a role in the separation/shedding vortex. At present, these issues are not well understood. In addition, the current implementation of effective control methods is often based on a specific operating condition. If the working conditions are constantly changing, it is questionable whether these control measures are still effective and, if so, how they should be changed. As a result, it is difficult to come to a definitive conclusion about such things as the amount of control, the incidence/suction angle, and the frequency of control of the unstable means. An important source of these problems is that the interaction between different control methods and vortex structures at the mechanism level is not clear enough.

Theoretical research usually refines the dominant features of some typical vortex structures and summarises their internal laws or physical mechanisms to obtain some general conclusions. Orszag (1971) used the Orr–Sommerfeld equation based on the N-S equation to analyse the stability of plate shear flow. The Stuart–Landau model was established to analyse the flow in the critical state (Stuart, 1958; Stuart, 1967), and it was later used to analyse the shedding vortex of the cylinder (Thompson and Gal, 2004). To analyse the unsteady motion of the shedding vortex of a cylinder, the van der Pol equation was used (Skop, 1995) and developed into the van der Pol-Duffen equation to explain the flow control mechanism (Marzouk et al, 2007). A simplified cross-directional motion model (SCDM) similar to the van der Pol-Duffen equation was developed by our team (Huang et al, 2017) to analyse cascade separation flow and its flow control mechanism. These theories and models were further developed and used in subsequent research studies (Theofilis, 2003; Akhtar et al, 2009; Ku et al, 2015). In summary, the theoretical research on the blade suction surface separation flow is relatively deficient and incomplete compared with the numerical and experimental research, which causes difficulties in the in-depth understanding of the separation/shedding vortex and the adoption of appropriate methods to suppress it.

In order to improve and complete the theoretical understanding of the blade suction separation/shedding vortex and to lay the foundation for adopting an accurate, effective, and relatively universal flow control method, a two-dimensional vortex model is introduced in this paper. The main contents of this paper can be divided into the following three parts: first, the blade-divergent passage and its main internal flow structures are introduced, on the basis of which a two-dimensional vortex model for the blade suction shedding vortex is introduced (Section 2, Section 3). Then, three typical external factors are studied individually depending on the model, and an unsteady flow control concept based on negative circulation is proposed (Section 4, Section 5). Finally, numerical simulation is carried out to verify the effectiveness of the negative circulation flow control (NCFC) method in comparison with the conventional unsteady flow control (Section 6).

2 Flow structures in a blade-divergent passage

2.1 Research object and numerical simulation

In this study, a blade-divergent passage established by our team is used. A blade is placed at the corner of the passage, which is

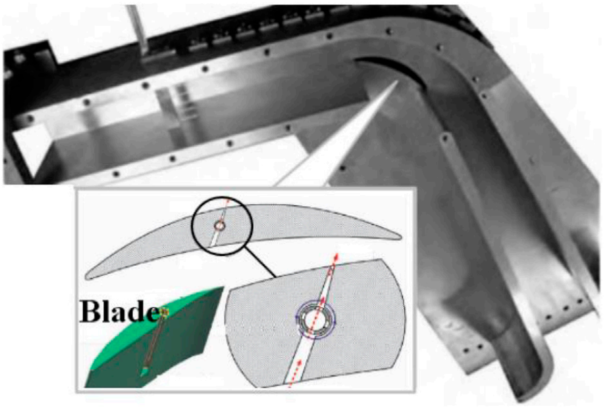

FIGURE 1
Structure diagram of the blade-divergent passage.

derived from a stator blade provided by China Gas Turbine Establishment (CGTE), as shown in Figure 1. The inlet width is 34.3 mm, and the outlet width is 55.5 mm. The blade chord length is 80.0 mm. More details can be found in Hong and Huang (2017) and Zhu et al (2015). In our previous study, an unsteady jet flow control driven by the pressure difference between the blade suction and pressure surfaces was investigated. Here, we compare it with our new flow control method in the following section through numerical simulation.

Two-dimensional numerical calculation is adopted for the blade-divergent passage by large eddy simulation (LES). The length of the entire calculation domain is about 6.25 times chord length in total, about 1.25 times chord length at the inlet, and 4 times chord length at the outlet. The Reynolds number is about 1.8×10^5, and the non-dimensional wall distance $y^+ \approx 1$. The grid height of the first wall layer is set to be 0.001 mm. Figure 2 shows the computational gird of the blade-divergent passage (the bypass flow is useful only for flow control). By comparing the relationship between the flow rate and the inlet Mach number with the number of calculation grids, the results no longer change with the number of grids when the number of grids exceeds 80,000, as shown in Figure 3. Therefore, for an uncontrolled blade-divergent passage, a grid of 90,000 numbers is used. A velocity inlet of magnitude 35 m/s is given for the blade-divergent passage, corresponding to the Mach number Ma ≈0.1 referred to in the experiment. The outlet is set to be a pressure outlet with a static pressure of 0 Pa (gauge pressure). The solid wall is adiabatic with no slip conditions. The time step is 1×10^{-5} s with 20 iterations per time step. Based on the results of this paper, an average CFL number of 0.45 can be obtained, which is lower than the value of 1.0 suggested by Ferziger and Peric (2002) and Balduzzi et al (2016a). Furthermore, according to Balduzzi et al (2016b), each time step for a rotating impeller should be between 0.135° and 0.405°. If the time step of 1×10^{-5} s used in this paper corresponds to this angular range, the impeller speed would exceed 800,000 RPM, which would satisfy most impeller calculation needs. By comparing the shedding vortex frequency, relative total pressure loss coefficient, average pressure, and other parameters under different conditions, it is shown that the experimental and numerical simulation results are in good agreement (Zhu et al, 2015; Hong and Huang, 2017). Therefore, the numerical simulation adopted in this paper has a certain degree of credibility.

2.2 Flow structures in the passage

Basically, the flow field is considered to have entered a state of unsteady convergence when the average mass flow rate and other channel parameters remain unchanged, and the instantaneous parameters show periodic fluctuations. We select the flow fields in one period after unsteady convergence (the shedding vortex frequency $f_0 \approx 266$ Hz (Zhu et al, 2015; Hong and Huang, 2017)) for analysis.

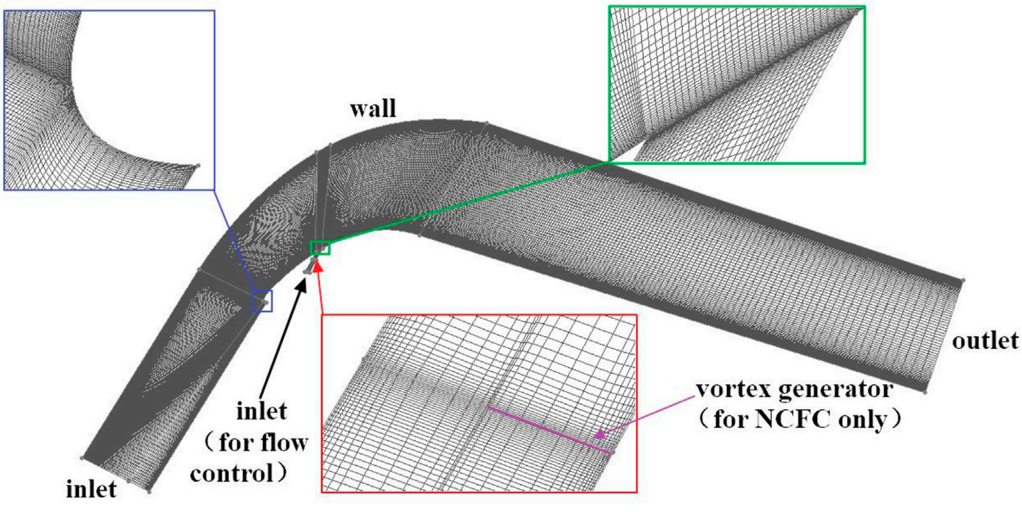

FIGURE 2
Computational grid of the blade-divergent passage.

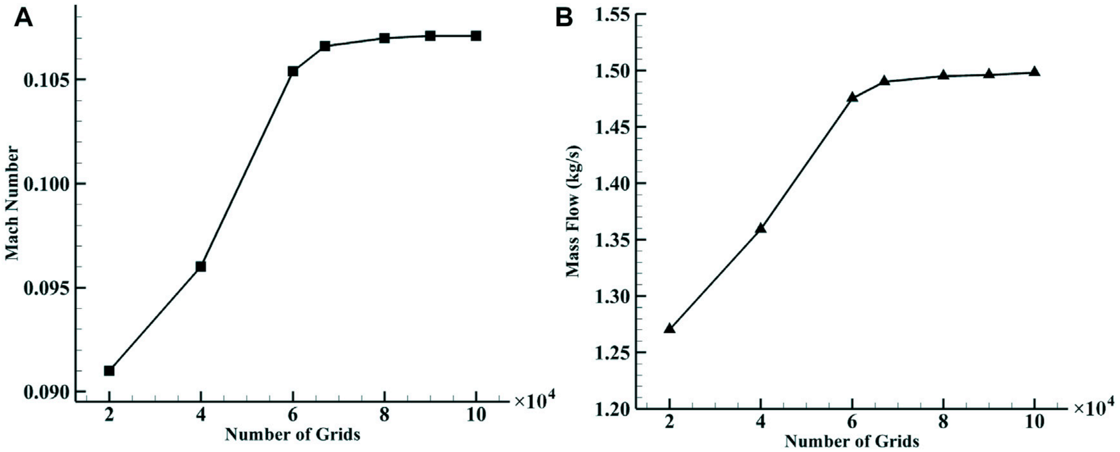

FIGURE 3
Variation of the main aerodynamic parameters of the uncontrolled flow field with the number of grids. **(A)** Variation of the inlet Mach number with the number of grids. **(B)** Mass flow variation with the number of grids.

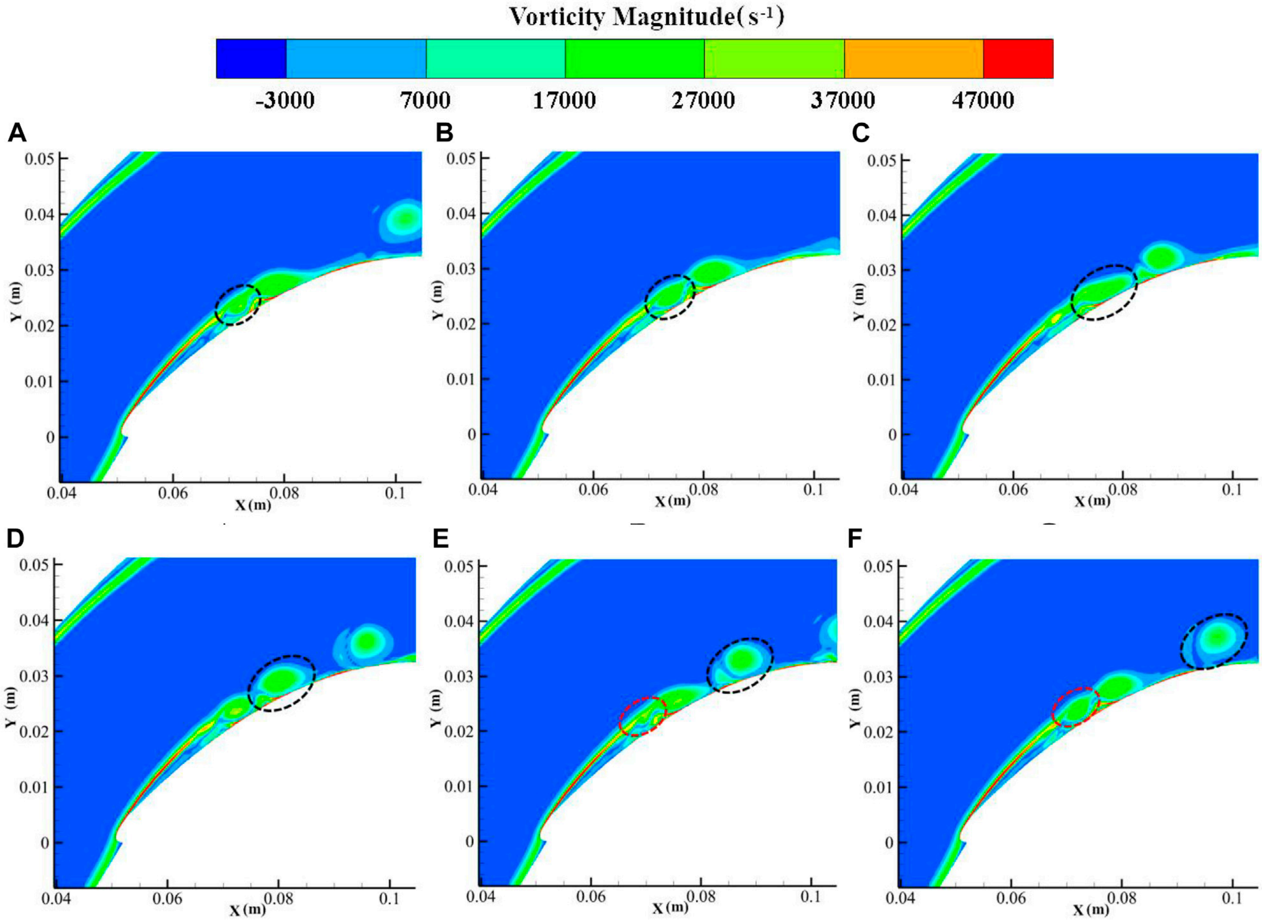

FIGURE 4
Flow structures in the blade-divergent passage without control. **(A)** 1/6T. **(B)** 2/6T. **(C)** 3/6T. **(D)** 4/6T. **(E)** 5/6T. **(F)** 6/6T. (*i*/6T means *i*/6 of one shedding vortex period).

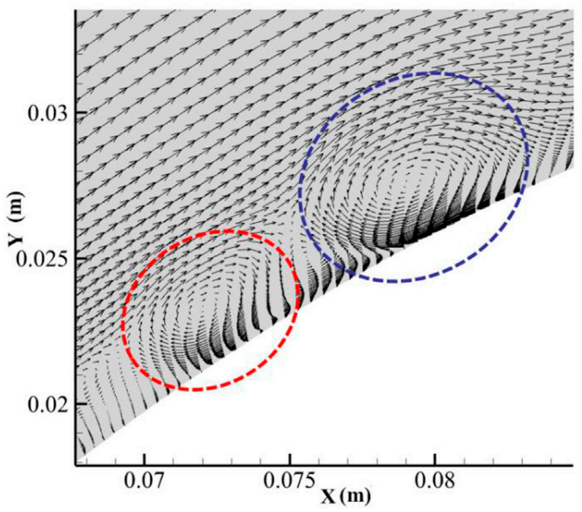

FIGURE 5
Velocity vector at 3/6T.

Figure 4 shows the vorticity distribution of the flow field at different times in one shedding vortex period. It can be seen that under the influence of the unfavourable pressure gradient and the curvature, the airflow begins to become unstable on the curved wall due to the K-H instability, causing the vortex layer to roll up and form a small-scale shedding vortex (shown by the dotted line at 1/6T). The curled vortex extends in the curved channel from 2/6T to 4/6T. At 5/6T, a new shear layer instability occurs (shown with the red dotted line at 5/6T). Finally, it spreads further downstream along the main flow.

It can also be seen from Figures 4, 5 that the profile of the shedding vortex at the blade suction surface is elliptical. The irregularity of the ellipse is due to the coupling of small-scale vortices to the shedding vortex. When we extract the dominant vortex structure using special technology, such as the dynamic mode decomposition (DMD) method, the regularity of the elliptical vortex becomes clear (Hong and Huang, 2017). This is the main reason why we introduce an elliptical vortex model instead of a circular vortex, which is usually used.

3 The two-dimensional vortex model for the blade suction separation flow

As we have presented the details of the two-dimensional vortex model (Hong et al, 2022), we will only give a brief introduction to the model's principles and results. The region where vorticity is concentrated in a two-dimensional inviscid flow field is called the vortex patch. For example, the vortex core of a Rankine vortex is the simplest circular vortex patch often used by researchers to analyse vortex structures. In general, the boundary shape of a vortex patch of any shape should change continuously as the vortex patch moves. There is a special case: an elliptical vortex patch with uniform vorticity will rotate on itself at a constant angular velocity and remain unchanged; this type of vortex is called a Kirchhoff elliptical vortex. The constant angular velocity is expressed by the following formula:

$$\Omega = \frac{ab}{(a+b)^2}, \tag{1}$$

where a and b are the long and short axes of the ellipse, respectively. From the previous CFD results, the core region of the blade suction shedding vortex is very close to the Kirchoff elliptical vortex. Therefore, our research is based on the elliptical vortex.

$$\nabla^2\Psi = 0 \tag{2}$$

Based on the elliptical vortex model, we can divide the flow field inside the blade-divergent passage into the following two parts: inside the ellipse, the vorticity is known and its velocity field is determined; and the outside of the ellipse is equivalent to an elliptical column affected by the passage flow. Finally, the two parts are combined to give the total velocity field.

First, the governing equation of the stream function outside the elliptical vortex is

$$\boldsymbol{V}_b\cdot\boldsymbol{n} = -\Omega y\frac{\partial y}{\partial s} - \Omega x\frac{\partial x}{\partial s} = -\Omega r\frac{\partial r}{\partial s}, \tag{3}$$

where $r^2 = x^2 + y^2$, $\boldsymbol{V}_\mathrm{b}$ is a point velocity on an ellipse surface, $\boldsymbol{n}$ is the unit outer normal vector, and s is the surface arc length measured counterclockwise. On the other hand, if we express the normal velocity with a stream function, then the normal velocity has the following form:

$$\boldsymbol{V}_b\cdot\boldsymbol{n} = \frac{\partial\Psi}{\partial s}\boldsymbol{n}_x - \frac{\partial\Psi}{\partial s}\boldsymbol{n}_y = \frac{\partial\Psi}{\partial s}. \tag{4}$$

Comparing Eqs 3, 4 and after integration, the surface stream function expression can be obtained as

$$\Psi_b = -\frac{1}{2}\Omega r^2 + \text{const.} \tag{5}$$

Then, we use elliptic coordinates (η, ξ) and assume that the velocity on the boundary of the elliptical vortex is close to the main flow velocity U due to the influence of the viscous force to obtain the stream function expression on the border

$$\Psi_b = -\frac{1}{2}\frac{U}{ab}c^2\cos 2\eta + \text{const}, \tag{6}$$

where the elliptic focus is $c^2 = a^2 - b^2$. Finally, when we combine the aforementioned surface boundary condition (6) with the governing Eq. 2, the condition that the velocity at infinity is 0, and the consideration that the elliptical vortex has a circulation $\Gamma = \pi ab\omega$, that is, the vortex flux passing through the cross-sectional area of the ellipse; the external stream function can be expressed as

$$\Psi^{(o)} = -\frac{1}{4}\frac{U}{ab}c^2 e^{2\xi_0}e^{-2\xi}\cos 2\eta - \frac{1}{2}ab\omega(\xi-\xi_0), \tag{7}$$

where the superscript "o" in the formula means external, ξ_o is the elliptic coordinate ξ on the border, and ω is vorticity.

Second, the governing equation of the stream function inside the elliptical vortex is

$$\nabla^2\Psi = -\omega. \tag{8}$$

We choose the stream function of the form

$$\Psi^{(i)} = \frac{1}{2}\omega\left(Ax^2 + By^2\right), \tag{9}$$

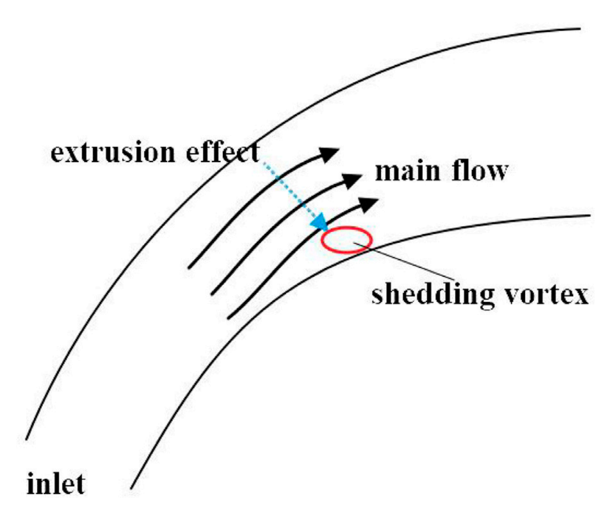

FIGURE 6
Schematic representation of the main flow extrusion effect.

where the superscript "*i*" in the formula means internal, and *A* and *B* are undetermined coefficients to be solved. According to the aforementioned equations and the continuity of the normal and tangential velocity components at the boundary between the inner and outer flows, we can obtain the final internal stream function

$$\Psi^{(i)} = -\frac{1}{2}\frac{U(a+b)c^2}{a^2b^2}\left(b\cosh^2\xi\cos^2\eta + a\sinh^2\xi\sin^2\eta\right). \tag{10}$$

4 Blade-divergent passage and its internal flow structures

The purpose of this section is to use the model introduced in the previous section to analyse the blade suction shedding vortex characteristics under some typical loads. In general, the flow in the passage is quite complex; even for the dominant coherent vortex structure, such as the shedding vortex, there are many factors acting on it. These complex factors are intertwined, making it difficult for us to identify which factors play a leading role or which factors trigger the phenomena we observe macroscopically. Therefore, our idea is to separate these factors and only consider what happens when a simple factor acts behind the vortex. In this part, we have analysed three typical factors of action in the blade-divergent passage, which we call the "main flow extrusion effect", the "main flow and wall viscous effect," and the "transport effect," respectively. Other factors can also be analysed and studied in this way.

4.1 Main flow extrusion effect

The description of the mainstream extrusion is shown in Figure 6. The dotted line in the figure represents a virtual extrusion. The low energy flow near the wall begins to break away from the wall and form a large-scale shedding vortex due to the effects of wall viscosity and back pressure. At the same time, the main flow turns into the shedding vortex due to the influence of the curved channel and causes a certain degree of extrusion, which will affect the structure of the shedding vortex.

To analyse and simplify this squeezing action, we set the coordinate origin at the centre of the ellipse; the *x*-axis and *y*-axis coincide with the long axis and short axis of the ellipse, respectively; and the extrusion action passes through the coordinate origin, so its corresponding stream function can be simplified as follows:

$$\Psi = \frac{1}{2}e\left(x^2 - y^2\right) = \frac{1}{2}ec^2\left(\cosh^2\xi\cos^2\eta + \sinh^2\xi\sin^2\eta\right), \tag{11}$$

where *e* is the strain rate strength that is determined here by the strength of the passage flow.

According to the superposition principle of harmonic functions, after the strain effect is applied to the original external stream function, the new external stream function becomes

$$\begin{aligned}\Psi_{ee}^{(o)} = {} & \frac{1}{2}ec^2\left(\cosh^2\xi\cos^2\eta + \sinh^2\xi\sin^2\eta\right) - \frac{1}{4}\frac{U}{ab}c^2e^{2\xi_0}e^{-2\xi}\cos 2\eta \\ & -\frac{1}{2}ab\omega\left(\xi - \xi_0\right),\end{aligned} \tag{12}$$

where the subscript "*ee*" means the extrusion effect. Continuity conditions for the stream function and tangential velocity on the ellipse boundary are satisfied, which provides

$$\begin{aligned}&\frac{1}{2}e\left(a^2\cos^2\eta + b^2\sin^2\eta\right) - \frac{1}{4}\frac{U}{ab}c^2\cos 2\eta \\ &= -\frac{1}{2}\omega\frac{ab}{(a+b)}\left(a\cos^2\eta + b\sin^2\eta\right),\end{aligned} \tag{13}$$

$$eab + \frac{1}{2}\frac{U}{ab}c^2\cos 2\eta - \frac{1}{2}ab\omega = -\omega\frac{ab}{(a+b)}\left(b\cos^2\eta + a\sin^2\eta\right). \tag{14}$$

The aforementioned two equations can be simplified to

$$\begin{aligned}&e\left(a^2\cos^2\eta + b^2\sin^2\eta\right) + eab - \frac{1}{2}ab\omega \\ &= -\omega\frac{ab}{(a+b)}(a+b)\left(\cos^2\eta + \sin^2\eta\right).\end{aligned} \tag{15}$$

So the ratio of the strain rate to vorticity is

$$e/\omega = -\frac{1}{2\big(\big(\varepsilon - \frac{1}{\varepsilon}\big)\cos^2\eta + 1 + \frac{1}{\varepsilon}\big)}, \tag{16}$$

whose value range is from −1/2 (ε + 1) to −1/2 (1/ε + 1), where ε = *a*/*b* is the axial ratio of the ellipse. From this, it can be seen that the extrusion effect of the main flow on the shedding vortex is opposite to the direction we set earlier, indicating that the extrusion of the passage flow actually plays a role in the stretching effect. When the fluid separates from the wall, the vortex will instead compress the main flow passage. The main flow seems to exert an entrainment effect on the shedding vortex. Meanwhile, we can conclude that the expansion of the shedding vortex has a range from −1/2 (ε + 1) to −1/2 (1/ε + 1) relative to the shedding vortex, and this value depends on the axial ratio of the ellipse. In short, the main stream has a suction effect on the shedding vortex, and its strength depends on the shedding vortex itself.

4.2 Viscous effect of the main flow and wall

The viscous effects include the fluid viscosity and the solid wall viscosity, as shown in Figure 7. During the formation of the

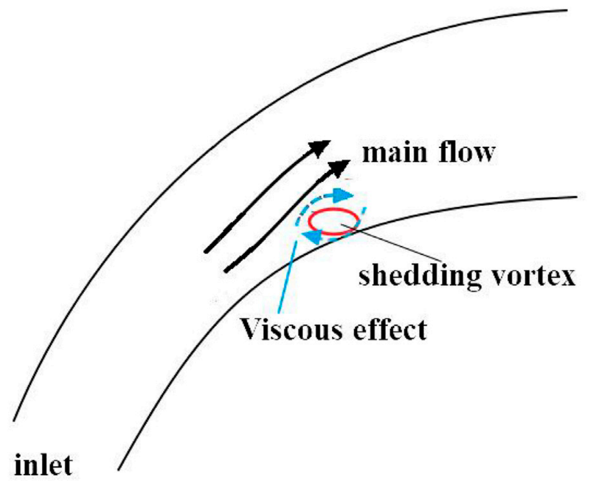

FIGURE 7
Schematic representation of the viscous effect.

backflow, the shedding vortex forms a relative motion with the main flow and the solid wall. The viscous acceleration effect of the main flow and the viscous stagnation effect of the wall are approximately equivalent to the formation of an additional circulation around the shedding vortex. As in the previous section, we set the coordinate origin at the centre of the ellipse and use a point vortex model for the additional circulation. The corresponding current function is

$$\Psi_{ve}^{(o)} = -\frac{\Gamma_0}{2\pi}\ln\left[c\left(\cosh^2\xi\cos^2\eta+\sinh^2\xi\sin^2\eta\right)^{1/2}\right], \tag{17}$$

where the subscript "*ve*" means the viscous effect. In addition, according to the continuity condition, we obtain

$$-\frac{\Gamma_0}{2\pi}\ln\left[\left(a^2\cos^2\eta+b^2\sin^2\eta\right)^{1/2}\right]-\frac{1}{4}\frac{U}{ab}c^2\cos 2\eta = -\frac{1}{2}\omega\frac{ab}{a+b}\left(a\cos^2\eta+b\sin^2\eta\right) \tag{18}$$

and

$$-\frac{\Gamma_0}{2\pi}\frac{ab}{a^2\cos^2\eta+b^2\sin^2\eta}+\frac{1}{2}\frac{U}{ab}c^2\cos 2\eta-\frac{1}{2}ab\omega = -\omega\frac{ab}{a+b}\left(b\cos^2\eta+a\sin^2\eta\right). \tag{19}$$

We can multiply Eq. 18 by 2 and add it to Eq. 19 to eliminate the second term to get

$$-\frac{\Gamma_0}{2\pi}\frac{ab}{a^2\cos^2\eta+b^2\sin^2\eta}-\frac{\Gamma_0}{2\pi}\ln\left(a^2\cos^2\eta+b^2\sin^2\eta\right) = -\frac{1}{2}ab\omega. \tag{20}$$

By analysing the aforementioned equation, we can get the maximum and minimum values of Γ_o/ω:

$$\left(\Gamma_0/\omega\right)_{max} = \frac{\pi ab}{1+\ln ab}, \tag{21}$$

$$\left(\Gamma_0/\omega\right)_{min} = \frac{\pi ab}{a/b+\ln b^2}. \tag{22}$$

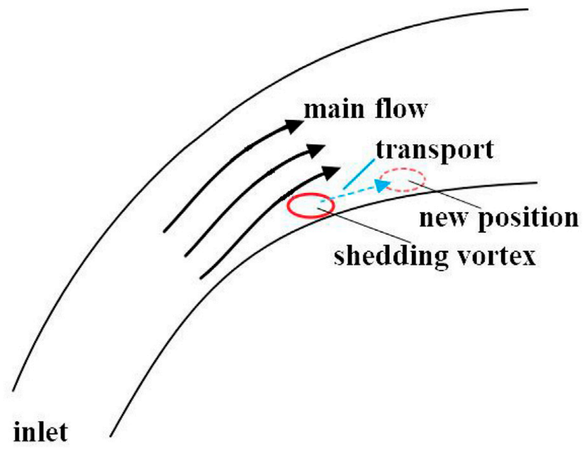

FIGURE 8
Schematic representation of the transport effect.

The aforementioned expression gives the range of Γ_o/ω, which is the range of values that the mainstream viscous force and wall friction can affect the shedding vortex. It can be seen that the viscous force depends on the long and short axes of the elliptical vortex. Further analysis shows that the minimum value of Γ_o/ω can only be less than 1 when both the long axis a and the short axis b are less than 1. In addition, in most cases, Γ_o/ω is greater than 1. In other words, in most cases, when the viscous force acts on the shedding vortex, its influence will even exceed that of the shedding vortex itself. Only when the scale of the shedding vortex is small can the effect of the viscous force be less than that of the vortex itself. This may be due to the small scale of the vortex, which makes the range of action of the viscous force not large enough.

4.3 Transport effect

As mentioned previously, the movement of the shedding vortex trajectory is the result of many factors, but from the perspective of lateral displacement, the effect of movement is more direct compared to other factors. The transport effect is discussed in this section, as shown in Figure 8.

Now, assuming that the shedding vortex is constant, we can write the stream function corresponding to the translational action as

$$\Psi = Ax - By + C, \tag{23}$$

where A, B, and C are constants determined by the strength of the passage flow. Since our analysis takes the long axis of the elliptical vortex as the x-axis, a simpler stream function can be written as

$$\Psi = -By. \tag{24}$$

Then, we replace B with e for notation consistency with the previous analysis. The external stream function becomes

$$\Psi_{te}^{(o)} = -ec\sinh\xi\sin\eta-\frac{1}{4}\frac{U}{ab}c^2e^{2\xi_0}e^{-2\xi}\cos 2\eta-\frac{1}{2}ab\omega\left(\xi-\xi_0\right), \tag{25}$$

where the subscript "*te*" means the transport effect. Using the continuity condition, we obtain

$$-eb\sin\eta-\frac{1}{4}\frac{U}{ab}c^{2}\cos 2\eta=-\frac{1}{2}\omega\frac{ab}{a+b}\left(a\cos^{2}\eta+b\sin^{2}\eta\right)\tag{26}$$

and

$$-eb\sin\eta+\frac{1}{2}\frac{U}{ab}c^{2}\cos 2\eta-\frac{1}{2}ab\omega=-\omega\frac{ab}{a+b}\left(b\cos^{2}\eta+a\sin^{2}\eta\right).\tag{27}$$

The aforementioned two equations can be combined as

$$-eb\sin\eta\left(2b+a\right)-\frac{1}{2}ab\omega=-\omega\frac{ab}{a+b}\left(a+b\right)\left(\cos^{2}\eta+\sin^{2}\eta\right)\tag{28a}$$

Finally, we get the ratio of the strain rate to vorticity

$$e/\omega=\frac{1}{2\sin\eta}ab/\left(2b+a\right)\tag{28b}$$

whose absolute minimum value is $ab/2\ (2b+a)$. This reflects the influence of the passage flow on the shedding vortex trajectory. Unlike the extrusion and viscous effects, the transport effect has no upper limit. In addition, relative to the original vortex, the minimum effect depends on both the long and short axes of the shedding vortex. This is equivalent to creating a flow condition to generate a shedding vortex in the blade-divergent passage, and if the passage flow is strong, its influence on the shedding vortex will also increase.

5 Negative circulation flow control technology

As mentioned previously, it can be seen that the intensity ratio of the transport effect to the shedding vortex has only a minimum value, which means that the effect is a necessary condition to affect the shedding vortex. Therefore, from a flow control point of view, we are not willing to spend much energy on controlling this effect. For the main flow extrusion effect, if we take a conventional ellipse with axis ratio $\varepsilon = 2$, the maximum intensity ratio of the extrusion effect to the shedding vortex can be obtained from Eq. 16 as 1/3. Comparing this value with the minimum value of Γ_0/ω (Eq. 22), which is greater than 1 in most cases, we can conclude that the influence of the extrusion effect on the shedding vortex will be much greater than that of the viscous effect. Therefore, an appropriate flow control method that we adopt should be to weaken or better inhibit the viscous effect. Here, we propose that the jet flow control should include an action opposite to the viscous effect to offset it, i.e., to produce an action opposite to the point vortex we introduced earlier, which we call NCFC technology.

Figure 9 shows a jet flow control device based on NCFC technology. A vortex generator can be set in the jet channel to produce a negative circulation effect. In order to eliminate the influence of the jet inlet on the control effect and to create fully developed vortices in the bypass tube, we have increased the length of the bypass tube accordingly. It is worth mentioning that the NCFC technology may also be applicable to unsteady suction flow control methods. Although the unsteady control method will use the principles of frequency locking, phase locking, and some other mechanisms (Huang et al, 2017), NCFC technology may further improve its efficiency.

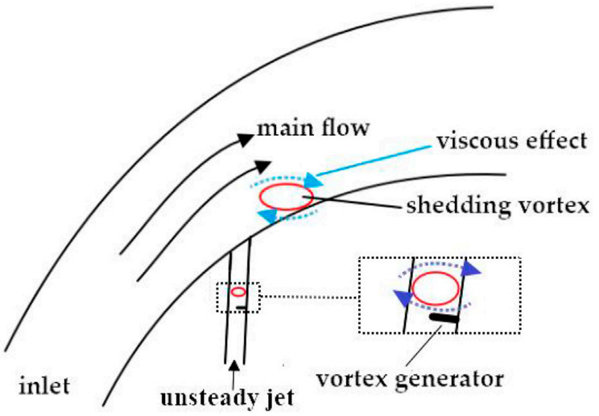

FIGURE 9
Schematic representation of a NCFC method for jet flow control.

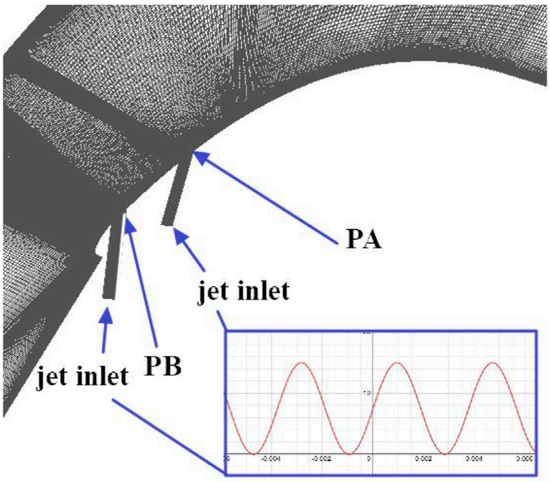

FIGURE 10
Locations of the jet flow control.

5.1 Blade-divergent flow with and without NCFC devices

To simulate the jet, we set up a bypass flow connected to the main flow passage. Two positions are studied. In the first case, the bypass flow is located at the position of about 25% chord length (marked as PA), which is the generation point of the shedding vortex, so this situation is considered to weaken the shedding vortex. In the second case, the bypass flow is located at the position of about 10% chord length (noted as PB), where the flow starts to separate, so this case is considered to suppress the secondary flow. The incident angle is about 35, and the control frequency is the same as the

TABLE 1 Performances of the blade-divergent passage under different conditions.

	Position	$\overline{m}_{\mathrm{jet}}/\overline{m}_{\mathrm{in}}$	$\bar{\omega}_{\mathrm{rel}}$	Position	$\overline{m}_{\mathrm{jet}}/\overline{m}_{\mathrm{in}}$	$\bar{\omega}_{\mathrm{rel}}$
Unsteady jet	PA	0.019%	4.8%	PB	0.021%	−15.6%
	PA	0.19%	−5.9%	PB	0.21%	−19.5%
	PA	1.92%	−14.8%	PB	2.1%	−7.8%
Unsteady jet with NCFC	PA	0.019%	−6.7%	PB	0.021%	−24.4%
	PA	0.19%	−27.8%	PB	0.21%	−23.4%
	PA	1.92%	−19.3%	PB	2.1%	−22.8%

shedding vortex frequency. Figure 10 shows the two locations and the situation when applying NCFC technology. The bypass flow inlet is set as the velocity inlet, and its expression is as follows:

$$V_t = V_m\left(\sin\left(2\pi f_0 t\right) + 1\right)/2, \tag{29}$$

where V_m is the jet velocity amplitude, f_0 is the shedding vortex frequency, and t is the flow time. In order to understand the mechanism of unsteady flow control and NCFC technology, we have studied PA and PB under three flow controls with different jet flow mass rates by varying V_m. The relative pressure loss coefficient is used to measure the control effect, defined as

$$\bar{\omega}_{\mathrm{rel}} = \frac{\bar{\omega}_{\mathrm{c}} - \bar{\omega}_0}{\bar{\omega}_0} \times 100\%, \tag{30}$$

where $\bar{\omega}_{\mathrm{c}}$ and $\bar{\omega}_0$ are average pressure loss coefficients of the controlled flow field and the uncontrolled flow field, respectively. $\bar{\omega}_{\mathrm{rel}}$ can be calculated by

$$\bar{\omega}_{\mathrm{c}} = \frac{\overline{m}_{\mathrm{in}} \cdot \bar{p}_{\mathrm{in}} + \overline{m}_{\mathrm{jet}} \cdot \bar{p}_{\mathrm{jet}} - \overline{m}_{\mathrm{out}} \cdot \bar{p}_{\mathrm{out}}}{\overline{m}_{\mathrm{in}} \cdot \bar{p}_{\mathrm{in}} + \overline{m}_{\mathrm{jet}} \cdot \bar{p}_{\mathrm{jet}}}, \tag{31}$$

where $\overline{m}_{\mathrm{in}}$ is the average mass flow at the main flow inlet; $\overline{m}_{\mathrm{jet}}$ is the average mass flow at the jet inlet; $\overline{m}_{\mathrm{out}}$ is the average mass flow at the main flow outlet; $\bar{p}_{\mathrm{in}}$ is the average total pressure at the main flow inlet; $\bar{p}_{\mathrm{jet}}$ is the average total pressure at the jet inlet; $\bar{p}_{\mathrm{out}}$ is the average total pressure at the main flow outlet. Table 1 shows the performance of the blade-divergent passage under different operating conditions.

5.2 Flow control for the shedding vortex

By observing the relative loss coefficient of each scheme at the PA position in Table 1, we can draw the following conclusions: 1) the application of unsteady flow control can reduce the loss coefficient of the blade-divergent passage, and the application of the NCFC method is generally more effective than the application of the conventional method; 2) with the NCFC method, there is an optimum injection to achieve the optimum control effect. When the injection is 0.2% of the main flow, it is almost saturated. At this point, further increasing the injection will cause the efficiency to decrease (indicating that the energy consumed by the flow control will reduce the economy of the flow efficiency improvement); 3) when conventional flow control is used, the control efficiency increases with the increase of the injection in a relatively wide range (the injection is 0.019%–1.9% of the main flow). We can also see that the efficiency of the NCFC method is higher by comparing the characteristic that the NCFC tends to be saturated when the injection is small.

Figures 11, 12 show the flow structures in the blade divergence passage with the NCFC method and with conventional flow control. From the figures, it can be seen that the shedding vortex can be stabilised on the curved blade surface after using the NCFC method, while the development of the shedding vortex after excitation is similar to that of the uncontrolled flow (Figure 4). In addition, the size of the shedding vortex restrained by NCFC is also smaller than that of the conventional method. As a result, the area of the low-velocity zone on the blade surface is smaller than that of the conventional method undergoing NCFC (shown in Figure 13). Figure 14 shows the velocity vector and the interaction of the main flow and the bypass flow. We can see that a vortex is generated in the bypass with the NCFC method and moves downstream. When the vortex moves to the junction of the main flow and the bypass, it can better mix the flows. However, there are no such flow structures for momentum exchange with the conventional method. So we can see from Figure 11 that there is no shedding vortex at the interface between the jet and the main stream, whereas in Figure 12, there is still a shedding vortex at this location.

5.3 Flow control for separation flow

In this study, flow separation occurs at the leading edge of the blade, so we set the flow control position at 10% chord length. Table 1 also shows the performance comparison between conventional flow control and the NCFC method. From the table, we can see that conventional flow control has a positive effect on the suppression of flow separation. Even a small injection mass can improve the performance of the blade-divergent passage. However, as the incident flow increases, its efficiency decreases. The law of jet mass flow and control effect is different from that of PA. For the NCFC method, it performs well under different incident flow rates, and the performance improvement is similar under different incident flow rates. This reflects that the NCFC method is not sensitive to the injection flow mass to inhibit flow separation. Overall, the performance improvement of the NCFC method is slightly better than that of the conventional method.

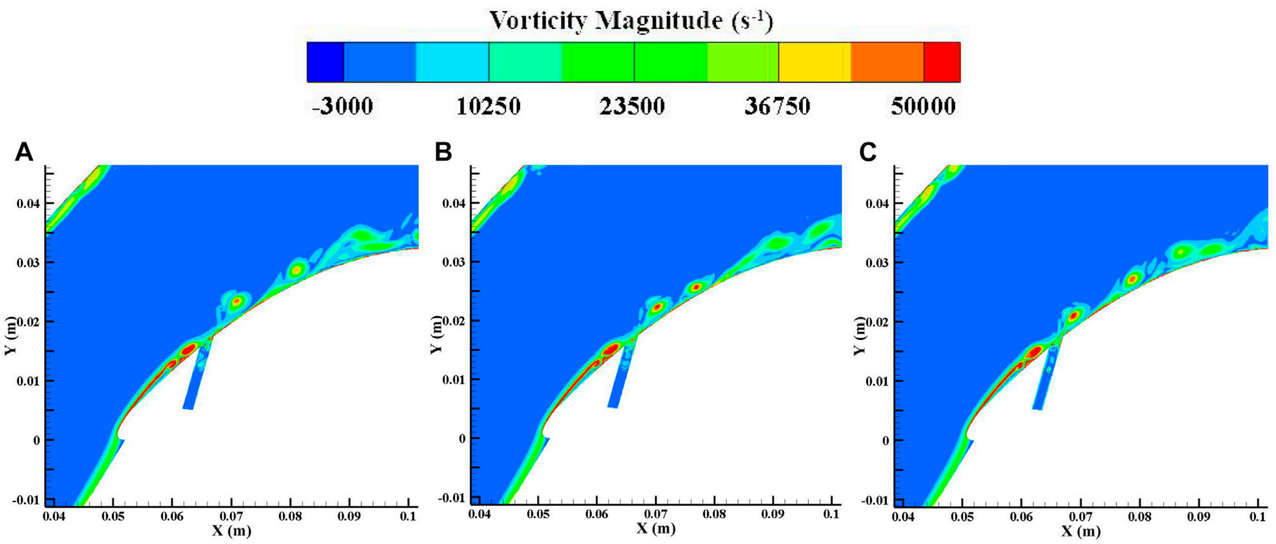

FIGURE 11
Flow structures in the blade-divergent passage with NCFC technology at PA. **(A)** 1/6T. **(B)** 3/6T. **(C)** 5/6T.

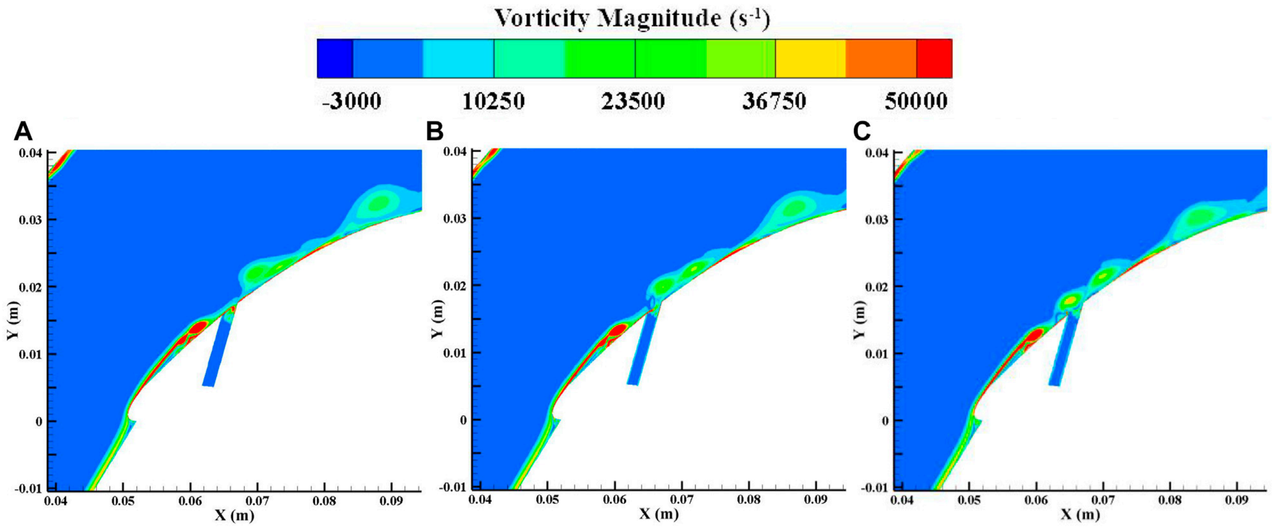

FIGURE 12
Flow structures in the blade-divergent passage with conventional flow control at PA. **(A)** 1/6T. **(B)** 3/6T. **(C)** 5/6T.

Figure 15 shows a comparison of instantaneous vorticity with conventional flow control and the NCFC method under large injection masses. Figure 16 shows the instantaneous velocity contribution. It can be seen from the two figures that the NCFC method uses the vortices generated in the bypass to enhance the momentum exchange in the main flow, which is similar to a common vortex generator technology. However, conventional flow control uses a jet to accelerate the low-energy flow at the blade surface. Since the shedding vortex is not generated at position PB, the leading edge separation could be considered a stable flow, so applying unsteady flow control at this position actually takes advantage of the “steady” part of the jet.

6 Discussion

From the aforementioned analysis, we have reason to believe that the NCFC method utilises both the unsteady effect and the negative circulation effect, so its performance is superior to the conventional unsteady flow control technology under most

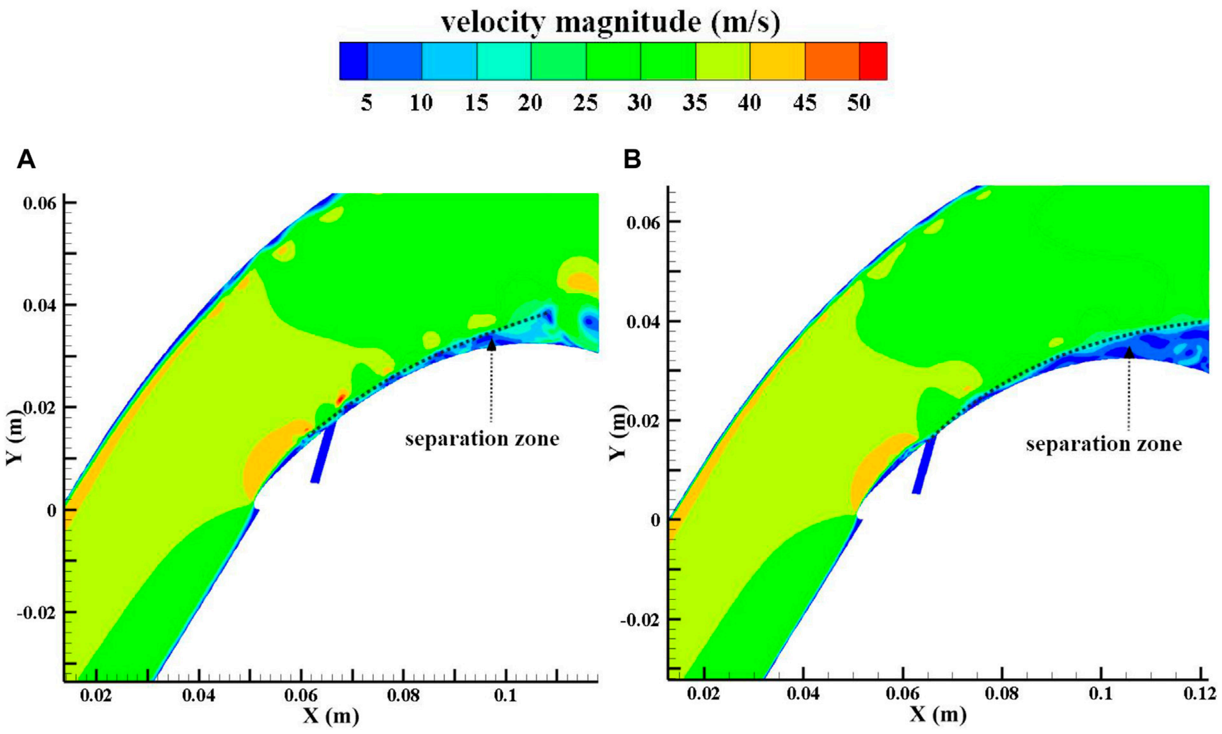

FIGURE 13
Velocity distribution at 3/6T. **(A)** NCFC method. **(B)** Conventional flow control.

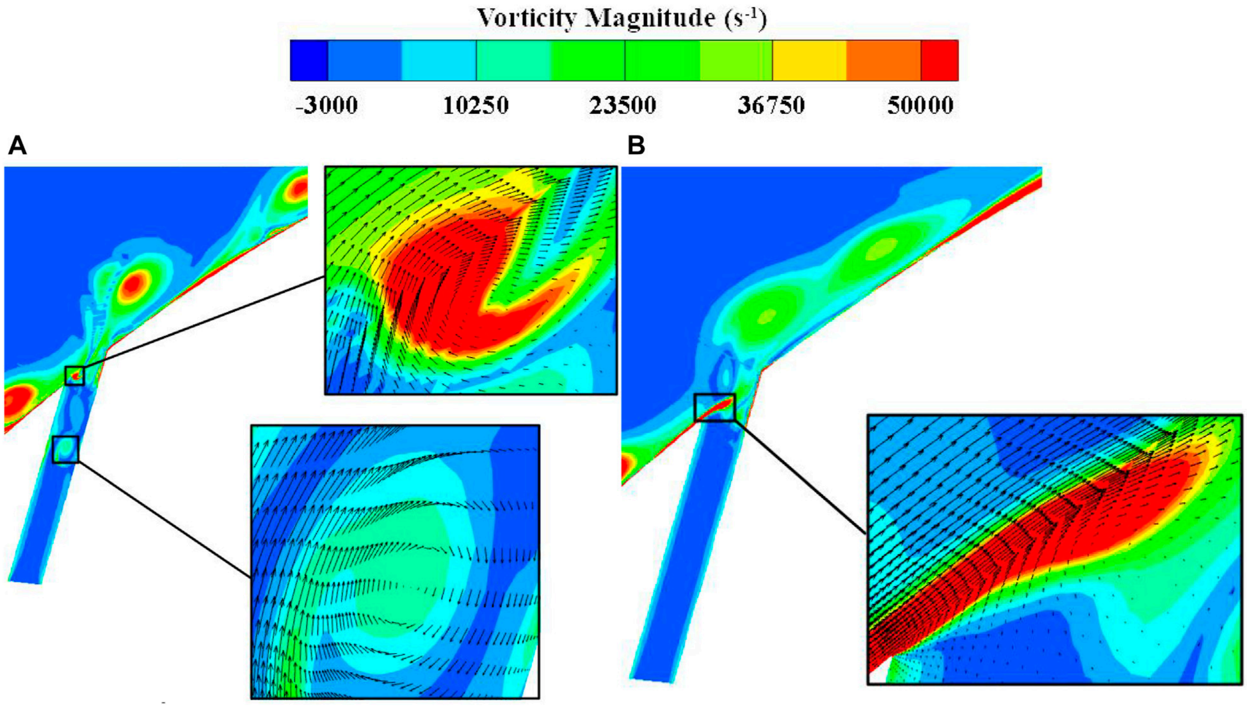

FIGURE 14
Vectors in the bypass flow. **(A)** NCFC method. **(B)** Conventional flow control.

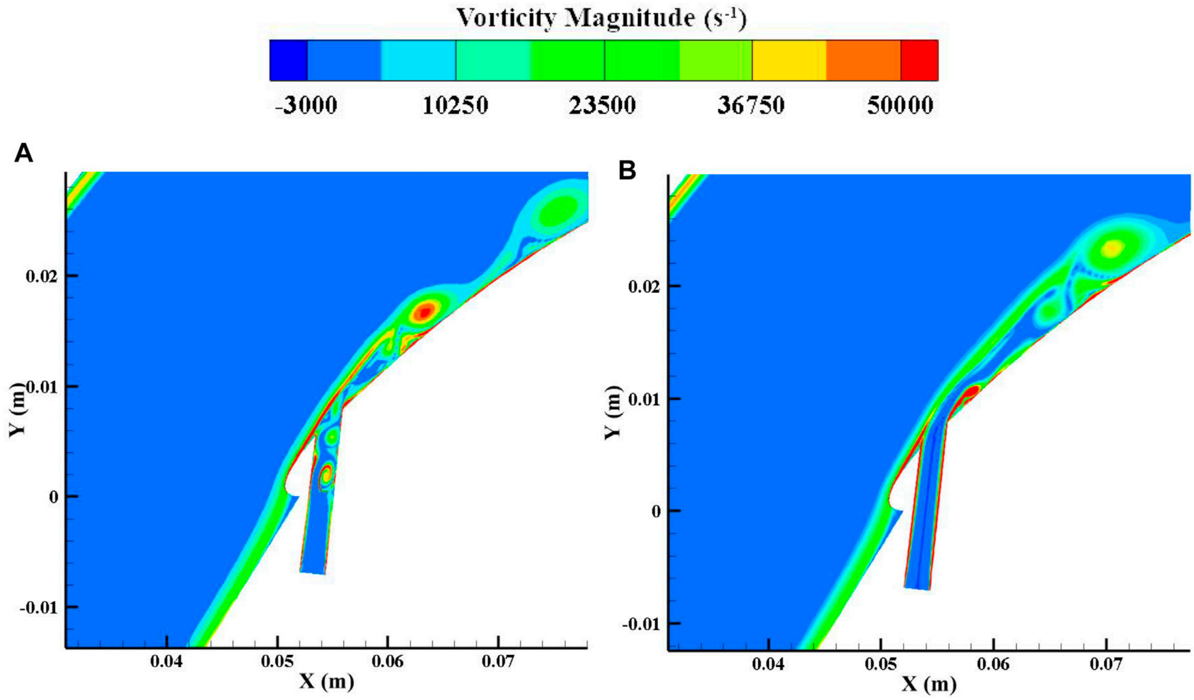

FIGURE 15
Instantaneous vorticity distribution of the large injection flow mass rate. **(A)** NCFC method. **(B)** Conventional flow control.

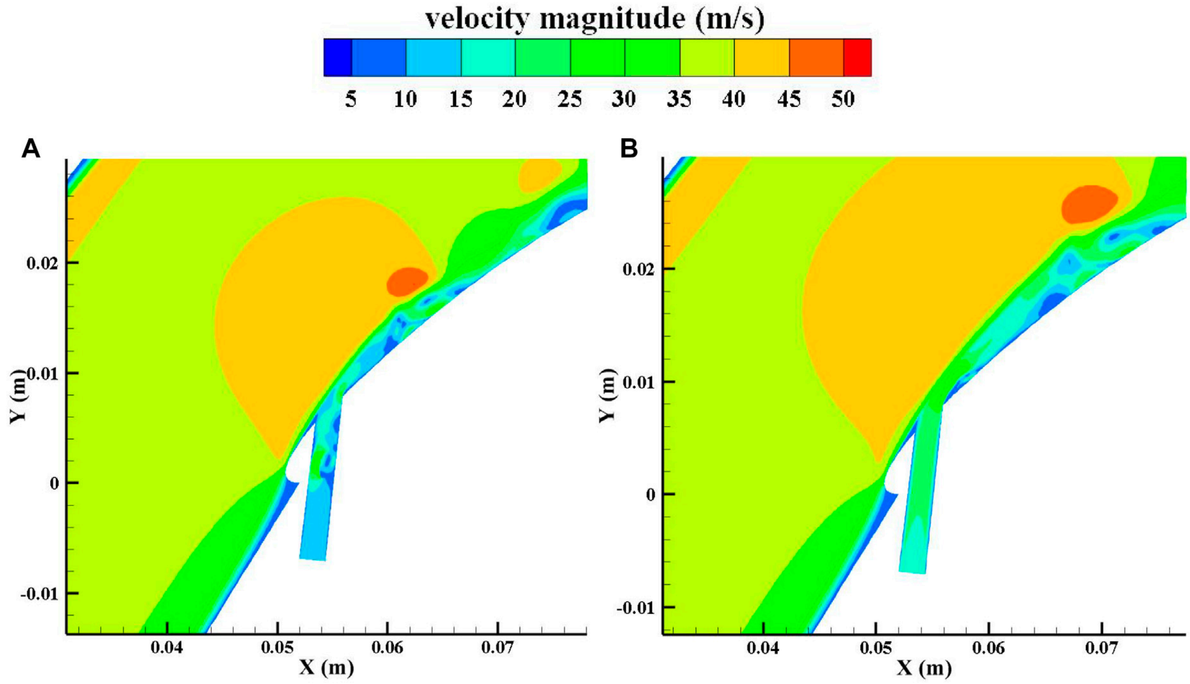

FIGURE 16
Instantaneous velocity distribution of the large injection flow mass rate. **(A)** NCFC method. **(B)** Conventional flow control.

working conditions. In addition, we recommend using the NCFC method with a medium injection intensity (about 0.2% of the main flow mass) because, in this case, the NCFC method performs well in both shedding vortex suppression and separation flow control.

In our previous studies, we found that flow control was most effective when positioned near the separation point of the shedding vortex (Lu et al, 2022). Other researchers have investigated the sensitivity of the control position (Amitay et al, 2001) (Shojaefar et al, 2005). So one of the issues we need to look at is the sensitivity of the location of the control point. However, the reality is that as the operating conditions of compressors and such fluid machines change, this can lead to variations in pneumatic parameters such as the angle of attack, so that setting the control point at a single fixed position may be effective in some operating conditions but fail in many others. Moreover, through our research into NCFC technology, we found that this method was less sensitive to the location of the control point. We therefore analysed two locations: PA (similar to our previous studies, set close to the separation point) and PB (quite some distance in front of the shedding vortex separation point). As the data in Table 1 show, the control effect is still positive, although the setting at position PA is less effective than the setting at PB when the energy input is small. When the energy input increases, the control effect does not differ much from the setting at PB. Therefore, our conclusion and recommendation is to set the control point upstream of the predicted shedding vortex separation point to account for changes in operating conditions or to partially resolve the uncertainty in the location of the separation point.

7 Conclusion

In order to improve and complete the theoretical understanding of the blade suction shedding vortex and to lay the foundation for the adoption of a proper flow control method, a two-dimensional vortex model is introduced in this paper and numerical simulation is carried out for verification. The conclusions are as follows:

(1) An elliptical vortex is used to analyse the behaviour of the shedding vortex in a blade-divergent passage. Three typical external factors are studied individually depending on the model: the main flow extrusion effect, the main flow and solid wall viscous effect, and the transport effect. These factors can also be combined to analyse more complex situations.

(2) The transport effect on the shedding vortex is a necessary condition to influence the shedding vortex. The effect of the extrusion effect will be much greater than that of the viscous effect on the shedding vortex. Therefore, a flow control concept based on negative circulation is proposed to compensate for the viscous effect, which is known as NCFC.

(3) An NCFC device is designed and realised by a vortex generator installed in a tube connected to the blade surface through a hole. Through numerical simulation, it is found that the NCFC method is superior to conventional unsteady flow control for improving the performance of the blade-divergent passage in most cases.

(4) There is an optimum injection to suppress the shedding vortex with NCFC, which is about 0.2% of the main flow mass. However, with conventional unsteady flow control, the control efficiency increases with increasing injection over a wide range, implying that NCFC is more efficient than conventional flow control for the shedding vortex.

(5) The control mechanism of the NCFC and conventional unsteady flow control for the separation flow is similar to that of a steady flow control. The former uses a vortex to increase the exchange between the main flow and the low-energy flow at the blade surface. The latter uses injection to accelerate the low-energy flow close to the blade.

(6) Due to its high efficiency in shedding vortex control and its insensitivity to separation flow control, the NCFC method is highly recommended for adapting to the changing flow field under variable operating conditions in practice.

Data availability statement

The original contributions presented in the study are included in the article/Supplementary material; further inquiries can be directed to the corresponding author.

Author contributions

SH carried out the establishment of the model, presentation of strategies, data analysis, and wrote the first draft. WL assisted in the establishment of a model and the improvement of strategies. XX assisted in data analysis and polished the manuscript. LQ helped with the revision of the manuscript. All authors contributed to the article and approved the submitted version.

Funding

This research was funded by the Zhejiang Provincial Natural Science Foundation of China, Grant No. LQ20E060004. This research was also supported by the Fundamental Research Funds for the Ningbo University of Technology.

Acknowledgments

The authors are also grateful to Huang Guoping (NUAA) for technical aspects.

Conflict of interest

The authors declare that the research was conducted in the absence of any commercial or financial relationships that could be construed as a potential conflict of interest.

Publisher's note

References

Abdolrahim, R., Hamid, M., and Bert, B. (2019). Active flow control for power enhancement of vertical axis wind turbines: Leading-edge slot suction. *Energy* 189, 116131. doi:10.1016/j.energy.2019.116131

Akhtar, I., Marzouk, O., and Nayfeh, A. (2009). A van der Pol-Duffing oscillator model of hydrodynamic forces on canonical structures. *J. Comput. Nonlinear Dyn.* 4 (4), 041006. doi:10.1115/1.3192127

Amitay, M., Smith, D., Kibens, V., Parekh, D., and Glezer, A. (2001). Aerodynamic flow control over an unconventional airfoil using synthetic jet actuators. *AIAA J.* 39 (3), 361–370. doi:10.2514/2.1323

Braunscheidel, E., Culley, D., and Zaman, K. (2008). "Application of synthetic jets to reduce stator flow separation in a low speed axial compressor," in In 46th AIAA aerospace sciences meeting and exhibit, Nevada, United States, January, 2008, 7–10.

Balduzzi, F., Bianchini, A., Ferrara, G., and Ferrari, L. (2016a). Dimensionless numbers for the assessment of mesh and timestep requirements in CFD simulations of Darrieus wind turbines. *Energy* 97, 246–261. doi:10.1016/j.energy.2015.12.111

Balduzzi, F., Bianchini, A., Maleci, Riccardo., Ferrara, Giovanni., and Ferrari, L. (2016b). Critical issues in the CFD simulation of Darrieus wind turbines. *Renew. Energy* 85, 419–435. doi:10.1016/j.renene.2015.06.048

Chen, J., Lu, W., Huang, G., Zhu, J., and Wang, J. (2017). Research on pulsed jet flow control without external energy in a blade cascade. *Energies* 10 (12), 2004. doi:10.3390/en10122004

Chen, S., Tu, T., Zeng, C., and Meng, Q. (2022). Modal analysis of compressor cascades with sweeping jet actuator and pulsed jet for active flow control based on large Eddy simulation. *Aerosp. Sci. Technol.* 131, 107997. doi:10.1016/j.ast.2022.107997

Choi, M., Baek, J. H., Oh, S. H., and Ki, D. J. (2008). Role of hub-corner-separation on rotating stall in an axial compressor. *Trans. Jpn. Soc. Aeronautical Space Sci.* 51 (172), 93–100. doi:10.2322/tjsass.51.93

Feng, Q., Hou, A., Liu, R., Zhou, B., and Zhang, M. (2022). Separation flow and blade dynamic response characteristic of compressor at high attack angle. *J. Beijing Univ. Aeronautics Astronautics* 43 (7), 1410–1418. doi:10.13700/j.bh.1001-5965.2016.0912

Ferziger, J., and Peric, M. (2002). *Computational methods for fluid dynamics*. 3. Berlin, Germany: Springer.

Gbadebo, S. A., Cumpsty, N. A., and Hynes, T. P. (2008). Control of three-dimensional separations in axial compressors by tailored boundary layer suction. *J. Turbomach.* 130 (1), 011004. doi:10.1115/1.2749294

Gbadebo, S. A., Cumpsty, N. A., and Hynes, T. P. (2005). Three-dimensional separations in axial compressors. *J. Turbomach.* 127 (2), 331–339. doi:10.1115/1.1811093

Giorgi, M., Luca, C., Ficarella, A., and Marra, F. (2015). Comparison between synthetic jets and continuous jets for active flow control: Application on a NACA 0015 and a compressor stator cascade. *Aerosp. Sci. Technol.* 43, 256–280. doi:10.1016/j.ast.2015.03.004

Hong, S., Chi, J., Xiang, X., and Lu, W. (2022). Theoretical model and numerical analysis of the tip leakage vortex variations of a centrifugal compressor. *Aerospace* 9 (12), 830. doi:10.3390/aerospace9120830

Hong, S., and Huang, G. (2017). Introducing DMD method to study dynamic structures of flow separation with and without control. *Acta Aeronautica Astronautica Sinica* 38 (8), 120876. doi:10.7527/S1000-6893.2016.120876

Huang, G., Lu, W., Zhu, J., Fu, X., and Wang, J. (2017). A nonlinear dynamic model for unsteady separated flow control and its mechanism analysis. *J. Fluid Mech.* 826, 942–974. doi:10.1017/jfm.2017.321

Ku, W., Girvan, M., and Ott, E. (2015). Dynamical transitions in large systems of mean field-coupled Landau-Stuart oscillators: Extensive chaos and cluster states. *Chaos* 25 (12), 123122. doi:10.1063/1.4938534

Lei, V. M. (2006). *A simple criterion for three-dimensional flow separation in axial compressors*. Ph. D. thesis. Cambridge, United States: Massachusetts Institute of Technology.

Liesner, K., Meyer, R., Lemke, M., Gmelin, C., and Thiele, F. (2010). "On the efficiency of secondary flow suction in a compressor cascade," in In Proceedings of the ASME Turbo Expo 2010: Power for Land, Sea, and Air, Glasgow, United Kingdom, 14–18 June 2010.

Likiewicz, G., Kabalyk, K., Jaeschke, A., Grapow, F., Kulak, M., Stajuda, M., et al. (2020). Unstable flow structures present at different rotational velocities of the centrifugal compressor. *Energies* 13 (16), 4146. doi:10.3390/en13164146

Lu, W., Huang, G., and Wang, J. (2022). Analysis of pulsed suction flow control behavior based on a nonlinear reduced-order model. *Aerosp. Sci. Technol.* 122, 107410. doi:10.1016/j.ast.2022.107410

Ma, D., Li, G., Yang, M., and Wang, S. (2018). Research of the suction flow control on wings at low Reynolds numbers. *Proc. Institution Mech. Eng. Part G J. Aerosp. Eng.* 232 (8), 1515–1528. doi:10.1177/0954410017694057

Marzouk, O., Nayfeh, A., Akhtar, I., and Arafat, H. (2007). Modeling steady-state and transient forces on a cylinder. *J. Vib. Control* 13 (7), 1065–1091. doi:10.1177/1077546307078737

Matejka, M., Popelka, L., Safarik, P., and Nozicka, J. (2008). "Influence of active methods of flow control on compressor blade cascade flow," in In Proceedings of the ASME Turbo Expo 2008: Power for Land, Sea, and Air, Berlin, Germany, June, 2008, 9–13.

Orszag, S. (1971). Accurate solution of the Orr–Sommerfeld stability equation. *J. Fluid Mech.* 50 (4), 689–703. doi:10.1017/S0022112071002842

Shojaefar, M., Noorpoor, A., Avanesians, A., and Ghaffarpou, M. (2005). Numerical investigation of flow control by suction and injection on a subsonic airfoil. *Am. J. Appl. Sci.* 2 (10), 1474–1480. doi:10.3844/ajassp.2005.1474.1480

Skop, R. A. (1995). "A nonlinear oscillator model for vortex shedding from a forced cylinder. Part 2: Shear flow and axial diffusion," in Paper presented at the The Fifth International Offshore and Polar Engineering Conference, The Hague, The Netherlands, June, 1995, 11.

Stuart, J. (1967). On finite amplitude oscillations in laminar mixing layers. *J. Fluid Mech.* 29 (3), 417–440. doi:10.1017/S0022112067000941

Stuart, J. (1958). On the non-linear mechanics of hydrodynamic stability. *J. Fluid Mech.* 4 (1), 1–21. doi:10.1017/S0022112058000276

Tang, Y., Liu, Y., and Sciubba, E. (2020). Aerodynamic investigation of datum and slotted blade profiles under different mach number conditions. *Energies* 13 (7), 1673. doi:10.3390/en13071673

Theofilis, V. (2003). Advances in global linear instability analysis of nonparallel and three-dimensional flows. *Prog. Aerosp. Sci.* 39 (4), 249–315. doi:10.1016/S0376-0421(02)00030-1

Thompson, M., and Gal, P. (2004). The Stuart-Landau model applied to wake transition revisited. *Eur. J. Mech. B-fluids* 23 (1), 219–228. doi:10.1016/j.euromechflu.2003.09.012

Yang, Z., Mao, X., and Liu, B. (2021). Numerical investigation of secondary flow control by boundary layer suction on the end-wall in a highly-loaded axial compressor cascade. *J. Aeronautics, Astronautics Aviat.* 53 (4), 483–496.

Yousefi, K., and Saleh, R. (2015). Three-dimensional suction flow control and suction jet length optimization of NACA 0012 wing. *Meccanica* 50 (6), 1481–1494. doi:10.1007/s11012-015-0100-9

Zhu, J., Huang, G., Fu, X., and Fu, Y. (2015). Characteristic of controlling flow separation in divergent curved channels by pulsed jet. *J. Aerosp. Power* 30 (12), 2942–2948. doi:10.13224/j.cnki.jasp.2015.12.018

Frontiers in Energy Research

TYPE Original Research
PUBLISHED 05 July 2023
DOI 10.3389/fenrg.2023.1180607

A study on the multi-objective optimization method and characteristic analysis of installation locations of submersible mixer for sewage

Fei Tian[1], Chen Yang[1]*, Erfeng Zhang[1], Dehua Sun[1], Weidong Shi[2] and Yonghua Chen[3]

[1]School of Energy and Power Engineering, Jiangsu University, Zhenjiang, China, [2]School of Mechanical Engineering, Nantong University, Nantong, China, [3]Yatai Pump & Valve Co., Ltd., Taixing, China

OPEN ACCESS

EDITED BY
Kan Kan,
College of Energy and Electrical Engineering, China

REVIEWED BY
Qiang Gao,
University of Minnesota Twin Cities, United States
Zhaohan Li,
Lam Research, United States

*CORRESPONDENCE
Chen Yang,
✉ 2222106001@stmail.ujs.edu.cn

RECEIVED 06 March 2023
ACCEPTED 03 April 2023
PUBLISHED 05 July 2023

CITATION
Tian F, Yang C, Zhang E, Sun D, Shi W and Chen Y (2023), A study on the multi-objective optimization method and characteristic analysis of installation locations of submersible mixer for sewage.
Front. Energy Res. 11:1180607.
doi: 10.3389/fenrg.2023.1180607

In this study, the performance of submersible mixers in sewage treatment was improved by optimizing the installation position parameters of the mixer. The aim was to enhance the average flow velocity and mixing efficiency in the pool. The study employed ISIGHT software, integrated with Creo Parametric 6.0 software and ANSYS Workbench 2020 software, to analyze the factors affecting mean flow velocity and completed a multi-objective optimized design using Non-dominated Sorting Genetic Algorithm (NSGA-II). The study used the ISIGHT software to analyze the factors affecting mean flow velocity in the pool. The installation position parameters of the submersible mixer were selected as design variables. The study employed Creo Parametric 6.0 software to create a three-dimensional model of the pool and the submersible mixer. ANSYS Workbench 2020 software was used to simulate fluid flow in the pool. The Non-dominated Sorting Genetic Algorithm (NSGA-II) was used for multi-objective optimization. The results of the study indicated an increase of approximately 0.021 m/s in average flow velocity and an improvement of approximately 0.47% in mixing efficiency compared to pre-optimization values. The effective axial propulsion distance and effective radial diffusion radius were significantly increased by 6.71% and 8.33%, respectively, after optimization. The fluid distribution in the pool became more uniform, and the low-speed zone was greatly reduced, resulting in an enhanced flow state of the fluid in the pool and a strengthened mixing effect. The study provides insights into the control of the submersible mixer's installation position to improve the average flow velocity inside the pool. Automatic optimization of submersible mixer installation locations using the ISIGHT software can effectively improve mixing efficiency, overall plant operating efficiency, and economic benefits in sewage treatment plants. The multi-objective optimization platform based on the ISIGHT platform for wastewater treatment mixer installation location can be successfully applied in engineering practice.

KEYWORDS

submersible mixers, multi-objective optimization, numerical simulation, NSGA-II, ISIGHT platform

1 Introduction

The submersible mixer is an efficient submersible mixing and pushing device (Yan et al., 2009). It is typically utilized in sewage treatment plants, a variety of pools and oxidation ditches and landscape environments for conservation equipment, among others. The impeller of the submersible mixer is driven by the motor through rotating and stirring to achieve the creation of water flow and water circulation in the pool, uniform mixture, so that the suspended matter is effectively suspended from the bottom, improve water quality and increase the oxygen content of water (Tian et al., 2022a). The energy consumption and efficiency of submersible mixers greatly affect the operation and development of the water treatment industry, with its special economic and social benefits (Qiu, 2021).

In the actual engineering application, the flow phenomenon of submersible mixers is more complex. The water flow collides with the pool wall and produces rebound, sometimes causing backflow, vortex and other conditions. The flow field characteristics of the mixing pool are influenced by several factors. These factors include the hub ratio, the installation position, the angle of the mixer, blade clearance, blade placement angle, etc. Optimizing the layout of the mixer, the design of the pool shape and the structure of the mixer are conducive to enhancing mixing efficiency and achieving desirable mixing effects (Liu et al., 2022). Therefore, the study of optimal design for submersible mixer is an important direction for engineering design.

Many studies have been conducted on the optimization design of submersible mixer performance, using methods such as experiment, numerical simulation, and theoretical calculation. For example, Chen et al. adopted numerical simulation to optimize the arrangement of the mixer using clear water as the study medium. The results showed that the mixer arrangement near the inlet would increase the area of the central low-velocity region (Chen et al., 2020). Xu et al. studied the flow field distribution in the pool under two cases of submersible mixer installation depth of 3 m and 5.72 m, using clear water flow as the medium. The results indicated that the submersible mixer installed near the bottom of the pool formed a high-velocity flow area on the bottom surface of the pool (Xu and Yuan, 2011). Tian et al. studied the external characteristics of submersible mixers when they were located in four different positions in the pool. The study found that the best mixing was achieved when the impeller centre axis of the submersible mixer was 600 mm from the pool bottom, the blades were at least 200 mm from the pool bottom and the ratio of wall width to wall narrowness was 4:3 (Tian et al., 2013). Jin et al. studied the sewage-sludge two-phase flow model using numerical simulation and concluded that after reducing the installation position of the submersible mixer, the flow velocity formed by the mixer at the bottom of the mixing pond increased and the sludge settling weakened. When the distance between the centre of rotation of the mixer impeller and the bottom wall of the pond was reduced to 0.4 m, there was no longer any obvious sludge deposition in the mixing pond (Jin and Zhang, 2014). Xu used computational fluid dynamics method to analyze the flow field characteristics and hydro-mechanical performances of submersible mixers. The results indicated that the performance of the mixer was greatly improved by optimally setting the motor speed, blade clearance, blade placement angle, installation angle and with or without guide shell (Xu, 2016). Additionally, Tian et al. studied the solid-liquid two-phase flow field of a submersible stirrer using a coupled CFD-DEM method and found that the location of particle aggregation was at the dead zone located at the junction of the vortex location and the wall of the pool, and that the vortex generated near the bottom and wall of the pool was an essential factor leading to particle aggregation (Tian et al., 2022b). These studies have demonstrated the impact of different installation locations on the flow field within the submersible mixer basin and have provided important insights into improving efficiency and mixing effectiveness. Nevertheless, conventional optimization methods require manual modification of design variables and the generation of multiple solutions for comparison, resulting in repetitive labor. Therefore, achieving automatic optimization of the submersible mixer installation location parameters without altering the overall pool structure is crucial.

With the rapid development of science and technology, the automatic optimization design of hydraulic machinery has become attainable through the utilization of high-performance platforms such as the ISIGHT software. Notably, numerous scholars have leveraged the ISIGHT platform for the analysis and study of hydraulic machinery's optimal design. For instance, Wen et al. employed the ISIGHT software with integrated MATLAB, GAMBIT, and FLUENT software to propose a multi-objective and automatic optimization design method for the movable guide vane of a Francis turbine. They used the non-dominated ranking genetic algorithm with the geometric parameters of the movable guide vane as the optimization variables, the total pressure loss of the inlet and outlet of the guide vane flow path, and the cavitation performance as the objectives. The results indicated a 10.4% reduction in the total inlet and outlet pressure loss of the guide vane flow path and a 17.8% increase in the minimum static pressure on the guide vane (Wen et al., 2017). Subsequently, Wen et al. integrated GAMBIT and ANSYS FLUENT16.0 software based on ISIGHT software to propose an optimized design method for the crown profile of the runner of a low specific speed Francis turbine, which improved the turbine efficiency by 0.35% after optimization (Wen et al., 2018). Ding utilized the genetic optimization algorithm of the ISIGHT platform to optimize the turbine blade chord length with the mean and variance of the power coefficients at TSR = 4, 6, and 8 as the optimization objectives. The results demonstrated that increasing the chord lengths of the middle section and tip of the blade not only increased the power coefficient at the optimal tip speed ratio of the tidal energy turbine but also expanded the range of the optimal tip speed ratio, making it more applicable to engineering practice (Ding, 2020).

In addition, other studies have utilized the ISIGHT platform for optimizing designs of mixed-flow pumps, LB46 torque converter pump, and axial flow pump vanes. For example, Yang et al. utilized the NSGA-II algorithm and ISIGHT platform to optimize the design parameters of the worm housing section for a mixed-flow pump, resulting in a 3.02% increase in hydraulic efficiency and 2.81% increase in head. The high-efficiency zone of the pump was expanded (Yang et al., 2019). Fan utilized the multi-island genetic algorithm integrated into the ISIGHT platform to optimize the design of the LB46 torque converter pump wheel blades, resulting in an overall performance improvement in all cases (Fan, 2021). Similarly, He employed the ISIGHT platform combined with the NSGA-II optimization algorithm to perform a multi-objective optimization of the design parameters of the impeller and worm gear of the mixed-flow pump, resulting in improved hydraulic efficiency and head, and an expansion of the high-efficiency zone. The optimized pump also exhibited a more uniform and reasonable static pressure distribution, leading to reduced energy loss (He, 2019). Shi et al. e established an automatic optimization design platform for axial flow pump vanes based on the ISIGHT platform, which significantly improved the hydraulic performance of the vanes after optimization (Shi et al., 2014). Xia et al. designed an optimization platform for axial flow pump impellers using ISIGHT software and the multi-island genetic algorithm, resulting in improved hydraulic efficiency and an expanded efficient region after optimization (Xia et al., 2016). Lu et al. optimized the combination of impeller and guide vane of an ultra-high specific speed axial flow pump using the multi-island genetic algorithm integrated into the ISIGHT platform, resulting in improved efficiency of the design point, while the head remained almost unchanged (Lu et al., 2017). Wang integrated Pro/E, Gambit, and Fluent software into ISIGHT to develop a fully automated optimization method for centrifugal pump shaft surface projection diagrams based on CFD calculations, resulting in a 4.85% increase in optimized head and a 1.31% increase in hydraulic efficiency (Wang, 2011).

In the field of marine propeller design, recent studies have utilized the ISIGHT platform to establish optimization system and improve propeller performance. For example, Liu et al. applied ISIGHT software to integrate analysis modules, including type-value point calculation, model building, meshing, and simulation calculation, to analyze the effects of pitch, arch, longitudinal inclination, and chord length on propeller open water performance. The study revealed that pitch had the most significant impact on propeller open water performance, followed by chord length, arch, and longitudinal inclination. Furthermore, the quadratic and interactive terms between factors were found to have a more significant effect than longitudinal inclination (Liu et al., 2014). Similarly, Long et al. utilized the ISIGHT optimization platform to optimize the pitch distribution of a propeller, with the open water efficiency and minimum pressure coefficient at multiple radii as the objective function. The study found that optimizing propeller open water performance using a new anti-cavitation profile was effective (Long et al., 2011). Cheng et al. utilized the Design of Experiments method and optimization techniques combined with approximation methods based on the response surface model on the ISIGHT multidisciplinary optimization design platform to establish a new design engineering framework. The resulting optimization efforts led to improved propeller efficiency and minimum pressure coefficient (Cheng et al., 2008).

Overall, the ISIGHT platform has proven to be an effective tool for optimizing hydraulic machinery. It not only saves significant time and effort for designers, but also effectively enhances the performance of hydraulic machinery while reducing energy consumption. However, there is currently a lack of research on the application of the ISIGHT platform for optimizing submersible mixers. Therefore, the application of the ISIGHT platform holds great practical value for optimal design of submersible mixer installation locations.

This paper focuses on the submersible mixer for sewage and rectangular pool as the research objects, aiming to optimize the average flow velocity and mixing efficiency inside the pool. ISIGHT software is utilized as the optimization platform, which integrates Creo Parametric 6.0 software and ANSYS Workbench 2020 software. Analysis of influencing factors is performed using the design of experiment component packaged by ISIGHT. Multi-objective optimization design is accomplished through the non-inferiority ranking genetic algorithm in the optimization component packaged by ISIGHT. The ISIGHT software is employed to implement the automatic cyclic modeling and numerical analysis optimization process of submersible mixers, providing more efficient and intuitive ideas and methods to enhance the overall performance of submersible mixers.

2 Numerical calculation

2.1 Physical model

This study refers to an actual submersible mixer model and an actual pool model from a sewage treatment plant. In numerical simulations, submersible mixer models are typically replaced with impellers for simplification purposes. The computational domain comprises the water body of the pool and the water body of the impeller, with the pool dimensions and submersible mixer installation positions illustrated in Figure 1. The diameter of the impeller is 210 mm. The number of blades is 2, and the rotation speed is 1400 rpm. The submersible mixer is installed at a position 2000 mm away from the pool's side wall, 1000 mm above the pool's bottom, and 500 mm away from the pool's installation wall. Moreover, the length of the pool's installation wall is 4000 mm, the pool's depth is 2000 mm, and the adjacent pool wall's length is 5000 mm. The impeller is parallel to the installation wall of the pool and perpendicular to the bottom wall of the pool.

2.2 Meshing

The Fluid Flow (Fluent) module within ANSYS Workbench 2020 software was utilized to generate polyhedral, unstructured meshes for the pool's water body and impeller using the Mesh tool, as well as to encrypt the blade, the impeller and the pool contact surface. The simulation result of mesh independence verification is as Table 1. To validate mesh independence, the deviation of hydraulic thrust and torque values obtained from different mesh quantities can be compared with those of the actual model. When the number of grids was increased from 1,766,486 to 4,374,954, the hydraulic thrust decreased and subsequently increased and then decreased. The torque decreased and then increased and then decreased. Considering computational resources and accuracy, option 3 was chosen as the final mesh. In option 3, the simulated values of hydraulic thrust and torque exhibit minimal deviation from those of the actual model. The meshing of the submersible mixer and pool as shown in Figure 2. The mesh quality is above 0.3.

2.3 Basic equation

When the number of submersible mixers is small, it is common to adopt the multiple reference system method (MRF) for steady-state simulation, which is a widely used approach for simulating rotating machinery. Scalable Wall Functions are used near the wall and the free liquid surface of the pool is set to a rigid cover assumption with a residual convergence accuracy of 0.0001.

The continuity equation and momentum equation are represented by the following Equations 1 and Equations 2:

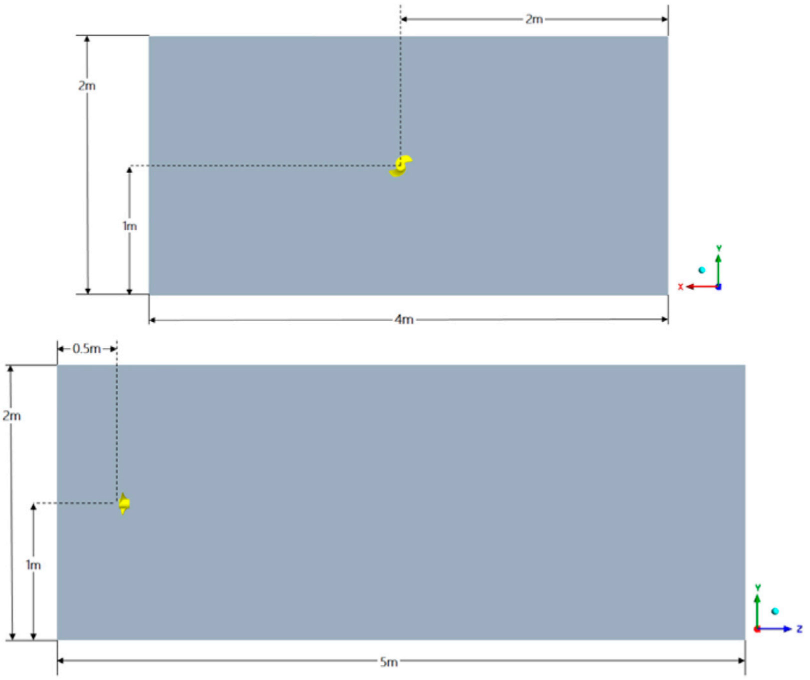

FIGURE 1
The pool and submersible mixer.

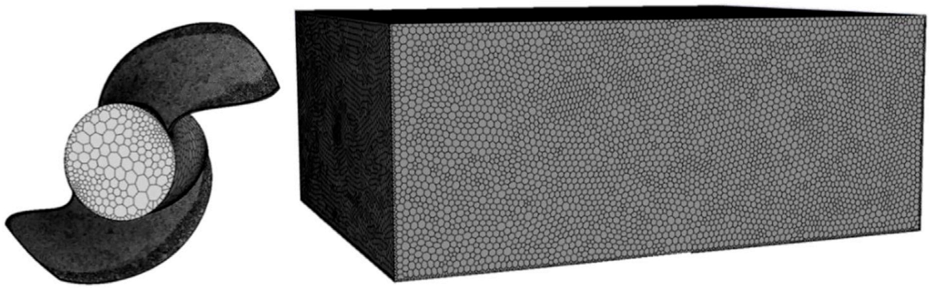

FIGURE 2
Meshing of submersible mixer and pool.

TABLE 1 Mesh independence verification.

Serial number	Mesh number	Hydraulic Thrust [N]	Torque [N·m]	Hydraulic thrust deviation/%	Torque deviation/%
1	1,766,486	241.76	10.96	20.88	9.6
2	2,707,747	230.53	10.35	15.27	3.5
3	3,863,064	217.52	9.73	8.76	2.7
4	4,029,750	216.17	10.19	10.09	1.9
5	4,374,954	215.39	9.89	7.70	1.1
6	Experiment (clear water)	200	10	-	-

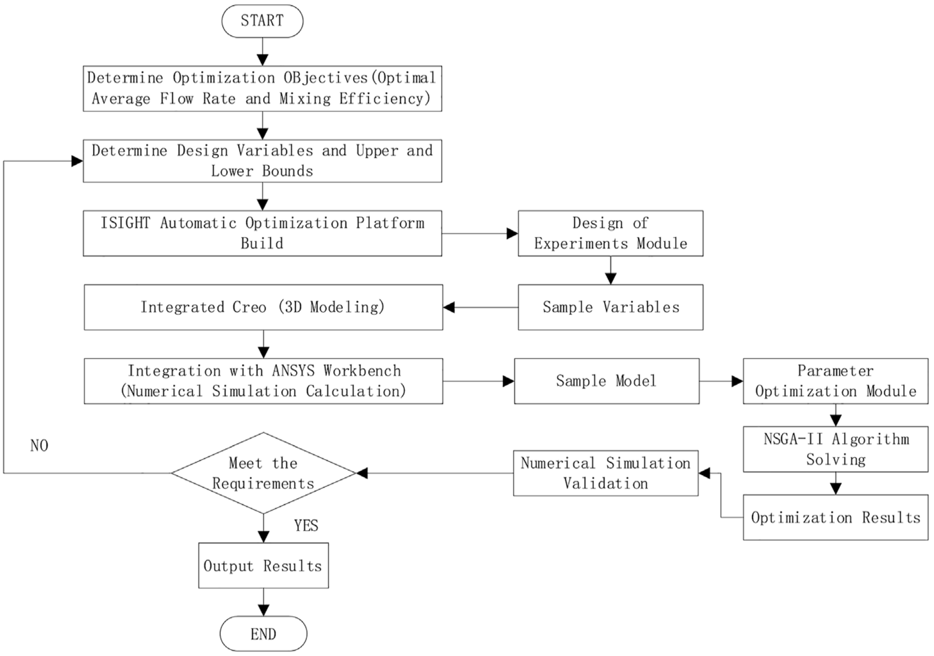

FIGURE 3
A flowchart for optimizing.

$$\frac{\partial u_j}{\partial x_j} = 0 \tag{1}$$

$$\rho \frac{\partial u_i}{\partial t} + u_j \rho \frac{\partial u_i}{\partial x_j} = -\frac{\partial p}{\partial x_i} + \mu \frac{\partial^2 u_i}{\partial x_j^2} + \rho f_i \tag{2}$$

By using the Realizable $k-\varepsilon$ turbulence model, the k equations are given in Eq. 3 and ε Eq. 4 respectively.

$$\frac{\partial(\rho k)}{\partial t} + \frac{\partial(\rho u_i k)}{\partial x_i} = \frac{\partial}{\partial x_j}\left[\left(\mu + \frac{\mu_t}{\sigma_k}\right)\frac{\partial k}{\partial x_i}\right] + G_k + G_b - \rho\varepsilon - Y_M + S_k \tag{3}$$

$$\frac{\partial(\rho\varepsilon)}{\partial t} + \frac{\partial(\rho\varepsilon u_i)}{\partial x_i} = \frac{\partial}{\partial x_i}\left[\left(\mu + \frac{\mu_t}{\sigma_\varepsilon}\right)\frac{\partial\varepsilon}{\partial x_j}\right] + \rho C_1 S\varepsilon - \rho C_2 \frac{\varepsilon^2}{k + \sqrt{\mu_t \varepsilon/\rho}} + C_{1\varepsilon}\frac{\varepsilon}{k}C_{3\varepsilon}G_b + S_\varepsilon \tag{4}$$

where t is time; u_i and u_j is the velocity vector; x_i , x_j is the position vector; ρ is the liquid density; f_i is the mass force; k is the turbulent energy; μ is the molecular viscosity; μ_t is the turbulent viscosity coefficient; σ_k is a constant; G_k is the turbulent energy production due to the mean velocity gradient; G_b is the turbulent energy production due to buoyancy effects; Y_M is the effect of compressible turbulent pulsations on the total dissipation rate; ε is the turbulent energy dissipation rate; σ_ε is the turbulent kinetic energy dissipation rate Prandtl number; $C_2, C_{1\varepsilon}, C_{3\varepsilon}$ are constants. $C_2 = 1.92$; $C_{1\varepsilon} = 1.44$; $C_{3\varepsilon} = 0.09$; $C_1 = max[0.43, \frac{\eta}{\eta+5}]$; $\eta = S\frac{k}{\varepsilon}$; $S = \sqrt{2S_{ij}S_{ij}}$; S_k and S_ε are user-defined source terms, which can be set according to different situations.

3 Optimization of submersible mixer using the ISIGHT platform

In this paper, we introduce an integrated platform for submersible mixer optimization design, which is built using the ISIGHT platform that integrates Creo Parametric 6.0 software and ANSYS Workbench 2020 software. The main objective is to maximize the average flow velocity and mixing efficiency inside the pool. The Task Plan component is employed to integrate the design of experiments module and parameter optimization module for global optimization design. Firstly, the design of experiments module is used to uniformly sample the design space, capturing the most effective design area in the entire space. Subsequently, the parameter optimization module is applied to optimize the design in the effective design area to obtain optimization results. Upon obtaining the optimization results, numerical simulation is performed to verify that the final optimization results meet the requirements. A flowchart for optimizing using the ISIGHT software is shown in Figure 3.

3.1 Optimization parameters determination

Parametric modeling is a crucial foundation for optimal design. In this study, a three-dimensional parametric model of the submersible mixer was built using Creo software. During the assembly of the pool and impeller water body, the installation position of the submersible mixer was constrained by the plane and XYZ coordinate system. The distance from the rotation center of the impeller of the submersible mixer to the side pool wall was defined as parameter A, the distance from the rotation center of the impeller of the submersible mixer to the bottom wall of the pool was parameter B, and the distance from the back of the submersible mixer to the installation wall was parameter C. The installation position parameters of the submersible mixer in the pool, i.e., A, B, and C, were selected as design variables in this study. An optimized design seeks an optimal solution that satisfies the objective function

TABLE 2 Initial values and value ranges of design variables.

Installation location parameters	Initial values	Range of values
A[mm]	2000	200–2000
B[mm]	1,000	200–1,000
C[mm]	500	200–800

within the constraints of the design variables and constraints. Therefore, establishing the correct numerical model is essential to the success of the optimized design as a whole. The numerical model for optimization in this study can be summarized as follows: the parameters of the submersible mixer installation are optimized to satisfy the constraints of the range of design variables and the effective mean flow velocity inside the pool, and the point within the pool with the highest mean flow velocity and efficiency value is sought.

3.1.1 Design variables

The three parameters A, B, and C were selected as the optimal design variables indicated in equation. The initial values and value ranges of these submersible mixer design variables are presented in Table 2.

$$X = [A、B、C] \tag{5}$$

Where A isthe distance from the rotation center of the impeller of the submersible mixer to the side pool wall, B is the distance from the rotation center of the impeller of the submersible mixer to the bottom wall of the pool, and C is the distance from the back of the submersible mixer to the installation wall.

3.1.2 Objective functions

The objective function in this study is to maximize both the average flow velocity and mixing efficiency in the pool, as shown in Equations and.

$$Max\ f_1 = \bar{v} \tag{6}$$

$$Max\ f_2 = \eta_{mix} \tag{7}$$

Where $\bar{v}$ is the average flow velocity inside the pool and η_{mix} is the mixing efficiency. 1) Average flow velocity inside the pool

The installation position of the best mixing effect is selected by selecting the maximum value of the average flow velocity inside the pool. This approach can directly reflect the mixing performance of the submersible mixer at different installation positions under the same impeller speed conditions. Thus, if a certain position of the submersible mixer in the pool results in the largest average flow velocity, it implies that the mixing effect is best at that position.

3.1.2.1 Mixing efficiency

Tian et al. (Tian et al., 2012) derived the efficiency estimation formula(9), which has been demonstrated to be significant in assessing mixing efficiency using numerical simulation techniques.

$$\eta = \frac{F^{\frac{3}{2}}}{3.14 D_Y M n} \times 100\% \tag{8}$$

FIGURE 4
Integration of ISIGHT.

Where: F is the hydraulic thrust, N; D_Y for the impeller diameter, m; M is the torque, N·m; n is the impeller speed, r/min.

3.1.3 Binding conditions

Zhang et al. (Zhang et al., 2014) proposed the effective mixing domain evaluation method that involves calculating the volume of fluid with an average flow velocity greater than or equal to 0.1 m/s as the effective mixing volume of the submersible mixer. Therefore, the constraint in this study is that the average flow velocity inside the pool must be greater than or equal to 0.1 m/s, as shown in equation.

$$\bar{v} \geqq 0.1 m/s \tag{9}$$

3.2 ISIGHT platform

The ISIGHT platform can integrate and manage complex simulation processes and use optimization algorithms to explore for superior parameter combinations, thus shortening the product development time and reducing the development cost. In this study, we established an automated optimization platform for diving mixers by integrating Creo Parametric 6.0 software and ANSYS Workbench 2020 software, as illustrated in Figure 4. Throughout each cycle, the ISIGHT platform allows for the real-time presentation of design parameter inputs and performance parameter outputs, enabling designers to conveniently monitor progress.

3.2.1 Optimal Latin hypercube design of experiments

The Design of Experiments methodology can be used to rationalize experimental arrangements, especially in cases involving small-scale tests, resulting in reduced test durations and lower costs. In this study, the optimal Latin hypercube was used to sample the optimized variables, and the design and results of the experiment are presented in Table 3. The desired experimental outcomes were achieved, and scientifically valid conclusions were drawn. To ensure analytical accuracy, the number of test points n and the total number of design variables N should satisfy the following relationship, i.e.,

$$n \geqslant (N+1)(N+2) \tag{10}$$

TABLE 3 Experiments design scheme and results.

Scheme	A [mm]	B [mm]	C [mm]	Average flow velocity [m/s]	Mixing efficiency [%]
1	1,354	303	738	0.132	35.81
2	892	713	631	0.157	35.33
3	246	815	569	0.150	35.29
4	1815	549	277	0.168	35.74
5	569	897	723	0.167	35.69
6	1954	323	369	0.155	35.91
7	431	631	754	0.153	35.74
⋮	⋮	⋮	⋮	⋮	⋮
41	2000	1,000	300	0.178	35.95

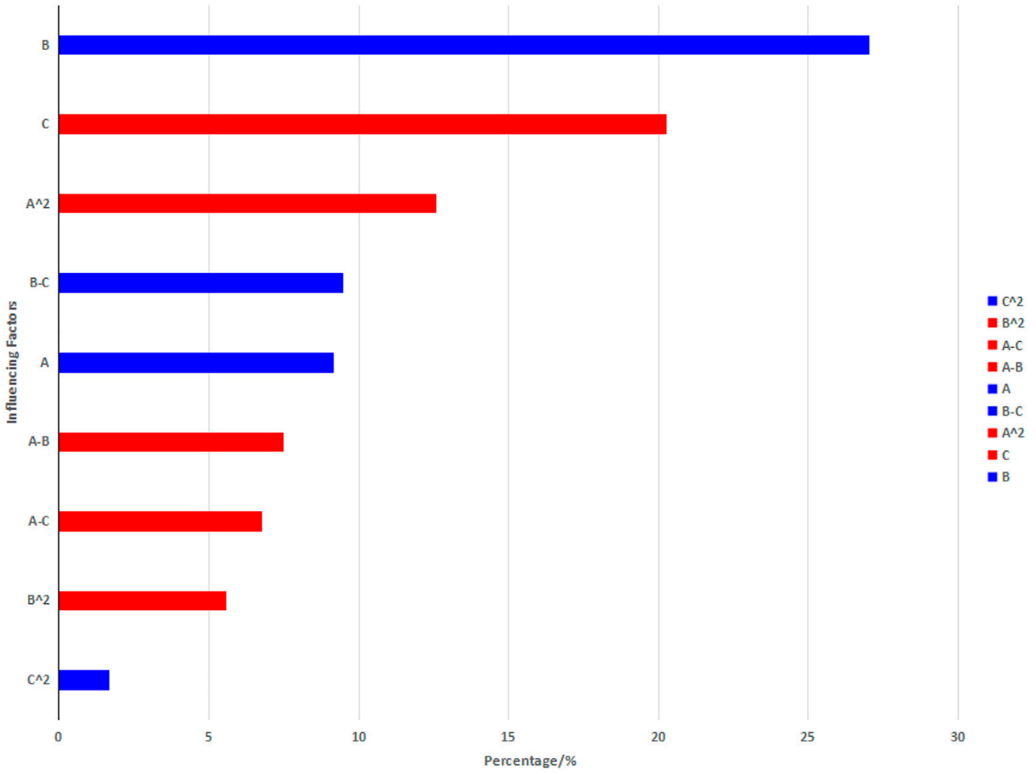

FIGURE 5
Pareto graph of the average flow velocity.

Consequently, the number of sample points is set to 41 according to Eq. 10 above.

3.2.2 Parameter optimization (NSGA-II)

When there are multiple optimization objectives, due to the conflicts between the optimization objectives, sometimes one optimization objective is improved, while simultaneously another optimization objective is deteriorated, it is difficult to find a solution that furnishes all the objective functions optimal at the same time. Therefore, it is used to optimize the multi-objective problem by Non-Dominated Sorting Genetic Algorithm (NSGA-II) (Srinivas and Deb, 1994; Li, 2008). For multi-objective optimization problems, there is usually a set of solutions that cannot be compared between them with respect to the overall objective function. It is characterized by the fact that it is impossible to improve any objective function without weakening at least one other objective function.

NSGA-II optimization algorithm flow for:

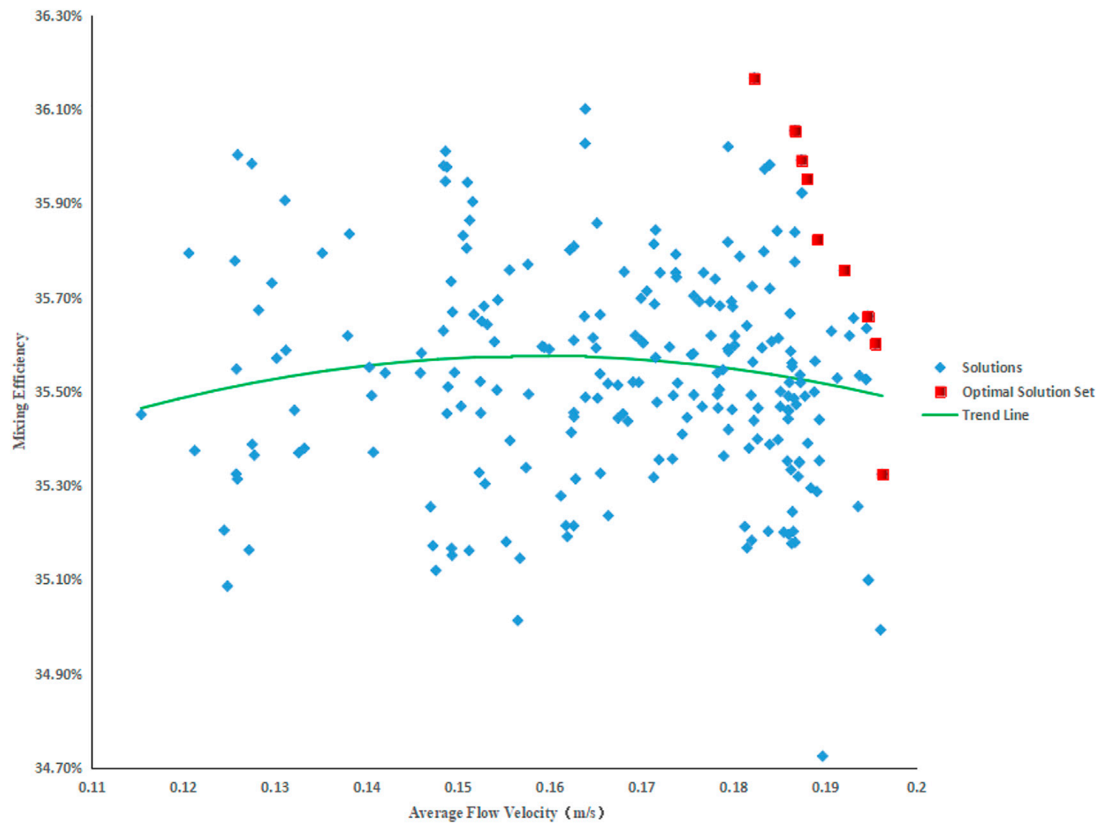

FIGURE 6
Pareto Frontier.

TABLE 4 Comparison of submersible mixer design parameters before and after optimization.

	A [mm]	B [mm]	C [mm]	Average flow velocity [m/s]	Mixing efficiency [%]
Before optimization	2000	1,000	500	0.161	35.70
After optimization	2000	1,000	207	0.182	36.17

a) In the first place, the population that randomly generates a certain number of individuals is regarded as the parent population.
b) During evolution, the current parent population is crossed and mutated to produce a subpopulation, and the parent population and subpopulation are combined to obtain a new population.
c) Comparing individuals in a new population two by two by their objective function vector using non-dominance sorting to divide all individuals in the population into multiple sequentially controlled Frontier layers.
d) Using crowding distance sorting, eliminate inferior individuals within layers with the same Pareto order.
e) In the case of individuals belonging to different Pareto layers, evaluate the superiority of individuals using the evaluation of Pareto superiority, thereby deriving the Pareto optimal set of solutions to the objective function.

4 Optimization results and analysis

4.1 Analysis of influencing factors

The sensitivity, correlation, interaction effect, and contribution rate of the factors on the average flow velocity inside the submersible mixer pool were obtained through the Pareto graph, which further analyzed the effects of the factors on mixing performance.

The Pareto graph reflect the percentage contribution of all factors to average flow velocity, with blue bars indicating positive effects and red bars indicating negative effects. As shown in Figure 5, the primary term factor that is most sensitive to the average flow velocity is variable B, while variable C is the next most sensitive. The secondary term of variable A and the interaction term of variable B and variable C have a greater impact on the average flow velocity than the factor variable A. The secondary term of variable B and variable C, the interaction term of variable A and variable B between

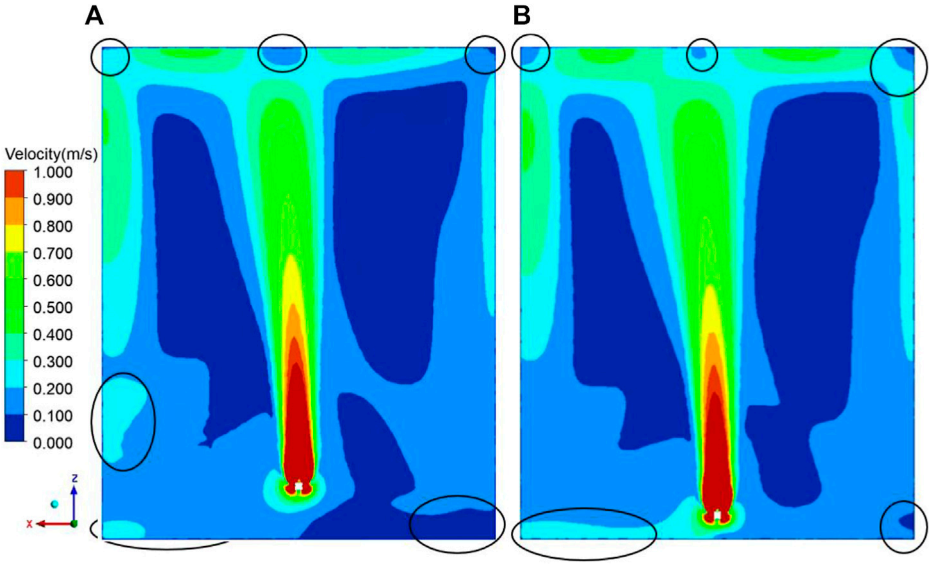

FIGURE 7
Velocity contour of ZOX cross-section: **(A)** Before optimization; **(B)** After optimization.

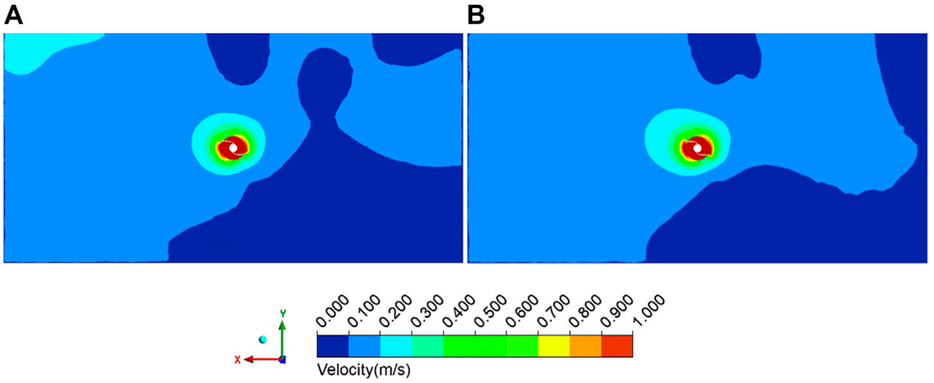

FIGURE 8
Velocity contour of XOY cross-section: **(A)** Before optimization; **(B)** After optimization.

factors, and the interaction term of variable A and variable C between factors have less significant effects on the average flow velocity than the primary term factor of variable A. The effect of the primary term on the average flow velocity of the two factors of variable B and variable A is positive, indicating that increasing these two factors is beneficial to increasing the average flow velocity within the constraint range. However, the effect of the primary term of variable C on the mean velocity is negative, meaning that decreasing this factor is beneficial to increasing the average flow velocity within the constraint range.

4.2 Pareto frontier

The global search method has been employed to obtain the Pareto Frontier solution for the genetic optimization of submersible mixer installation location parameters. The Pareto Frontier consists of a total of 241 solutions, represented by blue points. The optimal set of solutions, which take into account both the average flow velocity and mixing efficiency, are represented by the red points on the Frontier, as shown in Figure 6.

Prior to optimization, the average flow velocity within the pool was recorded at 0.161 m/s with a mixing efficiency of 35.70%. Following optimization, these values were improved to an average flow velocity of 0.182 m/s and a mixing efficiency of 36.17%. The observed increase in the average flow velocity was approximately 0.021 m/s, while the mixing efficiency was improved by approximately 0.47%, as compared to pre-optimization values. Table 4 provides detailed information regarding the submersible mixer installation position parameters and the corresponding mixing performance before and after optimization.

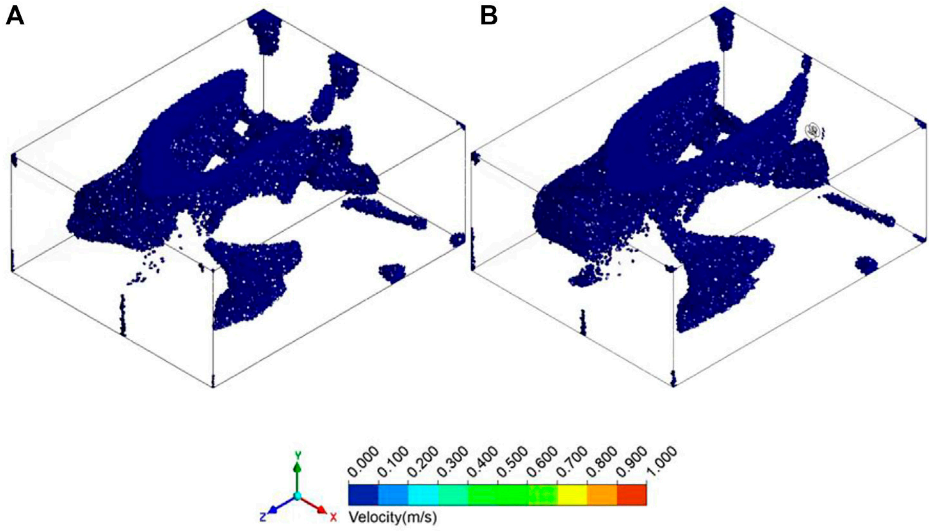

FIGURE 9
The distribution of mixing low-velocity zones: **(A)** Before optimization; **(B)** After optimization.

4.3 Comparative analysis of internal flow field before and after optimization

To verify the feasibility of the optimization method, we conducted flow field simulations using the same simulation method as the above simulations. The ZOX cross-section is parallel to the direction of the impeller rotation axis of the submersible mixer, and the XOY cross-section is perpendicular to the direction of the impeller rotation axis.

As shown in Figure 7, stirring the mixer generates a high-speed jet that pushes forward and then splits into two streams. One stream moves to the liquid surface and back to the impeller, forming a small circulating vortex, while the other stream pushes forward and collides with the pool wall, forming a large circulating vortex. The velocity contour of the ZOX cross-section shows the distribution of the z-axis velocity component in the pool. The red high-velocity zone in the contour indicates the areas where the velocity is the highest. Figure 7 demonstrates that the high-velocity zone increased in size after optimization, indicating that the optimization method was successful in increasing the mixing efficiency of the submersible mixer. The effective axial propulsion distance refers to the distance along the axial direction of the submersible mixer that effectively propels the water body under the condition that the flow velocity is maintained at or above 0.3 m/s (Tian et al., 2022a). This measure is important because it indicates how much of the pool is effectively mixed by the submersible mixer. Before optimization, the effective axial distance was 4.17 m, and after optimization, it increased to 4.45 m, representing a 6.71% increase in effective axial propulsion distance.

Additionally, the effective radial diffusion radius is the effective radius of perturbation of the water column section that is disturbed by the submersible mixer under the condition that the flow velocity is maintained at or above 0.3 m/s (Tian et al., 2022a). As shown in Figure 8, the velocity contour of the XOY cross-section demonstrated that the effective radial diffusion radius before optimization was 0.24 m, and after optimization, it increased to 0.26 m, representing a 8.33% increase in the effective radial diffusion radius.

4.4 Distribution of low-velocity zone distribution

For water velocities below 0.05 m/s in a certain area of the mixing pool, that area is defined as the low-velocity zone. Before optimization, the low-velocity zones were distributed at the edge junction and the top corner between the pool wall and the surrounding wall. The velocity of the circulation vortex flow was less than 0.05 m/s, and a large number of low-velocity zones appeared near the pool surface and the bottom wall surface of the pool close to the installation wall, as shown in Figure 9. The total volume of all low-velocity zones before optimization was 2949.93 dm^3, accounting for 7.37% of the total water mass volume. After optimization, the low-velocity zones in the pool wall and the edge junction and top corner of the wall surrounded by the pool were significantly reduced. The low-velocity zones near the installation wall surface of the pool bottom and surface were also significantly reduced. After optimization, the total volume of all low-velocity zones was 2607.79 dm^3, accounting for 6.52% of the total water mass volume. The low-velocity zones were significantly reduced after optimization compared to pre-optimization zones.

5 Conclusion

(1) After optimizing the installation position of the submersible mixer using the ISIGHT platform, the average flow velocity and mixing efficiency in the pool were significantly improved. The fluid distribution in the pool became more uniform, with a significant increase in the effective axial propulsion distance and effective radial diffusion radius. The low speed zone was greatly reduced, resulting in an enhanced flow state of the fluid in the pool and greatly strengthened mixing effect.
(2) These results demonstrate the potential of optimizing design to improve the performance of submersible mixers by taking into account factors such as the average flow velocity inside the pool,

mixing efficiency, effective axial distance, effective radial diffusion radius, and low-velocity zone volume.

(3) Through the design of experiments study, it was discovered that an increase in the distance from the rotation center of the impeller of the submersible mixer to the side pool wall and the distance from the rotation center of the impeller of the submersible mixer to the bottom wall of the pool within the constraint range led to an increase in the average flow velocity, while a decrease in the distance from the back of the submersible mixer to the installation wall within the constraint range had a similar effect. These findings can provide valuable insights into improving the average flow velocity inside the pool through the control of the submersible mixer's installation position. The use of the ISIGHT software for automatic optimization of submersible mixer installation locations can effectively improve mixing efficiency, overall plant operating efficiency, and economic benefits in sewage treatment plants. The multi-objective optimization platform based on the ISIGHT platform for installation location of submersible mixer for sewage can be successfully applied in engineering practice.

Data availability statement

The original contribution presented in the study are included in the article/supplementary material, further inquiries can be directed to the corresponding author.

Author contributions

Conceptualization, FT; methodology, FT; software, EZ; formal analysis, CY; investigation, YC; data curation, CY; visualization, DS; writing—original draft preparation, CY; writing—review and editing, FT; supervision, WS. All authors have read and agreed to the published version of the manuscript.

Conflict of interest

Author YC was employed by Yatai Pump & Valve Co., Ltd.

The remaining authors declare that the research was conducted in the absence of any commercial or financial relationships that could be construed as a potential conflict of interest.

Publisher's note

References

Chen, Y. F., Yang, C., Zhang, H., Xu, Y. F., and Xia, C. Z. (2020). Influence and optimization of mixer's arrangement of flow field of anoxic pool. *J. Drain. Irrig. Mach. Eng.* 38, 1045–1050.

Cheng, C., Li, F., and Leng, W. H. (2008). Design and optimization of propeller based on doe methods and approximation loop methods. *Comput. Appl. Softw.* 25, 70–72.

Ding, L. (2020). *Study on blade optimization and wavecurrent interaction of horizontal axis tidal turbines*. Zhejiang University. Master.

Fan, W. L. (2021). Isight-based optimization design of hydrodynamic torque converter pump vanes. *J. Chengdu Aeronaut. Voc. Tech. Coll.* 37, 62–64.

He, S. (2019). *Multi-objective optimization and cavitation characteristics of volute mixed-flow pump based on isight platform*. Jiangsu University. Master.

Jin, J. H., and Zhang, H. W. (2014). *A numerical simulation of submersible mixer in three-dimensional flow with sewage-sludge two-phase*. Water Hydropower, 159–162. China Rural.

Li, L. (2008). *Research on the application of multi-objective optimization strategy based on genetic algorithm*. Wuxi, China: Jiangnan University. Master.

Liu, Y., Lu, J. G., Yang, M. C., Chen, X. F., Wang, M. L., and Zhao, R. S. (2014). Feasibility of metal-organic nanotubes [Cu3(μ3-O)(μ-OH)(triazolate)2]+-coated fibers for solid-phase microextraction of polychlorinated biphenyls in water samples. *J. Nanjing Univ.Technol.(Nat. Sci. Ed.)* 36, 58–65. doi:10.1016/j.chroma.2014.11.058

Liu, Y. Y., Wang, W. S., Lu, X. F., Lang, X. L., and Zhao, H. W. (2022). Energy consumption and energy-saving ways of mixing in sewage treatment process. *China Environ. Prot. Ind.*, 35–38.

Long, W., Xie, W., Yang, X. H., and Qiu, L. Y. (2011). Multi-objective optimization of open water performance of propeller based on new anti-cavitation airfoil profile design. *Ship Sci. Technol.* 33, 56–60.

Lu, R., Yuan, J. P., Li, Y. J., and Jiang, H. Y. (2017). Automatic optimization of axial flow pump based on radialbasis functions neural network and cfd. *J. Drain. Irrig. Mach. Eng.* 35, 481–487.

Qiu, S. P. (2021). Research on application of submerged agitator in water treatment field. *Shandong Water Resour.*, 23–25.

Shi, L. J., Tang, F. P., Li, S. L., Li, Z., and Xie, D. Z. (2014). Hydraulic performance optimization research based on the isight platform of axial flow pump blades. *Fluid Mach.* 42, 16–20.

Srinivas, N., and Deb, K. (1994). Muiltiobjective optimization using nondominated sorting in genetic algorithms. *Evol. Comput.* 2, 221–248. doi:10.1162/evco.1994.2.3.221

Tian, F., Shi, W. D., He, X. H., Jiang, H., and Xu, Y. H. (2013). "Study on installation of the submersible mixer," in *6th international conference on pumps and fans with compressors and wind turbines*, 52. Icpf2013.

Tian, F., Shi, W. D., Lu, X. N., Chen, B., and Xu, L. D. (2012). Theoretical calculation and simulation analysis of submersible mixer effciency for wastewater treatment. *J. Agric. Eng.* 28, 50–54.

Tian, F., Zhang, E. F., Yang, C., Shi, W. D., and Chen, Y. H. (2022). Research on the characteristics of the solid-liquid two-phase flow field of a submersible mixer based on cfd-dem. *Energies* 15, 6096. doi:10.3390/en15166096

Tian, F., Zhang, E. F., Yang, C., Shi, W. D., and Zhang, C. H. (2022). Review of numerical simulation research on submersible mixer for sewage. *Front. Energy Res.* 9. doi:10.3389/fenrg.2021.818211

Wang, K. (2011). *Multi-conditions hydraulic design and optimization for centrifugal pumps and its application*. Jiangsu University. Doctor.

Wen, Z. N., Ba, D. C., Deng, W. J., and Yue, X. J. (2017). Application of isight to optimization design of francis turbine guide vane. *Mach. Des. Manu.*, 5–8.

Wen, Z. N., Zhang, Y. L., Ba, D. C., and Yue, X. J. (2018). Optimization method for the runner crown shape of a low specific speed francis turbine. *J.Northeast Univ.(Nat. Sci.)* 39, 839–843.

Xia, S. J., Yuan, J. P., Sun, X., Zhou, B. L., and Li, Y. J. (2016). Parametric modeling and multi-parameter optimization of axial-flow pump blade. *J. Drain. Irrig. Mach. Eng* 34, 597–601.

Xu, S. (2016). *Flow field analysis and operation optimization of submersible mixer*. Yangzhou, China: yangzhou University. Master.

Xu, W. X., and Yuan, S. Q. (2011). *Optimization design of submersible mixer based on a simulation study of agitated and engineering application*. Water Hydropower, 32–35. China Rural.

Yan, J. H., Huang, D. J., and Teng, G. R. (2009). Research on rural domestic sewage disposal of biologic disposal high efficiency blender. *J. Anhui Agric. Sci.* 37, 9606–9607.

Yang, J. J., He, S., and Li, X. J. (2019). *Multi-objective optimization design of volute mixed flow pump based on isight platform*. Water Hydropower, 176–180. China Rural.

Zhang, X. N., Zhao, J. Y., and Wang, W. H. (2014). Influence of submersible mixer installation angle with the mixing effect. *J. Beijing Inst. Civ.Eng. Archit.*, 48–51.

Frontiers in
Energy Research

Advances and innovation in sustainable, reliable and affordable energy

Explores sustainable and environmental developments in energy. It focuses on technological advances supporting Sustainable Development Goal 7: access to affordable, reliable, sustainable and modern energy for all.

Discover the latest Research Topics

See more →

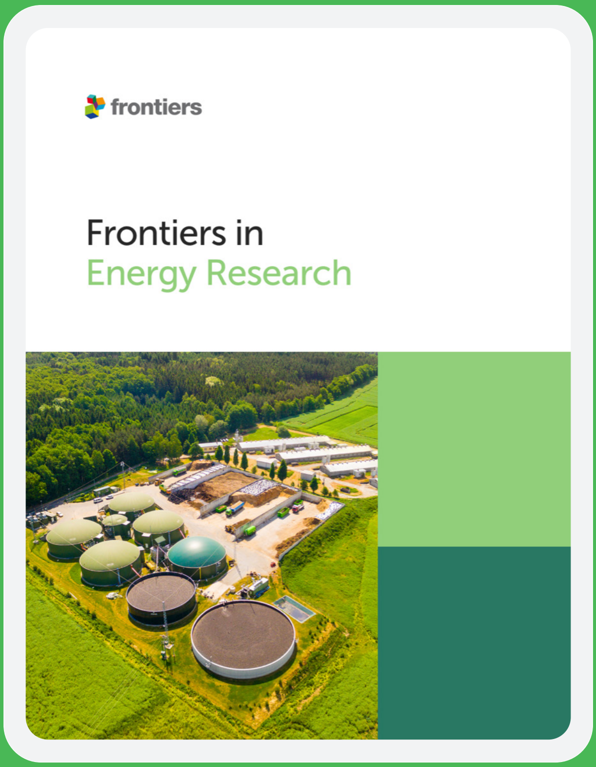

frontiers

Frontiers in
Energy Research

Frontiers

Avenue du Tribunal-Fédéral 34
1005 Lausanne, Switzerland
frontiersin.org

Contact us

+41 (0)21 510 17 00
frontiersin.org/about/contact

frontiers | Research Topics